Continuous flow for materials synthesis, assembly and crystallisation at Diamond: discovery and delivery of high value materials

Wayment, Lois

Award date:
2020

Awarding institution:
University of Bath

Continuous flow for materials synthesis, assembly and crystallisation at Diamond: discovery and delivery of high value materials

Lois Elizabeth Wayment

A thesis submitted for the degree of Doctor of Philosophy

University of Bath

Department of Chemistry

Supervisors: Professor Chick Wilson, Dr Karen Robertson, Professor Chiu Tang and Dr Dave Allan

March 2020

To Richard, Diane and Jodie

Abstract

The PhD project has implemented flow crystallisation / self-assembly methods compatible with Diamond beamlines. Specifically, monitoring of continuous crystallisation processes by a range of synchrotron radiation techniques have been developed in a series of *in situ* experiments, using bespoke crystallisers optimised for operation on the beamlines at the Diamond Light Source (DLS).

The technique of *in situ* X-ray diffraction (XRD) is applied to the continuous segmented flow crystallisation of highly polymorphic and pharmaceutically relevant model systems: Urea barbituric acid (UBA), carbamazepine (CBZ) and paracetamol (PCM). The cooling crystallisation processes yield crystalline powder and single crystals grown *in situ* within solution slugs in the flow crystallisation platforms KRAIC-D and KRAIC-S respectively. As a result of the steady-state operation employed in these crystallisers, events that evolve with time, such as polymorphic transitions and crystal growth, can be monitored. The KRAIC-D and KRAIC-S platforms were installed and data captured at the high-resolution powder diffraction beamline I11 and the small molecule single crystal beamline I19 respectively.

Chapter 1 contains a review of the literature of *in situ* XRD characterisation and flow crystallisation processes, which considers current limitations and opportunities for further investigation. The literature review provides context and builds towards the research project aims and objectives presented at the end of the first chapter. These objectives are targeted at the use of *in situ* XRD characterisation to provide additional insight to the pathway of crystallisation processes, which is unobtainable from offline analysis. In Chapter 2, the theory behind the analytical techniques used are described. In Chapter 3, the experimental methods implemented in this research project to achieve these research goals are reported.

Chapter 4 applies the synchrotron powder XRD technique at I11 in the study of the cooling crystallisation processes of UBA and CBZ in the KRAIC-D. In addition to unseeded crystallisations, investigation into the introduction of a controlled solid interface in the form of seeds of polymorphic purity introduced at pre-nucleation and post-nucleation stages is investigated. The use of integrated intensity values at various set-points along the length of the KRAIC-D provides an approach to investigate crystal growth. Engineering advances have been made to the KRAIC-D platform, allowing for optimisation to the crystallisation processes under investigation, as well as data capture capabilities. Significant advances to the data

analysis of this *in situ* powder XRD data have been achieved. Chapter 5 applies the synchrotron single crystal XRD technique at I19 in the study of the cooling crystallisation of PCM in the KRAIC-S. Seeding of the metastable PCM form II is investigated. Data processing in CrysAlisPro investigated the degree of crystals rotation with respect to the instrument. Comparison of single crystals grown *in situ* with single crystals of known crystal size, facilitated crystal sizing predictions of single crystals within the KRAIC-S. An automated data processing strategy using DIALS has also been devised, which allows data processing to be triggered after data acquisition. Chapter 6 explores crystal engineering for materials discovery of the profen family; co-crystallisation is investigated as an approach to improve physicochemical properties of profen targets. In addition to the discovery of new profen co-crystals, the study looks at accessing the multi-component materials *via* a wide range of crystallisation methods, as well as encompassing structural characterisation and property determination. Chapter 7 investigates *in situ* XRD monitoring of the slurrying crystallisation process of the IBU-ISO co-crystal discovered by crystallisation in Chapter 6.

In Chapter 8, conclusions from the findings in Chapters 4 to 7 are pulled together and patterns explored. Drawing on these overall findings, some suggestions for future work are also made.

In addition to the academic discovery achieved in this work, this PhD project contributes to the vision of the EPSRC National Centre in Continuous Manufacturing and Advanced Crystallisation (CMAC) and the Diamond Light Source. CMAC is an academic-industrial consortium, aimed at advancing the adoption of continuous manufacturing into the pharmaceutical industry. Diamond Light Source is the UK's national synchrotron science facility, which allows scientific research advances to be made, which extend beyond the capabilities of standard laboratory facilities. The significant synchrotron component of this project, which has advanced previous data collection and processing capabilities, provides a demonstration and offers additional potential to the beamtime experiments that can be investigated by synchrotron users in the future. Furthermore, the KRAIC-D and KRAIC-S crystallisation platforms developed in this PhD project can be used by Diamond users in the future; the principles of which are currently being translated to a laboratory based X-ray facility.

Acknowledgements

There are a number of people I would like to acknowledge for their contributions, both academic and personal, in helping me reach this milestone.

First, I would like to thank Professor Chick Wilson for offering me this fantastic opportunity to study for a PhD in Chemistry joint between the University of Bath and the Diamond Light Source synchrotron in Didcot. Chick's advice, expertise and guidance throughout my PhD and MChem studies has been invaluable and most memorable. Chick, I am forever grateful for all you have done for me.

Second, a massive thank you to my co-supervisor Dr. Karen Robertson for all your help, tenacity, detailed guidance, knowledge sharing and feedback. I have learnt so much and in working together, I have really developed my scientific thinking. Thank you also for providing feedback on my thesis.

Third, a huge thank you to my co-supervisor Dr. Mark Warren for all his help, guidance, knowledge sharing and feedback on the KRAIC-S work. I have thoroughly enjoyed developing data processing methods together and have learnt so much from working alongside you.

Fourth, to my great external collaborator Dr. Mark Levenstein, thank you for sharing your data processing expertise. I really enjoyed working together at the University of Leeds and at Diamond beamtimes.

The rest of the Wilson group have also been a constant support; in addition to their combined knowledge, their willingness to help and answer my never-ending questions has created a great learning environment for me. The support network for my Master's project was made complete by Dr. Lauren Agnew, a great foundation for starting my PhD studies. I have had the opportunity to carry out experiments at a number of facilities during my PhD including at the Diamond Light Source, on Beamlines I11 and I19, and at the Advanced Light Source on Beamline 12.2.1. I would also like to thank everyone who was a part of one of our beamtime teams or provided beamline support. For the KRAIC-D beamtimes: Dr. Karen Robertson, Dr. Mark Levenstein, Dr. Pierre-Baptiste Flandrin, Dr. Daniel Scott, Dr. Ruth Lunt and Pollyanna Payne. For the KRAIC-S beamtimes: Dr. Mark Warren, Dr. Karen Robertson, Dr. Daniel Scott, Pollyanna Payne, Dr. Lauren Hatcher and Dr. Lucy Saunders. For the *in situ* slurrying beamtimes: Pollyanna Payne and Dr. Lauren Hatcher.

Thank you to my Diamond supervision team: Dr. Dave Allan, Prof. Chiu Tang, Dr. Sarah Day and Dr. Mark Warren, for all your expertise and guidance in such an amazing working environment at the Diamond Light Source synchrotron. Thank you to the Research Complex at Harwell for the laboratory space to carry offline KRAIC-D runs, which was particularly beneficial in the run up to beamtimes.

Thank you to Dr. Thomas McGlone and Dr. Alan Martin for their support and help during my week at the University of Strathclyde and an additional thank you to Alan for continuing to take measurements on my behalf, once I had returned to Bath.

As a joint CMAC-Bath-Diamond PhD student, thanks go to the EPSRC Future Manufacturing Hub in Continuous Manufacturing and Advanced Crystallisation (CMAC) and Diamond Light Source for funding. Thank you to CMAC also for the opportunity to complete the Doctoral Training Centre in Continuous Manufacturing and Advanced Crystallisation. The intensive pharmaceutical training programme at the University of Strathclyde, comprising chemical engineering, pharmaceutical sciences and operations management including supply chain, was a fantastic learning opportunity and really heightened my interest in the pharmaceutical industry. Thank you to Dr. Mei Lee at GSK for being my mentor, I have hugely benefited from our Skype conversations about my project.

To the fantastic friends I have made including, Maria, Connie, Amelia, Ruth, Dan, Polly, Dan, Alex, Piba, Lauren, Aneesa, Lauren, Beth, Clare, Emma, Adam, Lucy, Stephen, Mark and Ben.

Finally, Mum, Dad and Jodie, your continual support and encouragement is so important, thank you so much. Mum and Dad, the fantastic opportunities you have given me during my education have led me here and I am forever grateful.

Table of Contents

List of Figures

List of Tables

List of Abbreviations

a.u. – Arbitrary Units

ACE – Acetone

ALS – Advanced Light Source

API – Active Pharmaceutical Ingredient

ATR – Attenuated Total Reflection

ATR-FTIR – Attenuated Total Reflectance Fourier Transform Infrared

BCS – Biopharmaceutics Classification System

CBZ – Carbamazepine

CCD – Charge Coupled Device

CCDC – Cambridge Crystallographic Data Centre

CFD – Computational Fluid Dynamics

CIF – Crystallographic Information File

CNT – Classical Nucleation Theory

COBC – Continuous Oscillatory-Baffled Crystalliser

CQA – Critical Quality Attribute

CRD – Cambridge Reactor Design

CSD – Cambridge Structural Database

Cu K_α – Copper K alpha

DAWN – Data Analysis WorkbeNch

DCM – Double Crystal Monochromator

DH – Dihydrate

DIALS – Diffraction Integration for Advanced Light Sources

DLS – Diamond Light Source

DSC – Differential Scanning Calorimetry

EH – Experimental Hutch

EPICS – Experimental Physics and Industrial Control System

EtOH – Ethanol

FBRM – Focused Beam Reflectance Measurement

FDA – Food and Drug Administration

FEP – Fluorinated Ethylene Propylene

FLU – Flurbiprofen

FP – Filter Paper

Fps – Frames per second

FTIR – Fourier Transfer Infrared

FWHM – Full Width Half Maximum

GDA – Generic Data Acquisition

GRAS – Generally Regarded as Safe

H_2O:IPA – water:isopropanol solvent mixture

HI – water:isopropanol solvent mixture (H_2O:IPA)

HIV – Human Immunodeficiency Virus

HR – Harmonic Rejection

HSM – Hot-Stage Microscope

HT – High Temperature (37.5 ℃)

IBU – Ibuprofen

IBU_ISO – Ibuprofen Isonicotinamide physical mixture

IBU-ISO – Ibuprofen Isonicotinamide co-crystal

ID – Internal Diameter

IMID – Imidazole

IPA – Isopropanol

IQR – Interquartile Range

IR – Infrared

ISO – Isonicotinamide

KETO – Ketoprofen

KRAIC – Kinetically Regulated Automated Input Crystalliser

KRAIC-D – Kinetically Regulated Automated Input Crystalliser for Diffraction

KRAIC-S – Kinetically Regulated Automated Input Crystalliser – Single Crystal

KRAIC-T – Kinetically Regulated Automated Input Crystalliser – Temperature Cycling

LAG – Liquid Assisted Grinding

LINAC – Linear Accelerator

max abs – maximum absorbance

MeOH – Methanol

min abs – minimum absorbance

Mo-K_α – Molybdenum K alpha

MS – Mass Spectrometry

MSZ – Metastable Zone

MSZW – Metastable Zone Width

MX – Macromolecular Crystallography

N_2 – Gaseous nitrogen

NG – Neat Grinding

NICO – Nicotinamide

NS – Neutral Solvent

NSAIDs – Non-Steroidal Anti-Inflammatory Drugs

Obs – Observation

OD – Outer Diameter

OXA – Oxaprozin

OXA_IMID – Oxaprozin and Imidazole physical mixture

OXA_ISO – Oxaprozin and Isonicotinamide physical mixture

OXA-IMID – Oxaprozin Imidazole co-crystal

OXA-ISO – Oxaprozin Isonicotinamide co-crystal

PAT – Process Analytical Technology

PCM – Paracetamol

PFPE – Perfluoropolyether

PMMA – Polymethylmethacrylate

Pos. – Position

PP – Polypropylene

PSD – Particle Size Distribution

PSD – Position Sensitive Detector

PTFE – Polytetrafluoroethylene

PVC – Polyvinyl Chloride

PVM – Particle Visualisation Measurements

PXRD – Powder X-ray Diffraction

QbD – Quality by Design

R1 – Rotation 1

R2 – Rotation 2

R3 – Rotation 3

RBF – round bottom flask

RF – Radiofrequency

RH – Relative Humidity

rpm – Revolutions Per Minute

RT – Residence Time

RT – Room Temperature

RTD – Residence Time Distribution

SAXS – Small Angle X-ray Scattering

SCGOGS – Select Committee on GRAS Substances

SCXRD – Single Crystal X-ray Diffraction

SMPT – Solution Mediated Phase Transformation

SSHB – Short strong hydrogen bond

TCI – Tokyo Chemical Industry

TGA – Thermogravimetric Analysis

TNT – Two-step Nucleation Theory

UBA – Urea-barbituric Acid

UV-Vis – Ultraviolet-Visible

v/v – volume by volume

VOF – Volume of Fluid

VT-PXRD – Variable Temperature Powder X-ray Diffraction

W1 – Window 1

W2 – Window 2

W3 – Window 3

Wt % – Weight Percent

X-FEL – X-Ray Free-Electron Lasers

X-piece – Cross-piece

XRD – X-ray Diffraction

XYZ – X-direction, Y-direction, Z-direction

Chapter 1 – Introduction

1.1 Context of Research

Crystallisation is a complex, multi-step process involving a sequence of competitive nucleation and growth events, where there is potential for various solid forms, known as polymorphs, to crystallise from solution.[1] In the context of crystalline pharmaceutical solids, the distinct differences in the molecular packing arrangements of the various polymorphic forms influences the physicochemical properties of the Active Pharmaceutical Ingredient (API), including solubility, dissolution, bioavailability and compressibility.[1-5] This variability in physical attributes dictates the need for additional excipients in the drug product, such as binders, glidants and disintegrants. Moreover, an in depth understanding of the polymorphic landscape of an API is vital in ensuring the correct form can be reproducibly manufactured and administered to patients. Control over polymorphism is paramount in overcoming production problems associated with polymorphism, such as the phenomenon of the ‘‘disappearing polymorph’’, as in the case of the HIV protease inhibitor Ritonavir.[6, 7] Manufactured by Abbott Laboratories, Ritonavir was introduced to the market in 1996, but just two years later was temporarily removed, as the original crystalline form could no longer be accessed. Instead, an unexpected more stable form (II) was produced in the crystalline product.[5] The significant drawback to the formation of form II was its lower solubility (as it is the thermodynamically stable form), which resulted in a reduced oral bioavailability, affecting the therapeutic effect of the drug.[8] This led to product withdrawal and a delay during reformulation before the drug was reintroduced to the market.[1, 6] Importantly, the prediction of the crystallisation route in yielding a particular crystalline form is difficult considering that post-crystallisation offline analysis reveals information on the outcome but not the route of the crystallisation process and without considering down-stream processing requirements such as filtration and drying.[9-12]

1.2 Types of Crystalline Compounds

Pharmaceutical compounds can exist in various solid forms, which can be broadly categorised as amorphous or crystalline. Crystalline materials contain a regular ordered array of components, whereas amorphous materials are not ordered in regular arrays; these solids are much more difficult to gain control over and are much less reproducible than their crystalline counterparts, so are rarely employed in the pharmaceutical industry.[13] The crystal structure

may be manipulated to improve physicochemical properties by exploiting the various single-component or multi-component crystal forms known as polymorphs, or the generation of novel molecular materials containing multiple components, which comprise the API crystallised with another molecular entity. In these multi-component materials the API is present in the crystal structure with solvent molecule(s), co-former molecules or ionised with another ionic component to produce solvates, co-crystals and salts respectively (Figure 1.1).[14-17]

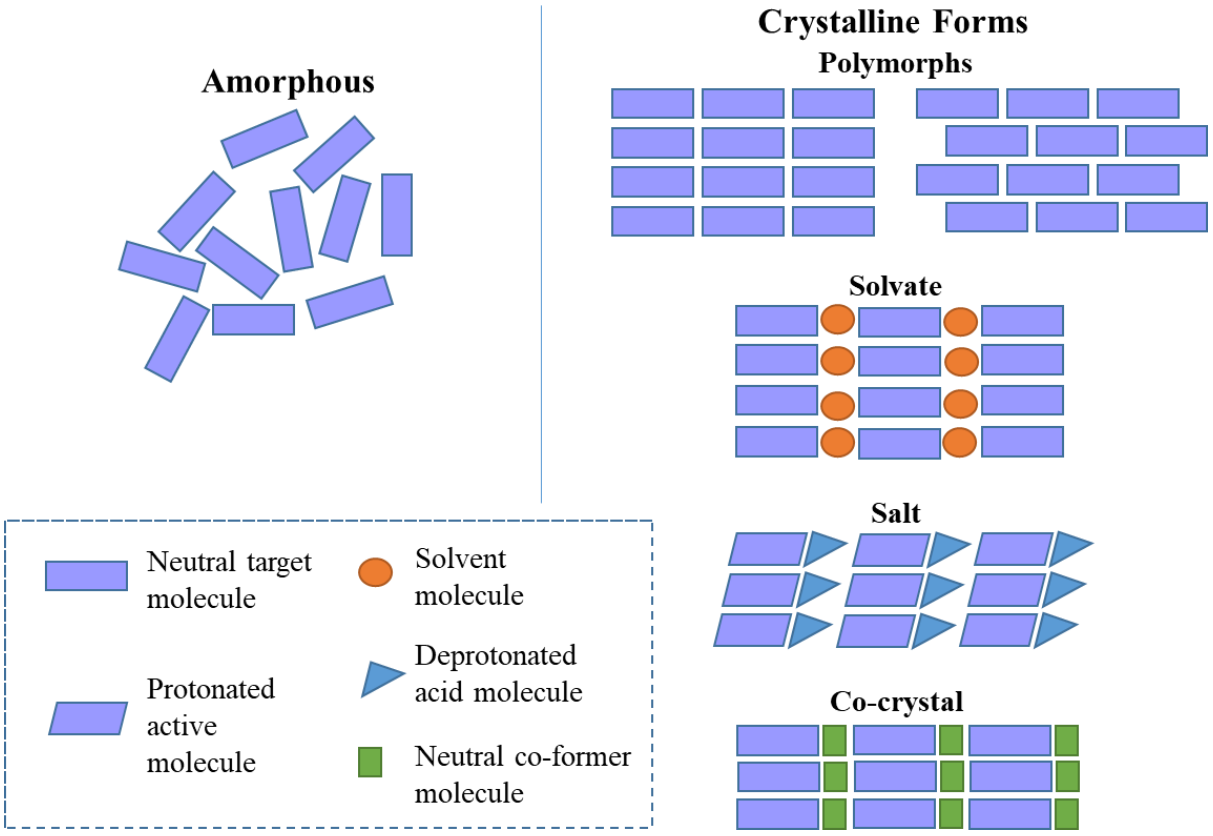

Figure 1.1 – Representation of crystalline forms including polymorphs and multi-component crystal systems compared to amorphous solids.

1.2.1 Polymorphism

Polymorphism is the ability of a single molecule or combination of different compounds to crystallise in multiple crystal forms, whilst still exhibiting the same chemical composition.[13, 18, 19] Polymorphism can be categorised into two types: conformational and packing.

Conformational polymorphism arises from the ability of flexible molecules to adopt more than one conformation in the solid state, with many examples in the literature. One well known

example is the multiple polymorphs formed by the molecule "ROY", due to its conformational flexibility.[20]

A good example of packing polymorphism is present for the pharmaceutically important drug paracetamol (PCM), which exists in two main structural forms under standard conditions: monoclinic PCM form I with a herringbone packing arrangement of molecules and orthorhombic PCM form II with parallel layers of molecules (Figure 1.2). PCM form I is the structural form formulated and administered, usually in tablet form, to ease mild to moderate pain. The layered structure of PCM form II enables the molecular layers to slide over each other. This structural feature leads to enhanced compressibility and solubility and as a result improved manufacturing and bioavailability of this API.[16, 21] PCM form II is metastable and must be formed in 100 % purity to avoid a polymorphic transition to the more stable PCM form I; presence of even trace form I causes the form II to form I transition. Crystallisation of pure form II has been highly challenging (though recent work has discovered new templated routes to its production),[22, 23] and as a result the form administered for low level pain relief is the less bioavailable form I. As PCM form I has a lower compressibility than form II, tablets of PCM are necessarily large due to the high percentage of excipients required to form a tablet.

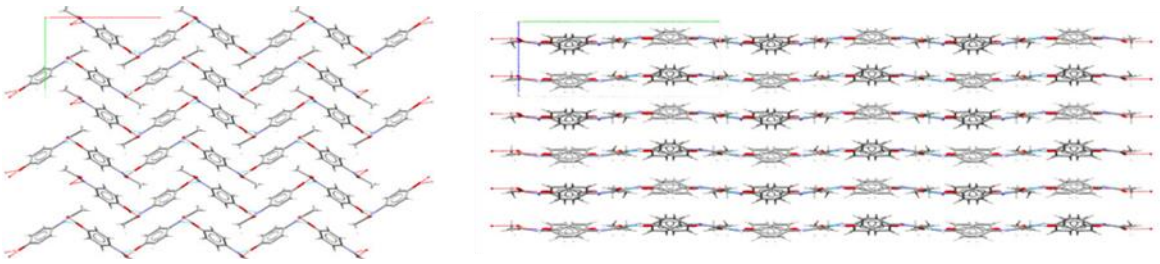

Figure 1.2 – The packing arrangements of the two main polymorphic forms of paracetamol (PCM) under standard conditions: PCM form I (left) and PCM form II (right), with CSD refcodes of HXACAN30 and HXACAN31 respectively.[24]

1.2.1.1 Thermodynamics of Polymorphism

The overriding goal of the development of any solid-state form is to establish the solid with optimal characteristics for the intended use,[21] which usually is the most thermodynamically stable polymorph.[13] This is because the thermodynamic polymorph is the only form, which does not tend to be susceptible to polymorphic transformation. On the other hand, a significant disadvantage of using the thermodynamic polymorph for a pharmaceutical application is that

the most stable polymorph is the least soluble due to its high crystal packing density and hence issues with low bioavailability are possible.

The relative stability of polymorphs can be attributed to their corresponding Gibbs free energies, where the most stable thermodynamic polymorph will possess the lowest free energy (Figure 1.3). Metastable polymorphs are thermodynamically unstable with higher free energies than the thermodynamic polymorph and thus are often formed under kinetic conditions.[18] Over time, metastable polymorphs will have the tendency to transform into the thermodynamically stable polymorph, where this polymorphic transition is driven by a reduction in free energy of the system, provided that the activation energy to polymorphic transformation can be overcome.[18, 25] This is captured in the concept of Ostwald's Law of Stages in which it is postulated that the system passes consecutively through each metastable polymorph *en route* to the stable form. The presence of even trace amounts of the thermodynamic polymorph will often seed the polymorphic transformation from the metastable to stable polymorph (as seen in the above example of PCM).

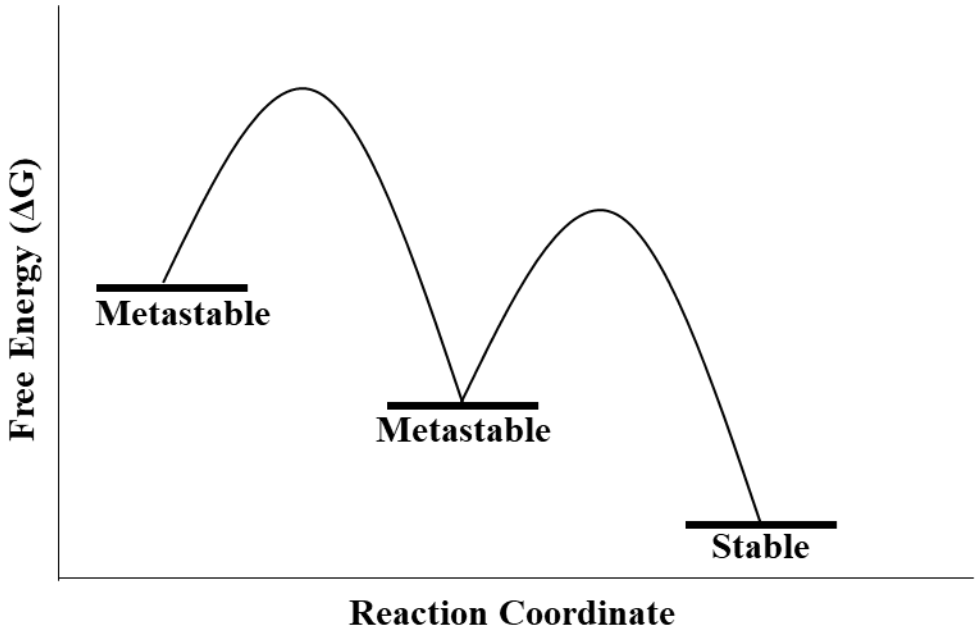

Figure 1.3 – The energy landscape of stable and metastable polymorphs.

Phase diagrams can be used to compare between monotropic and enantiotropic polymorphic systems, providing insight to the effect of temperature on the polymorphic form obtained (Figure 1.4). In a monotropic system, which is dimorphic, the relative orders of the solubility of polymorphs is independent of temperature and hence the solubility curves of the two

polymorphs do not cross. In an enantiotropic system, the relative solubilities of the two polymorphs are temperature dependent and therefore the solubility curves intersect at T_t, the transition temperature. At the point of intersection, a reversible solid-solid transition occurs between polymorph I and polymorph II. The enantiotropic phase diagram in Figure 1.4 shows that below the transition temperature, polymorph I is most stable, but after the transition temperature the relative stabilities of the two polymorphs have switched and now polymorph II is more stable. If the transition temperature exists below the melting point of both polymorphs, a transition from form I to form II will be observed upon heating.[9, 11, 13, 25]

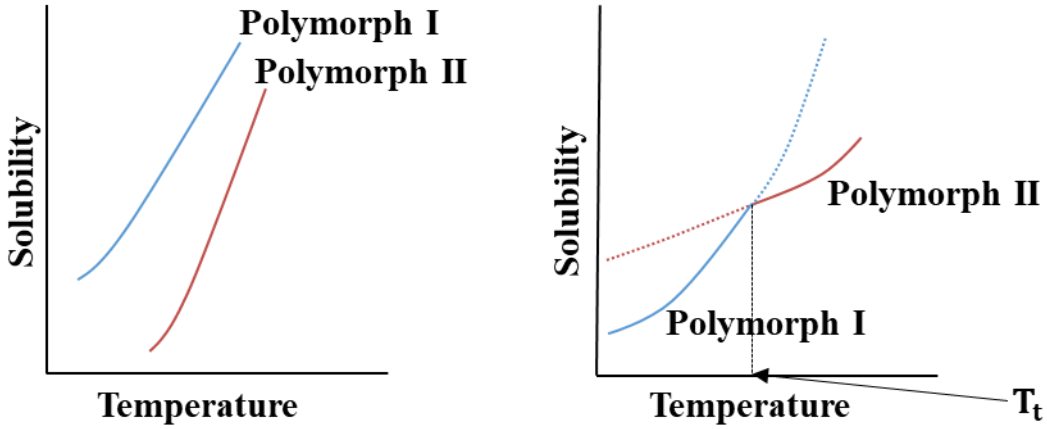

Figure 1.4 – Solubility curves in monotropic (left) and enantiotropic systems (right).

1.2.2 Solvates

In solute-solvent systems, it is possible for solvates to arise, where the solvent molecule is incorporated within the crystal structure and is present with the crystallising molecule in the unit cell. A solvate exhibits different physicochemical properties (melting point, bioavailability and compressibility properties) from those of the unsolvated form, which is important in the design of a drug product with specific requirements. Solvates are sometimes given the term pseudopolymorphs, but this is misleading as polymorphs occur in a unary system, whereas solvates belong to a binary system; it is therefore possible to differentiate between polymorphs and solvates by their position on the phase diagram.

1.2.3 Salts

A salt is a crystalline solid comprising of more than one type of ion; in pharmaceutical salts at least one of these ionic components includes an API. These charged entities are often generated

through proton transfer, leading to two oppositely charged components, held in the crystal lattice through both electrostatic attractions and intermolecular interactions.

The development of pharmaceutically important molecules in salt form is a common occurrence in the pharmaceutical industry, because of the frequently low aqueous solubility of neutral active molecules. In fact, around 90 % of potential APIs are classified as exhibiting low aqueous solubility. According to the Biopharmaceutics Classification System (BCS), drug substances can be categorised in terms of permeability and solubility: high permeability / high solubility, high permeability / low solubility, low permeability / high solubility and low permeability / low solubility.[14, 26] Introducing ionic components into the crystal lattice with the active molecule improves aqueous solubility as charged species dissolve more effectively in water, compared to the pure API form(s). The fundamental drawback to the formation of salts in pharmaceutical systems is that this relies on the active molecule being ionisable and thus restricts the choice of the API for pharmaceutical salt development.[17, 18, 27]

1.2.4 Co-crystals

Co-crystals are multi-component molecular materials comprising an API and co-former molecule or a second API in the crystal lattice, which exist as separate neutral entities and both of which are solids under ambient conditions. For pharmaceutical co-crystals the co-former should be benign and ideally a GRAS (Generally Regarded as Safe) molecule.[14-16]

1.2.4.1 Crystal Engineering and Multi-Component Crystallisation

Crystal engineering is an approach in which multi-component functional solid-state materials are designed through attempted prediction of intermolecular interactions with the aim of improving physicochemical properties with respect to those of the parent material. Co-crystallisation is a method for achieving crystal engineering goals through multi-component crystallisation whereby two or more molecules crystallise within the same crystal lattice (Figure 1.5).[16, 28-30] In co-crystallisation, the co-former molecule is utilised to direct the bonding and improve crystal packing to impart favourable physicochemical properties.[16, 31]

Molecular complexes designed in this way are seen as increasingly beneficial in the pharmaceutical industry where co-crystallisation can be used to prepare APIs with the potential of providing enhanced properties of existing materials; such co-crystals can also be patented as a new material. An example of a pharmaceutical co-crystal used in a drug product on the market is Betachlor, which was employed for its improved thermal stability over pure chloral

hydrate as an anti-inflammatory to treat diseases with a decreased adrenal gland function. In the crystal structure, the co-former molecule betaine forms tetramers of charge-assisted diol-carboxylate supramolecular motifs (heterosynthons) with the chloral hydrate API (Figure 1.6).[32]

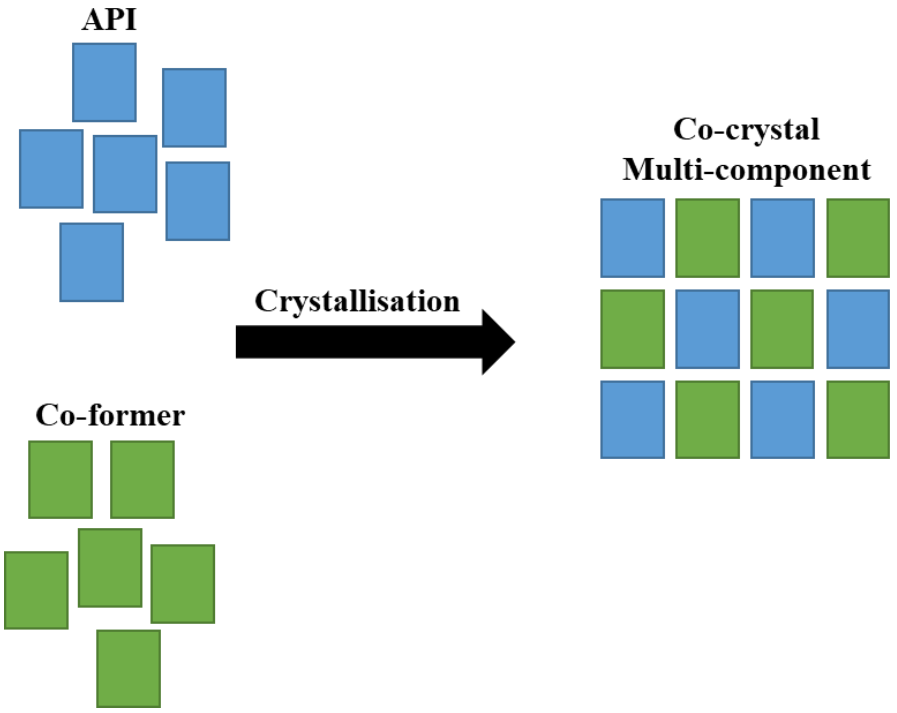

Figure 1.5 – Schematic representation of multi-component co-crystallisation involving API and co-former molecules.

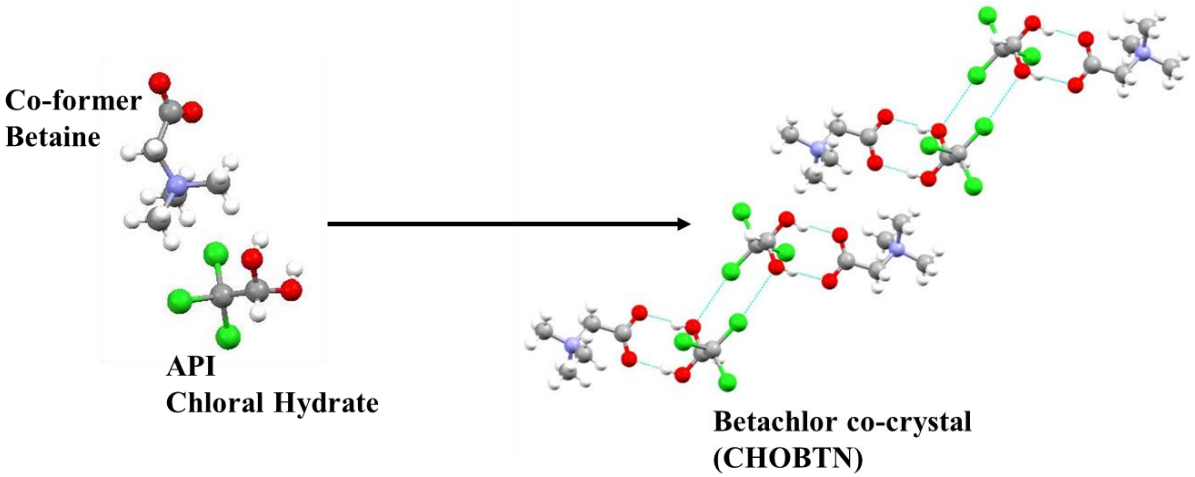

Figure 1.6 – Co-crystal formation of the pharmaceutical co-crystal Betachlor, with hydrogen-bonded chains of betaine and chloral hydrate molecules, forming a herringbone arrangement of molecules.[24, 33]

1.2.5 Intermolecular Interactions in the Solid State

1.2.5.1 Hydrogen Bonding

Hydrogen bonds often dominate the intermolecular interactions present in a molecular crystal structure, where molecules orient themselves to maximise the strength of the hydrogen bonding interactions. As a result of their directionality, hydrogen bonds largely govern the structure of extended materials.[34] A hydrogen bond is defined as an attractive electrostatic interaction between a hydrogen atom with a resulting partial positive charge, $H^{\delta+}$, by virtue of being covalently bonded to an electronegative atom A such as oxygen (O), fluorine (F) or nitrogen (N). The strength of the hydrogen bond is increased with increasing electronegativity of atom A.[35, 36] As a result of the partial positive charge associated with the hydrogen atom, the H atom is attracted to another electronegative atom B, containing a partial negative charge arising from polarisable π-electrons or a lone pair of electrons. A hydrogen bond A-H···B is a donor-acceptor bridging interaction, where H acts as a bridging atom between atom A and atom B. Atom A is the hydrogen bond donor, atom B the hydrogen bond acceptor.[36]

The strength of a hydrogen bonding interaction ranges from very strong, of comparable magnitude to a covalent bond, to much weaker interactions similar to the strength of van der Waals forces (Table 1.1). Most hydrogen bonds possess bond strengths between these two extremes. Electrostatic interactions dominate weak and moderate hydrogen bonds, as the hydrogen atom is more strongly attracted to atom A than atom B, whereas with increasing hydrogen bond strength, the nature of the hydrogen bond becomes more covalent as a more equal attraction exists between atom A and the hydrogen atom and the hydrogen atom and atom B. This equal atom attraction is indicative that the system may be close to undergoing hydrogen transfer; although in solution this is dictated by the pK_a values of the donor and acceptor molecules, this is not so clearly the case in the solid state. The closer the A-H···B bond angle to 180°, the stronger the hydrogen bond; linear hydrogen bonds of this type with very short A…B distances are often referred to as short strong hydrogen bonds (SSHBs).[34]

Table 1.1 – Properties of hydrogen bonds.[36]

Hydrogen bond property	**Strong**	**Moderate**	**Weak**
A-H···B interaction	Largely covalent	Largely electrostatic	Electrostatic
H···B bond length (Å)	~1.2-1.5	~1.5-2.2	2.2-3.2
A····B bond length (Å)	2.2-2.5	2.5-3.2	3.2-4.0
A-H···B bond angle (°)	175-180	130-180	90-150
Bond energy ($kcalmol^{-1}$)	14-40	4-15	1-4
Directionality	Strong	Moderate	Weak

1.2.5.2 Supramolecular Synthons and the Cambridge Structural Database (CSD)

Crystal engineering requires an understanding of intermolecular interactions; these intermolecular interactions are rationalised by the functionalities of the molecules present in the crystal structure.[37] The use of intermolecular interactions in the design strategy coupled with identification of the so-called supramolecular synthons that could potentially form, targets the prediction and control of the crystal structure.[34, 38, 39] A supramolecular synthon is employed to simplify the description of the crystal packing by only including those atoms important to the intermolecular interactions, allowing for a logical and regular route to understanding how the overall packing assembly in the crystal structure is built up.[14]

Information on how such units form can then be used in an attempt to predict the structures of other materials containing similar functionalities. This is the principle underlying the use of the Cambridge Structural Database (CSD)[24] in this area, which contains all reported crystal structures, including co-crystals, from the literature. The Cambridge Crystallographic Data Centre (CCDC) has developed search functions within the Mercury programme for exploring the wealth of structural information available in the CSD. The CSD is a valuable tool when designing new co-crystals in materials discovery, as trends in the interactions of existing co-crystals in the database can be used in the design strategy of new co-crystallisation attempts with the same targets involving alternative co-former molecules containing similar functional groups.

Assessing crystal structures directly based upon the molecular components is a simplification. The intermolecular interactions present in a crystal structure not only depend on the functional groups present in the molecules, but also the location and presence of other functionalities in

the local environment. Therefore, the use of the CSD in the design approach is rather as a guide as opposed to a rule for future attempts in crystal engineering.

Carboxylic acid moieties are utilised heavily in crystal engineering owing to their diverse hydrogen bonding potential; they also feature in the molecular structure of many pharmaceuticals.[30, 31] The formation of hydrogen bonding interactions between two carboxylic acid groups leads to the formation of a homosynthon. However, a CSD study carried by Steiner, found that instead of the formation of carboxylic acid homosynthons, carboxylic acids would instead preferentially bind to non-oxygen acceptors, such as pyridyl nitrogen atoms, provided these alternative sites are available. This leads to the formation of a heterosynthon, offering a suitable route to the formation of co-crystals (Figure 1.7).[40]

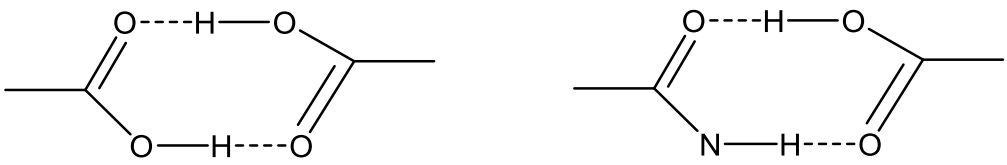

Figure 1.7 – Examples of a supramolecular homosynthon (left) and heterosynthon (right).

1.3 Crystallisation

Crystallisation is a phase change where randomly organised molecules, ions or atoms within a saturated solution condense to a regular and ordered crystalline solid. Crystallisation encompasses key areas of chemistry as well as chemical and process engineering, not only being useful as a purification and separation technique, but also as a means of producing new solid-state materials and functioning as a branch of particle technology.[25, 41, 42] Crystallisation is an important operation particularly in the pharmaceutical industry where the large majority (> 80 %) of commercially available APIs are delivered as a solid dosage form and thus require crystallising post-synthesis.[43]

Designing a crystallisation process to meet required product specification is a challenge. The pharmaceutical industry employs solution-based crystallisation for achieving desired product quality attributes including size, shape, purity and polymorphic form, where the control of these properties is paramount in subsequent down-stream processing such as granulation and tabletting.[44] Control over these aspects relies on an in-depth knowledge of the solubility and metastable zone widths (MSZWs) of each of the polymorphic forms in a variety of solvents. To

add to the variables requiring control, MSZWs will vary with scale of operation, intensity of mixing and the type of crystalliser employed. Control of the crystallisation process is governed by gaining control over both the nucleation and growth steps of crystallisation; thus, to gain fuller control the poorly understood process of nucleation requires improved understanding.[9, 11]

1.3.1 Solubility and Supersaturation

The starting point in the design of any solution-based crystallisation process is a thorough understanding of the solubility of the API in a given solvent. Solubility is defined as the maximum amount of solute able to dissolve in a given solvent or solvent mixture at a specified temperature.[11] A solution is classed as saturated when the solute concentration reaches the solubility limit; at which point dissolved and undissolved solute establish a thermodynamic equilibrium, illustrated by the equilibrium solubility curve in Figure 1.8.[11] Below the solubility limit, the solution is undersaturated and stable with respect to crystallisation. Above the solubility limit, the solution is considered to be supersaturated, where there is a greater amount of solute dissolved in the solution than the equilibrium value for saturation and therefore spontaneous nucleation can occur. Inside the metastable zone (MSZ), bounded by clear and cloud points in the turbidity method of solubility determination, primary nucleation cannot occur, however secondary nucleation can occur, in addition to crystal growth. Once the solubility of a solute-solvent system has been established at various temperatures, it is possible for the MSZW for that particular solute-solvent system to be established, shown as the distance between the equilibrium solubility and metastable boundary curves in Figure 1.8.[11, 25, 39] The temperature dependence of solubility can be represented on a phase diagram of concentration *versus* temperature (Figure 1.8).

The region in which a system can be classified as supersaturated but if undisturbed nucleation will not take place is known as the MSZ. For spontaneous nucleation to proceed, the system must pass beyond the MSZ *via* an increase in supersaturation of the system in to the so-called labile region. Nucleation is governed by kinetics, which dictates the size of the MSZ, which in turn dictates the extent of increase in supersaturation required to generate nuclei. Therefore, the nucleation and MSZW of a system exhibit innate variability with crystallisation environment, whereby experimental factors such as stirring and scale of crystallisation, as well as the presence of impurities have a significant impact on the MSZ.

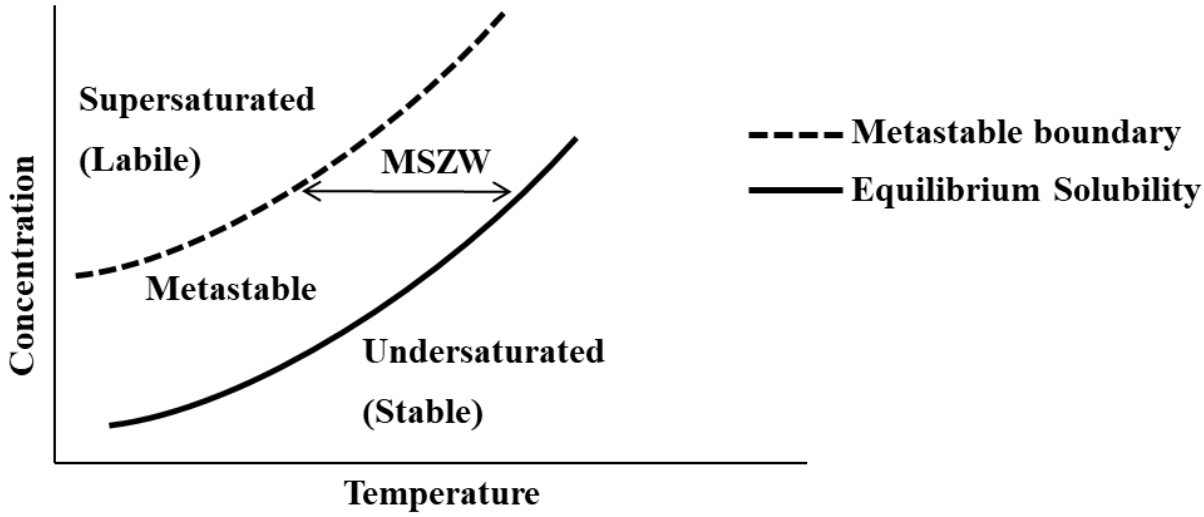

Figure 1.8 – Solubility curve (solid line), metastable boundary (dashed line) and MSZW highlighted as the region between the two curves.

The equilibrium solubility of a system is governed by thermodynamics and thus for a given solute-solvent system, the solubility behaviour will not be influenced by the crystallisation environment. Although the equilibrium solubility is a thermodynamic property, the metastable region is governed by kinetics. Importantly, until the crystallising system passes through the metastable region, the spontaneous nucleation occurring in the supersaturated region cannot proceed; this is known as the kinetic barrier to crystallisation. Supersaturation is the driving force of crystallisation as the solid and solute are no longer in equilibrium. To return the system back to equilibrium, solid material precipitates out of solution.[41]

Supersaturation can be expressed mathematically in a number of ways using the terms solution concentration (c) and the equilibrium solubility concentration (c*). Equation 1.1 considers the supersaturation (ΔC) as the difference between the solution concentration (c) and the equilibrium solubility concentration (c*) as the driving force for crystallisation, whereby the larger the value of ΔC, the greater the driving force for crystallisation. Equation 1.2 considers the same terms of solution concentration and the equilibrium solubility concentration but expressed as a ratio of the two terms, known as the supersaturation ratio, S. The value of S must be greater than 1 for the system to be supersaturated and thus for crystallisation to occur. Equation 1.3 describes the relative supersaturation, σ and is a dimensionless parameter.[10]

$$\Delta C = c - c^*$$

Equation 1.1 – Supersaturation expressed in terms ΔC – the difference between c – the solution concentration and c* – the equilibrium solubility concentration.

$$S = \frac{c}{c^*}$$

Equation 1.2 – The Supersaturation ratio, S.

$$\sigma = \frac{\Delta C}{c^*} = S - 1$$

Equation 1.3 – The relative supersaturation, σ.

1.3.2 Nucleation

The initial step in the process of crystallisation is the formation of crystal nuclei within the system, referred to as nucleation. These minute crystal nuclei are the centres for crystallisation. Once these nuclei have formed, their growth into crystallites can occur. Various mechanisms for nucleation exist; these are grouped as primary and secondary nucleation (Figure 1.9). Primary nucleation occurs without the presence of any crystalline particles (homogeneous seeds). Primary nucleation can be further categorised into homogeneous and heterogeneous depending on whether the nucleation is spontaneous or is induced by a foreign particle, respectively. Homogeneous primary nucleation can only be achieved once the concentration of the solution has moved through the MSZ and passed into the supersaturated region of the phase diagram. This type of spontaneous nucleation allows for little control to be exerted on the system, which will subsequently undergo crystal growth.

Heterogeneous nucleation can exist in both primary and secondary nucleation, dependent on whether nucleation occurs in the presence of foreign particles such as silica particles or seed crystals of the solute, respectively. Unlike homogeneous primary nucleation, heterogeneous primary nucleation can occur within the MSZ as the presence of these additional particles provide a surface for nucleation. The presence of a compatible surface within the solution reduces the Gibbs free energy barrier and thus the barrier to nucleation; therefore, it is possible for nucleation to proceed at lower levels of supersaturation than those required for spontaneous

nucleation. The presence of seed crystals of the desired solid form in secondary heterogeneous nucleation provides interfaces for nucleation from solution and growth of their crystalline polymorphic form in preference to other crystalline forms that could also be crystallised from the system. Outside of the intentional introduction of the desired polymorphic form through the use of seeds of polymorphic purity, the contact mechanism is the most common model proposed for secondary nucleation, where crystal-crystal, crystal-impeller and crystal-wall collisions create secondary nuclei.[9]

Secondary nucleation is a heterogeneous process whereby seed crystals of the desired polymorphic form are deliberately introduced into the system to promote crystallisation of this polymorphic form; [10, 11, 25] as an approach, seeding is thus more amenable to control.

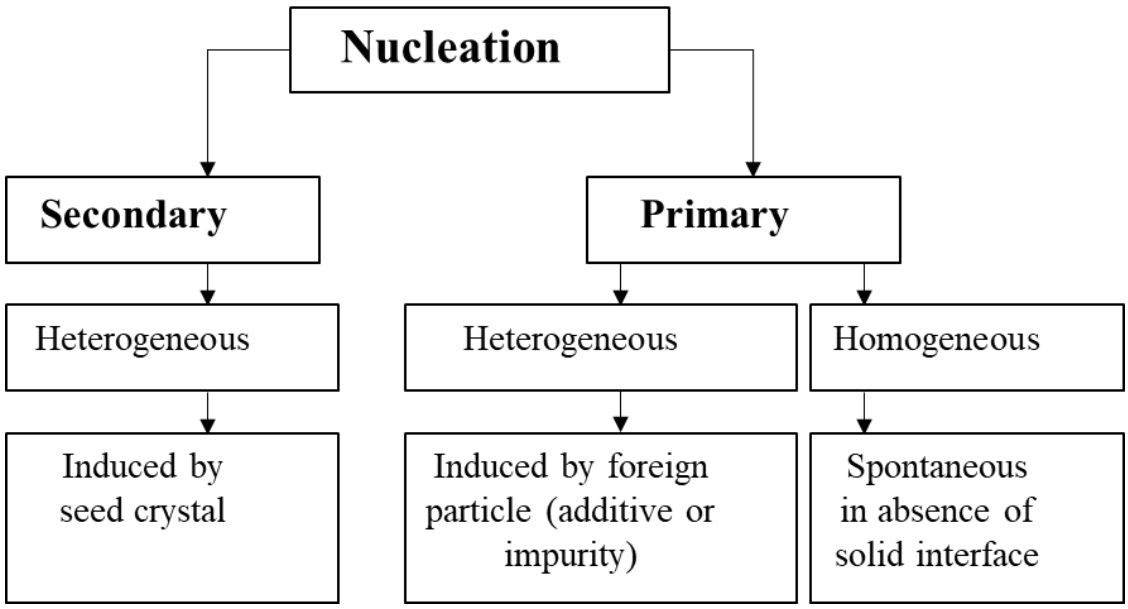

Figure 1.9 – The mechanisms of Nucleation.[11]

How nucleation occurs is poorly understood, however theories for the process by which nuclei are formed from a homogeneous solution exist. This ambiguity stems from the challenge in analysing nuclei, where the number of molecules contributing to the nuclei may range from as low as ten to several thousand individual molecules. It is unlikely that such number of nuclei in a cluster would evolve from a single collision, as the probability of so many molecules colliding simultaneously is low. Therefore, a more plausible suggestion to the formation of such nuclei containing so many molecules is a sequential addition of preferred orientation from a bimolecular collision, which builds step-wise; this is known as Classical Nucleation Theory

(CNT). As the size of the cluster reaches the critical cluster size (r_c), the intermolecular interactions within the cluster begin to be more favourable than the intermolecular interactions with surroundings in the system. Once the critical cluster size has been reached, the free energy of the nuclei decrease such that growth can occur and eventually a crystalline lattice has formed.[9-11, 45]

The free energy diagram for nucleation (Figure 1.10) indicates the critical nucleus size at which point the nuclei are stable and will not re-dissolve. This critical nucleus has an associated Gibbs free energy requirement, $\Delta G_{Critical}$. The outcome of whether particles re-dissolve or grow is governed by a resultant decrease in the Gibbs free energy of the particles.[9, 10, 45]

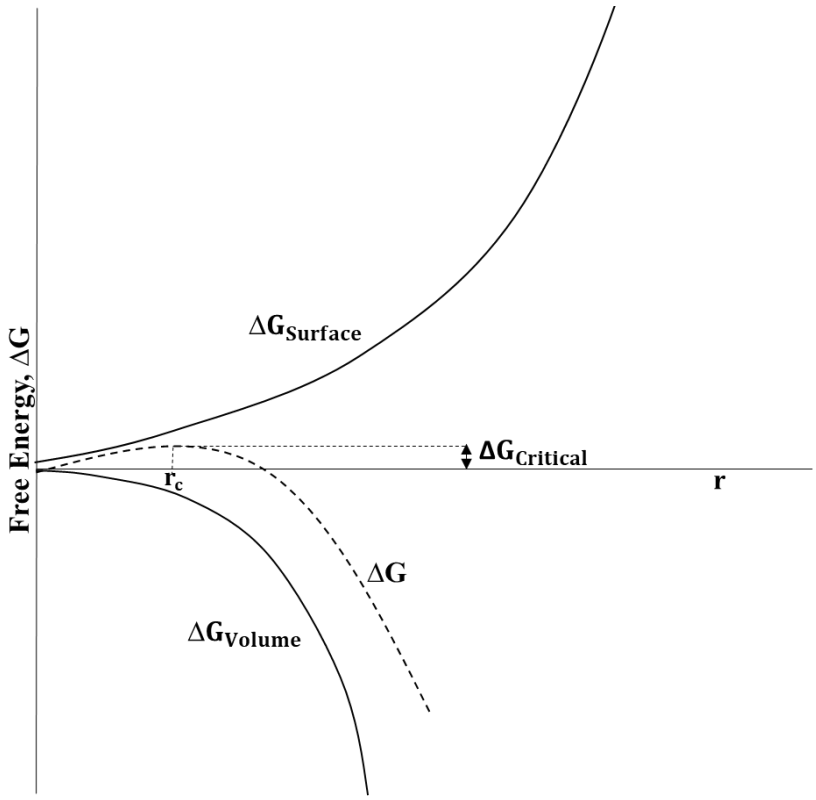

Figure 1.10 – Free energy diagram for nucleation, indicating the presence of the 'critical nucleus' size, r_c.[45]

Any nuclei which do not reach the critical cluster size simply re-dissolve in solution as they are unstable due to the large surface area / volume ratio, whereas once the clusters are at least equal to the critical cluster size or greater, the surface area / volume ratio has decreased to a point where the nuclei are stable and thus will not re-dissolve. The composition of this critical cluster is not known due to its minute size and short-lived nature, it is possible it is a well-defined crystallite or a more diffuse less-defined state.[10] CNT has limitations, such as the basic

presumption that one molecule is added to the growing cluster at a time. This seems unlikely considering that clusters have the tendency to aggregate and rearrange their orientations whilst building up to the critical cluster size. In fact, it is likely that the rate of molecular addition is greater than the ability of these molecules to orient themselves favourably, leading to regions of the solid exhibiting an amorphous nature. This effect can however be reduced through the introduction of seeds, which predetermines the crystal lattice of the saturated solution. [9, 10, 45]

This fundamental limitation to the CNT is the premise for the other nucleation theory, known as the two-step nucleation theory (TST). Although this TST model was initially proposed as the mechanism by which proteins crystallise, since then both theoretical and experimental studies have proven that the TST model is as applicable to small organic molecules as to macromolecules, highlighting its broad relevance to solution-based crystallisation.[45, 46] In the TST model, a cluster of sufficient size, much like that of CNT, is required to act as the centre for crystallisation, however in TST the particles within the cluster will rearrange themselves into a more favourable ordered structure larger than the critical nucleus size. This second step of cluster reorganisation is the rate-limiting step, where more complex structures take longer to reorganise themselves into the preferred arrangement (Figure 1.11).

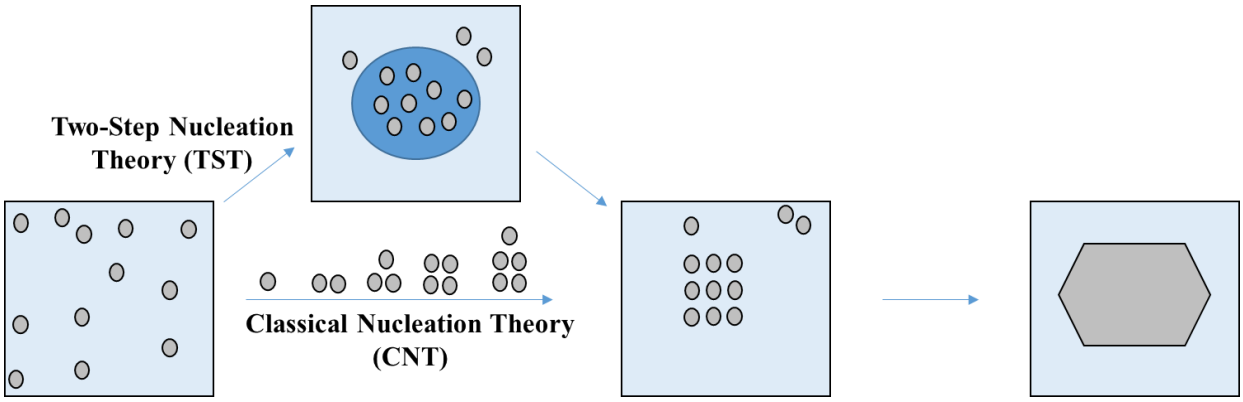

Figure 1.11 – Diagram comparing classical nucleation theory (CNT) and the two-step nucleation theory (TST).[45]

1.3.3 Crystal Growth

Once the nucleation process has occurred, the stage of crystal growth can proceed. Crystal growth involves the expansion of the stable nucleation centres formed in nucleation into macroscopic crystals. Exposing a crystal surface to a supersaturated solution causes the rate of movement of material to the crystal surface to exceed the rate of movement away from the

crystal surface, the net effect yielding crystal growth.[25] The ability of a crystal surface to attract this material within the supersaturated solution and use it for crystal growth is dependent on the level of attachment and the relative strengths of these interactions.

The basic principle for crystal growth relies on a build-up of layers, where new material, whether a molecule or cluster nucleus, first sheds its layers of solvent before bonding with the pre-existing crystal layers. The structure of a growing crystal surface may be categorised by the number of attachments: flat surface (F), growing step (S) and kink sites (K), which correspond to one, two and three attachments respectively (Figure 1.12).[9, 47] The greater the number of potential attachments the growth unit can make with the existing crystal surface, the greater the affinity of the growth unit to adsorb to the crystal surface and lead to crystal growth. This results in kink faces being the fastest growing and flat faces being the slowest crystal growth surfaces. The slowest growing flat faces determine the final morphology of the crystal.

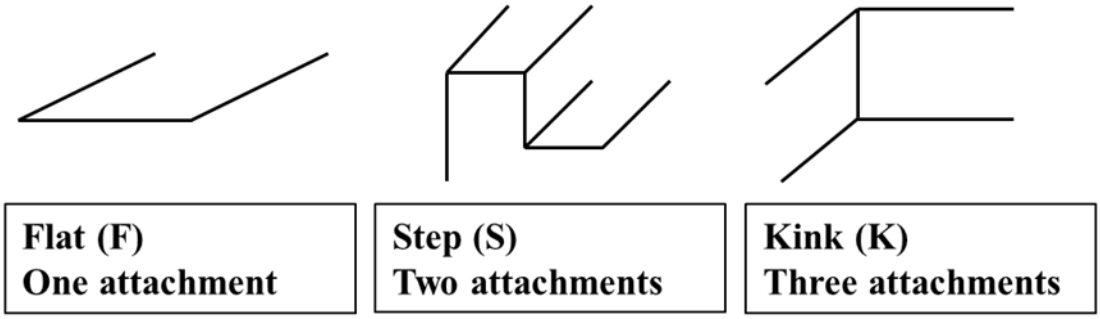

Figure 1.12 – Crystal surface structure containing flat (F), step (S) and kink (K) faces.[11]

Crystal growth is entropically an unfavourable process; a system will not preferentially drive to become more ordered, as this process exhibits a decrease in entropy. The crystal growth will only occur if growth sites with higher interaction energies can be created. The parameter α is defined to indicate which surfaces are likely to facilitate growth and develop multiple sites of interaction (Equation 1.4).[25]

$$\alpha = \frac{\Delta E}{kT}$$

Equation 1.4 – The α factor used to predict the relative ease of crystal growth, where ΔE = energy change, k = Boltzmann constant and T = temperature.

A low value of α corresponds to a surface with multiple growth sites available to facilitate crystal growth, whereas crystal surfaces with a large associated α term indicate that crystal

growth is difficult to achieve; in this case, special growth mechanisms are necessary. There are three common pathways with an increasing tendency for multiple site formation: continuous growth, surface nucleation and spiral growth.[9, 10, 25]

It is possible for a crystalline system to have a comparable affinity to the formation of the higher binding sites, such as kinks and steps. In these crystalline systems, the continuous growth mechanism is adopted and the α-factor must be less than 3. This continuous growth mechanism indicates that every solute molecule arriving at the crystal surface will find a growth site as the energy requirement to form a step feature is low. Hence, the growth rate for the continuous growth mechanism is linear and extends throughout the range of supersaturation. Crystalline systems rarely adopt the continuous growth mechanism as these materials do not possess sufficient roughness. In this case, rather than binding directly the majority of material approaching potential growth surfaces will either return to the solution phase of the system, or adsorb to previously deposited crystalline species already bound to a growth site; this preferential adsorption causes the formation of surface islands or nuclei (Figure 1.13).

Surface nucleation requires a larger α-factor than the continuous growth mechanism, in the range between 3 and 5. These surface islands eventually spread across the crystal surface as more solute molecules approach from solution leading to perpendicular growth in relation to the plane of the face. Surface islands produce both steps and kinks on the original crystal surface, which provide attachments for new crystalline material approaching the growth sites (Figure 1.13).

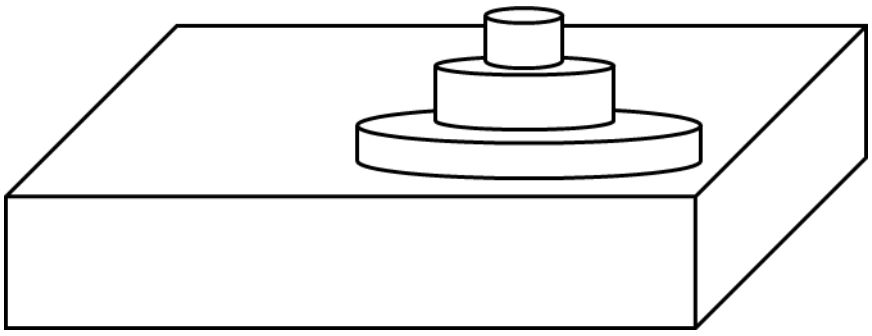

Figure 1.13 – Formation of surface nuclei / islands.

At α-factor values greater than 5, spiral growth or screw dislocation becomes the dominant mechanism and the formation of higher interactions such as kinks or steps is extremely difficult

(Figure 1.14). In this case, intermolecular interactions at the surface are increased, reducing the probability of surface nuclei formation, which ensures that the surface is flat. This growth mechanism utilises the fact that no crystal is perfect and therefore without defects, resulting in crystal surfaces which feature a self-generated step. Inherent lattice defects such as screw dislocations, a misalignment of the crystal lattice, permit spiral growth. These lattice defects could arise from heterogeneous growth *via* the addition of seeds crystals, additives or impurities to the crystalline system, each of which can impart stress during the growth process, leading to misalignment and in turn, points of emergence seen as steps. These vertical steps provide multiple binding sites for growth to occur.[25]

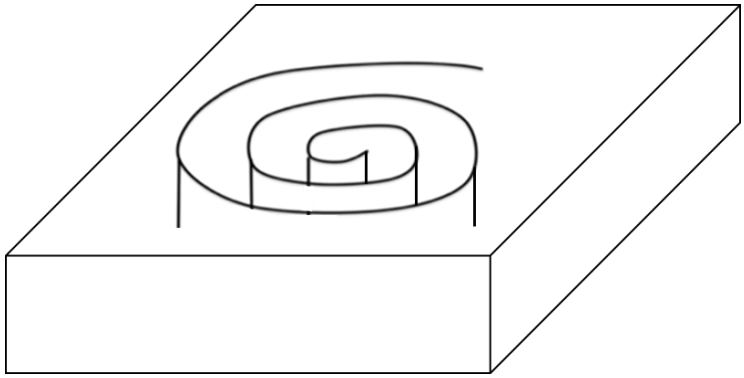

Figure 1.14 – The mechanism of spiral growth.

1.3.4 Crystal Morphology

In addition to the internal crystal structure, the crystal morphology or crystal habit – the external shape of the crystal system – is also of great importance.[10] The relative growth rates of the various crystal faces, which feature in a growing crystalline system, dictate the resultant morphology observed. The crystal morphology is described in terms of the set of crystallographic planes that show on the crystal surface, defined by their corresponding Miller indices, where the distance from the origin is proportional to the growth rate.[48] As an example, the (001) Miller index describes a face that grows parallel to both the crystallographic *a*- and *b*-axis and intercepts the *c*-axis.[25]

Crystal morphology influences both the crystallisation process and crystalline product. Crystal morphology can have a detrimental effect on secondary processing, where needles and plate-like crystals exhibit a low packing density, leading to blockages in the filtration steps due to the formation of an impervious layer (Figure 1.15). These undesirable morphologies influence

the viability of the crystallisation process. Crystal morphology also affects the end use of crystalline products, as crystal habit can modify the bioavailability of the drug product.

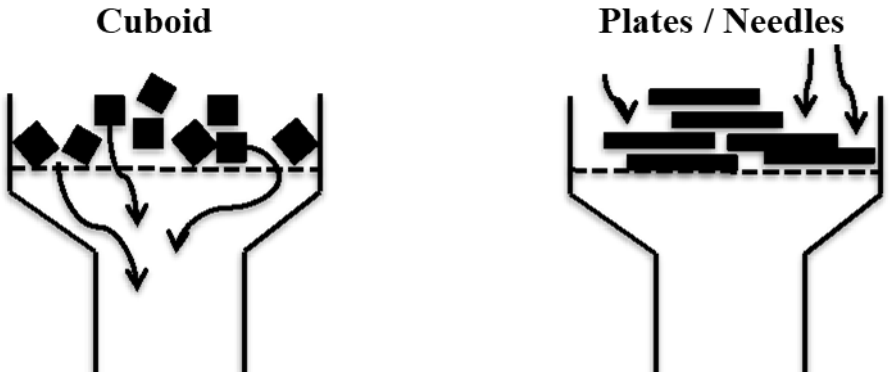

Figure 1.15 – Cuboid and plates/needle morphology comparison for filtration processing.[25]

1.3.5 Crystallisation Methods

The most common method of crystallisation employed in the pharmaceutical industry is solution-based crystallisation approaches.[46] In the pharmaceutical industry, early phase drug development involves version selection, in terms of exploring salts and co-crystals of an API, followed by a polymorph screen, an automated screening, which targets the thermodynamic form of the API material and aims to understand the polymorphic landscape.[49] 'Fit for purpose' crystallisation development is then carried out, ensuring that the crystallisation method will produce acceptable purity and yield, as well as the correct version and polymorph.

The choice of the crystallisation method is largely governed by the dependence of the solubility of the solute-solvent system on temperature. For instance, if the solubility of the system is only weakly dependent on temperature, then evaporative crystallisation or precipitation methods such as reactive or anti-solvent crystallisation methods are the most suitable choices. For systems that produce a steep solubility curve for concentration *versus* temperature dependence, then cooling crystallisation should be employed, in order to achieve sufficient yield.[11, 50]

1.3.5.1 Evaporative Crystallisation

In evaporative crystallisation methods, supersaturation of the solution is achieved *via* evaporation of the solvent. Initially the solution will be undersaturated; once the solution is left to evaporate at a suitable temperature, the concentration will increase due to evaporation of the solvent, the solution reaches the MSZ and eventually becomes labile (Figure 1.16). Once the solution has increased in concentration enough to meet the metastable boundary, the solution

is considered supersaturated (in the so-called labile region beyond the MSZ), at which point spontaneous nucleation can occur followed by crystal growth, whereby precipitation of crystalline material out of the solution causes a simultaneous decrease in the solution concentration, causing the system to returns towards the solubility curve. If the system is left to further evaporate, the saturation point will be reached once more and further crystal growth observed; this cycle continues until all the solvent in the solute-solvent system has evaporated. During evaporative crystallisation, the system is kept at constant temperature and the concentration of the solution is dependent on the solubility of the solute in the solvent. The crystallisation profile is dependent on the temperature and the volatility of the solvent.[9, 11, 25, 50]

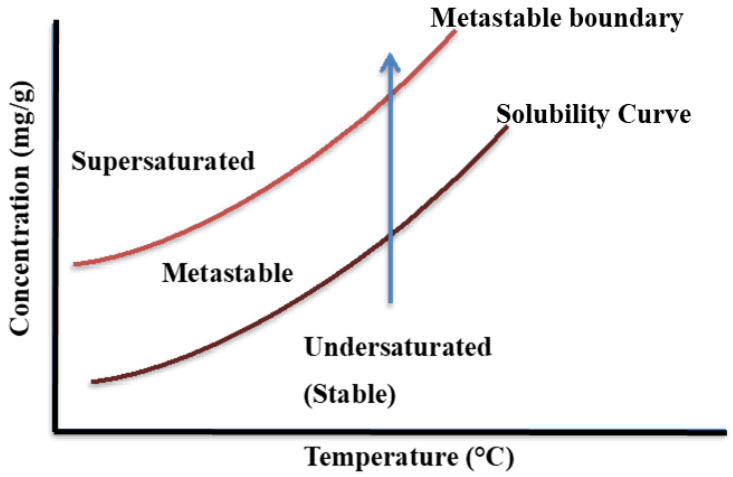

Figure 1.16 – Schematic of an evaporative crystallisation profile.

1.3.5.2 Cooling Crystallisation

A more advanced and controlled technique than evaporative crystallisation methods is cooling or temperature-controlled crystallisation, a favoured method of crystallisation for batch production.[51, 52] In cooling crystallisation, the system is cooled from the undersaturated to the supersaturated region. Much like in evaporative crystallisation, when the system reaches the metastable limit, nucleation and crystallisation is triggered and there is a subsequent decrease in concentration of the solution as some of the solute has precipitated out of the solution; this takes the system to within the MSZ. In the design of cooling crystallisation experiments it is important to ensure that the cooling of the system once it has achieved nucleation is controlled such that it remains in the metastable region to ensure no further primary nucleation may proceed, only growth. (Figure 1.17).

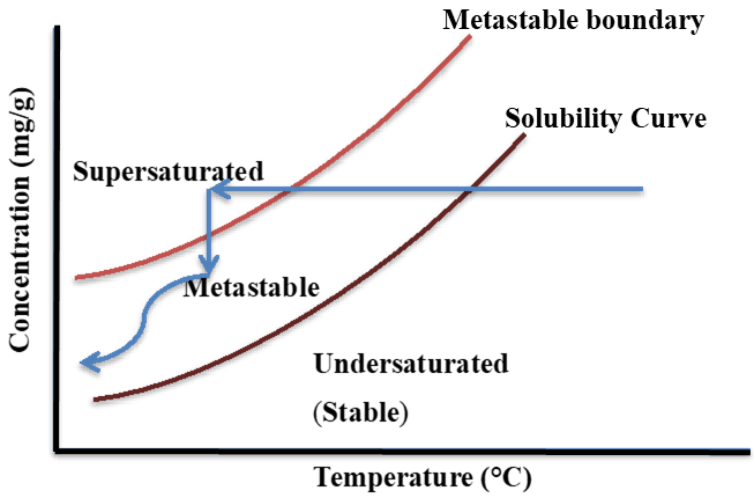

Figure 1.17 – Schematic of a cooling crystallisation profile.

As the MSZ is a kinetic phenomenon, its size varies with the crystallisation conditions, such as cooling rate, stirring rate and scale of the crystallisation. Under a faster cooling rate the system will not have the opportunity to reach equilibrium conditions and therefore the crystallisation occurs under kinetic control and thus is more likely to lead to the production of less stable polymorphs as opposed to the thermodynamic polymorph that is more likely in cases where the system has been allowed to reach equilibrium when slower cooling rates are employed.

1.3.5.3 Seeded Crystallisation

In seeded crystallisations, seed particles of the desired product either in dry form or as a seed slurry are added to the crystallisation to overcome the stochastic nature of nucleation by avoiding spontaneous nucleation in the system. The seeds are introduced when the growth solution is in the MSZ; the addition point must be carefully positioned, if the seeds are added when the temperature of the solution is too high the seeds will simply dissolve, however if seed addition occurs too close to the metastable boundary, then the increase in solute concentration (*via* seed crystal addition) risks spontaneous nucleation. Once the seeds are added, the solution is then cooled, maintaining stability within the MSZ. Seeding is commonly employed in the pharmaceutical industry to gain control over solid form and produce a narrower particle size distribution (PSD) than non-seeded crystallisations. [9, 11]

1.3.5.4 Anti-solvent Crystallisation

In anti-solvent crystallisation, a solvent in which the solute in the system displays poor solubility is added to an undersaturated solution. This anti-solvent addition increases the

supersaturation of the solution by essentially lowering the solubility curve so that the supersaturated region can be achieved at lower concentrations leading to crystallisation (Figure 1.18). The effect of dilution by addition of the anti-solvent is outweighed by the reduction in solubility caused by the addition of the anti-solvent to the system.

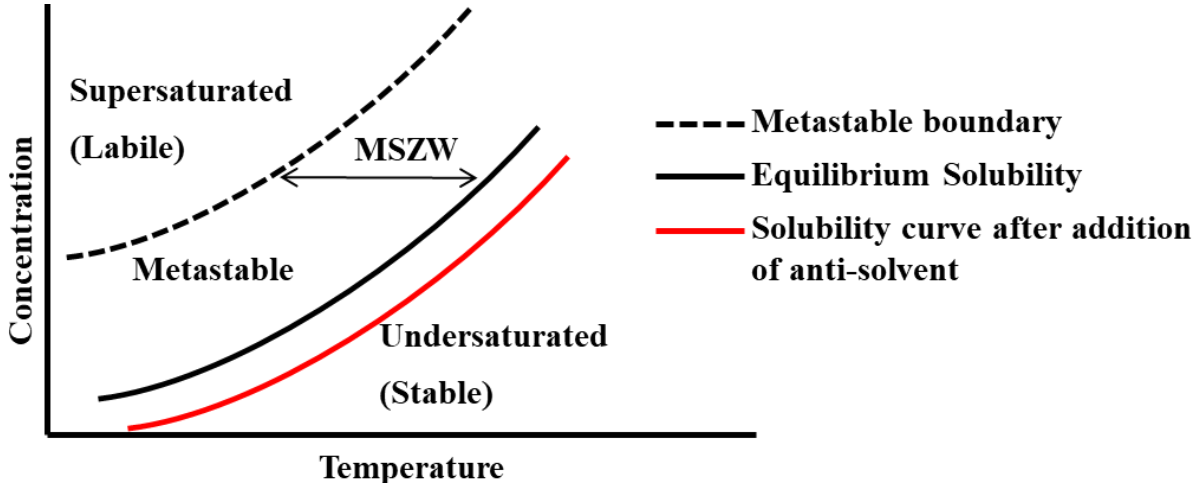

Figure 1.18 – Schematic of an anti-solvent crystallisation profile.

1.3.5.5 Reactive Crystallisation

Reactive crystallisation occurs when two or more compounds react within solution and the resultant product of the reaction is less soluble than the constituent starting components in the solvent system. Similar to anti-solvent crystallisation, this decrease in solubility and resultant increase in supersaturation causes crystallisation. The rate at which reactive crystallisation is achieved is dependent on the rate of reaction of the starting materials.

1.3.5.6 Slurrying Crystallisation

Solution mediated phase transformations (SMPTs) can be investigated *via* solution-mediated crystallisation techniques, known as slurrying. This method of crystallisation is a suspension technique, whereby an excess of solid is added to solvent and stirred for a period of time without complete solid dissolution. Some solid dissolution may occur in polymorphic systems, whereby dissolution of the metastable form and subsequent crystallisation of the stable form occurs during a SMPT. This method of crystallisation can be used to identify new polymorphic forms, to identify the thermodynamic form from concomitant polymorphs, or for screening for novel multi-components systems, such as co-crystals. The desired polymorph, obtained from slurrying crystallisations, can be tuned by varying experimental parameters such as slurrying time, stirring rate, temperature, solid loading and scale of operation.[8]

Systems that exhibit polymorphism in solution will undergo SMPTs, dictated by Ostwald's Law of Stages: first, the metastable phase will undergo dissolution, second, nucleation of the stable phase, third, growth of the stable phase will occur. This implies that a low-energy route to interconversion between polymorphic forms exists.[53] This transformation from the metastable to stable polymorph can be facilitated in solution as a result of the number of degrees of freedom molecules possess in this phase. Therefore, molecules in solution have the opportunity to re-orientate and re-align themselves so that as the molecules crystallise the free energy of the system is minimised. The SMPT is thermodynamically driven by the solubility difference between polymorphs.

If a dimorphic system contains monotropic polymorphs, where form I is the thermodynamic form and form II is the metastable form, the use of slurrying to facilitate SMPTs can transform form II into form I in solution. The SMPT can be achieved by addition of an excess of form II to a solvent, yielding a slurry suspension of form II. As the thermodynamic form is the least soluble, form I will be less soluble than form II and thus the solution will be supersaturated with respect to form I. Once form I crystallises from solution, the concentration of the solution decreases, which simultaneously allows additional form II to dissolve in solution. In turn this causes more nucleation and growth of the stable form I. This cycle proceeds until full conversion from form II to form I is complete.[54-56,57]

The same principle can also be applied to the formation of multi-component systems, such as co-crystals. The co-crystal A-B is comprised of single component A and single component B, where the co-crystal A-B exhibits a lower solubility in the particular solvent compared to the solubility of the individual components A and B in the same solvent. The thermodynamic relationship between the single components and multi-components facilitates the formation of the co-crystal (Figure 1.19). The co-crystal A-B could be accessed *via* a SMPT from a slurry containing an excess of the pure starting components A and B in the chosen solvent. The system is considered supersaturated with respect to component A and component B; the system will therefore be supersaturated with respect to the co-crystal A-B, provided the co-crystal exhibits a lower relative solubility in the chosen solvent. Once the system reaches supersaturation, nucleation of the co-crystal A-B can proceed in preference to crystallisation of either individual component. This cycle proceeds until full conversion from the starting components A and B to the co-crystal A-B is complete.[57]

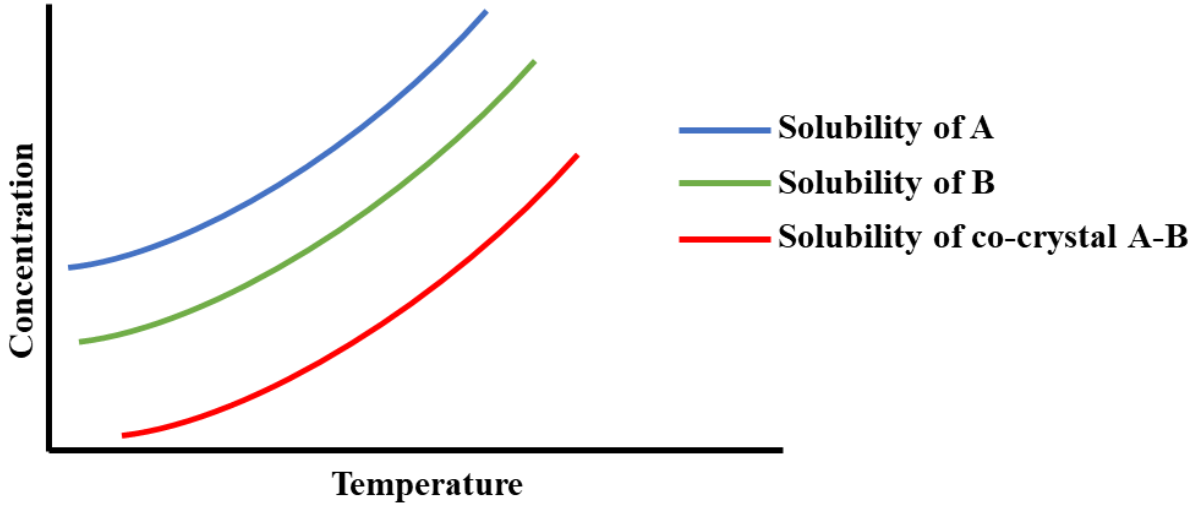

Figure 1.19 – Schematic of solubility curves of single components A and B, compared to the solubility curve of the multi-component co-crystal A-B.

1.3.5.7 Mechanochemical Crystallisation

Mechanochemistry refers to chemical reactions, typically of solid-state materials, achieved through the application of mechanical energy to the reaction system, either through neat grinding or the inclusion of minimal solvent, known as liquid assisted grinding (LAG). This approach can be applied particularly in the area of co-crystallisation, with the notable benefit of being less solvent intensive than solution-based crystallisation approaches. In addition, mechanochemical crystallisation is less dependent on the effects of solubility and solvent competition within a crystallising system compared to other crystallisation approaches.

Mechanochemistry can be applied to the crystallisation of organic molecular materials, as mechanical energy can overcome the intermolecular interactions present within crystal structures allowing the opportunity for other intermolecular interactions, perhaps between the target and co-former molecule in attempted co-crystallisations to be achieved. The high molecular mobility achieved through the application of mechanical energy to the crystallising system, offers the opportunity to manipulate polymorphic form as well as produce new molecular materials.[58-60] Both neat and LAG methods can be achieved using a traditional mortar and pestle or an automated mechanical ball mill apparatus.

In the case of LAG, minimal solvent is introduced along with the solid starting materials in preparation for grinding, to aid the formation of co-crystals. The incorporation of a small amount of solvent in the grinding of solids has been shown to increase the rate of solid-state

crystal formation.[61] The use of LAG can also encourage co-crystal formation in cases where the components have significantly different solubilities with respect to solution-based methods.

1.3.6 Continuous Manufacturing

Traditionally within the pharmaceutical industry, crystallisation is carried out *via* batch manufacturing methods. This standard approach utilises large stirred tank reactors, in which large volumes are being produced at one time.[42] Process steps in batch manufacturing are usually not fully integrated, leading to long lead times and large associated inventory costs. They are also generally energy intensive and use large amounts of solvent.

A technological shift to continuous production offers the opportunity to improve product quality and variety, reduce inventories, lower production costs in terms of time, energy usage and waste, as well as producing drug products on a variety of scales and enabling affordable personalised drugs to become a reality. However, a key drawback to the implementation of continuous processing is the complex and expensive regulatory procedure required to alter the current manufacturing methods (Table 1.2).[62] Although some pharmaceutical companies are employing continuous processing to produce drug products, the uptake of continuous crystallisation and manufacturing of pharmaceuticals and fine chemicals remains limited.

Table 1.2 – Opportunities for and barriers to Continuous Manufacturing.[62]

Opportunities for Continuous	**Barriers to Continuous**
1. Cost • Reduced capital investment due to smaller facilities and plant footprint • Operating costs are lower, due to reduced labour requirements, increased asset utilisation, cheaper development costs, lower energy requirements • Reduced inventory costs (less material handling and transport costs) **2. Product and Volume Flexibility** • System can be easily altered to change product mix (Product Flexibility)	**1. Regulatory** • Process Analytical Technology (PAT) and Quality by Design (QbD) not yet compliant • No regulatory body approval • No quality validation procedure • Sterility issues **2. Social** • Perception that it is only suitable for large scale • Lack of continuous technology experience

• System can be easily altered to respond to demand changes (Volume Flexibility) **3. Quality** • Improved process control (>5σ, right-first-time) • Less product rejection (*in situ* quality testing) • Integration of quality control and compliance (QbD) • Process safety and control **4. Responsiveness** • Move towards 'made-to-order' supply chain • Reduced time to market • Easier recycling • Minimised reaction time through better process parameter control • Little or no scale-up development required • Accelerated introduction of APIs to market **5. Rapid scale-up** • Ease of scale-up post clinical trial	**3. Process and Technology** • Lack of process and technology understanding • Unknown process development • Little knowledge about continuous crystallisation **4. Economics** • Resource availability • High initial start-up costs • Specialised equipment costs • Specialised personnel requirements

When shifting to the uptake of continuous processing methods, a range of fundamental differences must be considered. The key characteristics of stoichiometry, reaction time, reaction progress and steady-state are detailed in Table 1.3.

Table 1.3 – Comparison of the fundamental characteristics of batch and flow processing methods.[63]

Characteristic	Batch	Flow
Stoichiometry	Defined by the concentration and molar ratio of the starting components	Determined by the concentration of the reagents and the ratio of their flow rates
Reaction time	Time spent under the reaction conditions	Time spent in reactor – dependent on reactor volume and flow rates of reagents
Reaction progress	Time spent in reaction vessel	Dependent on distance travelled along reactor length
Steady-State	Uniform concentration of components throughout reaction vessel	Reactant concentration is steady with time but varies along reactor length

1.3.7 Flow Chemistry and Flow Crystallisation

The traditionally accepted advantages of flow chemistry include improved mixing and heat-mass transfer enabling precise control of both reaction and process parameters,[64, 65] but in addition the ability to carry out challenging chemistry not easily attainable in batch, such as photochemistry and reactions involving unstable intermediates, can also benefit from the adoption of flow chemistry.[66]

Furthermore, the ability to handle potentially hazardous materials within, for example, a microreactor, align well with the '12 Principles of Green Chemistry', emphasising safety as a key driver to the deployment of flow chemistry. The improved heat-mass transfer also means that this technology contributes to these 'Sustainable Development Goals' for greener and more sustainable chemistry solutions.[64, 66, 67]

Flow technologies can be used as a means to direct the synthesis and assembly of materials for which the crystalline structure is important for the resultant properties, whereby some of the conditions, such as very slow or very fast mixing and the use of very small volumes of reagents can be achieved in flow environments but not *via* batch methods. These conditions are inherent to the nature of flow environments; for instance, reproducible control over particle size is a direct result of a combination of homogeneous mixing conditions as well as temperature control.[65] Flow technologies can control the resultant structure through careful design of the ordering of reagents.[65]

In flow crystallisation the key attribute in confirming reactor efficacy is by the particle size distribution (PSD) of the crystalline product; the narrower the PSD, the higher the level of

homogeneity experienced within the reactor, which typically is the goal in crystallisation to meet critical quality attributes (CQAs) criteria.

1.3.7.1 Residence Time (RT)

In batch processing, the reaction time is determined by how long the batch reactor is held under a set of reaction conditions. In continuous processing, the reaction time is instead described by the residence time (RT), which refers to how long the reactants reside in the reactor. The RT depends on the volume of the reactor and the flow rates of the reactants.[63, 68]

In a tubular flow reactor, the RT can be calculated by the diameter and length of the tubing, along with the flow rate (s) (Figure 1.20 and Equation 1.5). The RT of a reaction can be varied through alterations to the size of the reactor, including bore size of the tubing, which alters the cross-sectional area, increasing the length of the tubing or adjusting the flow rates. There is an inversely proportional relationship between the flow rates employed and the RT, where at low flow rates this contributes to a longer RT in the reactor.

The RT with respect to chemical reactions and crystallisation processes requires optimisation; if the RT is too low, the chemical reaction may not have reached completion and similarly for a crystallisation process, without sufficient RT in the crystalliser crystal growth may not have time to happen, a desired polymorphic transformation may be incomplete resulting a polymorphic mixture, or the transition may not have even started to proceed. On the contrary, if the RT is too long undesirable phase transformations could occur, or simply the solution is occupying the crystalliser for no benefit. In any flow system, a distribution of residence times will exist as a result of the fluid dynamics of the system, not all molecules that enter the reactor spend the same time period in the reactor.[69, 70] This variance from the ideal residence time is known as the residence time distribution (RTD). During flow process optimisation, the RTD is minimised in order to maximise the consistency of the process. Strategies to reduce the RTD include enhanced mixing, alteration to the reactor geometry, reduction in solution viscosity and segmentation of flow.[70-72]

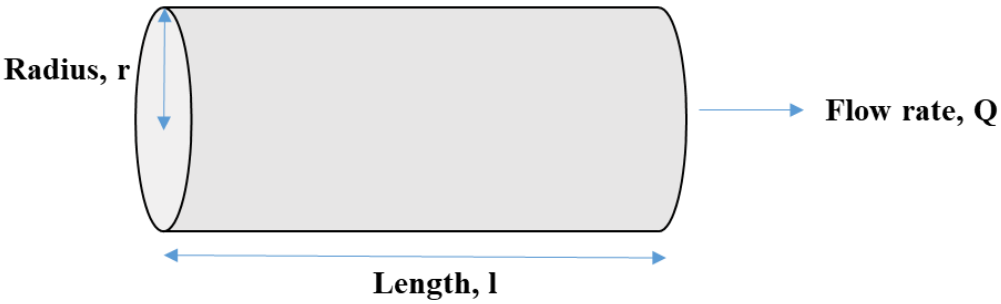

Figure 1.20 – Derivation of the operators for Residence Time calculation expressed in Equation 1.5 for a tubular reactor.

$$RT = \frac{\pi r^2 l}{Q} = \frac{V}{Q}$$

Equation 1.5 – Residence Time, RT calculated using r – radius of tubing (cm), l – length of tubing (cm), V – volume of tubing (mL) and Q – flow rate (mL/min).

1.3.7.2 Steady-State Operation

In a continuous flow reactor, the system can be considered to be operating at steady-state, provided at a given set point the concentration of a chemical species remains constant with time (Figure 1.21); however, in the event of precipitation or reaction, the concentration may differ with spatial point along the reactor.[73] Steady-state operation can only be achieved once the system has completed a start-up period at the desired flow conditions (including temperature and flow rate (s)), to allow the system to reach equilibrium. Similarly, the system will move into an unsteady-state after any alterations in process variables are made and thus the stage of start-up will need repeating in order to return the system to steady-state.[42, 70] Flow crystallisation processes, which suffer from blockages and issues with encrustation, will therefore experience disturbances to the pressure in the system, which causes the system to move from a steady to an unsteady-state. When continuous processes are operating at steady-state, in contrast to batch processes, which consistently operate under non-steady-state conditions, the continuous flow process has the capability to impart much more control over the particles in the system and therefore control over CQAs is significantly more achievable in flow compared to batch processing.[69, 74]

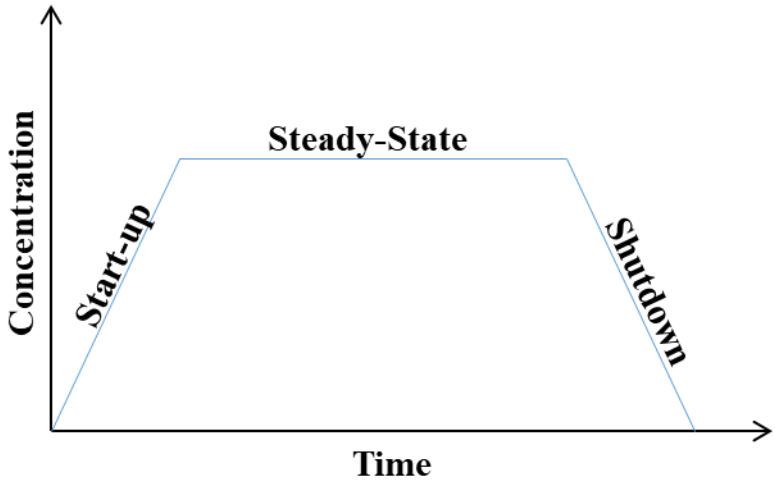

Figure 1.21 – Schematic of a single spatial point of a continuous flow process operating at steady-state, between the stages of start-up and shutdown.

In order to establish whether a flow system has reached steady-state operation, an inert trace material can be employed to monitor the progress of the reaction by measuring, for instance, the concentration of a dye trace using a spectrometer. The system is confirmed to be operating at steady-state once the concentration of the dye remains constant with time.[70]

1.3.7.3 Mixing, Mass and Heat Transfer

The adoption of continuous processing can accomplish improvements in mixing, mass and heat transfer, as a result of the improved surface area-to-volume ratio, compared to the low surface area-to-volume ratio in traditional batch methods. Typically, in batch, the large stirred tank reactor requires an outer heating jacket to regulate temperature, in which the transfer of heat within the reactor is inefficient, where components at the edge of a reactor are heated to a greater extent than particles in the centre. Similarly, the impeller employed at the centre of the reactor to facilitate mass transfer and mixing in the system, will provide a greater degree of mixing to particles at the centre of the reactor, but poor mixing to particles at the walls of the container.[68] The use of continuous processing methods imparts homogeneity on the system, which ensures that all particles experience similar conditions, in terms of RT, mixing, mass and heat transfer.

In continuous processing, a system can benefit from approaching the adoption of plug flow conditions (Figure 1.22), in which particles experience the same conditions over the same time period, due to a narrow RTD. Plug flow conditions such as uniform concentration, velocity and

temperature profiles can be achieved in a plug flow reactor (PFR). The PFR model assumes there is no mixing in the direction of the flow (no back-mixing), whereby only radial mixing occurs transverse to the flow, allowing the flow to travel through the reactor as a single 'plug' from the inlet to the outlet. A system operating under plug flow conditions is an idealised situation; however, designing a system that can maintain conditions close to plug flow is sufficient for the assumption to be held.[70]

The mixing behaviour in fluids can be broadly categorised into laminar, transitional and turbulent flow. The Reynold's number, R_e is a dimensionless mass transfer coefficient used to describe flow patterns in fluids, whereby the magnitude of R_e can be used to describe the type of flow present. The magnitude of R_e for a fluid can be determined from Equation 1.6. [68] A low R_e of < 2300 results in laminar flow dominating the fluid dynamics, an intermediate value of R_e, between $2300 < R_e < 4000$ results in transitional flow and large R_e values > 4000 correspond with turbulent flow. [63] Laminar flow features a radial distribution of velocities, where the maximum velocity and shortest residence time is achieved in the centre of the tubing, whilst the slowest moving particles with the longest residence times are those, which travel close and interact with the inside of the tubing.

The size of the reactor influences the flow regime accessible at a particular scale (Table 1.4). In microreactors and nanoreactors laminar regimes can provide efficient mixing, whilst at larger scale, turbulent flow is necessary to maintain the quality of the heat and mass transfer, which is obtainable from this intense and random motion of fluid. To achieve plug flow in a tubular reactor, a high velocity flow rate is necessary to generate turbulent mixing; however, this causes a reduction in the RT, which could be insufficient for completion of the reaction or polymorphic transformation. An alternative strategy to maintain sufficient mixing at larger scale is to employ segmentation into the flow based on the premise of immiscibility of different media (Figure 1.23), which allows plug flow conditions to be achieved irrespective of flow rate. Examples of segmented flow reactors are discussed in this work.

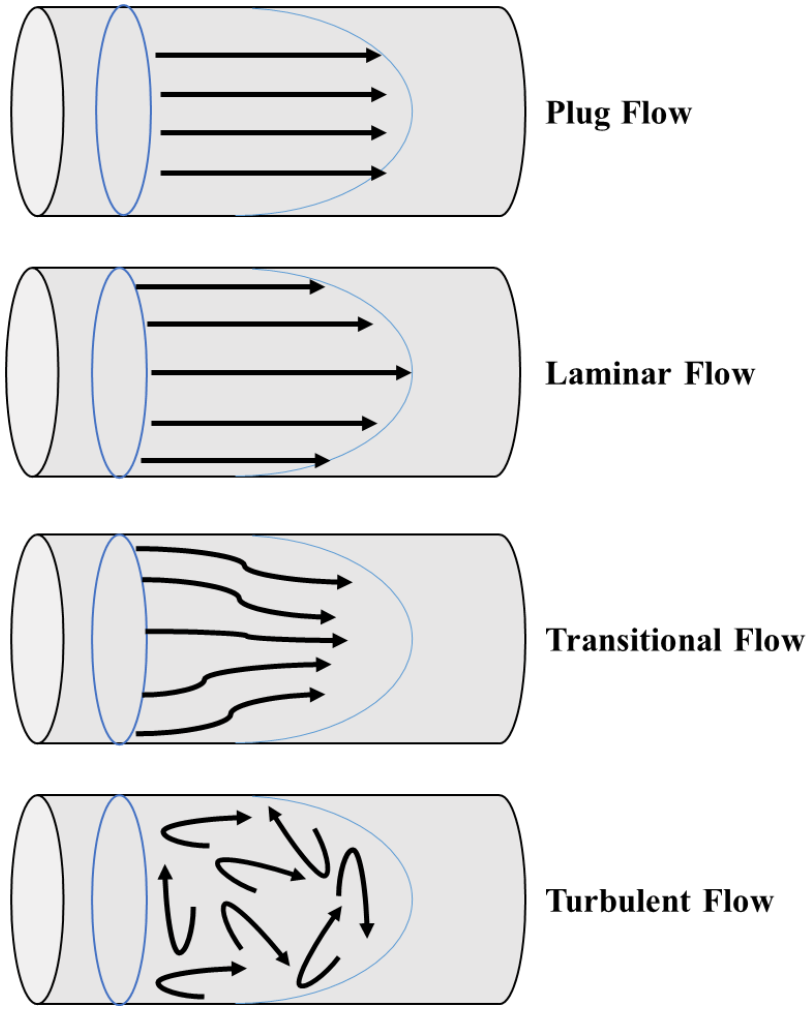

Figure 1.22 – Fluid flow profiles for the different types of fluid flow: plug flow, laminar flow, transitional flow and turbulent flow.

$$R_e = \frac{\rho v d}{\mu}$$

Equation 1.6 – Reynold's number, R_e, where ρ – density of the fluid (kg m^{-3}), υ – net flow velocity (m s^{-1}), d – diameter of the tube (m) and μ – dynamic viscosity (kg m^{-1} s^{-1}).

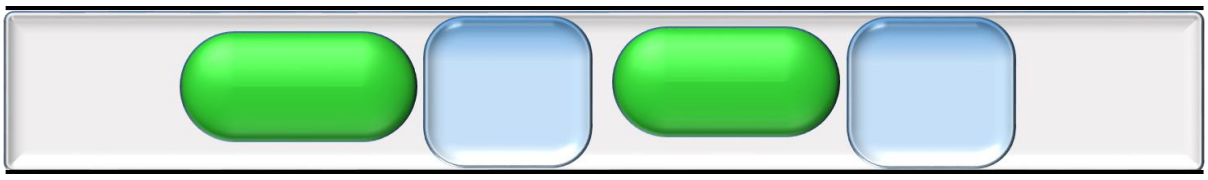

Figure 1.23 – Segmented flow comprising three immiscible media: media 1 (green), media 2 (blue) and media 3 fills the inside of the tubing (off-white).

Table 1.4 – Scale of reactor and corresponding flow regime.[63]

Scale	Characteristic size (m)	Flow regime
Nano	10^{-7}-10^{-9}	Laminar
Micro	10^{-7}-10^{-5}	Laminar
Meso	10^{-5}-10^{-3}	Laminar
Macro	10^{-3} and larger	Turbulent

1.4 Aims of Research

This work will focus on solid-state molecular materials discovery and crystallisation in a manufacturing context. These materials discovery and delivery methodologies were developed across the areas of flow crystallisation, materials science, analytical chemistry and reactor engineering. This research is relevant to the development of new pharmaceutical formulations with enhanced physical properties and continuous processing methods to manufacture these high value materials in an efficient, scalable and cost-effective manner.

The area of continuous crystallisation is in its infancy, with relatively limited understanding into how crystallisation occurs in a flow environment and thus its potential capabilities are also unknown. This PhD project has implemented flow crystallisation platforms at various beamlines on the Diamond Light Source (DLS) synchrotron. The major benefit with synchrotron studies is that the high intensity available for data collection times on these beamlines makes it possible to measure evolving crystalline materials as they grow in the reactor, allowing *in situ* characterisation to be carried out in flow as a function of crystallisation time. The pivotal importance of this is that online X-ray diffraction (XRD) analysis will facilitate this augmented understanding of crystallisation processes in a flow environment that the pharmaceutical industry requires, where presently understanding of the crystallisation process through diffraction is generally limited to analysis of the final crystalline product.

The project presented in this thesis looks at the development of capabilities for *in situ* diffraction of flow processes at Diamond Light Source (DLS), using segmented flow crystallisation platforms known as the KRAIC-D (Kinetically Regulated Automated Input Crystalliser – for Diffraction) and KRAIC-S (Kinetically Regulated Automated Input Crystalliser – Single Crystal). The design of these continuous platforms were developed and optimised for implementation on the Diamond beamlines I11 (High Resolution Powder Diffraction) and I19 (Small Molecule Single Crystal Diffraction). Studies of the crystallisation

of highly polymorphic and pharmaceutically relevant model systems were investigated in the KRAIC-D and KRAIC-S platforms both offline and online.

Another area of research presented in this thesis is the use of crystal engineering for the discovery of new multi-component materials, notably co-crystals of the profen family, using a range of crystallisation methods and techniques to evaluate the physical properties of these novel materials compared to their constituent profen API target.

Chapter 2 – Theory of Diffraction Methods

2.1 X-ray Crystallography

Knowledge of chemical structure is the fundamental basis to understanding a material's behaviour; in the solid state, it is also vital to understand the crystal structure. The study of crystal structure is termed 'crystallography', a fundamental analytical technique for structural determination of molecular materials.[75]

The technique of X-ray crystallography relies on the fact that distances between atoms in a molecule are of the same magnitude as the wavelength of X-rays, which are of the order of magnitude 1 Å. X-rays are diffracted by electrons within the atoms in the crystal structure and thus the resulting diffraction pattern allows for the relative position of atoms and the bonding behaviour between the different types of atoms in the molecular structure to be determined.[75, 76] X-ray diffraction analysis can be carried out using a range of diffraction techniques, most notably powder X-ray diffraction (PXRD) and single crystal X-ray diffraction (SCXRD), which comprise the diffraction analysis presented in this thesis.

2.1.1 The Crystal

A crystal is defined as a solid comprising of atoms or molecules, which are arranged in a systematic repeating manner that extends in three dimensions, where long-range order is exhibited throughout the solid. This repetition is effectively infinite on the atomic scale. This long-range order is also the origin of a number of well-defined properties of crystals, which allows for such properties to be designed in the crystallisation process. The building blocks are arranged symmetrically to maximise the level of interactions between the molecules, stabilising the crystal. The arrangement of the building blocks present within the crystal also affects the macroscopic crystal shape, known as morphology. The ordering of molecules of a particular substance can vary within the solid state, leading to the phenomenon of polymorphism. Both morphology and polymorphism are of pivotal importance within the crystallisation process in ensuring the desired physicochemical properties are achieved.[11, 75]

2.1.2 The Unit Cell

The unit cell is the simplest repeating unit that reflects the long-range order achieved in a crystal lattice. The unit cell can comprise a single molecule, part of a molecule, or a motif comprising of two molecules or more. The crystal lattice is built by displacements of the unit cell in three

dimensions. Restrictions on the unit cell parameters (Figure 2.1), with spatial dimensions (*a*, *b*, *c*) and angles (α, β, γ) leads to the seven crystal systems (Table 2.1 below).

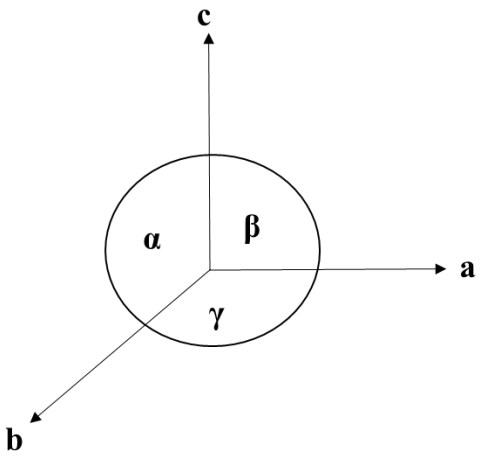

Figure 2.1 – Unit cell parameters labelled on unit cell axis.

In a crystal lattice, comprising of an ordered array of atoms, ions or molecules, a reference point can be selected and all points identical to this reference point are considered lattice points. All lattice points possess the same surroundings and their position relative to the repeating pattern / motif is identical, assuming that these points are in the bulk of the crystal and not at the crystal surface (Figure 2.2).[75, 77, 78]

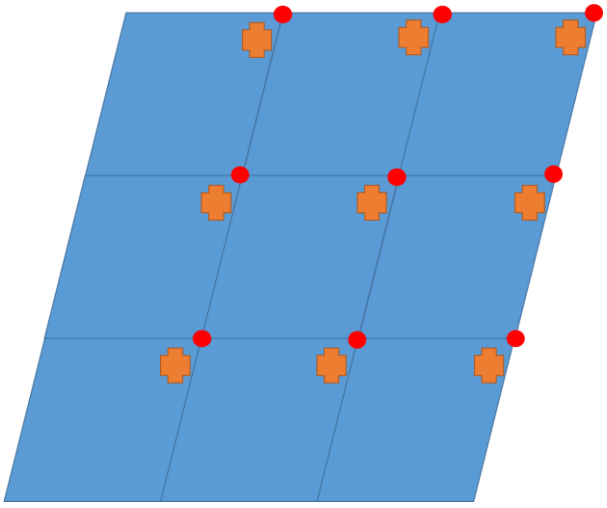

Figure 2.2 – A repeating array of lattice points found in a crystal lattice, where the orange cross represents a molecule and the red points are the lattice points, shown in two dimensions.

The arrangement of lattice points within the unit cell gives rise to four lattice types. Unit cells with lattice points only at the corners of the unit cell are referred to as Primitive (P). It is also

possible for lattice points to be positioned in the centre and on the faces of unit cells, leading to Body-Centred (I), Base-Centred (C) and Face-Centred (F) lattice types (Figure 2.3). These cell centrings lead to different numbers of lattice points per unit cell. The four lattice types combined with the seven crystal systems lead to fourteen unique Bravais lattices.

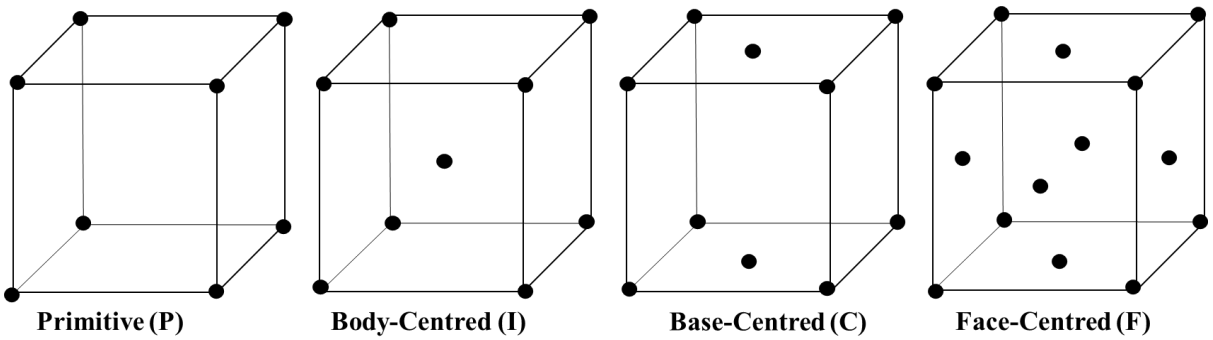

Figure 2.3 – Four lattice types: Primitive (P), Body-Centred (I), Base-Centred (C) and Face-Centred (F).

Table 2.1 – The seven crystal systems, ordered from highest to lowest symmetry.

Crystal System	**Unit Cell Parameters: Restrictions on Unit Cell**		**Lattice Types**
Cubic	$a = b = c$	$\alpha = \beta = \gamma = 90°$	P, I, F
Hexagonal	$a = b \neq c$	$\alpha = \beta = 90°$ $\gamma = 120°$	P
Trigonal (Rhombohedral)	$a = b = c$	$\alpha = \beta = \gamma \neq 90°$	P
Tetragonal	$a = b \neq c$	$\alpha = \beta = \gamma = 90°$	P, I
Orthorhombic	$a \neq b \neq c$	$\alpha = \beta = \gamma = 90°$	P, I, F, C
Monoclinic	$a \neq b \neq c$	$\alpha = \gamma = 90°$ $\beta \neq 90°$	P, C
Triclinic	$a \neq b \neq c$	$\alpha \neq \beta \neq \gamma$	P

2.1.3 Crystal Symmetry

Symmetry also exists inside the unit cell, leading to the concept of space groups that describe the spatial symmetry of molecules within the unit cell of a crystal lattice. The unit cell is generated from smaller asymmetric units related to one another by a combination of symmetry operations. There are six symmetry element types, which can be classified into translational and non-translational symmetry elements. There are four types of non-translational symmetry operations, which include rotation about an axis (*n*-fold = 2, 3, 4 and 6), reflection through a mirror, inversion through an inversion centre and rotary-inversion involving the rotation about an axis and inversion through a point (*n*-fold = $\bar{1}$, $\bar{2}$ and $\bar{3}$). The translational symmetry operations are compound operations, which comprise of a translation and non-translational symmetry element, which includes reflection or rotation. A glide plane involves a translation

followed by a reflection, whereas a screw axis involves a translation followed by a rotation operation. There are 230 unique space groups, arising from a finite number of possible symmetry element combinations, which are unevenly distributed across the fourteen Bravais lattices.[78, 79]

2.1.4 Lattice Planes

Two-dimensional planes (lattice planes) can be defined within the unit cell, in terms of their intercepts (*x, y, z*) with respect to the three cell axes (*a, b, c*), which gives insight into the orientation of a plane. The Weiss notation describes these points of interception, where these indices have values of integers or fractions of unit lengths. If a plane runs parallel to *a*, *b*, or *c*, the lattice plane does not intercept the particular axis and thus the Weiss notation is described by infinity, ∞. A more convenient notation, which unlike the Weiss indices does not contain fractions or infinities, is the use of Miller indices (*h, k, l*). Miller indices are related to Weiss indices, by a reciprocal relationship with any fractions cleared. For example, the plane intersecting the unit cell edges at *a*/2, *b*/2, *c*/2 would have Miller indices (2, 2, 2) (i.e. *a*/*h*, *b*/*k*, *l*/*c*). A group of lattice planes are each separated by the same spacing, known as the *d*-spacing and are situated parallel to each other. These lattice planes are described by the same Miller (*h, k, l*) set and are referred to as a family of crystal planes *hkl* of characteristic spacing d_{hkl}.[76]

2.2 Diffraction of X-rays by crystals

2.2.1 Generation of X-rays

The generation of X-rays may be achieved by accelerating electrons through a potential difference of 40-60 kV and colliding the electrons with a water-cooled metal anode target. These electrons are initially generated from a heated filament supplied by an alternating current. The majority of the kinetic energy of the electrons is wasted as heat, whilst a small proportion generates X-rays by collision with the metal atoms within the metal target.

X-rays emerging from a laboratory source are generated in an evacuated X-ray tube, in which collision of these high-energy electrons upon the metal target causes ionisation of an electron from a core atomic orbital. Subsequently, an electron from an excited state can lose energy to replace this core level electron, the energy difference between the electron in the higher level orbital and the core level is characteristic of the element used in the anode; the most frequent characteristic radiation used comes from the K_α and K_β transitions. These X-rays possess characteristic energies and are generated alongside a continuous spectrum of white radiation.

Usually monochromatic X-rays are employed and the K_α wavelength is selected preferentially. The X-ray wavelengths generated are characteristic of the metal of the anode target; the most common metals employed for X-ray tubes are copper (Cu-K_α) and molybdenum (Mo-K_α), with wavelengths of 1.5418 Å and 0.7107 Å respectively.[75, 80]

2.2.2 Scattering of X-rays by crystallographic planes

X-ray diffraction is widely used to characterise the structure of crystalline solids. X-ray diffraction employs the principle that in order to 'see' an object, the wavelength of the light radiation being utilised must be of similar magnitude to the size of the object. X-ray wavelengths (of the order of Angstroms (Å)) coincide with the order of magnitude for interatomic spacings, meaning that X-rays are the suitable choice for probing the internal structure to 'see' crystalline solids at the atomic scale.[76]

X-rays are scattered by electron clouds, whereby the strength of the scattering varies with the number of electrons present, relating to the atomic number of the element. A crystal of good quality yields a diffraction pattern of spots with varied intensity, produced by the scattering of X-rays. The diffraction pattern exhibits three features, which provide information on the properties of the crystal structure. The geometry of the pattern of spots gives insight to the lattice and unit cell geometry of the crystal. The diffraction pattern also exhibits symmetry, in both the positions of the diffraction spots, but more notably in the diffraction intensities of the spots in the pattern, which relates directly to the symmetry of the unit cell and thus gives information on the space group of the crystal lattice. Great variation in intensities of individual spots is apparent; these intensities hold all the available information about the relative positions of the atoms in the molecules that build up the crystal lattice.[75]

The underlying principle of X-ray diffraction geometry is expressed in Bragg's law, which determines the conditions by which diffraction is observed. Bragg's law regards X-ray diffraction as a reflection from sets of parallel lattice planes within the three dimensional lattice. The orientations of these lattice planes are described by the Miller indices: *h, k, l*. The perpendicular distance between the parallel lattice planes is denoted by the *d*-spacing, which can be mathematically related to the Miller indices (for an orthogonal unit cell with $\alpha = \beta = \gamma = 90°$) by Equation 2.1.

$$\frac{1}{d_{hkl}^2} = \frac{h^2}{a^2} + \frac{k^2}{b^2} + \frac{l^2}{c^2}$$

Equation 2.1 – *d*-spacing for an orthogonal unit cell represented in terms of Miller indices (*h*, *k*, *l*) and unit cell axes (*a*, *b*, *c*).

W. L. Bragg determined the conditions required for diffraction of X-rays and found that diffraction can be considered to behave like reflection from parallel planes constructed through lattice points, when the crystal is appropriately orientated in the X-ray beam. The angle of the incident X-ray beam (θ) must equal the angle of the 'reflected' X-ray beam for the diffraction to emerge from the scattering of the X-rays. In addition, to ensure that the waves from adjacent parallel planes will emerge in phase and constructively interfere (Figure 2.4), the path difference between X-ray beams must be an integral number (n) of the wavelength of the X-ray beam (λ), where θ is the angle of incidence on the lattice plane (Equation 2.2).

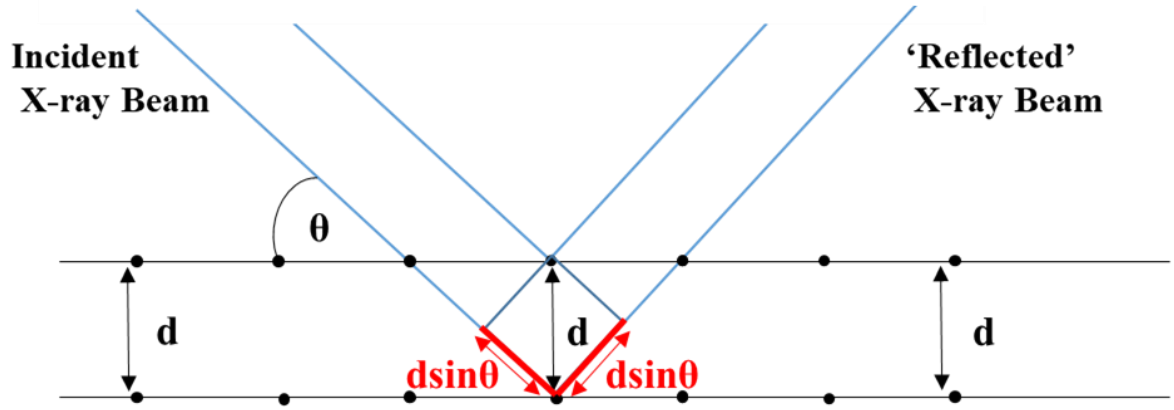

Figure 2.4 – The Bragg condition for the diffraction of X-rays from a set of parallel crystal planes.

$$n\lambda = 2d_{hkl}sin\theta$$

Equation 2.2 – Bragg's equation: the path difference requirement to observe X-ray diffraction.

2.2.3 The Reciprocal Lattice

An alternative approach to describing the 'direct' crystal lattice is to consider the reciprocal lattice. Instead of a set of parallel crystallographic planes *hkl*, situated in a particular orientation, which are separated by a particular *d*-spacing, the reciprocal lattice is built in reciprocal space through the use of vectors. The vectors normal to these families of crystallographic planes *hkl* are represented by lengths d^*_1 and d^*_2, which are inversely related

to the *d*-spacings d_1 and d_2 respectively (Figure 2.5). A family of crystallographic planes is therefore represented by a reciprocal lattice point positioned at the end of the reciprocal lattice vector of length *d** and whose direction relative to the reciprocal space origin, O is given by the normal to the corresponding *hkl* lattice plane. Each of the reciprocal lattice vectors represents a reflection from a diffraction pattern arising from a specific set of Miller planes. Assuming all of these vectors are related by the common reciprocal space origin, then the corresponding reciprocal lattice points will form a regular three dimensional array, known as the reciprocal lattice.[81]

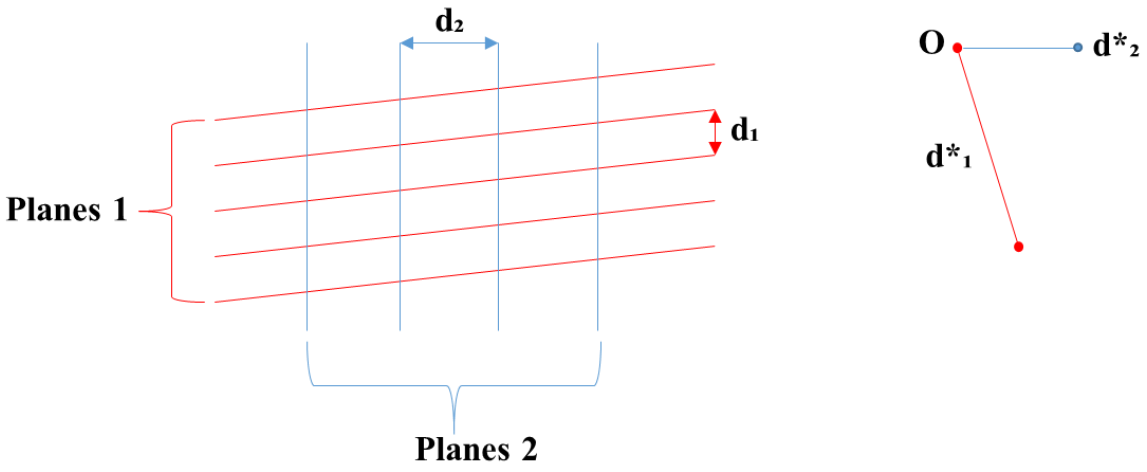

Figure 2.5 – Two families of parallel crystallographic planes *hkl* labelled as planes 1 and 2 separated by *d*-spacings of d_1 and d_2 respectively (left) and the normal to these families of planes from a common origin, O with lengths d^*_1 and d^*_2.[81]

The reciprocal lattice vector is a diffraction or scattering vector, containing information on both the magnitude of the interplanar *d*-spacing and the orientation of the Miller planes, which confirms whether the family of planes are in a diffracting position. The scattering vector bisects the incident and diffracted beams. Rearrangement of Bragg's Law (Equation 2.2), highlights a directly proportional relationship between the sine of the diffraction angle, θ, and the inverse of the *d*-spacing ($\frac{1}{d_{hkl}}$). As a diffraction pattern exists in reciprocal space, whilst a unit cell exists in real space, a large unit cell with larger d-spacings will have a compressed diffraction pattern.[81]

The crystal lattice in direct space is described by *a*, *b*, *c*, the corresponding reciprocal lattice is described by *a**, *b**, *c**. The relationship between direct and reciprocal lattice vectors is described in Equation 2.3.

$$\boldsymbol{a}^* = \frac{\boldsymbol{b}\times\boldsymbol{c}}{\boldsymbol{V}} \qquad \boldsymbol{b}^* = \frac{\boldsymbol{c}\times\boldsymbol{a}}{\boldsymbol{V}} \qquad \boldsymbol{c}^* = \frac{\boldsymbol{a}\times\boldsymbol{b}}{\boldsymbol{V}}$$

Equation 2.3 – The mathematical relationship between direct (*a*,*b*,*c*) and reciprocal lattice (*a**,*b**,*c**), with unit cell volume, V.

2.2.4 The Ewald construction

The Ewald construction is a geometrical expression of Bragg's Law, which can be used to determine when the Bragg diffraction conditions are satisfied for a crystallographic set of *hkl* lattice planes (Figure 2.6, left). In the Ewald construction, the limits of the Ewald sphere (E) are define by a sphere radius of $\frac{1}{\lambda}$, where λ is the wavelength of the incident X-ray beam passing through the middle of the sphere, with a crystal situated at the centre of sphere (E). The origin of the reciprocal lattice, O, is positioned at the point of intersection of the limits of sphere (E) with the emerging direct X-ray beam. The reciprocal lattice vector is perpendicular to the set of *hkl* crystallographic planes and has a magnitude of $\frac{1}{d_{hkl}}$. The conditions required for diffraction to be observed at point P are to rotate the reciprocal lattice about point O until a reciprocal lattice point cuts the sphere at point P; the magnitude of this distance OP is the magnitude of the normal to the set of the *hkl* lattice planes *d**. A limited number of reciprocal lattice points exist around sphere (E) corresponding with the limited number of observed reflections. The rotation of the Ewald construction about the reciprocal lattice centre O, leads to the 'limiting sphere' (L) (Figure 2.6, right), whose radius is the diameter of sphere (E), $\frac{2}{\lambda}$.

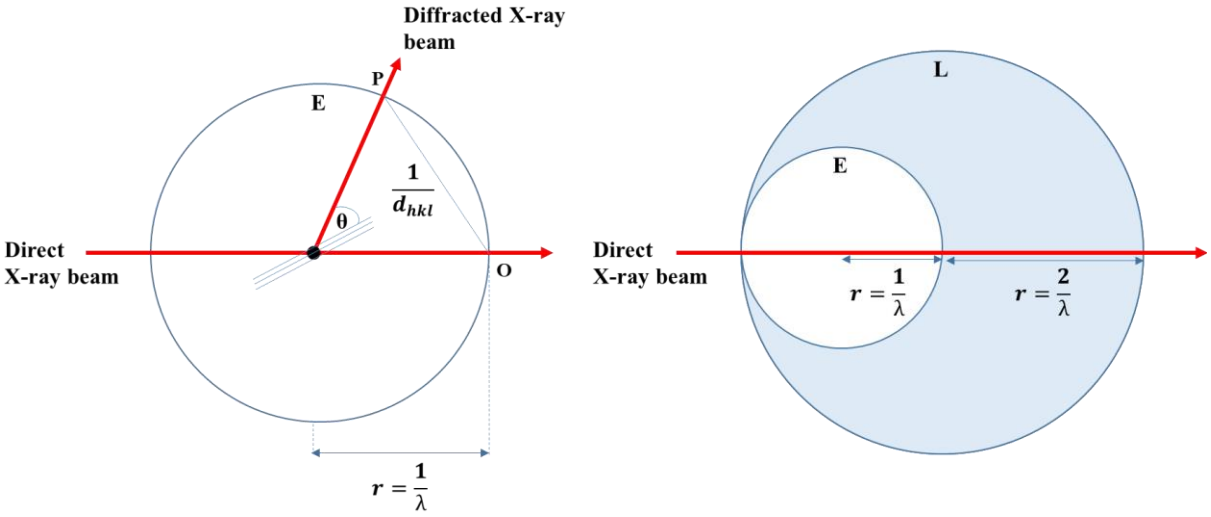

Figure 2.6 – The Ewald construction (E) (left) and the limiting sphere (L) of observable reflections (right).[81]

2.2.5 Scattering of X-rays by atoms

The scattering of X-rays by a crystal is from the electrons in the atoms, whose extent is of the same order as the X-ray wavelength. The path difference between X-rays scattered from different parts of the same atom thus results in destructive interference, leading to an angular dependence of the scattering as the X-rays become increasingly out of phase at higher scattering angles. This atomic scattering is expressed by the atomic scattering factor, f described in Equation 2.4, which considers the sum of the electrons from an atom, the contribution of which varies with scattering angle, θ (Figure 2.7).

$$\text{Atomic scattering factor, } f = \frac{Amplitude\ scattered\ by\ the\ atom}{Amplitude\ scattered\ by\ a\ single\ electron}$$

Equation 2.4 – Expression for the Atomic scattering factor, *f*.

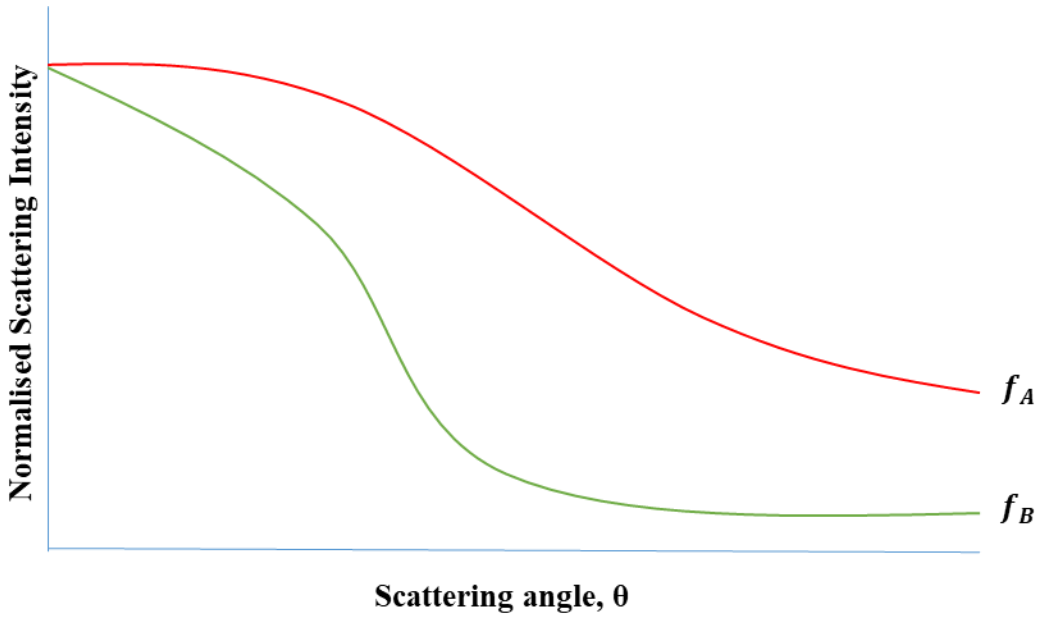

Figure 2.7 – Scattering factor functions f_A and f_B from atoms A and B, showing the relative fall-off of scattering with angle, θ for a heavier (A) and lighter (B) atom.

The intersection of the atomic scattering factor at the y-intercept, coinciding with a scattering angle of zero, indicates that X-rays are in phase and thus the atomic scattering amplitude equates to the atomic number of the atom, Z.[80]

The rate of fall off in scattering intensity with scattering angle is also impacted by the thermal motions of atoms, which effectively increases the extent of the electron density depending on the extent of the thermal motions and the type of atom; the associated thermal parameters

describing the atomic vibrations are an important aspect of a crystal structure determination. As can be seen in Figure 2.7, the fall-off of scattering with angle is more pronounced for lighter than heavier atoms; this, together with the intrinsically weaker scattering of atoms with fewer electrons, explains the difficulty that can be experienced in locating a hydrogen atom resulting from the single electron within the electron cloud as its X-ray scattering ability is low.

2.2.6 A single crystal diffraction experiment

In a single crystal X-ray diffraction experiment, a crystal is mounted onto a goniometer on a diffractometer and the crystal rotated about a fixed point, whilst being immersed in the X-ray beam. This rotation facilitates the maximum number of possible reciprocal lattice points to cut the Ewald sphere, resulting in the number of observable reflections to be maximised. This extent of rotation is achieved using a goniometer on a four-circle diffractometer set to Eulerian geometry with three possible axes of crystal rotation (ϕ, χ, ω). A fourth axis of rotation is achieved by a sweep of the detector along a 2θ vertical range used to observe the diffracted X-rays (Figure 2.8).[82]

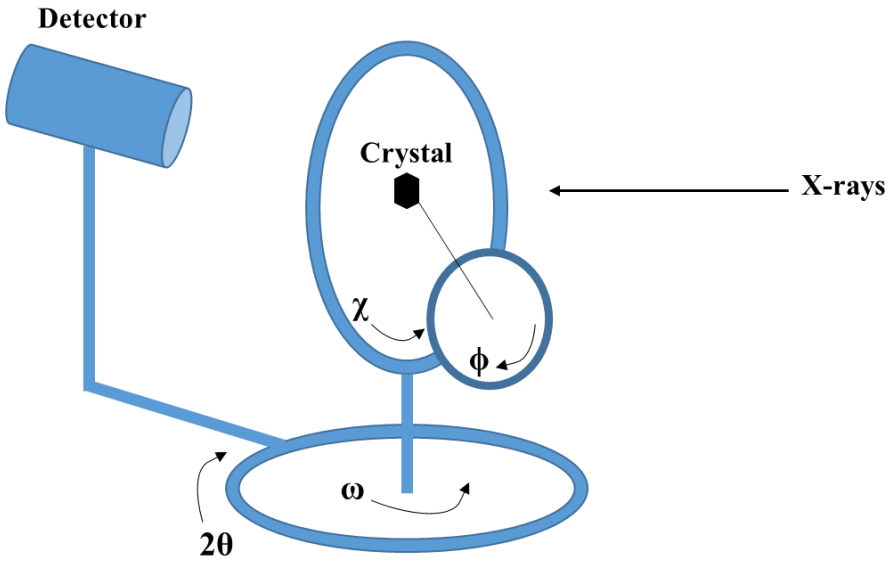

Figure 2.8 – Schematic representation of a four-circle goniometer with Eulerian geometry.

X-ray diffraction for structural determination *via* single crystal X-ray experiments is typically measured at low temperatures, whereby the single crystal is typically cooled to 100 K or 150 K by a cold nitrogen gas stream provided by a device such as a Cryostream. Low temperature sample environment is used for structural determination to reduce the thermal motion of atoms, which supresses the reduction in fall off of the atomic scattering factor with scattering angle.

A range of detectors can be employed to collect the diffraction data, including charge coupled devices (CCD)[83] and PILATUS hybrid pixel array detectors.[84] In a two-dimensional (2D) diffraction pattern produced from a single crystal experiment, the diffracted X-rays are observed as diffraction spots, which contain information about the crystalline material under analysis.

2.3 Crystal structure determination using X-ray diffraction

Measuring the diffraction of X-rays from a crystalline material, allows for the crystal structure to be determined, on the premise that the diffraction pattern is the Fourier Transform of the crystal structure.

2.3.1 Pattern geometry

2.3.1.1 Unit cell determination

The arrangement of the diffraction spots on a diffraction image is related to the geometry of the unit cell and the symmetry of the crystal. During cell indexation, the unit cell is determined through use of the orientation matrix, which includes information on both the (reciprocal) unit cell (through the determined d_{hkl}* values) and the diffractometer geometry. Using the diffraction positions of a relatively small number of reflections and their geometric relationship, the unit cell can be determined from a limited number of diffraction scans.[78] Further discussion of the orientation matrix is detailed in Chapter 5.

2.3.1.2 Symmetry and Space Group determination

Once the unit cell parameters have been determined, the crystal symmetry can usually be selected. The crystal symmetry and space group may be assigned by comparing the intensities of reflections which are equivalent by symmetry,[75] also taking into account the systematic absences in the diffraction pattern.

These systematic absences arise as a result of the fact that in the presence of certain symmetry elements, scattering due to symmetry related parts of the structure combine out-of-phase, resulting in reflections with zero intensity, such that they are considered ‘absent’. The absence of certain reflections can be attributed to lattice centring, which are referred to as general absences. For a primitive lattice type, no general absences arise, whilst reflections are absent in an I-centred lattice when the sum of $h + k + l$ is odd, in a B-centred lattice when $h + l$ is odd,

in a C-centred lattice when the sum of $h + k$ is odd and in an F-centred lattice when *hkl* integers are either all odd or all even integers.

Systematic absences in selected parts of the diffraction pattern occur due to the presence of the translational symmetry elements of glide planes and screw axes in the crystal structure, which result from the translation components of these symmetry elements. For example, the presence of a 2_1 screw axis along *b* means that reflections will be absent from the *0k0* planes when *k* is an odd integer.[76]

2.3.2 Reflection intensities

This relationship between diffraction pattern spots and the position of the atoms in the unit cell can be defined through information about the reflection intensities and how these relate to the electron densities of the atoms. In data collection, the intensities, I_{hkl}, of the diffracted X-ray beam are measured at reciprocal-lattice points that arise from each set of Miller planes (*hkl*)). The diffraction pattern produced from experimental methods is related to the arrangement of the atoms in the unit cell of the crystal through Fourier transformation, whereby the Fourier transform (FT) defines the important quantity known as the structure factor, F_{hkl}. The magnitude of the structure factor, F_{hkl} is equal to the square root of the intensity of each reflection, I_{hkl} (Equation 2.5). The structure factor, F_{hkl} is defined as the resultant of the waves scattered by all atoms in the unit cell in the *hkl* direction and is dependent on the scattering factor f_j and position (x_j, y_j, z_j) of each atom (Equation 2.6).

$$I_{hkl} = (F_{hkl})^2$$

Equation 2.5 – Square relationship between the intensity, I_{hkl} and structure factor, F_{hkl}.

$$F_{hkl} = \sum_{j=1}^{j=n} f_j cos2\pi\left(hx_j + ky_j + lz_j\right) + i\sum_{j=1}^{j=n} f_j sin2\pi\left(hx_j + ky_j + lz_j\right)$$

Equation 2.6 – Mathematical relationship between the structure factor, F_{hkl} and the atomic scattering factor, f_j, atomic positions, x_j, y_j, z_j of each atom and the Miller indices *hkl*.

Fourier transformation of the structure factor, F_{hkl} (Equation 2.7) in turn produces the electron density map, which allows the discovery of the atom locations in terms of electrons per cubic Angstrom (e A^{-3}) at all locations *x*, *y* and *z* in the unit cell, where *V* is the volume of the unit cell.[76] Atoms with higher atomic numbers will consequently be more prominent and be more

accurately determined within the unit cell. The structure factor for reflection *hkl* contains information on both the amplitude and phase of a wave diffracted from planes of the single crystal.[17]

$$\rho(x,y,z) = \frac{1}{V} = \sum_h \sum_k \sum_l F_{hkl} e^{-2\pi i(hx+ky+lz)}$$

Equation 2.7 – Mathematical relationship between the electron density ρ_{xyz} and the calculated structure factor, F_{hkl}^{calc}, atomic positions, x_j, y_j, z_j of each atom, the Miller indices *hkl* and volume of the unit cell, *V*.

Equation 2.5 gives rise to the phase problem: the experiment measures I_{hkl} and from this the magnitude of F_{hkl} can easily be obtained. However, the sign (+/-) or phase of the structure factor cannot be obtained from experimental measurements. The phase problem must be overcome as a lot of important information for the determination of electron density is contained within the phase. Each F_{hkl} value contains information about the positions of all atoms present from all symmetry related objects within the unit cell as stated by the space group. In order for the phases of the structure factors to be calculated, atomic positions must be known. Determination of these atomic positions can be carried out by a number of methods, including Direct methods and Patterson methods. The method should be chosen according to the atomic masses of the atoms present in the unit cell. For instance, for a structure containing heavy atoms, such as an organometallic crystal, the Patterson method approach should be adopted, whereas, for a purely organic molecule, direct methods should be chosen. It should be noted that direct methods could also be employed for heavy atom structures.[76]

In the Patterson methods approach, the observed structure factors are squared to produce a Patterson map (Equation 2.8), which does not require knowledge of the phases. A Patterson map contains peaks that correspond to vectors between pairs of atoms and shows the positions of atoms relative to each other. These peaks are proportional to the square of the atomic numbers of the atoms present, and so vectors between the heavier atoms will dominate the Patterson map allowing atomic positions to be determined for symmetry related heavy atoms.

$$P_{xyz} = \frac{1}{V} \sum_h \sum_k \sum_l (F_{hkl})^2 cos2\pi(hx + ky + lz)$$

Equation 2.8 – Mathematical relationship between the electron density ρ_{xyz} and the experimental structure factor, F_{hkl} , atomic positions, x_j, y_j, z_j of each atom and the Miller indices *hkl* and volume of the unit cell, *V*.

Direct methods are a trial and error method, whereby the phases of some of the structure factors are estimated according to the relationship between the phases of certain groups of reflections. If some strong reflections are assigned certain phase values this has implications for other strong reflections present. A restriction on the electron density is then imposed ($\rho(x,y,z)$ must be positive everywhere) and the resulting trialled phases from different permutations of the assigned phase values input into Equation 2.7 to produce an electron density map. The electron density map usually contains a recognisable fragment; the positions of this fragment can be input into the structure factor equation (Equation 2.6). The peaks in the electron density map are then interpreted to form an initial structural model; to generate approximate phases. Once this initial step is complete most non-hydrogen atoms have been accounted for and this process is then iterated (Fourier recycling) to generate all the atoms in the structure. Direct methods is best used for structures where the atoms present have similar scattering characteristics.[76]

2.4 Crystal structure refinement

Fourier recycling methods are used together with structural refinement to locate any missing atoms and to optimise the determined parameters for all atoms. For good quality data this should include the hydrogen atoms within the structure.

Fourier analysis on the calculated values of the structure factors produces an electron density map. This calculated electron density map is subtracted from the electron density map obtained from experimental data. From this, any further atomic positions not yet present in the model will appear as contours of electron density. These new atomic positions may now be used to recalculate structure factors and an updated electron density map; this iterative process continues until all atoms have been accounted for.

To minimise errors in the initial structural model, structural parameters, such as atom types, atom positions and displacement parameters require optimisation. Crystal structure refinement is carried out using least squares iterations on F^2. During the refinement process the structure factors resulting from the model (F_c) are compared to those from the experiment (F_o); the aim of the least squares refinement is to minimise the difference between the calculated and observed structure factors by use of a weighting approach (Equation 2.9). In this minimisation, each reflection is assigned a weight (w) reflecting the confidence in the accuracy of the measured intensity. The weight (w) of a reflection is inversely proportional to the estimated variance (σ) of the amplitude of the observed structure factor, F_o (Equation 2.10). Only the

magnitudes of F_o and F_c are compared as the corresponding phases of the structure factors are unknown from the experiment.

$$\sum w(|F_o|^2 - |F_c|^2)^2$$

Equation 2.9 – Least squares iteration comparing the calculated with the observed structure factors F_c and F_o respectively.

$$w = \frac{1}{\sigma^2({F_o}^2)}$$

Equation 2.10 – The weight (w) reflecting the confidence of an observed structure factor.

The progress of the refinement is monitored using the R-factor, a calculation of the agreement between the calculated and observed electron density maps, evaluated through the magnitudes of the structure factors (Equation 2.11). Throughout the refinement process the R-factor will decrease; high quality refinement is typically indicated by an R-factor of less than 5 %.

$$R = \sum \frac{\big||F_{obs}| - |F_{calc}|\big|}{|F_{obs}|}$$

Equation 2.11 – Mathematical relationship between R factor, R and observed and calculated structure factors, F_{Obs} and F_{Calc} respectively.

2.4.1 Constraints and Restraints

The optimisation of structural parameters in order to improve the structural model and reduce the corresponding R-factor may require the use of constraints or restraints. Constraints in least-squares refinement act to reduce the number of parameters involved in the refinement, either by expressing one parameter in terms of others, or by fixing the value of a parameter to a predefined value. For example, when proton disorder is present across a hydrogen bond, in order to refine the ratio of the site occupancy factors for each proton site, their sum is constrained to unity. On the other hand, the addition of restraint information to crystallographic least-squares refinement acts as extra information, leading to an increase in the overall number of observations. Restraints use a minimisation function involving a target value for a parameter which the actual restrained parameter will approach during refinement. For example, restraints may be applied to bond distances.[85]

2.5 Powder X-ray Diffraction (PXRD)

X-ray diffraction analysis can be used to analyse polycrystalline powders, whereby each individual, randomly oriented, crystallite yields its own diffraction pattern, which are superimposed on one another during powder averaging to yield an overall diffraction pattern representative of the bulk sample. Powder X-ray diffraction is usually carried out using a fixed wavelength (λ) method with a varying angle (θ). As powder samples are comprised of many randomly oriented crystallites, on exposure to X-rays, the Bragg condition is satisfied for a number of different *hkl* crystal planes simultaneously. For each diffraction peak the 2θ value is the same, however the direction of the diffracted X-rays will vary. This results in the diffracted X-rays being observed as Debye Scherrer cones, as a result of diffraction occurring from the same *hkl* crystal plane in a number of crystallites.[81] The intensity of these rings of diffraction may vary in intensity due to preferred orientation effects, which increases the intensity of certain peaks; the sample is often rotated during data collection to mitigate this issue. Preferred orientation effects can arise from a powder sample comprised of many plate-like crystals.

The cones or cone slices accessed by the detector are integrated to give the characteristic 1D PXRD pattern of intensity against 2θ (°), containing peaks for reflections from particular *hkl* crystal planes at 2θ positions related to the d_{hkl}, with intensity I_{hkl} (Figure 2.9). The position of peaks in a PXRD pattern are unique to each crystal structure and are determined by the unit cell parameters; these can therefore be used as fingerprinting tools when compared to the peak positions from crystal structures of polymorphic purity.[75, 81]

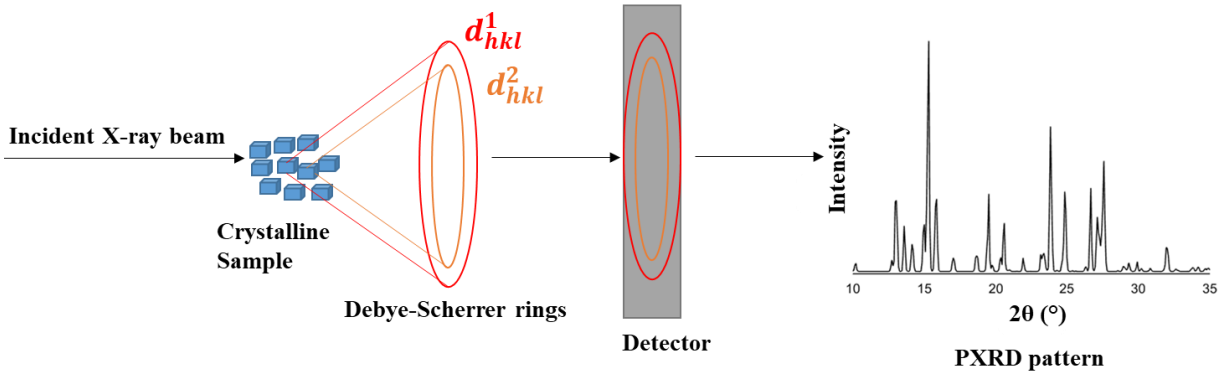

Figure 2.9 – Diffraction of a powder crystalline product, its detection and data conversion to a PXRD pattern.

2.6 Synchrotron Crystallography

Laboratory X-ray sources are appropriate for most offline routine diffraction analysis, however the use of synchrotron radiation at a synchrotron source is necessary for *in situ* X-ray diffraction techniques. Synchrotron radiation comprises electromagnetic radiation spanning the range from infrared (IR) radiation to X-rays, whereby synchrotron sources can generate tunable beams of electromagnetic radiation with intensities defined by 'flux' or 'brilliance' many orders of magnitude more intense than a laboratory source.[86, 87] The exceptionally bright X-ray beams obtainable at synchrotrons facilitates data collection of a quality and resolution not attainable through use of conventional X-ray sources. The brightness accessible at synchrotron sources has been further increased at third generation low-emittance light sources, through use of additional magnets known as insertion devices, such as undulators or wigglers. High brightness is fundamental for low bandpass detection and to achieve high angular and thus d-spacing resolution, whereby closely situated diffraction peaks, or those with weaker intensities, have the opportunity to be resolved.[87]

2.6.1 Synchrotron Radiation at Diamond Light Source (DLS)

Diamond Light Source (DLS) is the national synchrotron in the UK (Figure 2.10), it utilises highly accelerated electrons to produce extremely bright light in the form of intense and highly collimated X-ray beams. The electrons are generated in the electron gun from where they are accelerated to kinetic energies above the MeV range, corresponding to a speed approaching the speed of light, through a series of three particle accelerators, the linear accelerator (LINAC), the booster synchrotron and the storage ring. Once at speed, the electrons are injected in bunches into the storage ring, which is an evacuated ring shaped chamber.

Figure 2.10 – Aerial view of Diamond Light Source.[88]

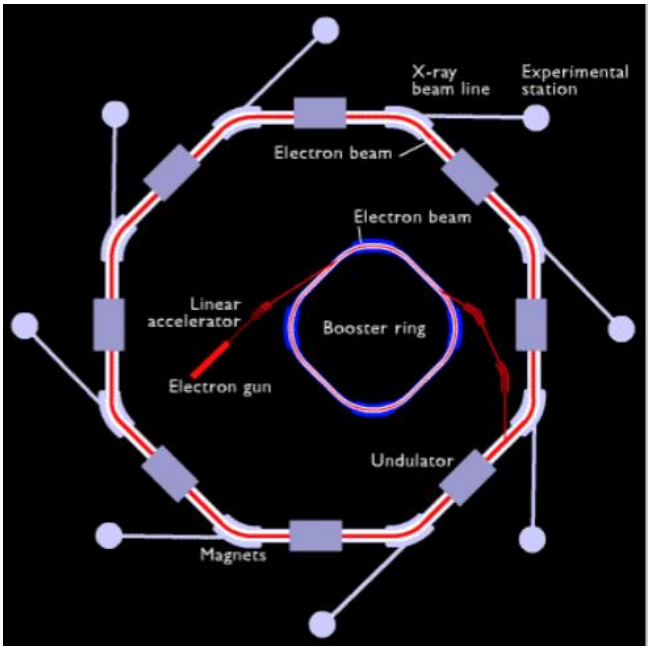

Figure 2.11 – The production of synchrotron X-ray radiation at Diamond Light Source, including the electron gun, linear accelerator, booster ring and electron beam around the synchrotron ring.[88]

The storage ring is not circular, but made of forty-eight straights connected with forty-eight bending magnets, to bend the electron beam. This bending causes the electrons to emit energy in the form of X-rays (Figure 2.11). These magnets work on the principle that if a moving electron intersects a magnetic field, which is perpendicular to the direction of travel, then the electron will experience a force perpendicular to both the direction of travel and the magnetic field. This force generates a centripetal acceleration causing the electron to move along a circular path and emit electromagnetic radiation. Radio frequency (RF) cavities are also present in sections along the storage ring to boost electron energy and momentum that has been lost due to the bending of electrons and electron collisions.

Insertion devices known as undulators or wigglers are also installed on the straight sections of the storage ring at Diamond (Figure 2.12), a third generation synchrotron – these are arrays of magnets that offer enhanced intensity and tunability of the generated X-ray beams. A wiggler can be considered as a series of bending magnets that alternate the direction of travel of the electrons to the left and right, causing a periodically ‘wiggling’ of the electron path. Undulators differ from bending magnets and wigglers, whereby these magnets comprise of alternating low field magnetic poles and thus as the electron beam passes through these magnets these electrons experience a series of inward and outward acceleration where radiation is emitted on each

'undulation'. Downstream of the undulator, the emitted radiation may overlap constructively or destructively, which results in a 'lumpy' spectrum, which consists of a fundamental frequency plus a series of higher harmonics. Undulators therefore can produce very intense single wavelength radiation by magnet parameter tuning.[86]

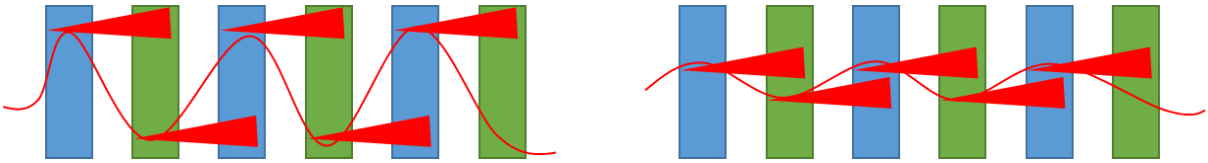

Figure 2.12 – Insertion devices: wiggler (left) and undulator (right) in principle differ only in the size of the excursions from a straight path that these insertion devices force the electrons to execute.[86]

The beamlines run off tangentially to the storage ring containing the bending magnets, whilst the beamlines are positioned parallel to the axes of the insertion devices.[86] A typical beamline set-up comprises an optics hutch, experimental hutch and control room. The synchrotron radiation emitted by the wiggler or undulator initially passes through the optics hutch, which carries out 'tuning' of the radiation by monochromation to the desired wavelength of radiation, whilst also 'focusing' the beam to the desired size and position for a particular diffraction experiment. Monochromation of the synchrotron beam is achieved using two crystal monochromators, whereby one of the crystals uses Bragg's law to filter out a narrow band of radiation, whilst the other redirects the beam in parallel to the incident beam back to its original path.[86] The monochromated beam is focused in both the horizontal and vertical direction using mirrors. The next section of a beamline is the experimental hutch where diffraction of the synchrotron X-rays from a crystalline sample is measured and the final section is the control room where the diffraction experiment is controlled and monitored.[86]

Chapter 3 – Experimental Techniques and Instrumentation

Chapter 3 details the range of techniques and instrumentation used for the preparation and characterisation of the materials under study in this research project in order to achieve the research goals outlined at the end of Chapter 1. This chapter provides a general overview whilst the more specific details are included in an experimental section in each results chapter.

3.1 Materials

The carrier fluid used in the segmented flow crystallisation experiments was a fluorinated perfluoropolyether (PFPE), commercially known as Galden SV110, which was sourced from Solvay.

In Chapter 4, urea (U) and barbituric acid (BA) were purchased from Sigma Aldrich (Steinheim, Germany) and carbamazepine (CBZ) was purchased from Molekula (Darlington, UK). All reagents were used without further purification. Laboratory grade solvents (methanol (MeOH) and ethanol (EtOH)) purchased from Sigma Aldrich were used for all crystallisations.

In Chapter 5, paracetamol (PCM) was purchased from Sigma Aldrich and used without further purification. Laboratory grade isopropanol (IPA) purchased from Sigma Aldrich was used in the solvent mixture 60:40 water:isopropanol (HI) for all crystallisations.

In Chapter 6, the four profen targets were sourced from TCI UK Ltd (Oxford, UK). All co-former molecules and laboratory grade solvents were purchased from Sigma Aldrich. All reagents were used without further purification.

In Chapter 7, ibuprofen (IBU) was sourced from TCI UK Ltd. The isonicotinamide (ISO) co-former molecule and laboratory grade IPA were purchased from Sigma Aldrich. All reagents were used without further purification.

3.2 Solubility and Metastable Zone Width (MSZW) Measurements

In Chapter 6, solubility measurements of the IBU and oxaprozin (OXA) pure target materials in 60:40 HI and acetone (ACE) respectively, a physical mixture of IBU and ISO (1:1 and 1:2 molar ratios) in 60:40 HI, as well as the pre-prepared co-crystal of IBU-ISO in 60:40 HI were carried out.

To establish the ability of a solid to dissolve in a solvent, solubility measurements were carried out, which allow for the concentration / temperature dependence of the solid material in a particular solvent to be understood. Solubility was measured by either turbidity or by visual observation. Turbidity measurements using the Technobis Crystal16® or Crystalline® at 1 mL and 5 mL scale respectively were performed at the University of Strathclyde. The Crystalline® also features particle viewer technology to allow real time imaging alongside the temperature and turbidity measurements. *In situ* images were acquired every minute, allowing for

visualisation of the complete crystallisation process. Visual observation measurements were conducted using the Cambridge Reactor Designs (CRD) Polar Bear Plus apparatus at the University of Bath.

3.2.1 Turbidity

Both the Crystal16® (Figure 3.1) and Crystalline® platforms operate by measuring the transmissivity of a laser through a sample in order to determine clear and cloud points through various heat and cool cycles respectively. The clear points are the temperatures at which the transmission reaches 100 %, marking full dissolution, whilst the cloud points correspond with when the transmission drops off from 100 % as nucleation and subsequent crystal growth occurs.

Solutions of varying concentration were prepared in 1.5 mL and 8 mL vials respectively for insertion into the Crystal16® and Crystalline® platforms. The vials were prepared by weighing a known amount of a pure or physical mixture of the constituent starting components under solubility investigation with 1 mL or 5 mL of solvent for the Crystal16® and Crystalline® platforms respectively. A concentration range for each system was investigated to yield a solubility curve. Vials were cycled through temperature cycles, where samples were heated from 20 °C to 70 °C and then cooled from 70 °C to 5 °C, *via* a Peltier thermoelectric device, using a heating and cooling rate of 0.3 °C min^{-1} with magnetic bottom stirring of 800 rpm to provide agitation to the system.

Figure 3.1 – The Technobis Crystal16®.

For each concentration of a solid in solvent system, one replicate was conducted and the average cloud and the average clear point calculated across the three heat-cool cycles, to yield a single cloud and a single clear point temperature at that particular concentration. The clear and cloud points denoted by the red and green circles respectively, mark the intersection of the

temperature *versus* time and transmission (%) *versus* time plots superimposed in Figure 3.2. The clear points denote the solubility points leading to a solubility curve when investigated over a concentration range. The region between the cloud curve and clear curve is referred to as the metastable zone (MSZ).

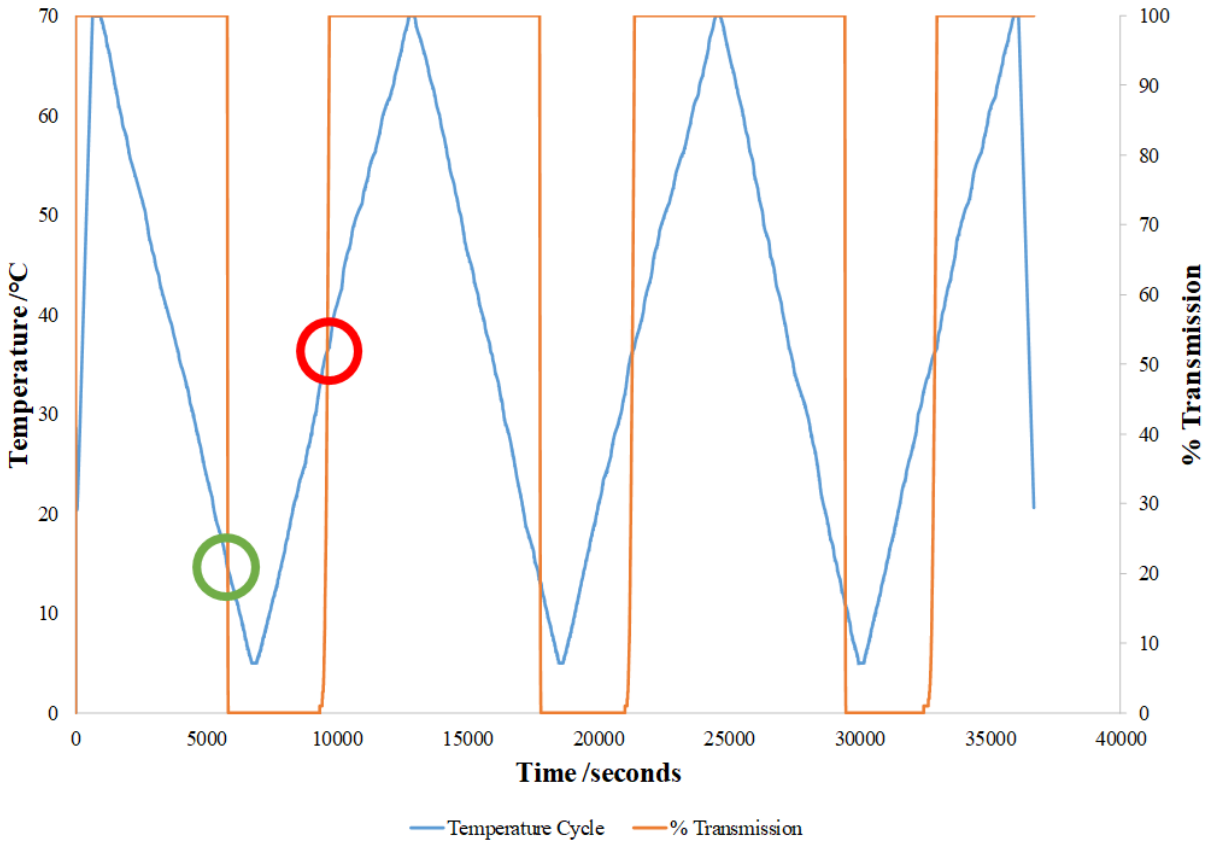

Figure 3.2 – Temperature (°C) *versus* time (seconds) plot (blue) superimposed with transmission (%) *versus* time (seconds) plot (orange) for repeat heat-cool cycles in the Crystal16® and Crystalline® platforms. Clear and cloud points are highlighted by red and green circles respectively.

3.2.2 Visual Observation

For these experiments, the CRD Polar Bear Plus crystalliser was used to allow for controlled heating and mixing of the sample to ascertain the dissolution temperature when a known amount of solid was added to the solution (Figure 3.3). A 50 mL round bottom flask with a working volume of 20 mL of the chosen solvent was allowed to equilibrate at 0 °C for 10 minutes before any solid was added. Magnetic bottom stirring was set to a stirring rate of 700 rpm. Once the solvent had equilibrated at 0 °C, small increments of solid of known mass were added and allowed to dissolve and the corresponding temperature noted. The solution was heated at a rate of 0.2 °C min^{-1} and further increments of solid were added to the solution.

As the temperature of solution increased the additional solid dissolved and the corresponding temperature of solid dissolution was noted before subsequent increments of solid were added. This process was repeated until the solution reached a temperature of 50 °C. The masses added were used to calculate the concentration of solution and this, coupled with the observed dissolution temperatures, yielded solubility curves of concentration *versus* temperature. In cases where the solution turned into a cloudy emulsion as the concentration was increased (similarly observed with in-line cameras during turbidity measurements in the Crystalline®) the solubility measurements were stopped before the 50 °C final heating temperature was reached. The visual observation experiments were repeated three times for each solid in solvent combination to ensure statistical reproducibility.

Figure 3.3 – The Cambridge Reactor Designs (CRD) Polar Bear Plus Crystalliser, featuring overhead stirring.

3.3 Crystallisation Methods

A range of crystallisation methods were investigated: evaporative, mechanochemical including neat grinding (NG) and liquid assisted grinding (LAG), slurrying and cooling crystallisations in both batch and continuous platforms were investigated for a range of systems. The various

crystallisation methods were employed to control polymorphic form or investigate co-crystal formation for materials discovery.

3.3.1 Evaporative Crystallisation

In Chapter 6, for the evaporative screen aimed at multi-component material formation, the four profen family materials were investigated with a range of co-formers. The solubilities of the two components are similar in the particular solvent, to result in a symmetric ternary phase diagram, otherwise the crystallisation outcomes do not reflect the input materials. A mass of 20 mg of the profen family target with initially the corresponding mass of co-former, calculated from a 1:1 molar ratio of target:co-former was weighed into a 7 mL vial with 1-2 mL of solvent. The use of sonication was employed to promote dissolution. If complete dissolution had not been achieved after 30 minutes of room temperature sonication in a sonic bath, heat was applied to the sonicator or more solvent was added to achieve complete dissolution. Once the solid was fully dissolved, plastic caps which had four small holes pierced in them were placed on the sample vials. The samples were then left undisturbed to allow for solvent evaporation and subsequent crystallisation. All crystallisations conducted in this way were set up to contain both starting materials, with the intention of forming a multi-component system. In addition to the different stoichiometries of starting materials, a variety of different evaporation temperatures were also investigated: 5 °C (placed in fridge), room temperature, 30 °C, 40 °C and 50 °C. For the elevated evaporation temperatures a hot-plate with a DrySyn attachment were used for temperature control. The samples were observed for any crystallisation and the crystals were harvested before complete evaporation of the solvent, in an aim to keep any unwanted impurities in the solution phase. The crystals were analysed *via* polarised optical microscopy as well as Powder X-ray Diffraction (PXRD) and Differential Scanning Calorimetry (DSC) in order to determine if a new phase had been accessed, when compared to the PXRD patterns and DSC traces of the starting materials.

3.3.2 Mechanochemical Crystallisation

In Chapter 6, mechanochemical crystallisations investigate the use of mechanical energy in achieving desired phases, either through multi-component formation or obtaining the desired polymorph. For materials discovery, initial experiments investigated a 1:1 molar ratio of target:co-former using 40 mg of the profen family target, where the components were ground by hand for 5 minutes using a mortar and pestle, either neat (NG) or using a few drops of solvent (LAG). When an excess of one or both of the starting components was evident in the

PXRD and DSC data, the grinding time was increased to 30 minutes to provide additional mechanical energy to favour co-crystal formation. An alternative strategy to yield a pure co-crystal from grinding approaches would be to alter the stoichiometric ratio of the starting components by decreasing the relative molar ratio of the component present in excess in the PXRD data.

3.3.3 Slurrying Crystallisation

Slurry crystallisations are a suspension technique used to investigate solution-mediated phase transformations (SMPTs) in solution. Slurry techniques can be used for multi-component material formation or establishing the thermodynamic form from concomitant polymorphs through competitive slurrying.

3.3.3.1 Multi-component Slurrying Experiments

In Chapter 6, small-scale slurries were prepared by a 1:1 molar ratio of a physical mixture of the starting components using ~200-400 mg of the profen target and the chosen co-former. A small amount of solvent was then added to the solid materials in 7 mL or 20 mL vials for slurries mediated in 2 mL and 10 mL of solvent respectively. The 20 mL vials were placed in the CRD Polar Bear Plus crystalliser and the 7 mL vials in a hot-plate with a DrySyn attachment for temperature control at 20 °C and 30 °C respectively. Magnetic bottom stirring (250-350 rpm) was used for agitation. A variety of solvent media were used (ACE, EtOH, IPA, H_2O and 60:40 HI), depending on the specific study being undertaken. Once the sample was prepared and under agitation, it was important to ensure that not all the solid dissolved and an excess remained, maintaining the suspension. If the slurry dissolved, a pre-weighed post addition of solid was added to the solution to establish a slurry that would remain a suspension after equilibration. The systems were left slurrying for a predetermined amount of time, for 24 hours and 1 week for 10 mL and 2 mL slurry investigations respectively, before being filtered and dried at room temperature. The slurry product was then analysed for solid form identity by PXRD and DSC. Full experimental parameters can be found in Chapter 6.

In Chapter 7, to investigate potential short-lived crystal phases undergoing SMPTs, *in situ* slurrying in capillaries was carried out at beamline I11. To investigate early stage slurrying crystallisation of IBU and ISO 1:1 in a physical mixture compared to the pre-prepared IBU-ISO co-crystal, slurrying crystallisations were carried out in 1-2 mL of 60:40 HI for 5 minutes,

to ensure the physical mixture was homogeneously mixed before loading the slurry into a borosilicate capillary. The precise sample preparation is detailed in Chapter 7.

3.3.3.2 Competitive Slurrying

In Chapter 4, competitive slurrying experiments using two polymorphic forms in a 1:1 molar ratio in the solid mixture were slurry mediated in solvent for a slurrying time of 4 minutes, in which the slurry time represents the residence time between adjacent windows in the KRAIC-D under the flow conditions employed in the experiments. These experiments aimed to establish whether a polymorphic transformation would occur between adjacent windows when a mixture of polymorphic forms were present in solution slugs. For the CBZ model system, competitive slurrying of the metastable CBZ form II and thermodynamic CBZ form III slurry mediated in EtOH were investigated, whilst for the UBA model system, the concomitant UBA form I and UBA form III slurry mediated in MeOH were investigated. A mass of ~150-200 mg of this mixture was placed into 7 mL glass vials and 1-2 mL of the chosen solvent (CBZ in EtOH, UBA in MeOH) was added. A hot-plate with a DrySyn attachment was used to allow for both magnetic bottom stirring set at 350 rpm and temperature control at 20 °C. After slurrying the polymorphic mixtures for 4 minutes, the slurries were then filtered *via* vacuum filtration and left to dry at room temperature before being analysed by PXRD. Full details can be found in Chapter 4.

3.3.4 Cooling Crystallisation

Cooling crystallisation was investigated by both batch and continuous processing methods. In Chapter 6, batch crystallisations were carried out in the CRD Polar Bear Plus crystalliser, whilst a range of platforms were investigated for continuous processing: KRAIC (Chapters 4, 5 and 6), KRAIC-D (Chapter 4 and Chapter 6) and KRAIC-S (Chapter 5) platforms.

3.3.4.1 Batch Cooling Crystallisation

In Chapter 6, small-scale cooling crystallisations with a working solvent volume of 1 mL were carried out in 1.5 mL vials using the CRD Polar Bear Plus crystalliser with magnetic bottom stirring. For co-crystallisation experiments, the two components were weighed into vials and the appropriate amount of the chosen solvent added. The vials were placed in the appropriate insert in the Polar Bear Plus crystalliser and stirred at a rate of 400 rpm. Cooling profiles were designed based on the solubility behaviour of the solid in the particular solvent. The vials were initially heated to the start temperature at a heating rate of 10 °C min^{-1} and dwelled at

temperature for an hour to ensure complete dissolution. Once the starting components had completely dissolved, the temperature programme switched to controlled linear cooling, initially at a cooling rate of 0.05 °C min^{-1}, which was increased to more appropriate cooling rates adopted in industry of 1 °C min^{-1}. The final temperature was chosen between 20 °C and 5 °C, depending on the temperature of crystallisation, the vials then dwelled at the final temperature for a specific amount of time before being filtered *via* vacuum filtration, dried at room temperature and then analysed by PXRD and DSC for solid form identity.

For cooling crystallisations at scale, between 20 mL and 200 mL working volume of solvent was placed in round bottom flasks (RBFs) inserted into the CRD Polar Bear Plus crystalliser. Overhead stirring was provided by an external motor and shaft, to ensure efficient mixing and mass transfer. The starting components were weighed and added to the solvent in the RBF and heated at 10 °C min^{-1} to the starting temperature. The cooling rate adopted for these larger scale crystallisations was 1 °C min^{-1}. Similar to the small-scale batch crystallisations, the vials dwelled at the initial temperature for 1 hour before commencing the cooling programme to ensure complete dissolution. The vials also dwelled at the final temperature to ensure sufficient crystalline material was available for analysis, with the dwell time the same across all the scales to allow for direct comparison between the various batch scales. Full experimental details on individual systems are provided in the relevant sections in Chapter 6.

3.3.4.2 Continuous Cooling Crystallisations in the KRAIC / KRAIC-D / KRAIC-S platforms

Continuous cooling crystallisations of model systems CBZ in EtOH and UBA in MeOH (Chapter 4), as well as continuous co-crystallisation of the novel material IBU-ISO in 60:40 HI (Chapter 6) were investigated in the KRAIC (Kinetically Regulated Automated Input Crystalliser) (Figure 3.4) and KRAIC-D (Kinetically Regulated Automated Input Crystalliser – for Diffraction) platforms (Figure 3.5, left).

In Chapter 5, the KRAIC-S (Kinetically Regulated Automated Input Crystalliser – Single Crystal) was used as a cooling crystallisation platform suitable for *in situ* Single Crystal X-ray Diffraction (SCXRD) characterisation in flow at beamline I19 (Figure 3.5, right). The cooling crystallisation process of paracetamol (PCM) in 60:40 HI in the KRAIC-S platform allowed for single crystals within solution slugs to be grown *in situ*. Optimisation of a slug triggering mechanism was used to achieve indexation from a single diffraction frame and after refinement

and integration of a series of images; the images could be scaled and merged allowing for full structural solution, *via* a serial-crystallography type approach.

The cooling crystallisation processes were optimised offline in the KRAIC platform, to yield powder and single crystals crystallising in solution slugs suitable for appropriate analysis. For *in situ* X-ray diffraction (XRD) analysis, the KRAIC-D and KRAIC-S were installed at the high-resolution powder diffraction beamline I11 (Figure 3.5, left) and the small molecule single crystal beamline I19 respectively at Diamond Light Source (DLS) (Figure 3.5, right).

Figure 3.4 – Bath-developed KRAIC platform.

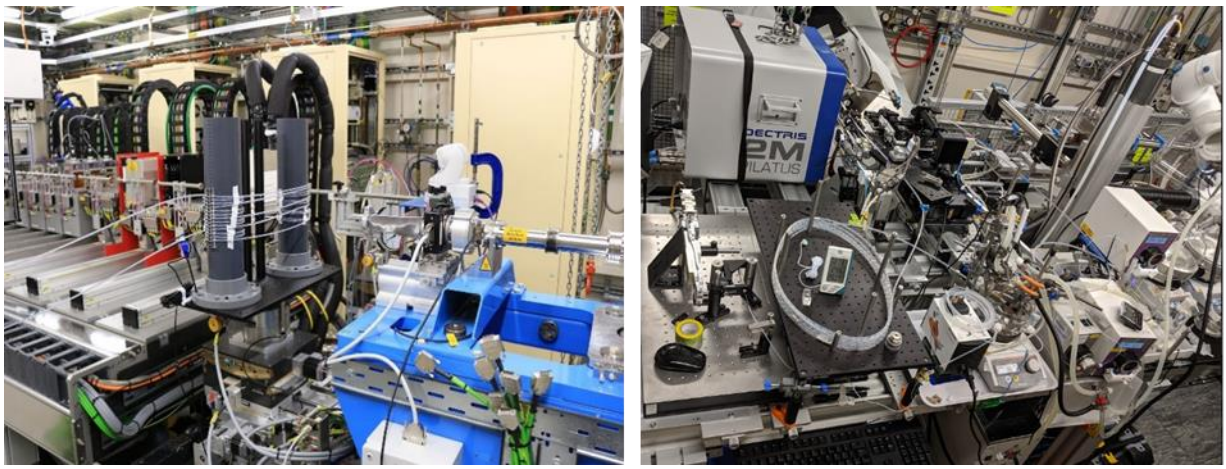

Figure 3.5 – Installation of the KRAIC-D at I11 (left) and installation of the KRAIC-S at I19 (right).

Segmented flow employed in the KRAIC, KRAIC-D and KRAIC-S platforms incorporates three phases: two liquid components, the carrier fluid and the crystallising solution, with one gas phase (air) to achieve tri-segmented flow (Figure 3.6). To achieve segmentation, a cross-piece (X-piece) was utilised, whereby the three separate streams combine at the mixer piece / segmentor; on the premise of immiscibility this combination results in a segmented net flow.

Segmentation facilitates plug flow operation in these flow crystallisation platforms, where particles experience good mixing conditions and are well suspended. Plug flow operation helps mitigate some of the inherent issues associated with moving solid particles in a flowing environment. For instance, the opportunity for sedimentation was reduced and the loss of homogeneity caused by adhesion of particles to the reactor walls was also reduced. This liquid-liquid segmentation prevents any back mixing within the crystalliser and thus all particles experience the same conditions, imparting homogeneity as a result of this steady-state operation. For instance, particles spend the same amount of time within the reactor, which varies depending on the reactor length, flow conditions and was quantified by the residence time (RT). The immiscible carrier fluid was a perfluoropolyether (PFPE) with favourable wetting properties to prevent the crystallising solution nucleating on the solid surface by physically removing the solution flow from the reactor walls and thus preventing unwanted secondary nucleation from occurring during the crystallisation.[72]

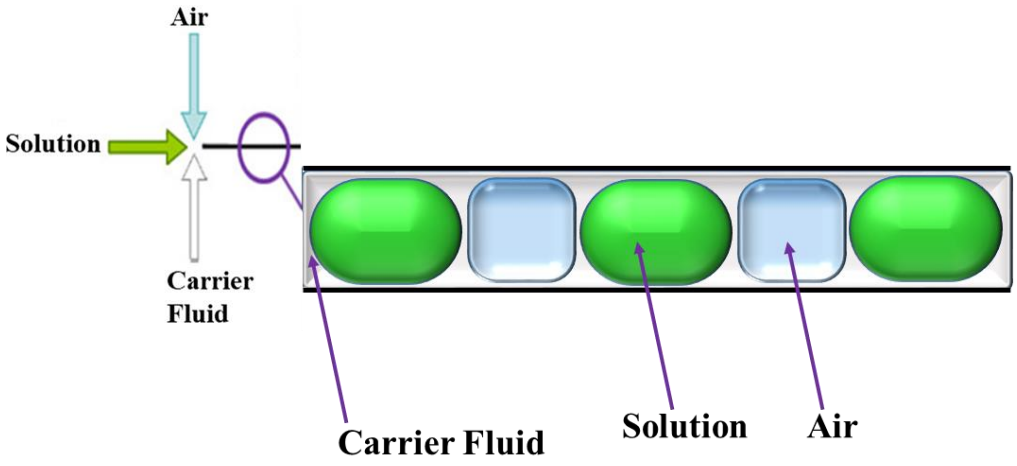

Figure 3.6 – Schematic of tri-segmented flow through the combination of three separate streams at the X-piece.

The three phases were independently pumped under temperature control to the point of combination at the X-piece; the use of temperature control prevents crystallisation from occurring before segmentation was achieved. The X-piece was contained in a custom-made glass segmentation water bath sat on a hot-plate to provide temperature control. The temperature of the system until the water bath was maintained at the temperature of the crystallising solution feed, using jacketed tubing, which was controlled by an external circulator. The crystallising solution and priming solvent feeds were contained separately in 2 L RBFs each on a hot-plate with a DrySyn attachment. The hot-plates provide heating and stirring of the solutions to ensure the crystallising solution was completely dissolved and if the

priming solvent was a solvent mixture, the mixing ensured the priming solvent was homogeneous ready for delivery. Once segmentation was achieved and the net segmented flow emerged from the heated water segmentation bath, no additional temperature control was imparted on the system. The system was left to cool on its own accord, resulting in crystallisation *via* air-cooling.

The crystallising solution (or priming solvent during equilibration of the system) was pumped using an SF-10 peristaltic pump designed to lessen the effects of pulsation. The air and carrier fluid were each pumped using gear pumps. Employing separate pumps for each of the components in the tri-segmented flow allows complete control over the platform and facilitates flexibility in both crystallisation and reaction-based experiments. Variation in pump speeds and the reactor length, allows for kinetic regulation to be imparted in the system and the RT (time for a particular crystallisation volume segment to transit the device from establishing segmentation to the end-piece) to be optimised. Importantly, this allows for solution-mediated kinetic changes, particularly polymorphic transitions, to be optimised or removed as required.[72]

The body of the KRAIC platform comprises a single extruded length of Fluorinated Ethylene Propylene (FEP) 15 m in length, with an internal diameter (ID) of 3.6 mm, resulting in a total crystalliser volume of 121 mL. As a result of the segmentation employed in the KRAIC crystalliser, only 61 mL of the total crystalliser volume comprises the crystallising solution. The net flow rate of the segmented flow through the KRAIC was typically 8.3 mL/min, contributing 2 mL/min from the crystallising solution, 4.18 mL/min and 2.1 mL/min for the air and carrier fluid flow rates respectively. This means that a 1 L crystallising solution feed will enable a 2 hour operation time, which was markedly longer than traditional flow crystallisation platforms such as a Continuous Oscillatory-Baffled Crystalliser (COBC), which for the same feed volume, would only facilitate a crystallisation run for 25 minutes.[72]

An end-piece was seamlessly attached to the FEP tubing outlet ready for product recovery *via* vacuum filtration. The downward slope introduced by the widening of the end-piece was designed to achieve both recovery of carrier fluid from the solution *via* recovery holes and propulsion of crystals towards the filtration unit. These carrier fluid recovery holes were simply a number of holes at the bottom of the tubing, which allow the preferentially wetting carrier fluid to pass through, but not the crystallising solution. Recovery of the carrier fluid will reduce the overall net flow of the system, which could lead to blockages, so this was mitigated by the

incorporation of a neutral solvent (NS) towards the outlet (Figure 3.7). The NS was employed upstream of the carrier fluid recovery system using a gear pump, to maintain the net flow, as the velocity of the solution was increased at the point of addition and will therefore prevent encrustation in the pipeline and reduce contact time of particles with the reactor walls. The NS must be miscible with the crystallising solution and will not alter the solubility properties of the solution. Thus, the NS will not dissolve any of the solid particles in the crystallising solution, or lead to precipitation of particles from the filtrate, such as impurities, or more crystals of the target material, which will negatively affect the particle size distribution (PSD). The NS selected was usually the pure solvent used in priming (and the solvent used in the crystallising solution), cooled in an ice bath.[72]

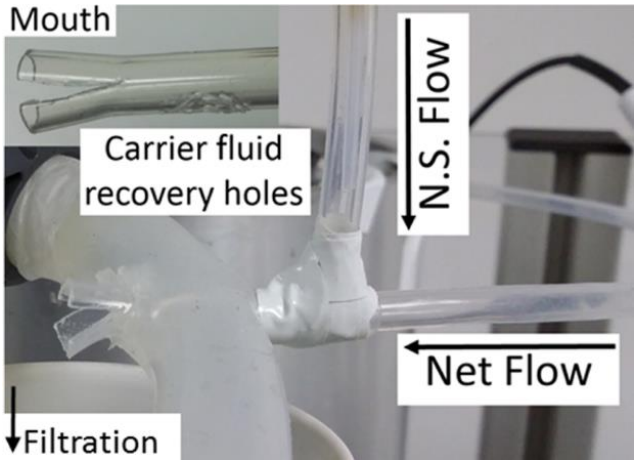

Figure 3.7 – End-piece set-up in the KRAIC, KRAIC-D and KRAIC-S platforms including the carrier fluid recovery holes and the NS inlet, adapted from Robertson *et al.*[72]

For each KRAIC, KRAIC-D and KRAIC-S run, the experimental RT was measured to ascertain the crystallisation time, whilst also ensuring that the various pumps were operating at the desired programmed rates. Particular attention was taken to the flow rate of the air pump, which had the tendency to lessen over time as air is compressible. To mitigate this reduction in flow rate over time, the air gear pump was primed with the solvent used for priming to wet the inside of the pump.

To ensure the KRAIC, KRAIC-D and KRAIC-S platforms were operating at steady-state, the system requires priming with pure solvent in place of the crystallising solution before any crystallisation run commences. The flow rates and temperature conditions utilised during priming were identical to those employed in the crystallisation run. The system will typically

require a couple of residence times to reach steady-state operation; this will also ensure any impurities from the inside of the tubing were removed. As a result of the steady-state operation obtained in the segmented flow, the solution passing a set point along the reactor length will always be at the same stage of the crystallisation process irrespective of the experiment time, enabling in-depth investigations into events that evolve with time, such as polymorphic transitions.

The materials from which the KRAIC-D was constructed were compatible with *in situ* operation on synchrotron radiation beamlines. For instance, the X-ray beam was focused at the hydrophobically coated Kapton® viewing windows, which were incorporated into the KRAIC-D design to facilitate X-ray penetration and minimise background interference at set points along the length of the crystalliser (Figure 3.8). The distance between windows was 2.623 m, to ensure the residence time was sufficient from when segmentation was established at the X-piece and between analytical points, so that crystallisation events such as polymorphic transitions will be observed within the length of the crystalliser.

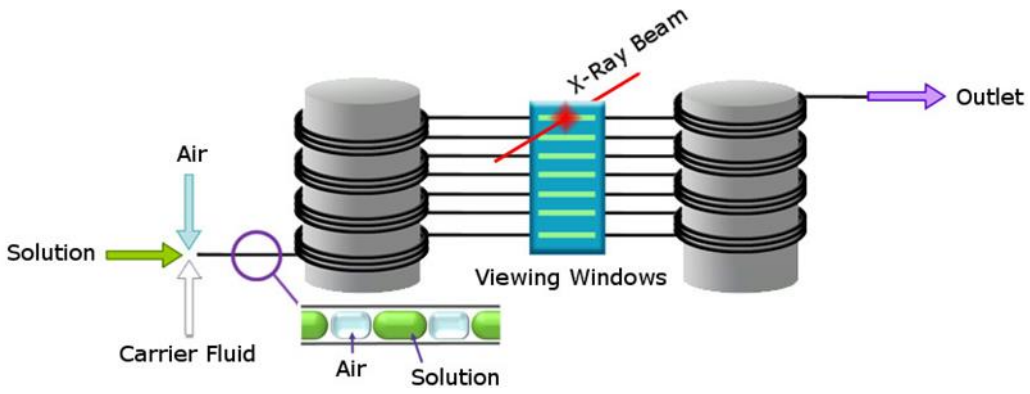

Figure 3.8 – Schematic of KRAIC-D showing segmented flow and position of viewing windows.

The body of the KRAIC-D tubular reactor was constructed of FEP, which is flexible and transparent to allow for visual monitoring of the crystallising solution, allowing identification of potential blockages. The Kapton® windows and Polytetrafluoroethylene (PTFE) unions comprise the viewing section of the KRAIC-D. The PTFE unions providing a join between the Kapton® analysis points and the rest of the FEP body.

Use of X-ray transparent Kapton® windows incorporated into the KRAIC-D at I11 was not employed for the KRAIC-S at I19 and instead the scattering resulting from the reactor was subtracted during data processing. Thus, the entirety of the KRAIC-S was built from a single

extruded length of FEP to set up a single coil of tubing for the main body of the KRAIC-S. The viewing section, where the X-ray beam focusses on the single crystal in the solution slugs, is comprised of FEP supported by a motorised stage, employed to oppose the net segmented flow, such that a single crystal can be artificially 'held' in the X-ray beam for sufficient time to obtain enough diffraction spots for indexing from a single frame. As a single crystal is held in the X-ray beam during data collection, due to the self-mixing provided by the bolus flow in the solution slugs the crystal is rotating, which allows for data across a range of orientations with respect to the X-ray beam to be obtained. A pump-probe approach is employed, based on a slug triggering mechanism, whereby a laser / diode is continually monitoring the segmented flow, coupled with the known net flow rate and distance from the laser trigger to the X-ray beam is known. The motorised stage can be prompted to translate as a single crystal in a solution slug passes the X-ray beam, whereby the X-ray beam can be switched on / off to only collect data on crystallising solution slugs. The developmental work and set-up associated with the slug triggering mechanism is detailed in Chapter 5.

The experimental conditions including concentration and temperature control, together with the flow parameters, varied greatly for the various KRAIC-D experiments (and corresponding KRAIC experiments), the detail of which can be found in Chapter 4 and Chapter 6. Similarly, the experimental detail for the various KRAIC-S (and the associated KRAIC) runs can be found in Chapter 5.

3.3.5 Seeded Cooling Crystallisation

To investigate the impact of introducing a controlled solid interface into the cooling crystallisation within the KRAIC-D platform, an additional T-piece inlet was inserted into the platform at pre- and post-nucleation stages of the crystallisation process. The introduction of a seed addition port allowed for a seed slurry to be transferred using an SF-10 peristaltic pump into the KRAIC-D. The slurry of seeds of polymorphic purity were introduced into the cooling crystallisation at room temperature. The detail of the slurry preparation, including slurry stability testing, as well as stability testing of the slurry through an SF-10 peristaltic pump was detailed in Chapter 4. The seeding cooling crystallisation experiments of the KRAIC-D installed at I11 DLS investigated the model systems CBZ in EtOH and UBA in MeOH. The seed slurry introduced into the cooling crystallisation of CBZ in EtOH was the thermodynamic CBZ form III delivered in EtOH. The impact of seeding on the cooling crystallisation of UBA in MeOH looked at the concomitant form UBA form III in polymorphic purity, introduced at

pre- and post-nucleation stages, whilst the dominant form UBA form I was only introduced at the pre-nucleation seeding port. Both UBA form I and III slurries were mediated and delivered in MeOH. The solvents employed in the delivery of the slurries were selected to match the solvent employed within the cooling crystallisation. The seeded KRAIC-D experimental set-ups are illustrated and described in detail in Chapter 4.

Seeding of the metastable PCM form II using an FEP coil into the cooling crystallisation of PCM in 60:40 HI in the KRAIC-S is detailed in Chapter 5. For seed solution delivery into the KRAIC-S, instead of an SF-10 pump as detailed for delivery into the KRAIC-D, a syringe pump coupled with a piston connected through a T-piece was used upstream of the sample loop. The net flow was delivered at room temperature using the syringe pump, while the piston provided oscillation to the system. The PCM form II seeds suspended in the carrier fluid were pre-loaded into the coil before delivery into the KRAIC-S. The seeded experimental set-up is illustrated and described in detail in Chapter 5. In Chapter 4 and Chapter 5, for each seeding experiment, the seed solutions were prepared immediately before use.

3.4 Analytical Methods

3.4.1 Powder X-Ray Diffraction (PXRD)

Laboratory Diffraction Analysis

PXRD was used in this work as a "fingerprinting" tool to characterise the crystal structure of polycrystalline solid products, including potential co-crystals produced during the crystallisation trials. Pattern comparison is used as the main approach; matching (of peak positions and hence of unit cell parameters) was expected for experiments targeting optimised production of known solid phases, while mismatched patterns were targeted in the case of materials discovery (the observed PXRD should not match those of either starting materials or known products containing these, indicating a product with a distinct unit cell).

Bruker D8 Advance Diffractometer

For the majority of laboratory powder diffraction analysis, a Bruker D8 Advance Diffractometer set in flat plate mode, equipped with monochromatic Cu-K_α (λ = 1.54056 Å) radiation in reflection geometry at 298 K was used to analyse powder samples. The crystalline samples were lightly ground and placed onto a glass slide, which was then mounted onto a glass flat-plate with a non-diffracting adhesive substance. The diffraction pattern of the powder sample was obtained between $2\theta = 5 – 40°$.

STOE STADI P Diffractometer

Later laboratory work conducted at the University of Bath (in 2019) used a STOE STADI P diffractometer with Cu-$K_{\alpha 1}$ radiation (λ = 1.54045 Å). The samples were prepared by placing some crystalline powder onto a transparent, zero-diffracting acetate foil in the sample holder. A secondary acetate foil was placed over the top of the sample, before being secured in the sample holder. The samples were evaluated at room temperature (298 K) and a diffraction pattern was obtained between $2\theta = 2 – 75°$.

In Chapter 4, the crystalline material resulting from CBZK and CBZKD experiments was not ground during sample preparation in order to avoid evoking a polymorphic transformation resulting from grinding of the sample.

Synchrotron Diffraction Analysis

Beamline I11, the High-Resolution Powder Diffraction beamline at DLS (Chapter 4 and Chapter 7)

The High Resolution Powder Diffraction Beamline I11 at DLS was used for the powder synchrotron studies presented in Chapter 4 and Chapter 7 of this research project. Beamline I11 utilises a combination of very high angular resolution, high count rates and controlled environmental conditions to achieve detailed structural analysis of polycrystalline materials.

The synchrotron X-ray radiation supplied to I11 is provided by an in-vacuum U22 undulator insertion device located in the main electron storage ring. The undulator is 2 m in length, comprising of an array of 90 permanent magnets, exhibiting a period length of 22 mm. This insertion device produces an X-ray beam energy ranging from 5-30 keV, where the highest flux was achieved at medium energies between 11-20 keV, decaying quickly beyond 20 keV.[89]

The optics hutch at I11 contains various components: primary slits designed to trim the white beam from the undulator, a cryo-cooled Double Crystal Monochromator (DCM) equipped with a pair of Si(111) crystals, double bounce harmonic rejection (HR) mirrors, two sets of monochromatic slits and an embedded intensity monitor (Figure 3.9). The distance between the two crystals comprising the DCM was altered to maintain the fixed-exit beam geometry across all energies.[89]

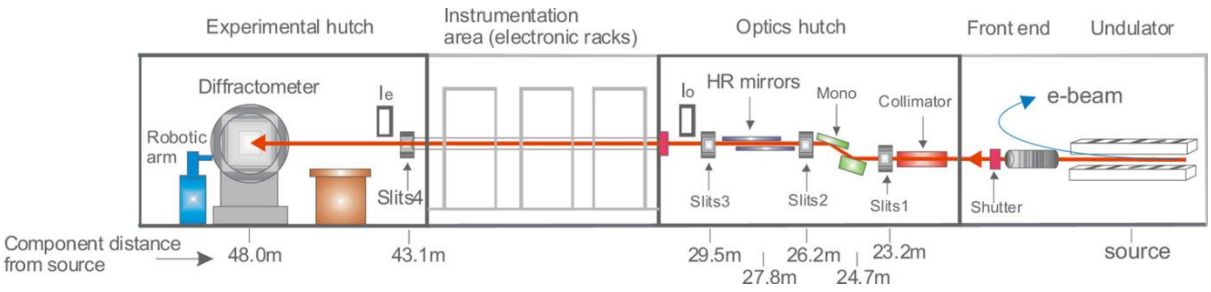

Figure 3.9 – A schematic of the beamline I11 layout at DLS, which shows the main components along with the approximate distances from the undulator X-ray source, adapted from Thompson *et al.*[89]

The two experimental hutches downstream of the optics hutch take beam controlled by an X-ray shutter. They house different experimental setups designed to support complementary areas of structural science. Synchrotron Powder XRD studies of highly polymorphic model systems and novel multi-component materials in this research project have been carried out in both experimental hutches (EH1 and EH2). Both EH1 and EH2 are designed for high-resolution and time-resolved diffraction data whilst EH2 offers the additional benefit of having physical capacity to house non-routine experiments, which require advanced experimental set-ups, such as the KRAIC-D. The key benefit in EH2 being situated downstream of EH1, allows experimental set-up to be carried out whilst EH1 is still taking beam (Figure 3.10).

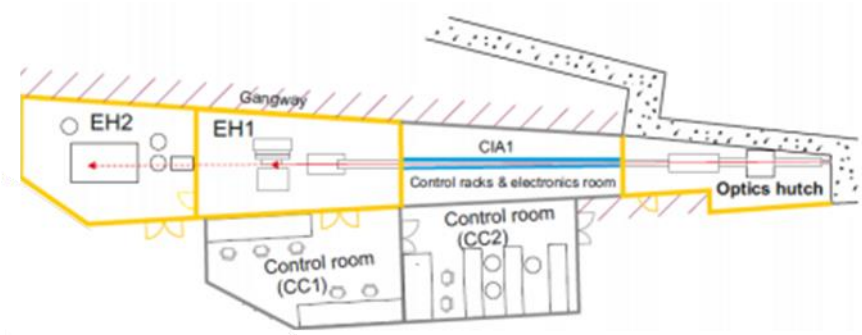

Figure 3.10 – A schematic of the beamline I11 layout at DLS.[90]

In Chapter 4, EH2 was utilised for *in situ* XRD characterisation of cooling crystallisations in the KRAIC-D, to investigate crystallisation events that evolve with crystallisation time. This was made possible due to the design and steady-state operation mode of the KRAIC-D, in which the reactor provides highly reproducible reaction conditions. A 15 keV X-ray beam energy, corresponding to a wavelength of 0.8265 Å, was employed to maximise flux. The beam size employed was 1 mm x 1 mm, compatible with a typical 7 mm plug length. The diffraction was detected using a 2D CCD (Charge Coupled Device) Pixium RF4343 detector, operating at

10 frames per second (fps), which was sufficient to isolate scattering from plugs in a proportion of frames.

In Chapter 7, EH1 was utilised for the *in situ* XRD characterisation of slurrying crystallisations in capillaries to benefit from both high-resolution and rapid data collection to monitor time-resolved changes in solution phases over a range of crystallisation periods. The wavelength of X-ray radiation used was 0.8265 Å, equating to a beam energy of 15 keV. The beam size of 0.5 mm x 2.5 mm was compatible with the sample size, where slurry samples were loaded into 1 mm borosilicate capillaries. The experimental capillary set-up was traditional for PXRD data collection at I11, whilst the sample state, whereby a slurry was loaded directly into a capillary, was non-routine and novel. Chapter 7 provides a demonstration for protocol development for *in situ* characterisation of slurrying crystallisation. As these slurrying investigations were time-resolved, a wide-angle PSD (Position Sensitive Detector) Mythen detector was employed due to its fast data acquisition rate of < 1 s per pattern. The diffraction patterns of the slurry samples were obtained between $2\theta = 2 – 92°$ at room temperature. Variable temperature powder X-ray diffraction (VT-PXRD) measurements were investigated across the same 2θ (°) range, within the temperature range 293-400 K through use of a Cryostream Plus. The heating / cooling rate employed was 0.8 °C min^{-1}, with each 5 °C incremental change in temperature accompanied by a 3 minute equilibration period before data collection.

The data collection process was controlled through the in-house Generic Data Acquisition (GDA) software whilst the data processing for the KRAIC-D EH2 work and the EH1 slurrying in capillaries investigations were carried out using Matlab® and DAWN[91] (Data Analysis WorkbeNch) software packages respectively.

3.4.2 Single Crystal X-ray Diffraction (SCXRD)

SCXRD was used in two ways in this work. For potential new co-crystals, SCXRD gives a rapid route to the determination of unit cells from single crystal samples resulting from crystallisation trials. For structures that were confirmed by unit cell screening to be novel, SCXRD was the method then used to allow for full structural determination, revealing molecular geometry and packing. Potential co-crystals were initially screened and the unit cell parameters from the pre-screening experiment compared with the unit cell parameters of the starting materials, including various polymorphic forms, found in the Cambridge Structural Database (CSD).[24] Provided the unit cell parameters were different, indicating a new crystal phase has

been discovered, and where the single crystal was of sufficient quality to yield quality diffraction data, a full data collection to yield structure solution could be carried out. A crystal of good diffraction quality has reflections that have a good intensity and occur to a high resolution (typically $d_{min} < 0.84$ Å), that do not overload at low angle and which are not split. The novel crystal structures presented in Chapter 6 were determined using SCXRD, conducted using both laboratory and synchrotron sources. The choice of X-ray source was selected on the basis of the quality of the crystals produced in the evaporative crystallisation trials; crystallisation products which yielded very small crystallites or weakly diffracting single crystals required a synchrotron source for structure solution.

SCXRD analysis was also used in this work to investigate structural solution of single crystals grown *in situ* in solution slugs in a segmented flow crystalliser known as the KRAIC-S. Synchrotron X-rays on I19 were employed as a non-invasive *in situ* characterisation technique to monitor tumbling crystals within moving droplets, the use of a high flux source with fast data collection times that a synchrotron source provides was fundamental for this *in situ* XRD single crystal analysis.

3.4.2.1 Optical Microscopy

The selection of quality single crystals for traditional laboratory and synchrotron single crystal diffraction studies was carried out using polarised light microscopy. A single crystal of suitable quality for analysis exhibits well define crystal edges and faces, whilst also being free from cracks or any additional tiny crystallites attached to the single crystal surface. A microscope fitted with a polarising lens was used to determine the crystallinity of the solid. When viewed under polarised light, a single crystal will 'extinguish' when rotated as the high degree of order within the crystalline structure causes the crystal to act as a polariser. Optical microscopy was also a useful tool for assessing a crystal's size and shape (morphology), which can give an indication of solid form, provided the various polymorphs exhibit distinct differences in habit. The crystal size also indicates the extent of crystal growth.

Laboratory Diffraction Analysis

Two in-house X-ray diffractometers were used in the SCXRD studies of the multi-component materials discovered in this research project. SCXRD data were recorded on the Rigaku Oxford Diffraction[92] (previously Agilent Technologies) SuperNova and Gemini A Ultra CCD diffractometers. Both of these diffractometers have a dual source sealed tube with both Cu-$K_{\alpha 1}$

(λ = 1.54045 Å) and Mo-$K_{\alpha 1}$ radiation (λ = 0.71073 Å) with microfocus sources allowing for high X-ray flux to be delivered to the sample. Both of the single crystal diffractometers utilise a graphite monochromator and have a four-circle kappa goniometer, with an Agilent[93] Eos S2 and Atlas CCD detectors for the SuperNova and Gemini A diffractometers respectively.

Although the specific components vary across diffractometers, the general experimental set-up remains the same (Figure 3.11). The four-circle κ goniometer allows for movement of the single crystal through each of the three diffractometer axes (κ, ϕ, ω), as well as the 2θ of the detector, allowing for a complete set of diffraction data to be collected.

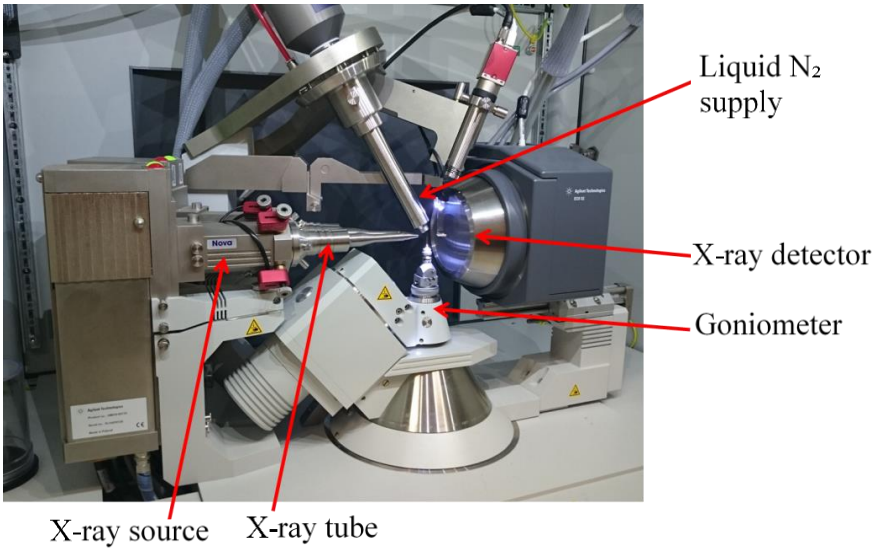

Figure 3.11 – The experimental set-up for a laboratory SCXRD diffractometer, pictured is the Rigaku Oxford Diffraction SuperNova diffractometer.[92]

All single crystals were isolated from the bulk sample, cleaned in a viscous oil, Fomblin®, and the crystal mounted onto the looped Kapton® filament attached to a magnetic mount. Once the temperature of the diffraction experiment was set at the desired temperature, the magnetic mount was then placed on the diffractometer goniometer head. The crystal was centred in the X-ray beam position by adjustments to the vertical and horizontal axes of the goniometer head. Once screening of the mounted single crystal of good diffraction quality is complete, full structural determination can be performed. A recommended data collection strategy is suggested at the end of the pre-experiment used for crystal screening. The strategy suggests the required exposure time per diffraction image necessary to obtain diffraction data to the required resolution, values of I/σ, as well as the completeness for accurate structure determination from

the data collection. These parameters are typically a d-spacing 0.8 Å resolution, an I/σ of 15, a redundancy of five and a completeness of 98 %. The extent of reciprocal space to be sampled during the data collection is also to be decided, in terms of the requirements of the unique data for the particular crystal system. If time permits, collection of a full hemisphere of data is recommended to access all unique reflections.

The sample temperature was controlled by a flow of liquid nitrogen using an Oxford Diffraction Cryojet apparatus. VT-SCXRD measurements can be achieved by altering the temperature controlled by this liquid nitrogen flow device. The exposure times were dependent upon the system being studied, the details of which can be found in the relevant results chapters.

Both the Supernova and the Gemini A Ultra CCD diffractometers were equipped with the Rigaku-Oxford diffraction software CrysAlisPro,[94] which was used to collect, index and prepare data for structural interpretation. This was then analysed in the SHELXT (structure solution using a dual-space iteration starting from a Patterson superposition, through use of the charge flipping algorithm to generate more random phases) and SHELXL (least squares refinement) programs, used to solve and refine the crystal structure respectively. Both programmes were executed as part of the GUI Olex2 (version 1.2.10) software package from OlexySys Ltd. Visualisation and analysis of the crystal structures produced was then conducted in Mercury (version 4.2.0).

Synchrotron Diffraction Analysis

Single crystal synchrotron X-ray diffraction studies of crystalline material in this research project were carried out at two synchrotron facilities: Diamond Light Source (DLS), UK[88] on beamline I19, at Harwell and the Advanced Light Source (ALS), USA[95] on beamline 12.2.1, at the Lawrence Berkeley National Laboratory. The theory of synchrotron crystallography was described in Chapter 2. The high intensity of synchrotron X-rays is advantageous for demanding crystalline systems, with a high degree of structural disorder or where crystallisation trials produce weakly diffracting samples, or extremely small crystallites where laboratory sources could not provide structural solution.

Beamline I19, the Small Molecule Single Crystal beamline at DLS (Chapter 5)

Beamline I19 was used predominately for the single crystal synchrotron studies in this research project. I19 offers high-flux, along with tuneable-wavelengths dedicated to single crystal

structure determination of small-molecule systems, including under a variety of conditions and sample environments, such as high pressure.[96]

Beamline I19 is located on a 5 m straight-section of the storage ring, where an in-vacuum U21 undulator source provides the highly intense 5-28 keV energy range, with an associated 0.44-2.48 Å wavelength range (Figure 3.12). Wavelength selection of the synchrotron X-rays emerging from the storage ring was achieved using a cryo-cooled double crystal monochromator (DCM) situated in the optics hutch, equipped with a Si(111) crystal set. The double crystals select the 5-28 keV synchrotron radiation range, whilst also maintaining the fixed-exit beam geometry. The X-ray beam was focused downstream of the DCM in the optics hutch using a pair of bimorph mirrors, which independently focus the beam in the horizontal and vertical axes. Once focused, the beam was directed towards the experimental hutches, where the sample was situated, ready for data collection. The dimensions of the mirrors were matched to the beam divergence and the beam's 3 mrad incidence angle, which ensures the beam footprint was maximised over the mirrors. The focused beam exhibits a Gaussian profile with a Full Width Half Maximum (FWHM) of 90 μm horizontally by 60 μm vertically and 185 μm horizontally by 130 μm vertically for the first and second experimental hutches (EH1 and EH2), respectively. The beam size can be altered by defocusing / refocusing the bimorphs, which provides opportunity to optimise for a range of sample sizes. The beam size was selected to ensure that the sample was completely immersed in the primary beam. The experimental hutches were able to take beam, by opening an X-ray shutter.[96]

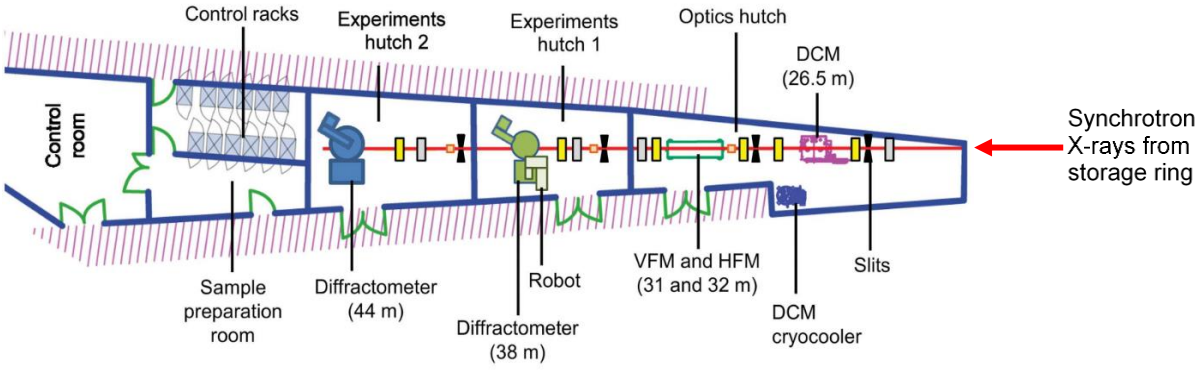

Figure 3.12 – A schematic of the beamline I19 layout at DLS.[97]

EH2 offers the physical capacity to house non-routine experiments, which require advanced experimental set-ups, such as the KRAIC-S. The key benefit in EH2 being situated downstream of EH1, is to allow experimental set-up to be carried out whilst EH1 is still taking beam.

Data were collected in EH2 using Si(111) monochromated radiation at the Ag edge (0.4859 Å) on a Newport[98] four-circle diffractometer in κ geometry equipped with a DECTRIS[99] PILATUS 2M hybrid pixel detector (Figure 3.13). The diffraction data was collected by the in-house GDA software. Image data from the PILATUS 2M detector was displayed and analysed using the data visualisation and image manipulation software Albula.[100] Data processing trials were carried out 'by hand' using the CrysAlisPro (Version 40.53) software package, whilst automated data processing was carried out using the in-house software DIALS (Diffraction Integration for Advanced Light Sources)[101, 102] and Xia2 using a pre-package of DIALS.

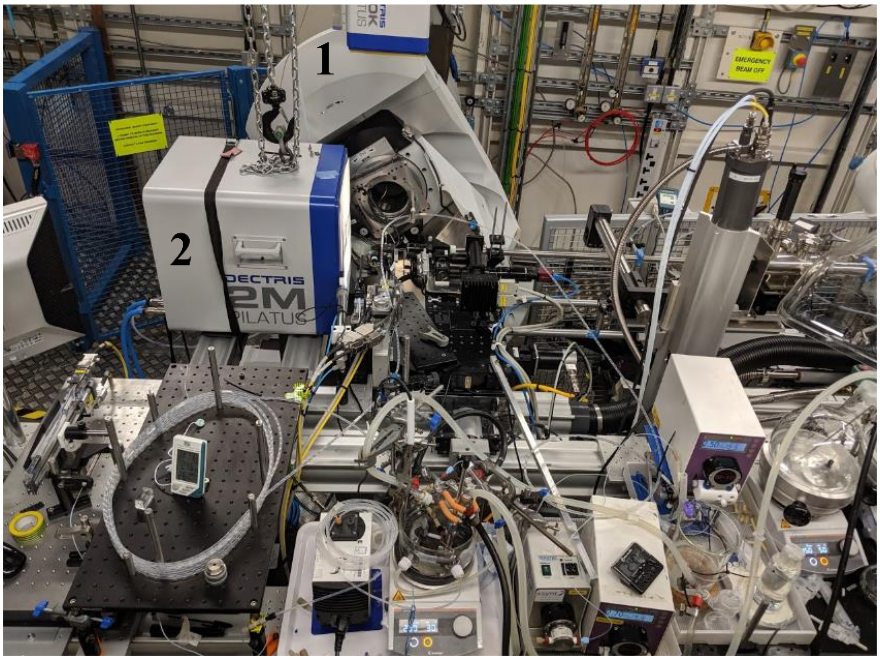

Figure 3.13 – The experimental set-up of the KRAIC-S at EH2, I19 DLS, featuring **1)** Newport[98] four-circle diffractometer and **2)** DECTRIS[99] PILATUS 2M detector.

To ascertain crystal growth at various set points along the length of the KRAIC-S platform where crystals were grown *in situ*, standard data collections of known crystallite sizes were analysed in EH2 as a reference. The integrated intensity values of the PCM form I and PCM form II crystallites of known sizes were collected *via* the traditional SCXRD data collection methodology and compared to the integrated intensity values of single crystals in solution slugs captured in flow in the KRAIC-S.

Beamline 12.2.1, the Small Molecule Crystallography beamline at ALS (Chapter 6)

A recently upgraded superbend beamline 12.2.1 with wavelength ranges of 0.5-2 Å, coinciding with a beam energy of 6-24 keV, suitable for chemical crystallography was installed at the ALS.[95] Beamline 12.2.1 features a parabolic collimating mirror where the X-rays were directed into a Kohzu double crystal Si(111) monochromator followed by a second toroidal mirror, which focuses the beam at the sample positioned in the X-ray hutch. An extremely small beam focus spot of 30 μm x 80 μm was available. Beamline 12.2.1 employs a Bruker D8 laboratory diffractometer with a PHOTON II CPAD detector, in which temperature control was achieved using an Oxford Cryostream 800+. Transmission filters were applied to the incoming beam dependent on the attenuation / diffraction characteristics of the sample, the details can be found in Chapter 6.[103, 104] The data were collected using the Bruker AXS Apex2 software and processed using the Bruker AXS Apex2 with SADABS-2014/5 software packages.

The exposure times for each SCXRD data collection were dependent on both the analytical approach and the material under analysis (full details can be found in the relevant results chapters).

Thermal analysis

3.4.3 Differential Scanning Calorimetry (DSC)

DSC is used to determine the thermal properties of the solid material under study. The information obtained includes melting point, phase transitions, desolvation, decomposition among others. Comparing the thermal events of the profen family co-crystals, with those of the constituent starting components can indicate co-crystal formation when the thermal events differ from the starting materials or confirm the presence of pure or excess starting material when the DSC traces match the DSC traces of the starting materials. This DSC trace comparison is similar to the pattern comparison approach used in the PXRD analysis.

For DSC measurements, between 1-10 mg of powdered sample was weighed and placed into a Tzero aluminium pan and then sealed with a Tzero aluminium lid by the use of a crimping device. The pan containing the powdered sample under study was placed next to an empty reference pan, within a Thermal Advantage (TA) Instruments Q20 DSC. This DSC instrument was equipped with Thermal Advantage Cooling System 90 and operated with a dry nitrogen purge gas at a flow rate of 18 cm^3 min^{-1}. The average heating rate was 10 K min^{-1}. The DSC procedure was devised with TA software whereby specific heating and cooling programmes

could be set including heating and cooling rates, in addition to temperature limits. The data were collected using the software Advantage for Qseries. The resultant endothermic and exothermic events that occurred during the heat-cool cycles were recorded and the Universal Analysis software was used to evaluate the resulting DSC traces.

3.4.4 Thermogravimetric Analysis (TGA) coupled with Mass Spectrometry (MS)

Thermogravimetric (TG) analysis coupled with Mass Spectrometry (MS) allows for the thermal decomposition pathway of a material to be understood, by measuring the weight loss of a sample as a function of temperature. TG is often coupled with MS to allow the identity of the components lost during sample heating to be confirmed. TGA is used to monitor the desolvation of a sample and additionally the stoichiometry of a solvate can be quantified. TGA was used in Chapter 6 to analyse the Oxaprozin-Imidazole (OXA-IMID) solvate structure.

Thermogravimetric Analysis (TGA) was conducted using a Setsys Evolution TGA 16/18 in tandem with a Mass Spectrometer (MS). Once the instrument had been calibrated and a background sample of an empty aluminium crucible run under air, a small powdered sample (1-5 mg) was placed into a 170 μL aluminium crucible which was placed onto the internal instrument balance. The sample was then subject to a pre-programmed heating profile, 5 ^{o}C min^{-1} between 20 °C and 400 °C and the mass loss of the sample was recorded with respect to the temperature. The data collection and processing were carried out using Calisto. Any evolved gas was run through the attached MS for analysis.

MS was coupled with the TG analysis using an OmniStar GSC 320 from Pfeiffer Vacuum, under an argon atmosphere (2.3 bar outlet pressure) controlled using Pfeiffer Vacuum Quadera software. In the experimental set up, the MS was programmed to detect the first four significant MS peaks of the ethanol solvent used in the evaporative crystallisation experiment. The signals of these peaks were recorded throughout the temperature regime and plotted alongside the TG curve, as a function of temperature; this allowed the solvent mass loss step to be identified and the stoichiometry of the OXA-IMID solvate to be quantified.

3.4.5 Hot-Stage Microscopy (HSM)

Hot-Stage Microscopy (HSM) combines microscopy with thermal analysis to allow the thermal behaviour of crystalline materials to be visualised as a function of temperature and time. The basic configuration of the hot-stage microscope includes an optical microscope equipped with a digital camera, a heating stage sample chamber coupled to a digital programmable temperature

controller and a computer with software to record HSM images and videos from the digital camera. HSM was used in Chapter 6 to analyse the OXA-IMID solvate structure and monitor solvent evolution from the sample.

A single crystal or a small quantity of the crystalline material produced from an evaporative crystallisation experiment was mounted onto a glass slide with the use of a low-diffracting oil, Fomblin®, which was then placed into a Mettler Toledo FP82 hot stage set up equipped with a Leica DM1000 Microscope. The crystalline sample was subject to specified heat programmes using the FP90 Processor whereby it was possible to define the initial and final temperature as well as the heating rate. The resultant thermal activity, such as melting of, or solvent evaporation from, the sample was recorded using an Infinity 2 microscopy camera.

3.4.6 Spectroscopy

3.4.6.1 Fourier Transform Infrared Spectroscopy (FTIR)

Infrared (IR) spectroscopy uses the IR region of the electromagnetic spectrum to probe the rotations and vibrations of molecular bonds in organic molecules. The IR radiation is absorbed by molecules at characteristic resonant frequencies that are directly related to the bond vibrations in the molecule and hence are characteristic of a particular functional group.[105]

Fourier transform IR (FTIR) increases the sensitivity of IR measurements by employing an interferometry approach in which the interference pattern generated by recombination with the reference beam can be Fourier transformed to produce the IR spectrum. The use of FTIR spectrometers is adopted as the standard approach in modern IR spectroscopy. The benefit of using an FTIR spectrometer include decreasing the sample size required for analysis and decreasing the time required for acquisition of the spectrum. In Chapter 6, FTIR spectroscopy was used as an approach to monitor co-crystal formation by comparison to the spectra of the starting profen targets, as well as the hydrogen bonds produced in the co-crystal formation, evident from the visualisation of the co-crystal in Mercury after SCXRD analysis.

The FTIR spectra were recorded at room temperature using a Perkin Elmer FTIR Spectrometer in the range 4000-500 cm^{-1} with an ATR (Attenuated Total Reflection) sampling accessory. Multi-component co-crystal formation can be established by comparison with the constituent starting materials prepared by the same crystallisation method. The functional groups of focus

were C=O and N-H due to their hydrogen bonding capabilities often observed during co-crystal formation.

3.4.7 Process Analytical Technology (PAT)

3.4.7.1 Inline Ultraviolet Visible Spectroscopy (UV-Vis) monitoring

Ultraviolet-Visible (UV-Vis) spectroscopy uses the UV and visible regions of the electromagnetic spectrum to interact with matter, which causes electronic transitions, in which electrons are promoted from the ground state to a high-energy state. UV-Vis absorption is principled on the Beer-Lambert law, which states that the attenuation of light is related to the properties of the material through which the light is travelling (Equation 3.1), including the concentration.

$$A = \varepsilon cl$$

Equation 3.1 – The Beer-Lambert law, where A = Absorbance, ε = molar extinction coefficient, c = concentration and l = path length.

Chapter 4 looks at UV-Vis monitoring to investigate dye addition into solution slugs as a technique to optimise seeding addition into the KRAIC-D. An Ocean Optics UV-Vis spectrometer with an in-line z-path flow cell monitored the concentration of dye *via* the 870 nm peak with a data step value of 5 ms. The intensity of wavelength 870 nm was followed as it gave the most discernible difference from the air spectra. As the absorbance value for the dye spectrum at this particular wavelength was lower than that for the air and carrier fluid media, local minima were monitored during the UV-vis analysis. The local minima absorbance values and time difference taken over a 1 minute time period were then compared for consistency of dosing quantities (abs), slug volume and separation (in s).

Chapter 4 – *In situ* X-ray Diffraction (XRD) Analysis of Continuous Segmented Flow Cooling Crystallisation in KRAIC-D at High Resolution Powder Diffraction Beamline I11 Diamond Light Source – Urea-barbituric acid (UBA) and Carbamazepine (CBZ)

The research presented in Chapter 4 comprises a research collaboration between the Wilson Group at the University of Bath with the Kapur and Meldrum groups at the University of Leeds. The other researchers who contributed to various aspects of this work include: Dr. Mark Levenstein (University of Leeds),[106] Dr. Pierre-Baptiste Flandrin,[107] Dr. Daniel Scott and Dr. Ruth Lunt (University of Bath).

The work presented in this chapter has been published in Analytical Chemistry: Dynamic Crystallization Pathways of Polymorphic Pharmaceuticals Revealed in Segmented Flow with Inline Powder X-ray Diffraction.

Mark A. Levenstein[#], Lois Wayment[#], C. Daniel Scott, Ruth Lunt, Pierre-Baptiste Flandrin, Sarah J. Day, Chiu C. Tang, Chick C. Wilson, Fiona C. Meldrum, Nikil Kapur, and Karen Robertson ([#]These authors contributed equally).

Analytical Chemistry **2020** 92 (11), 7754-7761, DOI: 10.1021/acs.analchem.0c00860

4.1 Introduction and Aims

In order to gain more control over crystallisation processes, an improved understanding of these processes is required. The use of more controllable and reproducible crystallisation methodologies, coupled with a means of continually monitoring the process through *in situ* analysis techniques, provides a means to achieve this. For example, *in situ* monitoring of a solution-mediated polymorphic transformation (SMPT) from form II to form I of the pharmaceutically relevant rifampicin in a 100 mL jacketed glass crystalliser in three solvents at 30 °C was investigated. The SMPT of rifampicin was monitored online using Focused Beam Reflectance Measurement (FBRM) and Raman spectroscopy. It was found that the factors controlling the polymorphic transformation differed with solvent selection. The transformation process was controlled by dissolution of form II in heptane, whilst in hexane and octane the

process was initially controlled by dissolution of form II and then by the growth of form I. This *in situ* study thus provided mechanistic insight.[108]

More relevant to this results chapter, *in situ* synchrotron powder X-ray diffraction (PXRD) studies have been used to monitor the SMPT of the potent anti-inflammatory agent flufenamic acid from the metastable form I to the stable form III during the wet granulation process. The resulting experimental data obtained from this study were used to test and validate a predictive model for polymorphic transformations during the wet phase of granulation, based on mass transport and crystallisation kinetics. Real time monitoring provided the opportunity for real-time control of the granulation process; altering the granulation time can alter the polymorphic outcome.[109] In a study by Ouyang *et al.*, the polymorphic transformation from α-glycine to γ-glycine during an ionic liquid-mediated crystallisation process was achieved through evaporation of water. Droplets of the target solution were spotted in the middle of the cavity of the glass sample holder and the crystallisation process of glycine was monitored *via in situ* PXRD by monitoring the change in intensity of characteristic diffraction peaks.[110]

Online PXRD analysis was employed to investigate chemical and structural transformations of coordination polymers and metal-organic frameworks carried out by mechanochemical reactions. The mechanochemical reactions were carried out in an in-house built milling vessel and analysed by *in situ* synchrotron X-ray diffraction (XRD) monitoring, whereby the real-time characterisation was achieved without disturbing the milling process.[111, 112]

Online PXRD analysis was employed to monitor the formation and growth of nanoparticles, as well as to monitor phase transitions and to determine crystallite size. The formation and growth of $CoSb_2O_4$ nanoparticles using different precursor stoichiometries were followed in real time using *in situ* synchrotron PXRD. The crystallite size can be fine-tuned between 14 nm and 17.5 nm under nonstoichiometric conditions, whilst crystallites twice as large are found in stoichiometric ratios. A similar study employed *in situ* synchrotron XRD analysis to study the formation, growth and phase transformation of colloidal monodisperse spherical copper sulfide nanocrystals synthesised in dodecanethiol. For these studies of the $CoSb_2O_4$ nanoparticles and the copper sulfide nanocrystals, the precursor was injected into a custom-made sapphire capillary set-up, which was subsequently pressurised and heated to the desired temperature, whilst time-resolved XRD patterns were acquired at 5 seconds and 9 seconds intervals respectively. These studies demonstrate the use of *in situ* synchrotron XRD analysis

to provide information on how to control the size and phase of these nanoparticle systems as a function of time and temperature.[113, 114]

These online PXRD studies have been limited to batch processing methods. Batch environments exhibit limitations such as inhomogeneity, with respect to mixing and heat transfer. In addition, for large stirred-tank reactors, it is only possible for a fraction of the vessel to be probed and thus the analysis may not necessarily be representative of the bulk sample.

Flow technologies offer the potential for the area of analysis (for example, the size of the X-ray beam), to be compatible with the size of the reactor, resulting in representative sampling of the crystallisation process compared to traditional batch reactors. At the micro and nanoscale, the flow of fluids is confined such that turbulence is essentially suppressed, which leads to predictable flow paths and controlled mixing conditions, where polymorphic form can be more reliably predicted and thus the desired form can be accessed for manufacture.[115] However, milliscale crystallisers operate over a more suitable scale of production of crystallisation processes in the pharmaceutical industry to facilitate high-throughput screening at scale. In increasing the scale of operation from nanoscale to milliscale, dramatic changes in flow behaviour are apparent, whereby the flow of fluids in milliscale crystallisers exhibit turbulent behaviour. This turbulent flow results in unpredictable crystallisation pathways compared to nanoscale systems and emphasises the importance of *in situ* XRD for improved understanding. Although the area of continuous crystallisation is not in its infancy, relatively little understanding into how crystallisation occurs in a flow environment has been achieved to date and thus its potential capabilities are also unknown.

In the work presented, a flow crystallisation platform based upon the KRAIC,[72] known as the KRAIC-D (Kinetically Regulated Automated Input Crystalliser for Diffraction), which employs tri-segmented flow and achieves crystallisation through cooling, was installed on the High Resolution Powder Diffraction beamline I11 at the Diamond Light Source (DLS) synchrotron. In this segmented flow environment, each droplet of crystallising solution only equates to a volume of *ca.* 0.2-0.4 mL; coupled with the corresponding flow rate and the associated data acquisition time per slug this means that observing crystallisation *in situ* is not to date accessible with laboratory-source diffractometers due to the small volume of diffracting material passing the beam at any given time. This problem with analysis is rectified through the use of the high flux available at synchrotrons. The use of synchrotron radiations rectifies

the inherent issues with low intensity of diffraction and a high signal:noise ratio. The higher intensity of X-rays available at synchrotron facilities allows diffraction from crystallites to be discerned above the scattering of the solvent, whereby solution slugs contain a significant solvent contribution compared to the low density of crystallites in solution slugs passing the X-ray beam. Furthermore, segmented flow provides highly reproducible environments for crystallisation, such that at a given set point along the length of the crystalliser, once steady-state operation has been reached, the crystallisation process will always be at the same stage of the crystallisation irrespective of the experiment time. This reproducibility in nucleation and crystal growth times allows events that evolve with time, such as polymorphic transformations, to be captured without time constraint.

Two pharmaceutically relevant and highly polymorphic systems of interest, which comprise the materials focus for this study, are the model systems urea-barbituric acid (UBA) and carbamazepine (CBZ).

CBZ is the API in Tergetol®, which is used as an anti-seizure medication and to relieve neuropathic pain (Figure 4.1). CBZ has five anhydrous polymorphic forms, as well as solvates and co-crystals;[116] the various polymorphs possess distinct habits.[117] CBZ form III is the thermodynamic form under ambient pressure, whilst CBZ form II is often formed from solution-based crystallisations.[1] According to Ostwald's rule of stages, the less stable polymorph will often nucleate first and will subsequently undergo polymorphic transformation(s) before reaching the most stable polymorph.[118] As a result of Ostwald's step rule, it can be postulated that a polymorphic transformation from CBZ form II to CBZ form III could be observed in the crystallisation process, where the initial polymorphic outcome is largely dictated by the mixing conditions.[1]

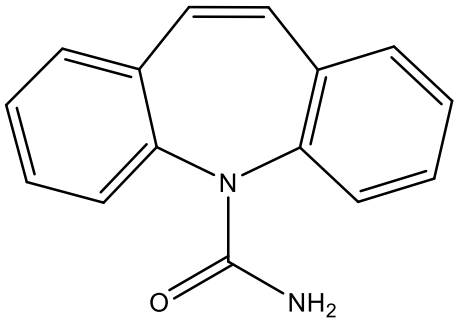

Figure 4.1 – Chemical structure of carbamazepine (CBZ).

UBA is a co-crystal of urea and barbituric acid (Figure 4.2). It exhibits improved solubility from barbituric acid, which is a precursor material to the barbiturate family of compounds. The barbiturates such as phenobarbital act as central nervous system depressants providing anaesthesia and used in the treatment of epilepsy and migraines.[119] UBA is a polymorphic co-crystal with four known forms, three of which have been fully characterised, two of which have very similar Gibbs Free energies and exist concomitantly; a mixture of these two, UBA form I and UBA form III, are often obtained as a mixture from cooling crystallisations.[51, 120] It has been previously reported that UBA form I is the stable form crystallised from cooling under ambient conditions,[51] whilst charge density calculations reported from Gryl *et al.*[121, 122] suggest otherwise. Thus, the use of *in situ* XRD characterisation could provide evidence to unravel the true stability relationship between UBA form III and UBA form I during crystallisation.

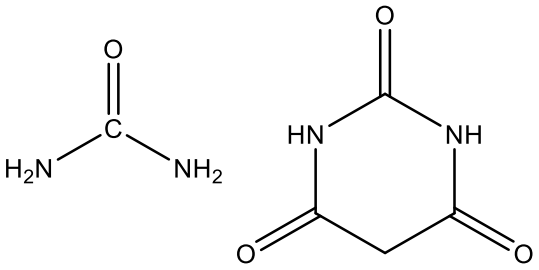

Figure 4.2 – Chemical structure of the components urea (left) and barbituric acid (right), which comprise the co-crystal system urea-barbituric acid (UBA).

This chapter investigates the relative stabilities of the various polymorphic forms for both the CBZ and UBA model systems, *via* unseeded and seeded cooling crystallisation *via* flow methodologies. This work will elucidate the crystallisation pathways for CBZ in ethanol (EtOH) and UBA in methanol (MeOH). As well as polymorphic transitions during unseeded crystallisation, the effect of introducing a controlled solid interface through the use of seed crystals of polymorphic purity, added at various set points along the length of the crystalliser, will be presented. The use of seeds in a range of pure polymorphic forms will augment the understanding of the polymorphic landscape by establishing whether seeding dictates the polymorphic outcome. In addition to analysing the final crystalline product, *in situ* monitoring *via* XRD characterisation will allow the crystallisation processes to be continually monitored, allowing the various phases and transformations during the processes to be revealed.

The pivotal importance of investigating flow crystallisation processes *via* online XRD analysis is to contribute to the augmented understanding of crystallisation processes in a flow

environment required by the pharmaceutical industry. *In situ* XRD analysis of continuous segmented flow milliscale crystallisation in the KRAIC-D platform at I11 is thus reported here for the pharmaceutical compounds CBZ and UBA.

4.2 KRAIC-D Design and Overview

The custom designed KRAIC (Kinetically Regulated Automated Input Crystalliser) is a milliscale continuous crystalliser, which employs liquid-segmented flow to achieve plug flow conditions and mixing throughout the reactor length, in order to optimise critical quality attributes (CQAs), such as form and particle size distribution (PSD). The liquid-segmented flow employed in the KRAIC platform comprises the crystallising solution to achieve crystallisation through cooling, carrier fluid to coat the inside of the tubing and prevent crystallisation on the reactor walls and air to improve mixing and slug regularity.[72]

An adaptation of the KRAIC developed by Dr. Karen Robertson at the University of Bath, to ensure the segmented-flow crystalliser was suitable for in-beam operation at DLS, led to a collaboration with the Kapur and Meldrum groups at the University of Leeds. Dr. Karen Robertson, Dr. Mark Levenstein and Dr. Pierre-Baptiste Flandrin conceptualised, designed and built the KRAIC-D. The design and materials used to construct the KRAIC-D are selected to ensure compatibility for in-beam operation at beamline I11, DLS. The two cylindrical supports in Figure 4.3a provide a means to add length to the crystalliser as the fluoroethylene propylene (FEP, 3.18 mm internal diameter (ID)) body of the KRAIC-D is wrapped around the cylinders. These cylinders are positioned to provide distance and, as a result of steady-state operation, choice of residence time between the various analytical set points along the crystalliser length. Wrapping the FEP tubing around the two columns provides a slight but constant upward gradient for the segmented flow, which is beneficial for the controlled fluid dynamics within the system. These plastic cylinders also provide heat insulation for the tubing coils and as a result prevent heat sink effects. The cylinders are set far enough apart such that unnecessary strain is not put upon the viewing section where the custom polytetrafluoroethylene (PTFE) unions provide a join between the viewing section (consisting of short lengths of Kapton® tubing) and the rest of the FEP body (Figure 4.3a). A constant ID is maintained throughout the entirety of the KRAIC-D crystalliser, including the KRAIC-D body, PTFE unions and Kapton® windows.

The viewing section comprises X-ray transparent Kapton® windows, to ensure minimal background diffraction results from the tubing. The windows are strategically placed along the length of the crystalliser to monitor the crystallisation process at various stages, where a given distance equates to a specific crystallisation time, irrespective of the experiment time due to the steady-state operation of the flow crystalliser. For the experiments reported here, the Kapton® analysis tubes are positioned at 6.4 m, 9.0 m and 11.7 m for windows 1, 2 and 3 respectively along the crystalliser length. Data are acquired by translation of the KRAIC-D platform on a motorised XYZ stage, which facilitates movement between windows in the Z-direction (Figure 4.3a). The motorised stage also allows traversing in the X-direction, along the windows, to allow multiple scans to be acquired at each window position, whilst also maximising the operational lifetime of each Kapton® window before damage of the coating from the X-ray beam renders them unusable. The Kapton® windows are hydrophobically coated with a commercially available water repellent, known as Aquapel®, to ensure preferential wetting of the carrier fluid (perfluoropolyether, PFPE (Galden®)); the treatment procedure is detailed in Section 4.3.1. This window treatment ensures that crystallisation occurs away from the inner walls of the tubing, removing the solid interface, which ensures that nucleation proceeds spontaneously by primary homogeneous nucleation (in an unseeded crystallisation run) and prevents sedimentation and encrustation.

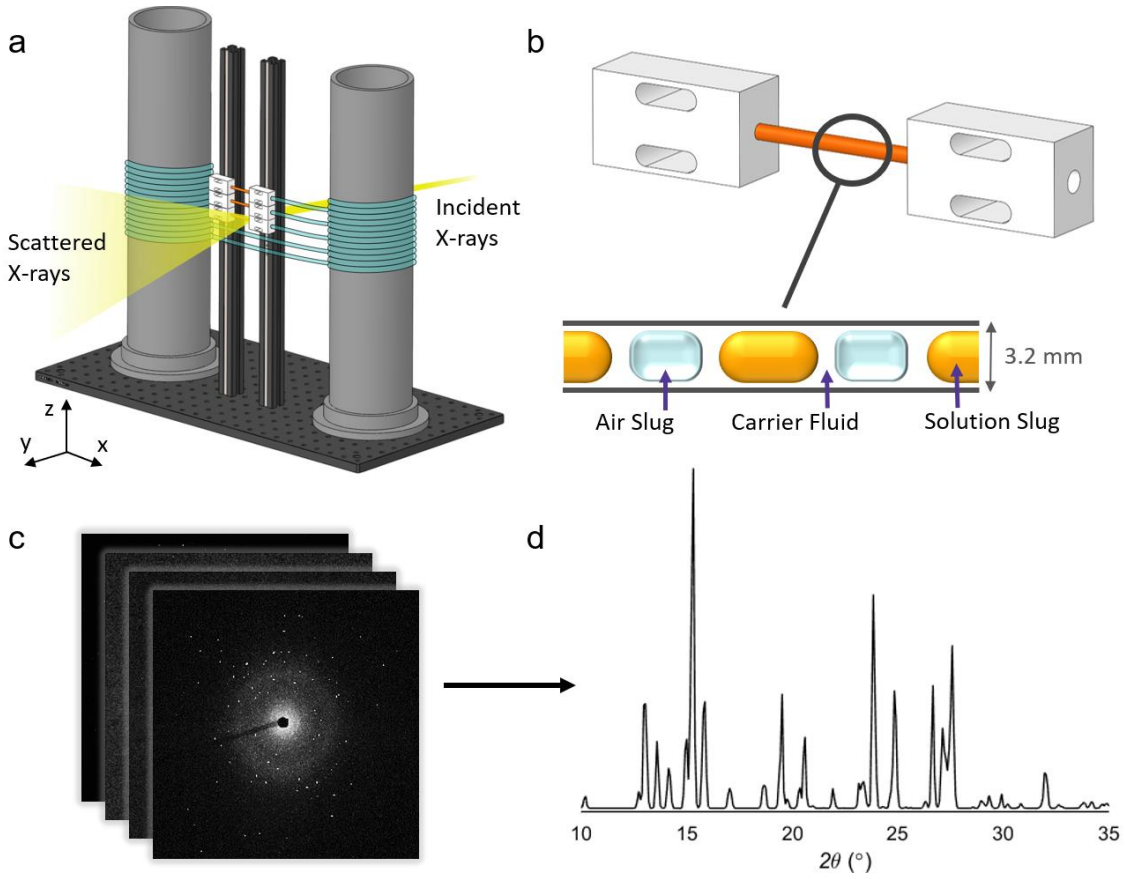

Figure 4.3 – (**a**) Diagram of the KRAIC-D by Dr. Mark Levenstein, operating in transmission mode with X-ray penetration initiated behind the window section, (**b**) enlarged view of a single analysis window comprising a Kapton® tube and two PTFE unions (inset shows the triphasic (solution, air, and carrier fluid) plug flow), (**c**) accumulation of 2D diffraction pattern frames from 100 ms exposures which are combined to achieve (**d**) the 1D diffraction plot (shown here is a combined scan of CBZ form II).

4.2.1 Union Detail

The PTFE unions designed by Dr Mark Levenstein provide a join between the viewing section containing the Kapton® windows (Kapton®, 3.188 mm ID, 3.38 mm OD) and the rest of the FEP body of the KRAIC-D (FEP, 3.175 mm ID, 4.76 mm OD). The joining of the Kapton® windows within the unions is improved by the use of a silicone sealant used to prevent leakages. The PTFE unions are designed to ensure a continual ID of 3.19 mm) with little to no perturbation to the flow as detailed in Figure 4.4.

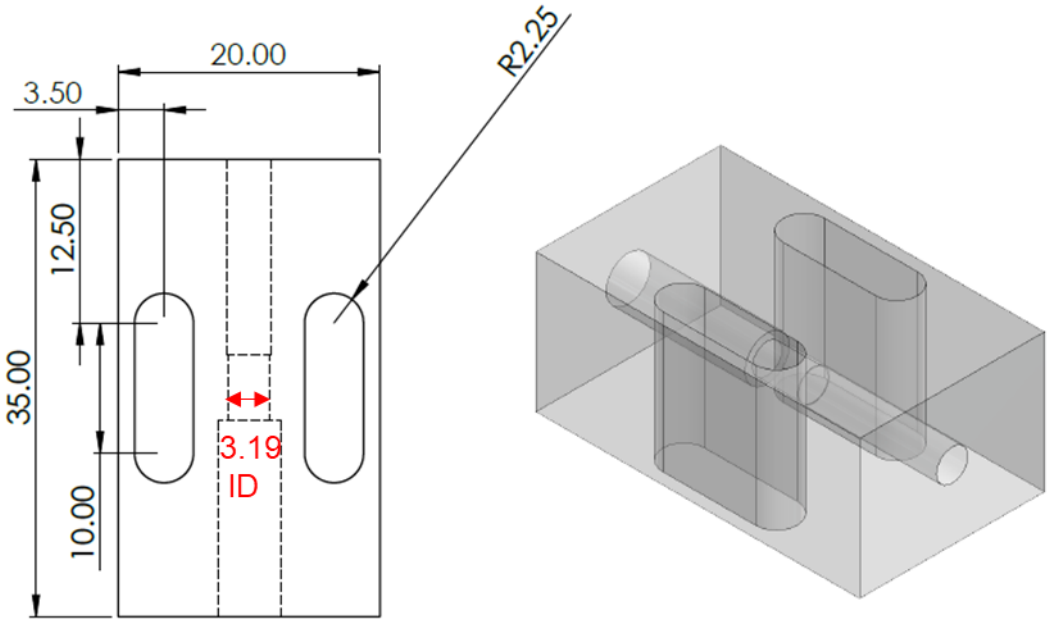

Figure 4.4 – Computer-aided drawing (CAD) of PTFE unions by Dr. Mark Levenstein, with all measurements set to mm, with the ID of the union equalling the ID of the KRAIC-D body, highlighted in red.

4.2.2 Experimental Set-up

Segmentation is achieved on the premise of immiscibility of the three phases, where separate streams of crystallising solution, air and carrier fluid are all transferred under temperature-controlling jacketed tubing to ensure a constant, well-defined temperature start point before the flows combine at a glass cross-piece (X-piece, 3 mm ID) (Figure 4.5a).

A circulator bath is used to control the temperature of the tubing jackets and transfer tubes (Figure 4.5d). The X-piece sits in a temperature-controlled segmentation water bath comprising a custom glass water bath *via* a hot-plate with magnetic bottom stirring. The temperature is actively regulated until segmentation is achieved to prevent crystallisation occurring before segmentation; once the flow is segmented heated temperature control is removed to allow the cooling crystallisation to proceed *via* air cooling of the solution within the crystalliser tubing. Depending on how rapidly nucleating the crystallising system is, coupled with the concentration and temperature conditions, further temperature controlled tubing such as a section of sub-ambient jacketed crystalliser tubing (represented by the nucleation promoter) may be required to promote nucleation as the crystallisation process is optimised (Figure 4.6).

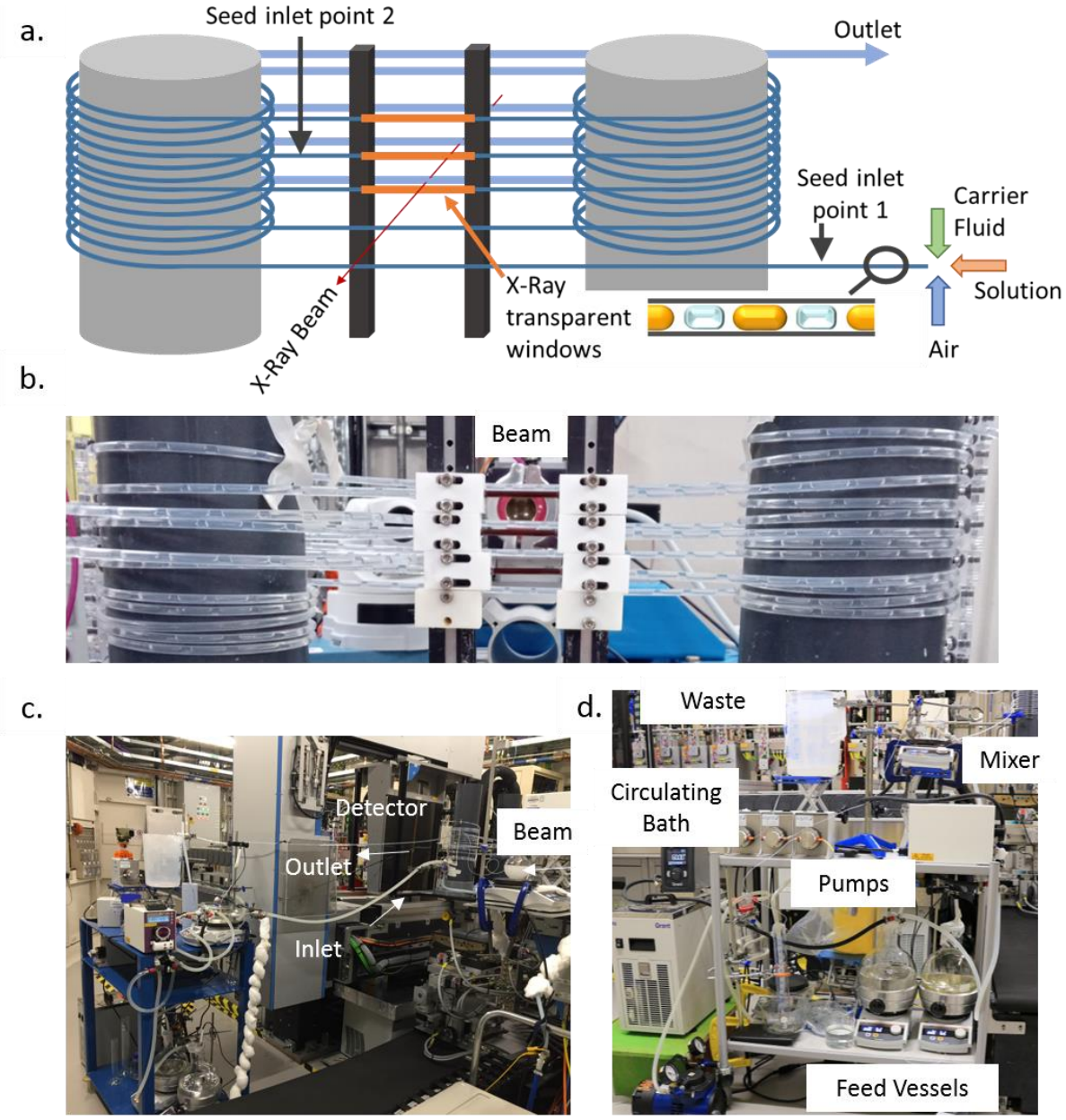

Figure 4.5 – (**a**) KRAIC-D schematic highlighting X-ray transparent windows and seed inlet positions. (**b-d**) Photographs of the KRAIC-D in experimental hutch 2 (EH2) of beamline I11 at Diamond Light Source showing (**b**) KRAIC-D analysis section with beam outlet behind, (**c**) detector and trolley positioning, (**d**) trolley with pumping, segmentation, and fluidic apparatus.

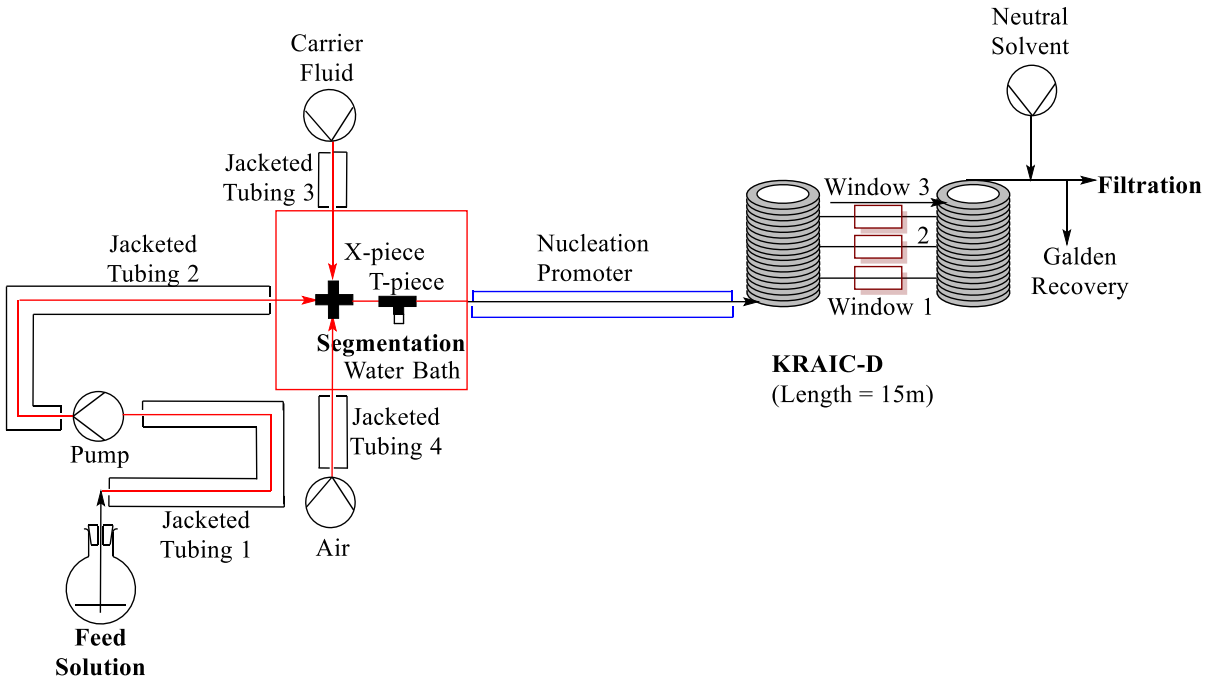

Figure 4.6 – Schematic of KRAIC-D unseeded experiments.

A peristaltic pump (Vapourtec SF-10), designed to lessen pulsation with respect to standard peristaltic pumps whilst maintaining compatibility with crystallising solution transfer, was employed for the crystallising solution, whilst the air and carrier fluid were transferred using gear pumps (Ismatec ISM895E). For seeding crystallisation runs, an additional SF-10 peristaltic pump was utilised to introduce the seed slurry into the crystallisation at the pre-nucleation and post-nucleation seeding ports (Figure 4.5a).

4.2.3 Seeding Inlets

For experiments where the influence of introducing a controlled solid interface through seeding was investigated, the experimental set-up required adaptation to accommodate this addition.

4.2.3.1 Seed Inlet Geometry and Flow Rate ratio Optimisation

The previously optimised unseeded crystallisation set-up required development to allow for an additional inlet to introduce the seed slurry into the system. The considerations for this development include the type of connector component used to introduce the slurry, with consideration to the material of which it is composed, the bore size of the component and the orientation of the connector. The component that facilitates the introduction of the seeds must be a 3-way connector, such as a Y-piece or a T-piece, where the net-segmented flow emerging from the X-piece can combine with the seed stream, resulting in a seeded net-flow. The material

from which this connector is made, such as glass or polypropylene (PP), will affect the wettability and in turn the segmentation. The flow conditions also require optimisation, as the relative flow rates of the various streams will affect the seed dosage into a solution slug. The incorporation of additional material within the segmented flow also relates back to the bore size of the connector. For instance, a connector with a smaller bore size, whilst maintaining the same flow rates and thus the same volume of fluid passing through in a given time, maximises the chance of incorporation of the seed material into the solution slug rather than the generation of separate slugs comprising only the seed slurry. The generation of novel solution slugs during seed addition assumes the immiscible activation barrier, which depends on the surface tension of the segmented media in the tubing, is overcome.

4.2.3.2 Seed Addition Monitoring using inline UV-vis Spectroscopy

The use of a dye allows for the addition of the seed stream to be evaluated not only visually but also using UV-Vis spectroscopy. For the purpose of UV-Vis analysis, the seed slurry comprised an ethanolic solution containing ~0.8 g/L of Eosin Y in ethanol, which was continually stirred *via* round bottom stirring with a magnetic stirrer. The dye solution was introduced into the segmented flow system *via* one of three connectors under trial: PP T-piece (2 mm ID), PP Y-piece (3 mm ID) and glass T-piece (3 mm ID). The different connector geometries allow for connector material, connector design and orientation, as well as bore size to be evaluated for optimal seed delivery (Figure 4.7). The seed connector was introduced directly after the X-piece where segmentation is established by adopting the same in-series configuration illustrated in the unseeded experiments (Figure 4.6), using a short section of Marprene® tubing, chosen both for its chemical resistance and for the fact that the semi-rigid Marprene® provides a strong join between the glass X-piece and the seed connector.

For the purpose of this developmental study, rather than the segmented flow entering the KRAIC-D platform, instead a 1 m length of FEP tubing (ID 3.18 mm) was connected to the end of the segmentor and dye inlet using a short section of Marprene® to the 3-way seed connector. To monitor the dye incorporation into the segmented flow, an Ocean Optics UV-Vis spectrometer connected to an in-line z-path flow cell was attached directly to the outlet of the 1 m length of FEP tubing using a PP screw thread connector and ferrule. The tri-segmented flow emerging from the X-piece comprised ethanol for the solution slugs, carrier fluid (Galden® SV 110) and air delivered at flow rates of 2.1 mL/min for ethanol and 4.18 mL/min each for air and the carrier fluid.

Figure 4.7 – Images of segmentation X-piece connected to (clockwise) PP T-piece, glass T-piece and PP Y-piece seed / dye inlet connectors for seeding optimisation studies.

To ascertain the identity of each of the components of the segmented flow featuring in the UV-Vis spectra, background spectra of each of the pure components (ethanol, air, carrier fluid and Eosin Y in ethanol solution) were recorded separately and background subtraction carried out (Figure 4.8). The UV-Vis spectrometer was set to scan across a range of wavelengths (200-1000 nm), to determine the single wavelength most appropriate for analysis of Eosin Y in relation to the other media. A wavelength of 870 nm was selected as the spectrum at this wavelength shows the most discernible differences in absorption between air and Eosin Y, given potential issues with detector blackout due to absorbance values of >1 at 250 nm and 590 nm.

The UV-Vis spectrum of carrier fluid was not observed from the spectra obtained during segmented flow; this can be attributed to the high density of the carrier fluid meaning sufficient volume of carrier fluid does not pass the laser beam path for identification.

The flow conditions investigated in these experiments are summarised in Table 4.1, with each flow rate combination trialled for the X-piece connected to either a PP T-piece, glass T-piece or PP Y-piece connector. This allowed flow rate optimisation, as well as connector material optimisation and choice of geometry to yield the best segmentation in terms of slug size consistency and dye addition (dosing) regularity to the solution slugs.

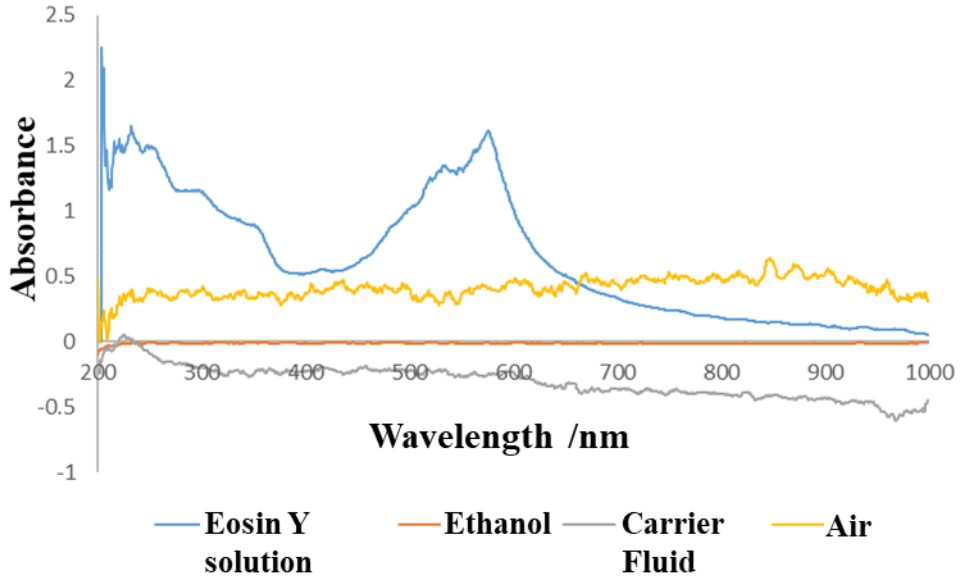

Figure 4.8 – Full UV-Vis spectra of all three phases in dye studies of seeding inlet optimisation (ethanol trace measured to confirm background subtraction).

Table 4.1 – Flow rates for the dye and solution feeds used in seed optimisation study.

Flow rate of dye /mL/min	1								2
Flow rate of solution /mL/min	1	1.2	1.4	1.6	1.8	2	2.5	3	2

Comparing the relative absorbance trends for the pure air and Eosin Y spectra, at 870 nm the air absorbs more strongly than Eosin Y and thus it was decided to focus on local minima of the absorbance values for monitoring the delivery of the dye (Figure 4.9).

The time interval between the local minima absorbance values gives an indication of the dosing from the resulting concentration of dye within a solution slug, but this will also be dictated by the slug sizes of the various media and the consistency of the segmentation. It is important therefore to make comparisons between the spectroscopic data and visual observations of the segmentation to make reliable judgements on the optimal seed delivery set-up. Regularity in segmentation and thus slug distances is observed as a horizontal line for the time interval (in increments) between the acquisition of adjacent data points.

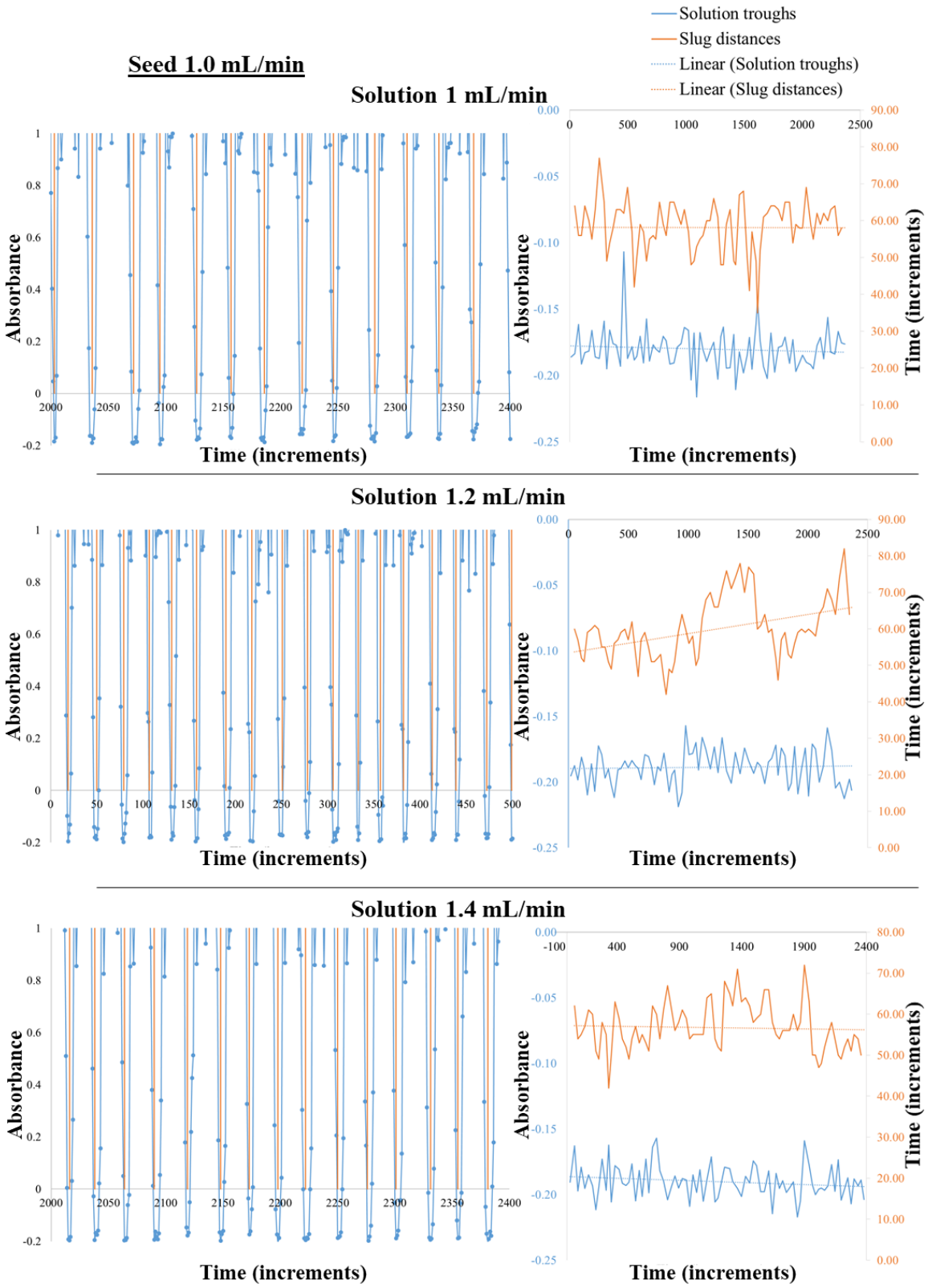

Figure 4.9 – 870 nm peak absorbance *versus* time (5 ms increments) for 1 mL/min seed flow rate, with 1.0, 1.2 or 1.4 mL/min solution flow rate, with a PP T-piece (used for optimal seeding configuration). N.B. orange vertical bars show location of detected local minima (left) and the corresponding slug analysis chart for each flow rate combination featuring solution troughs (blue) and slug distances (orange) (right).

The visual observation of the segmented flow corresponding with the UV-vis data presented in Figure 4.9 for the various flow rate combinations using the PP T-piece connector is presented in Table 4.2. Image 3 in Table 4.2 corresponding with a solution flow rate of 1.4 mL/min and seed flow rate of 1 mL/min exhibits the most homogeneous segmentation coupled with the lowest dosage addition of the dye to each solution slug, whilst mitigating against sedimentation. The PP T-piece set-up yields the lowest dosage of dye into the solution slugs consistent across all flow rate combinations, compared to the glass T-piece and PP Y-piece configurations; the corresponding UV-vis data and segmentation images for the same flow rate combinations are presented in Appendix 4.2 and 4.3 respectively. As a result of the low and consistent dosing of dye into solution slugs provided by the PP T-piece, this was selected as the most appropriate connector for this application.

As the flow rate of the solution feed is increased, the size of the solution slugs proportionally increases, which subsequently results in the segmented flow appearing less homogeneous, which is reflected in both the UV-vis data and corresponding slug analysis plots (Figure 4.9) as well as by visual observations (Table 4.2). This inverse relationship between the magnitude of the flow rate and segmentation homogeneity is consistent across all the connectors, as evident from the data presented in Appendix 4.1, 4.2 and 4.3. The absorbance data for all the seed inlet geometries and flow rate ratios are detailed in Appendix 4.4.

Table 4.2 – Images of segmentation corresponding with a range of flow rate combinations for the solution feed and seed addition.

Flow rate of seed mL/min	1								2
Flow rate of solution mL/min	1	1.2	1.4	1.6	1.8	2	2.5	3	2.5
Image of Segmentation	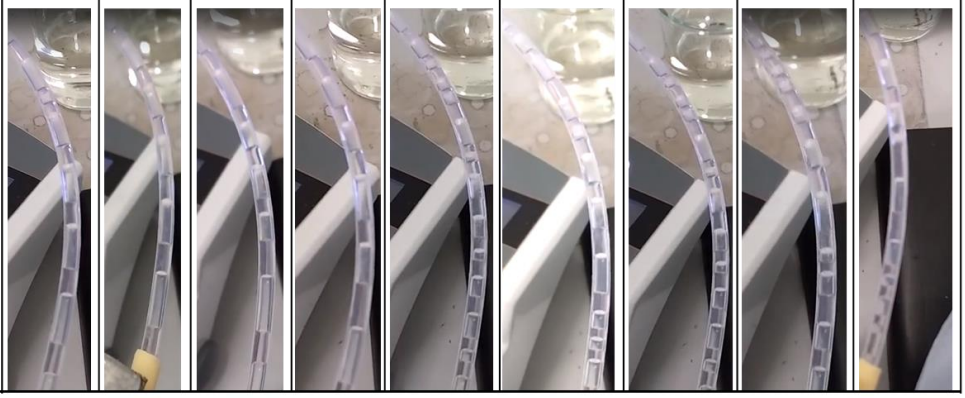								

4.2.4 Seed Generation and Slurry Stability Studies

4.2.4.1 CBZ Seed Generation and Feed Slurry Stability

A study of pure CBZ form III seeds and seed solution stability was performed through a range of slurry densities (altered by CBZ in EtOH concentration), stirring rates and slurrying times (Table 4.3). This allows for the elucidation of form delivery parameters in order to access CBZ form III in polymorphic purity, allowing the form of seeds delivered into the KRAIC-D to be established reliably and to be reproducibly accessed.

The slurry is prepared and delivered at room temperature into the cooling crystallisation during *in situ* analysis experiments and therefore this study only considers a slurry temperature of 20 °C. Importantly the temperature of the experimental hutch (EH2) at beamline I11 varies greatly depending on the outside temperature, the circulator bath, water bath and feed solution will all emit heat, additionally contributing to the temperature of the room. The temperature will affect the slurry density through change in solubility and therefore investigating a concentration range helps account for these slight variances in temperature. The CBZ stock used in the crystallisations is the thermodynamic form CBZ form III (Appendix 4.5 (CBZ starting material)).

Table 4.3 – Experimental parameters for seed stability testing of CBZ form III in EtOH.

Concentration of CBZ in EtOH /mg/mL	Slurrying time /hrs	Stirring rate /rpm	Slurrying Temperature /°C
40	1	300	20
45	2		
50	3		
55			
60			

Concentration of CBZ in EtOH

Varying concentrations of CBZ slurry mediated in EtOH at a stirring rate of 300 rpm for 1 hour yielded CBZ form III. A representative CBZ DH peak at 9° 2θ is also evident in the PXRD patterns for 40, 50 and 55 mg/mL CBZ in EtOH (Figure 4.10), while concentrations of 45 and 60 mg/mL CBZ in EtOH produce CBZ form III in polymorphic purity. Slurrying CBZ in EtOH at a stirring rate of 300 rpm for 2 and 3 hours across the same concentration range each produced CBZ form III in polymorphic purity. Obtaining seeds of polymorphic purity at these longer timescales is beneficial, particularly considering that even though the slurries are made

just before use, the nature of in-beam operation including blockage mitigation result in slurry preparation and delivery timeframes typically of hours.

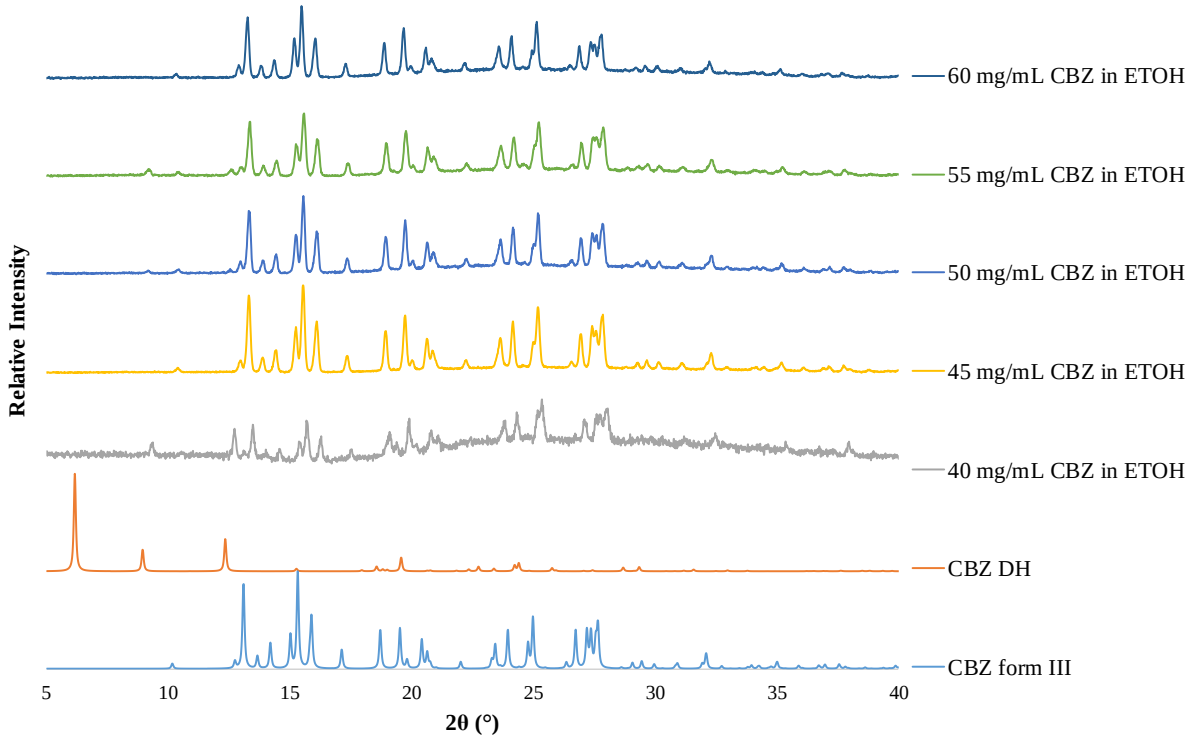

Figure 4.10 – PXRD patterns showing CBZ form III stability in EtOH at 300 rpm for a slurrying time of 1 hour at 20 °C.

Slurrying Time

To access the metastable CBZ form II, Ostwald's rule of stages would suggest that shorter slurrying times could yield CBZ form II forming initially, which may be isolated provided the metastable form can be isolated before transforming to the thermodynamically stable CBZ form III. Formation of the metastable CBZ form II will be kinetically driven, thus an increase in stirring rate may promote the formation of this metastable form (Table 4.4). Slurrying CBZ in EtOH at an increased rate of 400 rpm for 10, 20 and 30 minutes before filtration, yielded CBZ DH (Figure 4.11). Experiments at these various slurrying times were investigated over the full 40-60 mg/mL CBZ in EtOH concentration range. The results for the 40 mg/mL CBZ in EtOH are reported here, but the polymorphic outcome was the same across the full concentration range and over the various slurrying times (Figure 4.11 and Appendix 4.5).

The stirring rate and slurrying time have a greater impact on polymorphic outcome compared to concentration. When CBZ in EtOH is slurried at a stirring rate of 500 rpm, a polymorphic

transformation is observed from CBZ DH to the thermodynamic CBZ form III between 10 and 20 minutes respectively (Figure 4.12 and 4.13) consistent across the full concentration range.

A complete summary of all the CBZ seeding stability testing including the experimental conditions and the corresponding polymorphic outcome is given in Table 4.5.

Table 4.4 – Experimental parameters for CBZ form II slurry stability testing.

Concentration of CBZ in EtOH /mg/mL	Slurrying time /mins	Stirring rate /rpm	Slurrying Temperature /°C
40	10	300	20
45	20	400	
50	30	500	
55	60		
60	120		
	180		

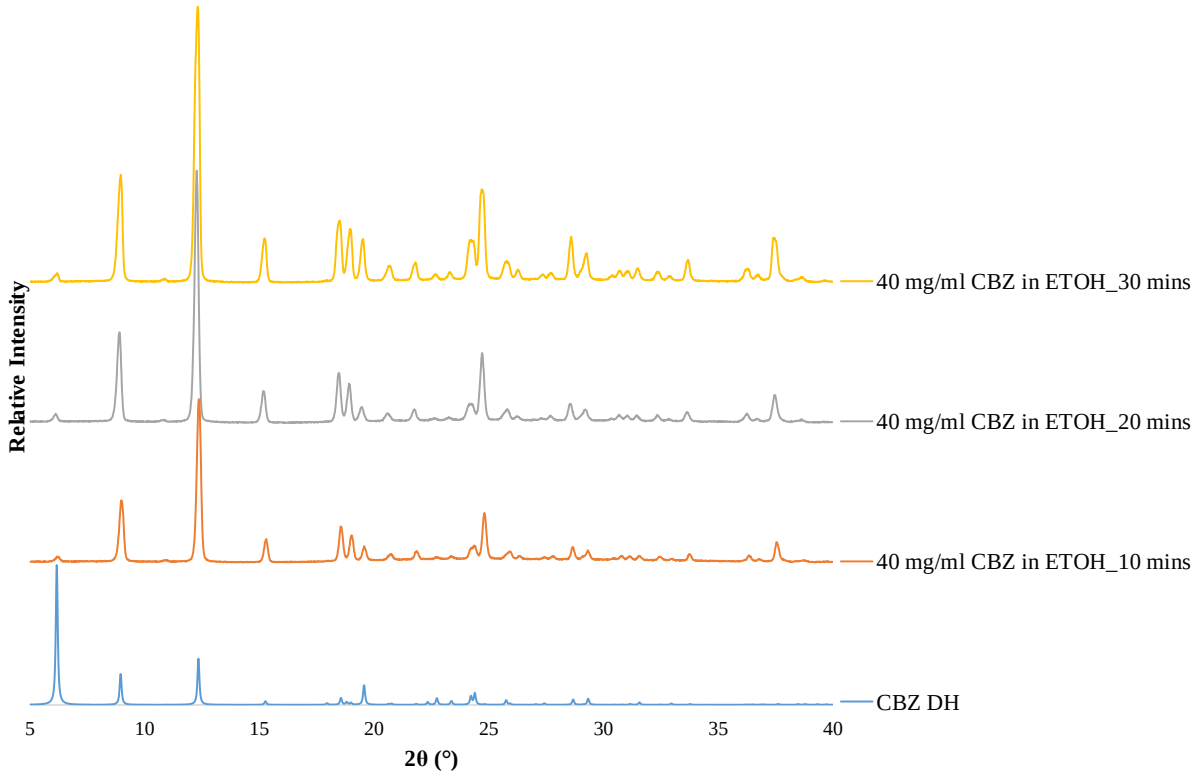

Figure 4.11 – PXRD patterns for CBZ form II slurry testing at 400 rpm over various slurrying times at 20 ℃.

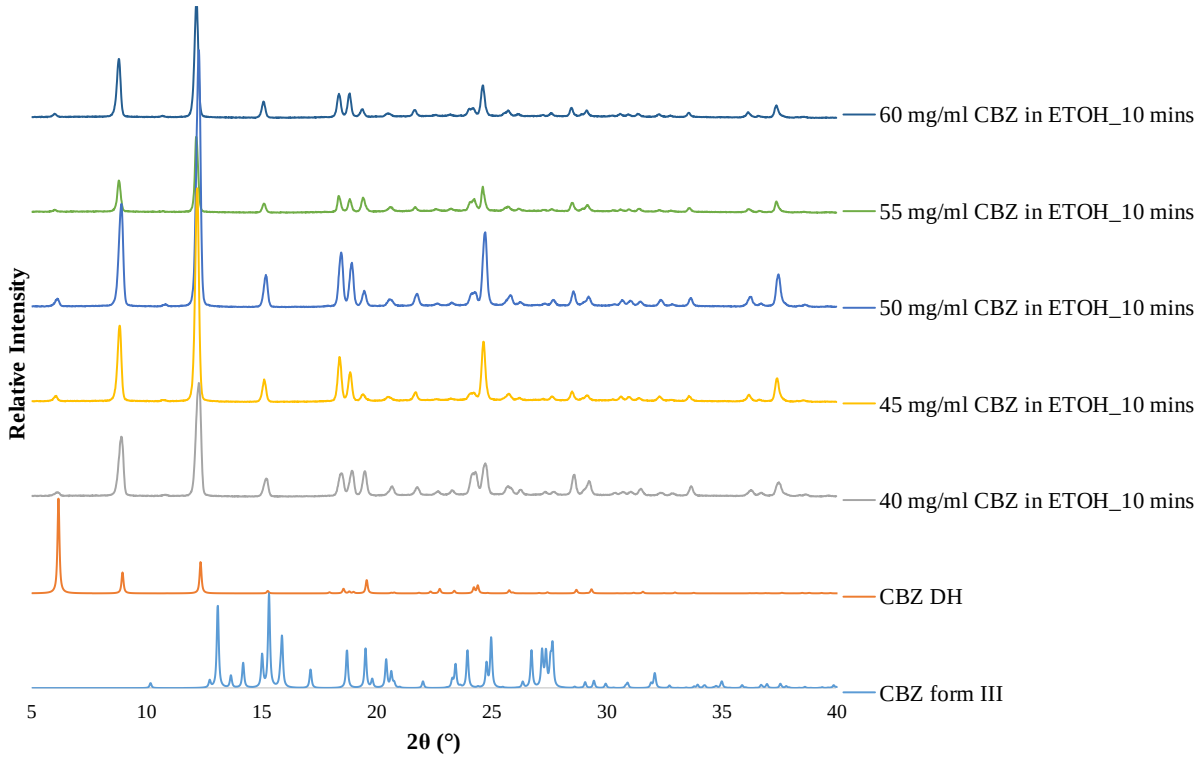

Figure 4.12 – PXRD patterns of varying concentrations of CBZ in EtOH at 500 rpm for 10 minutes slurrying time.

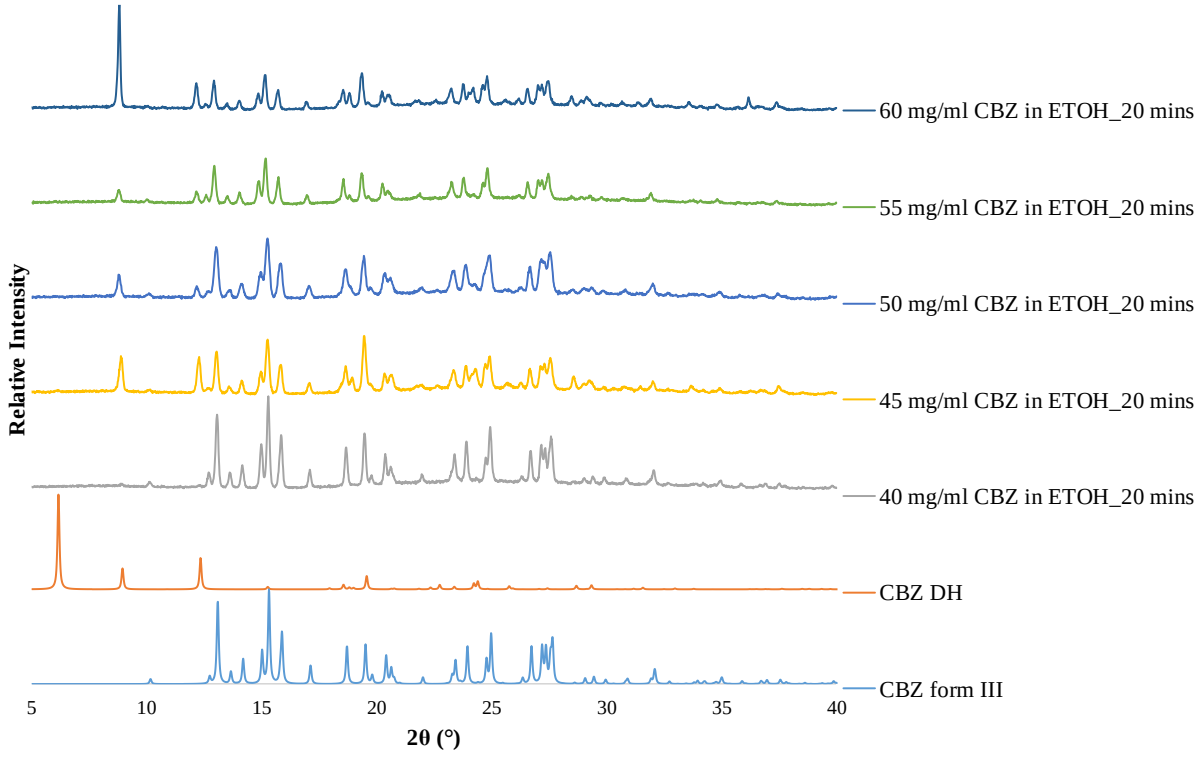

Figure 4.13 – PXRD patterns of varying concentrations of CBZ in EtOH at 500 rpm for 20 minutes slurrying time.

Table 4.5 – Summary of CBZ seeding stability testing.

<table>
<tr><th rowspan="3">Concentration of CBZ in EtOH /mg/mL</th><th colspan="9">Stirring Rate /rpm</th></tr>
<tr><td colspan="3">300</td><td colspan="3">400</td><td colspan="3">500</td></tr>
<tr><th colspan="9">Slurrying Time /mins</th></tr>
<tr><td>10</td><td>20</td><td>30</td><td>10</td><td>20</td><td>30</td><td>10</td><td>20</td><td>30</td></tr>
<tr><td>40</td><td>CBZ form III</td><td>CBZ form III (not pure)</td><td>CBZ DH</td><td colspan="3" rowspan="4">CBZ DH (slight variance in peak around 20° 2θ)</td><td>CBZ DH</td><td rowspan="4">CBZ form III (not pure – representative DH or form II peak)</td><td>CBZ form III</td></tr>
<tr><td>45</td><td>CBZ form III (not pure)</td><td>CBZ form III</td><td>CBZ form III</td><td>CBZ form III</td></tr>
<tr><td>50</td><td rowspan="3">CBZ form III</td><td rowspan="2">CBZ form III (not pure)</td><td>CBZ form III (not pure)</td><td>CBZ form III (not pure)</td></tr>
<tr><td>55</td><td rowspan="2">CBZ form III</td><td>CBZ form III</td></tr>
<tr><td>60</td><td>CBZ form III</td><td>CBZ form III</td></tr>
</table>

4.2.4.2 Pumping Stability Testing

Slurry delivery uses the SF-10 peristaltic pump from Vapourtec UK to transfer the slurry suspension from the slurry feed, through the pump to the filtration unit, or in the case of seeded KRAIC-D runs, towards the KRAIC-D. Slurry delivery experiments were used to ensure that the solid form of the CBZ does not change as the seed suspension is pumped through the SF-10, where the movement of the slurry through the flexible tubing inside the SF-10 pump or the action of the rotor resulting in compression of the flexible tubing could cause a grinding effect leading to a change in polymorphic form. It is important to establish that the seeds of polymorphic purity obtained from the seeding experiments maintain form and purity when the slurry is delivered through the SF-10 pump towards the pre- and post-nucleation seeding inlets in the KRAIC-D. Achieving precise control over the form of CBZ introduced into the KRAIC-D allows reliable comparisons with the unseeded KRAIC-D runs, as well as understanding the effect of introducing a controlled solid interface into the crystallisation process.

In addition to solid form, it is important to establish the weight percent (wt %) of solid delivery from the pump and thus the seed dosing in the KRAIC-D experiments. The stability of CBZ samples through the SF-10 was investigated using the set-up in Figure 4.14. The slurry

suspension is pumped through the SF-10 pump at a flow rate of 1 mL/min, in order to collect a 5 mL aliquot, each sample is collected over 5 minutes through Buchner funnel filtration.

The slurry is produced by overhead stirring of a seed solution of 50 mg/mL CBZ in EtOH (prepared at 100 mL scale), stirred at a rate of 500 rpm for 2 hours. Once equilibration of the slurry suspension was established for 5 minutes, the slurry was delivered through a SF-10 pump and subsequently collected *via* vacuum filtration. The slurry delivery parameters and wt % solid loading of CBZ in each sample aliquot are summarised in Table 4.6 and 4.7 respectively.

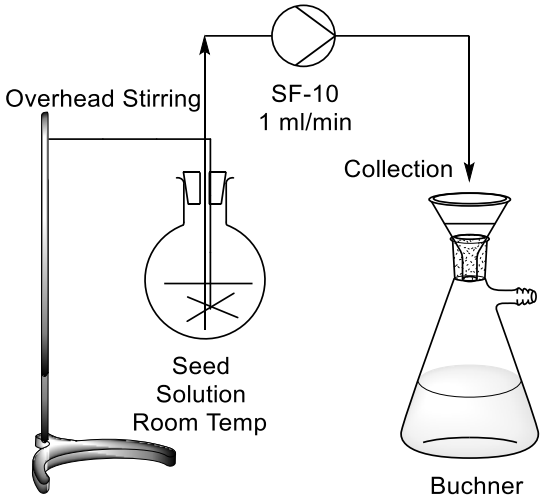

Figure 4.14 – Schematic of experimental set-up for CBZ form III seed solution pumping stability studies.

Table 4.6 – CBZ slurry delivery parameters.

Flow rate (mL/min)	1
Collection time (mins)	5
Collection volume (mL)	5
Predicted solid from excess from 50 g/kg	45.5
Predicted wt% CBZ solid in CBZ slurry	2.93

Table 4.7 – Slurry wt % of CBZ form III seed solutions used for pumping stability studies *via* collection of 5 mL aliquots.

Sample aliquot	**Mass on filter paper /g**	**Wt %**
A1	0.1123	0.68
A2	0.1561	1.40
A3	0.1646	1.53
A4	0.157	1.41
A5	0.1629	1.51

A6	0.172	1.65
A7	0.1771	1.74
A8	0.1416	1.16

The PXRD data confirms solid form consistency across the eight aliquots collected for offline analysis, where CBZ form III was crystallised with a representative CBZ DH peak also evident at 9° 2θ for the majority of the aliquots (Figure 4.15). Aliquots A2 and A6 yielded CBZ form III in polymorphic purity and thus as there is no obvious transformation point between prepared slurry form and obtained aliquot it can be confirmed that passing the CBZ slurry mediated in EtOH through the SF-10 peristaltic pump does not impact form and the slurry remains stable over the full collection time.

The wt % solid loading remains relatively consistent throughout, only resulting in a blockage within the pump 44 minutes 30 seconds into the slurry delivery experiment, at A9 where no solid was drawn through the line and the experiment was stopped. Consistent with this, during the beamtime experiments it was found that a slurry would not be continually delivered into the KRAIC-D for more than 45 minutes.

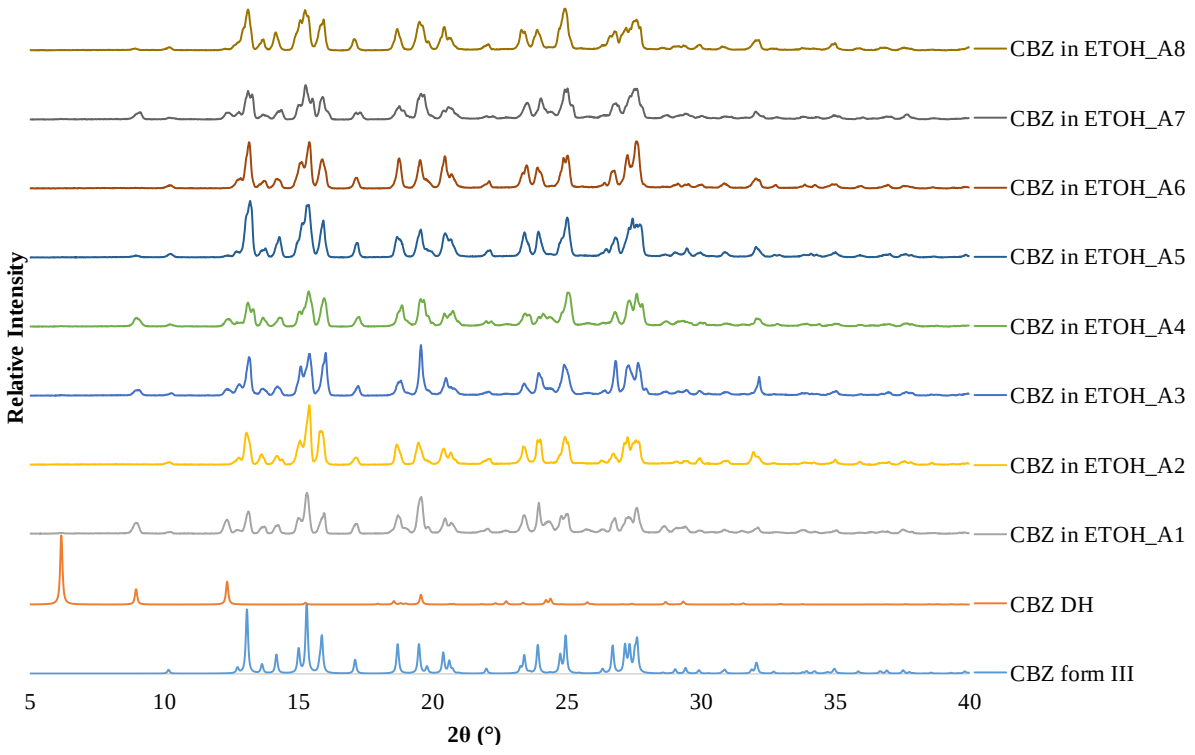

Figure 4.15 – PXRD result of CBZ form III seed solutions pumping stability studies.

4.3 Platform Development and Optimisation

4.3.1 Kapton® Window Treatment

The surface of the Kapton® windows are inherently slightly hydrophilic and thus modification by surface activation with a plasma cleaner, followed by the application of a commercial fluorinated water repellent (Aquapel®) is required, to match the hydrophobic surfaces of the PTFE unions and FEP body of the KRAIC-D.[123]

The Kapton® windows were made hydrophobic using a chemical treatment process with Aquapel® adapted from Mazutis *et al.*[124] Kapton® tubes were prepared by initially cleaning the tubes thoroughly with acetone (ACE) or EtOH, followed by drying the tubes with an air or nitrogen (N_2) stream. A Kapton® tube was placed in the plasma cleaner with the plasma stream pointing down the tube. A negative glow discharge with a 20 mA current was applied to the tubing for 15 seconds. After activating the surface of the tubing with the plasma cleaner, the tubing was placed in a centrifuge tube, which contained 7 mL of Aquapel®. The tubing was soaked in the hydrophobic treatment for 1 minute with rotation to ensure the tubing was completely coated. The tubing was removed from the Aquapel®, dried again with an air or nitrogen (N_2) stream and subsequently washed once more with ACE or EtOH. Water was run down the tubing to check the coating was complete and no beading occurred.

4.3.2 Aquapel® Coating Deterioration

The hydrophobic coating was shown to deteriorate after overexposure to the X-ray beam, where the Aquapel® was susceptible to beam damage and beading was observed on the inside of the Kapton® tubing. To combat this, beam exposure at any given tube location was reduced and limited to 51 frames of a 0.1 second exposure before traversing by 1 mm increments along the length of a Kapton® window using the X-translation stage. The translation increment along the Kapton® tubing is compatible with the size of the 1 mm x 1 mm X-ray beam.[107]

4.3.3 Blockage Mitigation

Blockage mitigation must be considered when crystallisation is occurring in flow. Strategies to deal with blockages include providing a seamless join when tubing, unions and mixer pieces are connected to prevent perturbation to the flow, which could cause encrustation. The wettability of the carrier fluid to the inner wall of a tubular reactor / crystalliser must be optimised to ensure crystallisation is occurring away from the solid interface by ensuring the crystallising solution does not come into contact with the crystalliser walls. As the crystallising

solution does not ordinarily interact with the crystalliser walls, a solid surface to allow for nucleation does not exist and thus the solution slugs exist in a highly metastable state until crystallisation is achieved; a tiny perturbation to the flow could thus cause interaction with a solid surface and in turn could lead to encrustation.

Strategies to deal with potential blockages during crystallisation in the KRAIC-D platform include by-pass tubes of 3.18 mm ID FEP tubing of similar length to the Kapton® windows, connected to the rest of the FEP body with zero volume unions, comprising of FEP of slightly larger bore size, which provide a seamless join. This approach improves the crystallisation run time and maximises time for data collection. During process optimisation the mitigation of blockages originating from the PTFE union joins was investigated *via* the removal of the unions (Figure 4.16). To provide a seamless join between the Kapton® windows and the FEP body, the FEP ends required heat treatment.

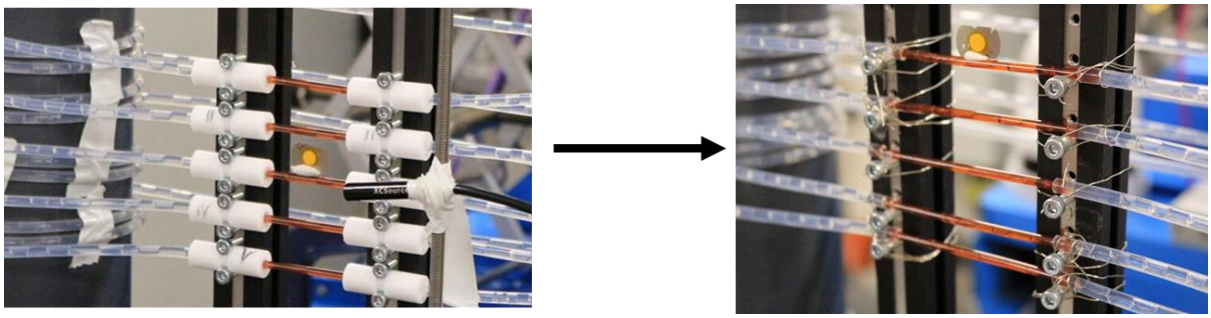

Figure 4.16 – Removal of PTFE unions as part of blockage mitigation strategy.

Heat treatment of the FEP ends altered the surface chemistry of the inside of the FEP tubing, altering the preferential wetting of the carrier fluid, which led to perturbation of the segmented flow at the FEP ends and thus this blockage mitigation strategy is not a suitable alternative to the PTFE union set-up. In addition, due to beam damage of the Kapton® windows in the KRAIC-D set-up, it is necessary to retain the PTFE unions to allow window replacement. As the unions had to be retained, other methods were employed for blockage mitigation. These were minimising X-ray exposure time at a given analysis point to avoid X-ray damage to the hydrophobic coating at the exposure point and also ensuring the Kapton® windows contain flush edges through a developed cutting procedure (Section 4.3.4).

4.3.4 Thin Wall Tubing Cutting Procedure

The polyimide (Kapton®) tubing (3.38 mm OD, 3.188 mm ID) from American Durafilm (Moorseville, NC) was extruded rather than wound and required cutting into approximately 7.5 cm lengths for the Kapton® windows. The use of Kapton® tubing wound in preparation is not appropriate in this case as winding produces subtle joins in the tubing, which can alter the surface properties and prevent the carrier fluid preferentially wetting the inside of the tubing.

A 3.18 mm metal rod was filed to fit neatly within the 3.188 mm Kapton® tubing to prevent distortion of the delicate tubing during cutting. A radial cutting pattern was then employed using a tubing cutter to guide a straight cut in the tubing, whilst ensuring a flush finish. A flush finish to the Kapton® tubing is necessary to provide as seamless a join as possible with the PTFE unions (Figure 4.17).

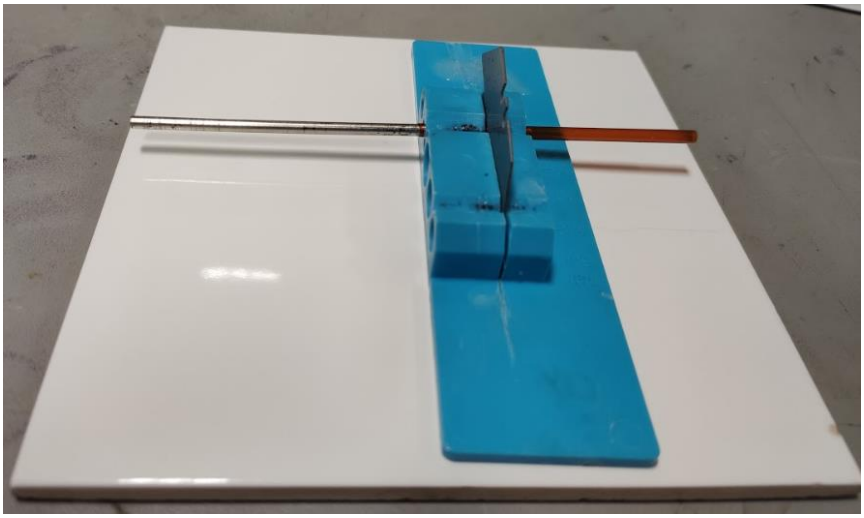

Figure 4.17 – Photograph of Kapton® tube cutting set-up.

4.4 Cooling Crystallisations

All continuous crystallisation runs are initially cleaned and primed with segmented flow comprising carrier fluid, air and the pure solvent used in the crystallising solution. During priming the conditions such as flow rates and temperature are matched to those adopted in the crystallising run to ensure the system is allowed to perform at steady-state operation. All transfer tubing jackets and the segmentation bath were usually set to the same temperature as the feed solution. The system usually requires at least one residence time (the time taken for the media to travel from the point of segmentation to the end-piece) to reach steady-state conditions. The time taken to reach steady-state operation can be attributed to the flow

conditions adopted by the pump. The pumps do not operate under the same plug flow conditions as the rest of the system, instead the pumps operate under laminar flow and thus time is required for the concentration to reach equilibrium, which then must pass through the whole crystalliser to outlet, which is dependent on the residence time.

At the end of the KRAIC system, before filtration employed for offline analysis, the segmented flow undergoes carrier fluid recovery and the resulting loss in flow rate due to this recycling of the carrier fluid results in the need for an additional inlet to maintain the overall flow rate and prevent a build-up of material at the end-piece. This additional inlet flow is termed the neutral solvent (NS), comprising the solvent used in the crystallising solution chilled in an ice bath. The NS is selected on the basis that its introduction into the system (using a Gear pump, Ismatec ISM895E) will not cause further crystallisation or dissolution.[72] Crystal recovery *via* vacuum filtration was only used for supporting offline analysis. For most of this work where *in situ* diffraction analysis was carried out, the NS was often not chilled in an ice bath and thus was not considered neutral and contributed to dissolution. Therefore, the NS employed in the beamtime experiments was used to aid carrier fluid rather than solid recovery.

After any major blockages or detrimental changes in segmentation, such as issues with wettability, are observed, the system was washed with pure hot solvent to dissolve any crystalline material and impurities on the inside of the crystalliser. Removing the segmentation and operating at high flow rates of approximately 10 mL/min cleans the inside of the tubing most effectively.

During priming, the feed solution (CBZ in EtOH or UBA in MeOH) is prepared and allowed to reach dissolution at the set temperature for approximately an hour. For all experiments additional temperature-controlled tubing of 1.07 m length of FEP (hereafter termed ‘nucleation promoter’) is connected directly after the segmentation water bath and prior to the air-cooled 15 m FEP, should additional cold temperature be required to aid nucleation.

In the case of CBZ in EtOH, additional temperature control using the nucleation promoter set to 10 °C was required, whilst for UBA in MeOH the conditions were optimised without the need for the additional temperature control, so the jacket of the nucleation promoter was left air-filled and under ambient temperature.

4.4.1 Seeded Cooling Crystallisations

Seeded cooling crystallisations operate similarly to an unseeded run, but with an additional inlet to which the seed is introduced in a slurry using a PP T-piece (see Section 4.2.3). The seeding ports are positioned either pre-nucleation in a T-piece after the X-piece (0.05 m) in the segmentation bath, or post-nucleation in a T-piece positioned after window 2 (9.1 m). The seeding port positions relating to two distinct stages of pre- and post-nucleation in the crystallisation process were determined from an unseeded crystallisation run.

4.4.1.1 Pre-nucleation Seeding

When seeding was introduced before primary nucleation, the seed inlet comprised a PP T-piece (2 mm ID) connected shortly after the glass X-piece through compressed flexible tubing (Marprene®, 3.18 mm ID) held flush on either side of the T-piece to limit any perturbation to the segmented flow (Figure 4.18).

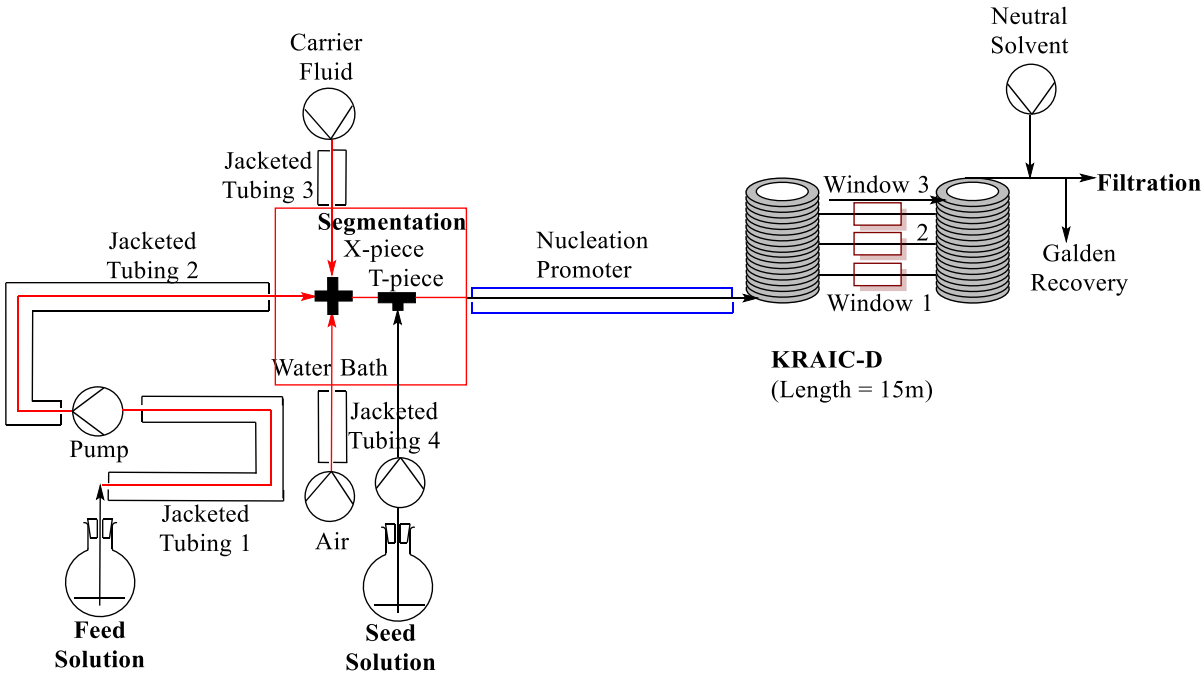

Figure 4.18 – Schematic of KRAIC-D showing seeding position for pre-nucleation seeding experiments.

4.4.1.2 Post-nucleation Seeding

When seeding was introduced after primary nucleation, the pre-nucleation seed inlet was capped and an additional seed inlet comprised a joined section of 3.18 mm FEP tubing with a 2 mm hole on the top and a Marprene® sheath to seal the port connected shortly after window 2 (Figure 4.19).

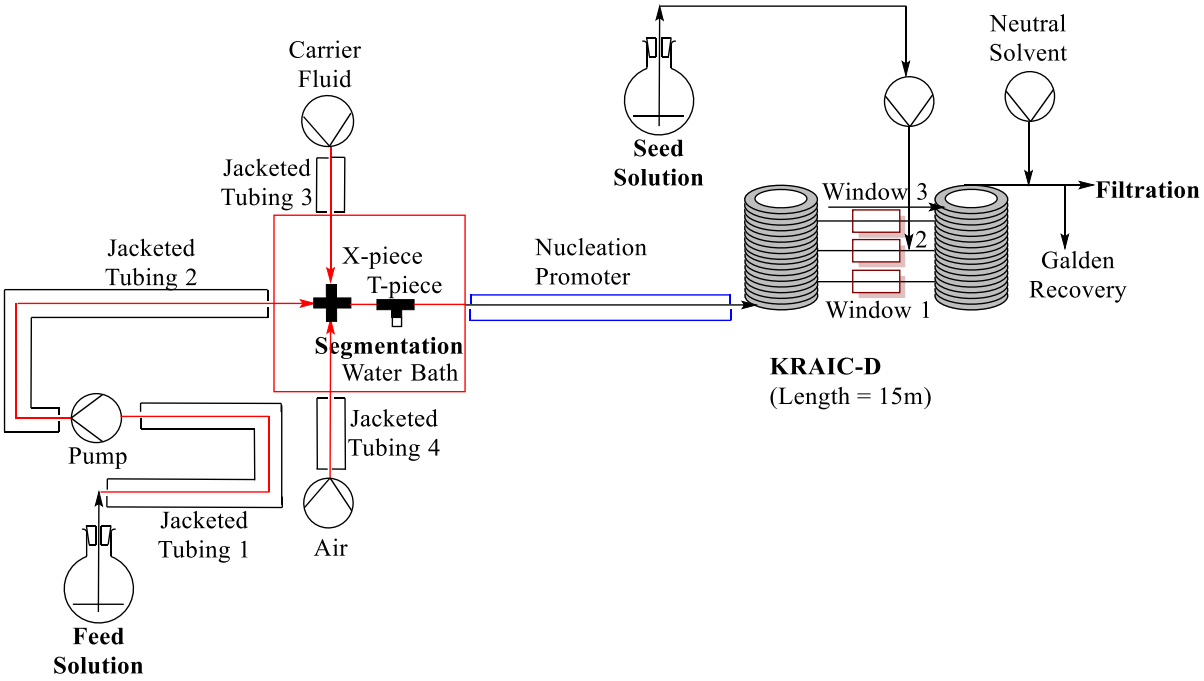

Figure 4.19 – Schematic of KRAIC-D showing seeding position for post-nucleation seeding experiments.

The difference in material between the pre- and post-nucleation seeding ports can be attributed to where the crystallising solution sits on the concentration / temperature dependent solubility curve. For post nucleation stages in the crystallisation process, the solution slugs exist in a highly metastable state where any changes in material from the Kapton® or FEP body could cause changes in preferential wetting and thus nucleation upon the walls of the crystalliser, which in turn could lead to blockages. As a result, instead of the PP T-piece, the use of an FEP union with a comparable inlet bore size to the PP T-piece was chosen for the seeding port to mitigate against these issues. For pre-nucleation stages, the PP-T piece was chosen for the connector as the best material to achieve preferential wetting of the carrier fluid. A change in material from FEP to PP at this early stage in the crystallisation process was possible as the solution slugs had just been segmented and are at a higher temperature so have not yet reached the metastable zone from cooling.

4.5 Data Capture and Analysis Procedure

4.5.1 Data Capture

Powder diffraction data were collected in a serial crystallography-like approach, where diffraction data from a range of scans, obtained from a range of slugs at the same analytical residence time (RT) position were integrated to build a statistical average of crystalline form

and growth at a set point along the length of the crystalliser.[125] As the system is operating at steady-state and the crystalline material in the solution slugs is grown *in situ*, different set points can be related to the different stages in the crystallisation process, imparting knowledge on the crystallisation pathway adopted with time.

In situ XRD characterisation was performed at Diamond beamline I11, using an X-ray beam of 15 keV energy, corresponding with a wavelength of 0.82437 Å with a 2D CCD detector (Pixium RF4343) operating at 10 frames per second (fps). The energy of the X-ray beam was chosen to maximise flux, which is particularly beneficial for poorly diffracting samples. As the stream of crystallisation media passes the X-ray beam continually, the X-ray damage caused to each crystallite by the high flux X-ray beam is minimised. The size of the X-ray beam used was 1 mm x 1 mm to maximise the area probing crystallite detection, whilst the beam remained compatible with the sample size, by being completely immersed in the average 7 mm to 1 cm slug length and 3.18 mm slug diameter. The net flow resulting from the flow rates of the three separate streams produced an average slug velocity of between 12 and 22 mm/s equating to a dwell time in the beam of 455 to 830 ms calculated from a 1 cm average slug size.

The background was an important consideration as the sample, in addition to not being static, also comprises three separate media: air, carrier fluid and the solvent background from the crystallising solution. The frame collection rate was designed to be faster than the net flow, ensuring that most frames contain only one of the three components in the tri-segmented flow. As a result, each scan comprised 51 frames of a 0.1 second exposure; a short exposure time was selected for each frame to maximise the signal-to-noise ratio.

4.5.2 Data Analysis Procedure

To process and analyse the high volume of diffraction data obtained during synchrotron experiments, collaborator Dr. Mark Levenstein developed an automated Matlab® script to interrogate each frame and determine the origin of the scattering.[106, 123] An empirical approach to background subtraction was adopted, whereby within each scan a frame of solvent scattering without crystalline diffraction was selected for use in background subtraction. Careful background subtraction was carried out ‘by hand’ to ensure the background was representative of the experimental conditions for the particular scan, together with an appropriate threshold value.

These processed frames are then combined and azimuthally integrated to generate a composite 1D diffraction pattern (Figure 4.3c and d). Finally, this process is repeated with data from each window, where five 10.1 s scans (each of 51 individual 100 ms frames with 100 ms dead-time between frames) per window are combined to obtain a picture of the average diffraction from crystals present at that particular residence time in the crystallising solution slugs. Five scans were chosen to be statistically relevant, recognising that not all scans will contain diffraction, particularly those at earlier analysis points along the length of the crystalliser where sufficient growth may not have been achieved. It is therefore possible to estimate the diffraction 'hit rate' at a given set point by considering how many of the five scans contain diffraction. The five scans included for each window were selected to span the full range of scans taken from different times in an individual experimental run to be representative of the entire crystallisation and avoid data being skewed by a potential short-lived flow instability. Each diffraction pattern presented in this chapter from an *in situ* experiment will comprise 255 frames of a 0.1 second exposure. Diffraction patterns are presented at the Cu Kα characteristic wavelength (1.5406 Å) for comparison to reference data.

When comparing diffraction patterns, it is important to consider the uncertainty in 2θ resulting from the 3.19 mm ID of the Kapton® window analysis points, within which depth the observed crystals can reside at any distance as they pass the incident X-ray beam. The sample-to-detector distance was calibrated by mounting a ceria sample on the centre of the Kapton® tubing, thus there is an error margin of 1.6 mm either side of the calibration centre. Thus a crystal passing through the analysis window residing close to the tubing wall is situated at a different sample-to-detector distance to a crystal passing through the centre of the tubing and there is an associated angular uncertainty in 2θ due to the width of this milliscale flow channel. This uncertainty has an angular dependence, which reaches a maximum value at 45°, which equates to a 2θ drift of approximately ±0.14° for diffracted X-rays with a sample-to-detector distance of 324 mm. An inverse relationship exists between the sample-to-detector distance and the associated uncertainty in angle; as the sample is moved further from the detector, the uncertainty in the angle reduces.

In addition to the uncertainty in 2θ due to the variance in sample-to-detector distance resulting from the ID of the Kapton® windows, there is also a smaller effect due to the finite pixel size on the detector. For these *in situ* experiments on I11, the detector was chosen to operate in the faster detector mode, whereby groups of pixels are merged into a single pixel, binned into

296 x 296 μm blocks of 2 x 2 pixels. With increased pixel size, the uncertainty in angle also increases, with a maximum uncertainty of 0.025°. The uncertainty associated with the size of the pixels on the detector is thus significantly smaller than the error associated with the variance in the sample-to-detector distance.

4.6 Growth Studies

Within the Matlab® script, an integrated intensity value for each scan is produced. To express the crystal growth at a set point along the length of the crystalliser, the five integrated intensity values can be illustrated in a box and whisker plot. The limits of the box express the upper and lower quartile, while the median is highlighted by a red line. The whiskers denote the highest and lowest integrated values amongst the five values. The default Matlab® box plotting method is adopted, which extends the whiskers to any data that falls within 1.5 x interquartile range (IQR). Any data outside this region is instead plotted with a red cross.

Representing the spread of the integrated intensity values, or area under the diffraction pattern at each window with a box and whisker plot, indirectly allows for the crystal growth in a crystallisation process to be interpreted visually. The diffraction intensity can be correlated to the number of nuclei and the relative crystal growth of the system at a set point along the crystalliser length. The growth profile can therefore be mapped and compared across unseeded and seeded crystallisation runs. It is important to consider that in the case of seeded crystallisations, additional crystalline material with an associated integrated intensity is injected into the system, so the crystal growth between windows will not be quantifiable (Appendix 4.6).

4.7 Polymorphic Monitoring of Carbamazepine (CBZ)

CBZ exists in five anhydrous polymorphic forms, as well as a dihydrate (DH) form (Figure 4.20).[116, 126] The metastable CBZ form II is known to crystallise from solution and CBZ form III is the thermodynamic form,[1] therefore these two forms can be expected in this study. It is important to recognise that even though absolute ethanol is the solvent utilised in these cooling crystallisations, once absolute ethanol is exposed to the atmosphere, the ethanol will uptake some water from the atmosphere and thus CBZ DH may also emerge from this study.[127]

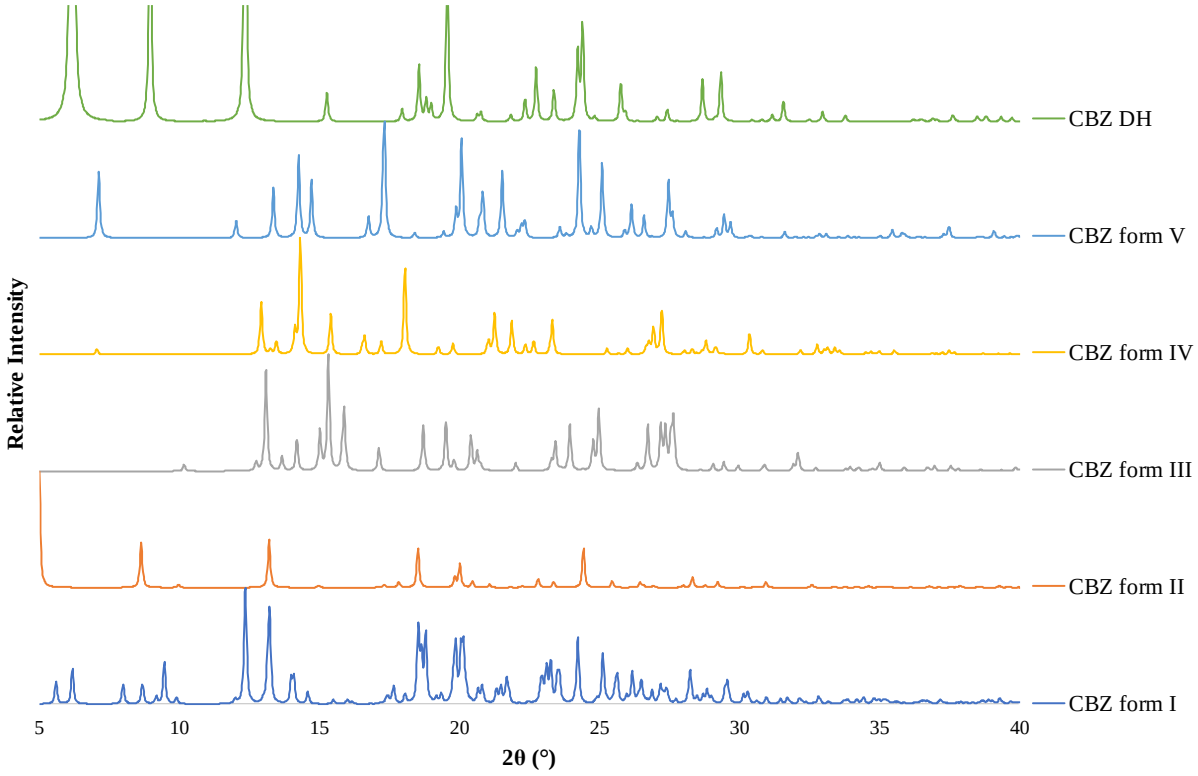

Figure 4.20 – PXRD patterns of the five anhydrous forms of CBZ and CBZ DH reference patterns simulated in Mercury[33] (Refcodes: CBMZPN11 (CBZ form I), CBMZPN03 (CBZ form II), CBMZPN01 (CBZ form III), CBMZPN12 (CBZ form IV), CBMZPN16 (CBZ form V) and FEFNOT (CBZ DH, orthorhombic interpretation of space group)). The intense peaks between 5-13° 2θ for CBZ DH have been truncated to ensure clarity of less intense peaks for comparison.

CBZ form III is the stable form at room temperature (RT), which is enantiotropically related to form I; form I can be produced by holding form III at 185 °C for 10 minutes to induce the phase transformation.[128] CBZ form I is the preferred CBZ polymorph at high temperature.[129] CBZ form II can be accessed by cooling crystallisation from ethanol, propan-1-ol, isopropylbenzene and dichloromethane.[1, 128, 130, 131] CBZ form IV has not been reported from solution based crystallisation techniques, but instead this metastable form has been accessed by spray drying.[132] A computationally assisted approach was adopted to selectively produce CBZ form V through calculations of structurally similar molecules, which indicated their potential to act as a solid-state template. The calculations and subsequent experimental trials found that CBZ form V could be accessed by templating the growth of CBZ from the vapour phase onto the surface of a dihydrocarbamazepine form II crystal.[133]

Sypek *et al.* investigated the influence of experimental conditions on polymorphic outcome, as well as possible polymorphic transformations during the cooling crystallisation of CBZ from

anhydrous EtOH. The study showed that stirring was the most notable controlling factor in dictating the initial polymorphic outcome of CBZ, where quiescent conditions yielded CBZ form II crystals, which subsequently underwent slow transformation to the stable form III.[1]

The phase transformation between CBZ form II and form III during cooling crystallisation from propan-1-ol was investigated by Zhao *et al.*, through use of in-line PAT techniques: Attenuated Total Reflectance Fourier Transform Infrared (ATR-FTIR), Focused Beam Reflectance Measurement (FBRM) and Raman.[134, 135] This study confirmed an enantiotropic relationship between forms II and III, with an associated transition temperature of 34 °C. A similar study carried out by Liu *et al.* using *in situ* FBRM and PVM confirmed a transition temperature of 40 °C from the same solvent system.[130] The paper reported that the cooling rate affected the polymorphic outcome, whereby an increase in cooling rate from 0.2-0.5 K min^{-1} reduced the quantity of CBZ form II in the crystalline product.[130] The polymorphic transformation of the metastable CBZ form II to the thermodynamic form III is not dependent on the solvent choice of crystallisation, as studies have shown the transformation proceeding from both EtOH and propan-1-ol solvents.[1, 130] However, the rate of transformation can be altered by solvent choice and purity of the CBZ starting material.[1]

Guidelines for solvent selection on the premise of 'Black's rule', which states that the solubility of a solvent-solute system will double in concentration every 20 °C increase in temperature, have been proposed.[136] Adhering to this rule for solvent selection during the design of a cooling crystallisation process, will ensure an adequate yield. Other selection criteria exist including a maximum temperature (T_{max}) of approximately 60 °C, to minimise solvent loss due to evaporation, highlighting the importance of T_{max} reaching a temperature at least 5-10 °C below the boiling point of the solvent. Criteria for a cooling crystallisation with respect to concentration are also factors for consideration, where the solubility should be equal to 50-150 g/L at T_{max} to ensure the final slurry remains mobile. Equally, if the final solubility is less than 5 g/L, the precipitation of impurities is deemed more likely than the solute.[136] On the basis of these selection criteria, the evidence of polymorphic transformations from cooling CBZ in EtOH, as well as the impact of mixing conditions on polymorphic outcome, EtOH was selected as the most suitable solvent for the *in situ* monitoring of the cooling crystallisation of CBZ.

The temperature dependence and enantiotropic relationship between CBZ polymorphs make this a suitable model system to investigate *via* cooling crystallisation in the KRAIC and

KRAIC-D platforms. The benefit of using the KRAIC-D platform here is that an understanding of the polymorphism of CBZ in EtOH as a function of crystallisation time can be gained, by installing the KRAIC-D and monitoring this system on beamline I11.

4.7.1 Offline KRAIC / KRAIC-D Experiments: CBZ in ethanol (EtOH) (CBZK/KD)

To develop the flow crystallisation process of CBZ in ethanol (EtOH) for in-beam operation in the KRAIC-D, developmental work optimised offline was carried out in the KRAIC and KRAIC-D platforms. The KRAIC and KRAIC-D are operationally identical with one exception; the KRAIC comprises a single extruded length of 15 m of FEP tubing, whilst the KRAIC-D requires Kapton® windows and PTFE unions to connect the various lengths of FEP tubing (total 14 m).

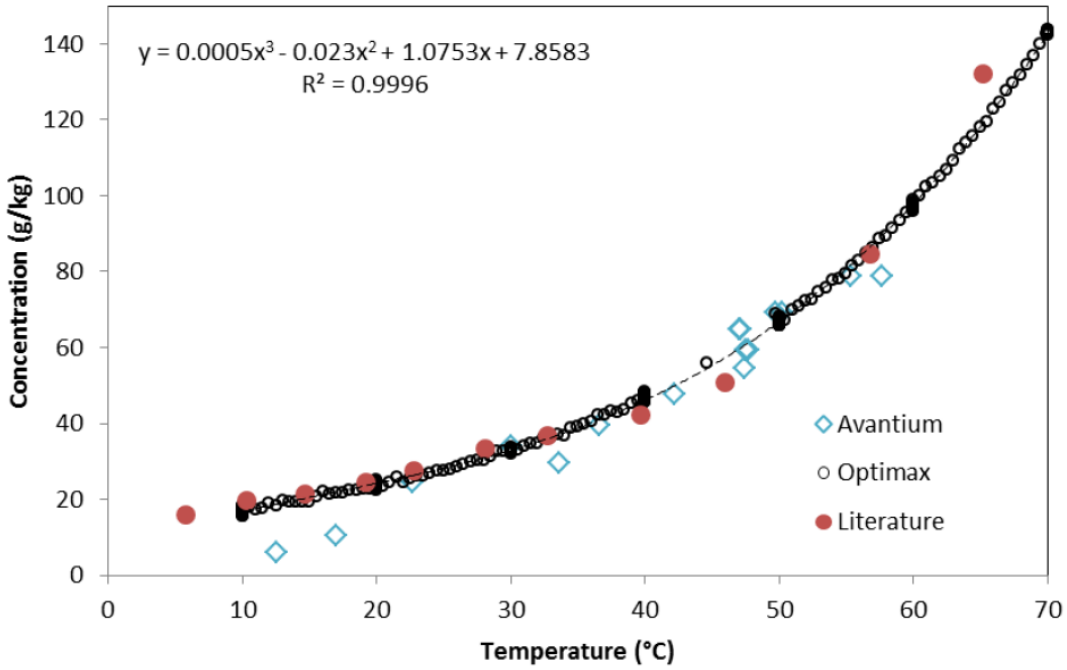

Figure 4.21 – CBZ in EtOH solubility curve adapted from N. Briggs thesis.[137] Avantium: turbidity data collected on 8 mL parallel crystallisation system. Optimax: collected in a 1 L stirred tank crystalliser with ATR-FTIR as the method of detection. Literature curve: laser monitoring technique determined by the synthetic method.[138] The data from each of the methods defined are overlaid.

Initial concentrations of CBZ in EtOH and corresponding temperature conditions were based upon the solubility curve of CBZ in EtOH.[137] The concentration used for the unseeded CBZ in EtOH KRAIC (CBZK1) and KRAIC-D runs (CBZKD1-2 and CBZKD6), as well as seeded KRAIC-D runs (CBZKD3-5) was based on the solubility curve at 50 °C (feed temperature), equating to a concentration of 66.6 g/kg (52.5 g/L) CBZ in EtOH (Figure 4.21). The

crystallisation parameters used in the unseeded 52.5 g/L CBZ in EtOH KRAIC (CBZK1) and KRAIC-D (CBZKD1-2 and CBZKD6) runs as well as CBZ form III seeded KRAIC-D offline runs (CBZKD3-5) are summarised in Tables 4.8 and 4.9.

Table 4.8 – Flow rates (in mL/min) used for all KRAIC (CBZ unseeded), as well as (offline and online) KRAIC-D runs: unseeded, † 'pre-seed pos.' and 'post-seed pos.' refer to the flow rates prior to and after the post-nucleation seeding inlet.

						Total (excl. NS)	
	Carrier fluid	**Air**	**Neutral solvent (NS)**	**Solution**	**Seed**	**Pre-seed pos.†**	**Post-seed pos.†**
CBZ unseeded	2.1	4.18	12.5	2.4	N/A	8.68	8.68
CBZ III pre-nucleation seeded	2.1	4.18	12.5	1.4	1	8.68	8.68
CBZ III post-nucleation seeded	2.1	4.18	12.5	2.4	1	8.68	9.68

The experimental set-up for the unseeded CBZ in EtOH KRAIC (CBZK1) run is illustrated in Figure 4.22. The experimental set-up for offline unseeded CBZ in EtOH KRAIC-D (CBZKD1 and CBZKD5) runs is represented in Figure 4.23.

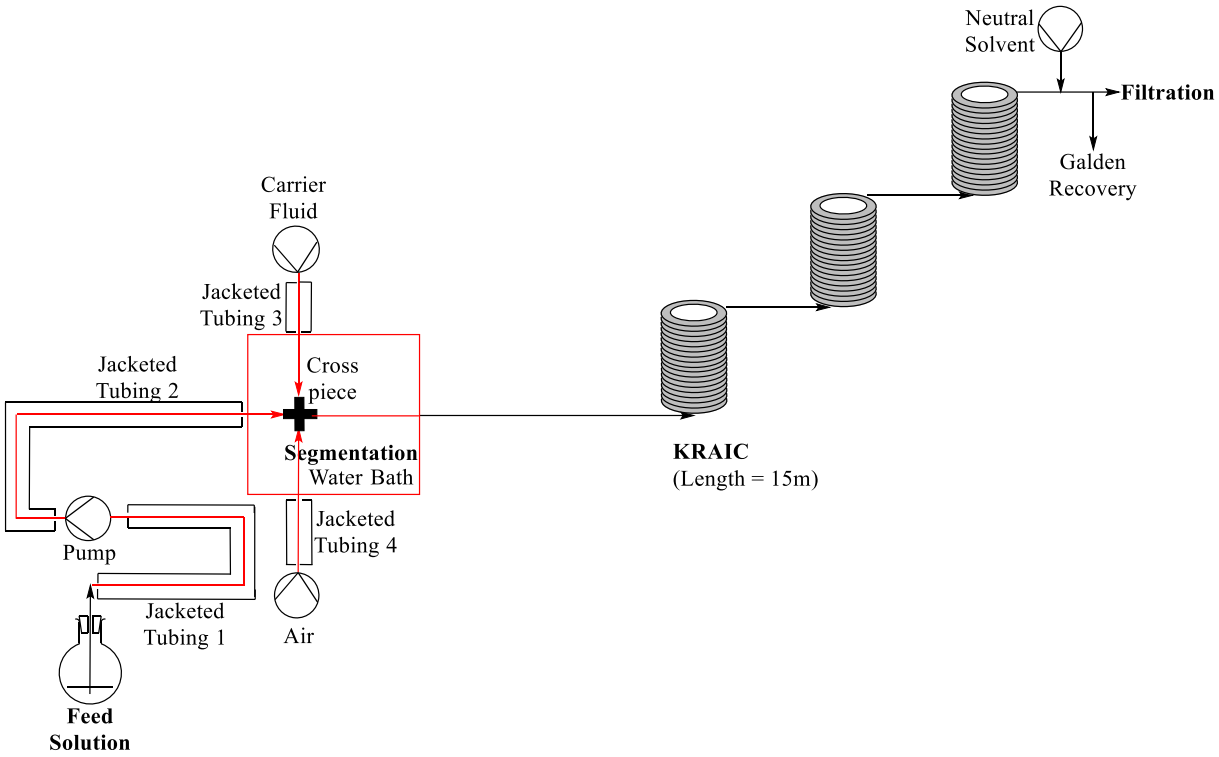

Figure 4.22 – Schematic of the experimental set-up for the unseeded CBZ crystallisation in EtOH run in the KRAIC (CBZK1).

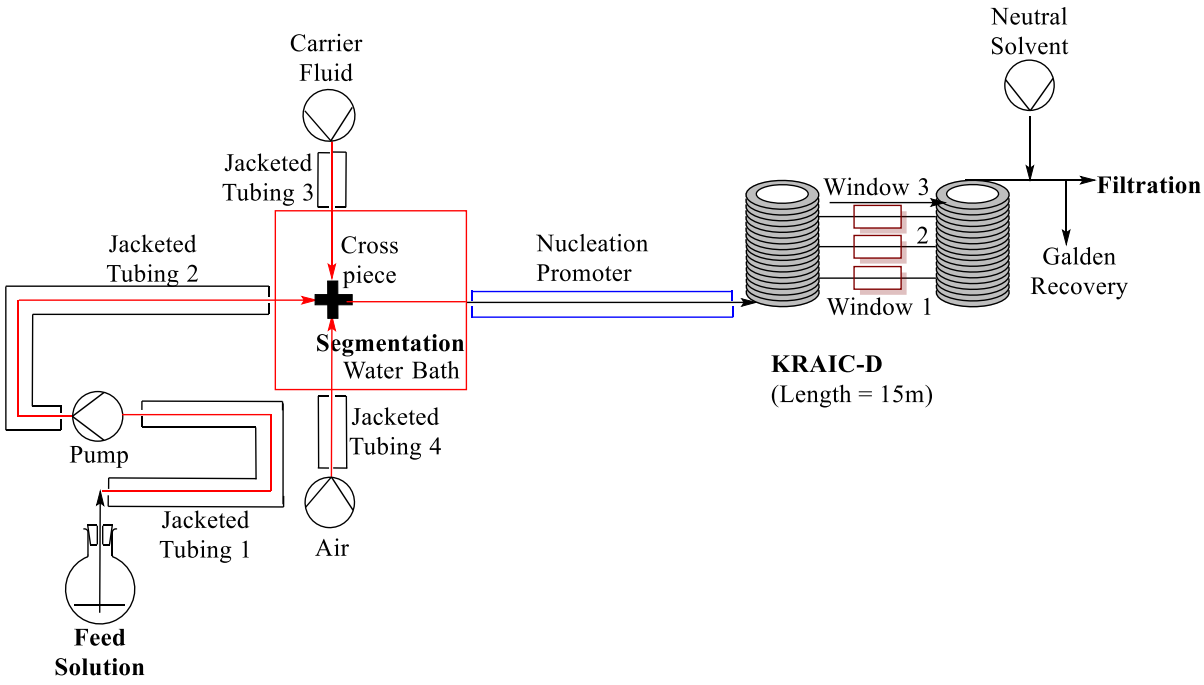

Figure 4.23 – Schematic of the experimental set-up for the offline unseeded CBZ crystallisation in EtOH runs in the KRAIC-D.

The experimental conditions including platform set-up, feed concentration and seed wt % solid loading are summarised in Table 4.9, as well as experimental residence times at various analytical points for the offline CBZK1 and CBZKD1-6 runs in Table 4.10. CBZKD2 investigated the impact of the removal of the PTFE unions on the crystallisation product and process, whilst all other CBZKD runs employed the PTFE unions.

Table 4.9 – Experimental parameters including feed concentration, seed loading and experimental set-up for CBZ offline experiments in the KRAIC and KRAIC-D are identified by CBZK and CBZKD respectively.

Experiment	CBZ Feed Solution (g/L EtOH)	Seeding wt %	Experimental Set-up
CBZK1	52.5	N/A	No T-piece, unseeded KRAIC Fig. 4.22
CBZKD1	52.5	N/A	No T-piece, unseeded KRAIC-D Fig. 4.23, with unions
CBZKD2	52.5	N/A	No T-piece, unseeded KRAIC-D Fig. 4.23), without unions
CBZKD3	52.5	2.9	Pre-nucleation seeded KRAIC-D, Fig. 4.18
CBZKD4	52.5	2.9	Pre-nucleation seeded KRAIC-D, Fig. 4.18
CBZKD5	52.5	2.9	Pre-nucleation seeded KRAIC-D, Fig. 4.18
CBZKD6	52.5	N/A	Capped T-piece, unseeded KRAIC-D, Fig. 4.6

Table 4.10 – Experimental residence times for various analytical set points along the length of the KRAIC-D for CBZ offline experiments (CBZKD). N.B No residence time measurements were taken for CBZKD2. The difference between CBZKD1 and CBZKD2 is attributed to the removal of the unions, which would reduce the length of the crystalliser slightly for CBZKD2.

Experiment	**Nucleation Promoter J5 (mins:secs)**	**Window 1 (mins:secs)**	**Window 2 (mins:secs)**	**Window 3 (mins:secs)**	**Total Residence Time after segmentation (mins:secs)**
Length	**1.07 m**	**6.47 m**	**9.07 m**	**11.77 m**	**14 m**
CBZK1	N/A	N/A	N/A	N/A	16:27
CBZKD1	1:10	5:51	8:33	11:40	14:46
CBZKD3	1:02	5:23	7:52	10:31	12:48
CBZKD4	-	-	-	-	13:03
CBZKD5	-	-	-	-	12:51
CBZKD6	-	8:28	12:09	16:05	19:06

CBZK1

Initial temperature control of the feed, circulator and segmentation bath was set to 55 ℃. Even after reductions in temperature of the segmentation bath from 50 ℃ to 35 ℃ in 5 ℃ increments to promote nucleation, no crystallisation was observed after 1 hour into the crystallisation run. Ice was then introduced into the segmentation water bath, as a crude way to provide insight as to whether additional temperature control in the form of a nucleation promoter could promote crystallisation at this concentration. Ice in the water bath led to a reduction in temperature of the water bath to 13-15 ℃, which resulted in crystallisation observed in the first coil, where agglomerates of needle crystals appeared in the solution slugs, which would suggest crystallisation of CBZ form II; however, the PXRD data for CBZK1 also shows the presence of CBZ DH (as shown in Figure 4.24 below). CBZKD experiments after CBZK1 required the use of the nucleation promoter, thus the use of additional cold temperature control introduced after the segmentation water bath was the key finding from experiment CBZK1.

Offline measurements by PXRD of CBZ produced in the KRAIC platform (CBZK1) from EtOH indicated that CBZ DH was the resultant form with additional diffraction peaks attributed to CBZ form III, whilst crystallisation in the KRAIC-D yielded CBZ form III when unions were present (CBZKD1) and CBZ form II without the use of unions (CBZKD2) (Figure 4.24). The CBZ in EtOH KRAIC-D run (CBZKD1) with PTFE unions experienced a leakage between a Kapton®-union join and thus evaporation of EtOH at this join could have caused crystallisation of CBZ form III and led to seeding of the evaporation product through the

crystalliser. It has been reported that evaporation of CBZ in EtOH yields CBZ form III,[128] which could explain the formation of the thermodynamic form in this run. Experiment CBZKD6 of unseeded CBZ in EtOH yielded CBZ form II. The CBZ in EtOH form III pre-nucleation seeded KRAIC-D (CBZKD3-5) runs trialled offline produced CBZ form III, indicating that seeding largely dictates polymorphic outcome, whilst CBZKD3 does not yield CBZ form III in purity, due to additional peaks at 8° 2θ (Figure 4.24).

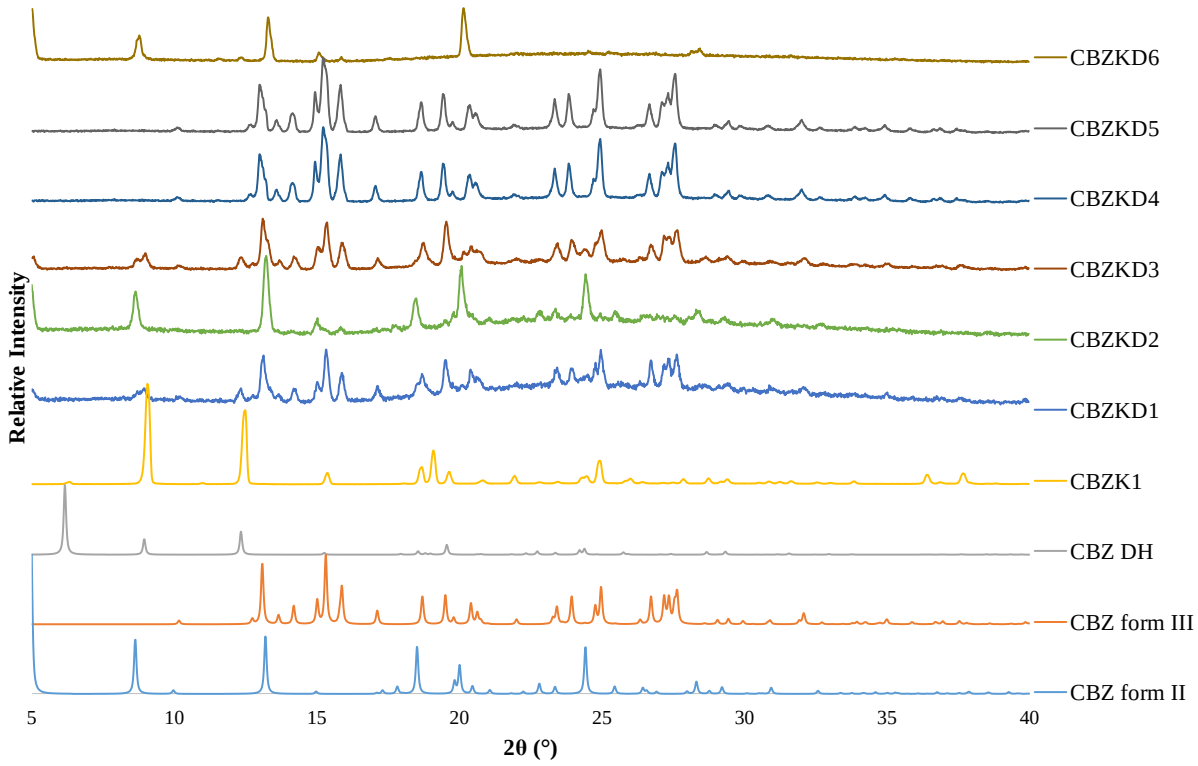

Figure 4.24 – PXRD patterns of CBZ in EtOH in KRAIC and KRAIC-D platforms identified as CBZK and CBZKD respectively compared to the reference patterns simulated in Mercury[33] (Refcodes: CBMZPN03 (CBZ form II), CBMZPN01 (CBZ form III) and FEFNOT (CBZ DH)).

To ascertain the yield achieved by the various crystallisation runs, sample collection *via* vacuum filtration was carried out over a residence time (Table 4.10 above), summarised by the various yields in Table 4.11. The collection time is presented with the corresponding yield, as product recovery over a full collection time was not always possible due to blockages.

Table 4.11 – Yield and polymorphic outcome of crystallisation for CBZ offline experiments (CBZK and CBZKD).

Experiment	Crystallisation?	Mass Collected (g) (Collection Time)	% Yield	Polymorphic Form
CBZK1	Yes – after cooling segmentation bath below RT	-	-	CBZ DH
CBZKD1	Yes	FP1: 0.1955 (7 min)	FP1: 22.2	Impure CBZ form III with CBZ DH
CBZKD2	Yes	FP2: 0.1957 (10 min)	FP2: 15.5	CBZ form II
CBZKD3	Yes	FP1: 0.0814 (10 min) FP2: 0.2024 (15 min) FP3: 0.0724 (6 min)	FP1: 6.5 FP2: 10.7 FP3: 9.6	Impure CBZ form III with CBZ DH
CBZKD4	Yes	FP1: 0.0716 (35 min 48 sec)	FP1: 1.6	CBZ form III
CBZKD5	Yes	FP1: 0.073 (unknown collection time)	-	CBZ form III
CBZKD6	Yes	FP1: 0.0379 (17 min)	FP1: 1.8	CBZ form II

The yields presented in Table 4.11 show great variance between crystallisation runs and also between different collections (FP1 and FP2), within the same experiment. Accurate determination of the yield for a given run proved difficult, as common blockage problems and flow rate adjustments in regards to the air pump, particularly evident for CBZKD4 and CBZKD5, resulted in inaccurate collection times and yields. Encrustation problems were experienced at unions, inside the SF-10 pumps used for both the seed and solution lines and in the FEP tubing if this was distorted. Offline *ex situ* analysis carried out using a laboratory source X-ray diffractometer have shown the metastable CBZ form II is crystallised from unseeded KRAIC-D (CBZKD2 and CBZKD6) runs. Offline measurements from pre-nucleation seeded CBZ form III (CBZKD3-5) KRAIC-D runs yields CBZ form III, indicating that seeding dictates polymorphic outcome. These offline investigations highlight the potential of CBZ in EtOH cooling crystallisation for online X-ray monitoring at Beamline I11.

4.7.2 Online KRAIC-D Runs at Beamline I11: CBZ in EtOH (CBZKDB)

The preliminary offline KRAIC (CBZK1) and KRAIC-D (CBZKD1-6) experiments presented in Section 4.7.1 provide a suitable start point for online CBZ KRAIC-D experiments at I11, which are presented by CBZKDB identifiers. A range of online cooling crystallisations were investigated during the beamtime, including unseeded (CBZKDB1 and CBZKDB2), pre-nucleation (CBZKDB3) and post-nucleation (CBZKDB4) seeded crystallisation experiments.

The experimental set-up, along with feed and seed slurry concentration for each of these CBZKDB beamtime experiments are summarised in Table 4.12, as well as temperature conditions and residence times at the three analytical set points (W1, W2, W3) (Table 4.13).

Table 4.12 – Experimental set-up, as well as concentrations of feed and seed solutions for the various CBZKDB beamtime experiments.

Experiment	**Set-up**	**Feed solution concentration CBZ in EtOH g/L**	**Seed Solution (wt%)**
CBZKDB1	T-piece Unseeded KRAIC-D (Fig. 4.7)	52.5	Unseeded (N/A)
CBZKDB2	T-piece Unseeded KRAIC-D (Fig. 4.7)	56.7	Unseeded (N/A)
CBZKDB3	Pre-nucleation Seeded KRAIC-D (Fig. 4.13)	52.5	3.0
CBZKDB4	Post-nucleation Seeded KRAIC-D (Fig. 4.14)	52.5	3.0

Table 4.13 – Crystallisation parameters for all CBZ runs, with temperature until segmentation and nucleation promoter defined in Figures 4.6, 4.18 and 4.19 ‡denotes RTs which are extrapolated from observed values.

					Residence time (min)			
	[Solution] (g/L)	**[Seed solution] (Wt %)**	**Temp. until segmenta-tion (°C)**	**Temp. of Nucleation Promoter (°C)**	**W1**	**W2**	**W3**	**End**
CBZ unseeded	56.7	-	55	10	8.7	12.6	16.7	19.3
CBZ III pre-nucleation seeded	52.5	3.0	55	10	8.7	12.6	16.7	19.3
CBZ III post-nucleation seeded	52.5	3.0	55	10	8.7	12.6	16.3‡	18.6‡

4.7.3 Unseeded CBZ in EtOH KRAIC-D at I11 (CBZKDB1 and CBZKDB2)

The initial concentration of 52.5 g/L CBZ in EtOH used in experiment CBZKDB1 with the temperature of the experimental hutch at 26 ℃ did not crystallise sufficient material for analysis, particularly at window 1 (W1) which is the earliest analysis point in the crystallisation

process. As a result, the concentration of the feed solution was increased to 56.7 g/L CBZ in EtOH for experiment CBZKDB2. The data obtained from online analysis of experiment CBZKDB2 is presented in Figure 4.25.

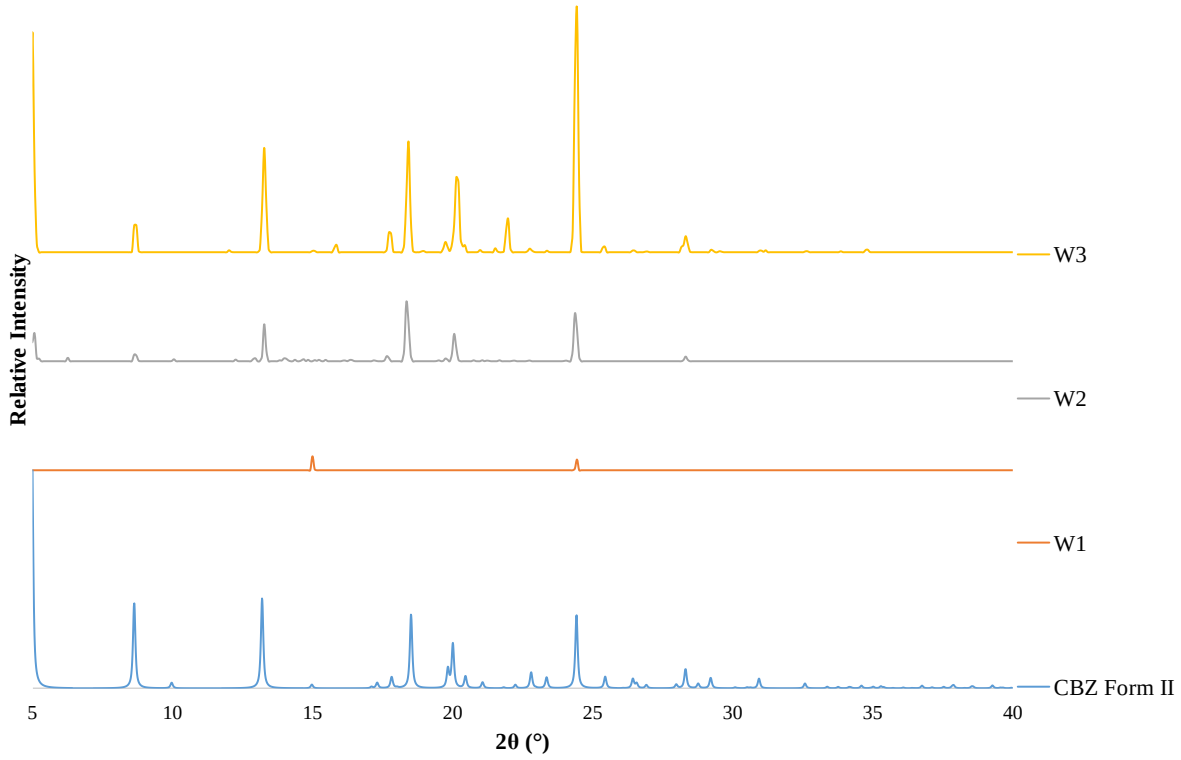

Figure 4.25 – PXRD patterns of CBZKDB2 unseeded CBZ in EtOH at W1, W2 and W3 in the KRAIC-D at I11. The scale of the experimental diffraction patterns has been adjusted for clarity (W1 scaled by a factor of 8 relative to W2 and W3) and converted into Cu Kα wavelength for comparison to the reference CBZ form II simulated in Mercury[33] (Refcode: CBMZPN03 (CBZ form II)).

For an unseeded CBZ in EtOH run in the KRAIC-D, the metastable CBZ form II is crystallised from the solution slugs at window 2 (W2) and window 3 (W3), indicated by representative CBZ form II peaks at 8°, 13° and 24° 2θ. W1 contains only two diffraction peaks, which also coincide with representative CBZ form II peaks (at 15° and 24° 2θ). The observation points equate to 8 mins 30 secs (6.4 m), 12 mins 20 secs (9.0 m) and 16 mins 20 secs (11.7 m) for W1, W2 and W3 respectively.

At W1, crystallisation is at much earlier stages within the crystallisation process, which explains the weak diffraction signal obtained at that point. A method was developed to determine the 'hit rate' at a given position to gauge the likelihood of observing diffraction at different crystallisation times. The hit rates, which quantify the probability of observing

diffraction in the total number of scans collected for each crystallisation run, are summarised for CBZKDB1 and CBZKDB2 in Table 4.14.

Diffraction was not observed for the beamtime experiment CBZKDB1, as indicated by the hit rate fractions and integrated intensity values at the analytical points of W1, W2 and W3. For experiment CBZKDB2, the hit rate and integrated intensity values increase from W1 to W3 as would be expected from the occurrence of crystal growth, the probability of the X-ray beam hitting crystallites in a solution slug increases. Importantly, the spread of the five integrated intensity values involved in the integration to produce a diffraction pattern are selected to reflect the hit rate when the number of scans collected exceeds five scans. This ensures that the five scans under analysis are representative of all of the data collected at a set point.

Table 4.14 – Integrated intensity values for growth plots for all crystallisation runs

Crystallisation run	**Window number**	**Hit rate of total number of scans collected**	**Integrated Intensity for 5 scan statistical sampling**
CBZKDB1	1	0/5	0
	2	0/5	0
	3	0/5	0
CBZKDB2	1	2/5	0.062 / 0.044 / 0 / 0 / 0
	2	4/5	0.822 / 3.394 / 5.887 / 0.028 / 0
	3	5/5	11.13 / 13.05 / 17.17 / 3.589 / 5.693

Growth plots represented by box and whisker plots at various set points (W1, W2, W3), provide an alternative visual approach to comparing crystal growth across the crystallisation process. The growth plots for the unseeded CBZ in EtOH KRAIC-D run convey the widely accepted exponential crystal growth mechanism. An increase in intensity was seen between the first (0.02 a.u. average intensity) and second (2.03 a.u. average intensity) windows with an even greater increase seen between the second and third (10.13 a.u. average intensity) windows (Figure 4.26). It should be noted that such comparisons are only semi-quantitative; CBZ form II exhibits needle-like morphology and thus dependent on the movement of the needles within the solution slugs and the high aspect ratio diffraction data may only capture a particular face of the crystals. This is analogous to the issues of preferred orientation in conventional PXRD.

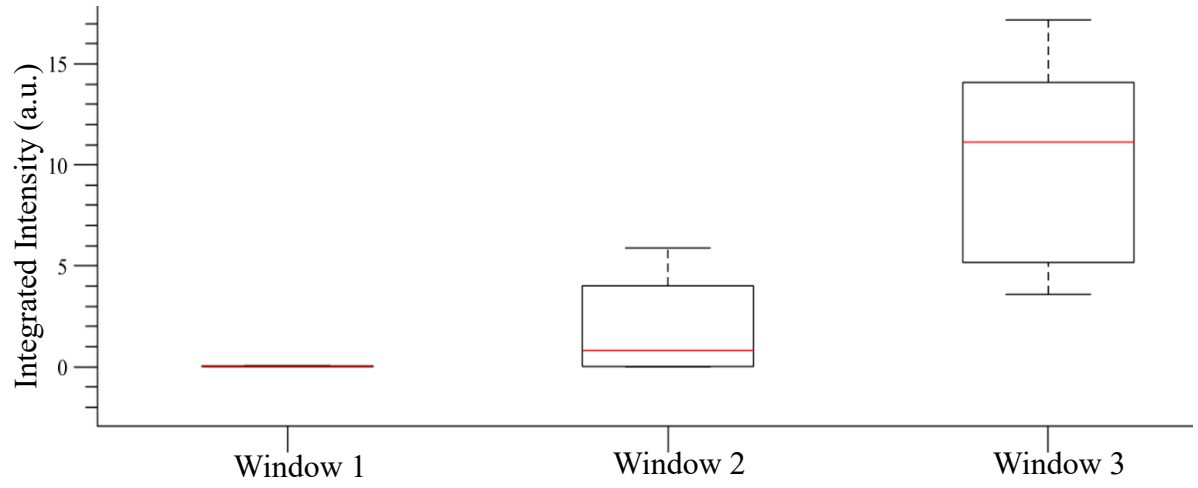

Figure 4.26 – Growth plots for CBZKDB2 unseeded CBZ in EtOH KRAIC-D run at I11.

4.7.4 Pre-nucleation Seeding of CBZ form III (CBZKDB3)

For CBZ form III seeded runs where pure CBZ form III is introduced as a slurry into the CBZ in EtOH cooling crystallisation at the pre-nucleation stage (CBZKDB3) (0.05 m, Figure 4.18 in Section 4.4.1), CBZ form III is observed across all windows, highlighting that pre-nucleation seeding with the thermodynamic form of CBZ dictates the polymorphic outcome (Figure 4.27).

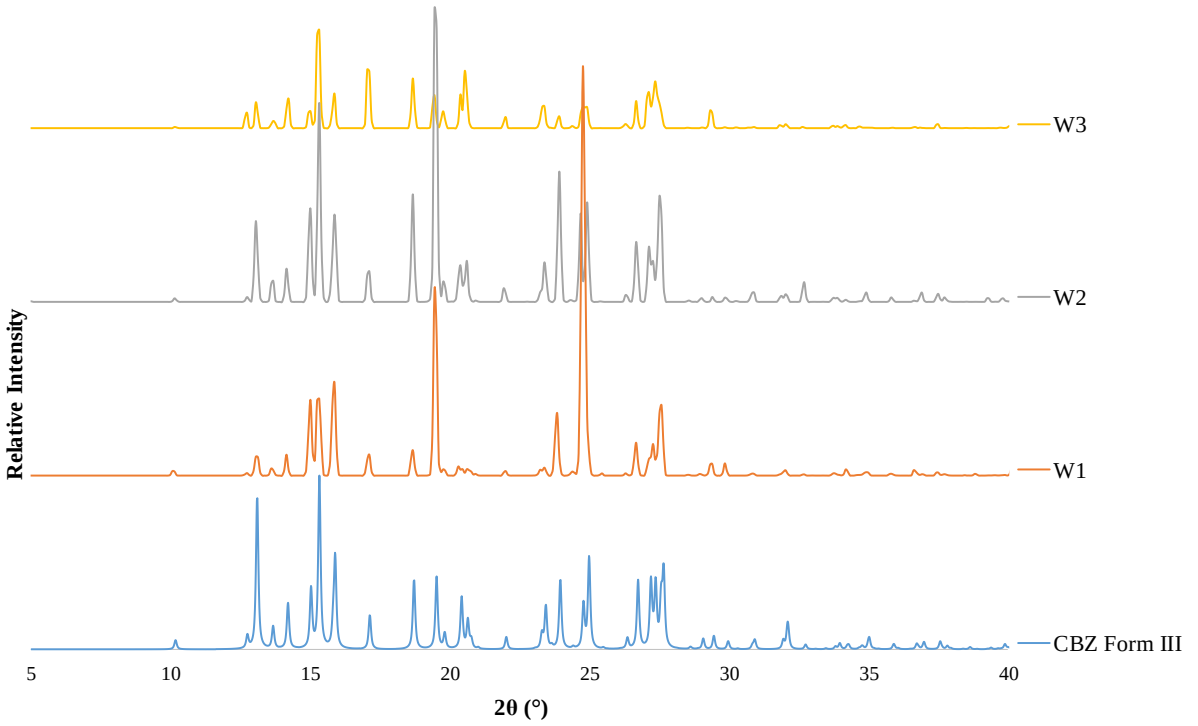

Figure 4.27 – PXRD patterns of CBZKDB3 pre-nucleation seeded CBZ in EtOH at W1, W2 and W3 in the KRAIC-D at I11, which have been converted into Cu Kα wavelength for comparison to the reference CBZ form III simulated in Mercury[33] (Refcode: CBMZPN01 (CBZ form III)).

The growth plots for the pre-nucleation seeded CBZ form III (CBZKDB3) cooling crystallisation in EtOH analysed in the KRAIC-D platform show consistency in integrated intensity values for CBZ across the three windows, implying the system reached equilibrium prior to W1 (Figure 4.28).

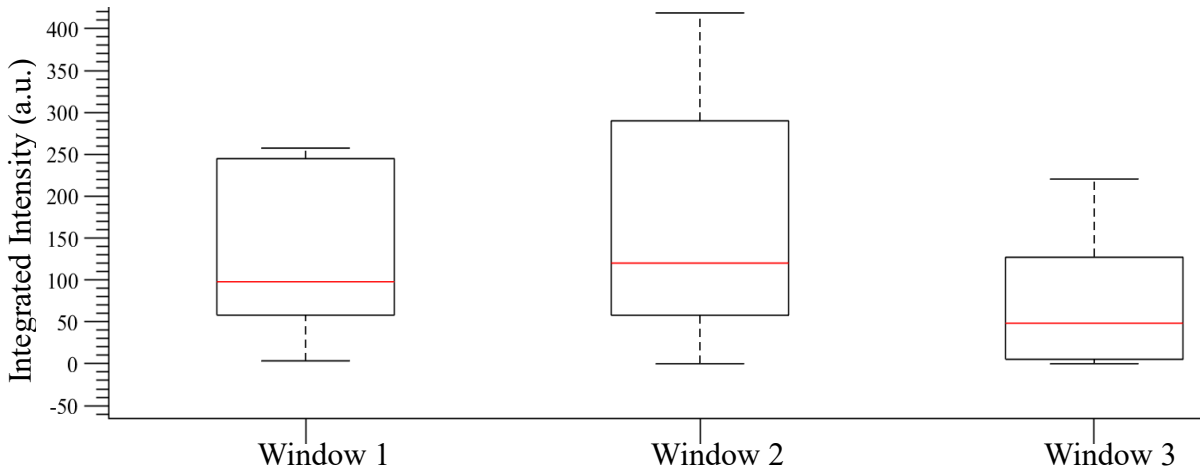

Figure 4.28 – Growth plots for CBZKDB3 pre-nucleation seeded CBZ form III in EtOH KRAIC-D run at I11.

4.7.5 Post-nucleation Seeding of CBZ form III (CBZKDB4)

For CBZ form III seeded runs where pure CBZ form III is introduced as a slurry at a post-nucleation stage, (CBZKDB4) after W2 (9.1 m, 16 mins 30 secs RT, Figure 4.19 in Section 4.4.1), into the crystallisation stream, CBZ form II is observed to have crystallised at W2, whilst only CBZ form III is detected at W3 (Figure 4.29).

For a post-nucleation seeded CBZ form III (CBZKDB4) crystallisation, a pronounced increase in integrated intensity is observed between W2 and W3, which is to be expected as additional crystalline material is injected between the two analytical windows (Figure 4.30).

Visually observing solution slugs passing W3, it was found that two habits could be observed to be physically separated based upon their different resulting interactions with the turbulent flow within the slugs. The crystal habits for CBZ form II and form III are distinctly needles and prismatic blocks respectively. The separation of form in a single solution slug could be rationalised by CBZ form II needles forming a cluster, which presents a higher drag force for the bolus flow and thus result in the clusters being pushed towards the rear of the slug. The blocks of CBZ form III have a correspondingly lower drag surface, which can overcome the bolus driving forces and take position in the front of the solution slug.

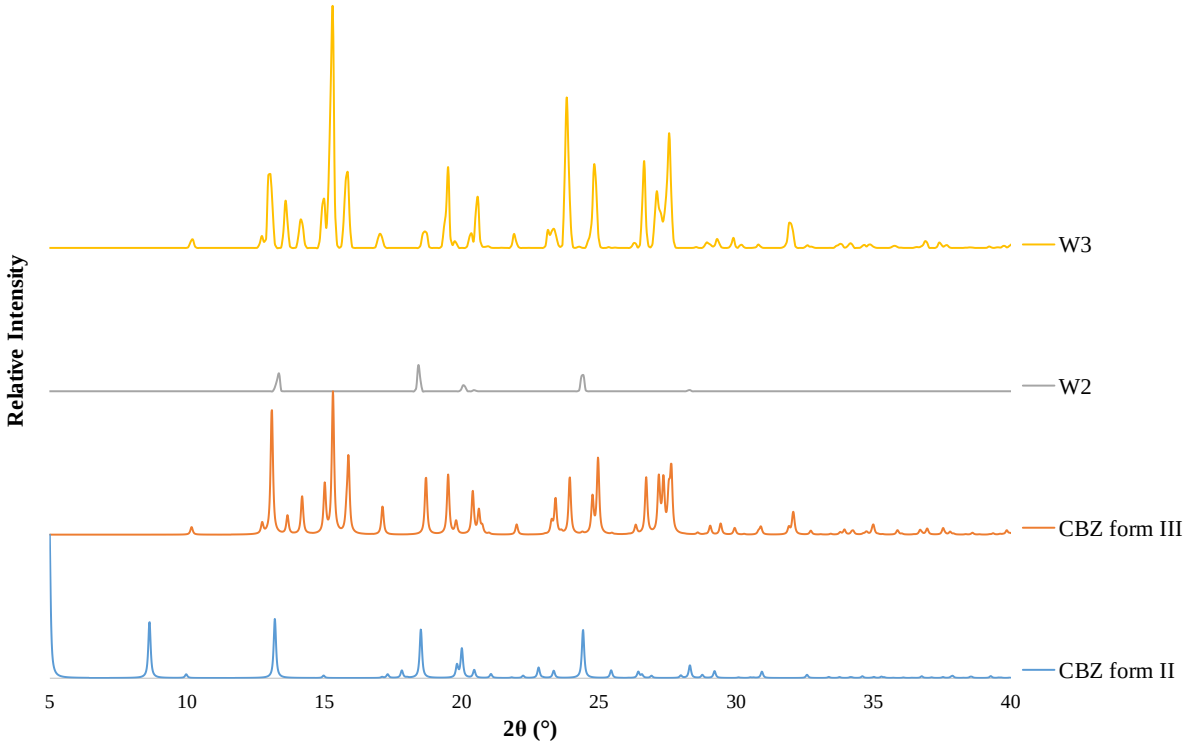

Figure 4.29 – PXRD patterns of CBZKDB4 post-nucleation seeded CBZ in EtOH at W2 and W3 in the KRAIC-D at I1. W2 is scaled by a factor of 20 relative to W3 for clarity and the diffraction patterns are converted into Cu Kα wavelength for comparison to the references CBZ form II and CBZ form III simulated in Mercury[33] (Refcodes: CBMZPN03 (CBZ form II) and CBMZPN01 (CBZ form III)).

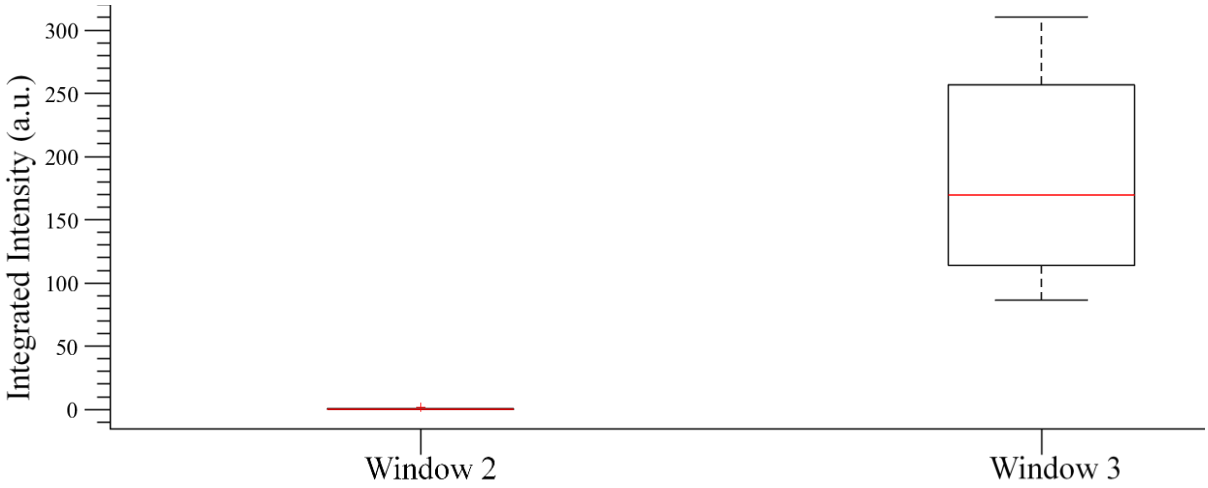

Figure 4.30 – Growth plots for CBZKDB4 post-nucleation seeded CBZ form III in EtOH KRAIC-D run at I11.

Both of these polymorphs do, however position themselves within the centre of the fore and rear eddy centres, the positions of which were predicted by computational fluid dynamic (CFD) simulations (Figure 4.31) performed by P.-B. Flandrin.[107]

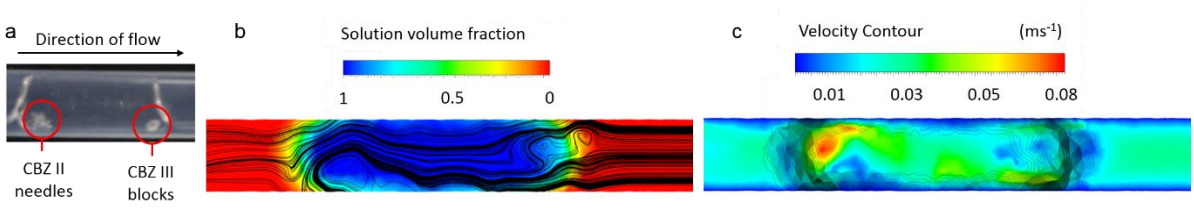

Figure 4.31 – **(a)** Photograph of CBZ form II needles and CBZ form III blocks separated by flow patterns in slugs, **(b)** CFD volume of fluid (VOF) image with flow streamlines overlaid, **(c)** CFD velocity contour image. N.B. CFD calculations were performed with Ansys Fluent by P.-B. Flandrin.[139]

4.7.5.1 Single exposure polymorph identification

Contrary to the visual observations of distinct habits, preliminary diffraction analysis only indicated the presence of CBZ form III after seeding. This could be because the diffracting power of CBZ form III is anticipated to be higher than that of the high aspect ratio needles of CBZ form II which, dependent on the needle orientation with respect to the X-ray beam, could reduce the observed diffraction intensity of CBZ form II with respect to form III. Furthermore, the empirical approach adopted for background subtraction during the data processing could also be reducing the chance of observing CBZ form II depending on the threshold chosen.

To investigate whether CBZ form II could be isolated not only visually but in the diffraction data, single frame analysis was investigated. As each frame is collected by a 100 ms exposure at intervals of 100 ms, the probing point within a solution slug is random and thus any position within a solution slug could be probed. Each frame that exhibited diffraction at W3 was analysed and in each case only CBZ form III emerged (Figure 4.32b), despite the visual observations that clearly showed needles and blocks physically separated within a single solution slug. The single frame analysis was also investigated at W2 before the CBZ form III seed solution was introduced and confirmed that sufficient diffraction data was collected within these frames to elucidate the presence of CBZ form II in this window (Figure 4.32a).

Investigation of individual frames did not isolate CBZ form II, which was postulated to be observed visually separated from CBZ form III in a single solution slug. However, the single frame analysis has highlighted that polymorphic identity of CBZ form II and CBZ form III could be clearly ascertained from single 100 ms exposures from W2 and W3, respectively (Figure 4.32). At W3, the vast majority of habit observed in the solution slug was needle and thus it is unlikely that diffraction data from these needles would not have been acquired during the data collection.

To address this, it is noted that in some studies CBZ form III has been found to exist as needles under certain conditions, *via* crystallisation in isopropanol[140] or in the presence of surfactants.[141] This may explain the separation of CBZ crystalline material on the premise of habit, whereby the needle and block morphologies are separated based on their different interactions with the flow paths in the solution slug. The lack of observation of CBZ form II in the PXRD patterns can be attributed to this unusual case of crystallising two different morphologies of CBZ form III in this segmented flow environment in the KRAIC-D.

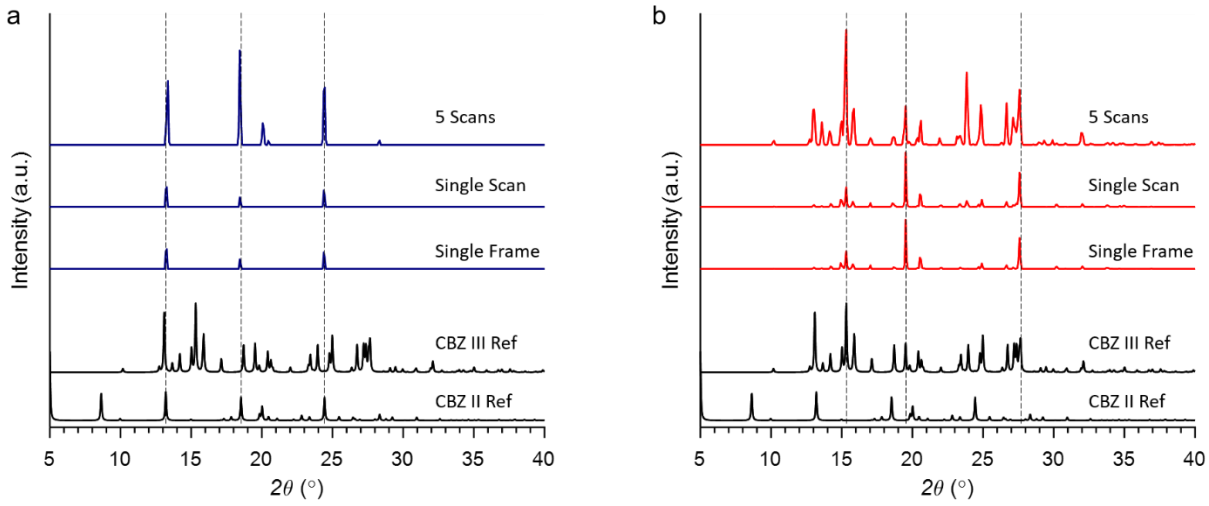

Figure 4.32 – PXRD patterns of CBZ obtained from post-nucleation seeded cooling crystallisation in the KRAIC-D at windows **(a)** W2 and **(b)** W3 comparing the data obtained from the combined scan method (5 scans), a single scan with a total of 51 exposures and a single 100 ms exposure (frame). The dotted lines are a guide to the eye for the identification of selected characteristic peaks of CBZ II and III in **(a)** and **(b)**, respectively. The experimental diffraction patterns have been converted into Cu Kα wavelength for comparison to reference data. (Refcodes: CBMZPN03 (CBZ form II) and CBMZPN01 (CBZ form III)).[33]

4.7.5.2 Offline slurrying of CBZ form II and CBZ form III

The initial visual observation of CBZ form II and CBZ form III potentially co-existing within a single solution slug evident from post-nucleation seeding of pure CBZ form III after window 2 prompted investigation into competitive slurrying of the two forms. To ascertain whether conversion between CBZ form II and CBZ form III would be expected between W2 and W3. Slurrying experiments were carried out wherein a slurry containing both polymorphs was stirred for the time between windows (4 minutes) and then filtered and analysed offline *via* PXRD. A physical 50:50 solid mixture of CBZ form II and form III was also prepared as a reference.

Offline slurrying experiments of CBZ II and III seed mixtures (Figure 4.33) indicate that a slight polymorphic transition can occur within the 4 minutes timeframe between the seeding inlet and W3. Importantly, the mixing conditions in the offline slurrying batch experiments using a round bottomed flask with magnetic bottom stirring differ from the mixing experienced within the solution slugs in the KRAIC-D. In the KRAIC-D experiment, this could result in a reduction in the amount of CBZ form II present at W3 to below detectable limits accessible by this *in situ* XRD characterisation and data processing technique. Alternatively, since the needle habit of CBZ form II shows consistency in shape and thus position within the solution slug is well defined, it is plausible that the random exposure rate of the solution slugs simply resulted in no exposures of the rear portion of the slug containing CBZ form II needles.

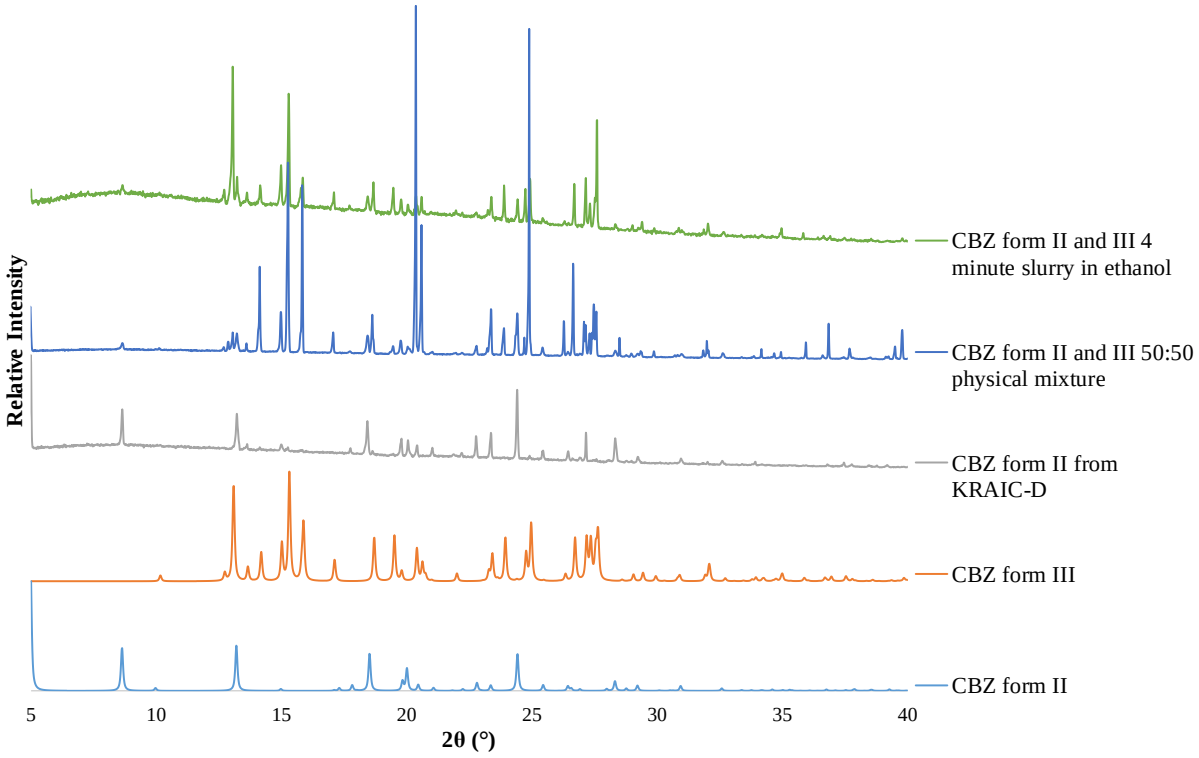

Figure 4.33 – PXRD plots of offline slurrying experiments of CBZ form II and III mixture showing some transformation towards CBZ form III in the 4 minute slurrying experiment.

4.7.6 Conclusions of CBZ *in situ* XRD Characterisation

An unseeded CBZ in EtOH cooling crystallisation yields the metastable CBZ form II across all analytical points. Seeding with the pure thermodynamic CBZ form III dictates the polymorph outcome at both pre- and post-nucleation stages. Visual analysis of post-nucleation seeding of CBZ form III suggested the presence of both CBZ form II needles and CBZ form III blocks in solutions slugs at W3, but this was not reflected in the diffraction data, where only

CBZ form III was identified from all diffraction from flowing droplets at W3. This could be explained by the fact that CBZ form III has been found also to exist in needle morphology under certain conditions.

4.8 Polymorphic Monitoring of Urea Barbituric acid (UBA)

The co-crystal system urea-barbituric acid (UBA) has four polymorphic forms at atmospheric pressure. UBA form I and form III exist concomitantly, whilst UBA form II is highly metastable and thus is not expected in this study.[122] The fourth polymorph UBA form X has been discovered recently during slurry experiments utilising urea and barbituric acid in a 2:1 ratio slurry mediated in 2 mL of methanol or ethanol stirred at a rate of 250 rpm maintained at 20 °C.[120] Concomitant production of polymorphs UBA form I and III is expected in the study described here. The concomitant nature of the UBA polymorphs has led to some debate regarding the identity of the thermodynamic form of UBA,[122] and this study aims to provide additional insight to the relative stabilities of UBA form I and III.

4.8.1 Offline KRAIC Experiments: UBA in methanol (MeOH) (UBAK1)

Experiments performed by a previous member of the group using the KRAIC platform without inline analytical capability[72] were reproduced here and similarly ascertained that a mixture of UBA form I and III were obtained from crystallisation in MeOH.

The crystallisation parameters for unseeded and seeded (both pre- and post-nucleation) experimental runs for UBA in MeOH are summarised in Table 4.15; the temperature zones controlled by the jacketed tubing and residence times dictated by the flow parameters are also highlighted.

The flow parameters used in the unseeded UBA in MeOH crystallisation runs (13.21 g/L and 14.09 g/L for urea and barbituric acid in MeOH respectively) in the KRAIC (UBAK1) and subsequent KRAIC-D (UBAKDB1), UBA form III (UBAKDB2 and UBAKDB3) and form I (UBAKDB4) seeded KRAIC-D runs are summarised in Table 4.16.

Table 4.15 – Crystallisation parameters for all UBA in MeOH runs with temperature until segmentation and nucleation promoter defined in Figures 4.6, 4.18 and 4.19, ‡denotes RTs which are extrapolated from observed values.

					Residence time (min)			
	[Solution] (g/L)	**[Seed solution] (wt%)**	**Temp until segmen-tation (°C)**	**Temp of Nucleation Promoter (°C)**	**W1**	**W2**	**W3**	**End**
UBA unseeded	Urea 13.21 BA 14.09	-	60	-	4.1	6.9	9.0	10.8
UBA I pre-nucleation seeded	Urea 13.21 BA 14.09	0.2	60	-	4.1	6.9	9.0	10.8
UBA III pre-nucleation seeded	Urea 13.21 BA 14.09	0.2	60	-	4.1	6.9	9.0	10.8
UBA III post-nucleation seeded	Urea 13.21 BA 14.09	0.2	60	-	4.1	6.9	8.8‡	10.4‡

Table 4.16 – Flow rates (in mL/min) used for all KRAIC and KRAIC-D runs, † ‘pre-seed pos. and ‘post-seed pos’ refer to the flow rates prior to and after the post-nucleation seeding inlet.

						Total (excl. NS)	
	Carrier fluid	**Air**	**Neutral solvent**	**Solution**	**Seed**	**Pre-seed pos.**	**Post-seed pos.**
UBA unseeded	4.18	4.18	12.5	4	N/A	12.36	12.36
UBA I pre-nucleation seeded	4.18	4.18	12.5	3	1	12.36	12.36
UBA III pre-nucleation seeded	4.18	4.18	12.5	3	1	12.36	12.36
UBA III post-nucleation seeded	4.18	4.18	12.5	4.33	1	12.69	13.69

The experimental set-up for unseeded UBA in MeOH KRAIC (UBAK1), which does not feature any additional temperature control after the segmentation water bath, is illustrated in Figure 4.22 in Section 4.7.1.

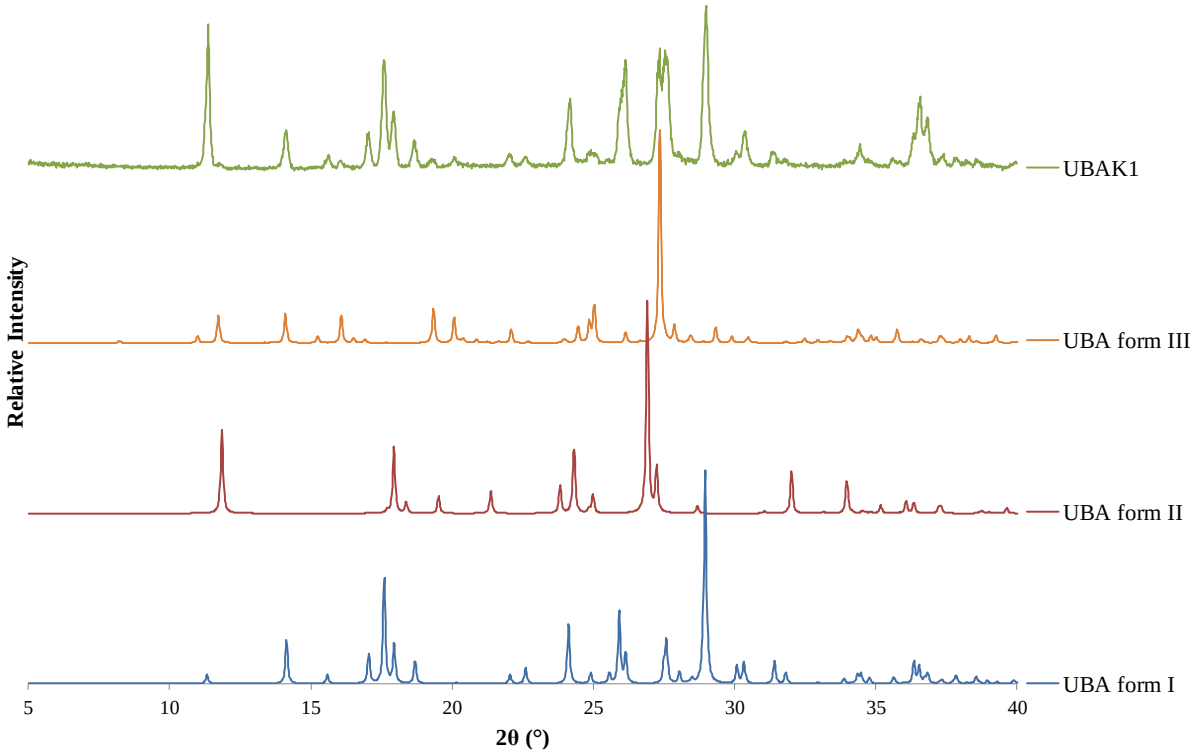

Figure 4.34 – PXRD of material collected from an unseeded offline KRAIC UBA in MeOH experiment (UBAK1) showing a mixture of UBA form I and III in the final product.

Offline PXRD analysis after filtration of the crystalline product emerging from the KRAIC platform (UBAK1) yields a mixture of UBA form I and III (Figure 4.34), which has also been reported in previous crystallisation studies of UBA.[72] This coexistence of UBA form I and III confirms UBA in MeOH shows the potential for a polymorphic transformation during crystallisation, which can be monitored by *in situ* XRD characterisation (UBAKDB).

4.8.2 Online KRAIC-D Runs at Beamline I11: UBA in MeOH (UBAKDB)

The preliminary offline KRAIC (UBAK1) experiment presented in Section 4.8.1 provides a suitable start point for online UBA KRAIC-D experiments at I11, which are presented by UBAKDB identifiers. A range of online cooling crystallisations was investigated during the beamtime, including unseeded (UBAKDB1), pre-nucleation (UBAKDB2 and UBAKDB4) and post-nucleation (UBAKDB3) seeded crystallisation experiments. The experimental set-up,

along with feed and seed slurry concentration for each of these UBAKDB beamtime experiments are summarised in Table 4.17.

Table 4.17 – Experimental set-up, as well as concentrations of feed and seed solutions for the various UBAKDB beamtime experiments.

Experiment	**Set-up**	**Feed solution concentration UBA in MeOH g/L**	**Seed Solution (Wt %)**
UBAKDB1	T-piece Unseeded KRAIC-D (Fig. 4.6)	13.21 (U) 14.09 (BA)	Unseeded (N/A)
UBAKDB2	Pre-nucleation form III Seeded KRAIC-D (Fig. 4.18)	13.21 (U) 14.09 (BA)	0.2 wt%
UBAKDB3	Post-nucleation form III Seeded KRAIC-D (Fig. 4.19)	13.21 (U) 14.09 (BA)	0.2 wt%
UBAKDB4	Pre-nucleation form I Seeded KRAIC-D (Fig. 4.18)	13.21 (U) 14.09 (BA)	0.2 wt%

4.8.3 Unseeded UBA in MeOH KRAIC-D at I11 (UBAKDB1)

For the unseeded UBA in MeOH KRAIC-D (UBAKDB1) run at I11, UBA form III was accessed in polymorphic purity at W1 (4.6 mins, 6.4 m), whilst W2 and W3 also show UBA form III, but a dominant UBA form I representative peak at 28.9° 2θ (3.09 Å; $(11\bar{4})$) begins to emerge at W2 (6.9 mins, 9.0 m). This representative UBA form I peak increases in intensity at W3 (9.0 mins, 11.7 m) (Figure 4.35). This progression in polymorphic form and dominance of the UBA form I polymorph signifies that a polymorphic transformation from UBA form III to I is occurring as the crystallisation process proceeds and UBA form I is the thermodynamic form in methanolic solution.

The growth plots for the unseeded UBA in MeOH KRAIC-D (UBAKDB1) run conveys a linear relationship between the average integrated intensity and position along the crystalliser length (Figure 4.36), but the extent of crystal growth is low in this case.

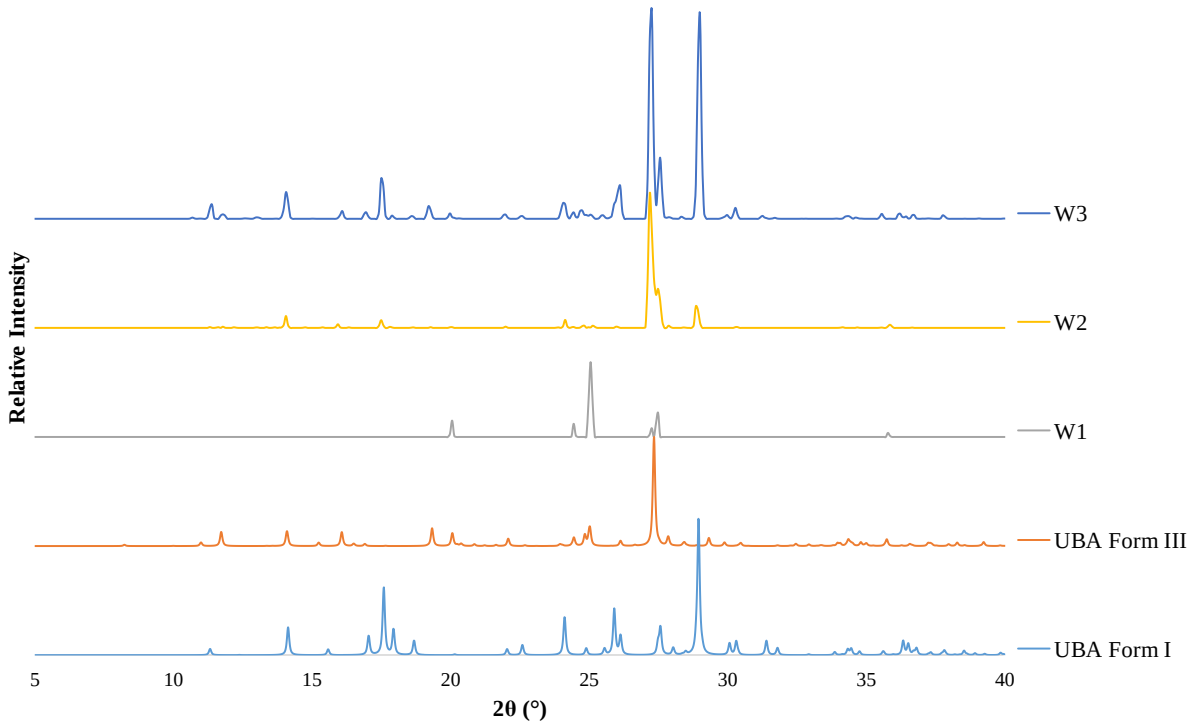

Figure 4.35 – PXRD patterns of UBAKDB1 unseeded cooling crystallisation of UBA in MeOH in the KRAIC-D showing a progression of UBA form III to form I in patterns obtained from W1 to W3. The scale of the experimental diffraction patterns has been adjusted for clarity (W1 scaled by a factor of 40, W2 by 3 relative to W3); the synchrotron data has been converted into Cu Kα wavelength for comparison to reference data. (Refcodes: EFOZAB (UBA form I) and EFOZAB02 (UBA form III)).

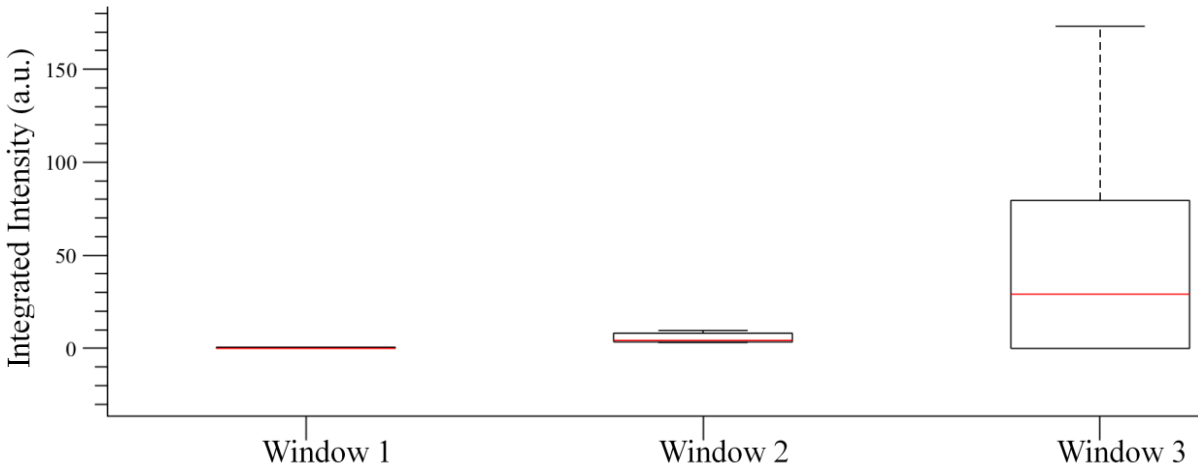

Figure 4.36 – Growth plots for a UBAKDB1 unseeded UBA in MeOH KRAIC-D run at I11.

4.8.4 Pre-nucleation Seeding of UBA form III (UBAKDB2)

For UBA form III seeded runs where pure UBA form III is introduced as a slurry at pre-nucleation stages (UBAKDB2) (0.05 m, Figure 4.18 in Section 4.4.1) into the UBA in MeOH

cooling crystallisation, UBA form III is observed across all windows, but the dominant UBA form I peak emerges again at ~29° 2θ for W2 and W3 set points along the KRAIC-D (Figure 4.37). Although small and apparently slightly shifted in 2θ, the intensity of this peak can be enhanced by combining 10 rather than 5 scans (Appendix 4.7). This demonstrates that seeding does not dictate polymorphic outcome and again implies that UBA form I is the thermodynamic polymorph.

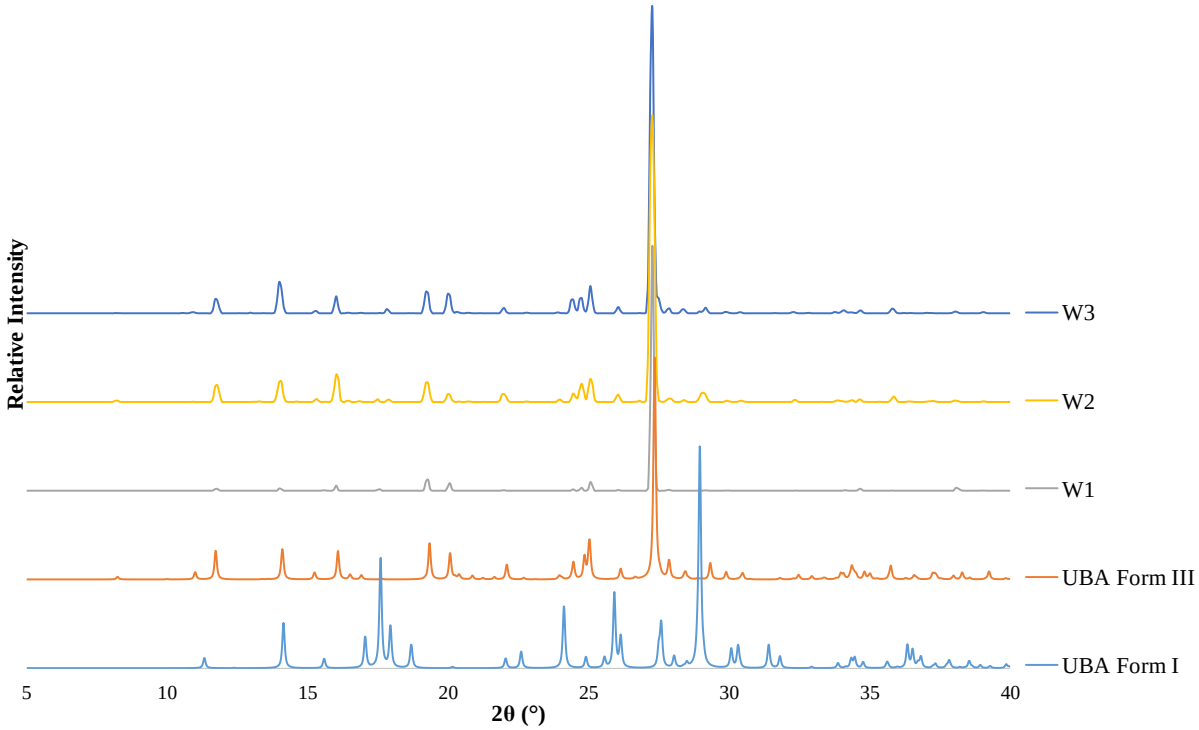

Figure 4.37 – PXRD patterns of UBAKDB2 pre-nucleation UBA form III seeded cooling crystallisation of UBA in MeOH in the KRAIC-D showing a progression of UBA form III to form I in patterns obtained from W1 to W3. The scale of the experimental diffraction patterns has been adjusted for clarity (W1 scaled by 5, W2 by 2.5 relative to W3); the synchrotron data has been converted into Cu Kα wavelength for comparison to reference data. (Refcodes: EFOZAB (UBA form I) and EFOZAB02 (UBA form III)).

The growth plots for the pre-nucleation UBA form III seeded UBA in MeOH KRAIC-D run conveys a linear relationship between the average integrated intensity and position along the crystalliser length (Figure 4.38), implying steady-state is not reached within the timeframe investigated. This crystal growth behaviour for a pre-nucleation seeded UBA in MeOH KRAIC-D run is similar to the crystal growth observed in the unseeded UBA in MeOH KRAIC-D experiment. The crystal growth results for UBAKDB2 show an increase in integrated intensity over the crystalliser length, in contrast to CBZKDB3 where CBZ form III

introduced at pre-nucleation stages led to a constant integrated intensity value over the crystalliser length.

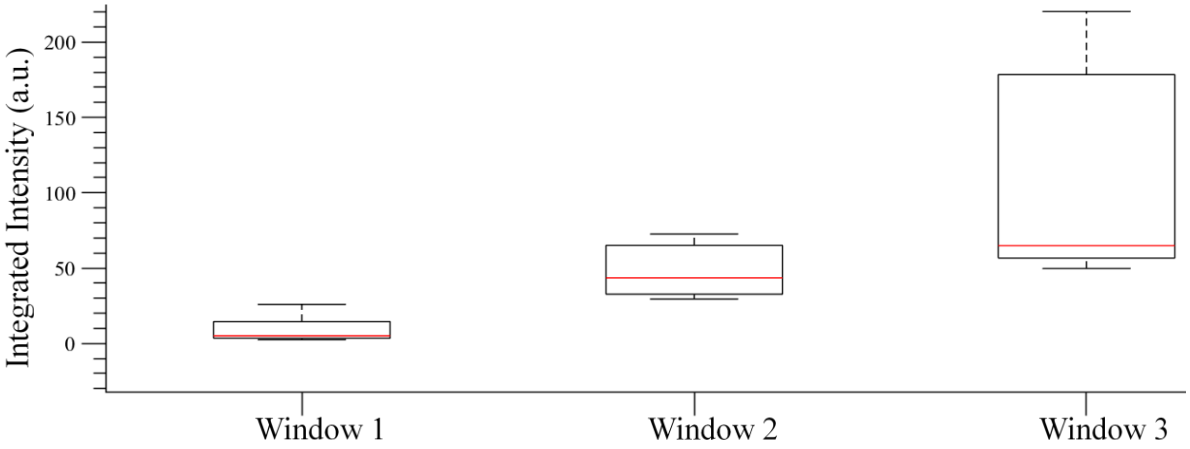

Figure 4.38 – Growth plots for UBAKDB2 pre-nucleation seeded UBA form III in MeOH KRAIC-D run at I11.

4.8.5 Post-nucleation Seeding of UBA form III (UBAKDB3)

Post-nucleation seeding with UBA form III after window 2 (UBAKDB3) (i.e. positioned after where UBA form I emerged at W2 in the unseeded experiments, Figure 4.19 in Section 4.4.1) further indicates a close relative stability of the two polymorphs with UBA form I emerging at W3 (Figure 4.39). However, unlike the unseeded cooling crystallisation of UBA in MeOH (UBAKDB1) presented in Section 4.8.3, UBA form I has not emerged at the analytical set point W2 for UBAKDB3, the polymorphic transformation occurs at a later stage in the crystallisation process and instead emerges at W3 (Figure 4.39).

For post-nucleation seeded UBA form III crystallisation (UBAKDB3), a pronounced increase in integrated intensity is observed between W2 and W3, which is to be expected as additional crystalline material is injected between the two analytical windows (Figure 4.40).

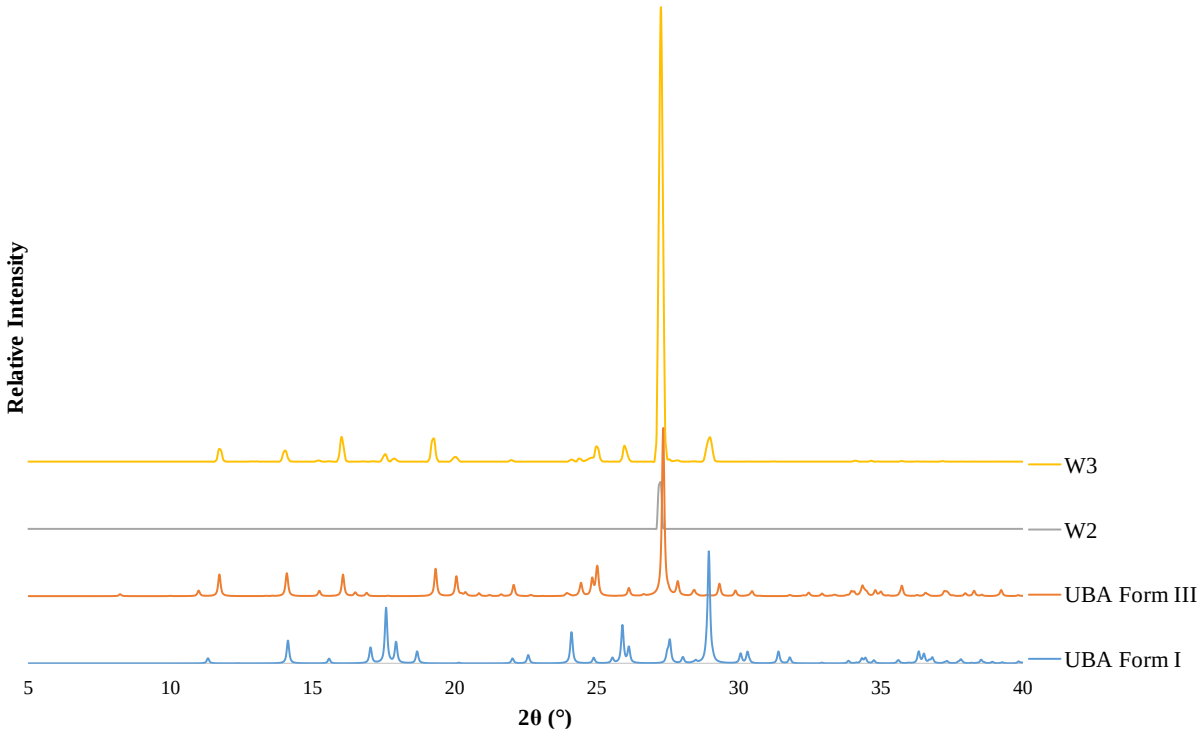

Figure 4.39 – PXRD patterns of UBAKDB3 post-nucleation UBA form III seeded cooling crystallisation of UBA in MeOH in the KRAIC-D showing a partial transformation of UBA form III to form I in the pattern obtained at W3. The scale of the experimental diffraction patterns has been adjusted for clarity (W2 scaled by 50 relative to W3); the synchrotron data has been converted into Cu Kα wavelength for comparison to reference data. (Refcodes: EFOZAB (UBA form I) and EFOZAB02 (UBA form III)).

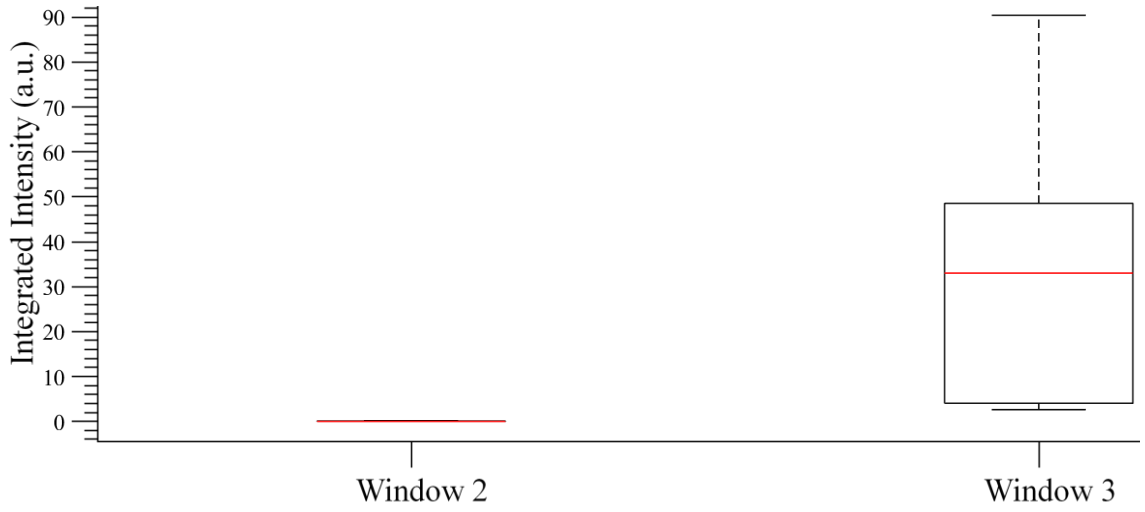

Figure 4.40 – Growth plots for UBAKDB3 post-nucleation seeded UBA form III in MeOH KRAIC-D run at I11.

4.8.6 Pre-nucleation Seeding of UBA form I (UBAKDB4)

For UBA form I seeded runs where pure UBA form I is introduced as a slurry at pre-nucleation stages (UBAKDB4) (0.05 m, Figure 4.18 in Section 4.4.1) into the UBA in MeOH cooling crystallisation, pure UBA form I is observed across W1 and W2, highlighting that seeding with the thermodynamic form in solution dictates the polymorphic outcome. Characteristic UBA form I peaks are evident across each of the analytical set points in the KRAIC-D (Figure 4.41).

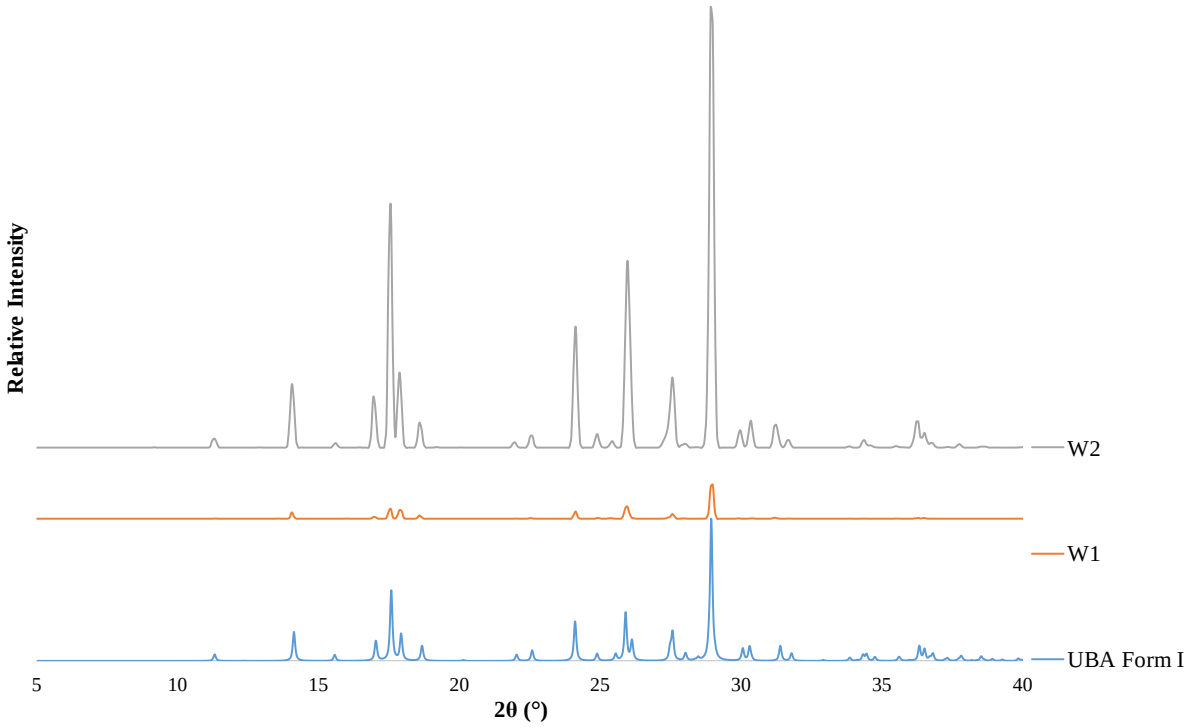

Figure 4.41 – PXRD patterns of UBAKDB4 pre-nucleation UBA form I seeded cooling crystallisation of UBA in MeOH in the KRAIC-D showing UBA form I at W1 and W2. The experimental diffraction patterns have been converted into Cu Kα wavelength for comparison to reference data. (Refcode: EFOZAB (UBA form I)).

For pre-nucleation seeded UBA form I crystallisation (UBAKDB4), a pronounced increase in integrated intensity is observed between W1 and W2 (Figure 4.42). Pre-nucleation seeding with UBA form I results in a greater increase in apparent crystal growth between W1 and W2 (increase of almost factor 20 in average intensity), when compared to pre-nucleation seeding with UBA form III. This implies UBA form I adopts a faster crystal growth mechanism compared to UBA form III, with average integrated intensity increase of factor ~5 between W1 and W2. This difference in relative growth rates of the two forms could be attributed to polymorphic conversion from UBA form III to I, which is occurring during the analysis time period for seeded form III crystallisations but not UBA form I seeded crystallisation runs.

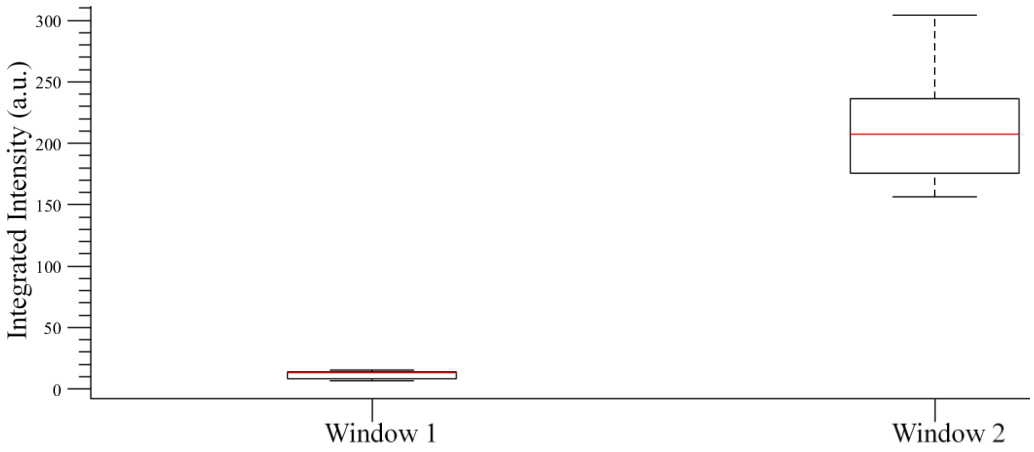

Figure 4.42 – Growth plots for UBAKDB4 pre-nucleation seeded UBA form I in MeOH KRAIC-D run at I11.

4.8.7 Stability of UBA Seeds

The polymorphic form of the UBA seeds used in the trials were tested after dry storage for over 12 months in a vial under standard laboratory conditions. Additionally, to ascertain whether conversion from UBA form III to UBA form I would be expected between windows, a slurry containing equal quantities of UBA form I and form III seeds was stirred in MeOH for 4 minutes, which equates to the residence time between adjacent windows. The UBA slurry was subsequently filtered and analysed offline *via* PXRD (Figure 4.43).

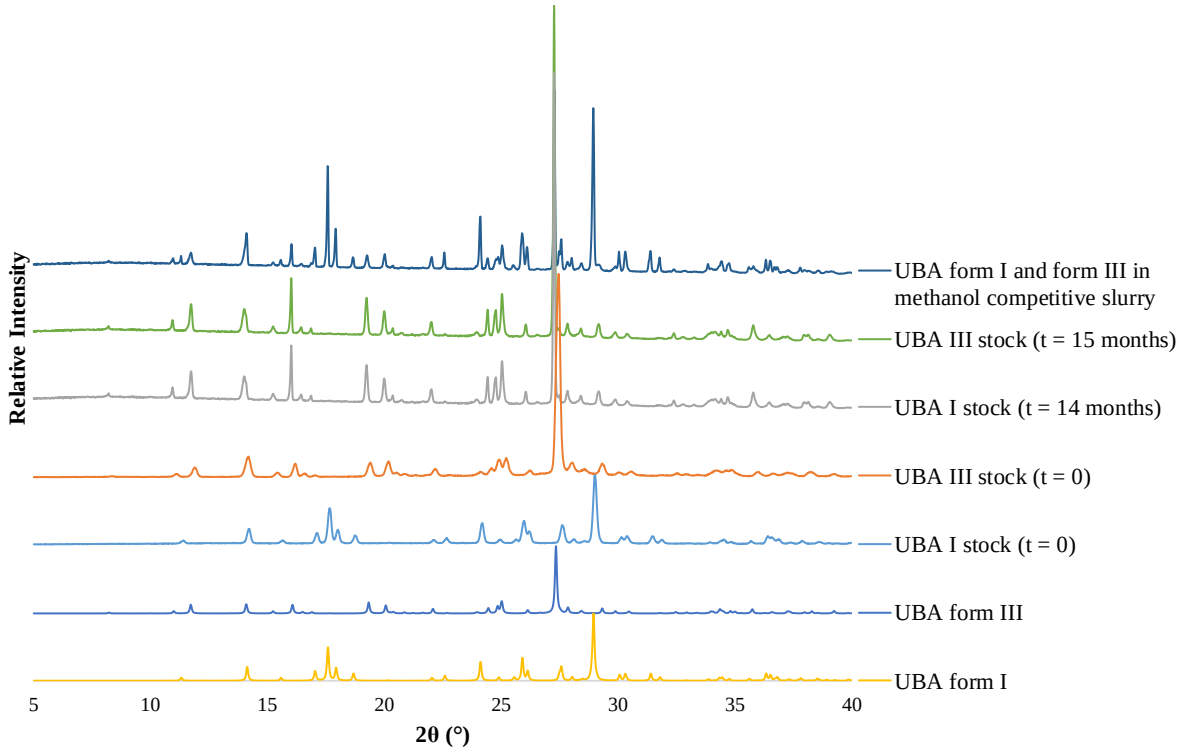

Figure 4.43 – PXRD plots of UBA form I and III seeds before and after dry storage for over 12 months and XRD pattern obtained from slurrying a UBA form I and III 50:50 mixture in MeOH for 4 minutes. N.B. UBA form I and III stock t=0 data taken on a Bruker D8 Advance, t=14/15 months and slurrying experiment taken on a STOE STADI P diffractometer.

Interestingly, the relative stability of the concomitant forms of UBA form I and III varies depending on whether the sample is dry or exists in solution. Under dry storage conditions within a 12 month period, it was found that UBA form I undergoes complete polymorphic transformation to UBA form III, whilst upon slurrying UBA form III for 4 minutes in MeOH, there is an incomplete conversion to UBA form I (Figure 4.43). The dry UBA form III seeds remained stable, maintaining form over the storage period. These findings clarify the discrepancy reported in the stability of UBA polymorphs; solid state transformation from UBA form I to form III,[120-122] but solution state transformation of UBA form III to form I.[51]

4.8.8 Conclusions of UBA *in situ* XRD Characterisation

In situ XRD has provided the first proof of a polymorphic transformation from UBA form III to UBA form I over the course of the crystallisation process in MeOH. Experiments seeded with UBA form I or UBA form III reinforce this finding. Seeding experiments with UBA form I at pre-nucleation stages yield UBA form I throughout analysis, whilst seeding at either pre- or post-nucleation stages with UBA form III shows a partial transformation from UBA form III

to form I emerging from W2 onwards along the length of the crystalliser. UBA form I is dominant in solution as seeding with UBA form III does not dictate the polymorphic outcome; partial transformation to UBA form I will occur. In contrast, dry samples of UBA form I showed a solid-state transformation to UBA form III from analysis after a one-year time period.

4.9 Comparison and Conclusions of model systems: CBZ and UBA

In situ powder XRD has been used to augment the limited understanding gained from offline analysis of the pharmaceutically relevant and highly polymorphic systems CBZ in EtOH and UBA in MeOH.

For CBZ in EtOH, an unseeded crystallisation run yielded the metastable CBZ form II. Unseeded crystallisation experiments of UBA in MeOH initially crystallises as UBA form III which, over the crystallisation process, undergoes incomplete transformation to UBA form I.

Introduction of a controlled solid interface in the form of pure polymorphic seed crystals dictated the polymorphic outcome of CBZ in EtOH but this was not the case for UBA form III seeded crystallisations in MeOH, whereby UBA form I emerged over the crystallisation time. Addition of the thermodynamic form of CBZ (CBZ form III) into the crystallisation at pre-nucleation stages produced pure CBZ form III throughout the observed crystallisation time. Whilst post-nucleation addition produced only CBZ form III from the diffraction data, visual observation confirmed the continued presence of CBZ form III needles separated in the same solution slug from the CBZ form III blocks. This finding has demonstrated the potential of segmented flow to be used as a polymorph separation technique, provided the polymorphs display distinct differences in habit. Seeding UBA in MeOH with pure UBA form III seeds did not dictate the polymorphic outcome, much like the unseeded UBA in MeOH run, UBA form I showed resilience and emerged over the length of the crystalliser. This gives indication to the relative stabilities of UBA form I and III, where there has been some contradictory views in the literature.[51, 120-122] The repeated incomplete transformation to UBA form I in seeded form III and unseeded runs, highlights that UBA form I is the thermodynamic form in methanolic solution. This finding is reaffirmed in UBA form I pre-nucleation seeding runs, where UBA form I is observed throughout the length of the crystalliser.

Whilst a combined scan method was preferred to encompass data from across many exposures to ensure a proportional representation of the crystallisation environment, where data across

five scans was selected to be statistically relevant, further diffraction analysis ascertained that polymorph identification could be achieved from individual 100 ms exposures. Table 4.18 summarises the phases of CBZ and UBA obtained from each experiment using the five-scan combined approach, listing the representative peaks identified in the diffraction patterns.

From the diffraction integrated intensity data, it was possible to gain insight into the different growth kinetics of the two crystallising systems from both unseeded and seeded environments. For an unseeded CBZ in EtOH run (CBZKDB2), the growth plots at the three analysis points along the length of the crystalliser are in agreement with the widely accepted exponential crystal growth mechanisms. In contrast, UBA in MeOH (UBAKDB1) shows less substantial growth with a linear dependence with respect to the crystalliser length. The differences in growth profiles for the unseeded runs of CBZ in EtOH and UBA in MeOH highlight the differences in MSZWs for the two solute-solvent systems and thus UBA did not require the additional temperature control provided by the 10 °C nucleation promoter, resulting in different cooling profiles for UBA and CBZ (Figure 4.44). The exponential crystal growth of CBZ in EtOH (Figure 4.45) relates to the delay in achieving nucleation and subsequent growth. The two crystallisation processes will also have different kinetics, different flow rates and corresponding residence times and thus the different analytical set points, which remain consistent across all experiments, are probing different stages in the growth kinetics of the two processes. In addition, during the unseeded UBA and form III seeded UBA crystallisations a polymorphic transformation was observed, whilst a transformation was not observed during the cooling crystallisation experiments of CBZ.

Table 4.18 – Qualitative summary of polymorphic expression observed in all KRAIC-D experiments. †A mixture of CBZ form III needles and CBZ form III blocks are visually separated in the flow paths within the solution slugs.

Model System	Experiment	Window	Form	Representative 2θ peaks
CBZ	Unseeded CBZ (CBZKDB2)	2 and 3	CBZ form II	8.7°, 13.3°, 18.4°, 24.4°
	Seeded form III pre-nucleation (CBZKDB3)	2 and 3	CBZ form III	15.3°, 15.8°, 17.1°, 24.9°, 27.5°
	Seeded form III post-nucleation (CBZKDB4)	2	CBZ form II	13.3°, 18.4°, 24.4°
		3	CBZ form III†	15.3°, 15.8°, 26.7°, 27.6°
UBA	Unseeded UBA (UBAKDB1)	1	UBA form III	27.3°, 25.0°
		2	UBA form I and form III	27.3°, 29.0°
		3	UBA form I and form III	27.3°, 29.0°
	Seeded (III) pre-nucleation (UBAKDB2)	1	UBA form III	27.2°
		2	UBA form I and form III	27.2°, 29°
		3	UBA form I and form III	27.2°, 29°
	Seeded (III) post-nucleation (UBAKDB3)	2	UBA form III	27.2°
		3	UBA form I and III	27.2°, 29°
	Seeded (I) pre-nucleation (UBAKDB4)	1	UBA form I	17.6°, 27.7°, 28.9°
		2	UBA form I	17.6°, 27.7°, 28.9°

The crystallisation behaviour of UBA in MeOH is reaffirmed by the growth plots for the seeded runs of UBA in MeOH. UBA form I pre-nucleation seeded runs have a much greater increase in apparent crystal growth between W1 and W2, compared to UBA form III pre-nucleation seeded runs, implying a faster crystal growth mechanism for form I over form III (Figure 4.46). This could be attributed to the polymorphic conversion of UBA form III to I which is taking place during the analysed time period for UBA form III seeded runs, but not for UBA form I seeded crystallisation runs.

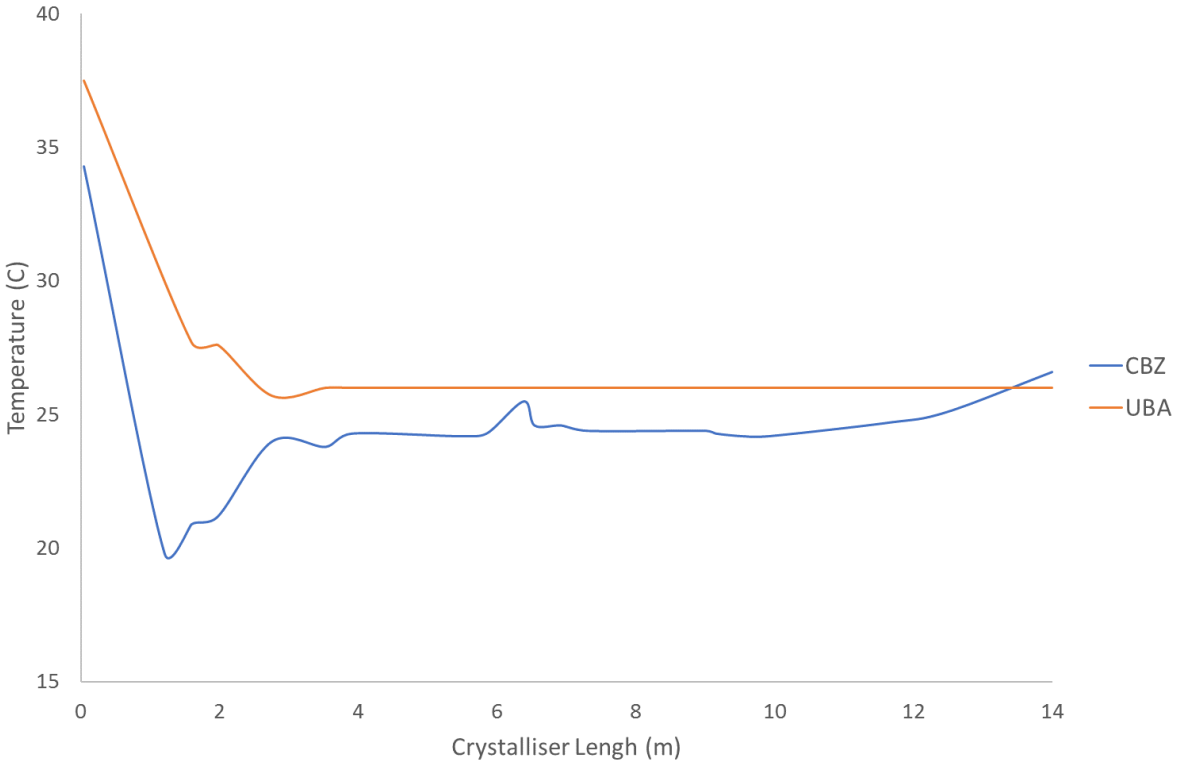

Figure 4.44 – Measure temperature profiles across KRAIC-D for CBZ and UBA experiments.

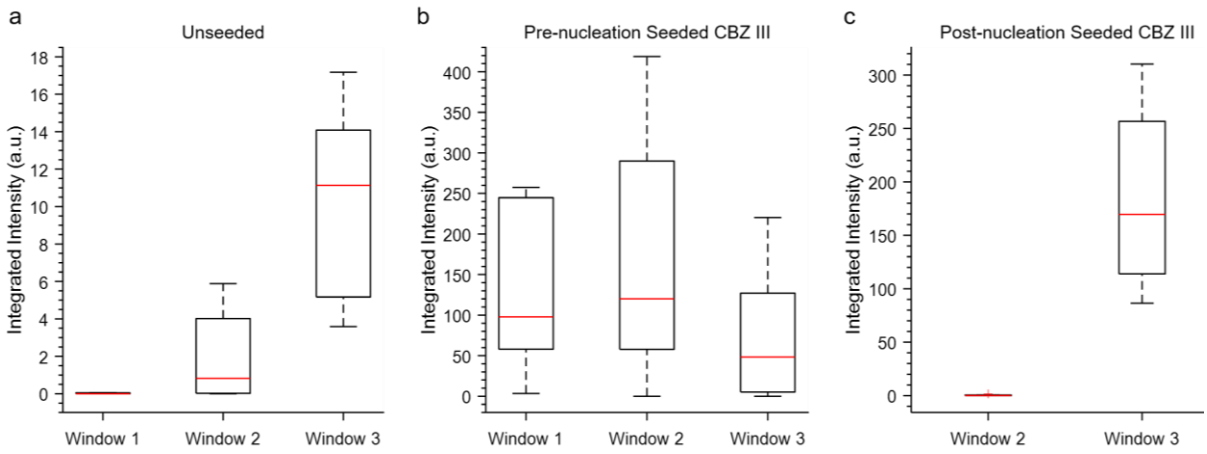

Figure 4.45 – Box plots of diffraction intensity for (**a**) unseeded (CBZKDB2), (**b**) pre-nucleation form III seeded (CBZKDB3), and (**c**) post-nucleation form III (CBZKDB4) seeded CBZ KRAIC-D experiments. N.B. red lines indicate the median intensity found in all frames containing non-solvent diffraction, boxes encompass upper to lower quartiles, and the absolute maximum and minimum intensity values are represented as whiskers.

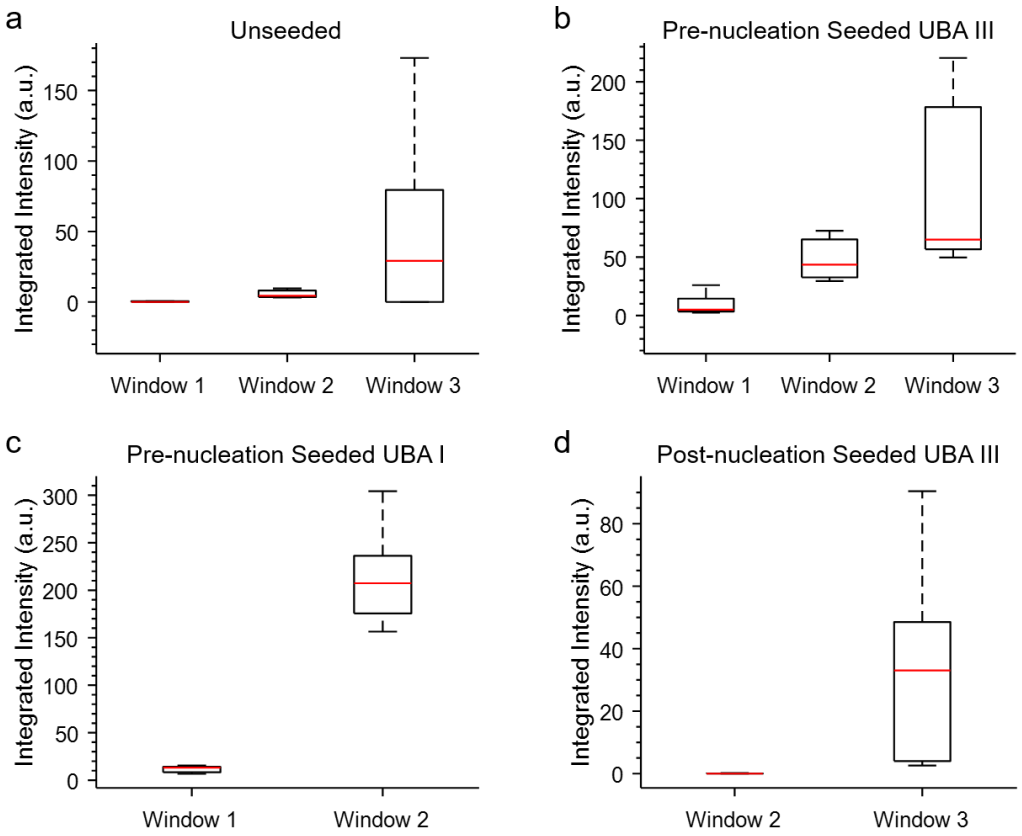

Figure 4.46 – Box plots of diffraction intensity for (**a**) unseeded (UBAKDB1), (**b**) pre-nucleation form III seeded (UBAKDB2), (**c**) pre-nucleation form I seeded (UBAKDB4), and (**d**) post-nucleation form III seeded (UBAKDB3) UBA KRAIC-D experiments. N.B. red lines indicate the median intensity found in all frames containing non-solvent diffraction, boxes encompass upper to lower quartiles, and the absolute maximum and minimum intensity values are represented as whiskers.

4.10 Overall Discussions and Conclusions

As a result of the steady-state operation of the KRAIC-D, an analytical set point will be at the same stage of the crystallisation process irrespective of the experiment time, which allows events that evolve with the crystallisation time, such as polymorphic transformations, to be investigated. Using both unseeded and seeded (pre- and post-nucleation) cooling crystallisation methodologies, the evolving crystal structures of the pharmaceutical compounds: CBZ in EtOH and UBA in MeOH were uncovered as a function of residence time by probing different set positions along the length of the tubular flow crystalliser, KRAIC-D.

In CBZ experiments, unseeded CBZ in EtOH crystallisations yielded the metastable CBZ form II. For seeded crystallisation runs, the seed addition point determined whether single or multiple polymorphs were observed throughout the crystallisation. Pre-nucleation seeded

crystallisations with the thermodynamic form CBZ form III produced CBZ form III throughout the length of the crystalliser, whereas addition of CBZ form III post nucleation once CBZ form II crystallised, yielded a mixture of morphologies, suggesting co-existence of CBZ form II and III. Only CBZ form III could be evaluated from the diffraction data, whereas visual observation suggested a potential mixture of the two forms in a single solution slug (distinguished by their characteristic morphologies, in which a significant proportion of crystalline material in the solution slug exhibited needle morphology). To examine the possible existence of the two forms from the diffraction data an alternative strategy to the five-scan combined method was examined, in which polymorph identification could be achieved from a single 0.1 second exposure. CBZ form II could still not be isolated from the single diffraction frames, in spite of the appearance of a significant proportion of needles in the visual observations. In the absence of diffraction evidence for CBZ form II, this can be explained by the fact that under some conditions, CBZ form III can exist in needle morphology.

The visual observation of the two morphologies and their separation in the slugs, however, showed that segmentation has the potential to facilitate polymorph separation on the premise that various forms might have different morphologies and thus different habits will interact differently in the bolus flow. The investigation of single frame analysis prompted by this observation has also highlighted that polymorph identification can be achieved from a single 100 ms exposure from flowing droplets.

It was observed that for an unseeded crystallisation of UBA in MeOH, a progression of polymorphs from UBA form III to form I occurred. In seeded UBA experiments, a single polymorph was observed throughout the process when seeded with UBA form I but in experiments seeded with UBA form III there was still an incomplete transformation into UBA form I, as observed in the unseeded run. The resilience of UBA form I in the presence of UBA form III seeds and the corresponding suppression of UBA form III in the presence of form I seeds suggests a preference for UBA form I in methanolic solution. Together, these results highlight the importance of coupling real-time structural analysis with the crystallisation of polymorphic pharmaceutical crystals and co-crystals.

The ability to investigate diffraction at different analytical length scales using this technique increases the number of materials and solution conditions that could benefit from this *in situ* characterisation. There is also the potential to extend this analytical method to augment the

crystallisation pathway understanding of other types of crystallisation methods, such as anti-solvent, reactive and slurrying crystallisations, in the KRAIC-D. The utility of the KRAIC-D thus potentially expands beyond fundamental research in academic laboratories to industrial pharmaceutical research and development (R&D) projects.

Chapter 5 – *In situ* X-ray Diffraction (XRD) Analysis of Continuous Segmented Flow Cooling Crystallisation in KRAIC-S at Small Molecule Single Crystal Beamline, I19 Diamond Light Source – Paracetamol (PCM)

The research presented in Chapter 5 comprises a research collaboration between the Wilson Group at the University of Bath with Dr. Mark Warren at Beamline I19 the Diamond Light Source. The other researchers who contributed to various aspects of this work include: Dr. Daniel Scott, Miss Pollyanna Payne, Dr. Lauren Hatcher (University of Bath), as well as Dr. Lucy Saunders, Dr. Graeme Winter and Dr. Ben Williams (Diamond Light Source).

5.1 Introduction and Aims

Serial Crystallography (the collection of data from a series of individual crystals to make a complete data set) is a method recently established to study the structures of macromolecules using synchrotron or X-FEL (X-Ray Free-Electron Lasers) sources. The intense synchrotron X-ray source and more intense X-FEL pulse of second and femtosecond timeframes respectively, can result in the destruction of any exposed microcrystal, in cases where larger single crystals cannot be grown, making serial data collection mandatory. This method of data collection requires a high-throughput serial approach to sample delivery. Of relevance to the present work, and the potential extension of the method to small molecule systems, this delivery of samples can be achieved using a microfluidic platform that has the ability to generate large numbers of identical droplets; this creates defined reaction chambers allowing continual sample replenishment during data collection.[123, 142]

Serial crystallography has received much attention in the field of protein crystallography, as a means to overcome the rate-limiting steps of obtaining diffraction quality crystals and handling crystals during transfer to the X-ray diffractometer.[143] Gerard *et al.* reported a microfluidic platform employed to address these issues. The crystallisation of a protein of pharmaceutical interest was achieved *via* tubing microfluidics, which facilitated both *in situ* and *ex situ* X-ray diffraction (XRD) analysis.[143]

The increasingly focused and brilliant X-ray beams available at synchrotron facilities reduce the requirements for both sample volume and data acquisition time, whilst high-resolution

diffraction data can be collected even from weakly diffracting crystals.[142, 144] Importantly, the rapid data acquisition times accessible at synchrotron sources allows a diffraction pattern to be collected before the onset of radiation damage, which is particularly beneficial to radiation sensitive samples.[142, 143] The requirements necessary for the serial sample delivery into the X-ray beam are imposed by both the experimental set-up and the properties of the sample. The sample must be compatible with the size of the X-ray beam, such that the sample is fully immersed in the X-ray beam. The sample must be reliably delivered to this X-ray interaction area at a constant and appropriate rate, to allow sufficient data to be collected while avoiding excessive radiation damage.[142]

Microfluidic techniques are appropriate for reducing sample volume, automation and high-throughput crystallisation approaches.[143] Microfluidics has the ability to produce hundreds to thousands of droplets with identical composition, compatible with serial crystallography approaches.[143] Most of the microfluidic devices used for *in situ* synchrotron studies have focused on the characterisation of protein crystals and small angle X-ray scattering (SAXS) of soft matter, such as surfactants[145] and biomolecules.[144] The majority of these studies have been performed with continuous flow[146] or static systems;[144] the analysis of flowing droplet systems is limited to SAXS to monitor the formation of nanoparticles[147] and protein assembly.[148, 149]

The millifluidic droplets or slugs achieved *via* segmentation of the flow in a milliscale crystalliser, such as the KRAIC-D reported in Chapter 4, offer reproducible crystallisation environments. Issues with radiation damage are also effectively eliminated by the short residence time of each droplet / slug in the X-ray beam.[123]

The use of serial crystallography approaches applied to structural solution using single crystals of small organic molecules grown *in situ* is unprecedented. This chapter investigates the use of segmented flow in a milliscale crystalliser to grow small organic molecule single crystals *in situ* through cooling crystallisation, coupled with *in situ* single crystal XRD analysis to achieve structural solution from single crystals contained in flowing droplets.

5.1.1 Data Requirements

One of the most notable challenges with this work is ensuring the appropriate crystallisation conditions to access a single crystal in a single solution slug. This is in contrast to the slurries crystallised in solution slugs in the KRAIC-D monitored at I11 presented in Chapter 4.

From the *in situ* XRD powder experiments presented in Chapter 4, individual diffraction images recorded from the polycrystalline sample within the solution slugs were converted relatively directly into 2D powder patterns for analysis. The KRAIC-D has been optimised for these *in situ* powder diffraction studies. In contrast, single crystal diffraction studies require the diffraction pattern to be indexed before any useful information can be extracted; achieving indexation from a single image of a small molecule system is challenging. This can be mitigated by obtaining multiple images from multiple orientations from a single crystal tumbling within a solution slug, which has to reside in the X-ray path (Figure 5.1) for a significant period (1-4 seconds). The tumbling of a single crystal in a solution slug presents multiple orientations with respect to the X-ray beam, a necessary requirement in diffraction experiments to sample a sufficient portion of reciprocal space, the extent of which is dependent on the crystal symmetry. To be able to "suspend" the crystal in the X-ray beam a re-design of the set-up is essential. The adaptation of the KRAIC platform for single crystal measurements on I19 will hereafter be known as the KRAIC-S (Kinetically Regulated Automated Input Crystalliser – Single Crystal).

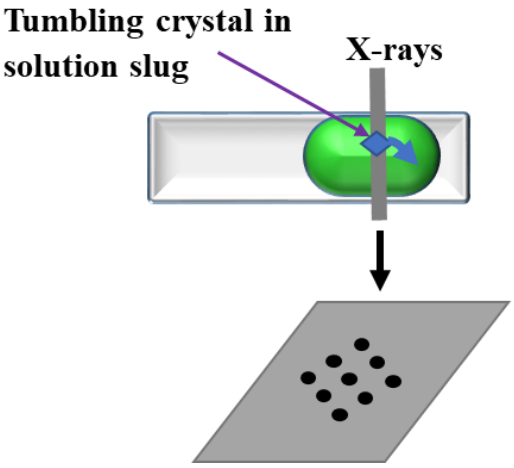

Figure 5.1 – Principles of the KRAIC-S flow cell implemented at I19.

Adaptations of the segmented flow apparatus for non-invasive single crystal structure determination is driven by the data requirements for this novel technique. As the X-ray source is in a fixed position and the segmented flow through the crystalliser cannot be stopped (as this would cause sedimentation and disrupt the mixing conditions within each slug), the only way to artificially "hold / suspend" the tumbling crystal in the X-ray beam is to use a motorised stage to translate the tubing in the opposite direction to the flow. The speed must equal and oppose the net flow rate within the KRAIC-S and the translation time / distance must be long

enough so the resulting diffraction data on a single diffraction image is sufficient for indexation.

Using data collected *via* standard methods, the typical minimum angular rotation required to index a crystal can be determined. This will then give an indication into how long each solution slug needs to reside in the X-ray beam; a suitable motorised stage can then be employed to move the tubing in the opposite direction to the segmented flow. A wedge of data is defined as a small sweep, which samples a small portion of reciprocal space.[150] Each wedge of data (range of angular rotation of the single crystal) will obtain a small slice of reciprocal space. For structure solution, hundreds of wedges at different orientation must be successfully scaled and merged. The longer the solution slug containing the crystals stays in the X-ray beam, the larger the wedge of data that can be collected, meaning fewer wedges need to be combined for structural solution.

5.1.2 Model System: Paracetamol (PCM)

Paracetamol (acetaminophen, PCM) is a common analgesic and antipyretic active pharmaceutical ingredient (API); the chemical structure is presented in Figure 5.2. PCM exists in five polymorphic forms, two of which can be accessed under high pressure conditions. The two forms of interest in this work are PCM form I, the thermodynamic form, and the metastable PCM form II. PCM form I (CSD Refcode: HXACAN30[24]) crystallises in the monoclinic space group $P2_1/n$, whilst PCM form II (CSD Refcode: HXACAN31[24]) crystallises in the orthorhombic space group *Pbca*. The different space groups associated with these polymorphs result from differences in packing which in turn results in differences in physiochemical properties of the solid forms of PCM. PCM form I adopts a herringbone arrangement of PCM molecules, whilst PCM form II adopts a layered structure (Figure 5.3).[151, 152] The layered structure of PCM form II means that the layers of molecules have the ability to slide over each other, resulting in a more soluble API, which is more easily compressible into a tablet.[152, 153]

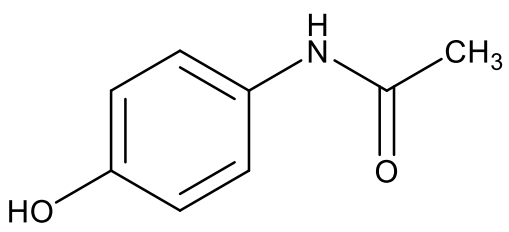

Figure 5.2 – Chemical structure of paracetamol (PCM).

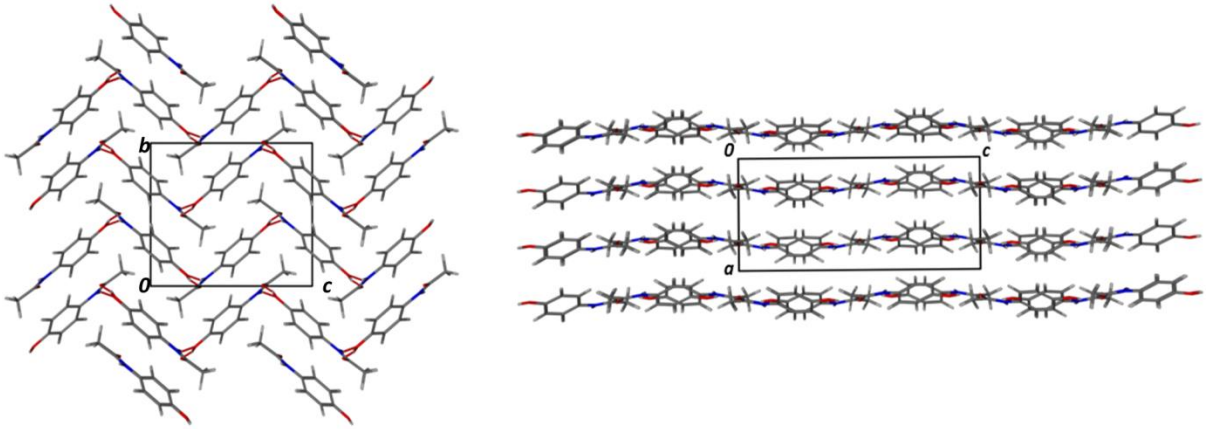

Figure 5.3 – The crystal structures of PCM form I (left) and PCM form II (right), displaying their distinct differences in packing arrangements of the two forms, adapted from Agnew *et al.*[151, 152]

The thermodynamic PCM form I and metastable PCM form II are easily distinguishable by single crystal X-ray diffraction (SCXRD) analysis due to distinct differences in space group and unit cell parameters (Table 5.1). In this study, crystal data including unit cell parameters are monitored to ascertain polymorphic form of single crystals grown and analysed *in situ*.

Table 5.1 – Crystal data including unit cell parameters of PCM form I and form II obtained from the CSD.[24]

Polymorph	**PCM form I**	**PCM form II**
CSD Refcode	HXACAN30	HXACAN31
Lattice type	Monoclinic	Orthorhombic
Space group	*$P2_1/n$*	*Pbca*
a /Å	7.091 (<1)	7.188
b /Å	9.211 (<1)	11.765
c /Å	11.597 (<1)	17.68
α /°	90.00	90.00
β /°	97.84 (<1)	90.00
γ /°	90.00	90.00
Volume /Å^3	750.387	1451.799
Z	4.0	8.0
Z′	1.0	1.0

These two polymorphs have also been shown to exhibit distinct differences in habit, where PCM form I displays octahedral geometry, whilst PCM form II produces needle-like morphology, when crystallised from ethanol.[154]

PCM was selected as the model system to be utilised as a proof of concept for this technique; it has been extensively studied in the solid state[153, 155-157] and the metastable PCM form II can

be selectively accessed in polymorphic purity;[22, 151, 152] the influence of introducing a controlled solid interface in the form of seeds introduced into the crystallisation can thus be understood.

5.2 Data Processing Trials

Data processing trials on previously collected datasets of strongly diffracting small organic molecules captured using a 0.2 second exposure per image were employed as standard test datasets to establish the minimum amount of data that could be used to achieve indexation and to obtain an instrument model used for all datasets. Two previously collected datasets were investigated: one from the small organic molecule cytidine (of size 40 x 30 x 20 μm^3), collected on the PILATUS 300K detector using a wavelength of 0.6889 Å at I19 EH2; the second from PCM (of size 90 x 50 x 20 μm^3), collected on the PILATUS 2M detector using a wavelength of 0.4859 Å at I19 EH2.

This information can then be used to predict how long the single crystal needs to be retained in the X-ray beam for successful indexation, and thus the length of translation needed from the motorised stage. Once this information is established, the experimental set-up can be designed and optimised.

5.2.1 CrysAlisPro Data Processing Trials

The aim of this work was to trial indexing of decreasing wedge sizes by processing existing data with known unit cells, which have previously been collected and solved at I19. These data processing trials investigated 180° (corresponding with a full dataset), 90°, 20°, 10°, 5°, 2°, 1° and 0.4° wedges of data. Each diffraction image corresponds to an angle of 0.2°, so for the 20° wedge, this coincides with 100 images. The wedge of data of the required width was selected during peak finding using CrysAlisPro (Version 40.53), with automated unit cell determination enabled. In cases where the unit cell was not found automatically, the unit cell parameters were input manually during cell indexation. The results of the data processing trials across the various data wedges, including unit cell parameters, total number of reflections and number of indexed reflections for the cytidine and PCM datasets are given in Tables 5.2 and 5.3 respectively.

Wedges of data of width 2° and above were successfully indexed in CrysAlisPro, finding the unit cell automatically without manual input. Wedges of at least 2° per frame collected from a

single crystal within a solution slug were thus assumed to be required for indexation from a single frame to be achieved.

Table 5.2 – Cytidine: the full 124° dataset was collected on a PILATUS 300K diffractometer and processed across a range of wedge sizes using CrysAlisPro.

Parameter	**Wedge of Data**			
	90°	**20°**	**10°**	**5°**
Unit cell finding (Auto)	Yes	Yes	Yes	Yes
a /Å	5.2287(12)	5.236(6)	5.236(10)	5.228(17)
b /Å	14.291(3)	14.388(19)	14.45(2)	14.55(4)
c /Å	15.118(3)	15.14(2)	15.15(2)	15.15(4)
α /°	89.967(16)	89.76(11)	89.56(14)	90.7(2)
β /°	89.972(17)	89.78(10)	89.74(15)	90.2(3)
γ /°	89.943(17)	89.62(10)	89.48(15)	89.7(3)
Volume /Å^3	1129.6(4)	1140(2)	1147(3)	1152(6)
Total number of reflections	338	65	36	16
Reflections indexed	319	61	33	15
% of indexed reflections	94.38	93.85	91.67	93.75

Table 5.3 – PCM: the full 180° dataset was collected on a PILATUS 2M diffractometer and processed across a range of wedge sizes using CrysAlisPro.

Parameter	**Wedge of Data**		
	180°	**90°**	**20°**
Unit cell finding (Auto)	Yes	Yes	Yes
a /Å	7.1039(4)	7.1039(6)	7.1022(17)
b /Å	9.3829(5)	9.3820(7)	9.380(2)
c /Å	11.7100(8)	11.7102(10)	11.708(3)
α /°	89.992(5)	90.020(7)	90.031(19)
β /°	97.402(5)	97.393(7)	97.405(19)
γ /°	90.010(5)	89.990(6)	89.973(19)
Volume /Å^3	774.02(8)	773.98(11)	773.5(3)
Total number of reflections	1600	820	177
Reflections indexed	1303	672	142
% of indexed reflections	81.44	81.95	80.23

Parameter	**Wedge of Data**			
	10°	**5°**	**2°**	**1°**
Unit cell finding (Auto)	Yes	Yes	Yes	Yes
a /Å	7.100(3)	7.103(5)	7.091(9)	7.077(16)
b /Å	9.386(4)	9.388(6)	9.394(12)	9.40(2)
c /Å	11.711(5)	11.714(7)	11.704(14)	11.718(11)
α /°	89.93(4)	90.04(5)	89.90(10)	89.86(13)

β /°	97.39(4)	97.41(5)	97.39(10)	97.27(13)
γ /°	90.00(4)	90.03(5)	90.07(11)	90.15(19)
Volume /Å^3	774.0(6)	774.6(8)	773(2)	773(3)
Total number of reflections	83	36	11	5
Reflections indexed	64	29	10	5
% of indexed reflections	77.11	80.56	90.91	100

5.2.2 Automated Data Processing Trials *via* DIALS

DIALS (Diffraction Integration for Advanced Light Sources) is a software suite for the analysis of crystallographic X-ray diffraction data, developed across synchrotron facilities including Diamond Light Source (DLS) and the Lawrence Berkeley National Laboratory in which the Advanced Light Source (ALS) is situated. The DIALS software encompasses spot finding, indexing, refinement and integration.[158]

DIALS was initially developed to process data from pixel-array detectors. The DIALS project provides an interface to the analysis of standard rotation datasets, as well as still-shot diffraction data of biological macromolecules, such as proteins, collected at synchrotron sources. Whilst DIALS was initially developed for analysis in macromolecular crystallography (MX), it can also be employed in chemical crystallography for the analysis of small organic molecules.[158] DIALS has previously been employed to process protein crystals randomly rotating within a droplet *via* the creep indexing routine. Protein crystals have corresponding large unit cells producing many diffraction peaks on a single image and thus indexing from a single image is facilitated, compared to small organic molecules in which much smaller unit cells produce significantly fewer diffraction spots on a single image.[159] The utilities that DIALS offer may be ideally suited for the processing of data collected from single crystals of small organic molecules randomly rotating within a solution slug in the KRAIC-S. Once a routine for DIALS processing has been established, each step can be automatically triggered after data collection, this can lead to full automation of processing. This improves on CrysAlisPro, which although user friendly can be slow (manual processing procedures can take days for a single collection run); the DIALS routine has the potential to process the same dataset in minutes.

Before the DIALS routine can be optimised, the data processing requirements for the KRAIC-S experiments need to be understood through use of data processing trials on existing data with a known unit cell. A comparable study to the CrysAlisPro work in Section 5.2.1 was carried out using DIALS (Version 2.1) to identify the minimum wedge of data that can be indexed

from a single image. These DIALS data processing trials investigated the same decreasing wedge widths for comparison with the CrysAlisPro data processing trials. In cases where the unit cell was not found automatically, the unit cell parameters were manually input during cell indexation. The results of the data processing trials across the various wedges of data, including unit cell parameters, total number of reflections and number of indexed reflections for the cytidine and PCM datasets are summarised in Table 5.4 and 5.5 respectively.

Table 5.4 – Cytidine: the full 124° dataset was collected on a PILATUS 300K diffractometer and processed across a range of wedge sizes using DIALS. Attempts to index a 1° wedge of data *via* manual input of unit cell parameters failed.

Parameter	**Wedge of data**				
	90°	**20°**	**10°**	**5°**	**2°**
Unit cell finding	Yes	Yes	Yes	Yes	Manual
a /Å	5.11896(6)	5.12581(11)	5.11742(15)	5.09039(15)	5.131(3)
b /Å	13.9854(8)	13.9430(19)	13.880(3)	13.746(3)	13.80(4)
c /Å	14.7781(8)	14.807(2)	14.794(3)	14.699(3)	14.908(19)
α /°	89.975(4)	89.941(12)	89.990(19)	90.31(2)	90.00
β /°	89.997(3)	90.162(6)	90.246(8)	90.253(9)	90.00
γ /°	89.964(3)	90.101(5)	89.803(8)	90.190(8)	90.00
Reflections unindexed	1055	48	28	13	6
Reflections indexed	231	223	110	59	19
% indexed reflections	82.0	82.3	79.7	81.9	76.0

Table 5.5 – PCM: the full 180° dataset was collected on a PILATUS 2M diffractometer and processed across a range of wedge sizes using DIALS.

Parameter	**Wedge of data**				
	180°	**90°**	**20°**	**10°**	**5°**
Unit cell finding	Yes	Yes	Yes	Yes	Yes
a /Å	7.10506(11)	7.1079(5)	7.1147(2)	7.1169(3)	7.1125(4)
b /Å	9.3846(2)	9.3860(6)	9.3969(4)	9.3990(7)	9.3965(8)
c /Å	11.7122(2)	11.7149(6)	11.7273(5)	11.7270(7)	11.7239(10)
α /°	89.9942(15)	90.014(2)	89.936(4)	89.934(6)	89.917(9)
β /°	82.5863(13)	82.598(3)	82.650(4)	82.642(6)	82.660(8)
γ /°	89.9889(14)	89.998(3)	90.046(4)	90.060(5)	90.059(7)
Reflections unindexed	566	286	65	27	13
Reflections indexed	2483	1291	287	138	65
% indexed reflections	81.4	81.9	81.5	83.6	83.3
Parameter	**Wedge of data**				
	2°		**1°**	**0.4°**	**0.2°**
Unit cell finding	Yes		Yes	Manual	Manual
a /Å	7.1245(10)		7.103(2)	7.108(3)	7.077
b /Å	9.402(2)		9.380(7)	9.370(11)	8.894
c /Å	11.743(4)		11.708(6)	11.704(9)	11.534
α /°	89.81(2)		90.0	90.0	90.000
β /°	82.70(2)		97.40(4)	97.42(6)	98.459
γ /°	90.101(17)		90.0	90.0	90.000
Reflections unindexed	5		3	0	0
Reflections indexed	25		12	8	5*
% indexed reflections	83.3		80.0	100.0	100

5.2.3 Automated Data Processing Trials *via* Xia2

Xia2 uses a pre-package of DIALS, whereby the various algorithms for the stages of spot finding, indexation, refinement, integration and scaling are achieved in a single command on behalf of the user.[159] The Xia2 data processing trials investigated the same decreasing wedge widths for comparison with the CrysAlisPro and DIALS data processing trials. In cases where the unit cell was not found automatically, the unit cell parameters were again manually input. Similar results were obtained as for the DIALS runs, with the full results across the various wedges shown in Appendix 5.1. However, Xia2 did not achieve indexation with as small a wedge of data as DIALS.

5.2.4 Data Processing Trials Conclusions

Using CrysAlisPro and DIALS *via* Xia2 processing methods, the smallest wedge of data that can be indexed is between 1-2°, whilst running the algorithms step-wise allowed DIALS to

index a wedge width of as small as 0.2° using manual input of the unit cell parameters to reduce the number of variables compared to reflections. The processing of multiple 2° datasets was attempted using DIALS, but this required further optimisation (see Section 5.5.2.2). The data produced from a randomly tumbling single crystal within a solution slug can benefit from the DIALS method of creep-indexing, following the orientation matrix in time as the crystal tumbles. The software can also be automated to process thousands of wedges and calculate the best set of wedges to merge for structure solution.

These initial data processing trials used diffraction data obtained on the PILATUS 300K and PILATUS 2M detectors. Whilst commissioning runs employed the PILATUS 300K detector, the beamtime experiments employed the PILATUS 2M detector for data collection. The larger PILATUS 2M detector results in more photons detected per image, thus allowing a wedge of data less than those accessed using the PILATUS 300K detector, resulting in finer slicing whilst also achieving indexation from a single image as a result of this larger detector.

5.3 KRAIC-S Design and Overview

The development of the KRAIC-S was carried out in collaboration with Dr. Mark Warren at the Diamond Light Source. As discussed above in Section 5.1.1, the set-up needs to facilitate translation to artificially "hold / suspend" the tumbling crystal in the X-ray beam. The data requirements of this *in situ* XRD technique dictated the design requirements. To minimise weight and bulk within the analysis area, as well as weight restrictions of the motorised stage, a single coil of tubing positioned away from the X-ray beam was employed, in which the crystallisation tubing can be pulled through the set-up to probe difference time-periods in the crystallisation process.

Although X-ray transparent Kapton® windows at various analytical points as featured in the KRAIC-D in Chapter 4 would be desirable to minimise background, a single extruded length of FEP (3.18 mm ID, 11 m length) was utilised for initial testing of the KRAIC-S. Although not optimal, a background subtraction can be performed to remove scattering resulting from the FEP before data processing. A practical advantage of using a single extruded length for the KRAIC-S allows for the FEP tubing to be threaded to monitor different lengths along the length of the KRAIC-S crystalliser; these different lengths scales equate to different crystallisation times in the crystallisation process. The removal of PTFE unions between FEP

and Kapton® windows should reduce the frequency of blockages compared to the KRAIC-D. Background subtraction from the diffraction data should also be more straightforward.

5.3.1 Experimental Set-up

As for the KRAIC-D, segmentation is achieved on the premise of immiscibility in the KRAIC-S. Separate streams of crystallising solution, air and carrier fluid are all transferred under temperature-controlling jacketed tubing to ensure a constant, well-defined temperature start point before the flows combine at a glass cross-piece (X-piece, 3 mm ID) (Figure 5.4). A circulator bath is used to control the temperature of the tubing jackets and transfer tubes. The X-piece sits in a temperature-controlled segmentation water bath comprising a custom glass water bath *via* a hot-plate with magnetic bottom stirring. The temperature is actively regulated until segmentation is achieved to prevent crystallisation occurring before segmentation; once the flow is segmented, heated temperature control is removed to allow the cooling crystallisation to proceed *via* air cooling of the solution within the crystalliser tubing. In contrast to the KRAIC-D, use of a temperature-controlled tubing segment as a nucleation promoter will be avoided in the experimental set-up of the KRAIC-S. Such a nucleation promoter could encourage the formation of multiple nucleation sites, which is not desirable when a single crystal is desired to crystallise per solution slug.

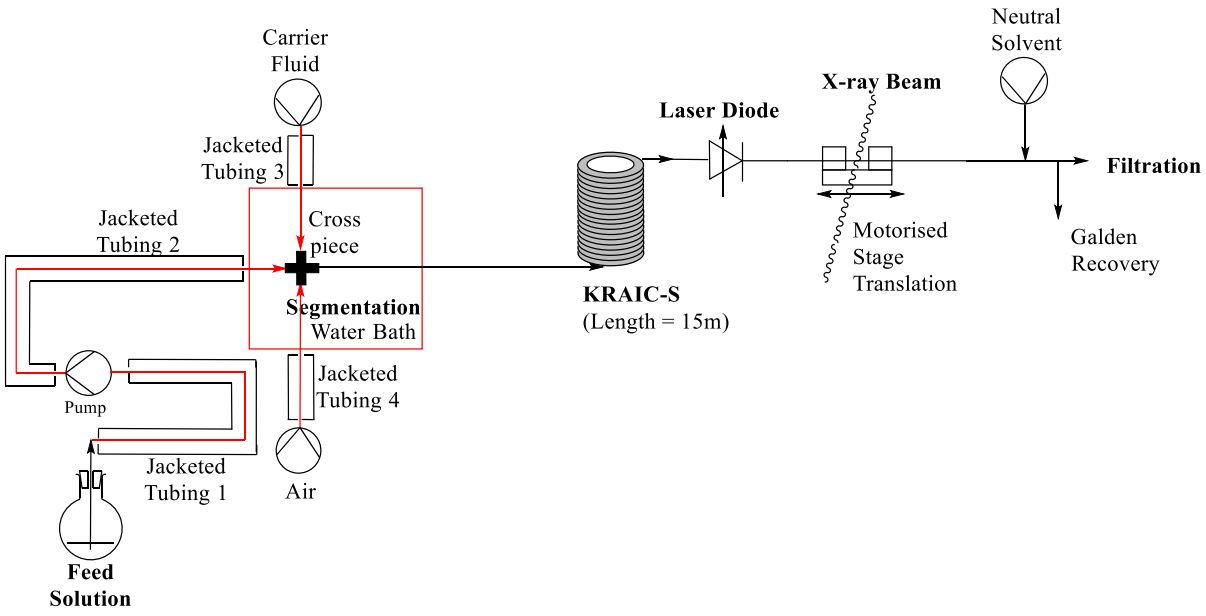

Figure 5.4 – Schematic of KRAIC-S unseeded experiments, featuring the original laser diode slug triggering set-up employed in the commissioning time experiments.

A peristaltic pump (Vapourtec SF-10) was employed for the crystallising solution and the air, whilst the carrier fluid was transferred using a gear pump (Ismatec ISM895E). For seeding crystallisation runs, an additional syringe pump (Syrris Asia) was utilised to introduce the single crystal seeds into the crystallisation at the pre-nucleation stage.

5.3.2 Seeding Coil Optimisation

To seek to ensure regularity in observing single crystals in solution slugs, an optimised seeding approach was employed to controllably introduce single crystals into the KRAIC-S crystalliser. In addition, introducing single crystal seeds of the metastable PCM form II, offers the potential to yield a different polymorphic outcome to the unseeded cooling crystallisation of PCM in 60:40 v/v water:isopropanol (HI). The challenge in introducing single crystals into the KRAIC-S is achieving regularity in seed dosing into every solution slug, coupled with the challenge in moving single crystals in a homogeneous stream through a suitable pump, through the seeding coil to the point at which segmentation is achieved.

The use of an orange dye pre-loaded into the sample loop facilitated visual observation of the seeding addition into the KRAIC-S. A water:isopropanol solvent mixture (60:40 HI), (~330 mg / 500 mL) of Eosin Y was prepared and continually stirred during the experiments through bottom stirring using a magnetic stirrer. The Eosin Y solution was pre-loaded into the FEP coil and added to the solution flow through a needle using a single syringe pump. The seed and solution streams combine with the air and carrier fluid to yield the tri-segmented flow with a net flow rate of 6.2 mL/min, comprising air (2.5 mL/min), carrier fluid (1 mL/min) and solution (2.7 mL/min). For the seed addition, flow rates of 50, 80 and 100 μL/min were trialled and it was found that 100 μL/min resulted in the most consistent addition of dye into each slug, confirmed by visual observation.

Initial seeding coil trials investigated the use of 1 mm ID FEP tubing resulting in a 2 mL volume with a single syringe pump. The delivery of the PCM form II suspended in 60:40 HI was successful using the single syringe pump, however the 2 mL volume only coincides with a 20 minute residence time, which is too short a time period for crystallisation runs. The delivery system of the PCM form II seeds needed optimisation, as the PCM form II seeds had the tendency to dissolve in the tubing. Instead of suspending the PCM form II seeds in solvent, delivering the seeds in carrier fluid ensures that the seeds will not dissolve and the seeds can

be introduced at room temperature. Carrier fluid was employed for the dispersant to prevent dissolution of the PCM form II seeds.

As part of the optimisation, the FEP tubing was replaced with a 1.5 mm ID, 12 mL volume tubing and seeds in carrier fluid were loaded into the FEP coil using a syringe. The seeds were then introduced from the sample loop into the KRAIC-S, at a rate of 100 μL/min, but did not progress along the tubing at all, as the larger bore size of the sample coil tubing did not provide sufficient back pressure to move the seeds along the tubing. This approach led to an uneven distribution of the PCM form II seeds and sedimentation within the FEP sample loop and thus an alternative approach was required.

To mitigate this issue with delivery, segmentation of the seeds in the 25 ft, 0.79 mm ID seeding coil was required. Segmentation of the seed delivery will reduce the consistency of the addition but will stop blocking issues and help with the overall seed delivery to the KRAIC-S system. Instead, PCM form II seed loading was carried out by segmenting the carrier fluid PCM form II suspension to prevent sedimentation. The air segmentation was achieved by removal / immersion / removal of the sample loop inlet in and out of the conical flask containing the PCM form II suspension carried out by hand. A pump was attached to the seed sample loop outlet to draw the segmented flow through the coil, to completely fill the loop before a seeding crystallisation run. The use of air segmentation to load the PCM form II into the FEP sample loop showed an improvement compared to the original method, which used a syringe to load the coil. However, a blockage occurred in the tubing despite segmenting the flow with air. The segmented flow required increased movement without a large increase to the net flow rate. Oscillation was thus introduced, rectifying this problem by providing additional movement to prevent the PCM form II crystals adhering to the tubing, but not altering the net flow, which would negatively impact the dosing of the seeds into the solution slugs (Figure 5.5).

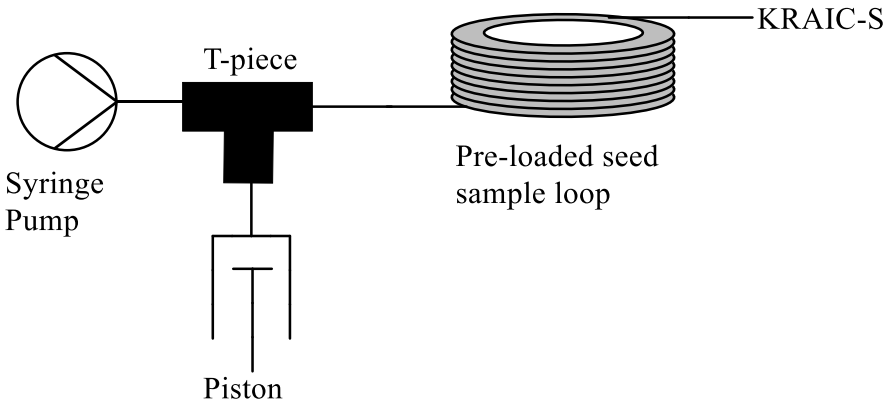

Figure 5.5 – Schematic of PCM form II seed addition *via* a carrier fluid suspension, in which the net flow is controlled by a syringe pump, whilst a piston provides an oscillation to the system.

A piston was employed to superimpose oscillation to the net flow *via* a T-piece. The net flow rate of 100 μL/min provided by the syringe pump, together with oscillation from the piston of ± 2 cm of 0.79 mm ID tubing maintains the overall flow rate from the seeding coil of 100 μL/min contributing to the net segmented flow of the KRAIC-S (Figure 5.6). The volume of the seeding coil is 3.38 mL, this coupled with the overall flow rate of 0.1 mL/min, equates to a suitable seeding run time of 34 minutes.

Once the PCM form II seeds were pre-loaded into the FEP sample loop before a crystallisation run, the outlet of the seed coil was passed through the segmentation water bath and introduced into the connector set-up in the segmentation water bath. Concerns with dissolution of the seeds at the raised temperature of the water bath were removed through the use of the inert carrier fluid, which will maintain the same solid loading at both room temperature and the raised temperature of the water bath.

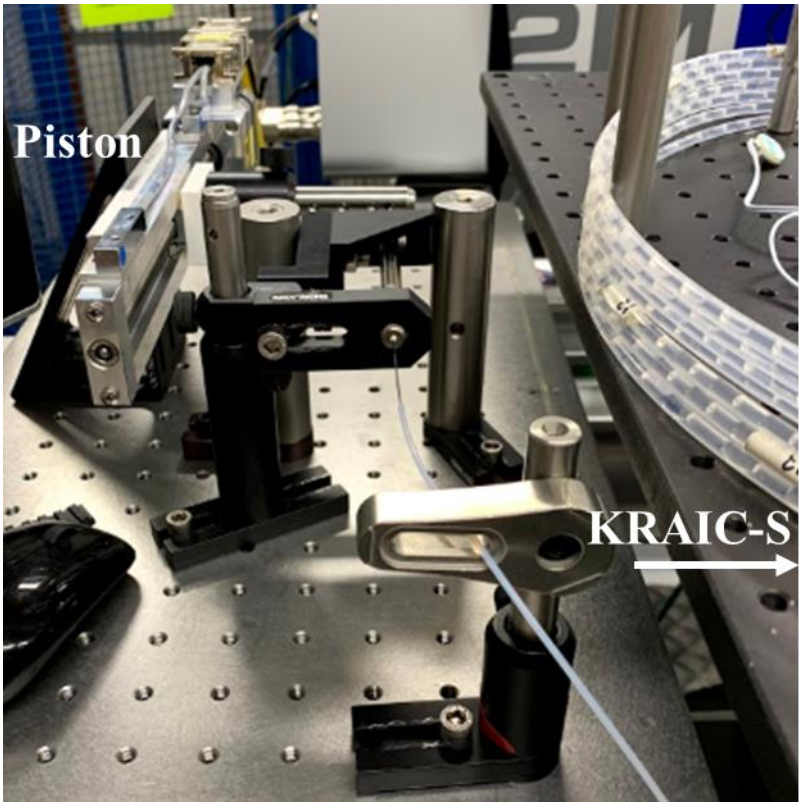

Figure 5.6 – Piston attached to a motorised stage to provide oscillation, with a needle connected to the coil tubing.

The connector set-up in the segmentation water bath comprised two polypropylene (PP) T-pieces (both 2 mm ID) arranged in series, with a needle (0.08 mm ID) through the centre of the first T-piece. The needle facilitated the addition of the PCM form II seeds to the solution, together with the carrier fluid. The net flow after the first T-piece was then further segmented using air *via* a second T-piece. The optimised seeding addition into the KRAIC-S is represented in the schematic in Figure 5.7 and installed at EH2 I19 in Figure 5.8.

5.3.3 Cooling Crystallisations

All continuous crystallisation runs are initially cleaned and primed with segmented flow comprising carrier fluid, air and the pure solvent mixture used in the crystallising solution. During priming the conditions such as flow rates and temperature are matched to those adopted in the crystallising run to ensure the system is allowed to perform at steady-state operation. All transfer tubing jackets and the segmentation bath were usually set to the same temperature as the feed solution. The system usually requires at least one residence time (the time taken for the media to travel from the point of segmentation to the end-piece) to reach steady-state

conditions. During priming, the feed solution (PCM in 60:40 HI) is prepared and allowed to reach dissolution at the set temperature for approximately an hour.

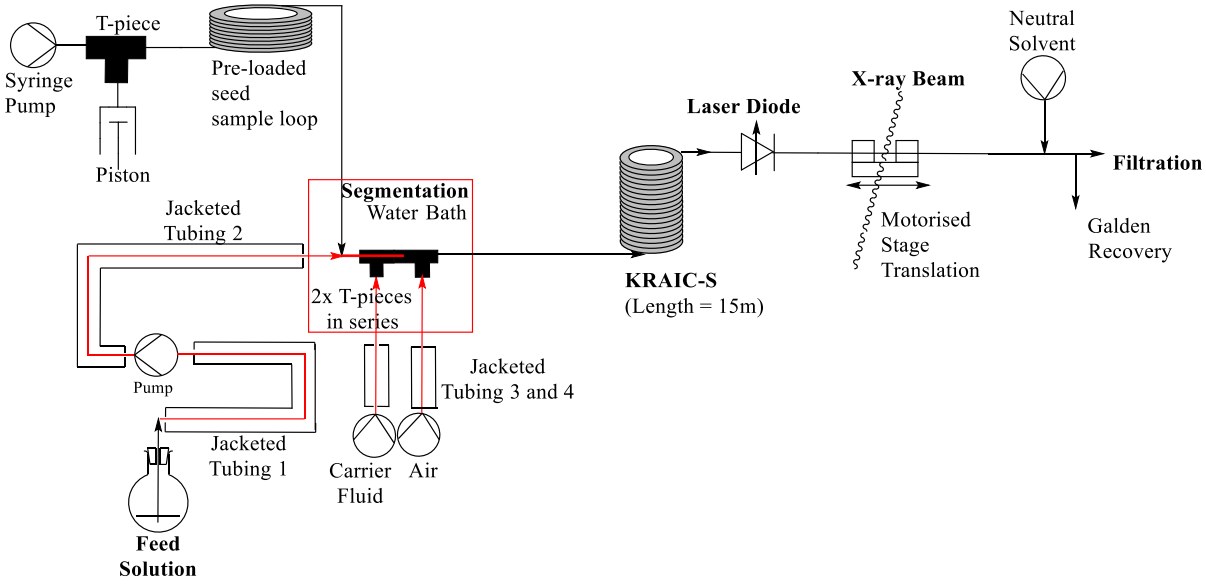

Figure 5.7 – Schematic of seeded KRAIC-S experiments (PCMKSS).

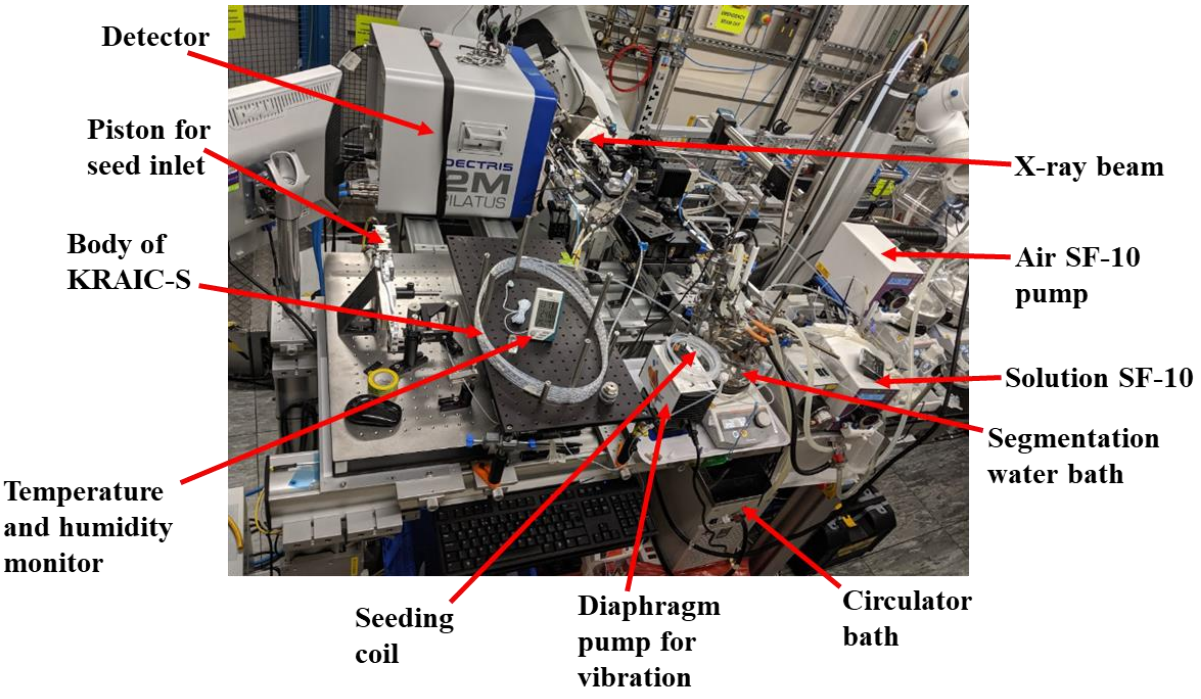

Figure 5.8 – Photograph of KRAIC-S installed in experimental hutch 2 (EH2) of beamline I19 at Diamond Light Source during the beamtime.

5.4 Slug Triggering

KRAIC-D experiments detailed in Chapter 4 on beamline I11 used a continuous collect strategy followed by advanced data processing to carry out background subtraction to remove any patterns without diffraction. The continuous collect strategy cannot be employed for analysis of single crystals grown *in situ* in the KRAIC-S as single images will not contain sufficient diffraction data for indexation and analysis. Triggering when a solution slug is passing the X-ray beam is therefore required to initiate translation of the motorised stage accurately in order to artificially suspended a single crystal in a solution slug in the X-ray beam during data acquisition.

Slug triggering testing was initially carried out offline in the KRAIC-D platform, looking at the effect upon a laser-photodiode pair when solution, air or carrier fluid passes through the laser beam, which changes the transmission and can be monitored on an oscilloscope read-out. A laser is focussed at a section of the FEP tubing containing the segmented media, which is flowing through the KRAIC-D platform (Figure 5.9). A photodiode reader (Canberra) is coupled to an oscilloscope (Tektronix) to measure the laser intensity (Beta CW 670 nm wavelength and 1 mW) through the tubing as segmented flow passes the laser beam.

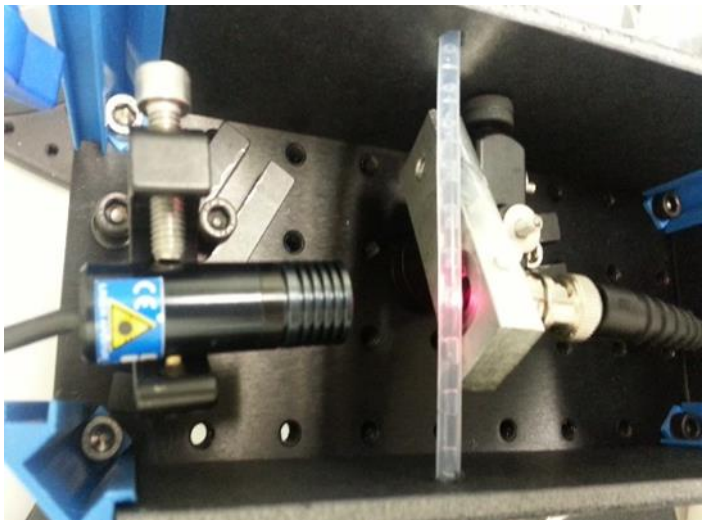

Figure 5.9 – The use of a laser on the segmented flow to provide an optical trigger.

The resulting pattern on the oscilloscope can be used to identify the different media (air, carrier fluid, solution) involved in the segmentation at a given point. The solution used in this investigation is water; tests on other solvent systems and crystallising solutions will need to be carried out, but water is appropriate for these initial investigations as good segmentation is

established due to the surface tension of water. This will then be used to design a triggering mechanism to control the translation stage to effectively suspend a solution slug containing a single crystal in the X-ray beam to collect a sufficient wedge of reciprocal space to achieve cell indexation from a single diffraction frame (Figure 5.10).

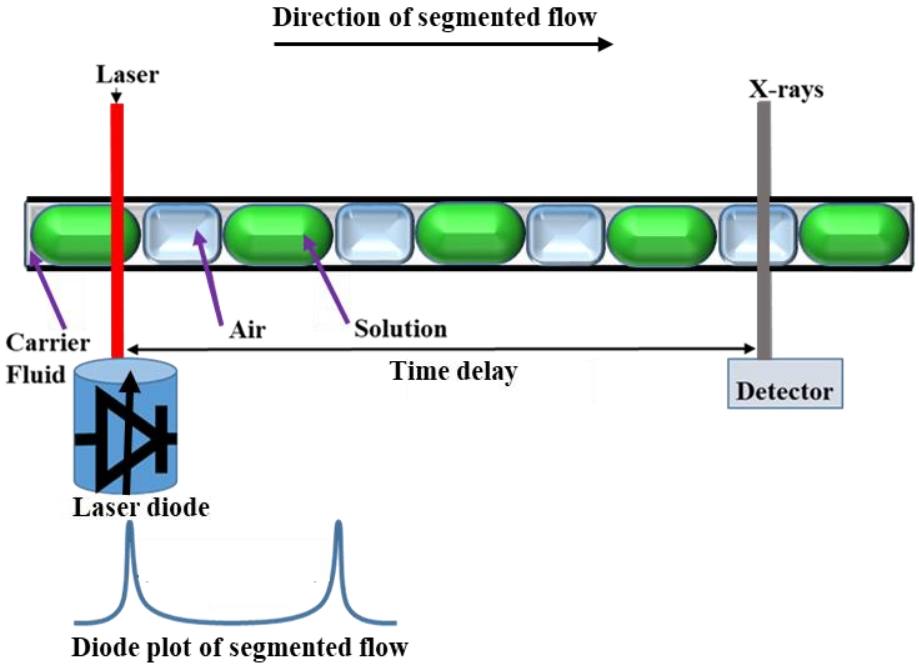

Figure 5.10 – Principles of the slug triggering testing.

The purpose of this work was to determine what media contributed to each of the features in the resulting oscilloscope pattern. To establish an understanding of these features a number of slug to air ratios were employed. To change this ratio, variation in the flow rates of each of the constituents in the segmented flow (air, carrier fluid and solution) were investigated. The detailed investigation is presented in Appendix 5.2.

The flow rate of the segmented flow is an accumulative effect of all pump rates. Combining the three separate flows using a X-piece connector, the speed of the motor would have to be 14 mm/s under a typical set of flow conditions (2.1 mL/min each for air and carrier fluid, and 1.6 mL/min for the solution). The tumbling / rotation speed of a single crystal within a solution slug is unknown. Assuming a single crystal rotates at 2° / second and a 2° wedge of data was required for indexation of a single frame, the time the crystal is required to be within the X-ray beam in order to obtain sufficient data to index a crystal would be one second, thus for the conditions described above, a motorised stage with the capability to travel a distance of 14 mm at a speed of 14 mm/s would be required.

This work established the basis for these signals to be used as an optical trigger for signalling when the X-ray beam should be on / off during data collection on I19.

The benefit of exploring the fastest and slowest flow rates in this work means that the entire range of translation distances established should be sufficient for any investigation of crystallisation processes when installing the KRAIC-S on I19. When optimising the flow rates during offline developmental work, it is important to consider the relationship between tumbling rate and flow rate, where it is probable that the faster the flow rate the greater the tumbling rate, which causes great variance in lattice orientation between adjacent diffraction frames. This could negatively impact indexation of adjacent diffraction frames, where reindexation of the unit cell obtained from the previous frame will be carried out during data processing.

5.4.1 *In vitro* Data Processing Optimisation

The purpose of the offline EH2 run at I19 was to use the findings from the data processing trials and slug triggering testing (Section 5.2 and 5.4 respectively), applied to the experimental set-up installed on the beamline (Figure 5.11). The requirements of the motor were also assessed, to establish whether the motorised stage initially employed had the capability to reach the required speeds and sufficient displacement calculated in the slug triggering testing. The calculated motor requirements were initially utilised, which can be altered by eye to ensure that the slug is artificially suspended in the camera under the initial flow rates employed. This is a useful approach for monitoring and 'following' a single slug, before X-ray experiments.

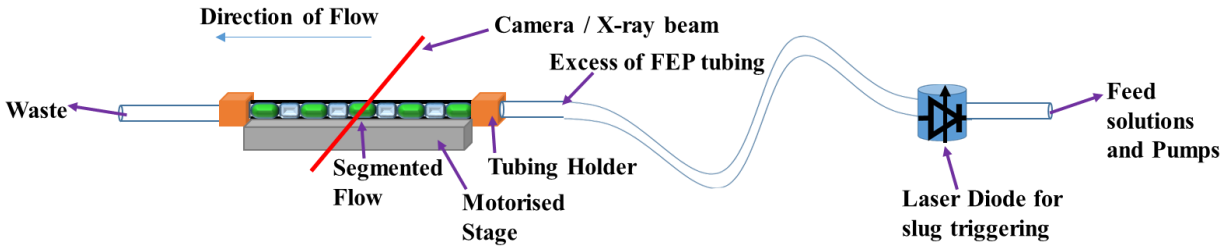

Figure 5.11 – Schematic of the initial translation / triggering set-up trialled for installation at EH2 I19.

The flow rates of each of the three separate streams employed to establish the tri-segmentation were controlled by separate pumps; the solution was controlled by an SF-10 peristaltic pump, while gear pumps were utilised for the carrier fluid and air streams. The solution employed

during the initial offline EH2 run was water, once optimisation was complete without solids; a crystallising solution of PCM in 60:40 HI was introduced.

The photodiode / laser assembly is placed upstream of the position where the FEP tubing crosses the X-ray beam. As the segmented flow passes the photodiode / laser assembly, the solution / air interface can be detected in advance, so that when that particular slug reaches the X-ray path the motorised stage (Figure 5.12) can be triggered.

In the initial slug triggering mechanism design employed in the commissioning time (PCMKSC), the photodiode / laser assembly is in a static position, separated from the motorised stage by an excess of FEP tubing, ensuring that the FEP pipeline does not become too taught as the motor moves after the optical trigger has been instigated.

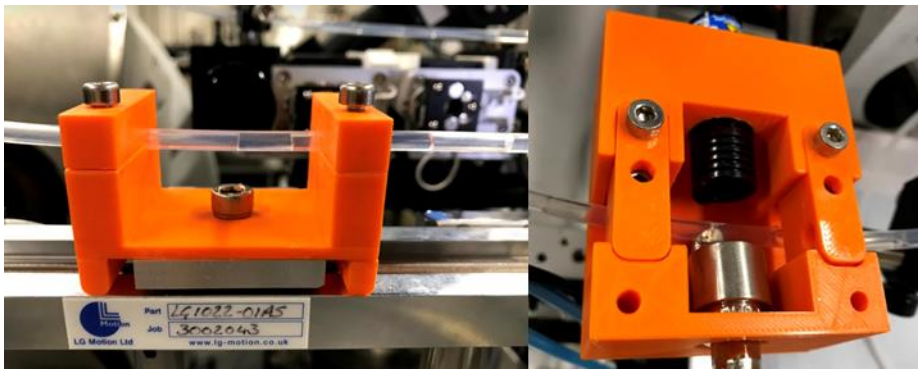

Figure 5.12 – FEP tube holder and motorised stage (left) and photodiode / laser box (right).

EPICS (Experimental Physics and Industrial Control System) was employed to continuously record the diode signals and was coupled with a Python script that plots the diode read-outs and monitors the diode plots by detecting when the signal goes above a specified threshold value. The larger the negative magnitude of the diode intensity, the higher the diode signal. This can then be used to trigger the motorised stage after a specified time-delay. Sampling of the signals is important, to allow the leading-edge trigger to be well defined allowing for an accurate optical read-out (Figure 5.13). It is also important that the sampling of signals is sufficiently rapid to minimise the associated uncertainty in the position of each slug. An increased sampling frequency would decrease this uncertainty and improve the accuracy of the optical triggering. Monitoring these diode plots during data acquisition allows for the regularity of the segmentation to be monitored; irregularities or changes to the diode read-out give an indication of a drop-off in slug triggering efficiency and any changes to the experimental

conditions, which cannot be visually monitored in the experimental hutch during data collection.

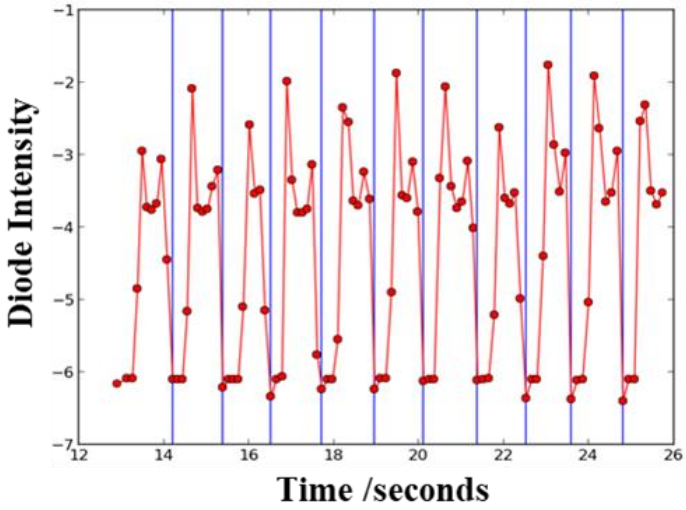

Figure 5.13 – Diode read-out produced from Python script, red data points correspond with the diode reading and the blue line corresponds with the leading edge detection.

Optimisation of flow rates to match motorised stage limitations

Both the individual flow rates of the three components, which contribute to the net flow and the size of the slugs, coupled with the speed and translation distance of the motorised stage, together need to ensure that a solution slug is artificially 'suspended' in the X-ray beam to collect sufficient data for indexing. A series of experiments were run to investigate this; the various parameters including the flow rates of the three media employed in the segmented flow, together with the slug separation and verdict of the trial are summarised in Table 5.6, with images of the resulting slugs in the Appendix 5.2.

Table 5.6 – Flow parameters and segmentation separation for the three trial combinations employed in the *in vitro* data processing optimisations.

Parameter		**Trial 1**	**Trial 2**	**Trial 3**
Flow rate /mL/min	**Air**	4.18	4.18	2.1
	Carrier Fluid	2.1	2.1	2.1
	Solution (water)	3.2	1.6	1.6
	Net	9.48	7.88	5.8
Distance between adjacent slugs /cm		3.2	4.2	2.6
Time separation between adjacent slugs /s		1.5	2	2
Motorised stage speed /mm/s		21	21	13
Verdict		Too fast	Too fast	Suitable

With a translation distance of 38 mm and a translation speed of 10 mm/s under the optimal flow conditions from these tests: air pump (2.1 mL/min), carrier fluid pump (2.1 mL/min) and solution pump, water (1.6 mL/min), the solution slug remains in the X-ray beam for nearly 4 seconds. This is sufficient for 38 images to be obtained, enough frames for unit cell determination. It would be possible to achieve a 4° to 8° wedge of data from this, depending on the speed of crystal tumbling. This is sufficient given that the data processing trials on CrysAlisPro and DIALS indicated a 2° and 0.2° wedge of data respectively would be required when the unit cell parameters are known.

5.5 Data Capture and Analysis Procedure

5.5.1 Data Capture

The X-ray beam is triggered to operate continuously during translation of the motorised stage, which is signalled from the slug triggering mechanism; depending on the net flow rate of the segmented flow, the translation may occur over 4 seconds during data acquisition of 40 images, which equates to a 0.1 second exposure per image. Single crystal diffraction data were collected in a serial crystallography-like approach, where each scan comprised data from a range of runs, where each run comprised a range of frames. Each run captured diffraction data on a single crystal within a single solution slug and data from a range of frames within a single run were analysed. Five datasets corresponding to five different single crystals were analysed for each set of experimental conditions to ensure statistical relevance. The various experimental conditions under investigation include two different analytical residence time (RT) positions (8.7 m and 6.7 m crystalliser lengths) for the unseeded cooling crystallisation of PCM in 60:40 HI, as well as PCM form II seeding experiments. For each of the five datasets analysed for each experiment, the diffraction frames were indexed and if this was achieved, refined to establish the extent of crystal rotation. Comparison of lattice rotations and intensity values for the unseeded crystallisation process at the two analytical RT points builds a statistical average of single crystal growth at a set point along the length of the crystalliser and allows crystal size to be compared with lattice rotations. As for other *in situ* experiments described, with the system operating at steady-state, different set points can be related to the different stages in the crystallisation process, imparting knowledge on the crystallisation pathway adopted with time.

Initial diffraction data obtained in the commissioning time (PCMKSC) were collected on a Dectris 300K PILATUS detector, whilst for subsequent beamtime experiments (PCMKSB) a

larger detector known as Dectris 2M PILATUS (Figure 5.14) was employed. This change to the large detectors facilitated the sampling of a larger part of reciprocal space, resulting in more reflections, which made indexation easier from a single image.

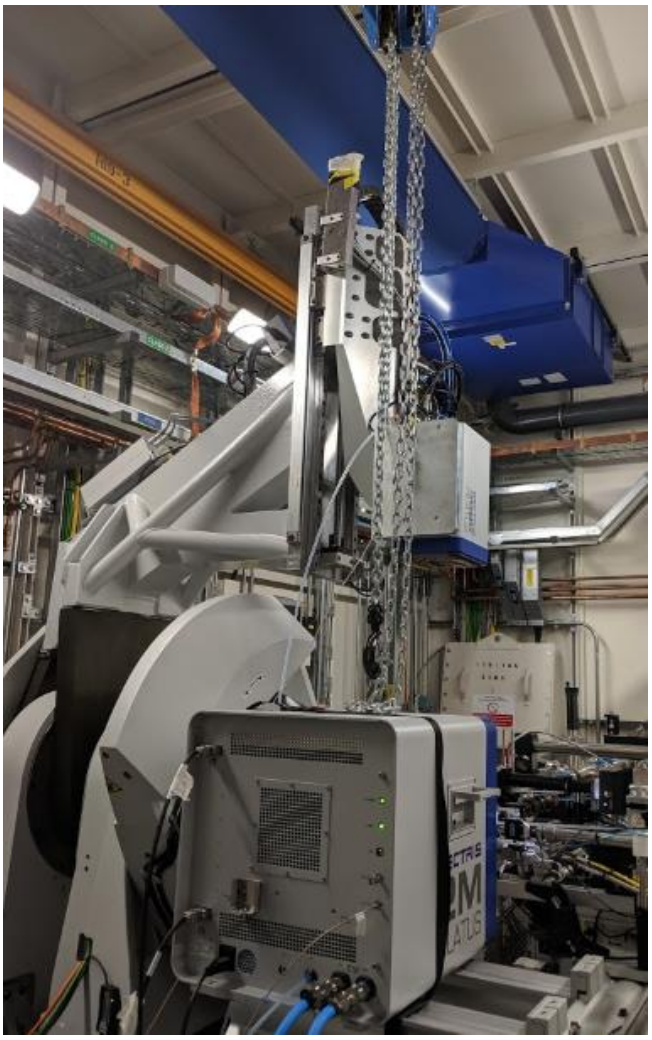

Figure 5.14 – Dectris 2M PILATUS detector employed for beamtime experiments (PCMKSB).

5.5.2 Data Analysis Procedure

5.5.2.1 CrysAlisPro

The data analysis procedure using CrysAlisPro (Version 40.53) was created and optimised. The PILATUS images and instrument model were imported into CrysAlisPro. A frame within the diffraction data was selected as a starting frame for initial unit cell finding, on the premise the frame contained sufficient diffraction but not too many spots as this could indicate the presence of a 'twinned' / multi-crystal. Peak hunting was carried out for this starting frame where diffraction spots were added manually before cell indexation. Provided the unit cell was

accessed automatically, cell refinement was carried out, whereby all lattice parameters were refined but only for the starting frame. For the monoclinic PCM form I, the unit cell angles were constrained with $\alpha = \gamma = 90°$, and for the orthorhombic PCM form II, all unit cell angles were constrained to 90°. For all subsequent frames, cell indexation was reindexed from the previous image and refinement was only carried out on lattice rotations relative to the instrument (R1, R2 and R3). For frames where cell indexation was not achieved initially or from the previous frame, the unit cell parameters of the polymorphic form could be input manually.

For each diffraction frame a range of information including the 2D diffraction image (Figure 5.15), unit cell parameters and lattice rotations after refinement (Table 5.7), a peak table for each diffraction frame and distribution histograms with respect to the reciprocal lattice (*a**, *b** and *c**-axes) (Figure 5.16) was collected. This information is useful for comparison with subsequent frames and subsequent runs, as well as between different types of experiment.

5.5.2.2 DIALS

The determination of the crystal orientation matrix from a single image requires tens of reflections, not always available from small unit cell materials. Improvements to the number of reflections per image can be achieved by employing a large pixel array detector. Thus, as noted above, for the beamtime experiments, a larger PILATUS 2M detector with dimensions 384 x 424 x 455 mm^3 was employed to increase the number of diffraction spots per frame. The detector was installed especially for the beamtime experiments; the precise detector position was thus determined and included post data collection, prior to any data processing.

The first attempt at processing the data using DIALS was to mimic the processing carried out previously in CrysAlisPro, whereby the same starting frames were selected. These starting frames in the various datasets were selected in CrysAlisPro data processing on the premise the image contains the most diffraction spots, whilst ensuring the diffraction coincides with a single crystal. The starting frame image is used for the initial indexing, then the rotation matrix of the next image is refined from this initial indexing.

After header correction was applied to the raw images, the header corrected images were imported into DIALS and the background associated with each diffraction frame was removed in preparation for the spot finding procedure. This was to mitigate issues associated with the

threshold selected for the spot finding and was successful in giving reliable spot location (Figure 5.17), which was particularly important to ensure sufficient diffraction data was found from a single image in order to achieve indexation.

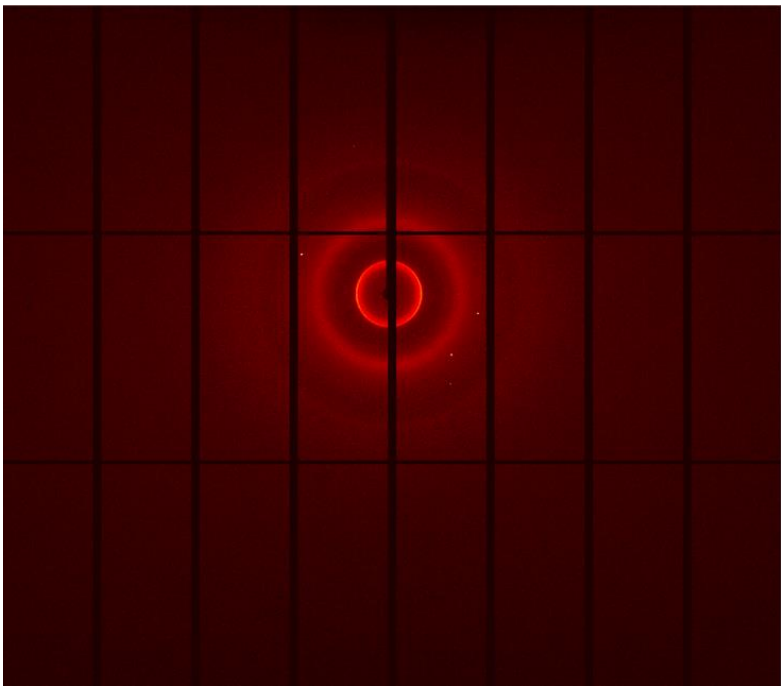

Figure 5.15 – 2D diffraction image from a PCM form II seeded crystallisation run.

Table 5.7 – Unit cell parameters (*a*, *b*, *c*, *α*, *β*, *γ*) and lattice rotations R1, R2, R3 after refinement from a PCM form II seeded crystallisation run.

Unit cell parameters	a /Å	11.6815
	b /Å	7.3393
	c /Å	16.9153
	α /°	90
	β /°	90
	γ /°	90
Lattice rotations	R1 /°	23.523
	R2 /°	-77.111
	R3 /°	-3.081

In comparison to the peak tables corresponding to the same diffraction frames in CrysAlisPro, which achieved cell indexation, the DIALS indexing routine was not able to index the single image to extract the orientation. In order to increase the number of diffraction peaks to achieve cell indexation, neighbouring diffraction images were merged, resulting in a larger wedge of data and thus an increasing sampling of reciprocal space per dataset. The benefit with fine

slicing is that the minimal amount of diffraction data per frame can be used to achieve cell indexation, whereby if a diffraction frame does not contain sufficient diffraction for indexation, a larger slice can be achieved by merging the fine slices together. The limiting factor is the smallest increment of a wedge of data sampled from reciprocal space.

For indexing, the unit cell parameters are fixed; reducing the number of parameters, and the detector distance is also constrained during cell indexation. The successfully indexed reflections are input into the refinement process.

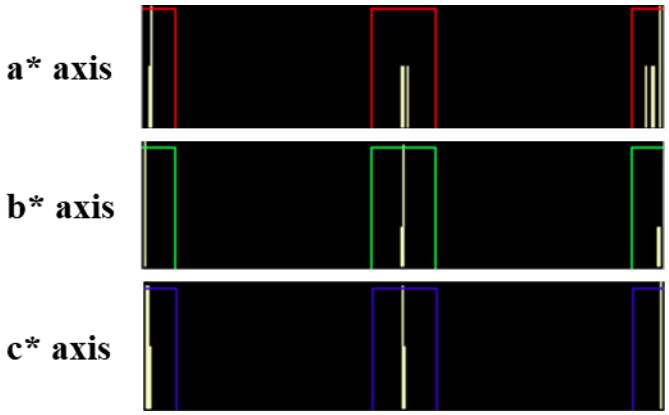

Figure 5.16 – Distribution histograms with respect to the reciprocal lattice: *a**-axis, *b**-axis and *c**-axis from a PCM form II seeded crystallisation run.

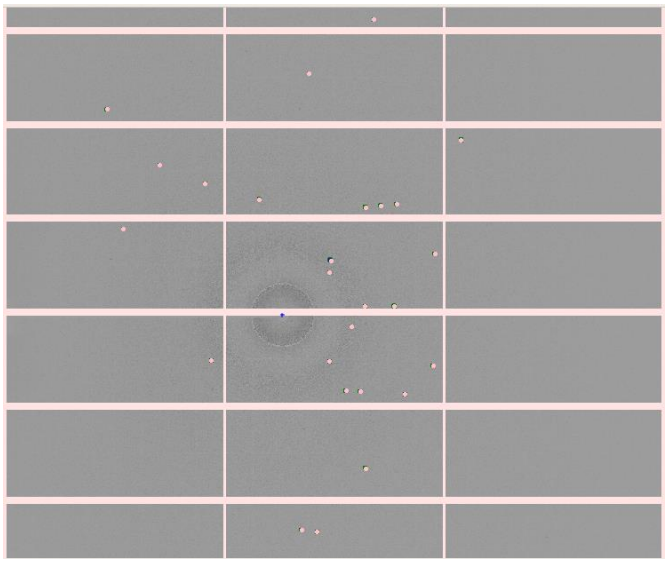

Figure 5.17 – Single diffraction frame after DIALS spot finding (background subtracted), with spots highlighted in pink.

With the increased number of peaks resulting from the merging of neighbouring images, it was possible to achieve indexation and obtain the orientation matrix from a single diffraction image. All the steps above were compiled into a Python script, facilitating complete automation of the DIALS processing procedure, which only takes a couple of minutes to complete.

This initial DIALS method provided a proof of concept for the novel *in situ* single crystal X-ray diffraction technique, however in contrast to CrysAlisPro, it was not possible to employ the starting frame to yield the first orientation matrix to then refine neighbouring images, as only single images were imported. The DIALS processing procedure was thus updated to import all of the data and only subtract a band of scattering from the FEP tubing as opposed to an entire background from the diffraction images. Background subtraction was also carried out around the beamstop and in this updated method, the spot finding, indexing, refinement and integration on the individual image occurs on the entirety of the datasets. A local indexing assignment method can be used on data that may not follow a conventional sweep about a given scan axis and is applied across all diffraction images in a dataset. After local indexing assignment, refinement, integration and scaling was carried out using DIALS. The integration stage was carried out using standard methods, generating p4p, hkl and ins files.

5.6 Growth Studies

Data from single crystals of known crystallite size measured on an optical microscope were collected *via* traditional single crystal data collection strategies at I19, using a 0.2 second exposure per image and subsequently processed using standard data processing procedures in CrysAlisPro (Version 40.53). Diffraction spots determined from a single crystal within a solution slug can be integrated and their intensities compared with the equivalent *hkl* reflections within the standard single crystal datasets. For a given *hkl* set of reflections, the intensity values corresponding with the single crystals of known crystal volume can be directly correlated, allowing estimation of the crystal size of the single crystals grown *in situ* in the KRAIC-S.

The concept of sufficient sampling must be considered; the intensity magnitudes of the complete rocking curve represented by a normal distribution function are sampled (Figure 5.18), as opposed to just the maximum average intensity value. The sampling is dependent on the fine slicing selected for data capture, illustrated by the red dotted lines in Figure 5.18, which causes the same *hkl* diffraction spot to reside on adjacent diffraction images and data from these spots in adjacent diffraction frames are accumulated to produce the total diffraction intensity.

For the single crystal slug datasets, the maximum average intensity coinciding with the centre of the *hkl* set was only accumulated with the intensity value of an adjacent frame ±1 either side of the maximum average intensity of the starting frame to mitigate the variabilities in intensity resulting from crystal rotation within the solution slug.

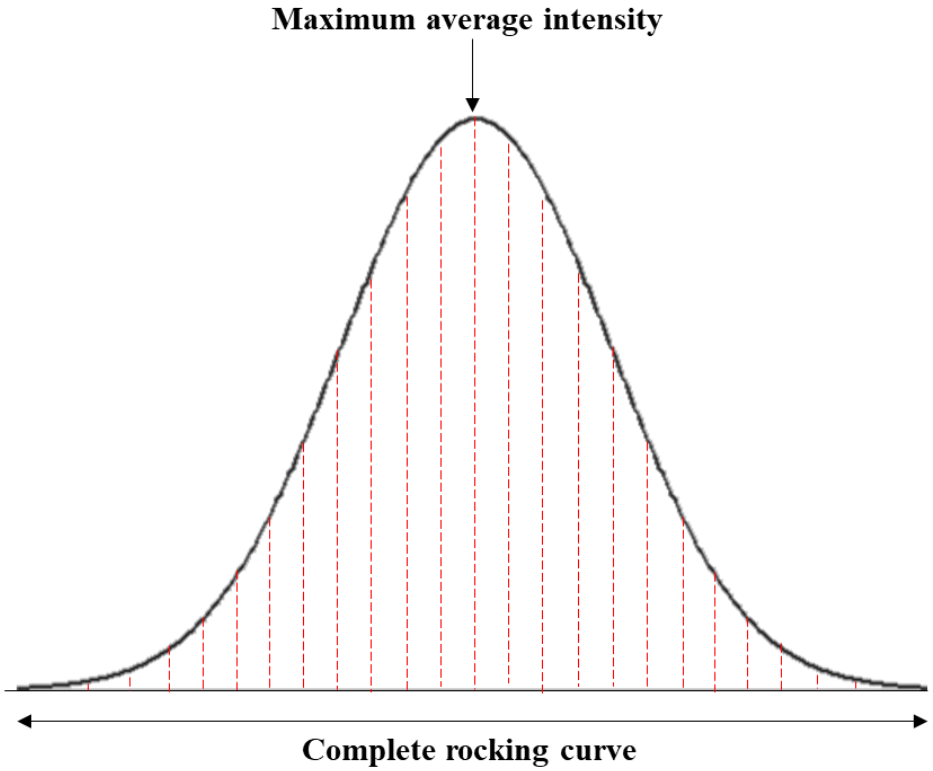

Figure 5.18 – Complete rocking curve represented by a normal distribution function.

5.7 Polymorphic Monitoring of Paracetamol (PCM)

5.7.1 Offline KRAIC Experiments: PCM in 60:40 H_2O:IPA (HI) (PCMK)

To develop the flow crystallisation process of PCM in 60:40 (v/v) H_2O:IPA (HI) to crystallise no more than one single crystal per solution slug, developmental work optimised offline was carried out in the KRAIC and KRAIC-S platforms. The KRAIC and KRAIC-S are operationally identical; unlike the KRAIC-D, these two platforms have a single extruded length of 15 m and 11 m of FEP tubing respectively. The only exception to this is that the KRAIC comprises three coils, one housed in a glass cylinder, whilst the other two coils are housed in aluminium cylinders, whilst the KRAIC-S is not housed and is instead wrapped around aluminium posts screwed into an aluminium breadboard base (ThorLabs). The difference in housing of the main FEP coil (s) may result in some differences in the residence time of

crystallisation through the length of the KRAIC and KRAIC-S crystallisers. It can be expected that crystallisation will occur at an earlier residence time in the KRAIC-S compared to the KRAIC as a result of increased air cooling. The crystallisation process required optimisation to ensure that crystallisation occurred by the residence time of the tubing holder positioned directly in front of the X-ray beam at I19 EH2, 6.7 m and 8.7 m for earlier stage and later stage crystallisation, respectively. The crystalliser length at the tubing holder / X-ray beam position was altered *via* threading of the FEP tubing. The standard crystalliser length at this analytical point was 8.7 m, which was used for all PCM form II seeded crystallisation experiments.

Initial concentrations of PCM in 60:40 HI and corresponding temperature conditions were based upon the solubility curve of PCM in 60:40 HI.[22, 152] The concentration used for the unseeded PCM in 60:40 HI KRAIC (PCMK) and KRAIC-S (PCMKS) runs, as well as seeded KRAIC-S runs (PCMKSS) was based on the solubility curve ($y = 68.596e^{0.0334x}$) at 29 °C (feed temperature). Referring to the solubility curve in Figure 5.19, this equates to a concentration of 182 g/kg (200 g/L with the density of 60:40 HI at 0.914 g/mL) PCM in 60:40 HI.

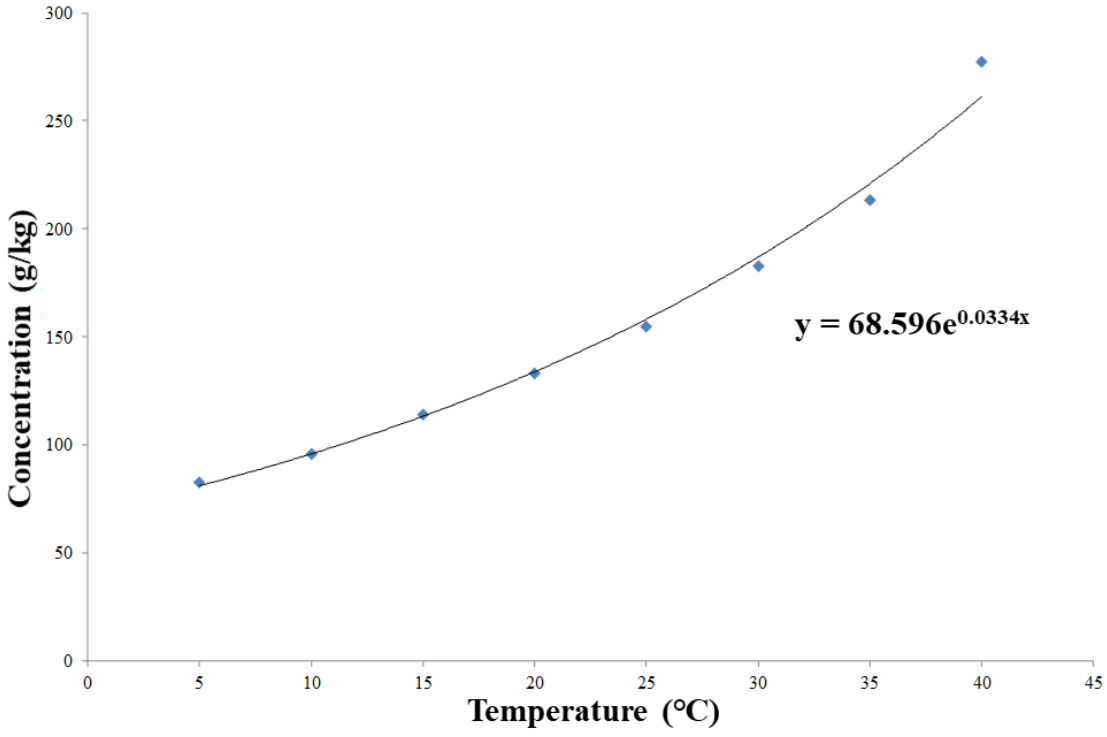

Figure 5.19 – Solubility curve of PCM form I in 60:40 (v/v) H_2O:IPA (HI) using data from Agnew[22, 152], fitted with an exponential trend curve.

The PCM in 60:40 HI cooling crystallisations in the KRAIC and KRAIC-S are categorised into offline experiments, identified as PCMK and PCMKS in the KRAIC and KRAIC-S platforms respectively. The online experiments are categorised into commissioning and beamtime experiments, denoted PCMKSC and PCMKSB, both carried out in the KRAIC-S, which is designed to be compatible with the size and data collection requirements of EH2 at I19.

The experimental set-ups for the various KRAIC offline crystallisation runs are presented in Figures 5.20 and 5.21, with the difference between the KRAIC set-ups being the presence and absence of a nucleation promoter after the segmentation water bath. The concentration of the PCM feed, the temperature control, flow rates and experimental residence times for the various experiments are outlined in Table 5.8, 5.9, 5.10 and 5.11 respectively. The measured cooling profiles for the unseeded PCM in 60:40 HI KRAIC cooling crystallisation experiments PCMK2-4 are shown in Figure 5.22.

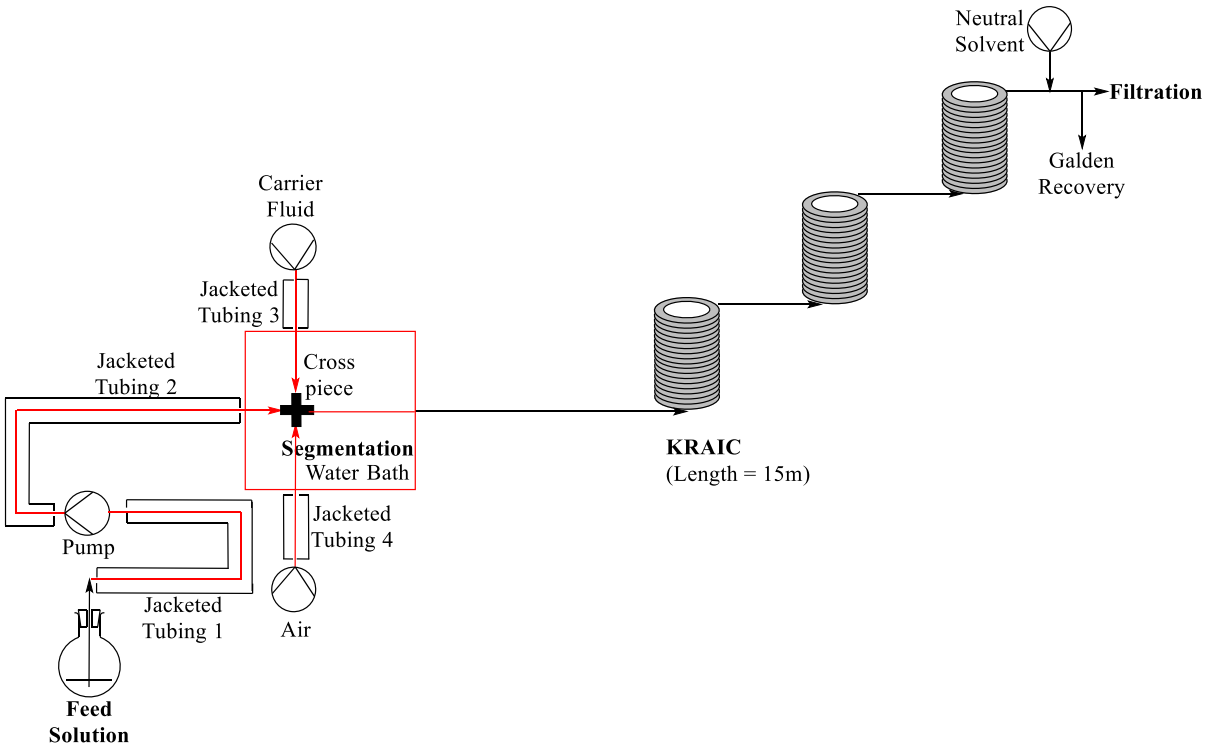

Figure 5.20 – Schematic of the experimental set-up for the unseeded PCM in 60:40 HI run, without a nucleation promoter in the KRAIC (PCMK1).

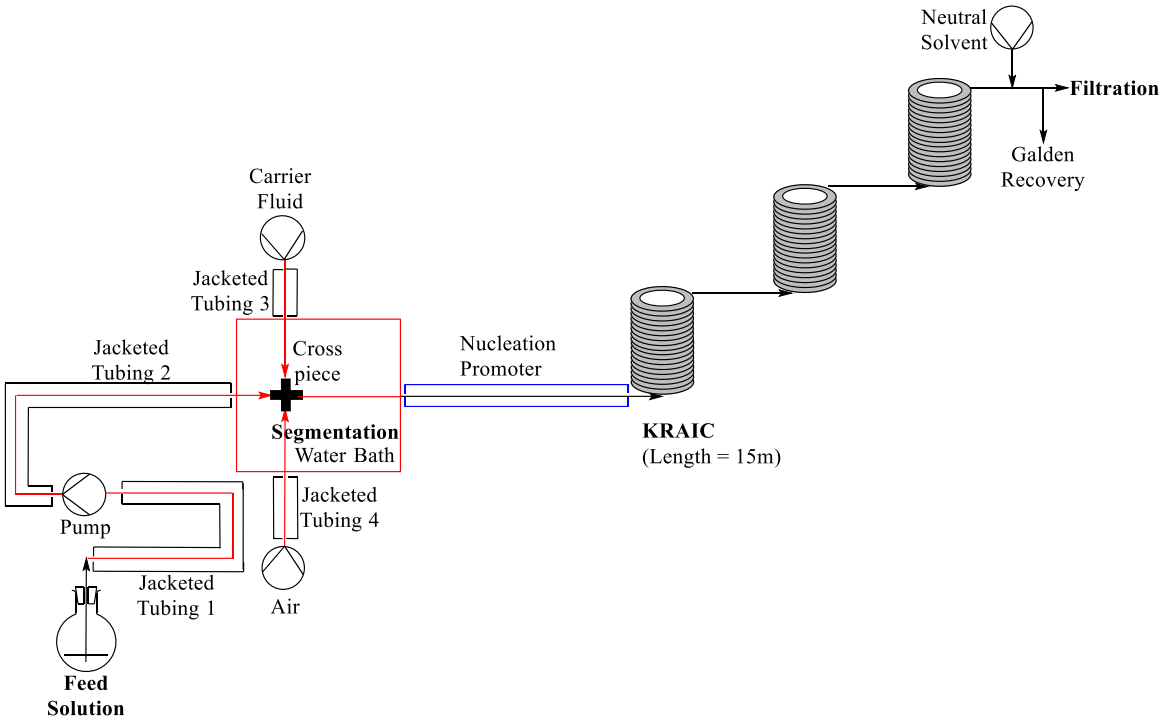

Figure 5.21 – Schematic of the experimental set-up for the unseeded PCM in 60:40 HI runs, with a nucleation promoter in the KRAIC (PCMK2-4).

Table 5.8 – Experimental parameters including feed concentration, seed loading and experimental set-up for PCM offline experiments in the KRAIC platform (PCMK).

Experiment	**Feed Solution (g/L 60:40 HI)**	**Experimental Set-up**
PCMK1	200	Unseeded, no nucleation promoter, Fig. 5.20
PCMK2	200	Unseeded, with nucleation promoter, Fig. 5.21
PCMK3	200	Unseeded, with nucleation promoter, Fig. 5.21
PCMK4	225	Unseeded, with nucleation promoter, Fig. 5.21

Table 5.9 – Set temperatures in the KRAIC platform *For PCMK1, the temperature of the water bath was reduced to 30 ℃ at 40 minutes into the run and subsequently the heating of the water bath was switched off and ice added to the bath (final temp 12.1 ℃) in attempt to promote nucleation. †For PCMK2 the temperature of the nucleation promoter was reduced to 5 ℃ at 1 hour 20 minutes into the crystallisation run. ‡For PCMK4, the nucleation promotor was turned on (from RT) to 10 ℃. #For PCMK4, 78 minutes into run the temperature of the tubing jackets was raised to 60 ℃.

Experiment	Set Temperature (℃)				Temperature of laboratory /℃
	Nucleation Promoter	Feed	Jacketed Tubing	Segmentation water bath	
PCMK1	N/A	45	45	40 (30)*	23.2
PCMK2	10 (5)†	50	45	40	22.9
PCMK3	5	50	45	40	21.5
PCMK4	RT (10)‡	50	50 (60)#	40	24.0

Table 5.10 – Flow rates (mL/min) used for all KRAIC runs. *For PCMK1, the flow rate of the solution was reduced to 1.4 mL/min to allow more time for crystallisation to proceed. Later on in PCMK1 the flow rate of the carrier fluid was reduced to 2.1 mL/min. #For PCMK2, the flow rate of the carrier fluid and feed were reduced to 2.1 mL/min and 1.5 mL/min respectively at 42 minutes, the flow rate of the feed was further reduced to 1 mL/min at 1 hour 12 minutes. ‡For PCMK4, 78 minutes into run the flow rate of the solution pump was increased to 3.6 mL/min.

Experiment	Flow rate / mL/min			
	Carrier fluid	Air	Neutral Solvent	Solution
PCMK1	4.18 (2.1)*	4.18	12.5	2.8 (1.4)*
PCMK2	4.18 (2.1)#	4.18	12.5	2.8 (1.5, 1)#
PCMK3	2.1	4.18	12.5	1.5
PCMK4	2.1	4.18	12.5	1.5 (3.6)‡

Table 5.11 – Experimental residence times for various set points along the length of the KRAIC for PCM offline experiments (PCMK) *For PCMK1, total residence time before solution flow rate reduction is shown, all other residence times quoted in PCMK1 refer to the reduced 1.4 mL/min flow rate for the solution. For PCMK2-4, residence times are measured before any alterations to the flow rates are carried out.

Experiment	Nucleation Promoter J5 (mins:secs)	Coil 1 (mins:secs)	Coil 2 (mins:secs)	Coil 3 (mins:secs)	Total Residence Time after segmentation (mins:secs)
PCMK1	N/A	~6	12:24	18:28	19:05
					13:45*
PCMK2	1:00	5:38	9:50	14:10	14:35
PCMK3	1:45	9:12	15:35	22:18	22:56
PCMK4	1:33	9:01	15:27	22:11	22:42

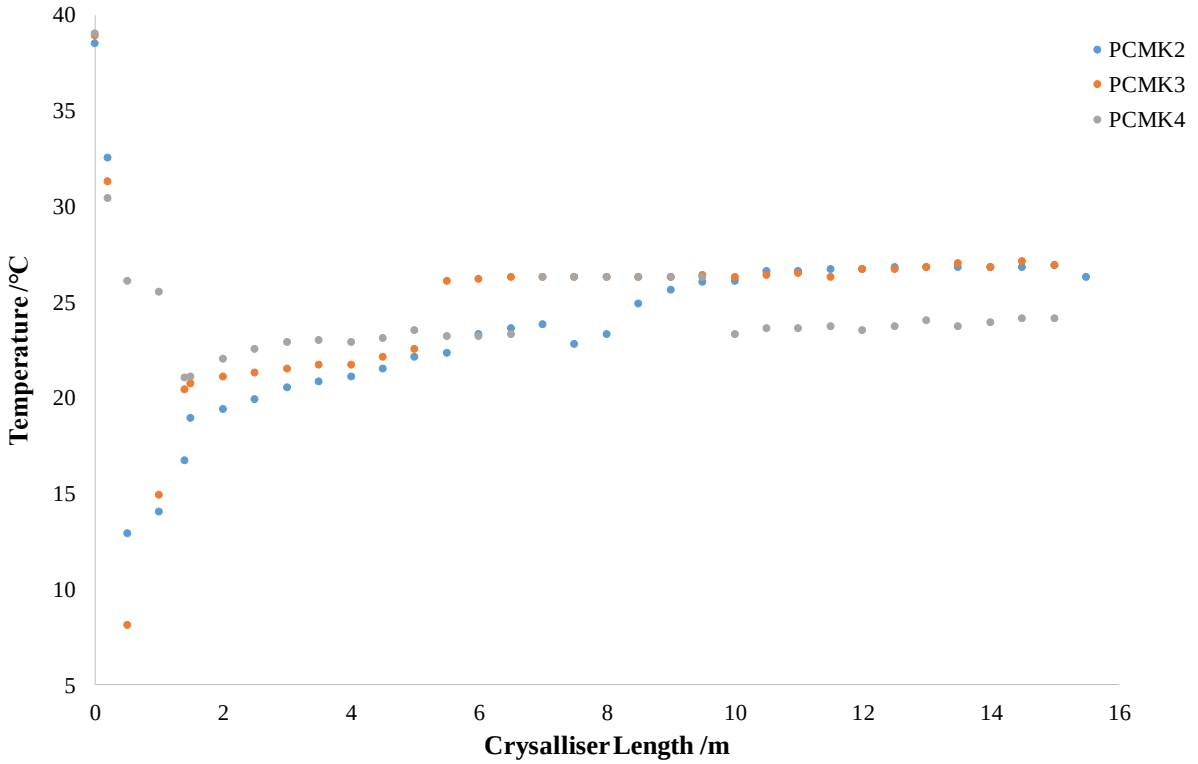

Figure 5.22 – Measured cooing profiles of temperature *versus* crystalliser length in the KRAIC for experiments PCMK2, PCMK3 and PCMK4.

PCMK1

After 40 minutes into the crystallisation run, no crystallisation was observed so the temperature of the water bath was reduced to 30 ℃ in an attempt to promote nucleation. The flow rate of the solution pump was also reduced to 1.4 mL/min at 1 hour 13 minutes to increase the residence time within the KRAIC to 16 minutes, allowing more time for crystallisation to proceed. The flow rate of the carrier fluid was also reduced to 2.1 mL/min at 1 hour 31 minutes to increase the residence time further to 19 minutes.

At 1 hour 37 minutes crystals were observed in the feed line and SF-10 solution pump. The lines were then switched to pure solvent and the system was cleaned / primed for 20 minutes before restarting the crystallisation run.

No crystallisation was observed after 30 minutes into the re-started run so the heating supplied to the water bath was switched off and ice added to the segmentation water bath to promote nucleation. The final temperature of the water bath was 12.1 ℃. At 52 minutes into the crystallisation run the feed was switched to cleaning / priming as crystallisation was observed in the solution pump, which led to a blockage in the solution pump.

The learnings obtained from PCMK1 was that a nucleation promoter maintained at sub-ambient temperatures was required to promote nucleation and subsequent crystallisation. The feed solution concentration could equally be increased for the same result, however the tendency of the solution pump to block suggests this would not be the most appropriate alteration in conditions. As a result of the blockage observed in the solution pump, the solution flow rate needs to be maintained at a high flow rate to avoid crystallisation in the line. The temperature of the jacketed tubing could also be increased to avoid crystallisation in the lines before segmentation is achieved.

PCMK2

The PCM solution re-used from PCMK1 did not dissolve at 45 ℃, so the temperature was raised to 50 ℃ to aid dissolution; this increase in dissolution temperature can be attributed to evaporation of the solvent. The flow rates of the carrier fluid and feed solution were reduced to 2.1 mL/min and 1.5 mL/min, respectively, at 42 minutes to increase the residence time. At 1 hour 12 minutes into the crystallisation run the flow rate of the solution feed was further reduced to 1 mL/min. Very sporadic nucleation and growth, equating to a single crystal in one single solution slug, was noted after 10 minutes of observations. The temperature of the

nucleation promoter was thus reduced to 5 ℃ at 1 hour 20 minutes to increase the extent of nucleation. Filtration to obtain yield from the crystallisation proved challenging as recovery of the carrier fluid was poor, which led to the formation of a filter cake resulting in filter clogging. The filter cake resulted from micro-crystals invisible to the naked eye in the slugs.

At 1 hour 24 minutes into the crystallisation run, encrustation was observed in the feed lines and the flow rate of the feed solution was returned to 1.5 mL/min. The feed was also switched to priming to avoid a blockage in the lines. The observation of single crystals after 1 hour 24 minutes could be attributed to the introduction of the nucleation promoter or could result from the previous blockage in the feed line.

PCMK3

The PCM solution was re-used from PCMK2. During the crystallisation run, no obvious crystallisation occurred in solution slugs, even with the nucleation promoter set to 5 ℃. Crystallisation was observed very sporadically in the solution slugs, with the earliest observation of crystallisation seen at coil 3 rung 3 (11.5 m). The crystals sometimes appear single in nature, highlighting the potential of PCM in 60:40 HI as a suitable system for growing single crystals *in situ* in the segmented flow crystalliser. Solid recovery was facilitated by vacuum filtration over a collection period of 23 minutes, with a corresponding mass of solid of 0.114 g, equating to a yield of 10.66 % for a measured outlet temperature of 27 ℃. The feed was switched to cleaning / priming at 1 hour 5 minutes into the crystallisation run.

PCMK4

The concentration of the PCM solution was increased to 225 g/L to increase the extent of crystallisation. Single crystals were observed exiting the KRAIC in irregular slugs; the first observable point of crystallisation occurred at coil 3 rung 4, 12 m along the length of the KRAIC. Solid was recovered from the outlet, where the crystallising solution exiting the KRAIC had a corresponding temperature of 24 ℃ obtained from readings measured using an internal temperature probe. During PCMK4, the first collection (FP1) was collected over 26.5 minutes with an associated mass of solid of 0.2311 g, equating to a yield of 8.07 %. The second collection (FP2) was collected over 11.25 minutes, giving a mass of 0.1741 g equating to a yield of 14.33 %. FP2, commencing 75 minutes into the crystallisation run, was not collected over an entire residence time due to the formation of a filter cake resulting from poor recovery of the carrier fluid. The filtration samples recovered from the KRAIC were viewed under a

microscope, providing confirmation that single crystals are formed under these conditions during the cooling crystallisation of PCM in 60:40 HI in PCMK4 (Figure 5.23).

It was noted that the single crystals did not appear to tumble sufficiently in solution slugs. Most of the crystals position themselves and grow at the back of a solution slug. This is a potential issue for data collection at I19, which uses 'crystal creeping' for indexing the crystal, based upon at least a 2° rotation angle. Conversely, substantial rotation is also undesirable, as between adjacent frames the orientation will alter so much that indexation may fail. A small 2° rotation angle may not be observable with the naked eye, so the minimal rotation of single crystals observed in the KRAIC runs offline may be sufficient for data processing requirements. The degree of rotation allowance was ascertained during the I19 commissioning time.

At a crystallisation run time of 78 minutes, encrustation was observed in the feed line. The flow rate of the feed solution pump was increased to 3.6 mL/min and the temperature of the tubing jackets increased to 60 ℃. The pump had to be stopped and cleared as the blockage was too severe. The SF-10 pump was changed and the feed line switched to priming solvent to clear the line at a flow rate of 5 mL/min.

The KRAIC crystallisation experiment PCMK4 showed that the flow rate adopted for the feed solution SF-10 pump was too low, which caused sedimentation and in turn encrustation in the pump and feed lines. As a result, the temperature of the feed requires increasing to avoid blockages observed before segmentation. Even though single crystals were clearly present in some of the solution slugs, their presence remained irregular and thus the concentration of the feed of PCM in 60:40 HI requires increasing.

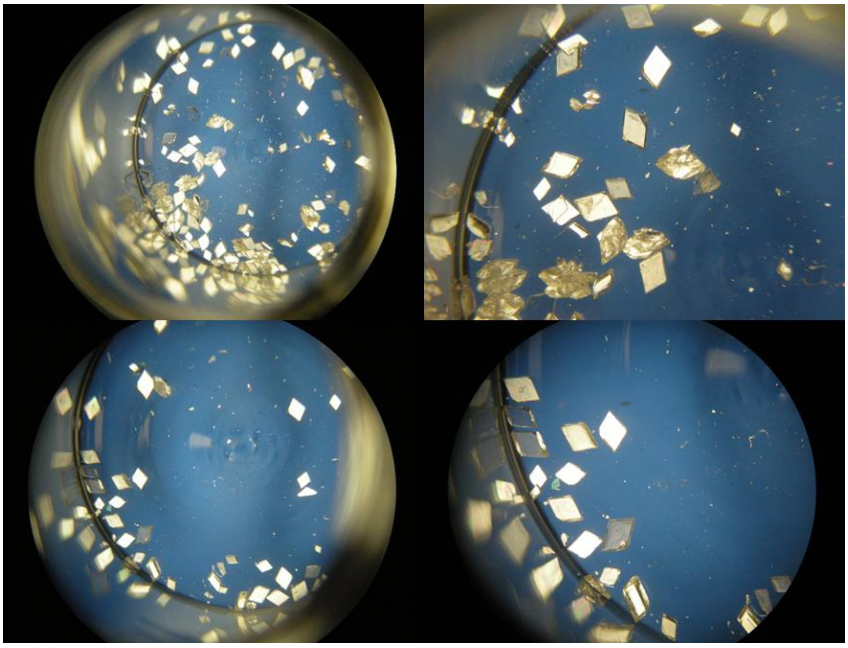

Figure 5.23 – Microscope images of FP1 (top) and FP2 (bottom) from PCMK4 vacuum filtration collections, with varying levels of magnification, lower (left) and higher (right) for each PCM collection sample.

Conclusions from offline PCMK experiments conducted at the University of Bath

The PCM single crystals have the tendency to position themselves at the back of solution slugs, knowledge of this is paramount in ensuring high precision from the slug triggering mechanism, as it is important that the position of where to suspend the slug in the beam is well understood, accurate and reproducible.

The flow rate and the temperature of the feed may be too low, which could be causing the recurring issues with blockages in the SF-10 solution pump and transfer tubes leading to the segmentation water bath. To mitigate these recurring issues, an increase in the flow rate of the solution pump, as well as raising the temperature control of the feed and transfer tubes was required.

The temperature of the laboratory varied by a few degrees between experiments PCMK1-4 (Table 5.9), which can result in marked differences in crystallisation outcome. The metastable zone width (MSZW) of PCM in 60:40 HI in the KRAIC is not known as a result of the uncontrolled cooling within the segmented flow platform.

Experiment PCMK4 at the increased concentration of 225 g/L PCM in 60:40 HI, may result in more single crystals in solution slugs with the introduction of cooling in the tubing jackets of the nucleation promoter.

Furthermore, the concentration of PCM in 60:40 HI may need to be raised further (250 g/kg PCM in 60:40 HI was employed by a previous group member to crystallise powder in solution slugs).[152] This may also require adjusting the temperature of the feed solution and the flow rate of the SF-10 solution pump.

5.7.2 Online KRAIC-S Runs at Beamline I19: PCM in 60:40 HI (PCMKSC and PCMKSB)

5.7.2.1 Commissioning Time at I19 EH2 (PCMKSC)

Offline KRAIC (PCMK) experiments presented in Section 5.7.1 yielded single crystals in solution slugs *via* visual observation, which highlights both the potential of PCM in 60:40 HI for *in situ* SCXRD monitoring and gives a suitable start point for online KRAIC-S experiments. The online KRAIC-S experiments at I19 are categorised into commissioning time and beamtime with unique identifiers PCMKSC and PCMKSB respectively.

During the commissioning time (PCMKSC) experiments, the unseeded cooling crystallisation of PCM in 60:40 HI was investigated. The experimental set-up, along with feed concentration and X-piece geometry for each of these PCMKSC commissioning time experiments are summarised in Table 5.12. The temperature conditions, flow rates and residence times for the PCMKSC experiments are summarised in Table 5.13, 5.14 and 5.15 respectively.

Table 5.12 – Experimental parameters including feed concentration and experimental set-up for the KRAIC-S platform used for the various experimental runs in the Commissioning time at EH2 I19 (PCMKSC).

Experiment	PCM Feed Solution (g/L 60:40 HI)	Experimental Set-up	Glass X-piece
PCMKSC1	225	Unseeded KRAIC-S, with nucleation promoter, Fig. 5.4	Uneven bore size 3 mm ID for feed inlet, 2 mm ID for air and carrier fluid inlets, with the net segmented flow at 3 mm ID
PCMKSC2	225	Unseeded KRAIC-S, with nucleation promoter, Fig. 5.4	Uneven bore size
PCMKSC3	225	Unseeded KRAIC-S, with nucleation promoter, Fig. 5.4	Uneven bore size
PCMKSC4	225	Unseeded KRAIC-S, with nucleation promoter, Fig. 5.4	Even bore size (3 mm ID for all inlets / outlet)
PCMKSC5	250	Unseeded KRAIC-S, with nucleation promoter, Fig. 5.4	Even bore size

Table 5.13 – Set temperatures in the KRAIC-S platform used for the various experimental runs in the Commissioning time at EH2 I19 (PCMKSC). *RT – room temperature.

Experiment	Set Temperature (°C)			
	Nucleation Promoter	Feed	Jacketed Tubing	Segmentation water bath
PCMKSC1	RT* (air filled)	50	50	40
PCMKSC2	RT (air filled)	55	55	40
PCMKSC3	RT (air filled)	55	55	40
PCMKSC4	RT (air filled)	50	55	40
PCMKSC5	RT (air filled)	50	55	40

Table 5.14 – Flow rates (mL/min) used for the various experimental runs in the Commissioning time at EH2 I19 (PCMKSC). *For PCMKSC3, the flow rates of the solution and air were altered to 2.1 mL/min and 2.5 mL/min respectively at 50 minutes into the crystallisation run.

Experiment	Flow rate /mL/min			
	Carrier fluid	Air	Neutral Solvent	Solution
PCMKSC1	2.1	4.18	12.5	1.5
PCMKSC2	4.18	4.18	12.5	1.5
PCMKSC3	2.1	1.5 (2.5)*	12.5	3.1 (2.1)*

PCMKSC4	2.1	3.1	12.5	1.5
PCMKSC5	2.1	3.1	12.5	1.5

Table 5.15 – Experimental residence times for various analytical set points along the length of the KRAIC-S in the various experimental runs in the Commissioning time at EH2 I19 (PCMKSC) N.B There are no residence times recorded for PCMKSC5, but they would be expected to be similar to PCMKSC4, which utilises the same flow rates. *A blockage in the solution feed was observed at this crystallisation time; as a result, the residence time may not be accurate. **The flow rate of the carrier fluid was briefly increased to 8.3 mL/min; therefore, the residence time of the outlet may not be accurate.

Position along KRAIC-S	**PCMKSC1 (mins:secs)**	**PCMKSC2 (mins:secs)**	**PCMKSC3 (mins:secs)**	**PCMKSC4 (mins:secs)**
Nucleation promoter	1:41	-	2:07	1:45
Rung 1	3:25	-	3:46	2:38
Rung 2	4:25	-	5:14	3:50
Rung 3	5:16	6:40	6:45	5:20
Rung 4	7:07	8:07	8:11	6:31
Rung 5	8:30	9:36	9:42	7:45
Rung 6	9:51	11:03	11:13	8:57
Rung 7	-	12:32	12:43	10:03
Rung 8	12:36	14:01	14:14	11:24
Rung 9	13:57	15:29	15:42	12:23
Rung 10	15:19	16:59	17:13	13:46
Rung 11	16:42	18:29	18:44	14:57
Rung 12	18:06	19:58	20:15	16:08
Rung 13	19:29	21:25*	21:44	17:23
Rung 14	20:51	22:55	23:13	18:33
Rung 15	22:14	24:25	24:10	19:45
Photodiode / Laser box	23:20	25:38	25:55	20:40
Tubing holder (X-ray beam)	23:28	26:22	26:42	-
Outlet	28:24	31:39	31:40**	-

PCMKSC1 and PCMKSC2

A blockage was observed 33 minutes into the crystallisation run in the SF-10 peristaltic solution pump. The temperature of the tubing jackets was increased from 50 °C to 55 °C for PCMKSC2, together with the introduction of foil added to the inlet of the SF-10 pump for insulation to mitigate blockages in the pump.

PCMKSC3

Some crystals were observed in the top of the KRAIC-S, but their presence was very irregular; some of the crystals comprised a single crystal within a single solution slug, whilst other solution slugs formed agglomerates of PCM. The PCMKSC3 experiment was ended 1 hr 10 minutes into the crystallisation run. The increased experiment time with respect to previous experiments can be attributed to a change in the SF-10 inlet and outlet tubing, where the bore size of the tubing has increased, reducing blockage issues in the solution pump.

PCMKSC4

For experiments PCMKSC1-3, a glass X-piece with uneven bore size was used. The segmentation observed in these experiments showed irregularity therefore, for PCMKSC4, a change in glass X-piece with even bore size for each inlet / outlet was adopted, which greatly improved the homogeneity of the segmented flow.

Some discrepancies in the slug triggering mechanism in terms of matching the translation of the motorised stage with the net flow rate of the segmented flow was observed; this could be altered experimentally by trialling different motor translation speeds to match and directly oppose the net flow. Inconsistency in which part of the solution slug was triggering the laser / photodiode box and thus held stationary in the camera / X-ray beam was experienced. This was attributed to a difference in height of the photodiode / laser box, which was at a lower position than the translation stage (calibrated to the X-ray beam), which was corrected. This in turn helped the consistency of the segmentation and also resulted in a reduction in the crystal tumbling of the single crystals in solution slugs.

PCMKSC5

Experiment PCMKSC5 used a higher concentration of PCM in 60:40 HI (250 g/L), to yield more single crystals in solution slugs. A single crystal within a solution slug was observed in the videos taken alongside the slug triggering mechanism to track these. The PCM single crystals have the tendency to position themselves at the back of solution slugs (Figure 5.24).

Figure 5.24 – 2D diffraction frame showing diffraction spots (left) with the corresponding solution slug held in the X-ray beam during data collection, captured by a camera positioned by the X-ray beam (right), the single crystal is positioned at the back of the solution slug highlighted by the red circle.

5.7.2.1.1 Commissioning Time Data Processing using CrysAlisPro

The lattice rotations with respect to the instrument corresponding to the PCM single crystal were found to be equivalent to a crystal rotation of 0.4° during data collection of each frame. This finding confirms previous data processing trials in Section 5.2.2 predicting that cell indexation could be achieved from a 0.2° wedge of data using the automated DIALS processing approach. The rotation is observed to be chaotic and not in a single direction, which is observable from the lattice rotations with respect to the instrument (Appendix 5.4).

Conclusions from Commissioning time conducted at Diamond Light Source

A fine balance exists between crystallising single crystals in enough solution slugs to index enough frames for full indexation, whilst also avoiding crystallisation of multiple crystallites within a solution slug. The key is to ensure that sufficient single crystals are crystallised *in situ* before the X-ray beam to allow around 20 datasets of single crystals to be collected, even if some solution slugs yield multiple crystallites as long as the latter can be processed.

During the commissioning time, the temperature of the experimental hutch was not regularly monitored. It was observed that very small changes in temperature greatly impact the crystallisation process and thus to mitigate these issues with temperature fluctuations, during subsequent beamtime experiments, the experimental hutch door remained closed except for entry and exit of the hutch in order to maintain constant temperature conditions. For beamtime

experiments, the temperature and humidity conditions of the experimental hutch were thus constantly monitored using a humidity / temperature sensor.

5.7.2.2 Slug Triggering Mechanism Optimisation

Both the offline EH2 run for rig development (Section 5.4.1) and the commissioning time described above employed a photodiode / laser box separated from the FEP tubing holder situated at the X-ray beam. This separation in the position of the slug trigger to the slug data collection at the X-ray beam not only led to both a time delay between trigger and data collection, which negatively impacted data collection efficiency, but also reduced the accuracy of the trigger due to alterations in the flow rate over the slug trigger distance. In terms of hit rate, single crystals resided in 1 in 10 solution slugs and the slug triggering mechanism successfully accessed the correct position of a single crystal in a solution slug for 1 in 20 attempts; the likelihood of obtaining data is thus only achieved 1 in 200 stage translations.

To mitigate these issues, an optimised design of the slug triggering mechanism was established, whereby the photodiode / laser box was instead installed on the motorised staged with the tubing holder. To make this design geometrically possible without the photodiode and laser colliding with the beamline optics, mirrors were employed to reflect the laser beam to the photodiode (Figure 5.25). The optimised slug triggering mechanism also incorporated a longer translation range from 42 mm in the original design to 118 mm, with corresponding operating translation windows of 38 mm and 60 mm for the original and updated slug triggering designs respectively (Figure 5.26). In addition, to avoid reductions in the flow rate of the air over time, which was observed repeatedly when using the gear pump in the offline EH2 run, the air pump was switched to an SF-10 peristaltic pump, allowing for the net flow rate to be more accurately maintained.

This updated slug triggering mechanism comprising of a single translation unit improved both the efficiency and efficacy of the slug triggering mechanism, as well as the single crystal hit rate. In the updated design, the delay time between slug triggering and X-ray data collection of a single crystal in a solution slug is significantly reduced from 44.63 seconds for the original slug triggering design (PCMKSC2) to 2 seconds for beamtime experiments with net flow rates of 9.86 mL/min and 6.2 mL/min for commissioning time and beamtime experiments respectively. This reduction in time delay from the original slug triggering set-up would have been greater if the net flow rate used in the commissioning time matched the lower flow rates

employed in the beamtime experiments. This design optimisation resulted in increased data collection efficiency. Furthermore, the slight variations in pump rates over the crystalliser lengths are mitigated in this new design as the trigger and analysis point are adjacent and thus the accuracy in accessing the single crystal in a solution slug after the optical trigger is much improved.

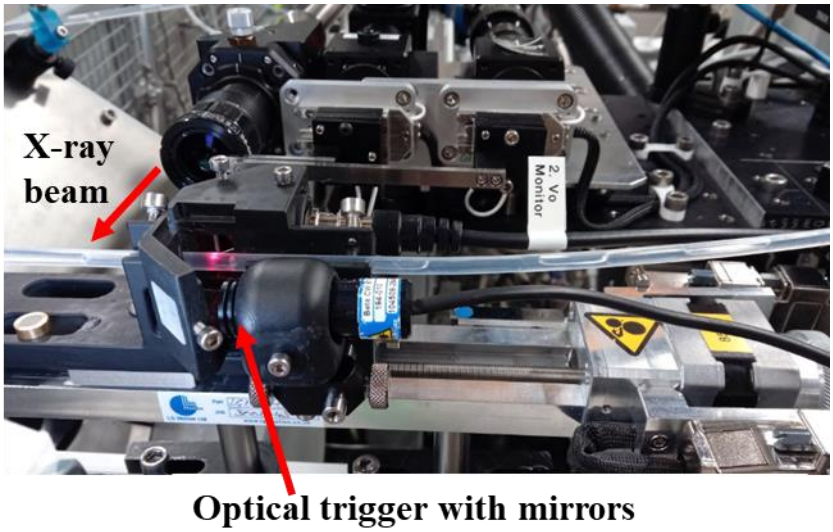

Figure 5.25 – Side on view of the updated slug triggering mechanism set-up featuring the photodiode / laser box with mirrors.

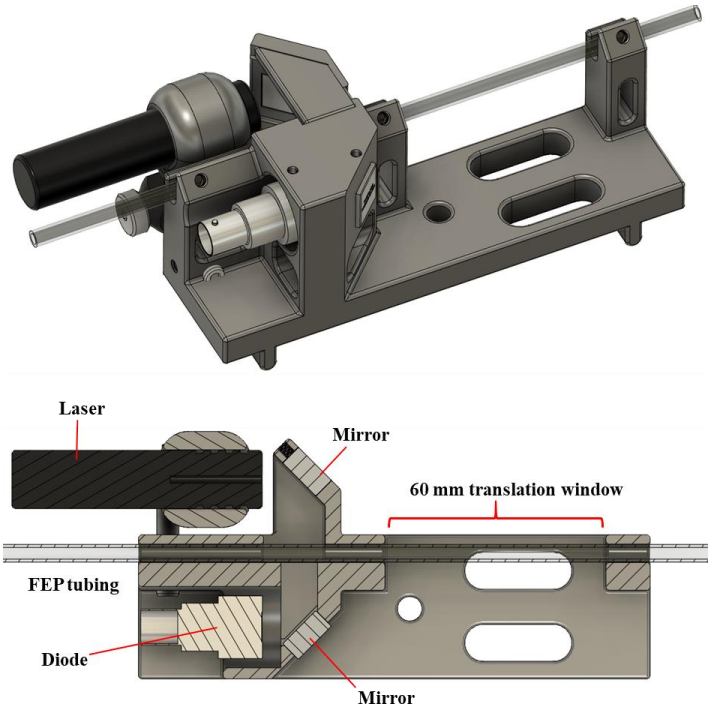

Figure 5.26 – CAD drawings of updated slug triggering mechanism design, above (top) and side (bottom) view.

5.7.2.3 Beamtime at I19 EH2 (PCMKSB)

Experimental conditions and observations for the various PCMKSB beamtime experiments, together with any changes to the flow rates, concentration and experimental set-up are presented and discussed in detail in Section 5.7.3 for CrysAlisPro and DIALS data processing.

Investigations into the effect of primary and secondary heterogeneous nucleation using silica particles and PCM form II seeds respectively on the crystallisation outcome in terms of crystal singularity and polymorphic outcome was investigated in the KRAIC-S. Secondary heterogeneous seeding was investigated through the addition of PCM form II seeds pre-loaded in a seeding coil and introduced into the KRAIC-S by careful dosing into the solution slugs. Primary heterogeneous seeding was investigated through the use of silica particles, which through addition to the PCM in 60:40 HI feed solution and subsequent removal of the feed inlet filters provided an amorphous surface to promote primary heterogeneous nucleation.

A range of online cooling crystallisations was investigated during the beamtime, including unseeded and homogeneous PCM form II seeded crystallisation experiments. The experimental set-up, including connector geometry, along with feed concentration for each of these PCMKSB beamtime experiments are summarised in Table 5.16. The temperature conditions, flow rates and residence times for the PCMKSB experiments are summarised in Table 5.17, 5.18 and 5.19 respectively. Importantly, for beamtime experiments PCMKSB3-5, the X-ray beam was focussed at 8.7 m along the length of the KRAIC-S, whereas for PCMKSB6 the X-ray analysis point focussed at 6.7 m along the KRAIC-S. To ensure platform versatility for the unseeded and seeded KRAIC-S experiments during the beamtime, the experimental set-up illustrated in Figure 5.27 was adopted, whilst the 8.7 m and 6.7 m analysis lengths were accessed by threading of the excess FEP.

PCMKSB1

During PCMKSB1 no active beam was present. For PCMKSB1 there is a difference in total residence time between priming and crystallisation of 42 seconds, however the time taken for a solution slug to travel from the start to the end of the tubing holder is the same. This travel time is the most fundamental part of the residence time for the slug triggering mechanism and the subsequent simultaneous trigger of the motorised stage and start of data collection for a single crystal.

The slug sizes were measured to be 2 cm during priming (without temperature control and with an empty water bath), which reduced to 1.5 cm during crystallisation. This can be attributed to the application of temperature control, which leads to a change in pressure and in surface tension as the viscosity of the media is reduced with an increase in temperature. In addition, there is a change from solvent to solution when moving from system priming to a crystallisation run, again changing the interfacial tension. The segmentation for PCMKSB1 is extremely regular, which is reflected in the associated photodiode / laser read-out (Appendix 5.5).

The use of silica particles to promote primary heterogeneous nucleation did not impact the regularity of single crystals in solution slugs and thus future PCMKSB experiments focussed on unseeded PCM in 60:40 HI experiments without additional silica non-crystalline particles.

Between experiments PCMKSB1 and PCMKSB2 the PILATUS 2M detector was installed; the chiller associated with this installation led to an increase in the room temperature of EH2 from 22.7 °C to 23.1 °C. The crystallisation conditions adopted in PCMKSB1 therefore correspond with a supersaturation ratio of 1.6. As a result of this slight increase in temperature, a corresponding increase in the concentration of PCM in 60:40 HI may be required to ensure that crystallisation occurs along the length of the crystalliser before the X-ray beam.

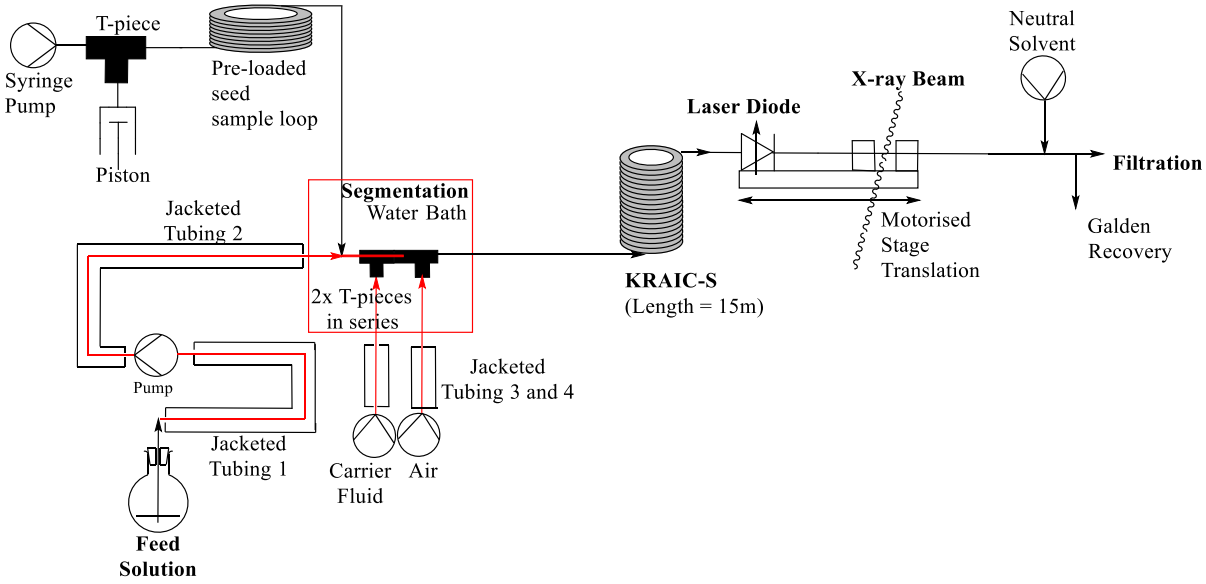

Figure 5.27 – Schematic of KRAIC-S used for unseeded (where the sample loop is disconnected) and seeded (with the sample loop) experiments with T-pieces in series configuration, featuring optimised slug triggering mechanism, whereby the laser diode resides on the motorised stage.

Table 5.16 – Experimental parameters including feed concentration, seed loading and experimental set-up for the KRAIC-S platform used for the various experimental runs in the Beamtime at EH2 I19 (PCMKSB).

Experiment	PCM Feed Solution (g/L 60:40 HI)	Mass of silica particles in feed /g	PCM Form II seeds? (Y/N)	Experimental Set-up	Connector piece(s) in segmentation water bath
PCMKSB1	240	1	N	Unseeded, Fig. 5.4	Even bore size Glass X-piece (3 mm ID)
PCMKSB2	245	N/A	N	Unseeded, Fig. 5.27	Two T-pieces in series with needle through centre of first T-piece
PCMKSB3	245	N/A	N	As for PCMKSB2	As for PCMKSB2
PCMKSB4	245	N/A	N	As for PCMKSB2	As for PCMKSB2
PCMKSB5	245	N/A	N	As for PCMKSB2	As for PCMKSB2
PCMKSB6	247	N/A	N	As for PCMKSB2	As for PCMKSB2
PCMKSB7	245	N/A	Y	Seeded, Fig. 5.27	As for PCMKSB2

Table 5.17 – Set temperatures in the KRAIC-S platform used for the various experimental runs in the Beamtime on I19 (PCMKSB). *For PCMKSB4 the temperature of the water bath was reduced to 35 ℃ at 1 hour 13 minutes into the crystallisation experiment, the bath reached 38 ℃ and 35 ℃ at 1 hour 15 minutes and 1 hour 40 minutes respectively. For PCMKSB4 the temperature of the water bath was further reduced to 32 ℃ at 2 hours 32 into the crystallisation run. #For PCMKSB5, the temperature of the water bath was reduced to 30 ℃ at 54 minutes.

Experiment	Set Temperature (℃)		
	Feed	Jacketed Tubing	Segmentation water bath
PCMKSB1	50	60	40
PCMKSB2	50	60	40
PCMKSB3	50	60	40
PCMKSB4	50	60	40 (35, 32)*
PCMKSB5	50	60	32 (30)#
PCMKSB6	50	60	40
PCMKSB7	50	60	30

Table 5.18 – Flow rates (mL/min) used for the various experimental runs in the KRAIC-S Beamtime on I19 (PCMKSB).

Experiment	Flow rate /mL/min				
	Carrier fluid	**Air**	**Neutral Solvent**	**Solution**	**Seed suspension**
PCMKSB1	1	2.5	2.1	2.7	0.1
PCMKSB2	1	2.5	2.1	2.7	N/A
PCMKSB3	1	2.5	2.1	2.7	N/A
PCMKSB4	1	2.5	6.26	2.7	N/A
PCMKSB5	1	2.5	6.26	2.7	N/A
PCMKSB6	1	2.5	6.26	2.7	N/A
PCMKSB7	1	2.5	6.26	2.7	0.1

Table 5.19 – Experimental residence times for various analytical set points along the length of the KRAIC-S in the various experimental runs in the Beamtime on I19 (PCMKSB). The various lengths along the KRAIC-S were calculated from the speed of the motorised stage employed in PCMKSB3 employed to directly oppose the net segmented flow at a rate of 6.47 mL/min and the residence times experimentally derived for PCMKSB3, where the X-ray beam is situated at 8.88 m, compared to measurement of the tubing of 8.7 m.

Position along KRAIC-S	Length along KRAIC-S /m	PCMKSB1 (mins:secs)		PCMKSB2 (mins:secs)	PCMKSB3 (mins:secs)
		During Priming	**During Crystallisation**		
Rung 1	1.16	1:27	1:30	1:26	1:26
Rung 2	2.30	2:45	2:52	2:46	2:49
Rung 3	3.44	4:03	4:13	4:07	4:13
Rung 4	4.55	5:19	5:33	5:27	5:35
Rung 5	5.65	6:34	6:52	6:45	6:56
Rung 6	6.73	7:48	8:10	8:03	8:16
Rung 7	7.82	9:02	9:28	9:21	9:36
Photodiode / Laser box	8.84	10:11	10:40	10:33	10:51
Start of tubing holder (X-ray beam)	8.88	10:13	10:42	10:34	10:54
End of tubing holder	8.95	10:16	10:46	10:39	10:59
Outlet	11.1	12:47	13:29	13:20	13:38

PCMKSB2

During PCMKSB2 no active beam was present. The crystallisation conditions adopted in PCMKSB2 correspond with a supersaturation ratio of 1.7. PCM crystals were observed

towards the back of solution slugs, where some of the crystals are singular and some are multiple. Crystal observations started at 27 minutes 50 seconds counted sequentially 1 in 34, 1 in 13, 1 in 30 and 1 in 5 slugs, with crystals observed at the end of rung 7. A second set of crystal observations was noted between 56 minutes and 1 hour 1 minute, where crystals were seen in 1 in 22, 1 in 12, 1 in 53, 1 in 28, 1 in 2, 1 in 4 and 1 in 51 solution slugs. Not all observations were of slugs containing just one crystal.

PCMKSB3

The input delay time for the slug triggering mechanism to consistently probe the same part of the solution slug was partially optimised, however some wavering in the slug positioning remains as a result of the speed of the photodiode output.

In addition, a build-up of crystals occurred at the end-piece; these were retrieved for crystal sizing to be used as standards for comparison to the crystal growth observed at various set points along the length of the crystalliser. To mitigate the blockages at the end-piece, the flow rate of the neutral solvent pump was increased to 6.26 mL/min.

PCMKSB4

The higher room temperature of EH2 appeared to be affecting the nucleation rate, as only two crystals were visually observed over a 20 minute period. The temperature of the water bath was therefore reduced from 40 ℃ to 35 ℃ at 1 hour 13 minutes, reaching the set 35 °C at 1 hour 40 minutes into the crystallisation run. A further reduction in temperature was applied to the water bath, where the temperature was changed to 32 ℃ at a crystallisation time of 2 hours 32 minutes. The statistics of crystal spotting at 2 hours 50 minutes was 1 in 133, 1 in 18, 1 in 33, 1 in 26 and 1 in 38 solution slugs.

PCMKSB5

To promote nucleation, the temperature of the water bath was reduced to 30 ℃ at 54 minutes into the crystallisation experiment, which took a further 4 minutes to reach the desired temperature. The temperature of EH2 was measured to be 23.9 ℃, which corresponds to a supersaturation ratio of 1.6.

PCMKSB6

To increase the number of slugs containing crystals, the concentration of the feed of PCM in 60:40 HI was increased to 247 g/L. To prevent the solution slugs producing multiple nucleation

sites yielding multiple crystals, the temperature of the water bath was returned to 40 °C. The first crystal was observed passing the beam at 23 minutes into the crystallisation time. The extent of single crystal formation remained too low, so a further increase in concentration of PCM was required. A post addition of 0.7502 g of PCM was made to the remaining 250 mL of solution to yield a concentration of 250 g/L; sufficient crystallisation was still not observed after 45 minutes. A further addition of 0.5017 g of PCM was made to the remaining 125 mL of solution, resulting in a PCM solution concentration of 254 g/L, however this did not increase crystallisation. Post additions are recognised as not the most accurate method for altering the concentration of solution, but provide a rapid means to gauge the effect of increasing the concentration. Once the concentration of PCM in 60:40 HI has been optimised for single crystal production, new solutions are made for improved accuracy of the concentration.

PCMKSB7

A stock of PCM form II previously made by L. Agnew[152] was used to investigate seeding of the metastable form into the cooling crystallisation of PCM in 60:40 HI in the KRAIC-S installed in EH2 at I19. The PCM form II sample preparation is detailed in Agnew *et al.*[22]

This experiment investigated the effect of PCM form II seeding on the cooling crystallisation of PCM in 60:40 HI in the KRAIC-S. The PCM form II seeds were suspended in carrier fluid, which was then loaded into the FEP coil with the use of air segmentation. The feed was switched from priming to the unseeded PCM in 60:40 HI solution 10 minutes before the syringe pump employed for the PCM form II seed coil, to ensure the concentration of the solution slugs had equilibrated and the PCM form II would not dissolve.

The increase in the net segmented flow arising from the additional 100 μL/min flow rate of the PCM form II seeds into the KRAIC-S resulted in the motorised stage operating at a speed too slow to directly oppose the net flow; this was thus altered.

For a PCM form II seeded crystallisation run (PCMKSS), the hit rate was observed to be 1 in 30, 6 in 50, 2 in 50, 1 in 9, 1 in 39, 11 in 13, 3 in 4, 2 in 2 and 2 in 5. Although these crystal hit rates show large variability between runs, each is improved from the previous slug triggering design.

5.7.3 Data Processing of Unseeded Cooling Crystallisations of Paracetamol (PCM) in 60:40 H_2O:IPA (HI) KRAIC-S at I19

For each type of experiment, as well as each analytical set-point along the length of the KRAIC-S (8.7 m and 6.7 m), five sets of data were processed and analysed to be statistically relevant, the corresponding experiment identifier for each of the datasets are summarised in Table 5.20.

The reflection statistics for each frame which was successfully indexed and refined within these datasets are summarised in Table 5.21; this information is useful for rationalising any significant changes in lattice parameters between frames within an experimental run. The reflection statistics show that the datasets analysed at 8.7 m corresponding with a crystallisation time of 10.7 minutes, compared to 6.7 m corresponding with 8.2 minutes crystallisation time, have more reflections per frame and a higher percentage of reflections involved in indexation. Additionally, indexation and refinement can be achieved across a greater number of adjacent frames at 8.7 m compared to 6.7 m along the KRAIC-S. These comparisons can be rationalised by crystal growth, whereby the intensity of spots is greater at 8.7 m compared to 6.7 m and thus manual spot finding is easier at 8.7 m.

Table 5.20 – Experiment identifier corresponding with each of the data sets processed for the unseeded crystallisation runs analysed at 8.7 m and 6.7 m along the length of the KRAIC-S.

Experiment type	Distance along length of KRAIC-S /m	Crystallisation time /mins	Set	Experiment identifier
Unseeded cooling crystallisation of PCM in 60:40 HI	8.7	10.7	1	PCMKSB3
			2-3	PCMKSB4
			4-5	PCMKSB5
	6.7	8.2	1-5	PCMKSB6

Table 5.21 – Reflection statistics corresponding with each of the datasets processed for the unseeded crystallisation runs analysed at 8.7 m and 6.7 m along the length of the KRAIC-S. *Denotes the starting frame employed for unit cell finding. #Frame was indexed but not enough reflections were available for refinement. †Frame required unit cell finding again. **Each diffraction run corresponds with a different single crystal, where five datasets corresponding with five different single crystals were analysed.

Crystallisation stage	Set** (Identifier)	Frames	Number of reflections	% of reflections indexed
Later – 8.7 m	1 (PCMKSB3)	3, 4, 6, 7, 8, 9†, 11, 12†, 25, 26, 27, 28, 29, 30†, 31#, 32, 33, 34, 35, **36***, 37, 38, 39, 40, 41, 42	18, 16, 8, 8, 8, 7, 12, 10, 19, 6, 10, 12, 7, 9, 3, 13, 16, 23, 20, 25, 25, 18, 26, 30, 17, 18	100, 100, 100, 100, 100, 100, 92, 100, 100, 100, 100, 100, 100, 100, 100, 94, 91, 100, 100, 100, 89, 100, 90, 100, 90
	2 (PCMKSB4)	**6***, 7, 8, 9, 10, 11, 12, 13, 14, 15, 17†, 18, 19, 22†, 24, 25	13, 9, 5, 8, 11, 8, 12, 12, 9, 8, 9, 13, 21, 11, 11, 7, 6	100, 100, 80, 100, 100, 100, 92, 100, 100, 100, 89, 77, 100, 91, 100, 86, 100
	3 (PCMKSB4)	4, 5, 6, 7, 8, 9, 10, **11***, 12, 13, 14, 15, 19†	18, 9, 11, 11, 10, 8, 12, 15, 11, 14, 22, 14, 10	78, 100, 100, 100, 100, 88, 100, 100, 91, 93, 100, 93, 100
	4 (PCMKSB5)	5†, 7, 9, 10, 11, 12, 13, 14, 15, 16, 17, **18***, 19, 20	6, 9, 7, 11, 8, 8, 12, 11, 8, 11, 6, 9, 10, 8	100, 100, 57, 100, 100, 50, 92, 100, 100, 82, 100, 100, 50, 88
	5 (PCMKSB5)	13, 14, 15, 16, 17, 19, 20, 21, 22, 23, 24, **25***, 26, 27, 28, 29, 30, 31, 32, 33, 34, 35, 36, 37, 38, 39, 40	10, 4, 8, 7, 6, 9, 9, 14, 10, 8, 8, 14, 19, 14, 11, 8, 11, 16, 8, 7, 7, 13, 10, 5, 5, 8, 6	90, 100, 89, 100, 100, 100, 90, 100, 100, 80, 100, 100, 79, 100, 100, 88, 73, 100, 88, 100, 100, 100, 60, 100, 80, 80, 83
Earlier – 6.7 m	1 (PCMKSB6)	13, 14, 15, 16, 17, 18, 19, 20, **21***, 22, 23	6, 20, 27, 19, 17, 21, 20, 14, 12, 8, 7	100, 65, 74, 74, 65, 90, 90, 100, 100, 100, 100
	2 (PCMKSB6)	28, 29, 30, 31, 32, **33***, 34, 35, 36, 37, 38, 39, 40, 41	17, 17, 15, 21, 23, 17, 11, 9, 9, 8, 7, 8, 13, 13	35, 35, 60, 43, 48, 71, 64, 67, 78, 100, 86, 75, 100, 69
	3 (PCMKSB6)	27, 28, 29, **30***, 31, 32, 33, 34, 35	11, 12, 17, 15, 11, 24, 9, 14, 6	45, 50, 65, 87, 91, 63, 67, 71, 83
	4 (PCMKSB6)	**20***, 21, 22, 23, 24, 25, 26, 27, 28, 29, 30, 31, 32, 33, 34, 35, 36	11, 14, 15, 14, 13, 19, 12, 9, 14, 19, 18, 14, 7, 9, 7, 6, 6	82, 64, 47, 57, 38, 53, 67, 67, 57, 68, 39, 36, 71, 56, 57, 67, 83
	5 (PCMKSB6)	**35***, 36	9, 5	89, 100

5.7.3.1 Monitoring later stage crystallisation using CrysAlisPro: 8.7 m along crystalliser length, crystallisation time of 10.7 minutes

Optimally the unit cell dimensions are fixed during the calculation of the rotation angles due to the very low data to parameter ratio (which can be as low as 1:1 for some frames; e.g. set 4, frame 9, which shows a large variance (Figure 5.28)). However, CrysAlisPro does not allow the unit cell dimensions to be fixed when refining rotation angles. The *a*-axis is shown to drift over time (Figure 5.28; the variance of the other unit cell parameters with time is presented in Appendix 5.6). This variance in unit cell parameters over time may be attributed to changes in the sample-detector distance as a single crystal rotates in a solution slug (± 1.59 mm).

Monitoring R1, R2 and R3 with respect to the instrument over time, allows the extent of single crystal rotation to be considered independently along three different 1-dimensional planes. The rotations of the single crystal analysed in set 5 at 8.7 m are presented in Appendix 5.6. These show that the rotation behaviour tends to be random.

5.7.3.2 Monitoring earlier stage crystallisation using CrysAlisPro: 6.7 m along crystalliser length, crystallisation time of 8.2 minutes

The same analysis approach using CrysAlisPro was also carried out on five datasets from diffraction scans acquired at 6.7 m along the length of the KRAIC-S. Again the *a*-axis across each of the frames showed variance over time, but in this case the *a*-axis parameter was consistently underestimated with respect to the 7.09 Å axis for PCM form I (HXACAN30) in the CSD (Figure 5.29). This can be attributed to the reduction in the number of reflections and reflection intensity at this earlier stage in the crystallisation process.

The R1, R2, and R3 lattice rotations of the single crystal analysed in set 5 at 6.7 m (Appendix 5.7) again show essentially random variations, which appear to be systematically smaller than for the 8.7 m position. If confirmed in further experiment such a reduction in tumbling rotation would affect the capability to gain indexing in the KRAIC-S. However, it must be noted that the different crystalliser lengths are not of course considering the same single crystal.

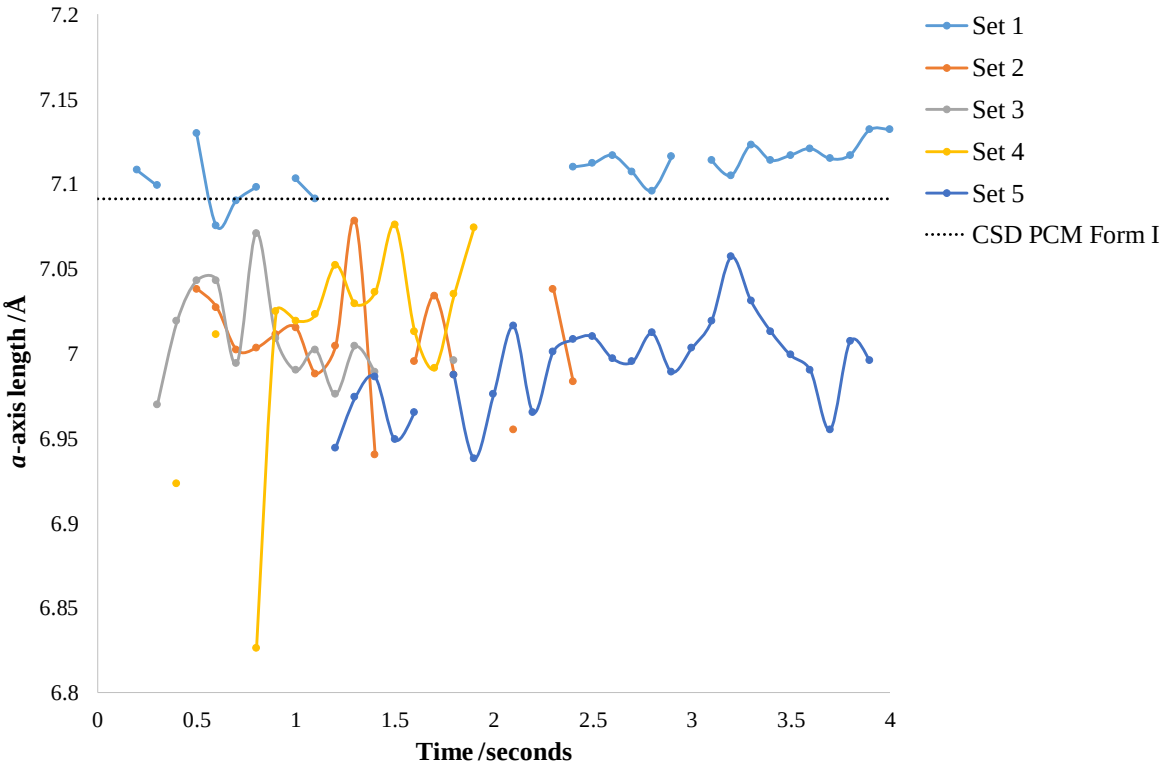

Figure 5.28 – *a*-axis lattice parameter over time for each of the five datasets at 8.7 m compared to the magnitude of the *a*-axis for PCM form I obtained from the CSD.

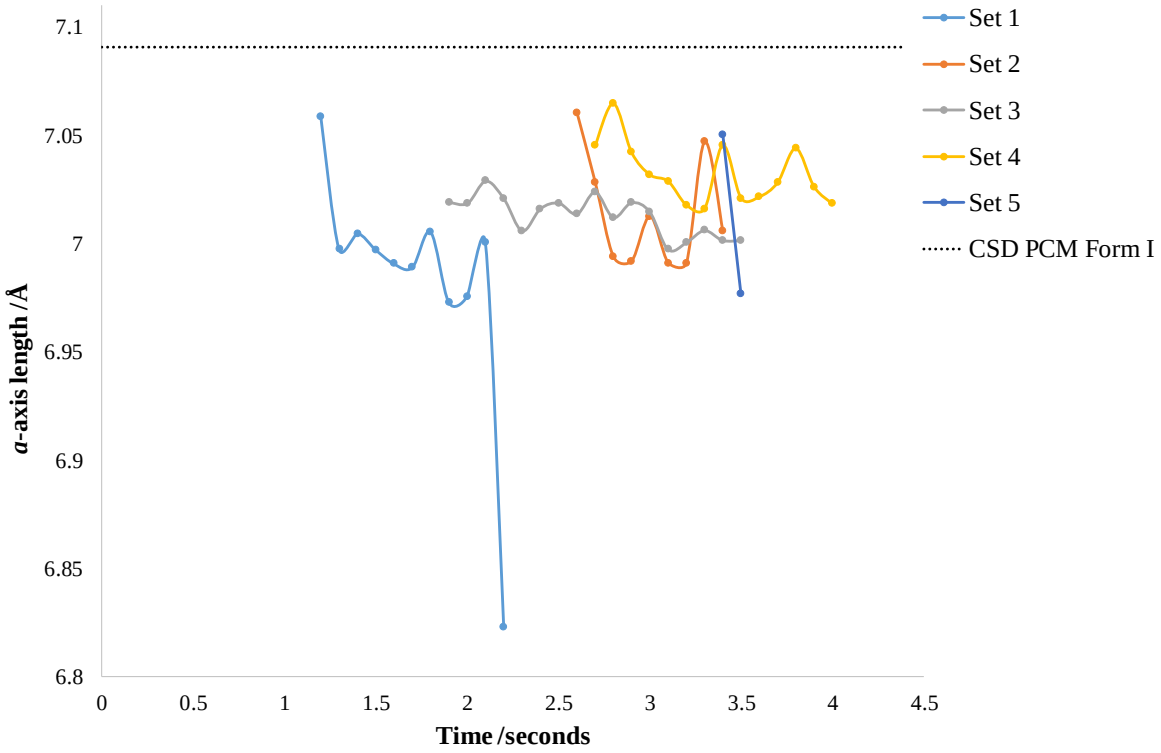

Figure 5.29 – *a*-axis lattice parameter over time for each of the five datasets at 6.7 m compared to the magnitude of the *a*-axis for PCM form I obtained from the CSD.

5.7.3.3 Comparison of Lattice Rotations at earlier and later stage crystallisation (6.7 m and 8.7 m crystalliser lengths)

Data acquisition at the different set points (6.7 m and 8.7 m) allows the extent of crystal growth, as well as the degree of lattice rotations with crystal size to be understood. Table 5.22 shows that the number of reflections and percentage of these reflections utilised in cell indexation increases with crystalliser length, as a single crystal grows between these two set points.

Table 5.22 – Reflection statistics of the indexed spots obtained from manual spot finding of adjacent frames in CrysAlisPro, corresponding with each of the datasets for the unseeded crystallisation runs analysed at 8.7 m and 6.7 m along the length of the KRAIC-S.

Crystalliser length /m	Dataset (Experiment Identifier)	# Reflections	% Indexed
8.7	1 (PCMKSB3)	384	96
	2 (PCMKSB4)	173	93
	3 (PCMKSB4)	165	94
	4 (PCMKSB5)	124	85
	5 (PCMKSB5)	255	95
6.7	1 (PCMKSB6)	171	88
	2 (PCMKSB6)	188	67
	3 (PCMKSB6)	119	69
	4 (PCMKSB6)	207	59
	5 (PCMKSB6)	14	95

As the PCM form I single crystal grows between 6.7 m and 8.7 m along the KRAIC-S, corresponding with 8.2 minutes and 10.7 minutes into the crystallisation process, the crystal rotates to a greater degree (Figures 5.30-5.32). This finding of an increase in the degree of crystal rotation with increasing crystal size can be attributed to differences in the interaction of the single crystal with the turbulent flow and may be of relevance in future experiment design.

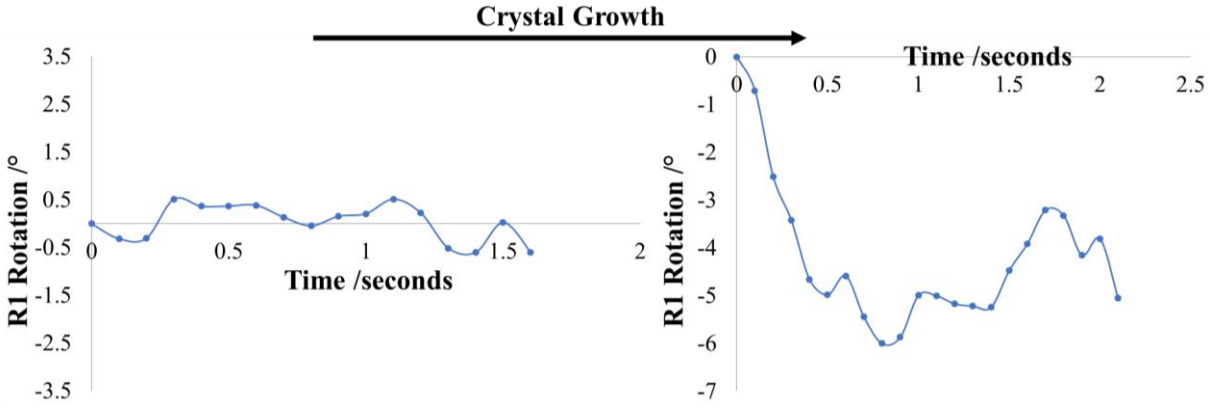

Figure 5.30 – R1 rotation with respect to the instrument over time as the crystal grows between 6.7 m and 8.7 m.

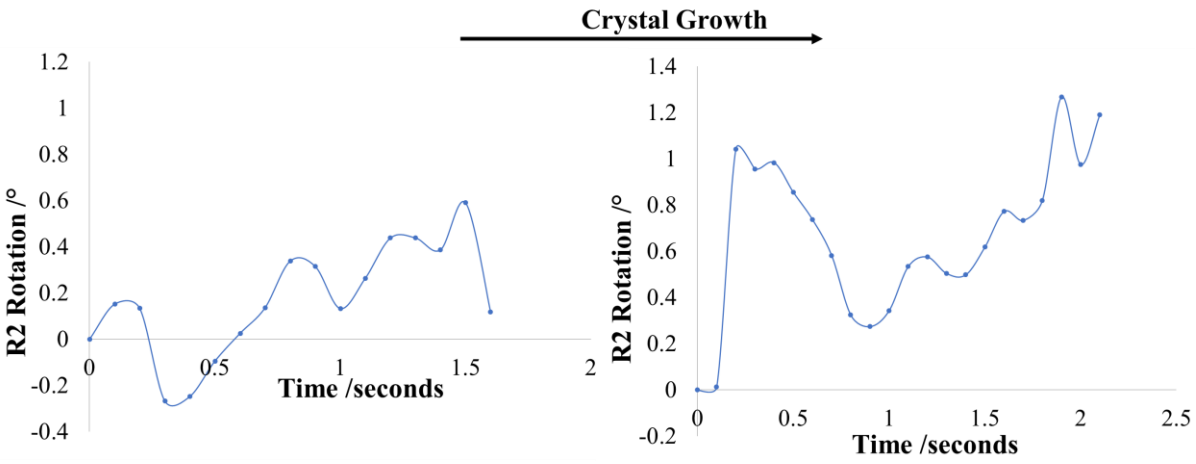

Figure 5.31 – R2 rotation with respect to the instrument over time as the crystal grows between 6.7 m and 8.7 m.

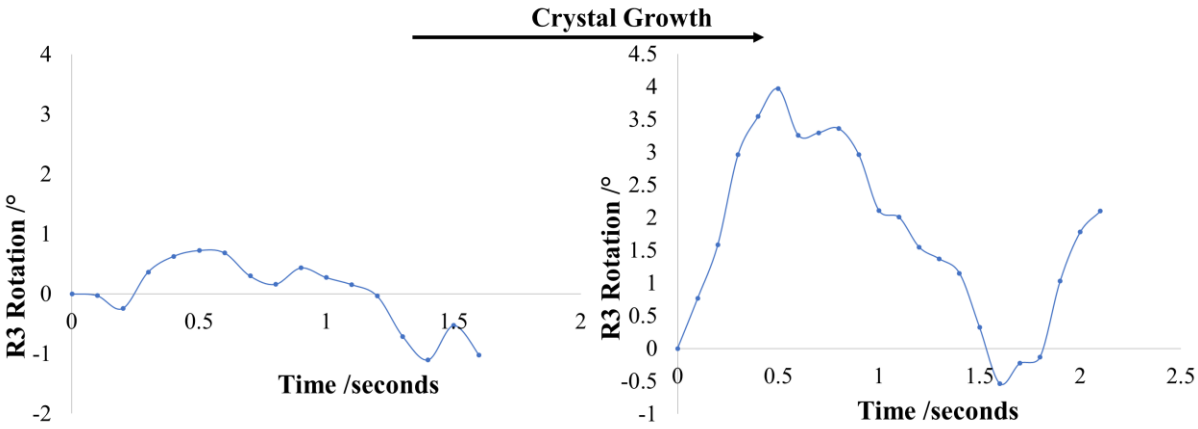

Figure 5.32 – R3 rotation with respect to the instrument over time as the crystal grows between 6.7 m and 8.7 m.

5.7.3.4 DIALS Processing Results

All data processing attempts from the various crystallisation runs were carried out manually using CrysAlisPro; the same analysis was also investigated *via* automated processing methodologies.

The DIALS automated processing was only carried out on data collected from the unseeded cooling crystallisation of paracetamol in 60:40 HI beamtime experiments (PCMKSB); five datasets were collected for both 8.7 m and 6.7 m crystalliser lengths along the KRAIC-S platform. Three of the ten datasets completed the entire DIALS data processing procedure, using the automated routine, two of the datasets failed at all stages and the remainder achieved

partial completion of the various data processing steps (Table 5.23). After initial spot finding, > 90 % indexation of the diffraction spots was achieved (Table 5.24), similar to the indexation achieved *via* CrysAlisPro processing (Table 5.22).

The DIALS data processing progress across the various datasets would proceed through the entirety of the process if the best processing routines for each of the algorithms were established. Merging of neighbouring datasets would also likely achieve a high success rate for completion of the DIALS process.

Table 5.23 – DIALS data processing progress for each of the ten datasets as those analysed in CryAlisPro at both 8.7 m and 6.7 m crystalliser length scale. Green denotes that the data processing stage was successfully completed, whilst red denotes that the data processing stage was unsuccessful.

Crystalliser length /m	Set	Experiment Identifier	Indexation	Refinement	Integration	Merging
8.7	1	PCMKSB3				
	2	PCMKSB4				
	3					
	4	PCMKSB5				
	5					
6.7	1	PCMKSB6				
	2					
	3					
	4					
	5					

Table 5.24 – Reflection statistics of the indexed spots obtained from spot finding, corresponding with each of the datasets processed using DIALS for the unseeded crystallisation runs analysed at 8.7 m and 6.7 m along the length of the KRAIC-S.

Crystalliser length /m	Dataset	# Indexed	# Unindexed	% Indexed
8.7	1	323	5	98.5
	2	224	0	100
	3	164	2	98.8
	4	135	3	97.8
	5	153	0	100
6.7	1	133	11	92.4
	4	103	4	96.3
	5	107	10	91.5

Monitoring the spot count over each of the diffraction frames in a dataset allows for the behaviour of the single crystal within a solution slug with respect to the X-ray beam to be

monitored. The single crystals monitored in the various datasets are generally shown to move in and out of the X-ray beam (Figure 5.33). In addition to monitoring the movement of the single crystal moving in and out of the X-ray beam through the spot count over the various frames, visual observations provide additional evidence of this behaviour.

The video capturing the motorised stage artificially suspend the single crystal in the X-ray beam during data collection also shows single crystal movement in and out of the beam in the ESI detailed in Appendix 5.8 (20190726_1928_0010_Unseeded PCM_8_7m_Set 4_Video). The movement of the single crystal analysed in dataset 5 at 6.7 m is also captured by visual observations in the ESI detailed in Appendix 5.8 (20190728_1614_0001_Unseeded PCM_6_7m_Set 5 Video). From the various observations, the correlation between crystals moving in and out of the beam and successful indexing was not established at this point.

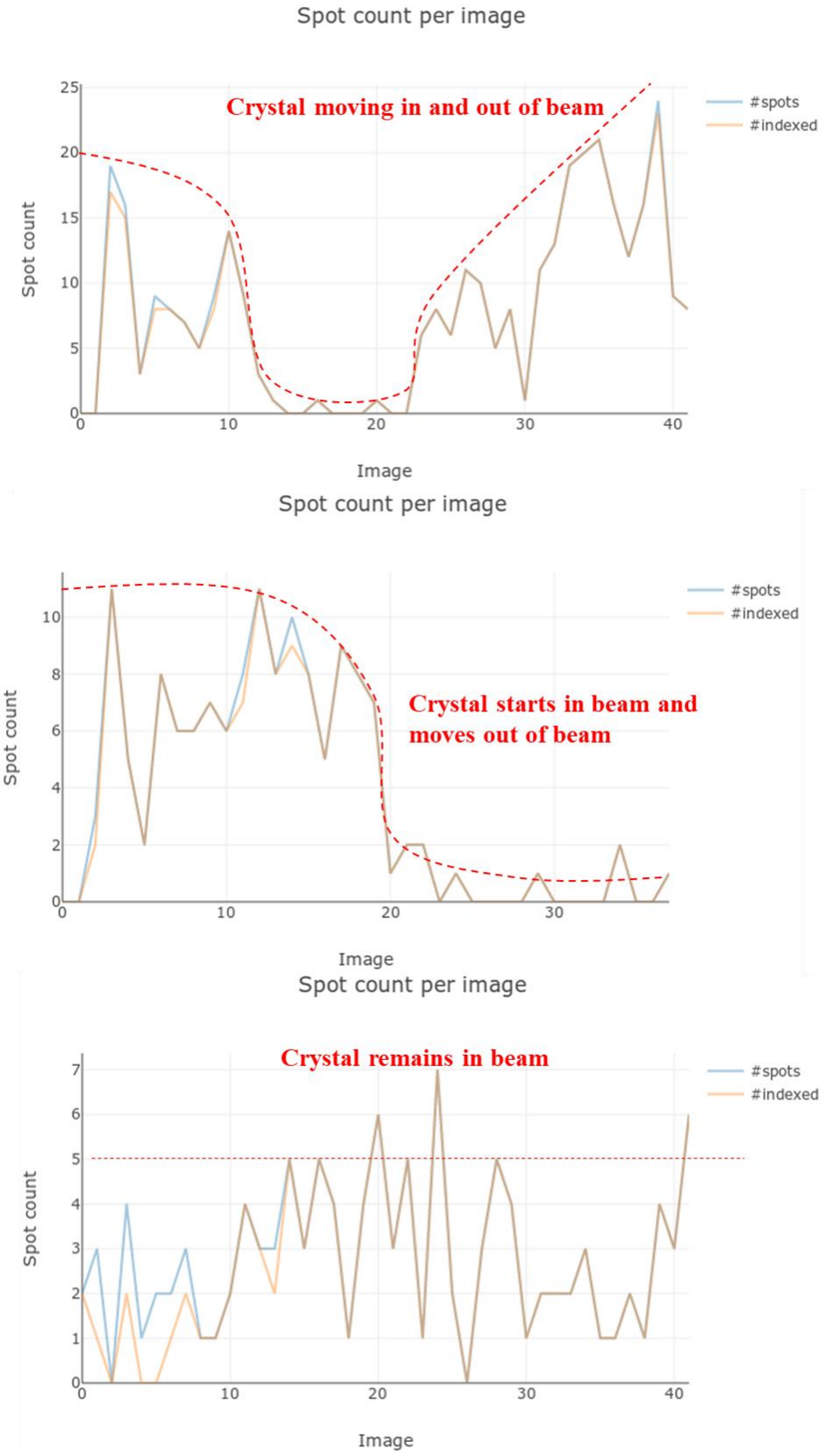

Figure 5.33 – Varying movement of a single crystal in the X-ray beam: Crystal moving in and out of beam for dataset 1 at 8.7 m (top), crystal starts in beam and moves out of beam dataset 4 at 8.7 m (middle) and crystal remains in beam dataset 5 at 6.7 m (bottom).

In contrast to the lattice rotations extracted from CrysAlisPro, which showed increased rotation at the later stage in the crystallisation process (8.7 m, 10.7 minutes crystallisation time), suggesting that crystal rotation increases with crystal size, DIALS processing suggested the opposite finding (Figure 5.34).

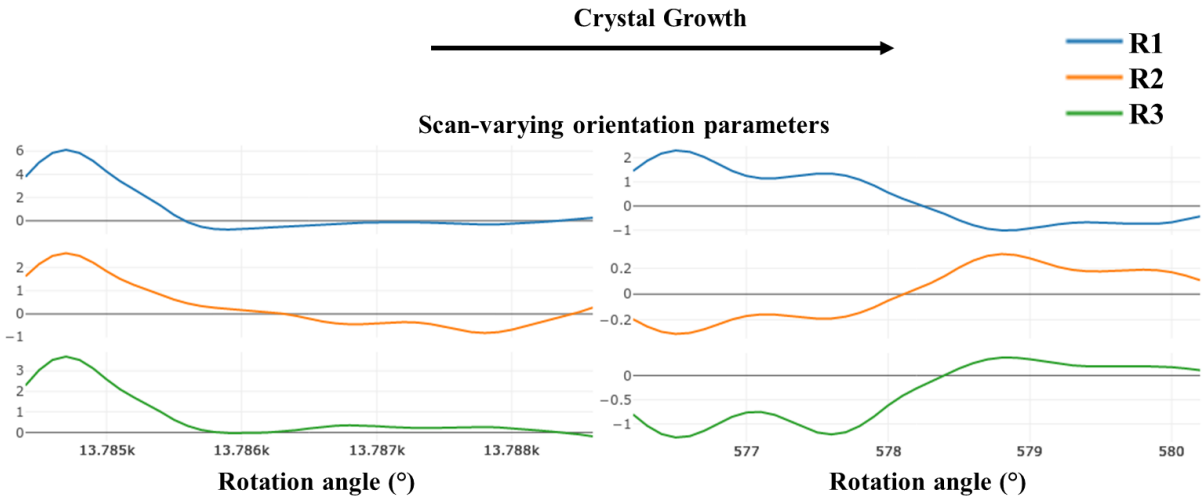

Figure 5.34 – Scan-varying orientation parameters for dataset 5 at 6.7 m and dataset 1 at 8.7 m, elucidating the relationship between the extent of crystal growth with lattice rotation using DIALS.

The difference in the extent of lattice rotation with crystal size suggested from the data processing methods of CrysAlisPro and DIALS can be attributed to differences in the various stages of the processing procedures, notably the automated spot finding in DIALS and the fact that DIALS processing is not dependent on successive frames all being indexed successfully. In addition, the unit cell parameters are fixed and input into the processing for DIALS, whilst CrysAlisPro the unit cell parameters are not input nor fixed during refinement. The lattice rotations across the run are acquired after the refinement stage.

To establish how the single crystal will tend to rotate in 3-dimensional dynamics, the sample's angular displacement from its original orientation rather than along the displacement axis direction can be considered (Figure 5.35). The overall sample tumbling angle with frame number as the crystal grows, shows a reduction in rotation, similar to the finding in 1-dimensions using DIALS, but contrasting to the finding in 1-dimensions using CrysAlisPro.

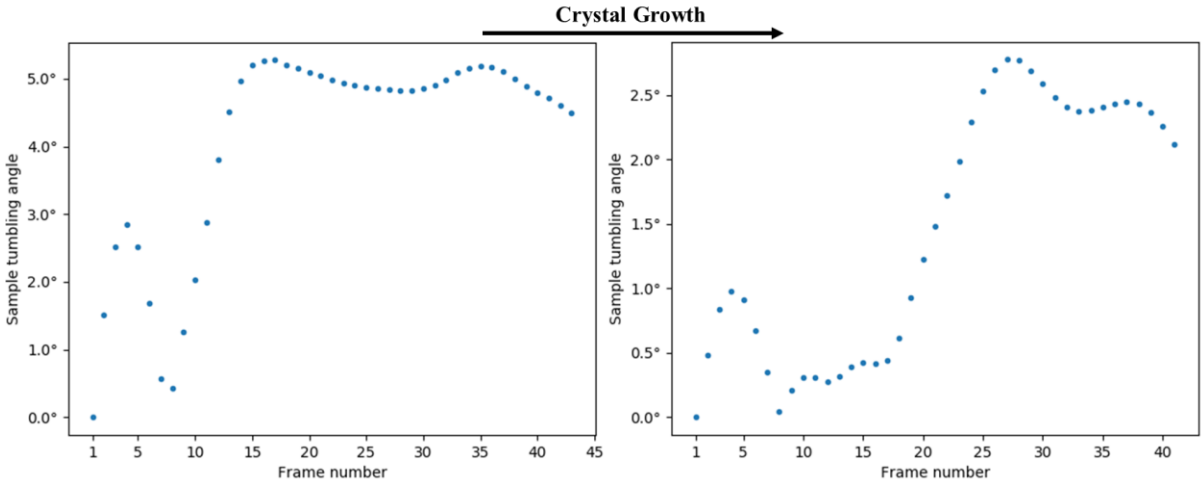

Figure 5.35 – Sample tumbling angle *versus* frame number for dataset 5 at 6.7 m and dataset 1 at 8.7 m, elucidating the relationship between the extent of crystal growth with overall lattice rotation using DIALS [combined rotration calculations courtesy of a Python script provided by Dr Ben Williams, DLS].

The merging statistics I/σ of 14 for dataset 1 at 8.7 m is of the magnitude required for standard collection datasets, typically of 15 (Table 5.25). Given the nature of the data collection strategy using the slug triggering mechanism, the completeness of a slug dataset was expected to be low, whilst dataset 1 at 6.7 m shows a reasonable completeness of 7 % considering the nature of the data collection. This completeness corresponds with one single crystal artificially suspended in the X-ray beam for 4.4 seconds and therefore it can be postulated that ~20 of these datasets would be required for full structure solution.

Table 5.25 – Merging statistics for dataset 1 at 8.7 m and dataset 5 at 6.7 m, that achieved the full DIALS processing procedure including the successful completion of the merging algorithm.

Merging Statistics	**Dataset 1 at 8.7 m**	**Dataset 5 at 6.7 m**
Resolution	2.86 – 0.54	5.33 – 0.54
Observations	285	742
Unique reflections	114	383
Redundancy	2.5	1.9
Completeness (%)	2.01	7.09
Mean intensity	36219.1	1970.0
Mean I/sigma(I)	14.1	1.8
R-merge	0.121	0.172
R-meas	0.147	0.232

5.7.4 Data Processing of Seeded PCM form II Cooling Crystallisation of Paracetamol (PCM) in 60:40 H_2O:IPA (HI) KRAIC-S (PCMKSS) at I19 using CrysAlisPro

For the PCM form II seeded experiments (PCMKSS), only four yielded diffraction suitable for indexation and only three of those identified PCM form II, whilst the other identified PCM form I. Each of these four sets were obtained from experiment PCMKSB7 (Table 5.26).

After indexation of the starting frame, none of the adjacent frames on any of the three sets from which PCM form II was positively identified could be either re-indexed from the current unit cell or indexed by manually inputting the PCM form II unit cell parameters. Furthermore, the adjacent frames to the starting frames selected for initial unit cell finding seldom contained diffraction on the 2D image. This indicates that the PCM form II crystals are moving in and out of the X-ray beam analysis region and thus it could be rationalised that the extent of crystal rotation for the PCM form II is much greater than the rotation found for the PCM form I single crystals; this may be a crystal morphology effect. This is further supported by visual observations (ESI in Appendix 5.8: 20190727_2355_0010_Seeded PCM form II_Set 2_Get Form II_Video). As the extent of rotation is so significant and moves beyond the X-ray analysis area, it is not possible to quantify the single crystal rotation of the PCM form II single crystals.

The fact that PCM form II was not produced in all seeded runs indicates that the PCM form II seed dosing efficiency could be improved. In addition, some of the datasets yielded multiple crystals in a single solution slug; therefore, the concentration of the seed could be reduced.

Table 5.26 – Reflection statistics corresponding with each of the datasets processed for the PCM form II seeded crystallisation runs in the KRAIC-S. *Denotes the starting frame employed for unit cell finding.

Set	Frames	Number of reflections	% of reflections indexed	Polymorph of single crystal
1	**3***	31	68	PCM form II
2	**2***	11	100	PCM form II
3	**3***	15	87	PCM form II
4	**3***	6	100	PCM form I

5.7.5 Crystal Sizing and Crystal Growth at various set-points

This work assesses whether it is possible to extract crystal size of single crystals grown *in situ* in the KRAIC-S, using a range of crystals of known size through the average intensity from a range of reflections manually integrated in CrysAlisPro. The assessment of crystal size would

ideally be carried out by merging fully processed and integrated data of the slug datasets compared to a range of standard datasets of suitable relative crystal sizes; however, these data are not generally available for the former.

The success of this crystal size prediction is reliant on many variables, including the intensity of individual reflections, which will be dependent on the crystal morphology. The morphology of single crystals grown under plug flow conditions in the KRAIC-S will differ from the batch of PCM used for crystal sizing standards. During data collection, depending on the position, orientation and morphology of a single crystal in a solution slug relative to the X-ray beam, it is possible that the beam will only partially hit the single crystal, which impacts the observed intensity of certain reflections. Furthermore, it is possible that only part of the rocking curve may be obtained for a reflection from a single crystal in a solution slug. This also relates to the extent of rotation of the single crystal in the solution slug. It would also not generally be possible to apply scaling of data from a single image for the single crystals grown *in situ*, whilst scaling will have been applied to the standard single crystal data collections.

Importantly, it is not possible to monitor crystal growth of the same single crystal in a solution slug at the various set points, but as the KRAIC-S is operating under steady state conditions, this analysis may provide a reasonable approximation for the size of the single crystals grown *in situ* in the KRAIC-S crystalliser. The growth profile of the crystallisations is not known under these conditions; fitting a linear trendline assumes a linear crystal growth mechanism, but an exponential crystal growth mechanism could be equally valid.

The sizes of the single crystals analysed for the standard datasets 1 and 2 (Table 5.27) were measured on an optical microscope to yield a benchmark for comparison to those grown *in situ* in solution slugs in the KRAIC-S. Assuming that size measurements of the larger single crystal corresponding with dataset 1 are more accurate than the small single crystal corresponding with dataset 2, dataset 1 was therefore used as the basis for scaling. The scaling ratio determined for standard datasets 1 and 2 of 4.74:1 is in good agreement with manual spot integration in CrysAlisPro across six *hkl* reflection sets, which gave a ratio of 5.62:1 (Table 5.28).

Table 5.27 – Crystal sizing parameters of standard datasets 1 and 2.

Crystal sizing parameter	**Standard dataset 1**	**Standard dataset 2**
Measured crystal dimensions /μm	150 x 120 x 20	90 x 50 x 20
Measured crystal volume / μm^3	360 000	90 000
Ratio from scaling and merging datasets 1 and 2 in XPrep	4.7492	1
Predicted crystal dimensions /μm	360 000	75 802

Table 5.28 – Integrated intensity values for the complete rocking curve across six *hkl* reflection sets for standard datasets 1 and 2.

Reflection set	***hkl***	**Standard dataset 1 (Rocking curve)**	**Standard dataset 2 (Rocking curve)**	**Scale (Rocking curve)**
1	0 1 -8	2929.75	377.75	7.76
2	-3 -2 -8	1659.25	322.5	5.14
3	4 3 -8	856	162.25	5.28
4	4 3 -9	1739.75	378.75	4.59
5	6 1 3	417.25	78	5.35
6	-5 -5 -5	396.25	71	5.58
				Average = 5.62

The crystal size prediction of single crystals crystallised in solution slugs in the KRAIC-S from standard single crystal datasets is slightly flawed as a result of the single crystals tumbling in and out of the X-ray beam, leading to inaccuracies in the observed intensity of reflections, and the assumption of a spherical crystal. The crystal size predictions could be improved by significantly increased sampling over a greater number of reflection sets, starting frames and standard datasets, whilst also comparing the growth results with the spot count statistics across the dataset. This increased sampling is not feasible using the manual crystal growth processing method used here; an automated crystal growth processing procedure would need to be outlined and optimised. Additionally, the size of the X-ray beam could be increased to immerse a solution slug, allowing for the single crystal to be continually monitored by the X-ray beam, however, additional background subtraction to remove the scattering from the 60:40 HI solvent in the solution slugs would also be required.

The crystal growth mechanism of the unseeded cooling crystallisation of paracetamol in 60:40 HI under these conditions is not known. Increasing the number of analytical set points could allow the crystal growth mechanism to be determined. Although the KRAIC-S operates under steady-state conditions, late nucleating crystals along the length of the KRAIC-S will be at an

earlier stage of the crystal growth process compared to earlier nucleating crystals monitored at the same set point. This would clearly affect estimates of crystal growth.

5.8 Overall Discussions and Conclusions

Data Processing Conclusions

CrysAlisPro provided a useful start point for indexing and refining the *in situ* single crystal XRD data to obtain information on the polymorph crystallised through cell indexation of a single diffraction frame. Lattice indexation and refinement on adjacent frames to the starting frame chosen for cell indexation allowed for lattice rotations to be monitored over time. CrysAlisPro allowed for the number of useful reflections per diffraction frame to be realised.

The key drawback to the use of CrysAlisPro is that the manual nature of the processing means that this data processing procedure is significantly time consuming, meaning that rapid data processing in parallel to beamtime experiments, which could potentially prompt alterations to experimental set-up and conditions, is not feasible. Furthermore, the unit cell parameters cannot be fixed and will shift after refinement; this greatly increases the number of variables and results in a poor data to parameter ratio. CrysAlisPro can only be employed for the single crystal data processing steps of indexation and refinement; it is not possible to carry out integration required for structural solution.

DIALS has the capability to mitigate against these key drawbacks highlighted in CrysAlisPro, whereby the data processing procedure can be fully automated, facilitating data checks during beamtime experiments and also allows a wealth of data to be processed in relatively minimal time on a timeframe of minutes. The use of DIALS was thus investigated and developed significantly during the project, in collaboration with Dr Mark Warren (Diamond Light Source). The unit cell can also be fixed in DIALS, greatly reducing the number of variables and thus improving the data to parameter ratio, which is particularly important in these single diffraction frame methods *via* this serial crystallography-like approach.

In contrast to CrysAlisPro, DIALS can carry out integration and image merging towards structural solution. Importantly, employing DIALS in this ‘proof-of-concept’ study allows the number of single crystals that need to be analysed to allow novel structure solution to be quantified, which is a fundamental question to be answered when selecting other crystallising systems in the future. The five datasets for each experimental condition investigated in this

study only resulted in a DIALS merging of one of the datasets, thus the merging of these integrated datasets for structural solution was not possible as a result of insufficient sampling. However, on the premise that the merged datasets at 8.7 m and 6.7 m achieved a completeness of 2 % and 7 % respectively, it would be expected that structural solution could be achieved from 20-50 of these datasets to sample the entire sphere, although due to symmetry of the lattice, this number of datasets could be reduced, whilst still achieving structural solution. Data capture utilises a continuous sweep of the X-ray beam, with the single crystal residing in the beam for 4 seconds, followed by data analysis using the automated DIALS processing procedure with a corresponding data analysis time of ~3-4 minutes; this results in a data capture and analysis time of only 5 minutes required for each dataset.

Experimental Set-up Conclusions

The KRAIC-S crystalliser, which employs segmented flow to yield solution slugs with an identical and highly reproducible crystallisation environment, is a suitable platform to carry out serial-crystallography type experiments. The accessible flow rates are compatible with the motorised stage translations to artificially ‘‘hold / suspend’’ a single crystal in the X-ray beam for sufficient diffraction data to be acquired for indexation. The slug triggering mechanism has been optimised into a single optical trigger and analysis unit, which greatly reduces the downtime between data acquisitions from 44 seconds to 2 seconds, but also improves the accuracy in the slug triggering tracking the current part of the solution slug, while maintaining equal but opposing speed of the motorised stage. This led to great improvements in the successful hit rate of single crystals by the X-ray beam, with the likelihood of obtaining data increased by a factor of 10 (to 1 in 20 stage translations) in the new design.

The cooling crystallisation process for PCM in 60:40 HI has been optimised to yield a single crystal within solution slugs. The crystallisation process is largely impacted by small fluctuations in temperature and therefore careful temperature control and maintenance mitigated this variability in the extent of crystallisation observed.

The seeding delivery system for PCM form II seeds into the cooling crystallisation of PCM in 60:40 HI in the KRAIC-S has been designed and optimised. Three diffraction runs were shown to yield PCM form II single crystals, whilst PCM form I was evident in a fourth run, indicating that the efficiency of seed dosing could be optimised further.

Future Work

Although the use of FEP tubing throughout the entirety of the KRAIC-S, including the analytical set point where the X-ray beam is focussed successfully mitigated against blockages, the FEP tubing contributed significantly to the background of the diffraction data. Therefore, future KRAIC-S experiments on I19 may employ an X-ray transparent hydrophobically coated Kapton® window similar to those employed in the KRAIC-D presented in Chapter 4. An alternative material to Kapton® would be Mylar®. Provided Mylar® can be prepared by extrusion, this is a more robust material and is colourless, allowing improved clarity of visual observations of single crystals in solution slugs. In addition, replacing the FEP with a material, which is transparent to X-rays will ensure that the tubing will not give rise to undue background in the diffraction patterns that would mask weak high resolution signals.

The main source of blockages in the KRAIC-S results from crystallisation of the PCM in 60:40 HI feed in the inlet / outlet of the SF-10 pump or inside the solution pump. To mitigate these sources of blockages, the use of positive displacement liquid transfer *via* Mass Flow Controllers (MFCs), which uses the transfer of pressure to accurately transfer media from the feed, is an alternative strategy to deliver the segmented flow through the KRAIC-S crystalliser.

The work presented on PCM in 60:40 HI in this chapter demonstrates the potential of the technique in terms of data collection and the associated information obtained from the data processing for other systems in the future. The serial-crystallography approach to data capture will be employed for the analysis of X-ray and photosensitive samples.

The use of the slug triggering mechanism can also be employed during data collection at I11 for future KRAIC-D experiments, which will greatly reduce the significant background subtraction previously employed in the continuous collect strategy, whilst also increasing the hit rate. The slug triggering can be used in future to avoid collecting unnecessary data at I11 with the KRAIC-D, such as background frames of the air slugs and the carrier fluid, thus removing time-consuming post-data collection analysis and allowing quick interpretation of the data quality allowing alterations to the experimental set-up to be made promptly.

Chapter 6 – Crystal Engineering for Materials Discovery: Co-crystals in the Profen family

6.1 Introduction and Aims of Research

The Biopharmaceutics Classification System (BCS) is a scientific framework to categorise drug substances based upon their aqueous solubility and intestinal permeability. According to the BCS, drug substances can be categorised in terms of permeability and solubility: high permeability / high solubility (BCS I), high permeability / low solubility (BCS II), low permeability / high solubility (BCS III) and low permeability / low solubility (BCS IV).[14, 26] The use of crystal engineering for materials discovery, to improve physicochemical properties of a drug through co-crystallisation of the API with a benign co-former, can provide a means of improving drug solubility as well as stability.[160]

Many APIs can be susceptible to polymorphic transformations, sensitive to moisture and exhibit the potential for solvent loss, whilst under the influence of raised temperature conditions.[52, 161, 162] This causes problems in hot climates where shelf life (also known as expiration dating period) of pharmaceuticals is reduced when an instability to heat is evident; this can result in the need for APIs requiring refrigerated storage, which is not always convenient for patients. The stability testing to ascertain an appropriate shelf-life should be suitably chosen to cover storage, shipment, and subsequent use of the pharmaceutical product.

Similarly, APIs can be susceptible to polymorphic transformations, as well as solvate formation, whilst under the influence of relatively mild humidity conditions. This instability to humidity can cause problems particularly when drug products are stored in humid countries before being administered, but also in early stages of the pharmaceutical supply chain, in drug production and transportation. The use of co-crystal formation can improve drug resistance to humidity changes, compared to the API alone, eliminating these undesirable phase transformations from occurring.[161, 162]

In addition to the discovery of new API-containing multi-component materials, with the target of optimising physical properties, the work presented in this chapter encompasses property determination and transfer of the process between different crystallisation methods for the production of these materials, offering an increased scale of production in preparation for

potential continuous flow crystallisation. These methods include evaporative, cooling, mechanochemical, slurrying and flow crystallisation (the last of these for one complex, IBU-ISO, only). These aspects are important in the context of the crystallisation basis of the overall project, whereby using these standard crystallisation techniques in batch allows for the discovery of novel materials. Some of these materials have the potential to be investigated in the novel KRAIC-D and KRAIC-S platforms coupled with the corresponding advanced data processing procedures presented in Chapter 4 and Chapter 5 respectively, driving capabilities towards novel materials crystallised in novel crystallisation platforms.

In order for the co-crystallisation of pharmaceutical co-crystals to be compatible with the safety and environmental requirements adopted in the pharmaceutical industry, where crystallisations are carried out in batch at scale, or *via* continuous production methods, careful selection of solvent is required. A solvent mixture of 60:40 water:isopropanol H_2O:IPA (v/v) is compliant with GRAS (Generally Regarded as Safe) Food and Drug Administration (FDA) classification, for deployment in industrial pharmaceutical processes and thus is a suitable solvent choice for batch scale-up and continuous crystallisation development. Co-crystallisation using a solvent mixture of 60:40 H_2O:IPA (60:40 HI) was investigated for a range of candidate co-crystal systems *via* evaporative, mechanochemical, slurrying and cooling methods, initially focused on batch scale-up towards continuous crystallisations. The use of 60:40 HI is an appropriate solvent choice as co-crystallisation can be achieved in pure IPA; although the pure APIs examined exhibit poor aqueous solubility, an aqueous solvent mixture offers the ability to achieve co-crystallisation whilst maintaining pharmaceutical compliance.

2-arylpropionic acid derivatives, also known as the profen family, are a sub-class of non-steroidal anti-inflammatory drugs (NSAIDs), comprising flurbiprofen, ibuprofen, ketoprofen, naproxen, tiaprofenic acid and oxaprozin. This work focuses on four of the profens: flurbiprofen (FLU), ibuprofen (IBU), ketoprofen (KETO) and oxaprozin (OXA) (Figure 6.1) all classified as BCS Class II, with poor solubility and high permeability, which impacts dissolution of the drug product, as well as the rate and extent of absorption of the solid oral dosage form.[26] Exploring co-crystal formation for these profens could help improve the inherent poor solubility of these targets, which have aqueous solubilities of 0.0105 mg/mL, 0.120 mg/mL, 0.0325 mg/mL and 0.184 mg/mL at room temperature for FLU,[163, 164] IBU,[165] OXA,[166] KETO,[167] respectively. Potential enhancements in physical properties of these target materials using a variety of API:co-former systems in various solvents at various temperature

regimes are explored. Investigations initially include evaporative crystallisations which are then translated into further crystallisation methods, including mechanochemical, slurrying and cooling, with a variety of API:co-former ratios in order to obtain significant coverage of the design space.

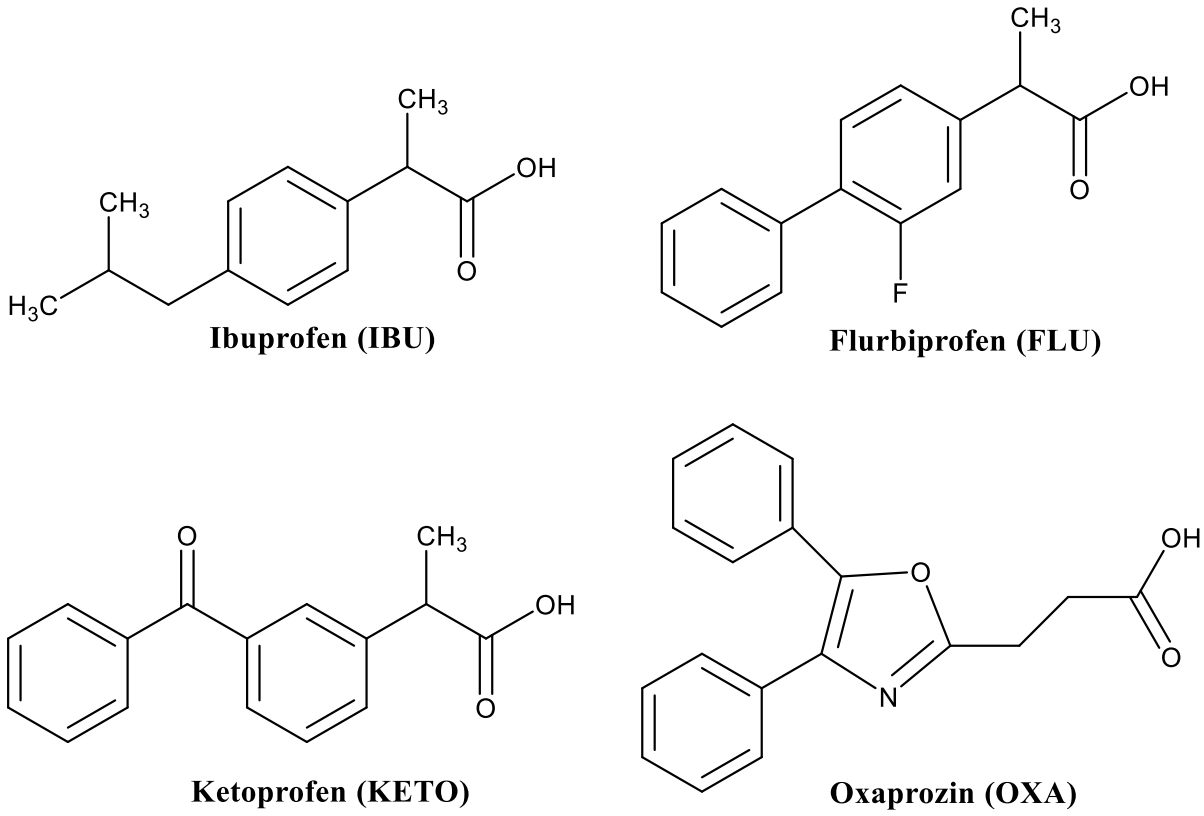

Figure 6.1 – Chemical structures of the target materials from the profen family.

A Cambridge Structural Database (CSD) search carried out of the four profen targets (Table 6.1) found that IBU exhibits two polymorphic forms each adopting the $P2_1/c$ space group, but featuring different lattice parameters. IBU form II (CSD refcode IBPRAC04) was accessed by Derollez *et al. via* annealing of the quenched IBU at 258 K and thus as this polymorph is not accessed under ambient conditions, this form is not expected nor considered in this study.[168] FLU features three polymorphic forms (FLU form I, II and III) and a hydrate form under ambient conditions whereas neither KETO nor OXA exhibit polymorphism. Whilst the profen targets of interest, with the exception of OXA, contain both enantiomeric forms, this work will primarily focus on the racemic form. Published examples of the profen family targets co-crystals typically feature pyridine rings or nitrogen-based substituents on benzene rings (Table 6.2 and Figure 6.2). There are no reported co-crystals of KETO currently in the CSD.[33]

Table 6.1 – CSD Refcodes for the four profen targets.

Profen Target	CSD Refcode
rs-Ibuprofen (IBU)	IBPRAC
rs-Flurbiprofen (FLU)	FLUBIP
rs-Ketoprofen (KETO)	KEMRUP
Oxaprozin (OXA)	OJURAO

Table 6.2 – CSD Refcodes for the existing co-crystals of the four profen targets.

Co-former molecule	IBU	FLU	KETO	OXA
4,4-bipyridine	HUPPAJ IJIHOZ IJIJAN	HUPPEN	-	OJUQOB
1,2-bis(4-pyridyl)ethane	OWIGEH	-	-	OJUQAN
Trans-1,2-bis(4-pyridyl)ethylene	-	HUPPIR	-	-
Nicotinamide	SODDIZ	QOBGAR	-	-
D/L-Proline	-	VEVMOB/ VEVMUH	-	-
2-aminopyrimidine	TAWSOB	-	-	-

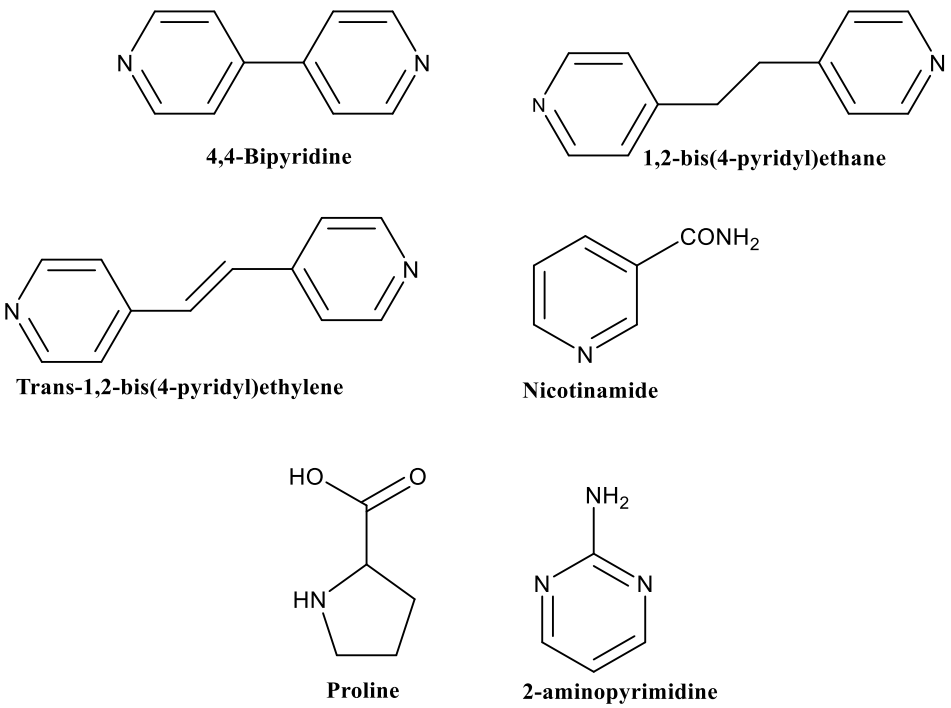

Figure 6.2 – Chemical structures of the co-former molecules involved in co-crystal formation with the four profen family targets.

On the basis of this CSD search, co-former molecules with nitrogen functionalities were selected, due to their proven ability in co-crystal formation with the profen family. Additionally

some GRAS molecules were selected, on the premise these molecules contained either a nitrogen or an oxygen functionality, such as a carboxylic acid or hydroxyl group, which have the potential to facilitate hydrogen bond formation. As GRAS molecules are considered pharmaceutically acceptable, incorporation of GRAS molecules in crystal engineering studies offers the potential to discover a novel pharmaceutical co-crystals, with the opportunity to be marketed as a drug product.[169] The chemical structures of the co-former molecules selected are shown in Figure 6.3.

6.2 Materials and Methods

IBU, FLU, OXA and KETO were purchased from TCI UK Ltd (Oxford, UK). All co-former molecules and laboratory grade solvents were purchased from Sigma Aldrich Chemie Gmbh (Steinheim, Germany). All reagents were used without further purification. The matrix of conditions for this profen family materials discovery screen, comprised four targets, fifteen co-formers, three solvents and five temperature regimes (Table 6.3).

Powder X-ray Diffraction (PXRD) and Differential Scanning Calorimetry (DSC) were initially used to screen all samples for the formation of a novel co-crystal(s). This led to the identification of three new co-crystals: IBU-ISO, OXA-ISO and OXA-IMID, which were structurally characterised using Single Crystal X-ray Diffraction (SCXRD) after single crystals of suitable quality were obtained through evaporative crystallisation methods. It should be noted that while IBU-ISO was discovered by the author in 2017, Walsh *et al.*[170] published the crystallisation of IBU-ISO in 2018 by a different crystallisation methodology and determined the X-ray crystal structure (CSD Refcode KIPPAD). The Walsh *et al.* study compares spray drying *versus* hot melt extrusion to engineer the pharmaceutical co-crystal IBU-ISO in an excipient matrix.

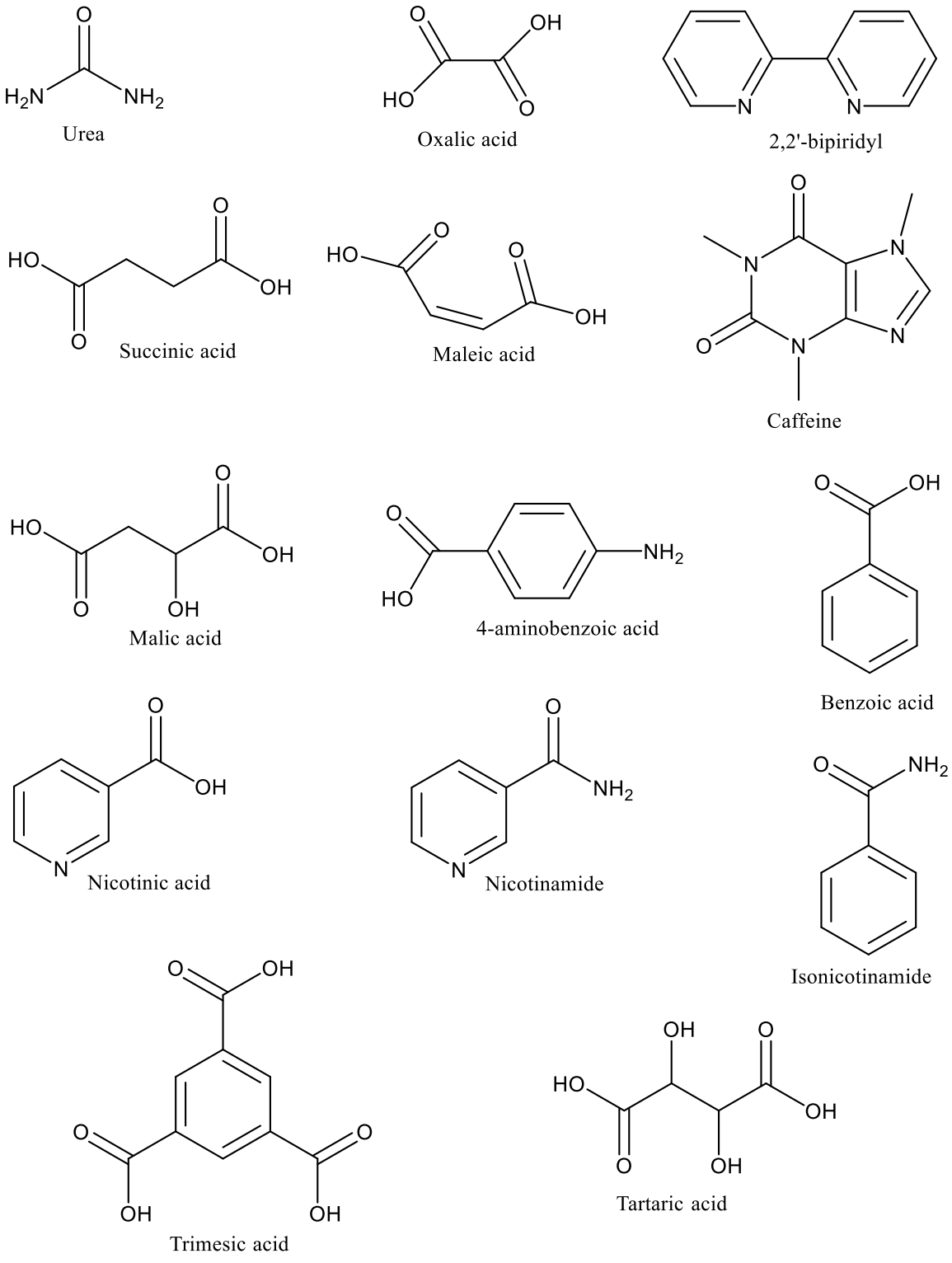

Figure 6.3 – Chemical structures of co-former molecules used in co-crystallisations with profen targets.

Table 6.3 – Matrix of conditions to be investigated for the materials discovery of the profen family *Classified as GRAS by the Select Committee on GRAS substances (SCOGS).

API	Co-former	Ratio	Solvent	Temp /°C
IBU	Urea*	1:1	Ethanol (EtOH)	4
FLU	Oxalic acid	1:2	Isopropanol (IPA)	18
OXA	Succinic acid		Acetone (ACE)	30
KETO	Maleic acid			40
	Benzoic acid			50
	4-aminobenzoic acid			
	Nicotinic acid*			
	Nicotinamide (NICO)			
	Isonicotinamide (ISO)			
	2,2-bipyridine			
	Trimesic acid			
	L-tartaric acid*			
	L-malic acid*			
	Caffeine			
	Imidazole (IMID)			

6.2.1 Evaporative Crystallisation for Co-crystal Screening

Small-scale evaporative crystallisations were prepared in 7 mL vials. The four profen family targets were combined in a 1:1 molar ratio with the co-former, using a consistent mass of 20 mg of the target. The API and co-former components were dissolved in minimal solvent (approximately 1-2 mL) at room temperature, with the use of sonication to aid dissolution of the materials. Once materials had fully dissolved, the lids were then punctured with four holes and left at the various temperature regimes detailed in Table 6.3, without the use of stirring, to allow for slow evaporation of the solvent (Figure 6.4).

Figure 6.4 – Welled DrySyn forms fitted on hot-plates for crystallisation *via* evaporation of the solvent at elevated temperatures of 30, 40 and 50 °C.

6.2.2 Mechanochemical Crystallisation

The co-crystals resulting from the evaporative screens were translated into both neat grinding (NG) and Liquid Assisted Grinding (LAG) methods using the same solvents as those in the evaporative screening, to investigate whether the use of mechanical energy could also favour the co-crystal formation achieved *via* evaporative crystallisation. The grinding was carried out in the same 1:1 molar ratio, by hand using a mortar and pestle, initially for 5 minutes and subsequently for 30 minutes. For the LAG, 3-4 drops of solvent were incorporated with the solid materials.

6.2.3 Slurrying Crystallisation

Solution Mediated Phase Transformations (SMPTs) can be investigated *via* slurrying crystallisation. This method of crystallisation is a suspension technique, whereby an excess of solid is added to solvent and stirred for a period of time without solid dissolution. This method can be used to investigate the effect of solution phases within a crystallisation process. The polymorph obtained from slurrying crystallisations can be tuned by varying experimental parameters such as slurrying time, stirring rate, temperature, solid loading and scale of operation.[8] All co-crystals obtained through evaporative crystallisation were translated into

slurrying techniques, which in addition to allowing novel polymorph identification, or providing a way to establish the thermodynamic form from concomitant polymorphs with similar Gibbs Free energies, can be used to screen for novel multi-component materials.

6.2.4 Cooling Crystallisation

All co-crystals resulting from the evaporative screening were also produced *via* controlled batch cooling crystallisations initially at 1 mL scale with a range of concentrations, progressing towards batch cooling crystallisations up to the 200 mL scale. After dissolution, the solution was subjected to a linear cooling regime with magnetic bottom stirring using the Cambridge Reactor Design (CRD) Polar Bear Plus crystalliser (Figure 6.5). The cooling rates investigated were increased from 0.05 to 1 °C min^{-1} (Appendix 6.1) over subsequent cooling crystallisations, towards the cooling rates adopted in industry. Translation of the batch cooling crystallisations to continuous flow crystallisations in the KRAIC / KRAIC-D platforms was established and optimised for IBU-ISO.

Figure 6.5 – Cambridge Reactor Design (CRD) Polar Bear Plus crystalliser for temperature controlled batch cooling crystallisations.

6.2.4.1 Solubility Measurements

To access the co-crystals *via* cooling, an understanding of the solubility behaviour of the various materials was required. Solubility studies were carried out on a physical mixture of the two starting components in a mixed solvent system of 60:40 (v/v) water:isopropanol (H_2O:IPA, HI) for each of the three profen family co-crystals using turbidity measurements in the Technobis Crystal16 at small (1 mL) scale initially.

The solubility of the physical mixture of IBU and ISO showed interesting 'oiling out' behaviour, which led to further investigation in the Technobis Crystalline at 5 mL scale, with in-line Particle Visualisation Measurement (PVM). Laser-based turbidity measurements and images are collected in parallel, allowing for improved accuracy compared to turbidity measurements alone. Both Crystal16 and Crystalline turbidity measurements were carried out at the University of Strathclyde, Glasgow.

6.2.5 Stability Testing

6.2.5.1 Thermal Stability

Samples of the three co-crystals and their IBU and OXA starting API targets, prepared by LAG in 60:40 HI for 30 minutes, were stored under moderate heat of 45 ℃, within a temperature controlled oven. The samples were subjected to thermal ageing and monitored over the course of a month. Sampling occurred each week *via* PXRD using the STOE STADI powder X-ray diffractometer and DSC.

6.2.5.2 Humidity Stability

The co-crystals were prepared for humidity storage by both mechanochemical methods using LAG for 5 minutes and slurrying techniques for 24 hours at 10 mL scale. Products of both of the crystallisation methods were investigated under moderate (20 ℃ and 46 % relative humidity (RH)) humidity conditions using a salt solution[171] over a 40 day period and analysed at various time intervals. In addition, the mechanochemical samples were also put under severe (45 ℃ and 80 % RH) humidity conditions using a controlled oven to ascertain the impact of this additional stress on the co-crystal.

Moderate humidity testing used a sealed plastic container filled with approximately 400 g potassium carbonate mixed with approximately 10 mL of deionised water. A humidity sensor was suspended on a plastic shelf within the sealed container (Figure 6.6). Severe humidity testing was carried out in a temperature and humidity controlled oven. The temperature and humidity conditions were allowed to equilibrate for 24 hours for both moderate and severe humidity conditions. The samples that were subjected to humidity ageing were monitored over the course of 4, 7, 14, 21, 28 and 40 days *via* PXRD. The initial experimental set-up and PXRD measurements were carried out by the author at the University of Strathclyde, Glasgow with Dr. Alan Martin, while data collected one week onwards was obtained in absence of the author.

A small quantity (10-50 mg) of sample was analysed using reflection Bragg-Brentano PXRD, collected on a Bruker D8 Discover diffractometer configured for θ/θ geometry, with Ni filtered $K_{\alpha 1,2}$ Cu radiation, λ = 1.540596 Å, line focused. Samples were mounted on a six position sample auto sampler. Samples were rotated at a rate of 15 rotations per minute throughout data collection to maximise particle sampling and minimise preferred orientation effects.

Figure 6.6 – Inside of humidity ageing unit containing raised ledge for humidity sensor (left) and humidity sensor within sealed plastic container containing salt solution slurry (right).

6.3 Analysis

Diffraction Analysis

6.3.1 Single Crystal X-ray Diffraction (SCXRD)

Ibuprofen Isonicotinamide (IBU-ISO)

SCXRD data for the IBU-ISO co-crystal was collected on an Agilent Technologies Supernova diffractometer, using Cu radiation (λ = 1.5406 Å) at 150 K. The sample temperature was controlled using an Oxford Diffraction Cryojet apparatus.

Due to the disorder in the initial structure of IBU-ISO co-crystal obtained from the laboratory diffractometer, attempts were made to improve data quality through use of the Advanced Light Source (ALS) synchrotron, Berkeley, USA. Data was collected at 150 K with a 17 keV X-ray source with 1 % and 10 % transmission filters applied to only the first run, with a 1 s exposure applied for all runs. Similar to that obtained using the laboratory source diffractometer, the IBU-ISO structure obtained from the synchrotron data suffered from disorder. In light of this, the IBU-ISO structure obtained from the Supernova laboratory diffractometer is presented, with disorder restraints applied to improve the structural model.

Oxaprozin Isonicotinamide (OXA-ISO)

SCXRD data for the OXA-ISO co-crystal was collected at the ALS synchrotron. Data were collected at 150 K with a 17 keV X-ray source with various transmission filters 0.1 % and 10 % for run 1, 10 % and 10 % for run 2 and 10 % and 25 % for runs 3, 4 and 5 applied to the 0.5 s exposure utilised for all runs.

Oxaprozin Imidazole (OXA-IMID)

SCXRD data were recorded on an Agilent Technologies Gemini A Ultra CCD diffractometer, using monochromatic Mo-Kα radiation (λ = 0.71073 Å). The diffractometer operated with use of an Atlas CCD area detector and an Oxford Instruments CryojetXL liquid nitrogen flow apparatus. The latter was used as a method of sample temperature control; data were collected in the range 150-340 K.

Both the Supernova and the Gemini A Ultra CCD diffractometers were equipped with the Rigaku-Oxford diffraction software CrysAlis Pro, which was used to collect, index and prepare data for structural interpretation, whilst the Bruker software equivalent Apex3 was utilised for the ALS synchrotron data. These data were then analysed in SHELXT using dual-space methods and SHELXL with least squares refinement programmes, used to solve and refine the crystal structure respectively. Both programmes were executed as part of the GUI Olex2 software package. Visualisation and analysis of the crystal structures produced was then conducted in Mercury.

Thermal Analysis

6.3.2 Thermogravimetric Analysis (TGA) coupled with Mass Spectrometry (MS)

Thermogravimetric Analysis (TGA) measures the mass loss of a sample as a function of temperature and thus can be an effective way to ascertain the stoichiometry of solvates (API:solvent molecule or API:Co-former:solvent molecule stoichiometric ratios). This is particularly important where a solvent may be present in non-stoichiometric quantities or non-uniformly within the lattice, and where this may depend on how tightly bound the solvent is within the crystal structure. In addition to quantifying the stoichiometry of solvates, TGA can be coupled with Mass Spectrometry (MS) in order to identify the gaseous phase evolving during the heating process. TGA also allows the decomposition behaviour of a material to be investigated.

6.3.3 Hot-Stage Microscopy (HSM)

A single crystal or a small quantity of the crystalline material produced from crystallisation was put onto a glass slide, which was then placed into a Mettler Toledo FP82 Hot-Stage set-up equipped with a Leica DM1000 microscope. The crystalline sample was subject to a specified heat program using the FP90 Processor, defining the initial and final temperature as well as the heating rate. The resultant activity, such as melting of the sample, was recorded using an Infinity 2 microscopy camera.

Spectroscopy

6.3.4 Infrared (IR) Spectroscopy

Fourier Transform Infrared (FTIR) spectra were recorded at room temperature using a Perkin Elmer FTIR Spectrometer in the range 4000-500 cm^{-1} with an ATR (Attenuated Total Reflection) sampling accessory. The profen family co-crystals prepared by LAG in 60:40 HI for 30 minutes were compared to the spectra from their constituent starting materials prepared by the same method. The functional groups of focus were C=O and N-H due to their hydrogen bonding capabilities often observed during co-crystal formation.

6.3.5 Particle Visualisation Measurements (PVM) Inline Images on Crystalline®

The Crystalline® platform features in-line particle visualisation technology with “through the vial” analytical capabilities, such as PVM to observe crystal formation and dissolution in real time, with images collected every minute monitored as a function of time and temperature.

Results and Discussion

6.4 Ibuprofen Isonicotinamide (IBU-ISO)

6.4.1 Evaporative Crystallisations of IBU-ISO

The PXRD patterns for IBU_ISO (IBU 20 mg) in a 1:1 ratio dissolved in approximately 2 mL of EtOH, IPA and ACE solvent systems, evaporated at 30 °C, indicate that each of these co-crystallisation attempts yielded the same potential co-crystal *via* evaporative methods, when compared to the PXRD patterns of the starting materials. The presence of new peaks, the most prominent at 2θ of 9°, not present in any of the starting material PXRD patterns (Figure 6.7), is evidence of co-crystal formation. Excess IBU is evident in each of the evaporative samples indicated by the representative IBU peak at 6° 2θ.

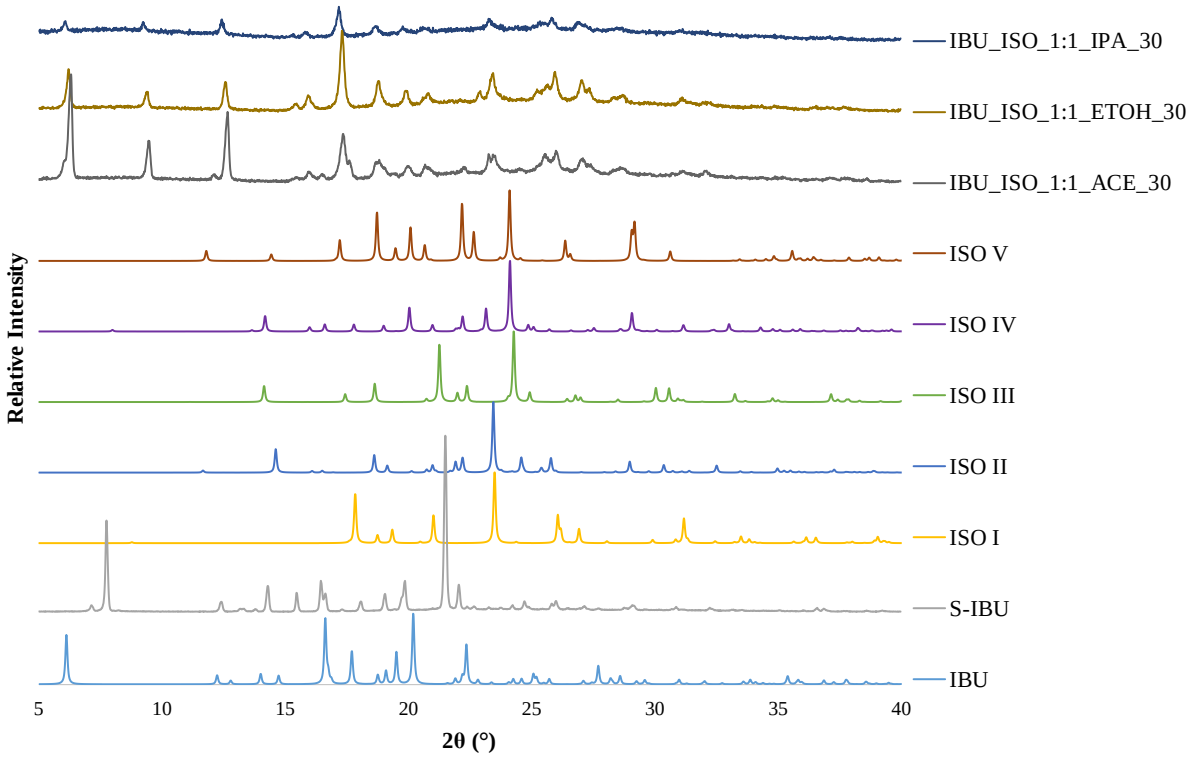

Figure 6.7 – PXRD patterns of the IBU-ISO 1:1 molecular complex prepared via evaporative crystallisation in three different solvents each at 30 °C, compared to the PXRD patterns of the constituent starting materials including various polymorphic, racemic and S-enantiomeric forms (Refcodes: IBPRAC (IBU), JEKNOC (S-IBU), EHOWIH01-05 (ISO I-V respectively)).

The same samples analysed *via* PXRD, were also analysed by DSC using a ramp rate of 10 °C min^{-1}. The DSC traces for IBU_ISO in a 1:1 ratio dissolved in these three solvent

systems, further indicate the formation of potential IBU-ISO co-crystal by evaporation. The DSC traces show an endothermic event around 121 °C for each of these attempted co-crystallisations, which does not correspond to a thermal event of either of the starting materials, which exhibit melting endotherms at 77 °C and 158 °C for IBU and ISO respectively (Figure 6.8). The DSC trace of IBU_ISO evaporated from ACE also features an additional endotherm around 70 °C, which can be attributed to excess IBU in the sample.

The DSC trace of ISO features a minor endothermic event around 120 °C, which required further investigation. A DSC trace of ISO at a significantly slower ramp rate of 1 °C min^{-1} (Appendix 6.2) allows further elucidation of this thermal event. The DSC data confirms this to be a very subtle endothermic event at 117 °C, compared to the sharp and intense endotherm attributed to the melting event of ISO at 158 °C; the melting endotherm of the co-crystal is at a higher temperature of 121 °C and is also sharp and intense. The melting point of the IBU-ISO co-crystal is intermediate between the two starting materials and thus has an increased thermal stability relative to the API IBU.

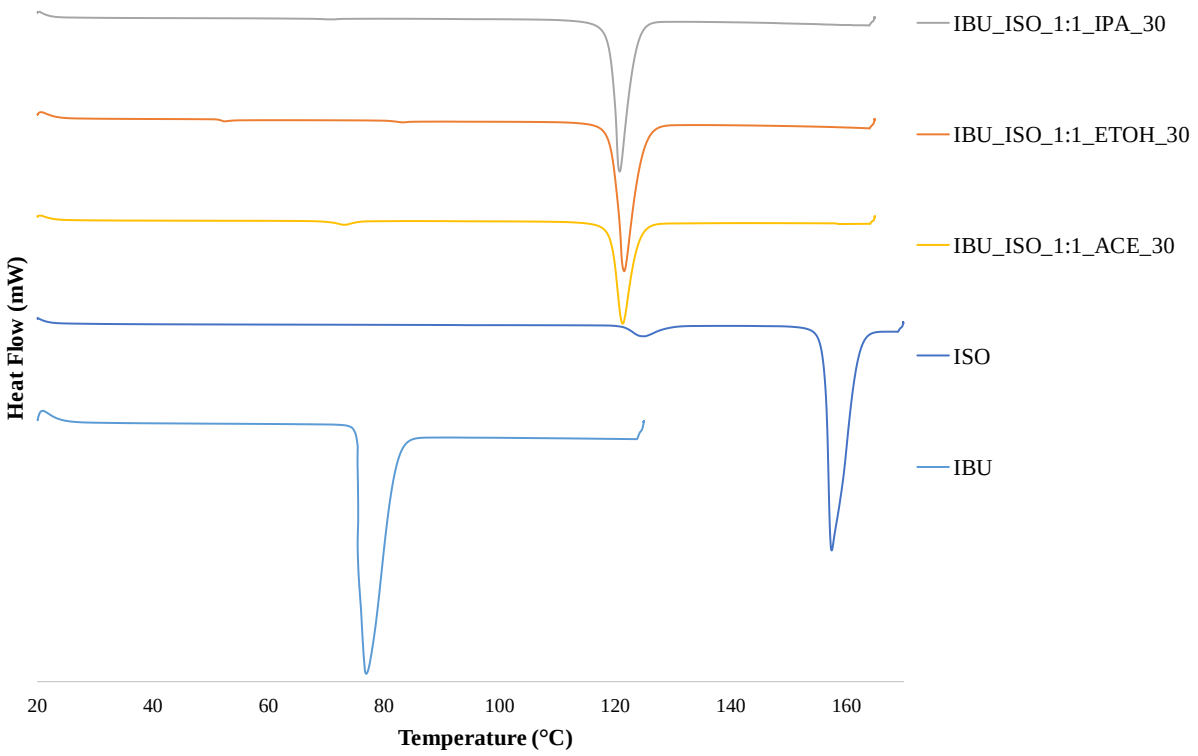

Figure 6.8 – DSC heat profile for the molecular complex IBU-ISO 1:1 prepared *via* evaporative crystallisation methods in ACE, EtOH and IPA solvent systems at 30 °C.

Structural determination of IBU-ISO

Masses of 20 mg of IBU and 11.8 mg of ISO (1:1 molar ratio) were dissolved in 2 mL of ACE and the solvent allowed to evaporate at 30 ℃ producing single crystals of suitable quality for analysis (Appendix 6.3). A suitable single crystal was subjected to SCXRD analysis; the crystal data for IBU-ISO is summarised in Table 6.4.

Table 6.4 – Crystal data and structural refinement parameters for IBU-ISO.

Empirical formula	**$C_{19}H_{24}N_2O_3$ ($C_{13}H_{18}O_2 \cdot C_6H_6N_2O$)**
Formula weight	328.40
Temperature /K	292.05(10)
Crystal system	Triclinic
Space group	$P\bar{1}$
a /Å	5.7031(3)
b /Å	11.5570(4)
c /Å	27.7335(18)
α /°	95.483(4)
β /°	93.695(5)
γ /°	102.004(4)
Volume /Å^3	1773.10(16)
Z	4
ρ_{calc} /g cm^{-3}	1.230
μ /mm^{-1}	0.084
F(000)	704.0
Crystal dimensions /μm	200 × 40 × 10
Radiation /Å	MoKα (λ = 0.71073)
2θ range for data collection /°	6.594 to 50.7
Index ranges	$-6 \leq h \leq 6$, $-13 \leq k \leq 13$, $-33 \leq l \leq 33$
Reflections collected	30522
Independent reflections	6467 [R_{int} = 0.0697, R_{sigma} = 0.0597]
Data/restraints/parameters	6467/196/518
Goodness-of-fit on F^2	1.156
Final R indexes [I>=2σ (I)]	R_1 = 0.1182, wR_2 = 0.2260
Final R indexes [all data]	R_1 = 0.1612, wR_2 = 0.2482
Largest diff. peak/hole /e Å^{-3}	0.67/-0.35

The IBU-ISO 1:1 co-crystal crystallises in the triclinic space group $P\bar{1}$, with two molecules of IBU and two molecules of ISO in the asymmetric unit. On co-crystal formation, a hydrogen bonding interaction is produced between the oxygen on the carbonyl group of the carboxylic acid of IBU and the amide nitrogen of ISO, depicted by the blue dotted line in Figure 6.9. The crystal structure of IBU-ISO contains the common acid-pyridine hydrogen bonded heterosynthon and intermolecular O-H···N hydrogen bond. The IBU and ISO molecules are

held together by a strong to moderate strength intermolecular hydrogen bond with a bond length of 2.608(5) Å and bond angle of 166.2° for O3-H3···N4, with the corresponding hydrogen-to-acceptor (H3···N4) bond length of 1.804 Å (Figure 6.9).

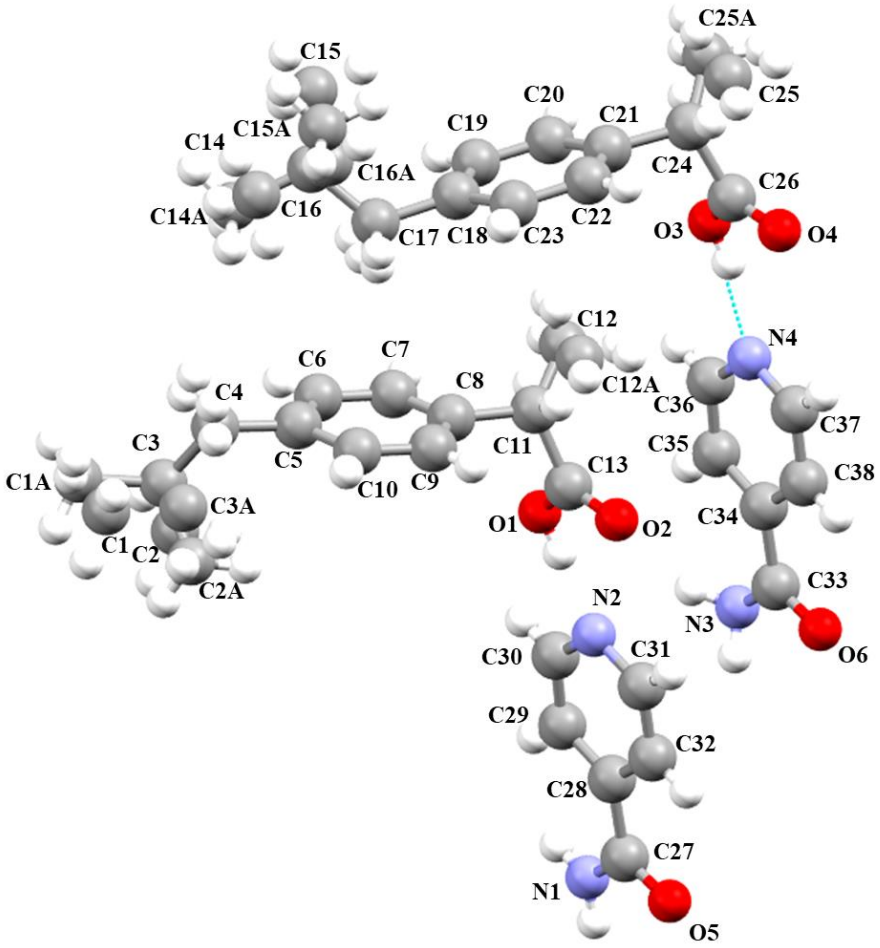

Figure 6.9 – The asymmetric unit of the novel co-crystal structure IBU-ISO.

Beyond the asymmetric unit, dimers of ISO containing hydrogen bonding between the amide nitrogen and the oxygen on the carbonyl group can be observed, whereby ISO dimers are formed through a $[R^2_2(8)]$ homosynthon (Figure 6.10). Also in the layers of molecules, a hydrogen bonding interaction is observed between the nitrogen on the pyridine ring in ISO with the oxygen on the alcohol group in the carboxylic acid functionality found in IBU. Intermolecular hydrogen bonds are also present between the layers, which is the same bonding interaction described for the asymmetric unit. The phenyl rings of the IBU and ISO units do not sit within the same molecular plane, with the angle relating the mean planes of the phenyl rings for the API and co-former molecule equating to 83.72°. The intermolecular hydrogen bond O3-H3···N4 also sits in another plane to the planes incorporating the sets of phenyl rings,

whereby the angle from this intermolecular hydrogen bond to the mean plane of the IBU and ISO rings equates to 87.28° and 24.80° respectively.

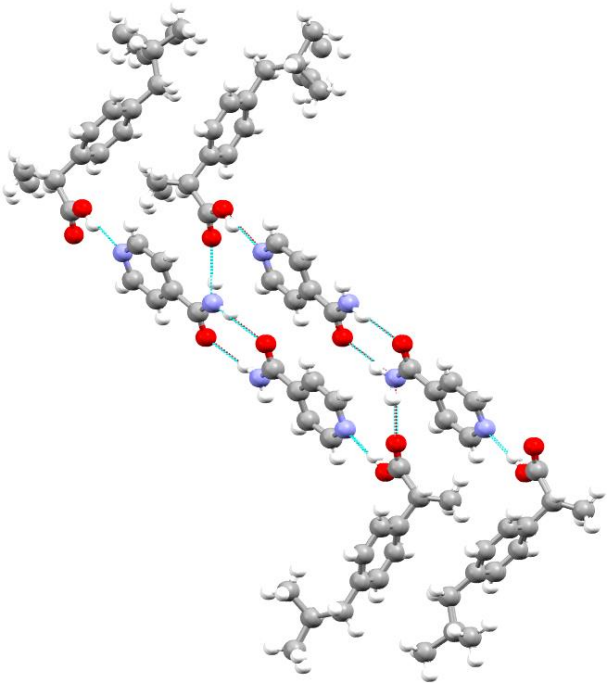

Figure 6.10 – The packing of the novel co-crystal structure IBU-ISO.

6.4.1.1 IR Spectroscopy of IBU-ISO

The IR spectrum of IBU-ISO shows an increase in the N-H stretching frequency of ISO on co-crystal formation, corresponding with the intermolecular hydrogen bond formation of O3-H3···N4. The C=O stretching frequency of IBU-ISO dimers, corresponding with C26-O4 within IBU and the carbonyl functional groups within the ISO dimers, is intermediate between the two starting components (Table 6.5 and Figure 6.11).

Table 6.5 – Comparison of IR stretching frequencies of key functional groups in IBU-ISO compared to the constituent IBU and ISO starting materials.

Vibration Frequency (cm^{-1})	IBU	ISO	IBU-ISO
N-H stretch	-	3362	3434 (H3···N4)
C=O stretch	1708	1656	1698 1681 (IBU C26-O4) (ISO dimers)

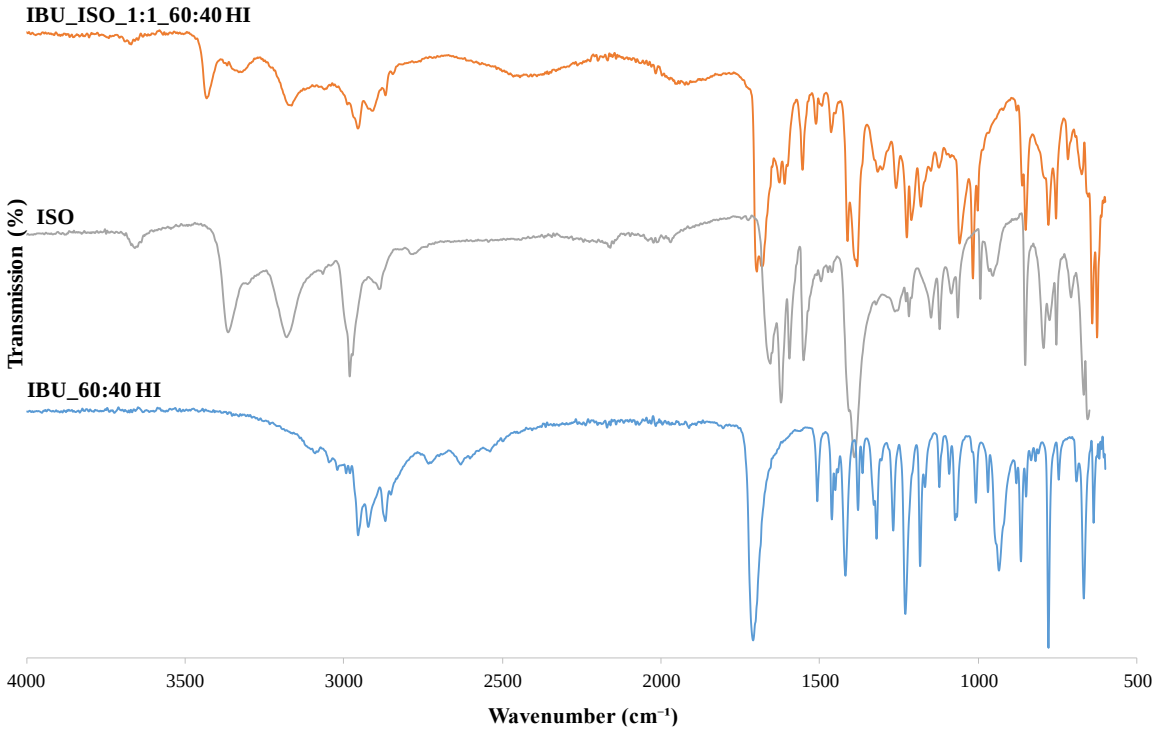

Figure 6.11 – FTIR spectra of IBU-ISO compared to the constituent IBU and ISO starting materials.

Comparing the predicted PXRD pattern of the IBU-ISO co-crystal with IBU-ISO crystallised from evaporative techniques and predicted patterns of the pure polymorphs of the starting components confirmed that a new co-crystalline material has been identified from evaporative crystallisation (Figure 6.12). Subsequent to this work, the PXRD pattern corresponding with the IBU-ISO co-crystal was found to match with the KIPPAD[170] co-crystal reported by spray drying and hot-melt extrusion.

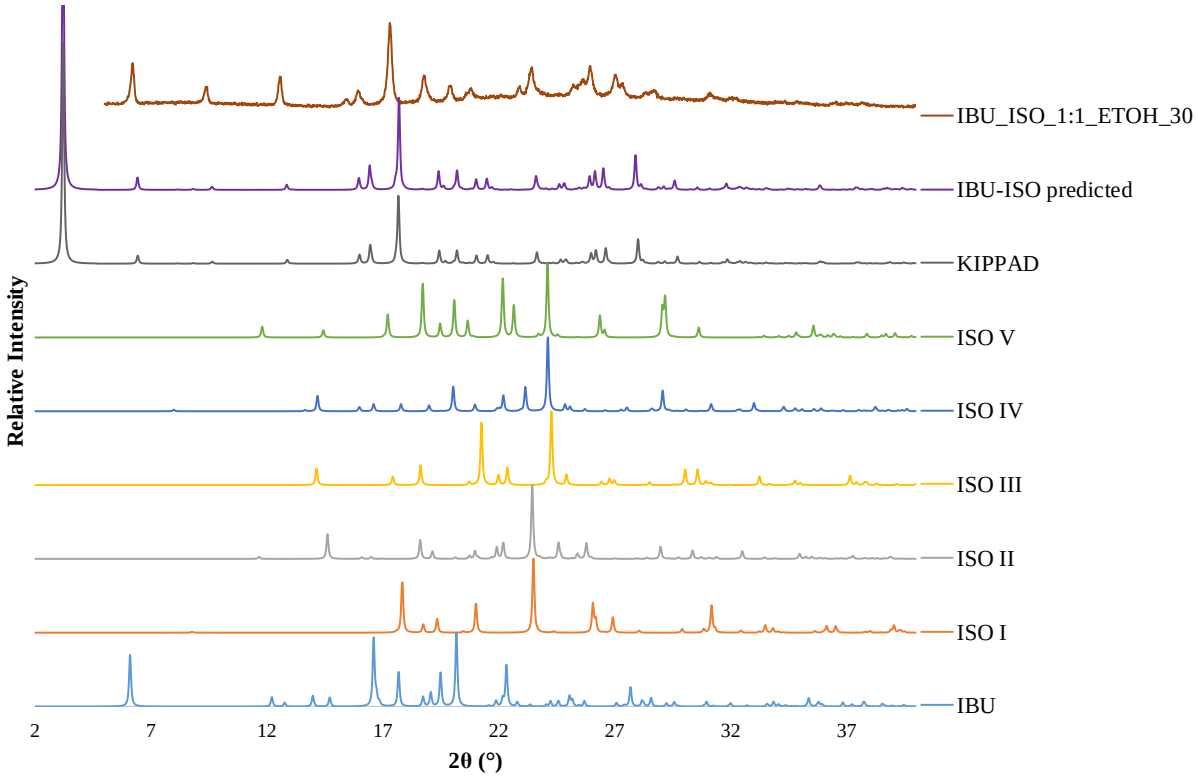

Figure 6.12 – PXRD patterns comparing IBU-ISO predicted pattern simulated in Mercury and IBU_ISO 1:1 evaporated from EtOH, with the PXRD patterns of the polymorphs of the pure starting materials as well as the KIPPAD[170] co-crystal obtained from Mercury (Refcodes: IBPRAC (IBU), EHOWIH01-05 (ISO I-V) respectively). The intense IBU-ISO peak at 2° 2θ has been truncated for clarity.

6.4.2 Mechanochemical Crystallisations of IBU-ISO

Once co-crystal formation for the IBU-ISO co-crystal had been achieved through evaporation and confirmed through SCXRD, PXRD and DSC analytical techniques; this system was translated into grinding approaches.

PXRD confirms the presence of IBU-ISO with an excess of starting material for all experiments presented in Figure 6.13. An increase in grinding time could lead to complete conversion to the co-crystal, or a change in stoichiometric ratio of the starting components could mitigate the excess starting material observed. The peaks are notably broader in the grinding samples than evaporative samples; this peak broadening can be attributed as inherent to the method of grinding, which reduces the particle size of the crystallites.

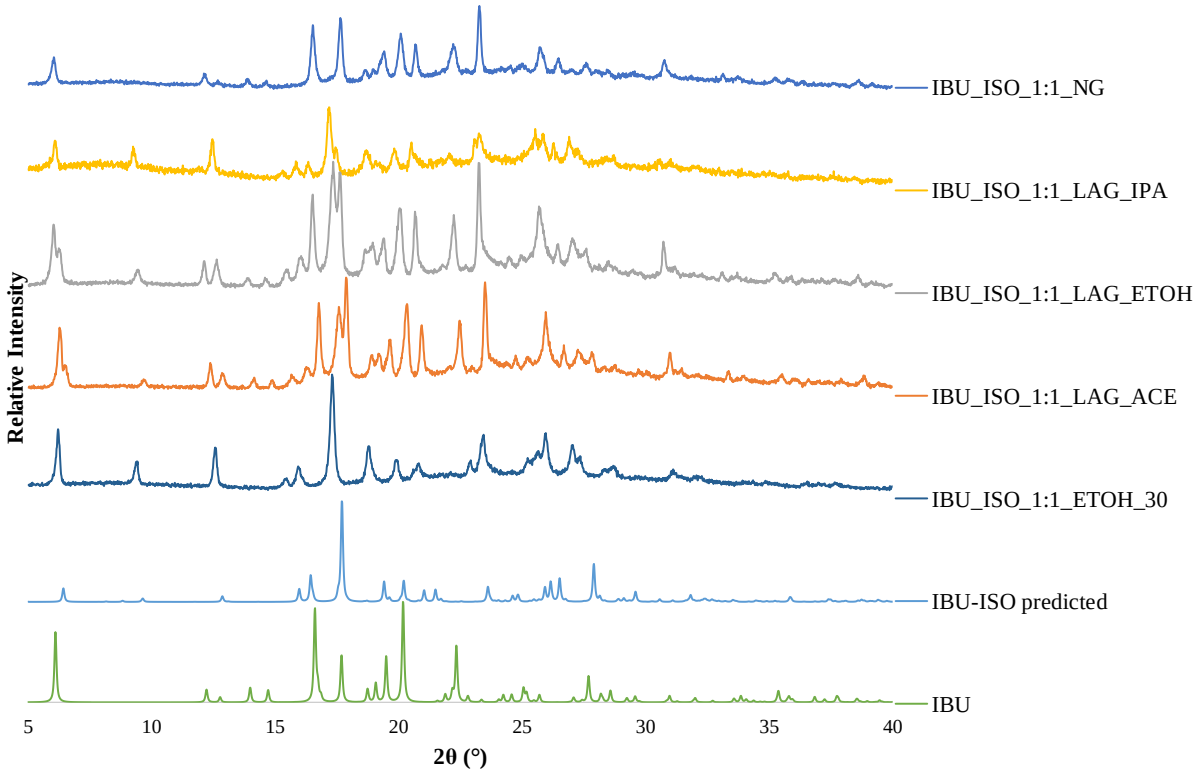

Figure 6.13 – PXRD patterns of the IBU-ISO 1:1 molecular complex prepared *via* mechanochemical crystallisation both NG and LAG in 3 different solvents, compared to the PXRD pattern of the IBU-ISO predicted pattern simulated in Mercury and IBU (Ref code: IBPRAC) and IBU_ISO 1:1 evaporated from EtOH powder patterns.

The DSC traces for IBU-ISO 1:1 co-crystals formed *via* LAG and NG approaches show similar events to those from the evaporative crystallisations. The DSC traces for these mechanochemical crystallisations, also feature an additional endothermic peak compared with the evaporative crystallisations, at approximately 71 °C, attributed to the presence of excess IBU starting material (Figure 6.14). This indicates that mechanochemical crystallisation for five minutes of IBU and ISO 1:1 does not achieve the co-crystal in 100 % yield, evident from both PXRD and DSC analysis; future attempts could look at IBU and ISO 1:2 ratio and an extended grinding time for the mechanochemical crystallisations.

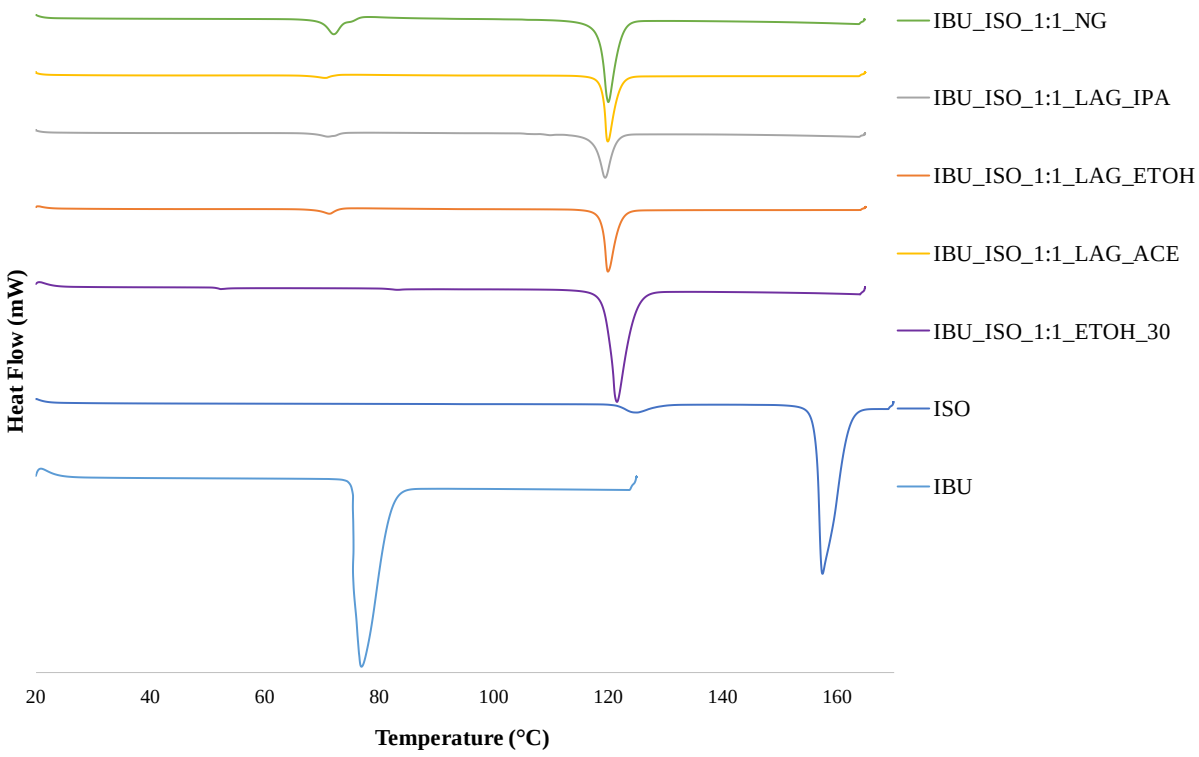

Figure 6.14 – DSC heat profile for the molecular complex IBU-ISO 1:1 prepared via mechanochemical crystallisations using both NG and LAG in ACE, EtOH and IPA solvent systems compared to the DSC trace of the IBU-ISO 1:1 crystallised from evaporation of EtOH, and those of the starting materials IBU and ISO.

6.4.3 Slurrying Crystallisations of IBU-ISO

Investigations into whether the IBU-ISO co-crystal could be accessed using small-scale slurry techniques were conducted using the same three solvents (ACE, EtOH, IPA), as those investigated in evaporative and mechanochemical techniques used to access the co-crystal previously. The slurries were prepared using a 1:1 molar ratio of IBU (400 mg) and ISO in 2 mL of solvent, left stirring at 250 rpm on a hot-plate with DrySyn attachment set to 30 ℃ for one week. After this stirring period, the resultant product was isolated from the solvent using vacuum filtration and left to dry for 24 hours before being analysed *via* PXRD and DSC.

The PXRD analysis carried out after slurrying a physical mixture of IBU_ISO 1:1 in various solvents for one week showed similar results to the evaporative and mechanochemical crystallisations, largely the IBU-ISO co-crystal, but with some additional peaks, which can be attributed to excess IBU starting material (Figure 6.15).

The DSC analysis on the same samples, showed some contrasting results across solvent systems. IBU_ISO slurry mediated in ACE and IPA solvent systems yielded a mixture of IBU and IBU-ISO co-crystal in both cases, whereas when EtOH was used the co-crystal was produced in purity (Figure 6.16). Melting of this co-crystal corresponds to the endotherm in the DSC data at 120 °C; additional peaks within the DSC traces from IBU and ISO slurry-mediated in ACE and IPA correspond to excess IBU.

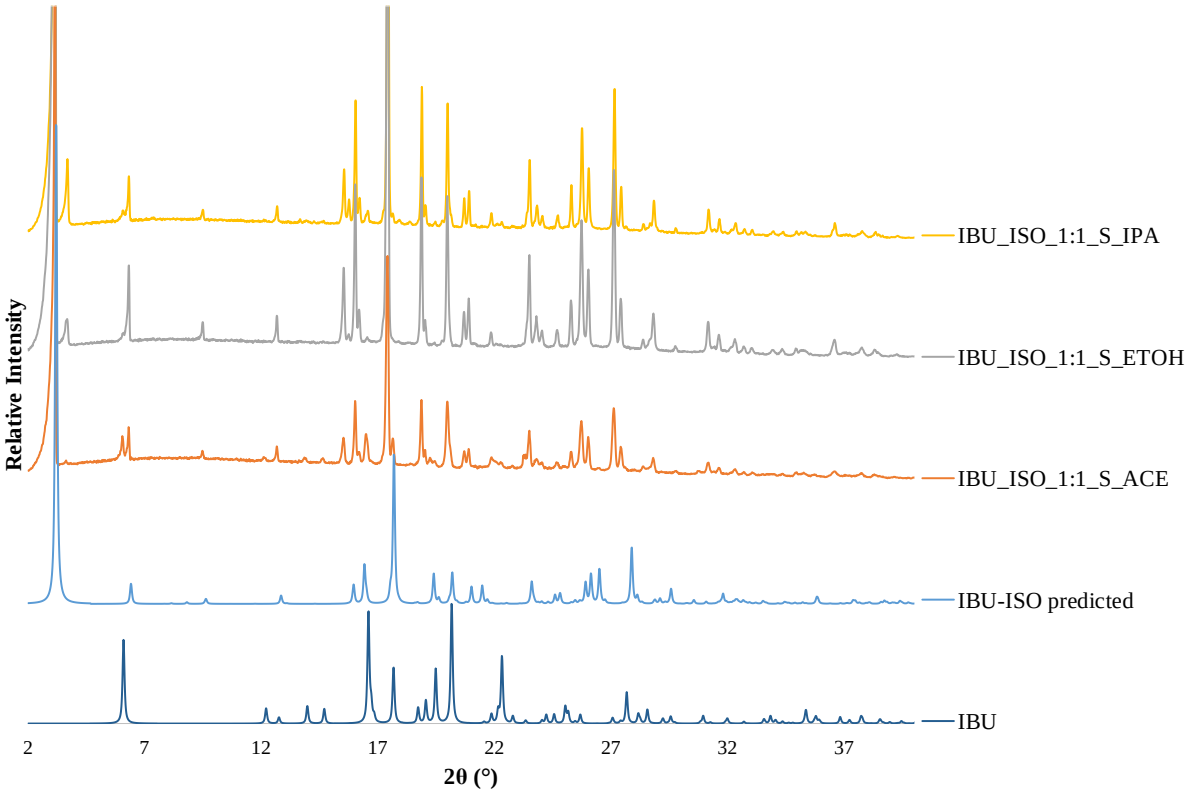

Figure 6.15 – PXRD patterns of the IBU-ISO 1:1 molecular complex prepared *via* slurrying crystallisations for 1 week in three different solvents systems (truncated in intensity), compared with the PXRD pattern of the IBU-ISO predicted pattern simulated in Mercury and IBU (Refcode: IBPRAC) powder pattern.

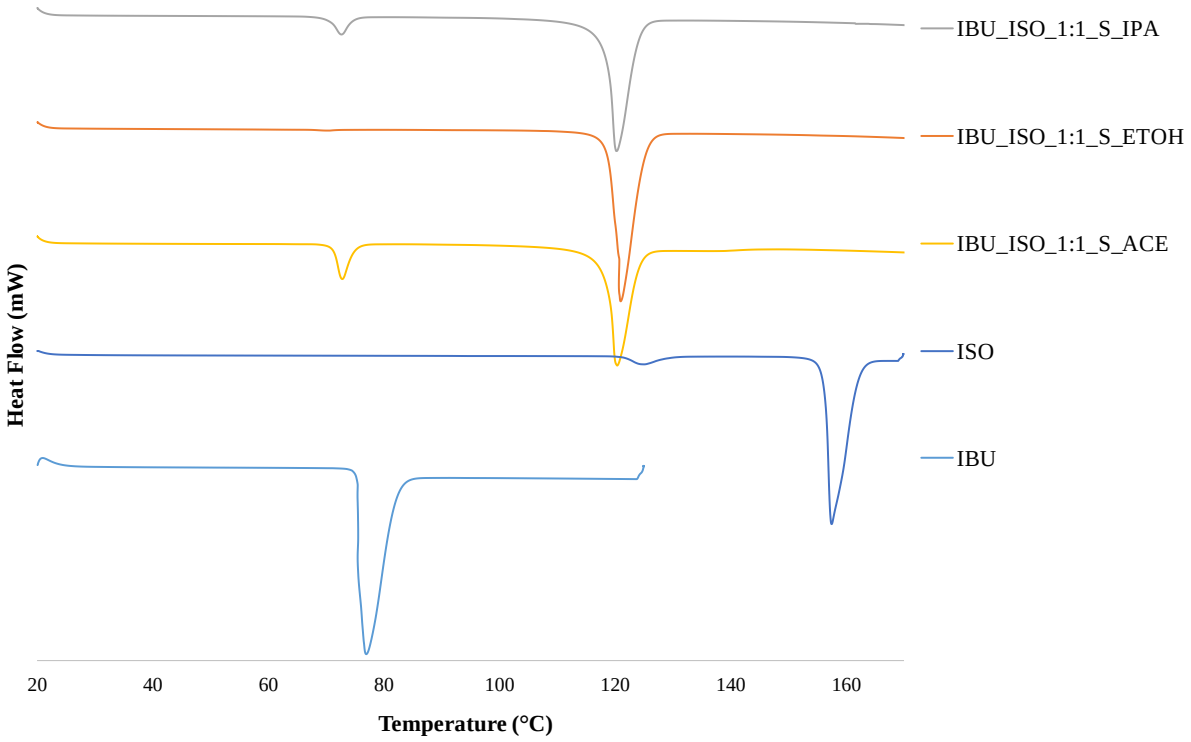

Figure 6.16 – DSC heat profile for the molecular complex IBU-ISO 1:1 prepared *via* slurrying crystallisation for 1 week in ACE, EtOH, IPA solvent systems.

6.4.4 IBU-ISO crystallisations in 60:40 water:isopropanol (HI)

PXRD analysis of attempted co-crystal formation of IBU-ISO in 60:40 HI yielded a mixture of IBU and IBU-ISO *via* LAG for 5 minutes and *via* evaporative crystallisation at 30 ℃, whilst slurrying for 24 hours at 20 ℃ produced pure IBU (Figure 6.17). This slurry result indicates that IBU is less soluble than the co-crystal and more thermodynamically stable. The PXRD analysis across the crystallisation methods is in agreement with the DSC analysis, which clearly show two endotherms at 78 ℃ and 120 ℃ confirming the presence of IBU and IBU-ISO respectively in both the evaporative and mechanochemical experiments. In contrast, slurrying IBU and ISO in 60:40 HI yielded a single DSC endotherm matching the melt of IBU (Figure 6.18).

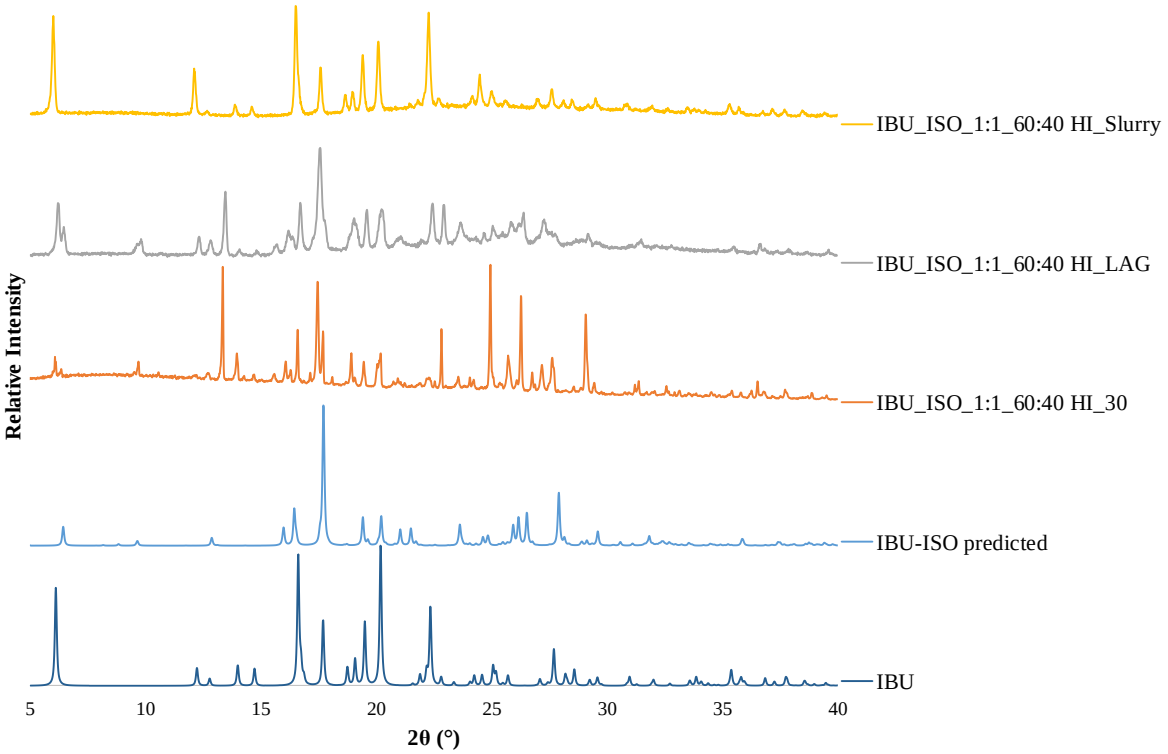

Figure 6.17 – PXRD patterns of the IBU-ISO 1:1 molecular complex prepared in 60:40 HI *via* various crystallisation methods: evaporative, LAG, slurrying at 20 °C at 10 mL scale for a slurry time of 24 hours, compared to the PXRD patterns of pure IBU and the IBU-ISO predicted pattern simulated in Mercury.

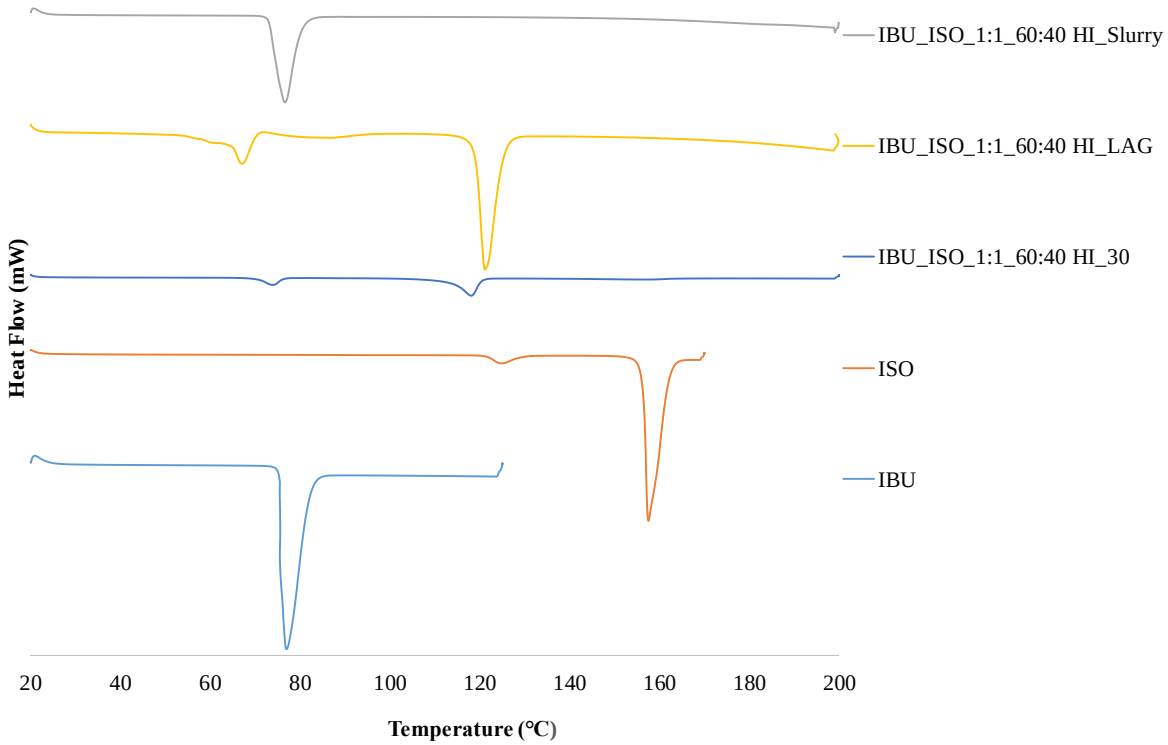

Figure 6.18 – DSC heat profiles of the IBU-ISO 1:1 molecular complex prepared in 60:40 HI *via* various crystallisation methods: evaporative, LAG, slurrying at 20 °C at 10 mL scale for a slurry time of 24 hours, compared to the DSC traces of pure IBU and pure ISO starting materials.

6.4.4.1 Relative Thermal Stability Studies of IBU-ISO

The thermal stability of the IBU-ISO co-crystal monitored over a month is shown in Appendix 6.4; the PXRD patterns and DSC traces sampled each week are the same, highlighting the stability of the IBU-ISO co-crystal on thermal ageing. The same analysis was carried out on the API IBU for comparison, which similarly shows resistance to 45 °C temperature conditions over a month (Appendix 6.5), confirmed by both PXRD and DSC analysis.

6.4.4.2 Humidity Stability studies of IBU-ISO

The IBU-ISO humidity stability results reported in Figures 6.19-6.21 show that the PXRD patterns exhibit changes over time, including the appearance of additional peaks between 13-18° 2θ, as well as peak broadening. The shift in PXRD patterns from seven days can be attributed to differing heights of the powder samples. This resistance to solid form changes of either solvate formation or dissociation into the constituent starting components, under either moderate or severe humidity conditions, shows the stability of IBU-ISO co-crystal prepared by both mechanochemical and slurrying crystallisations. A couple of additional peaks from excess IBU starting material are evident, as reported previously in the 5 minute mechanochemical crystallisations of IBU-ISO, so the samples did not consist of the co-crystal in purity at t=0.

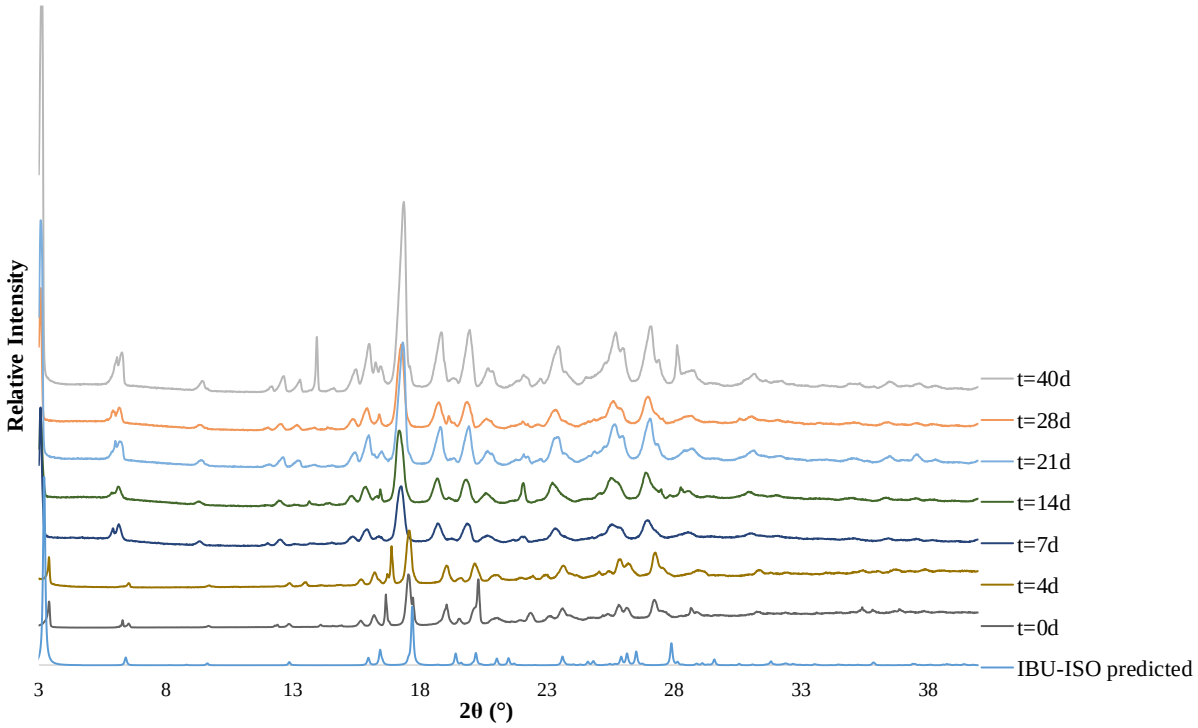

Figure 6.19 – IBU-ISO 1:1 prepared in 60:40 HI *via* LAG for 5 minutes – Humidity studies at 46 % RH monitored over 40 days. The intensity of the 3° 2θ peak for both the t = 28 and t = 40 days diffraction patterns has been truncated for ease of display and comparison.

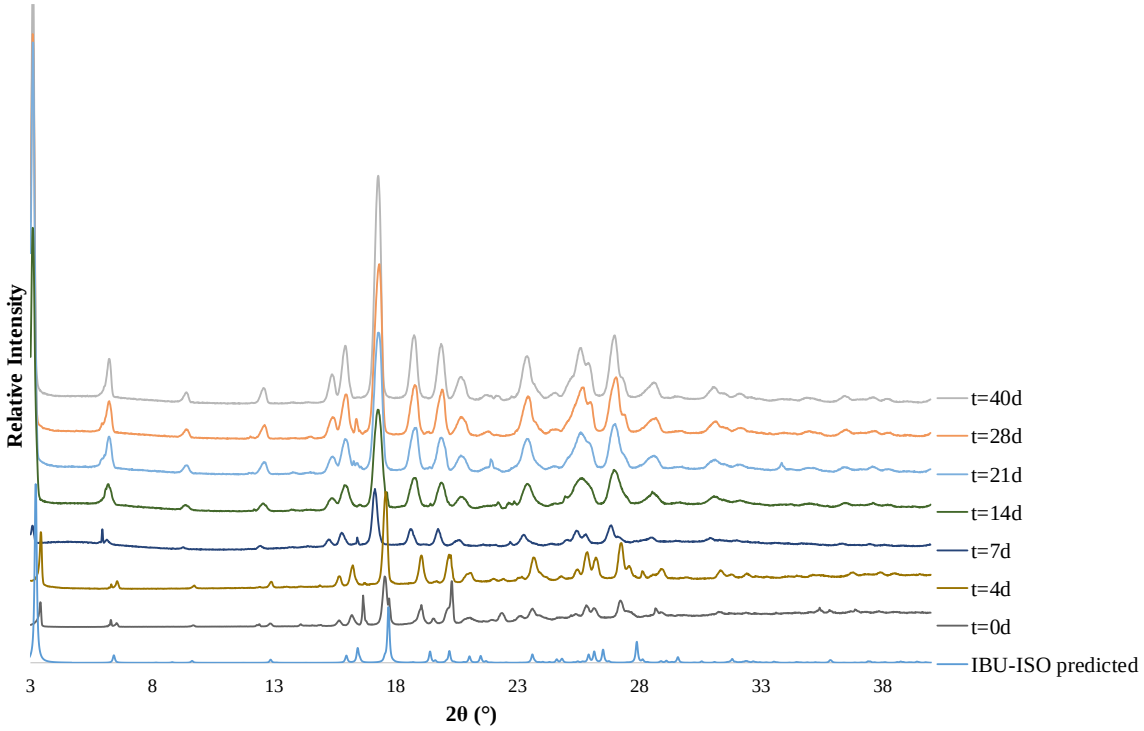

Figure 6.20 – IBU-ISO 1:1 prepared in 60:40 HI *via* LAG for 5 minutes – Humidity studies at 80 % RH monitored over 40 days. The intensity of the 3° 2θ peak for both the t = 28 and t = 40 days diffraction patterns has been truncated for ease of display and comparison.

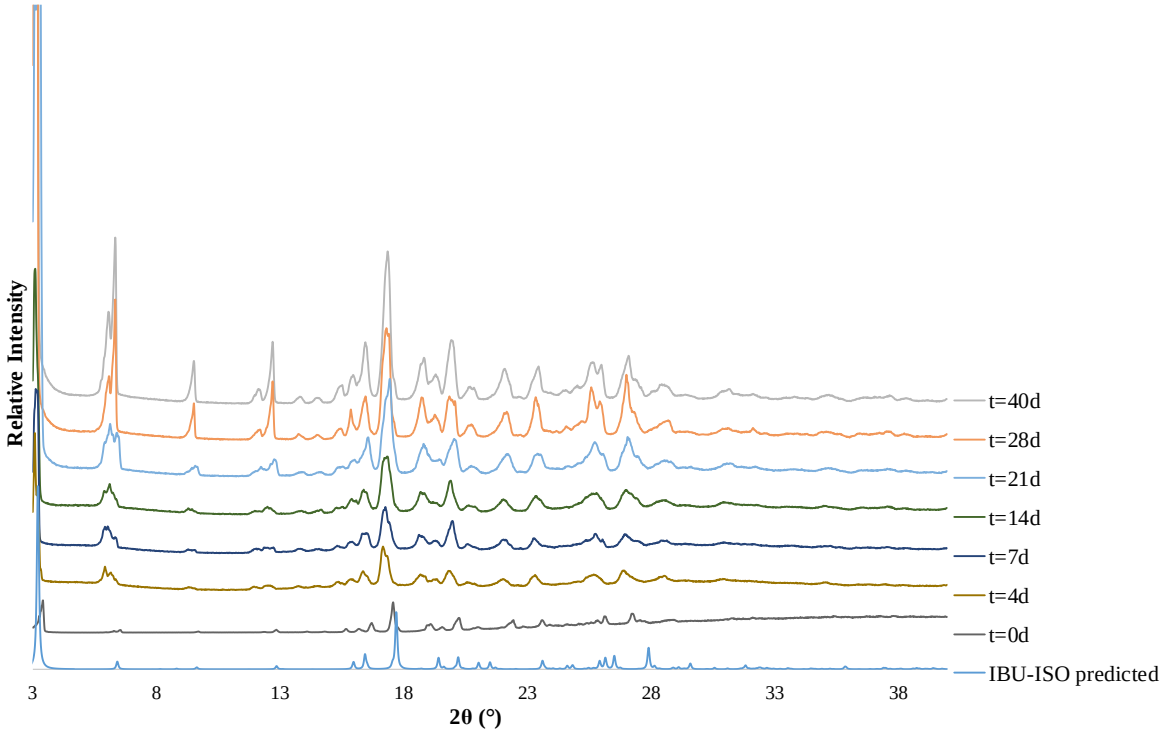

Figure 6.21 – IBU-ISO 1:1 prepared in 60:40 HI *via* for 5 minutes slurrying – Humidity studies at 46 % RH monitored over 40 days. The intensity of the 3° 2θ peak for both the t = 28 and t = 40 days diffraction patterns has been truncated for ease of display and comparison.

6.4.4.3 Solubility measurements of IBU ISO in 60:40 HI

Solubility measurements were carried out in preparation for translating the co-crystallisation of IBU and ISO into cooling crystallisation initially in batch and then into flow crystallisation in the KRAIC-D. Once the cooling crystallisation of the co-crystal has been designed from the physical mixture of starting components and the corresponding co-crystal accessed, analysis of the solubility behaviour of a pre-made co-crystal can be investigated, allowing for comparison between solubility of the physical mixture and the multi-component material.

6.4.4.3.1 Solubility by Turbidity

Solubility analysis to obtain a combined solubility of a physical mixture of IBU and ISO was carried out by turbidity measurements at two different scales using the Crystal16® and Crystalline® reactors at the University of Strathclyde. The platforms allowed the elucidation of solubility behaviour at 1 mL and 5 mL scale for the Crystal16® and Crystalline® respectively, with largely similar concentration / temperature dependence (Figure 6.22 and 6.24). Most interestingly, the data shows that the cloud points are observed at a lower corresponding concentration than the clear points, which is unusual behaviour and required further investigation.

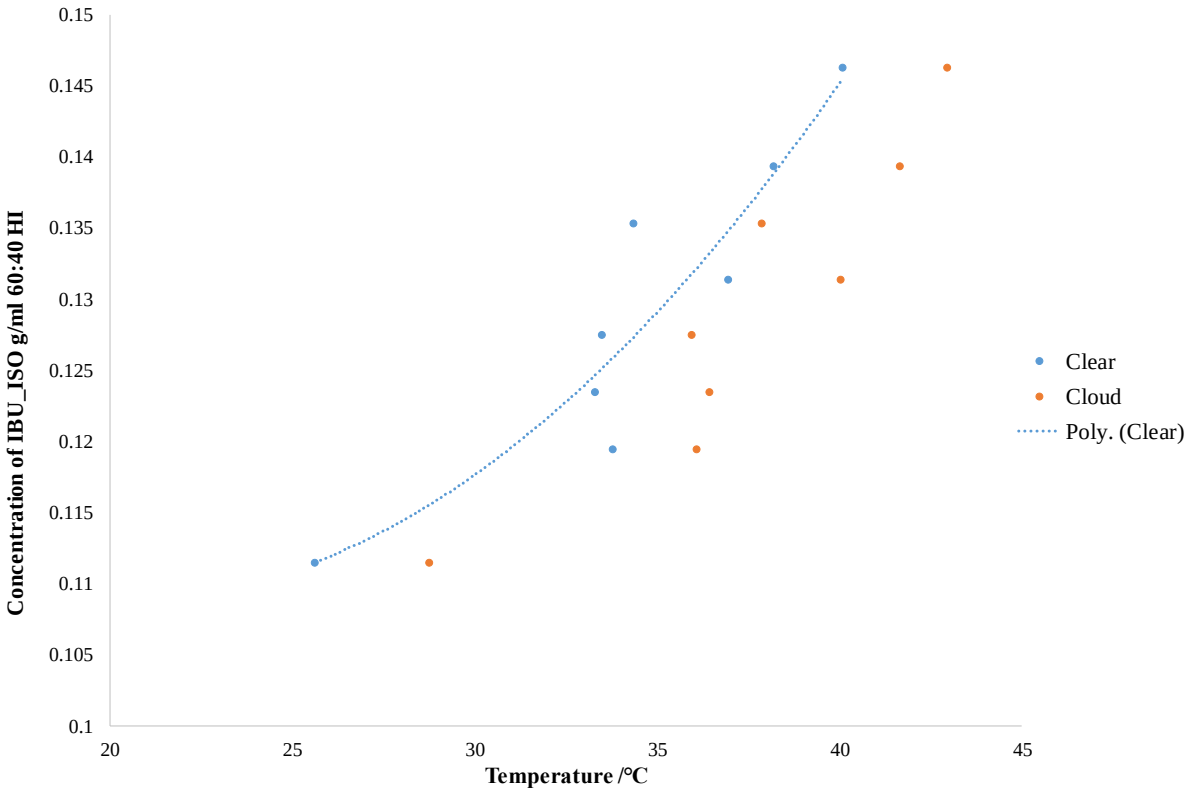

Figure 6.22 – Solubility curve of IBU and ISO 1:1 physical mixture in 60:40 HI at 1 mL scale in Crystal16®.

Observations of the vials within the Crystal16® after dissolving at 70 °C showed the phenomenon of 'oiling out'. This signifies that the solutions have reached supersaturation, but require an external stimulus to crystallise, which could explain the observation of cloud points at a lower temperature than the corresponding clear points.

The phenomenon of oiling out is evident in the literature; for example, Deneau *et al.* published an in-line study of oiling out and crystallisation of a pharmaceutical compound (which cannot be identified for commercial reasons) from a 50:50 v/v water-ethanol mixture.[172] The aim of the study was to improve knowledge of the process of oiling out, allowing for greater control to be imparted on the crystallisation process. *In situ* measurements using a FBRM (Focussed Beam Reflectance Measurement) probe and in-line PVM images, highlighted a number of events during the heat-cool cycles: dissolution, oiling out, coalescence of oil droplets, release of pharmaceutical compound from the droplets, nucleation and crystal growth. The solubility curve and the liquid-liquid phase separation boundary were also determined by FBRM, revealing that the two curves were largely separated at low temperature, whilst the MSZW decreased with an increase in temperature, until the curves merged into a single curve at high temperature.[172] This study highlights the importance of coupling turbidity measurements with in-line visual observations to monitor the phenomenon of oiling out, allowing for differentiation between crystallisation and oiling out in the turbidity cool cycles to be made.

Given these considerations, the choice of solubility limit from the turbidity data in the presence of the 'oiling out'[173] affecting the nucleation of the IBU_ISO in 60:40 HI was not clear. As the curves show overlap, it was chosen to focus on the cloud points on the solubility curve, acknowledging that the metastable zone (MSZ) is unknown.

To gain a greater understanding of the solubility behaviour of the IBU_ISO 1:1 physical mixture in 60:40 HI, in-line PVM images were collected during the three heat-cool cycles in the Technobis Crystalline® analysis, with images collected every minute throughout the temperature programme. The double spike in solubility (indicated by the orange stars in Figure 6.23) features only once in the repeat heat-cool cycles, indicating that this is a short-lived event. This double spike could be attributed to inhomogeneity of the oil droplets in the solution, whereby a reduction in oil droplets aligning with the beam path is evident from the increase in transmission at 750 minutes (45 000 seconds) into the turbidity analysis. Similar to findings from Deneua *et al*., the solubility of IBU_ISO 1:1 physical mixture showed a great variance

between the clear and cloud points at lower temperature, whereas at high temperature the MSZW is no longer distinguishable as the two curves merge (Figure 6.24).

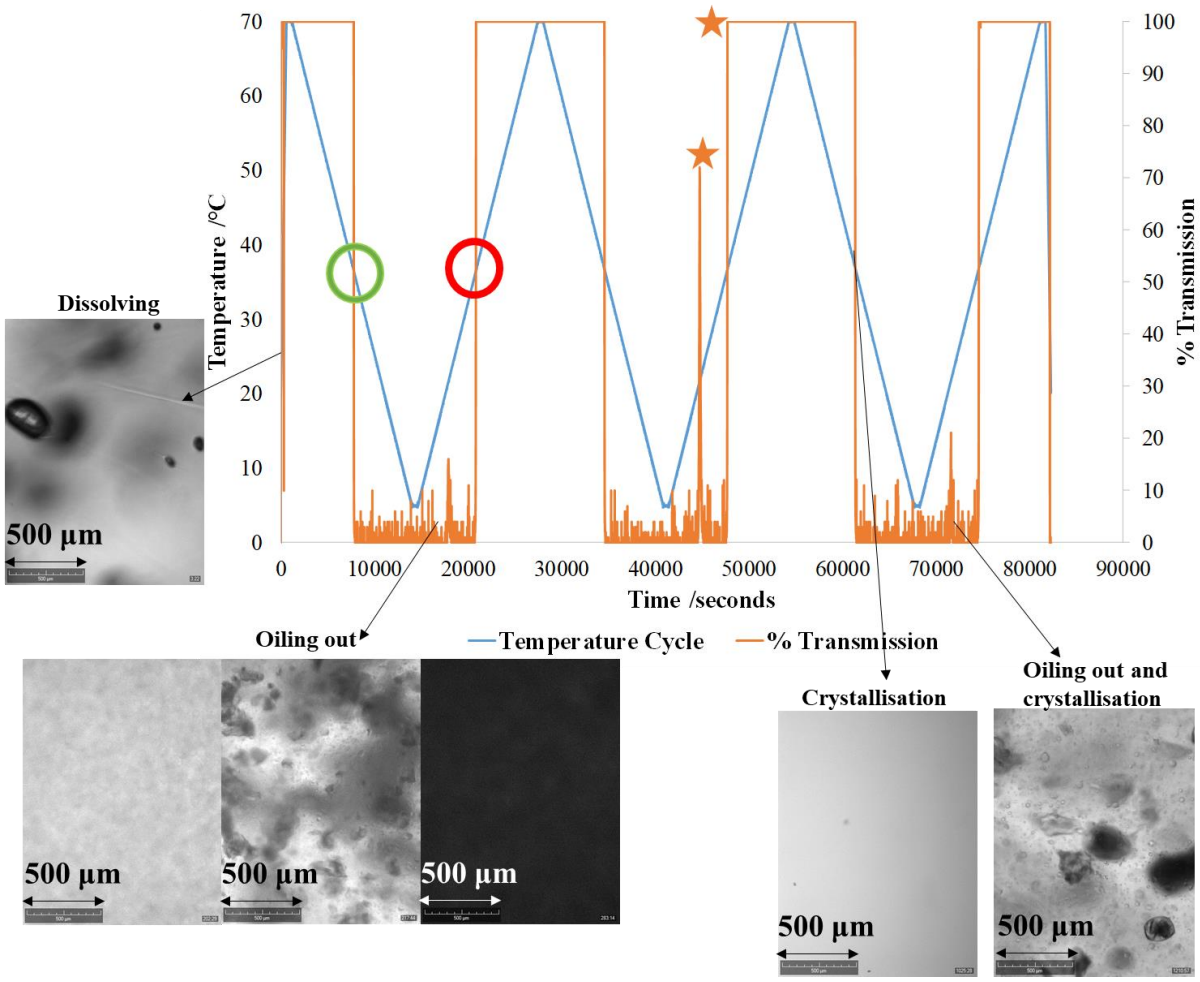

Figure 6.23 – Repeated heat-cool cycles to obtain clear (red circle) and cloud points (green circle) for IBU_ISO 1:1 physical mixture in 60:40 HI in Crystal16 and Crystalline® platforms. The heat-cool cycles presented coincide with a sample containing 0.4 g IBU and 0.474 g ISO in 5 mL 60:40 HI in the Crystalline®. The PVM images obtained alongside the Crystalline® turbidity measurements convey different stages of the crystallisation process at various time points. The unusual double spike in solubility is highlighted by the orange stars.

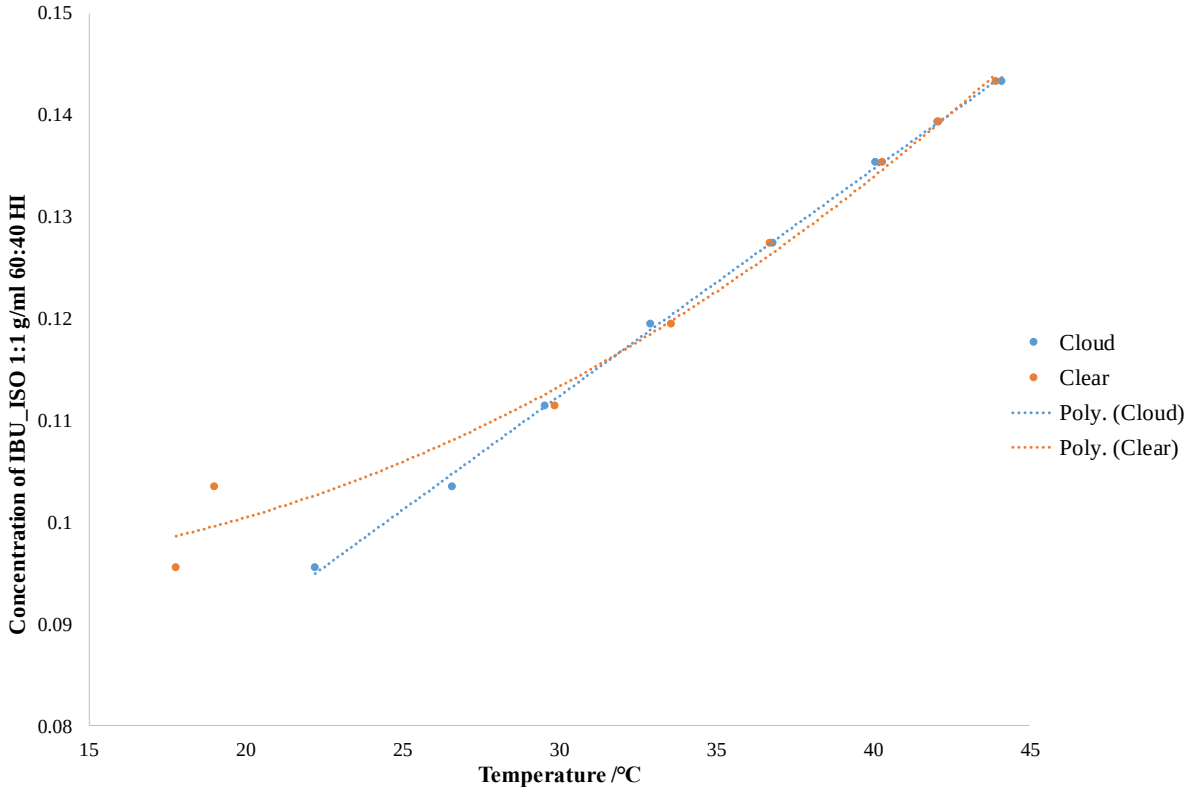

Figure 6.24 – Solubility curve of IBU and ISO 1:1 physical mixture in 60:40 HI at 5 mL scale in Crystalline®.

6.4.4.3.2 Solubility by Visual Observation

Due to the unusual solubility behaviour observed in both the Crystal16® and Crystalline® platforms, an alternative, visual observation, approach to solubility analysis was investigated. Incremental amounts of solid (either a physical mixture of starting components or a pre-prepared batch of the IBU-ISO co-crystal) were added to a saturated solution (20 mL volume) undergoing very slow temperature ramping. The temperature of dissolution is noted after each addition of solid.

The challenge with measuring the solubility of a multi-component system is the uncertainty in the material being measured. If the system dissociates into the constituent starting materials in solution, it is likely that the solubility of the least soluble component is being measured, although it is also possible that an initial physical mixture could phase transform in solution into the co-crystal, in which case solubility behaviour of the co-crystal can be obtained. It is therefore important to investigate the physical mixture and compare this to the starting individual components.

A physical mixture of IBU_ISO in 60:40 HI was investigated in both 1:1 and 1:2 stoichiometric ratios of IBU:ISO and compared with the pure IBU API (Figure 6.25) and ISO (Figure 6.26) starting components. Once the IBU-ISO co-crystal can be accessed in purity *via* cooling, it was then possible to ascertain whether this IBU co-crystal formation has improved the solubility compared to pure IBU. In each case, three repeats were investigated for reliability, in order to provide statistical relevance. The solubility of IBU was consistent across the repeat experiments, whereas the solubility of ISO showed great variance, particularly at low concentration / temperature and thus the data for ISO could not be fitted to an exponential curve. The solubility by visual observation of a physical mixture of IBU_ISO 1:1 in 60:40 HI is consistent between repeats at low temperature, but as the temperature is increased the variance between repeats increases (Figure 6.27). The greater variance in repeat observation measurements at higher temperature could be attributed to inconsistency in heating.

The heating programme was stopped when a cloud emulsion was produced (Figure 6.28). Importantly, an emulsion is observed for the parent compounds IBU and ISO, as well as for the physical mixture of IBU_ISO.

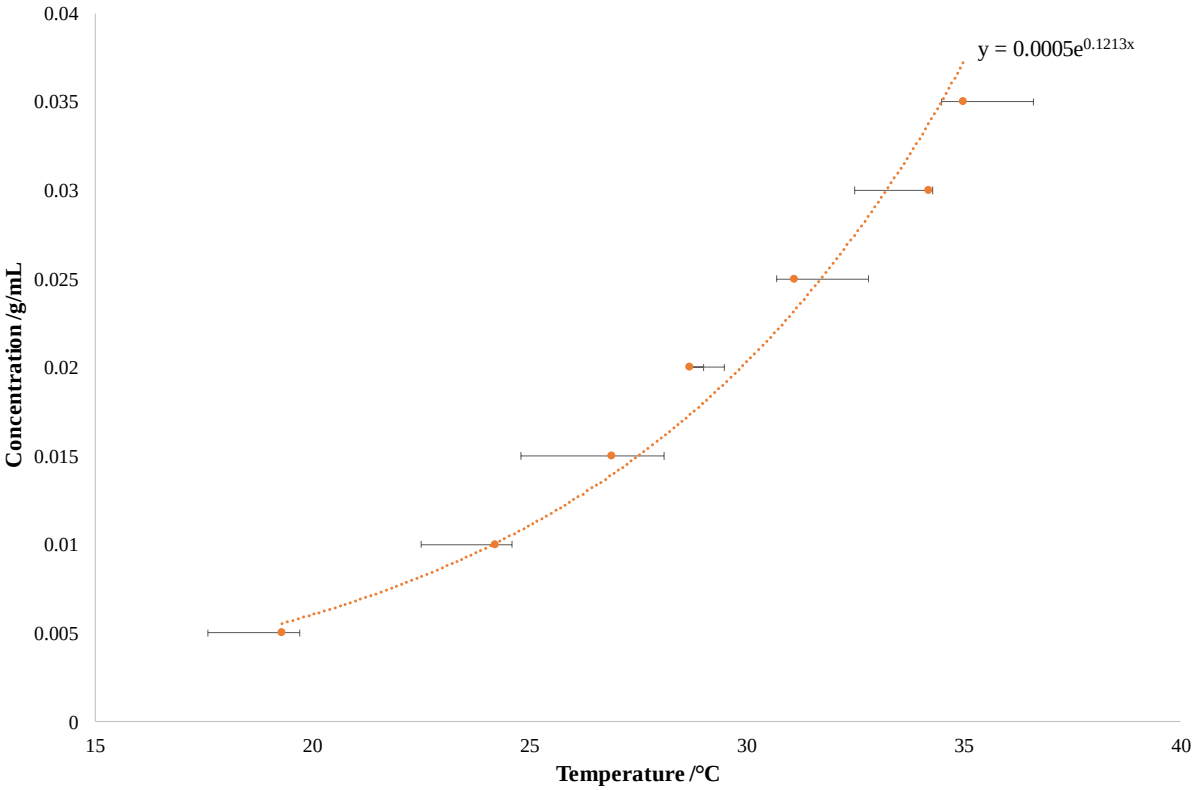

Figure 6.25 – Solubility of IBU in 60:40 HI *via* visual observation, three repeats Obs 1, 2, 3 with exponential trend curve to fit the median data.

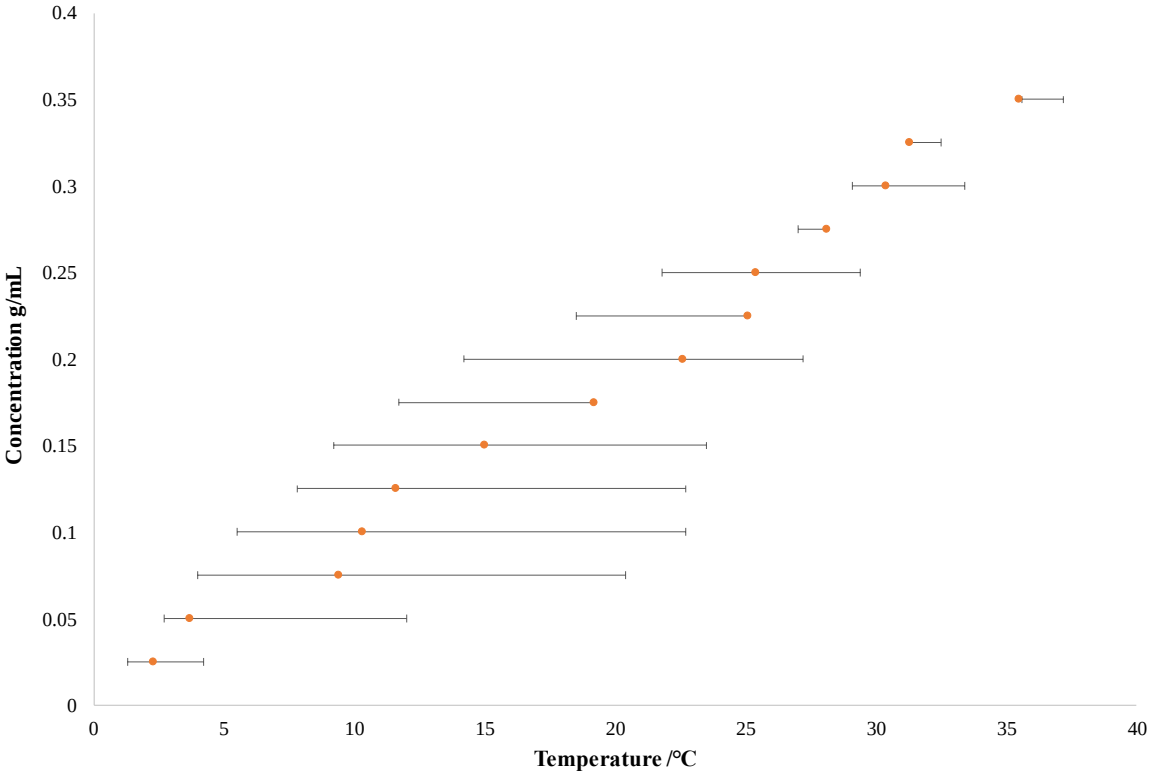

Figure 6.26 – Solubility of ISO in 60:40 HI *via* visual observation, three repeats Obs 1, 2, 3.

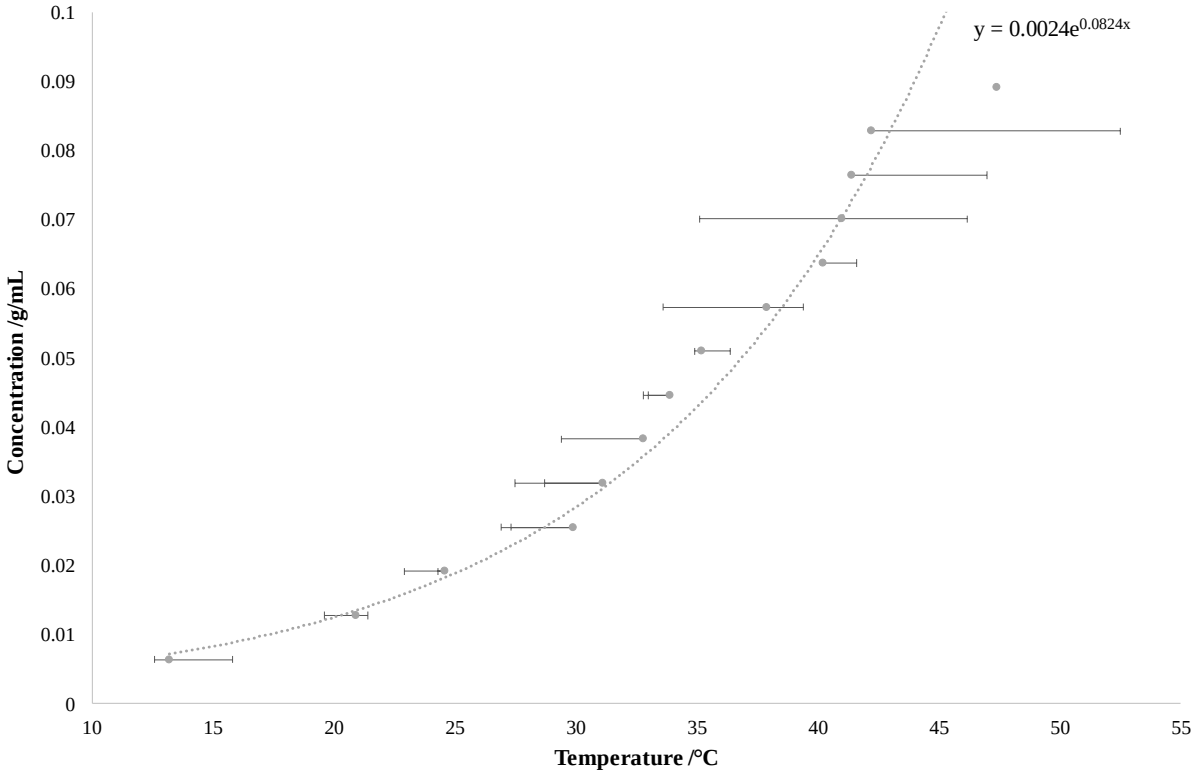

Figure 6.27 – Solubility of IBU_ISO 1:1 physical mixture in 60:40 HI *via* visual observation, three repeats Obs 1, 2, 3 with exponential trend curve to fit the median data.

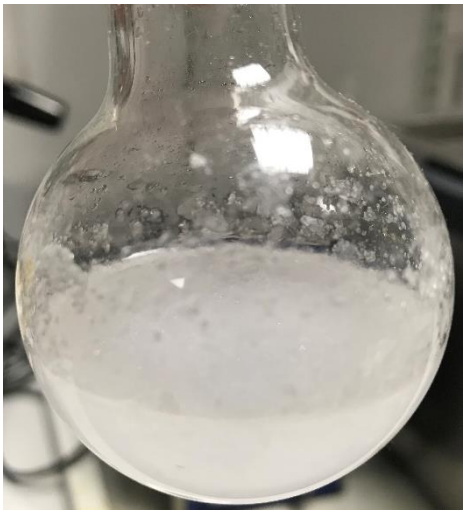

Figure 6.28 – Cloudy emulsion resulting from solubility of IBU_ISO 1:1 physical mixture in 60:40 HI.

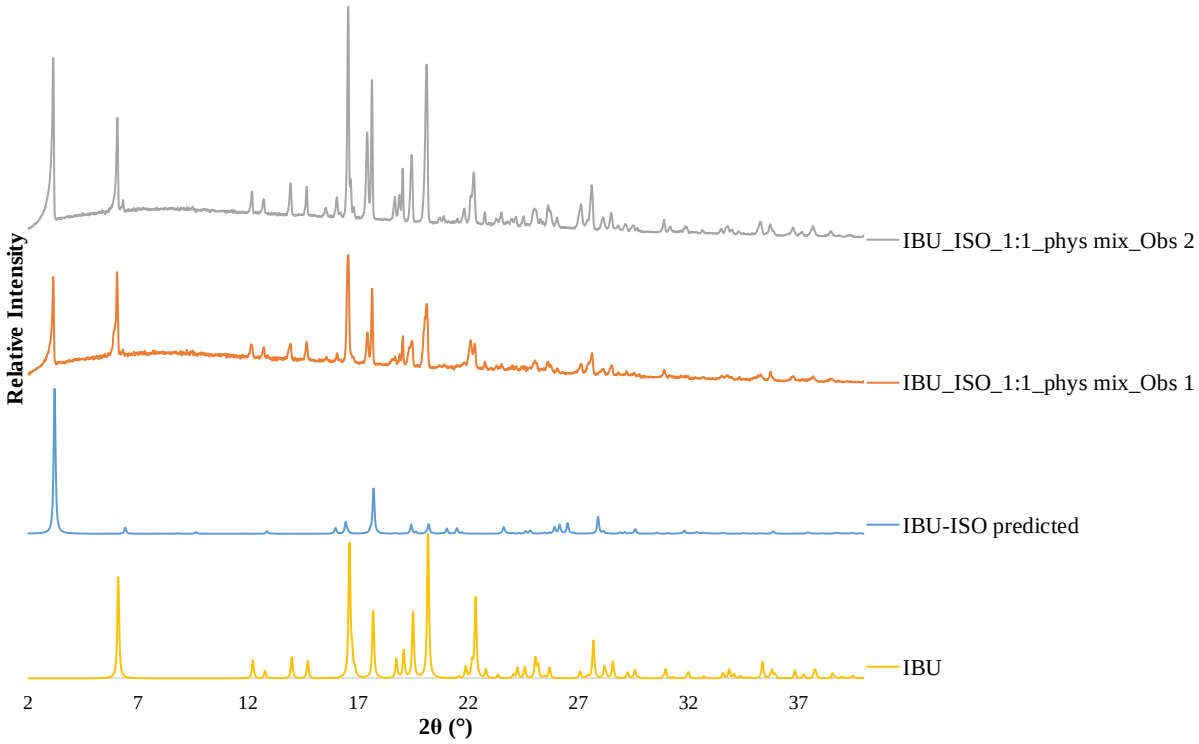

Figure 6.29 – PXRD patterns of the resultant crystalline material produced from the solubility by visual observation of the physical mixture (phys mix) of IBU and ISO in 60:40 HI, compared to the PXRD patterns of pure IBU and the IBU-ISO predicted pattern simulated in Mercury.

The resulting crystalline material produced once the heating regime was complete and the sample allowed to return to room temperature, produced a mixture of IBU and IBU-ISO co-crystal (Figure 6.29). This is in agreement with the solubility data presented in Figure 6.25 and 6.27, which is similar for IBU and the IBU_ISO 1:1 physical mixture respectively, so it can be

postulated that the IBU_ISO 1:1 physical mixture is largely measuring the solubility behaviour of IBU, or the solubilities could be very similar. The solubility measurements *via* visual observation did not yield the co-crystal in purity, therefore controlled cooling crystallisation experiments were carried out at 1:1 and 1:2 stoichiometric ratios of IBU:ISO to access the co-crystal in purity. Once the pure IBU-ISO co-crystal was accessed, this allowed for solubility analysis *via* visual observation of the pure co-crystal to be carried out and compared to the solubility behaviour of pure IBU in the 60:40 HI solvent mixture.

As the solubility behaviour of ISO in 60:40 HI is largely different to IBU and IBU_ISO 1:1 measured in the same solvent system, the solubility behaviour of IBU_ISO 1:2 physical mixture was investigated (Figure 6.30). The average solubility behaviour of IBU_ISO 1:2 is similar to the average solubility of IBU_ISO 1:1, particularly at high temperature, whereby the solubility curves will intersect above 40 °C. According to the equation for the exponential curves describing the solubility behaviour of IBU_ISO 1:1 and IBU_ISO 1:2, the concentration at 20 °C, equates to 0.0125 g/mL and 0.00691 g/mL for 1:1 and 1:2 respectively. As seen in Figure 6.27, the uncertainty in the data points presented in Figure 6.30 increases with increasing temperature; this could be attributed to poor heat transfer at higher temperatures.

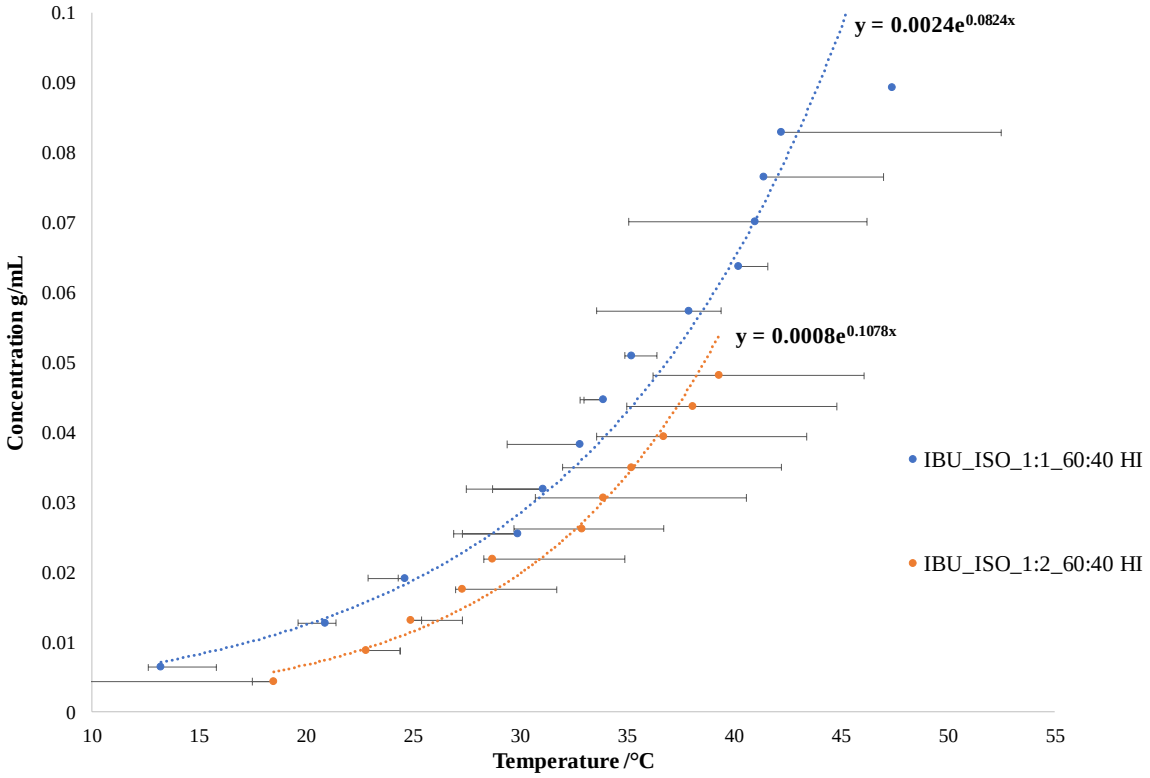

Figure 6.30 – Solubility of IBU_ISO 1:2 physical mixture in 60:40 HI *via* visual observation, three repeats Obs 1, 2, 3 with exponential trend curves to fit the median data.

6.4.4.4 Cooling Crystallisations of IBU-ISO

6.4.4.4.1 Batch *via* Polar Bear Plus from Cambridge Reactor Design (CRD)

The IBU-ISO co-crystal was translated into a cooling crystallisation regime as that crystallisation method is more easily controlled at larger scale, thus is widely adopted in the pharmaceutical industry. The quantities of IBU and ISO were initially based upon the room temperature solubility of the physical mixture of IBU_ISO 1:1 in 60:40 HI at 1 mL scale in the Crystal16®, which provides a suitable start point for a cooling crystallisation experiment. A concentration range was selected to ascertain the concentration dependence of IBU-ISO co-crystal formation (Table 6.6). The IBU_ISO 1:1 in 1 mL 60:40 HI samples were heated to 70 °C, followed by a 1 hour dwell time, to ensure complete dissolution before cooling to 5 °C at a cooling rate of 0.05 °C min^{-1}.

Table 6.6 – Quantities of each component and overall concentration of IBU_ISO 1:1 in 1 mL of 60:40 HI used in the initial cooling crystallisation trials at 1 mL in the CRD Polar Bear Plus crystalliser.

Vial	Moles of IBU /x10^{-4} moles	Moles of ISO / x10^{-4} moles	Concentration g/mL
1	3.88	3.88	0.1274
2	4.12	4.12	0.1353
3	4.24	4.24	0.1393
4	4.36	4.36	0.1462
5	3.39	3.39	0.1114
6	3.64	3.64	0.1194
7	3.76	3.76	0.1234
8	4.00	4.00	0.1313

A mixture of IBU and the IBU-ISO co-crystal is produced across the full concentration range, with slight shifts in the 2θ (°) positions (Figure 6.31). This is confirmed by DSC (Figure 6.32), in contrast to the pure co-crystal indicated in the DSC trace from the sample prepared by LAG.

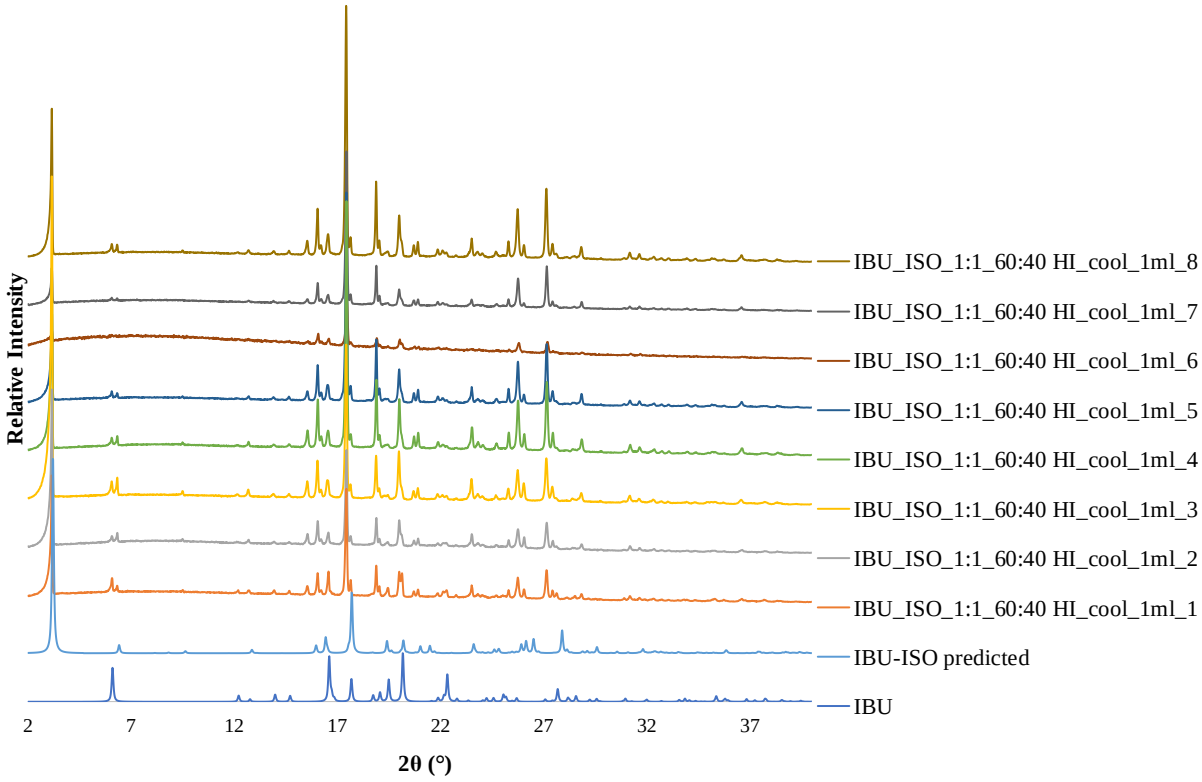

Figure 6.31 – PXRD of products from cooling crystallisations of IBU_ISO 1:1 in 60:40 HI at 1 mL scale over a concentration range performed in the CRD Polar Bear Plus crystalliser.

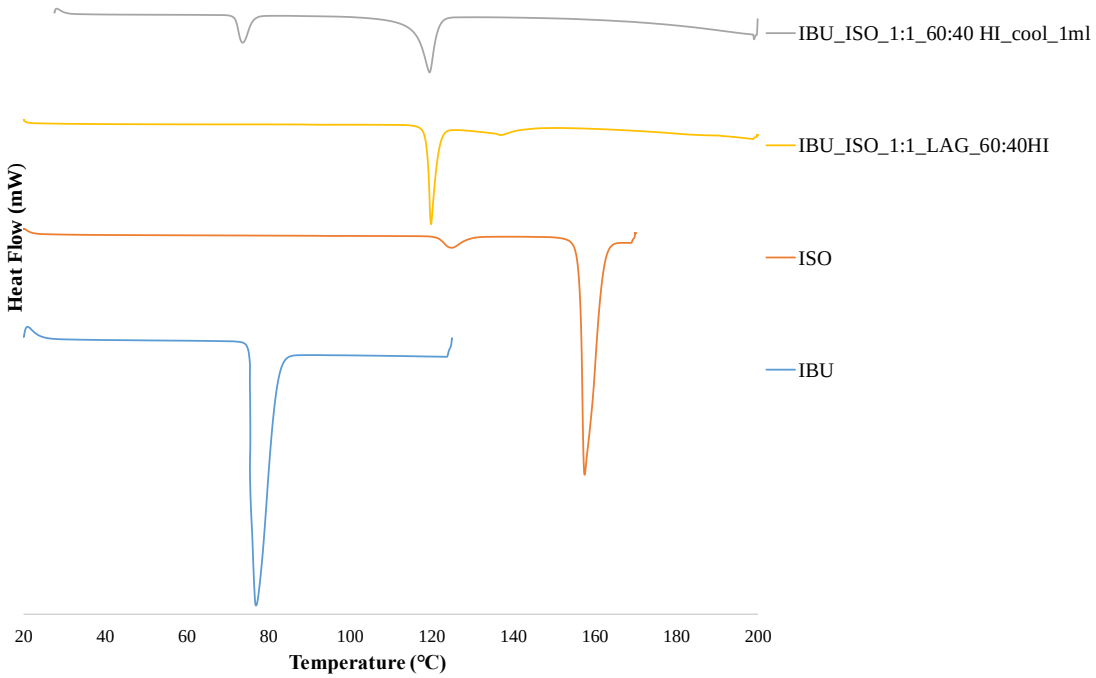

Figure 6.32 – DSC trace of cooling crystallisation of IBU_ISO 1:1 in 60:40 HI at 1 mL scale (vial 5) *versus* starting material DSC traces of IBU, ISO and the co-crystal IBU-ISO accessed *via* LAG in 60:40 HI for 30 minutes.

In subsequent cooling crystallisations, a 1:2 stoichiometric ratio of the IBU_ISO starting materials was used in an attempt to remove the excess IBU. In addition to altering the stoichiometric ratio of the starting components, to crystallise the IBU-ISO in purity, a faster cooling rate of 1 °C min^{-1}, comparable to those typically adopted in industry, was investigated. The PXRD patterns of the cooling crystallisations of IBU_ISO 1:2 in 60:40 HI at both 0.05 °C min^{-1} and 1 °C min^{-1} cooling rates are compared to the initial cooling crystallisation of a 1:1 stoichiometric ratio at the slower cooling rate in Figure 6.33.

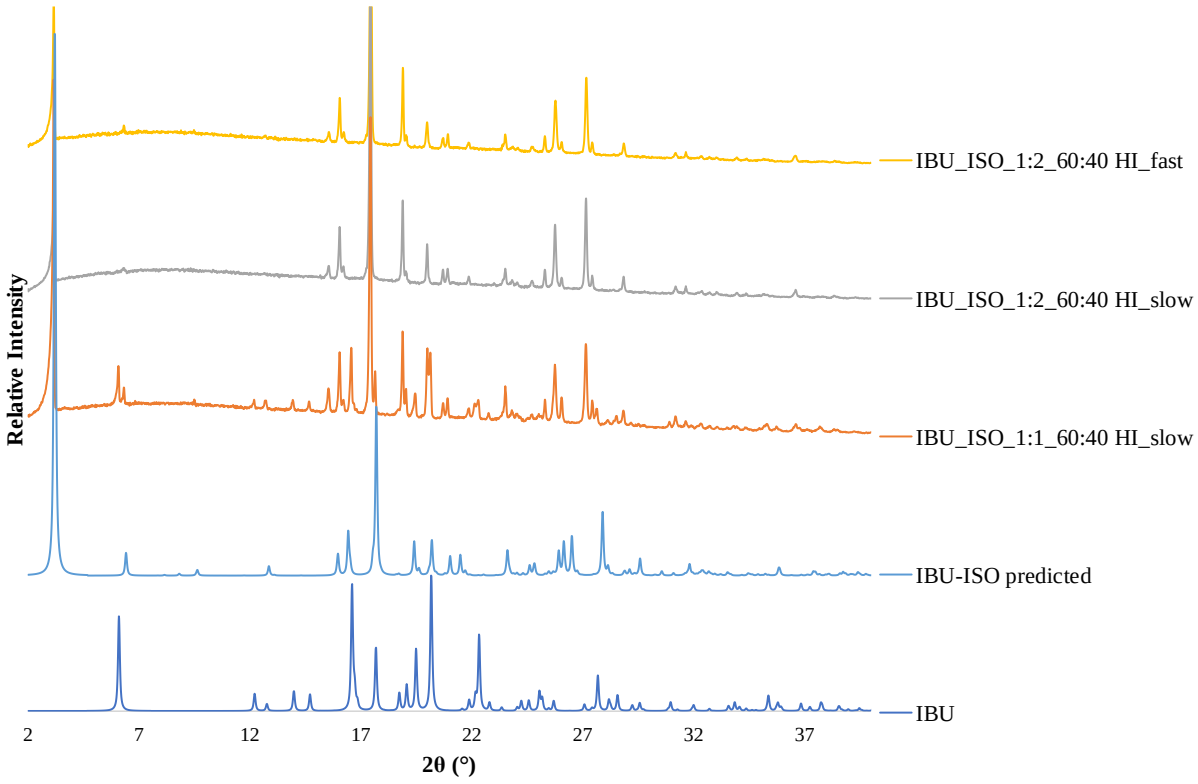

Figure 6.33 – PXRD of products of cooling crystallisations of IBU_ISO 1:1 and 1:2 in 60:40 HI at 1 mL scale cooled at 0.05 °C min^{-1} (slow) and 1 °C min^{-1} (fast) cooling rates performed in the CRD Polar Bear Plus crystalliser, with the intense peak at 17° 2θ truncated for clarity.

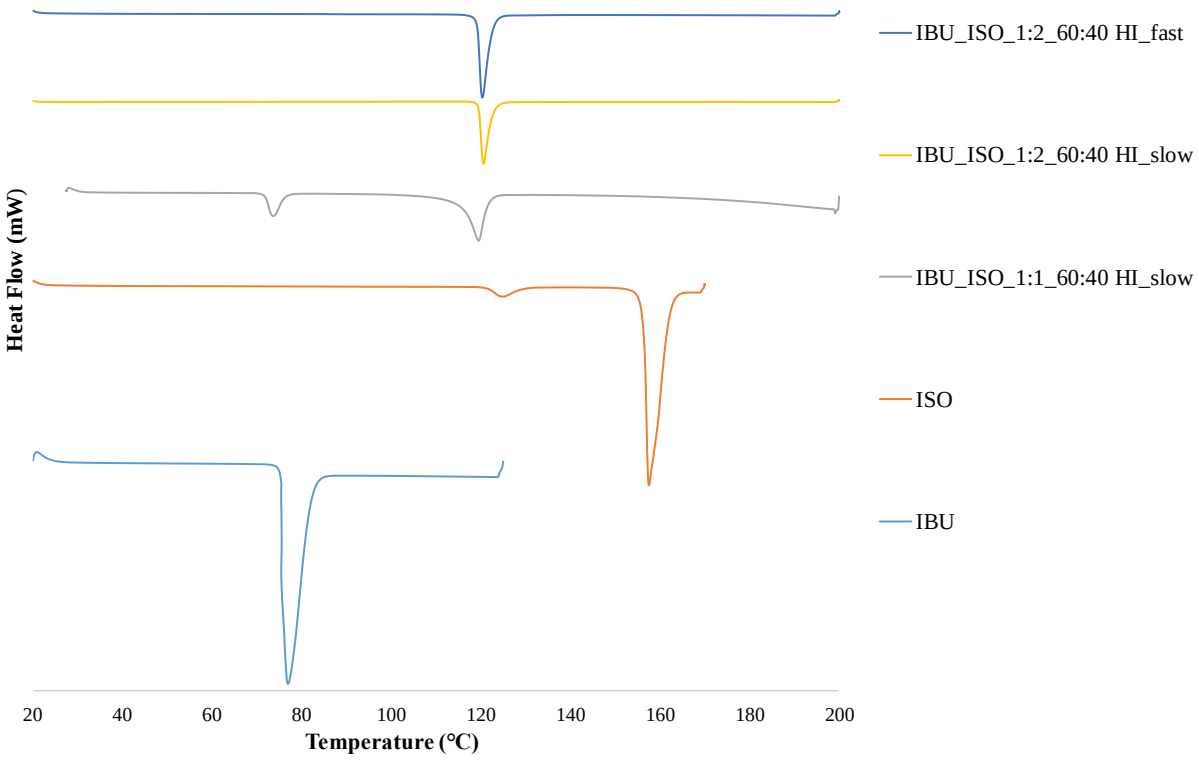

Figure 6.34 – DSC traces of cooling crystallisations of IBU_ISO 1:1 and 1:2 in 60:40 HI cooled at 0.05 °C min^{-1} (slow) and 1 °C min^{-1} (fast) cooling rates performed in the CRD Polar Bear Plus crystalliser at 1 mL scale *versus* starting material DSC traces of IBU and ISO.

The DSC traces of the IBU_ISO 1:2 in 60:40 HI cooled at both 0.05 °C min^{-1} and 1 °C min^{-1} features a single endothermic peak at 120 °C (Figure 6.34). Importantly, the reduction of the IBU in the IBU_ISO stoichiometric ratio resulted in the removal of the excess IBU peak, which featured in the previous IBU_ISO 1:1 in 60:40 HI DSC trace.

Production of the IBU-ISO co-crystal has also been successfully scaled up *via* cooling crystallisations to 200 mL scale at 1 °C min^{-1}, using both magnetic bottom (Figure 6.35) and overhead (Figure 6.36 and 6.37) stirring. There are no discernible differences in crystalline outcome from the different stirring methods, regardless of the difference in mixing homogeneity and shear.

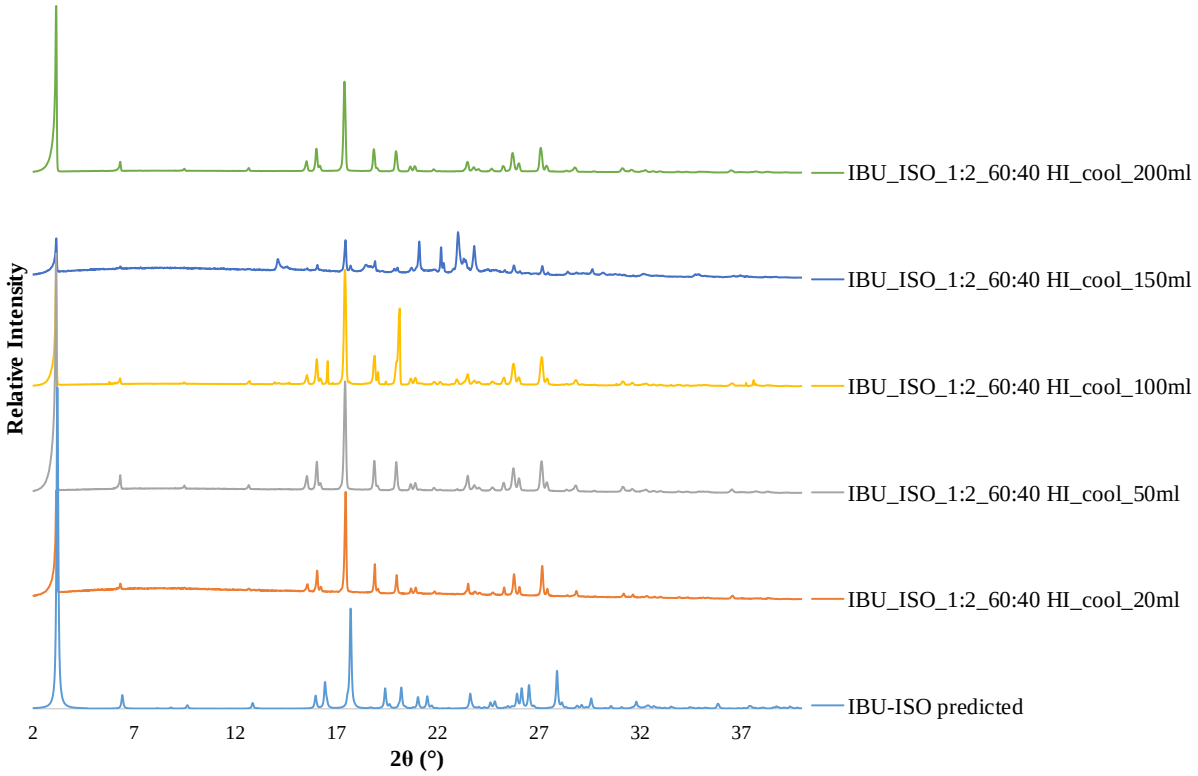

Figure 6.35 – PXRD of products from cooling crystallisations of IBU_ISO 1:2 in 60:40 HI scale-up with magnetic bottom stirring.

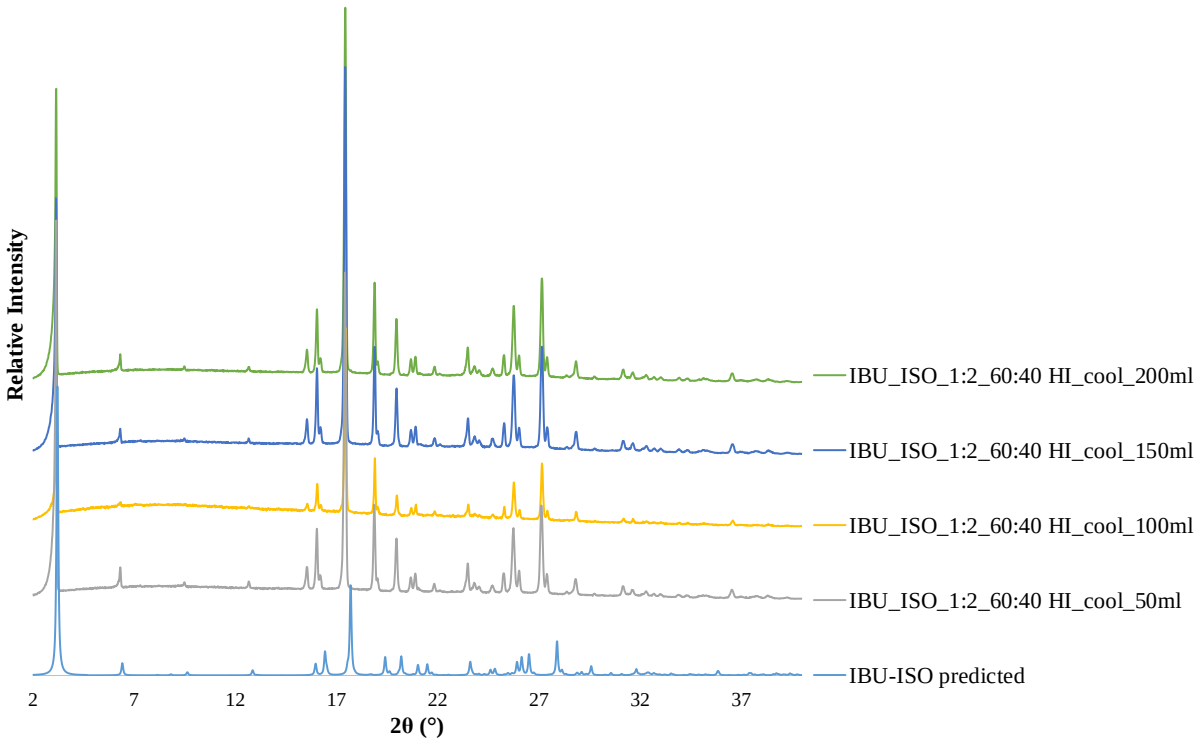

Figure 6.36 – PXRD of products from cooling crystallisations of IBU_ISO 1:2 in 60:40 HI scale-up with overhead stirring.

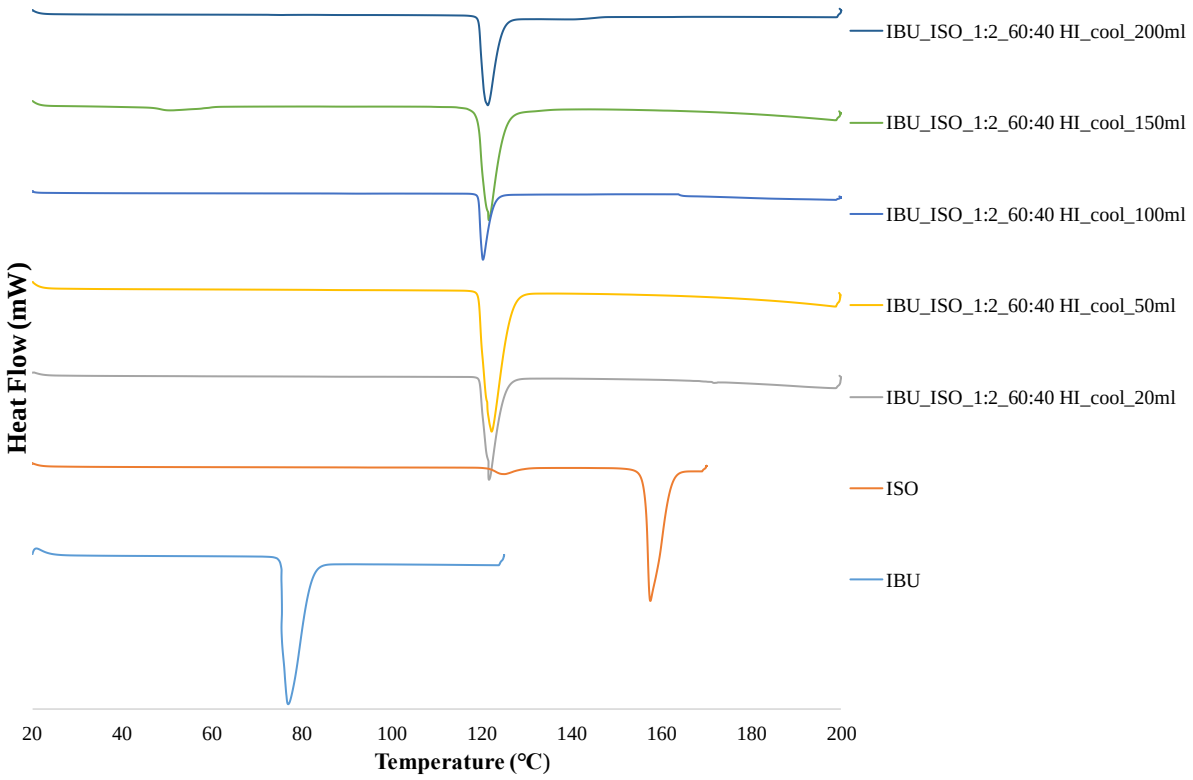

Figure 6.37 – DSC traces of cooling crystallisations of IBU_ISO 1:2 in 60:40 HI scale-up with overhead stirring.

The solubility of a physical mixture of IBU_ISO in 60:40 HI was investigated in both 1:1 and 1:2 stoichiometric ratios previously, and this can be compared with the solubility of the IBU-ISO co-crystal as this has been produced up to 200 mL scale *via* batch cooling (Figure 6.38).

Comparison of the IBU-ISO co-crystal solubility behaviour in 60:40 HI with IBU and IBU_ISO 1:2 physical mixture in the same solvent system shows that the IBU-ISO co-crystal is more soluble than both IBU in 60:40 HI and the IBU_ISO 1:2 physical mixture in 60:40 HI (Figure 6.38). Interestingly, the solubility behaviour of IBU in 60:40 HI and IBU_ISO 1:2 physical mixture in 60:40 HI show very similar exponential concentration / temperature dependence, so it can be postulated that the solubility of IBU is measured in the IBU_ISO 1:2 physical mixture. The solubility of IBU was only analysed to an upper limit temperature of approximately 40 °C for each of the repeats, as the IBU produced a cloudy emulsion and further analysis would not be accurate. This solubility study has shown that co-crystal formation has improved the solubility of IBU; for example by a factor of 5 at 20 °C.

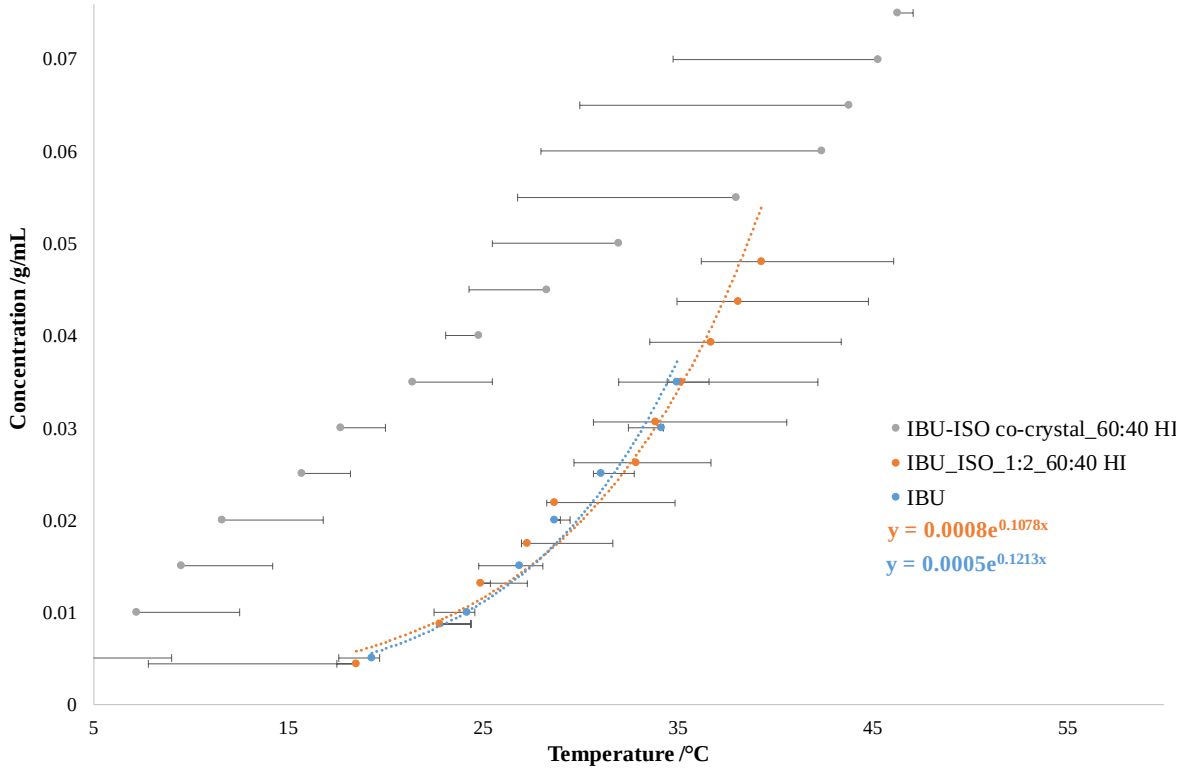

Figure 6.38 – Comparison of Solubility of IBU-ISO co-crystal with IBU in 60:40 HI and IBU_ISO 1:2 physical mixture *via* visual observation, three repeats Obs 1, 2, 3. The data for the solubility behaviour of the co-crystal IBU-ISO does not follow an exponential trend and therefore exponential fitting was not carried out.

6.4.4.5 Slurry stability testing of IBU-ISO co-crystal

Slurrying a physical mixture of IBU_ISO in 60:40 HI at 10 mL scale for 24 hours was previously shown to produce IBU. The stability of a slurry of the pre-made IBU-ISO co-crystal over a period of 48 hours, which is beyond the lifetime of the rate of release of a drug product in the gut, was investigated as a comparison to the behaviour of the physical mixture. In order to ascertain whether the co-crystal would remain intact as the multi-component material, PXRD and DSC analysis of aliquots sampled at various time points was carried out. Two temperatures were investigated, room temperature (RT) and 37.5 °C (HT – high temperature) to simulate temperature conditions in the gut. The co-crystal sample used in the slurry stability testing was prepared using IBU_ ISO 1:2 in 60:40 HI achieving co-crystal formation *via* cooling at 200 mL scale with the use of overhead stirring. The IBU-ISO co-crystal material produced from the cooling experiment was dried and confirmed to yield the co-crystal in purity *via* PXRD analysis presented in Figure 6.36.

Offline PXRD measurements of the pre-prepared IBU-ISO co-crystal slurried in 60:40 HI sampled over 2, 4, 6, 24 and 48 hours showed no discernible differences over time and yielded a mixture of IBU and IBU-ISO co-crystal at both RT and HT (Figure 6.39 and 6.41). ISO is significantly more soluble than IBU at room temperature, which causes an excess of IBU to crystallise when slurrying in solution, also evident from DSC analysis (Figure 6.40 and 6.42).

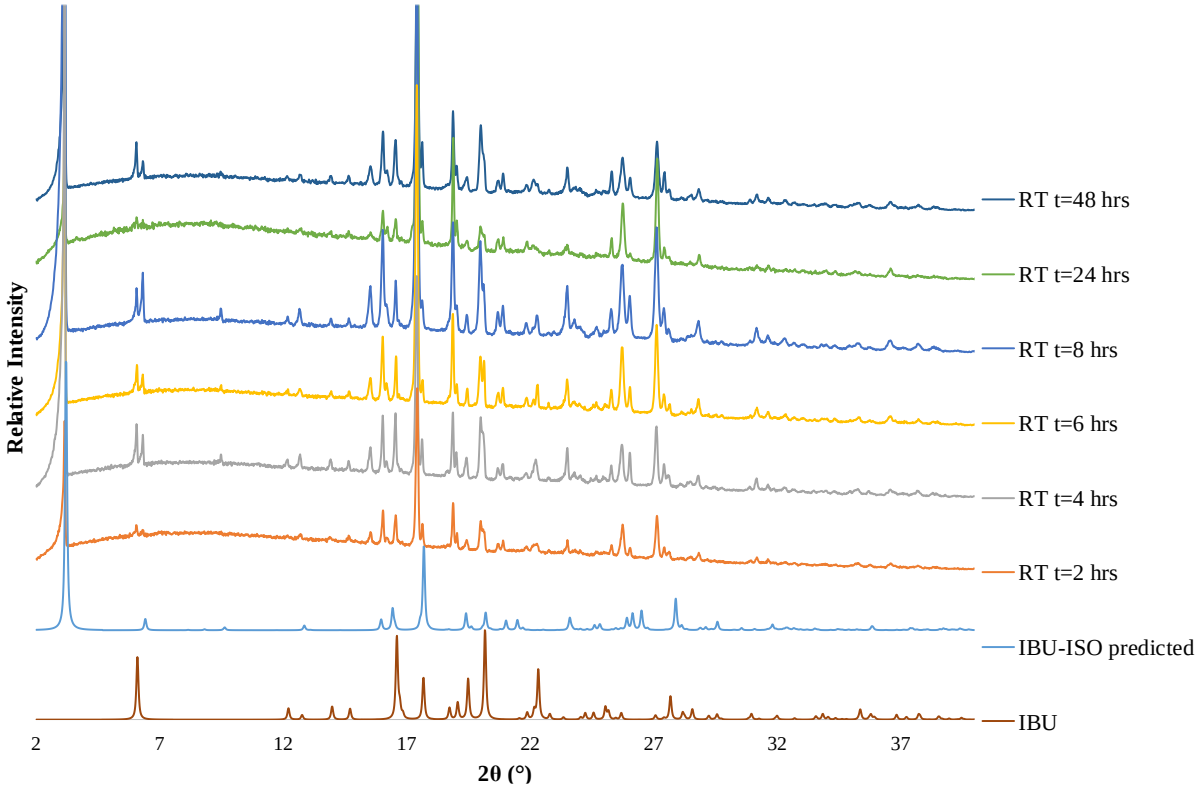

Figure 6.39 – PXRD patterns of IBU-ISO pre-prepared co-crystal used in 60:40 HI mediated slurry at room temperature (RT), sampled at t = 2, 4, 6, 8, 24 and 48 hours after slurry preparation. The intensity of the 2.5° 2θ peak has been truncated for ease of display and comparison.

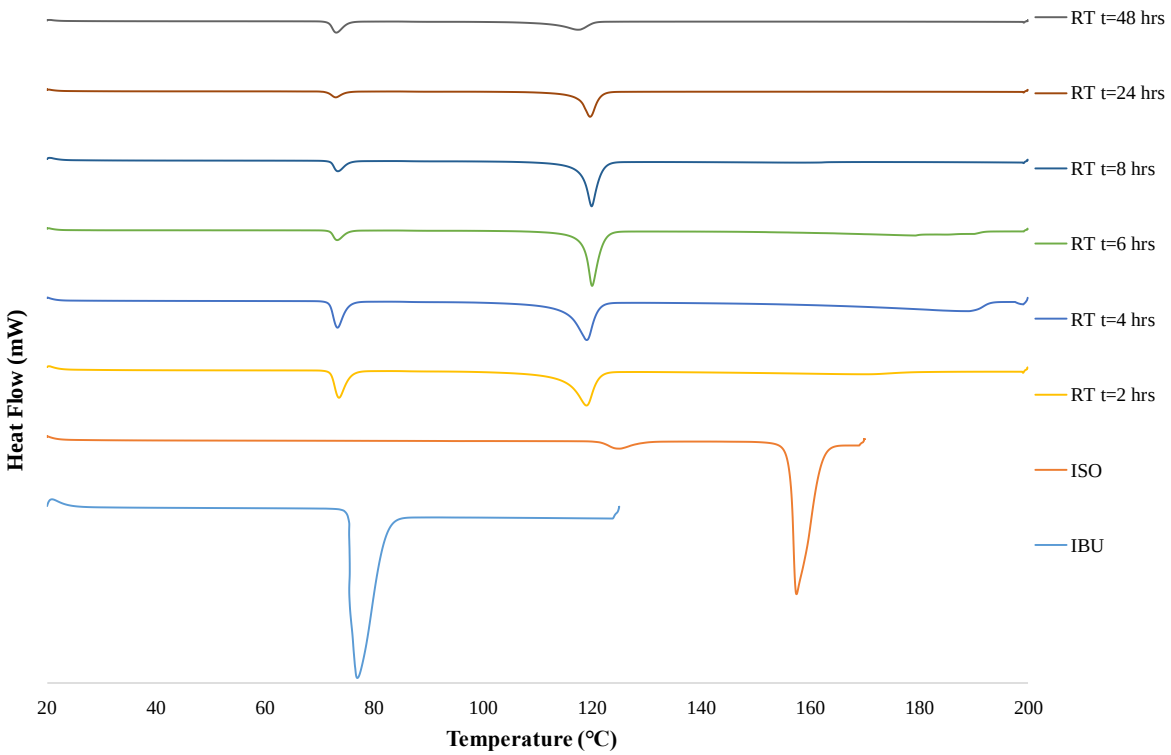

Figure 6.40 – DSC traces of IBU-ISO pre-prepared co-crystal used in 60:40 HI mediated slurry at room temperature (RT), sampled at t = 2, 4, 6, 8, 24 and 48 hours after slurry preparation compared to IBU and ISO starting material DSC traces.

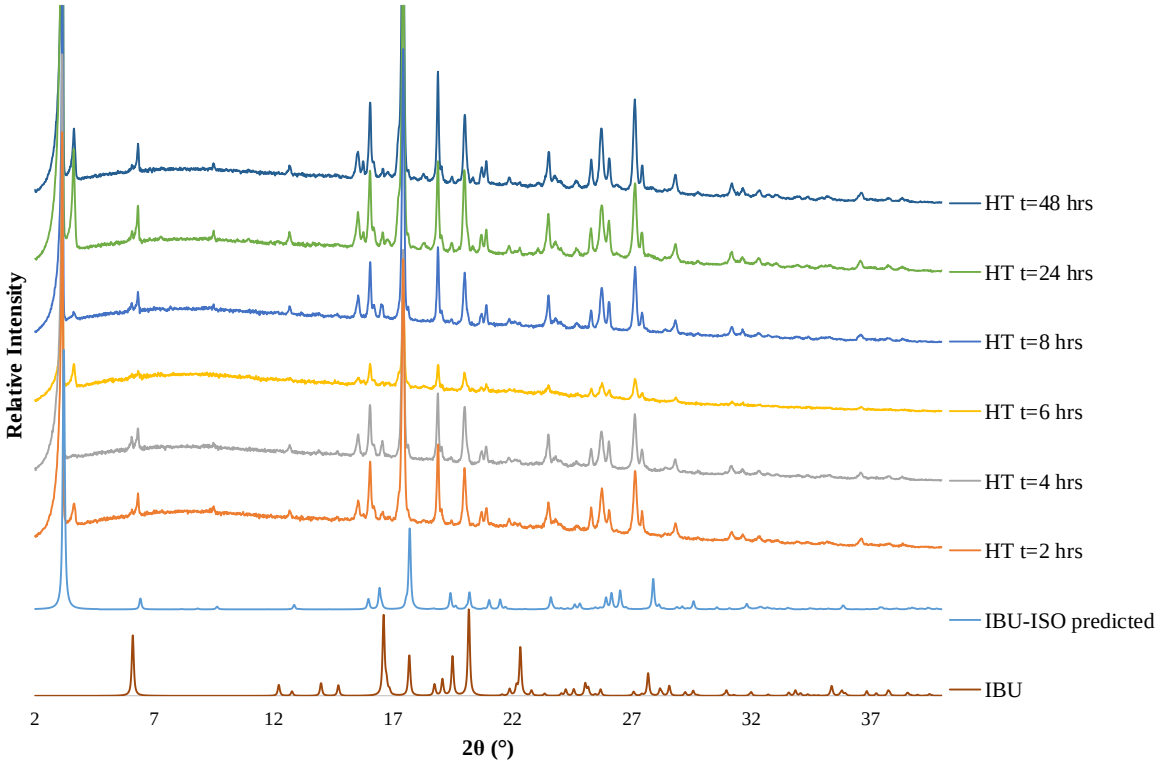

Figure 6.41 – PXRD patterns of IBU-ISO pre-prepared co-crystal used in 60:40 HI mediated slurry at 37.5 °C (HT), sampled at t = 2, 4, 6, 8, 24 and 48 hours after slurry preparation.

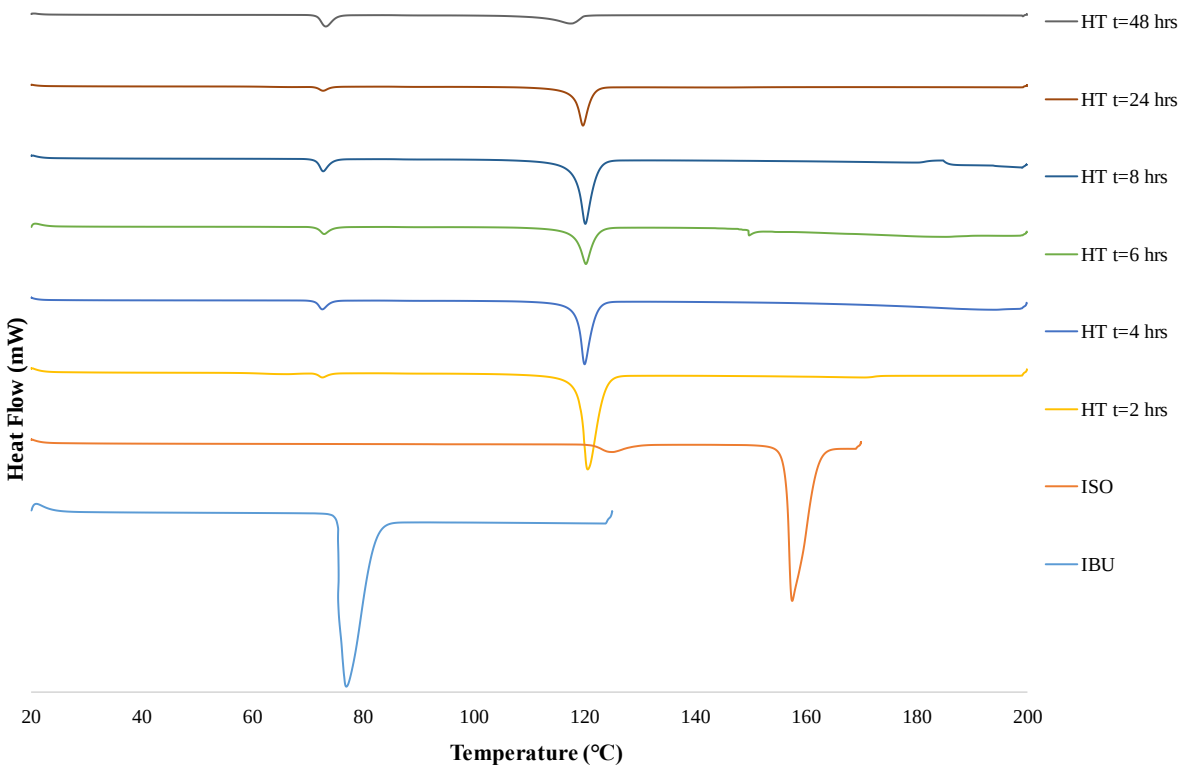

Figure 6.42 – DSC traces of IBU-ISO pre-prepared co-crystal used in 60:40 HI mediated slurry at 37.5 °C (HT), sampled at t = 2, 4, 6, 8, 24 and 48 hours after slurry preparation compared to IBU and ISO starting material DSC traces.

The endothermic event coinciding with the melting of IBU at 78 °C appears to become more prominent over time, while simultaneously the area of the co-crystal melting endotherm becomes less dominant. No endotherm corresponding with the melting event of ISO is evident even over time, confirming IBU is more stable and less soluble than ISO in 60:40 HI. Similarly, the switch in relative prominence of the IBU and co-crystal endotherms with time confirms that IBU is more stable and less soluble than the co-crystal in 60:40 HI.

6.4.4.6 Continuous Cooling Co-crystallisation in the KRAIC and KRAIC-D platforms: IBU-ISO in 60:40 HI (IBU-ISOK and IBU-ISOKD)

Formation of the IBU-ISO co-crystal has been achieved *via* batch cooling up to 200 mL scale; this highlights the potential of translating the production of this co-crystal *via* cooling into continuous crystallisation platforms, such as the KRAIC / KRAIC-D.

The solubility behaviour of IBU-ISO was previously investigated in the Crystal16® at 1 mL and *via* observation at 20 mL batch scales (Section 6.4.4.3**)**. The MSZ of IBU_ISO in 60:40 HI in the Crystal16® was not well known due to the unusual ‘oiling out’ behaviour and subsequent

relative concentrations of clear and cloud points at a given temperature. Nonetheless, the MSZ in the KRAIC / KRAIC-D platforms will not only be different to the 1 mL batch scale, but the MSZ cannot be ascertained in these platforms as the cooling is not controlled. The MSZW is dependent on the kinetics of the system and thus the use of segmentation will increase the MSZ, due to the removal of the solid-liquid phase boundary, the corresponding mixing strategy is an intrinsic recirculation within slugs.[174] It is expected that the concentration requirements in the KRAIC / KRAIC-D will be notably higher due to the use of segmentation and the gentle mixing conditions inherent to the bolus flow within each solution slug in these milliscale crystallisers. However, as the MSZW is unknown, initial experiments adopted a cooling regime close to the solubility curve.

To develop the flow crystallisation process of IBU_ISO 1:2 in 60:40 HI for in-beam operation in the KRAIC-D, developmental work optimised offline was carried out in the KRAIC. The experimental set-ups for the cooling co-crystallisation of IBU_ISO 1:2 in 60:40 HI for the KRAIC and KRAIC-D platforms are illustrated in Chapter 5 in Figure 5.20 and Figures 6.43-6.44 respectively. Depending on how rapidly nucleating the IBU-ISO system is, coupled with the concentration and temperature conditions, further temperature controlled tubing such as a section of sub-ambient jacketed crystalliser tubing (represented by the nucleation promoter in Figure 6.44) may be required to promote nucleation as the crystallisation process is optimised. The flow parameters and experimental conditions for the IBU-ISOK and IBU-ISOKD experiments are summarised in Tables 6.7 and 6.8 respectively.

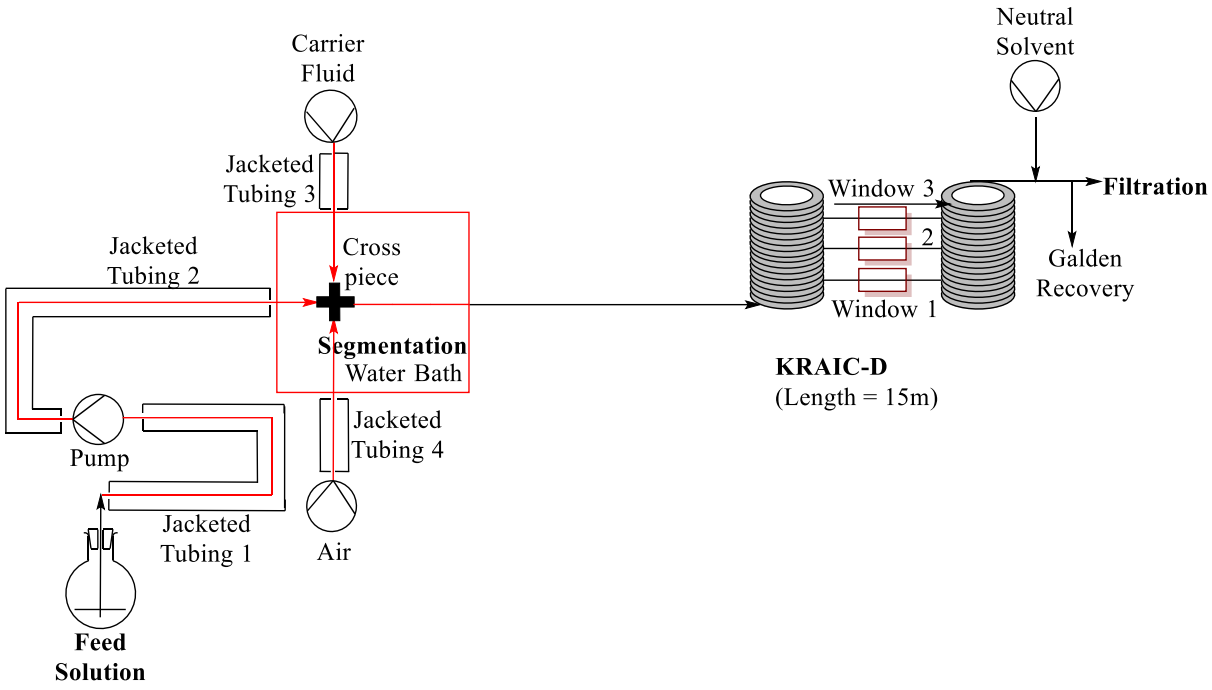

Figure 6.43 – Schematic of KRAIC-D IBU-ISO cooling co-crystallisation experimental set-up employed for IBU-ISOKD experiments1-3 at I11.

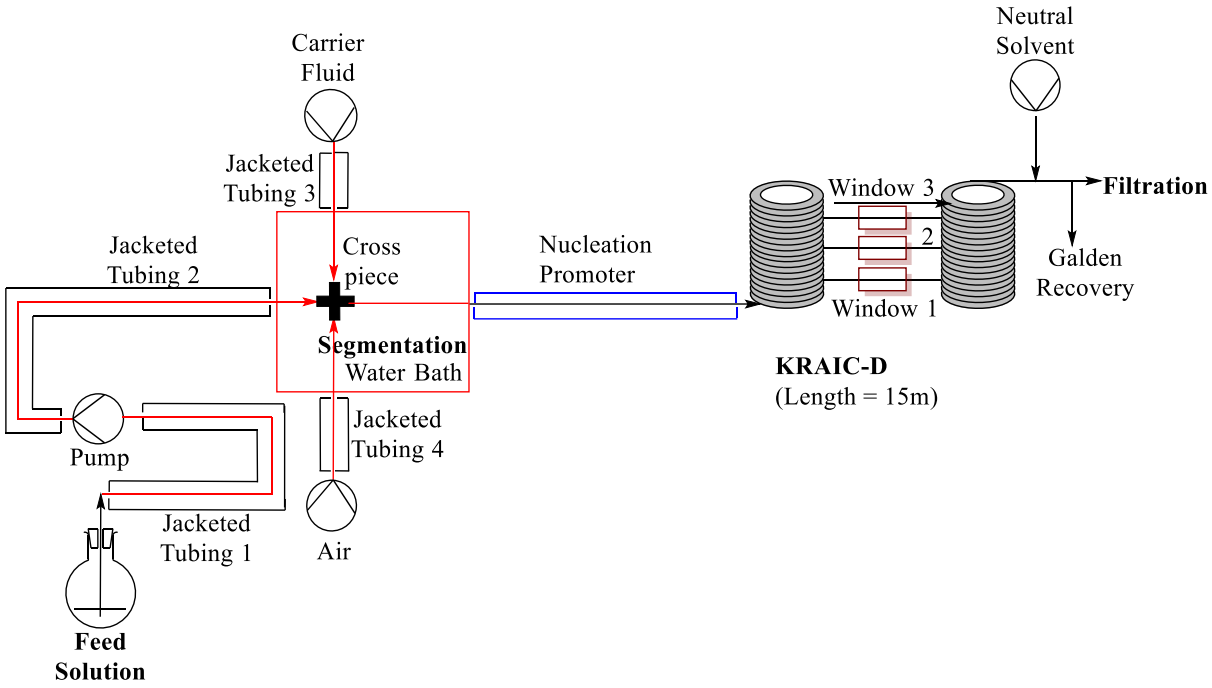

Figure 6.44 – Schematic of KRAIC-D IBU-ISO cooling co-crystallisation experimental set-up employed for IBU-ISOKD4 at I11.

Table 6.7 – Flow parameters for the continuous co-crystallisation of IBU-ISO in the KRAIC / KRAIC-D platforms, identified by IBU-ISOK and IBU-ISOKD respectively.

	Ismatec ISM895E gear pump			**Vapourtec SF-10**	**Total (excl. NS)**
	Carrier fluid	**Air**	**Neutral solvent (NS)**	**Solution**	
Flow rate /mL/min	2.1	4.18	12.5	1.6	7.88

Table 6.8 – Experimental parameters for offline KRAIC and online KRAIC-D experiments, identified by IBU-ISOK and IBU-ISOKD respectively. *Temperature was reduced to 40 ℃, 10 minutes into the crystallisation process. **Water bath set to 35 ℃ initially, increased to 40 ℃ at 15 minutes.

Experiment	**Concentration of IBU g/L**	**Concentration of ISO g/L**	**Temperature until segmentation (℃)**	**Nucleation Promoter**
IBU-ISOK1	40	47.4	50*	No
IBU-ISOK2	80	94.8	40**	No
IBU-ISOKD1	60	71.1	40	No
IBU-ISOKD2	70	83	40	No
IBU-ISOKD3	80	94.8	40	No
IBU-ISOKD4	60	71.1	40	Yes

IBU-ISOK1

The initial ratio of IBU_ISO 1:2 in 60:40 HI (40 g/L IBU, 47.4 g/L ISO) was selected (IBU-ISOK1). All temperature controls including feeds, the circulator used for the tubing jackets and the segmentation water bath, were set to 50 ℃; this was reduced to 40 ℃, as the feed solution had good solubility at room temperature. The experimental residence time (RT) was measured at 27 minutes. At 1 hour 36 minutes into the continuous run, no crystallisation had been observed; ice was thus introduced inside coil 1 at 1 hour 58 minutes, as a crude way to provide insight as to whether additional temperature control in the form of a cold tube could promote nucleation at this concentration. At 2 hours into the crystallisation run an emulsion was observed in the solution slugs in coil 1; this is consistent with the oiling out observed in the Crystalline® images in the solubility study of IBU_ISO 1:1 (Section 6.4.4.3.1). This emulsion re-dissolved in coil 2. Crystallisation was not observed under these conditions so an increase in concentration of the crystallising feed was required.

IBU-ISOK2

The concentration of IBU_ISO 1:2 in 60:40 HI was doubled to 80 g/L IBU and 94.8 g/L ISO in 60:40 HI to promote crystallisation. The circulator bath and feed solution were controlled at

40 °C, whilst the water bath was set to 35 °C and an ice bag was again placed inside coil 1. The previous flow parameters were maintained, whilst employing the same pumps, however a large decrease of 12 minutes in experimental residence time to 15.0 minutes was observed. The theoretical residence time for these flow rates is 15.1 minutes, suggesting that the residence time for IBU-ISOK1 is inaccurate.

Slugs in the emulsion phase were observed emerging from the 35 °C water bath, indicating that the ice bag in coil 1 may not be required at this increased concentration. Crystallisation was observed at 9 minutes into the crystallisation run at coil 1, rung 5. A number of crystals were observed in several slugs, with the extent of crystal growth in each slug sufficient to cause a blockage in coil 1. This suggested a reduction in feed concentration in addition to removal of the ice bag from the inside of coil 1 was required. The ice bag was removed from the inside of coil 1 and the temperature of the water bath was increased to 40 °C after a full residence time (15 minutes into the experiment time), after which slugs in the emulsion phase were no longer observed emerging from the water bath.

Samples under these conditions were collected to establish whether the IBU-ISO co-crystal was accessed in flow and the level of purity of the crystalline product. These samples were not collected for a full RT and due to blockages the flow rate was not always consistent over the collection time; a yield could therefore not be determined. Samples were taken at different times within the experiment for two collection periods: 15-30 minutes and 35-44 minutes for samples 1 and 2 respectively. The corresponding PXRD patterns IBU-ISOK2_sample 1 and IBU-ISOK2_sample 2 (Figure 6.45) show the IBU-ISO co-crystal is produced over both collection times, with sample 1 also containing some IBU starting material.

The corresponding DSC traces feature a single endothermic peak at 120 °C showing that the co-crystal had been accessed in flow consistently across two separate collection times (Figure 6.46). However, sample 1 is not pure with respect to the co-crystal, with a representative IBU peak at 78 °C. This difference in purity between the two samples could result from blockages; the KRAIC experienced a greater degree of encrustation for sample 1 compared to sample 2. The decrease in the extent of blockages between the two collection times can be attributed to an increase in temperature control, with the temperature raised for sample 2.

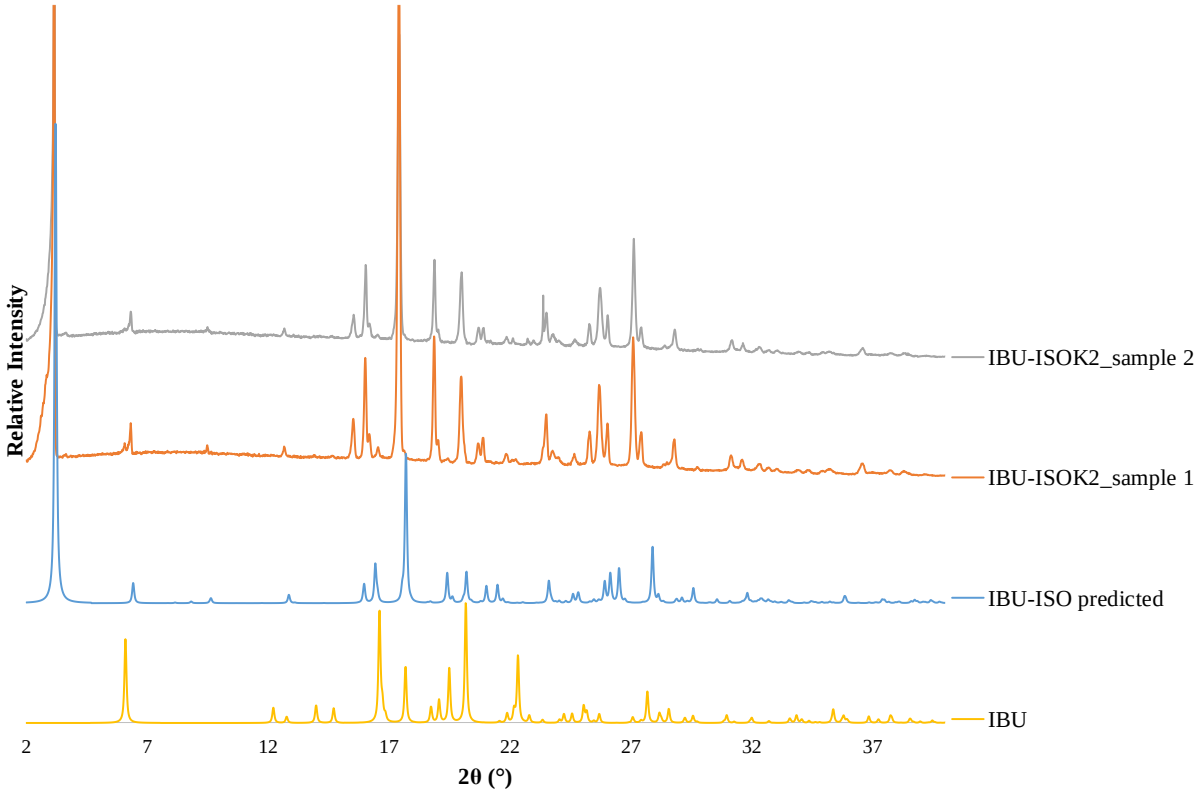

Figure 6.45 – PXRD patterns from experiment IBU-ISOK2, sample 1 and 2 were collected at 15 minutes and 35 minutes into the experiment respectively. The PXRD patterns for IBU-ISOK2_sample 1 and IBU-ISOK2_sample 2 have been truncated for clarity.

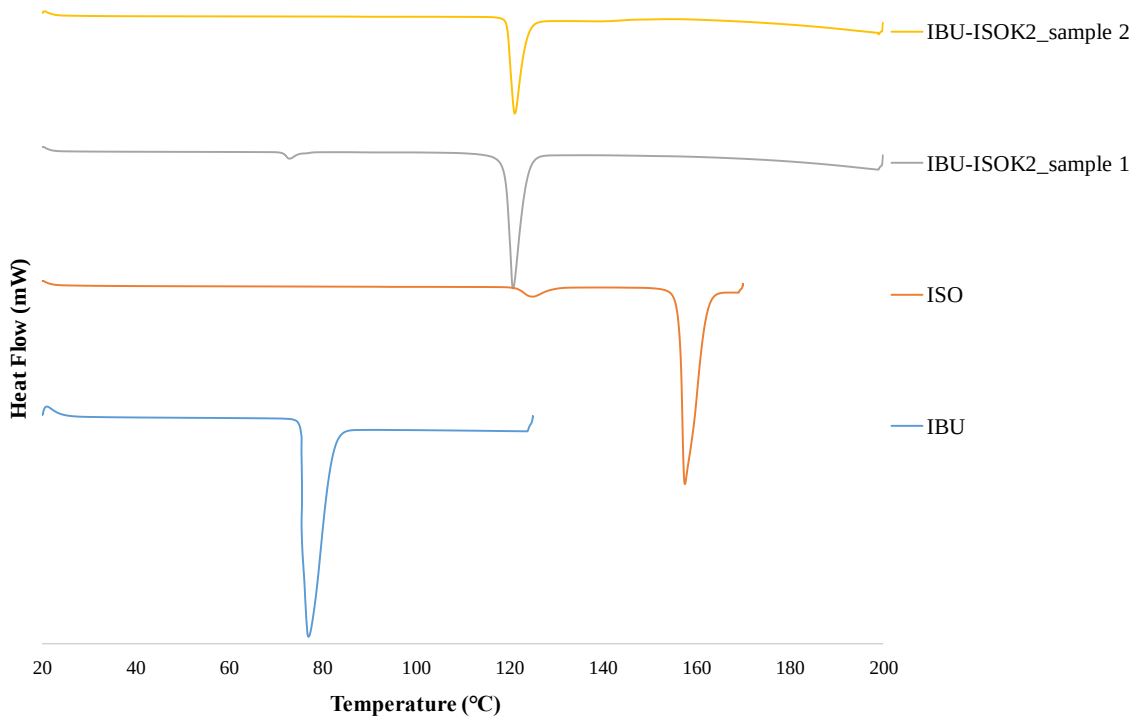

Figure 6.46 – DSC traces of IBU_ISO 1:2 in 60:40 HI in the KRAIC platform sampled at two different time points corresponding with experiment times of 15-30 minutes and 35-44 minutes compared to the DSC traces of the IBU and ISO starting materials.

The IBU-ISOKD1-2 experiments showed that the crystallisation process requires further optimisation in terms of concentration and temperature conditions to crystallise the IBU-ISO co-crystal in flow without blockages.

IBU-ISOKD1-4

Following the offline experiments, the cooling crystallisation of IBU-ISO in 60:40 HI was investigated in the KRAIC-D at I11 through *in situ* XRD characterisation (IBU-ISOKD). However, the initial suggested parameters from offline experiments in the KRAIC (reduced concentration, altered temperature control) did not yield crystallisation at I11 (IBU-ISOKD1 and IBU-ISOKD2). The conditions were altered accordingly towards those adopted in the KRAIC experiments IBU-ISOK1 and IBU-ISOK2 at Bath (Tables 6.7 and 6.8), but crystallisation was still not observed (IBU-ISOKD3). For experiment IBU-ISOKD4, the introduction of a nucleation promoter to encourage nucleation at 15 ℃ also did not produce crystallisation. Decreasing the temperature of the nucleation promoter to 10 ℃ caused crystallisation to occur uncontrollably, rapidly creating a blockage. This suggests that the MSZ in the KRAIC / KRAIC-D segmented flow platforms must be extremely narrow to move from no crystallisation to uncontrollable crystallisation with small changes in experimental conditions.

Another important conclusion from this work was that the blockages resulted from the oil phase preferentially combining with the Galden® (carrier fluid) in the segmented flow. This results in an emulsion comprising the carrier fluid and crystallising solution, whereby the crystallising solution has reached the ‘oiling out’ phase and thus on the premise of miscibility will preferentially combine and mix with the carrier fluid rather than the solvent in the crystallising solution slugs. This resulted in encrustation, which did not sit within a solution slug, but instead within the tubing interfacing with the walls of the inside of the FEP, whilst the segmented flow was simultaneously attempting to pass the blockage. This encrustation on the tubing contrasts with the plug shaped blocks usually observed when encrustation occurs in the KRAIC / KRAIC-D platforms. This highlights that the segmented flow utilised in the KRAIC / KRAIC-D is not suitable for every crystallisation process.

6.5 Oxaprozin Isonicotinamide (OXA-ISO)

6.5.1 Evaporative Crystallisations of OXA-ISO

The PXRD patterns for OXA (20 mg) and ISO (8.3 mg) in a 1:1 ratio dissolved in approximately 2 mL of EtOH, IPA and ACE, solvent systems, evaporated at 30 °C, confirm that EtOH and IPA solvent systems yield OXA starting material, whilst ACE yields a potential co-crystal *via* evaporative methods, when compared to the PXRD patterns of the starting materials including various polymorphic forms. The evidence of co-crystal formation is especially prominent from peaks at 8° and 13° 2θ, a peak not present in any of the starting material PXRD patterns (Figure 6.47). The PXRD patterns of pure OXA and potential OXA-ISO co-crystal are very similar and therefore DSC and structurally definitive SCXRD are particularly beneficial analytical techniques for the OXA-ISO system. The variance in crystalline outcome across the various solvent systems indicates the influence of solvent on co-crystal formation and highlights the importance of solvent screening in material discovery.

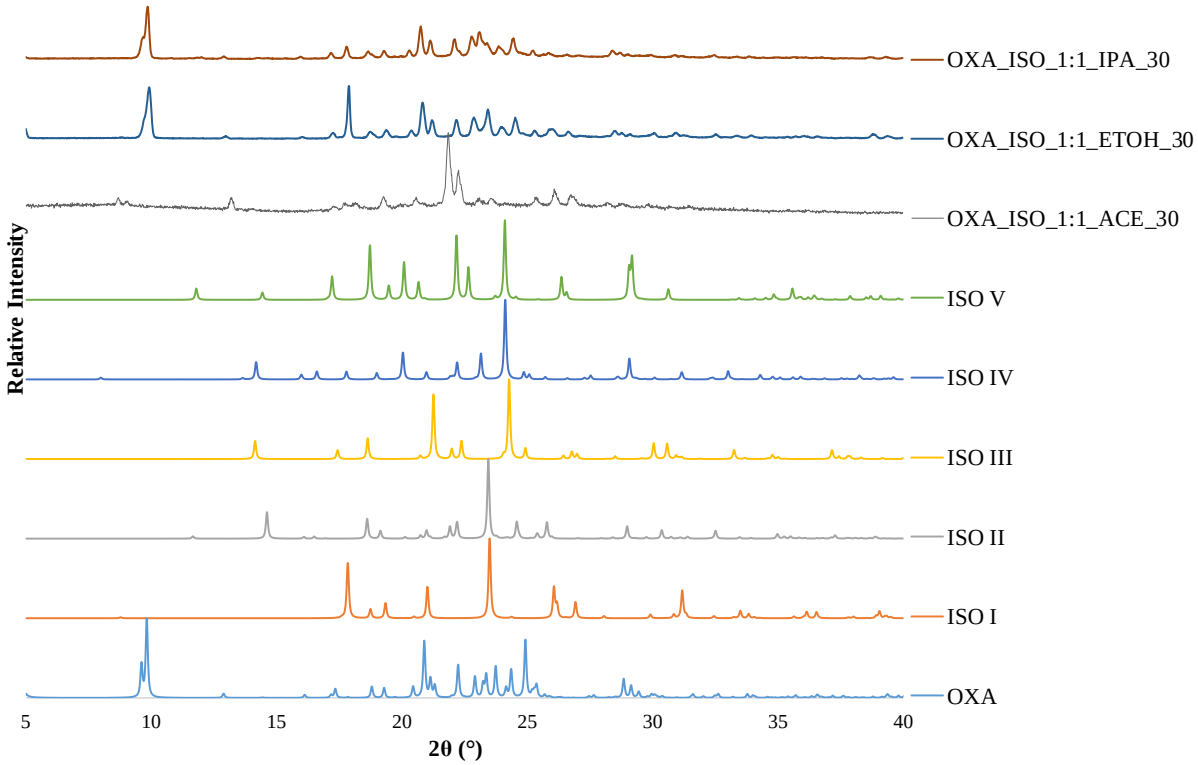

Figure 6.47 – PXRD patterns of attempted co-crystallisations of OXA-ISO prepared *via* evaporative crystallisations in three different solvents each at 30 °C, compared to the PXRD patterns of the constituent starting materials including various polymorphic forms (Refcodes: OJURAO (OXA), EHOWIH01-05 (ISO I-V respectively)).

The same samples analysed *via* PXRD, were also analysed by DSC using a ramp rate of 10 °C min^{-1}. The DSC traces for OXA-ISO co-crystallisation attempts in a 1:1 ratio dissolved in these three solvent systems, reconfirmed the possible formation of OXA-ISO, through the presence of an endothermic event around 124 °C for each of these attempted co-crystallisations. This endothermic event does not correspond to a melting event of either of the starting materials, which exhibit endotherms at 163 °C and 158 °C for OXA and ISO respectively (Figure 6.48). The co-crystal is confirmed in purity across all solvent systems from DSC analysis, with no OXA endotherm in any of the traces. This is contradictory to the indications from PXRD analysis, where access to co-crystal formation is only indicated from ACE.

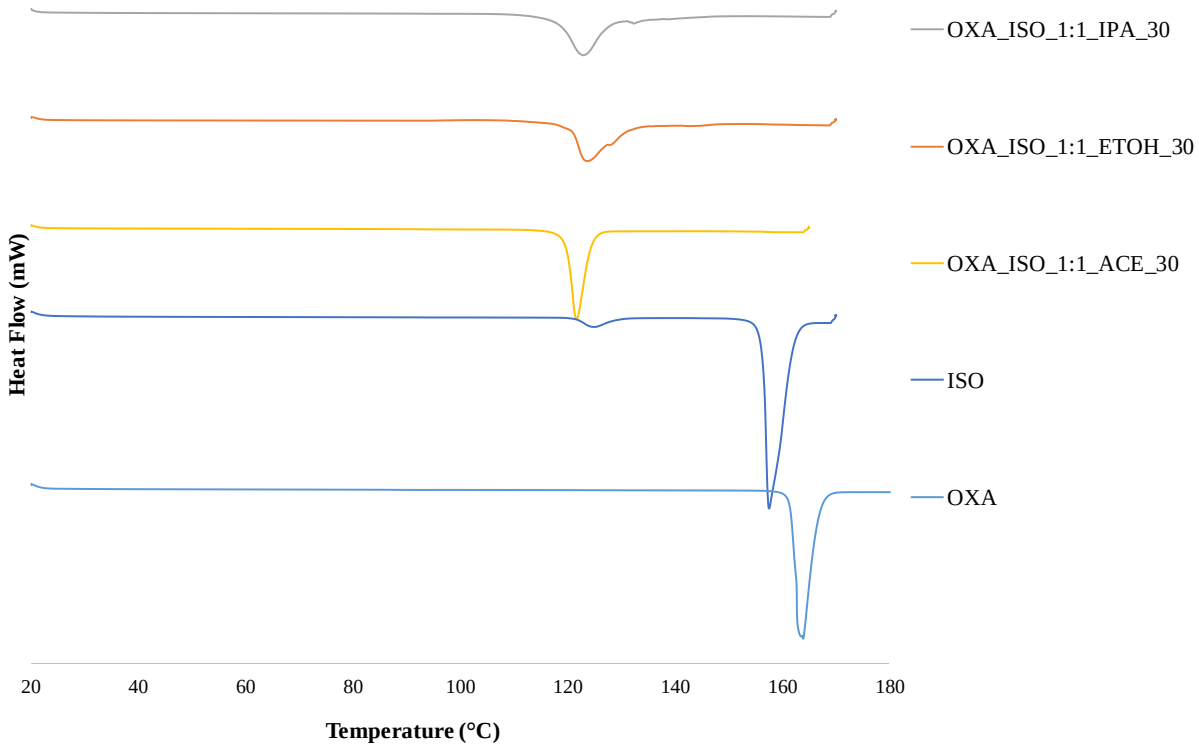

Figure 6.48 – DSC heat profiles for the molecular complex OXA-ISO 1:1 prepared *via* evaporative crystallisations at 30 °C in ACE, EtOH and IPA solvent systems.

Structural determination of OXA-ISO

A mass of 20 mg of OXA and 8.3 mg of ISO in a 1:1 ratio were dissolved in 2 mL of ACE and the solvent allowed to evaporate for one week at 30 °C *via* holes punctured in the lid of the vial, producing single crystals of suitable quality for diffraction analysis. A suitable single crystal was subjected to SCXRD analysis at the Advanced Light Source (ALS) synchrotron on

beamline 12.2.1, to determine the full 3D crystal structure of the novel co-crystal; the crystal data for OXA-ISO are summarised in Table 6.9.

Table 6.9 – Crystal data and structural refinement parameters for OXA-ISO.

Empirical formula	**$C_{24}H_{21}N_3O_4$**
Formula weight	415.12
Temperature /K	273.15
Crystal system	Monoclinic
Space group	*$P2_1/c$*
a /Å	19.3865(9)
b /Å	16.3714(8)
c /Å	39.7044(19)
α /°	90
β /°	103.510(2)
γ /°	90
Volume /Å^3	12252.9(10)
Z	24
ρ_{calc} /g cm^{-3}	1.3501
μ /mm^{-1}	0.098
F(000)	5226.9
Crystal dimensions /μm^3	160 × 40 × 20
Radiation /Å	ALS Synchrotron (λ = 0.7288)
2θ range for data collection /°	2.22 to 52.94
Index ranges	$-23 \leq h \leq 23$, $-19 \leq k \leq 20$, $-48 \leq l \leq 48$
Reflections collected	214902
Independent reflections	23371 [R_{int} = 0.1564, R_{sigma} = 0.0927]
Data/restraints/parameters	23371/0/1731
Goodness-of-fit on F^2	1.033
Final R indexes [I>=2σ (I)]	R_1 = 0.0767, wR_2 = 0.2013
Final R indexes [all data]	R_1 = 0.1019, wR_2 = 0.2364
Largest diff. peak/hole / e Å^{-3}	1.04/-0.48

The OXA-ISO 1:1 co-crystal crystallises in the monoclinic space group *$P2_1/c$*, with six molecules of OXA and six molecules of ISO in the asymmetric unit; the high Z' value (6) is discussed below. On co-crystal formation, a hydrogen bonding interaction is produced between the oxygen on the alcohol group of the carboxylic acid of OXA and the pyridine nitrogen of ISO forming a carboxylic acid:amide $R_2^2(7)$ heterosynthon, corresponding with the intramolecular hydrogen bond O11-H···N8 in Figure 6.49. Figure 6.49 displays half of the asymmetric unit containing two linked tetramers of molecules, allowing visualisation of the interaction between tetramers, whereby each tetramer comprises four molecules: two OXA and two ISO molecules. The other half of the asymmetric unit is similar to the half presented in

Figure 6.49 but with some changes in torsion angle of the phenyl rings. The OXA and ISO molecules are held together by a strong to moderate strength intermolecular hydrogen bond with a bond length of 2.628(3) Å and bond angle slightly offset from linearity, of 176(2)° for O11-H···N8, with the corresponding hydrogen-to-hydrogen donor length (H···N8) bond length of 1.59(3) Å (Figure 6.49).

Other hydrogen bonds are present in this complex asymmetric unit, including dimers of ISO (amide dimer $R_2^2(8)$ homosynthon) between the amide nitrogen and the oxygen on the carbonyl group (O12-H···N10 and N9-H··O13). This interaction happens twice for each of the functionalities on the adjacent molecules and is observed within the chains of molecules. Intermolecular hydrogen bonds are also present between the chains formed from the carbonyl oxygen on the carboxylic acid functionality of OXA with the amide nitrogen of ISO.

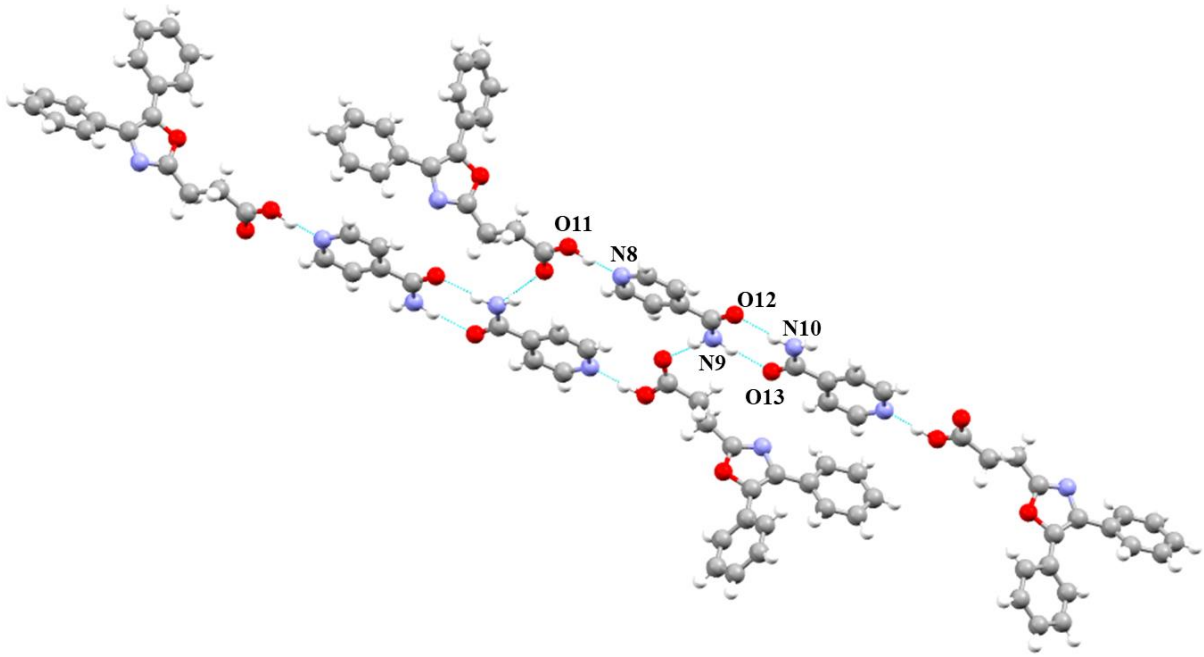

Figure 6.49 – Half of the asymmetric unit of the novel co-crystal structure of OXA-ISO.

Beyond the asymmetric unit, the extended structure is connected through π-π stacking. The packing diagram (Figure 6.50) features many molecules, each with slightly shifted orientations of the phenyl rings in a wave like arrangement. This twisting of the phenyl groups explains the large unit cell and high Z' value; the cell could not be reduced any more in PLATON calculations.

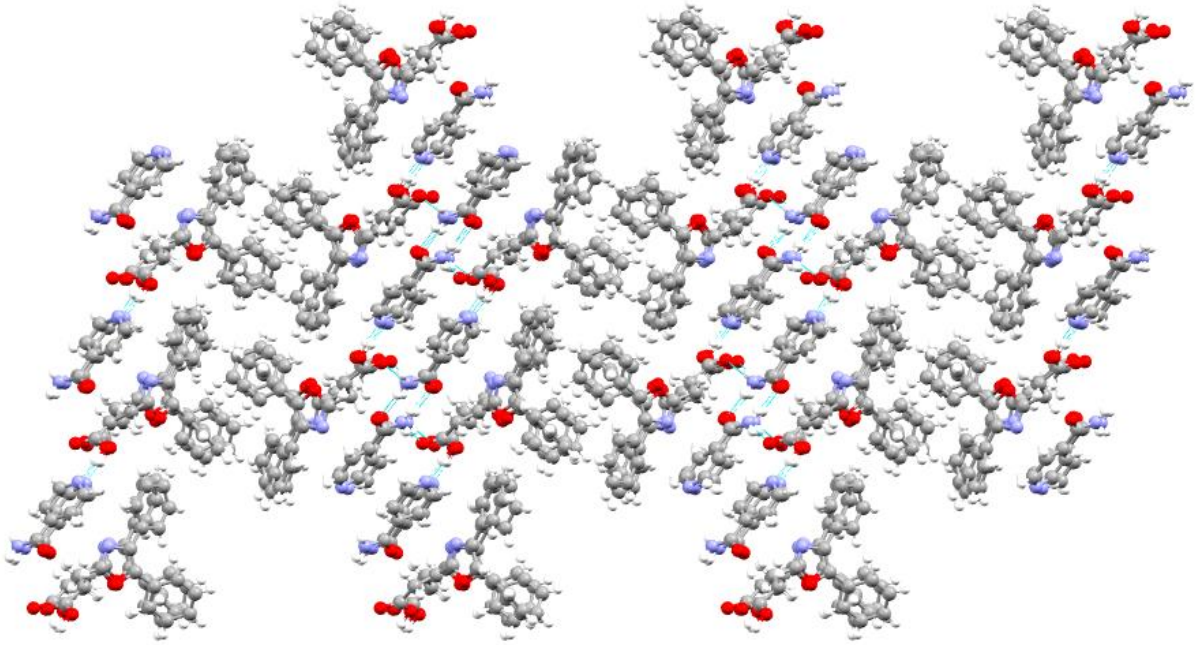

Figure 6.50 – The packing diagram of the novel co-crystal structure OXA-ISO, viewed down the crystallographic *b*-axis.

6.5.1.1 IR Spectroscopy of OXA-ISO

The IR spectrum of OXA-ISO compared to the constituent starting components of OXA and ISO shows a decrease in the N-H stretching frequency of ISO on co-crystal formation. One of the C=O stretching frequencies of OXA-ISO is intermediate with respect to the two starting components (Table 6.10 and Figure 6.51), while the other is very similar to the C=O stretching frequency of OXA.

Table 6.10 – Comparison of IR stretching frequencies of key functional groups in OXA-ISO compared to the constituent OXA and ISO starting materials.

Vibration Frequency (cm^{-1})	OXA	ISO	OXA-ISO
N-H stretch	-	3362	3337 (O11-H···N8)
C=O stretch	1719	1656	1715 1682 (C67=O11)

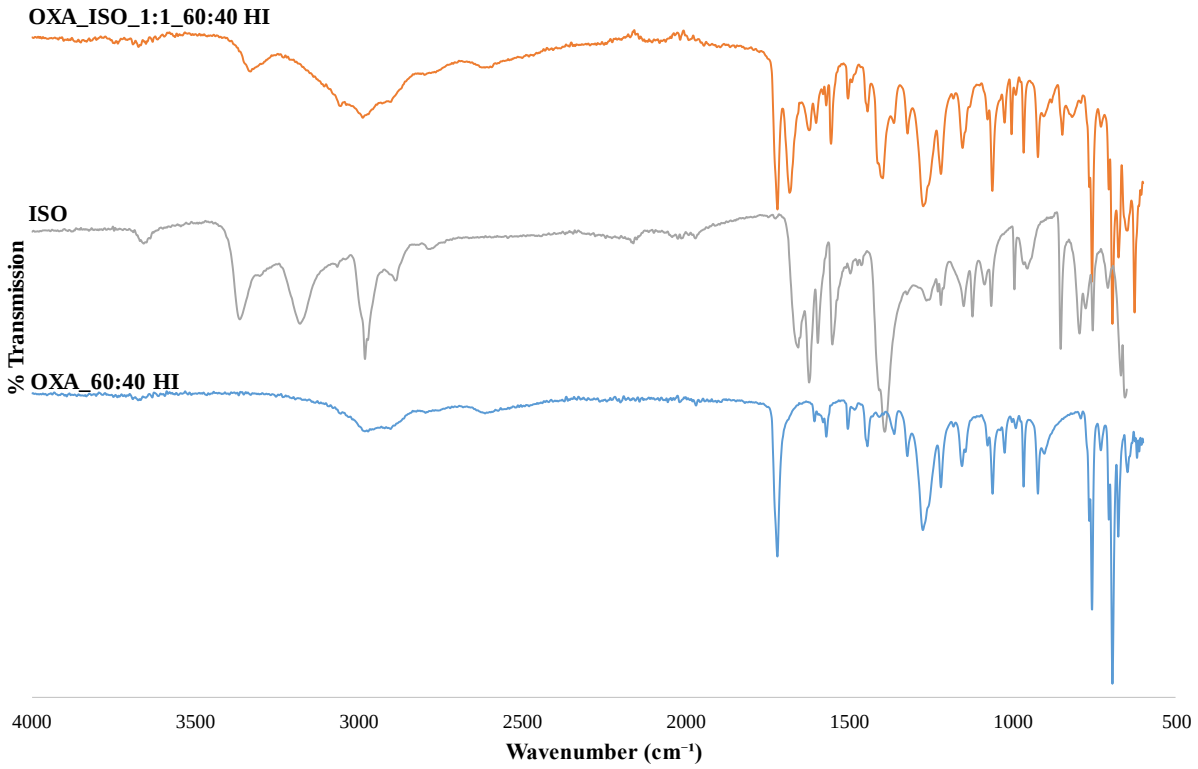

Figure 6.51 – FTIR spectra of OXA-ISO compared to the constituent OXA and ISO starting materials.

Comparing the predicted PXRD pattern of the OXA-ISO co-crystal (using Mercury Version 4.2.0), with the pure starting components obtained from the CSD and simulated in Mercury, a new co-crystalline material has been identified (Figure 6.52). Differentiating between co-crystal formation of OXA-ISO and re-crystallising the OXA API is challenging in this case as there are few discernible differences between the PXRD patterns of the two materials. An additional challenge in fingerprinting the PXRD patterns against the starting material and co-crystal is that the temperature of collection of the co-crystal is 150 K, whilst the various crystallisations will be analysed by PXRD at room temperature. Therefore, the slight shift in peaks, for instance the pair of diffraction peaks at 10° 2θ for OXA and OXA-ISO, could be shifted because of a different crystalline product or because of temperature effects. The OXA-ISO single crystal selected for SCXRD is not fully representative of the bulk sample of OXA_ISO 1:1 evaporated from ACE.

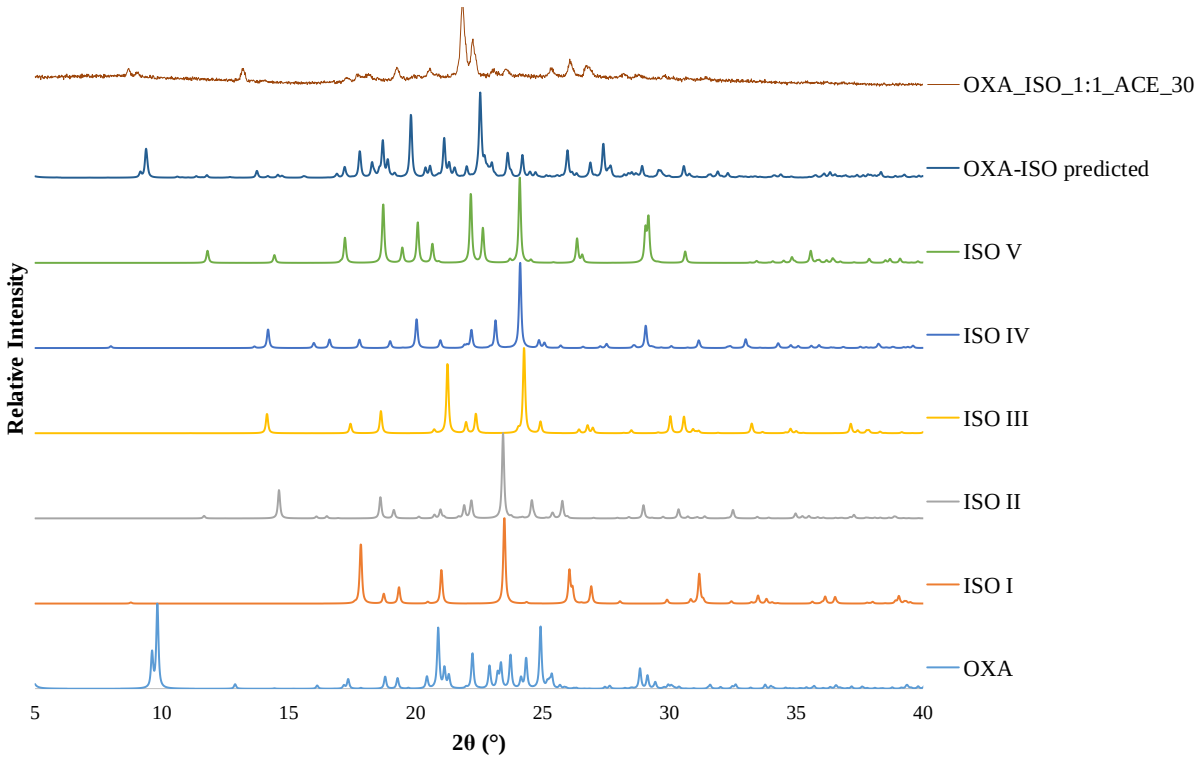

Figure 6.52 – PXRD patterns comparing OXA-ISO predicted pattern simulated in Mercury and OXA_ISO 1:1 evaporated from ACE, with the PXRD patterns of the pure starting materials obtained from Mercury (Refcodes: OJURAO (OXA), EHOWIH01-05 (ISO I-V respectively)).

6.5.2 Mechanochemical Crystallisations of OXA-ISO

Once co-crystal formation for the OXA-ISO co-crystal had been achieved through evaporation and confirmed through SCXRD, PXRD and DSC analytical techniques, this system was translated into grinding approaches. The OXA_ISO 1:1 sample prepared *via* NG and LAG across each of the solvents yields the same diffraction patterns, which can be identified as mainly OXA starting material, but with some additional representative OXA-ISO peaks aligning at 26° and 27° 2θ (Figure 6.53). Similar to the DSC traces from the evaporative crystallisations of OXA-ISO, the DSC traces for these mechanochemical crystallisations also feature a single endotherm at 120 °C, confirming co-crystal formation from thermal analysis (Figure 6.54).

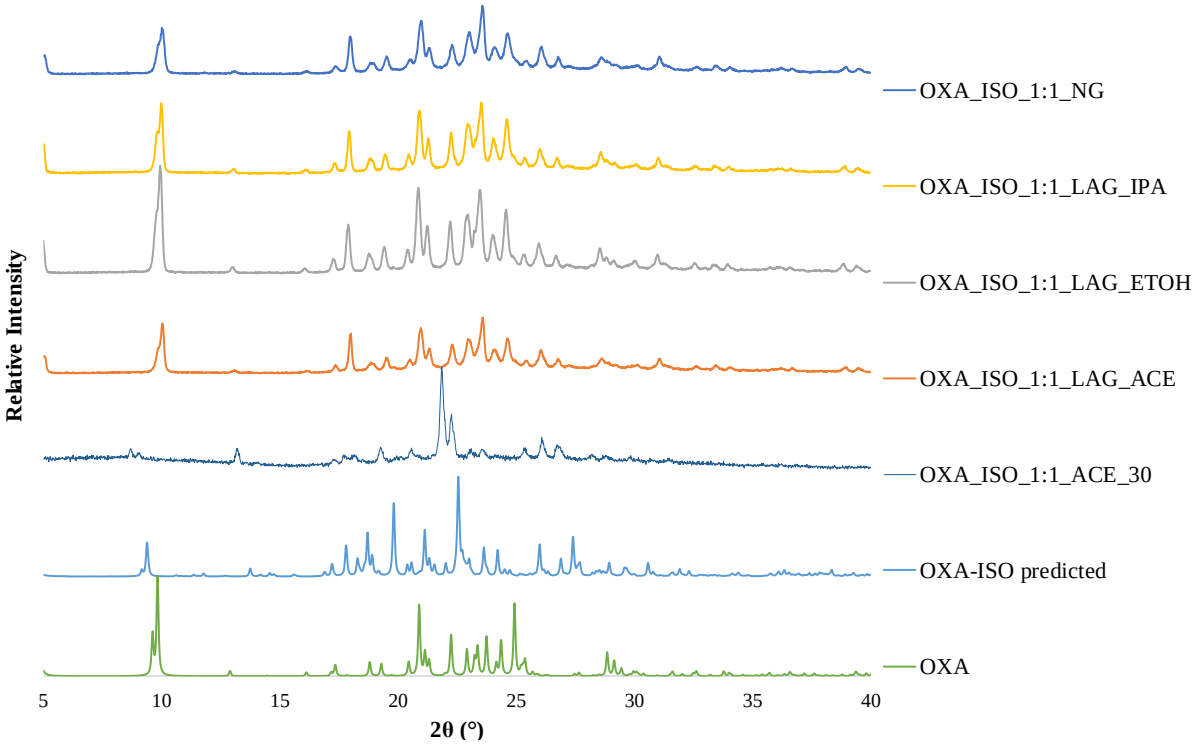

Figure 6.53 – PXRD patterns of the OXA-ISO 1:1 molecular complex prepared *via* mechanochemical crystallisation both NG and LAG in three different solvents, compared to the PXRD pattern of OXA_ISO 1:1 crystallised from evaporation of ACE, as well as OXA (Refcode OJURAO) and OXA-ISO predicted patterns simulated in Mercury.

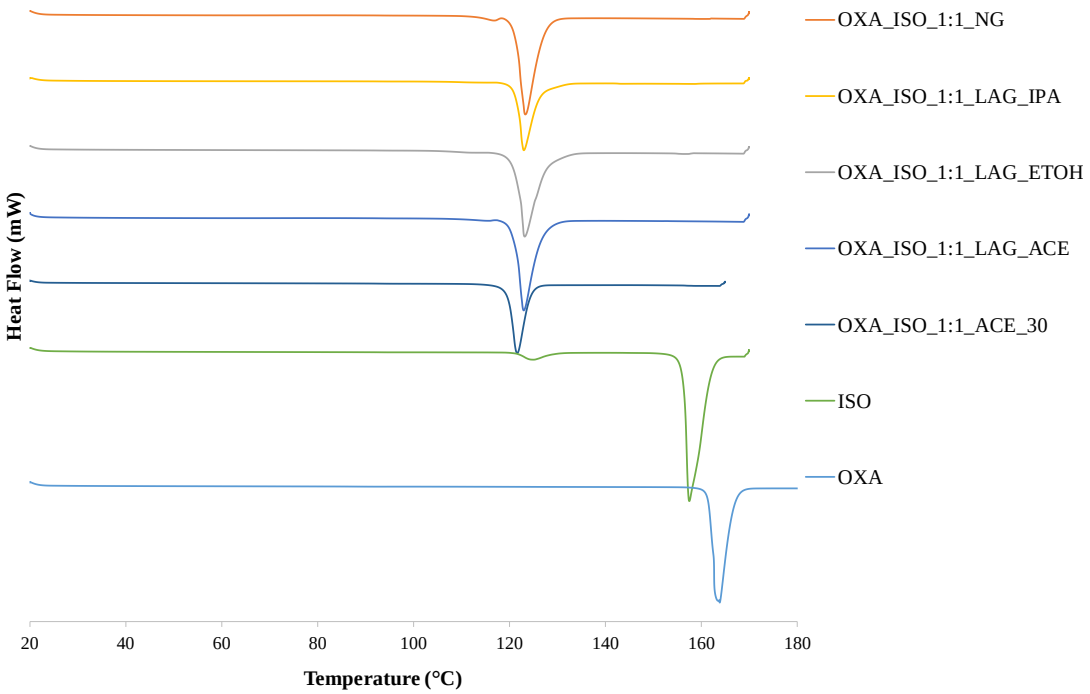

Figure 6.54 – DSC heat profile for the molecular complex of OXA-ISO 1:1 prepared *via* mechanochemical crystallisation using both NG and LAG in ACE, EtOH and IPA solvent systems, compared to the DSC trace of OXA_ISO 1:1 crystallised from evaporation of ACE, as well as the DSC traces of OXA and ISO starting materials.

Importantly, the discrepancy between PXRD and DSC analysis in addition to the data obtained from OXA-ISO crystallised *via* evaporative methods is also evident from these mechanochemical crystallisations. It can be postulated that a large proportion of the bulk sample is the OXA-ISO co-crystal, however the sample is not solely comprised of crystalline material, so co-crystal formation is not as prominent in the PXRD analysis as in the DSC analysis, where this thermal analysis has the ability to analyse amorphous material.

This indicates that mechanochemical crystallisation for 5 minutes of OXA and ISO 1:1 does not achieve the co-crystal in 100 % yield, evident from PXRD but not DSC analysis. An increase in grinding time could lead to complete conversion to the co-crystal, or a change in stoichiometric ratio of the starting components could mitigate the excess starting material observed.

6.5.3 Slurrying Crystallisations of OXA-ISO

Investigations into whether the OXA-ISO co-crystal could be accessed using small-scale slurry techniques were conducted using the same three solvents (ACE, EtOH, IPA) as those investigated in evaporative and mechanochemical techniques used to access the co-crystal previously. The slurries were prepared using a 1:1 molar ratio of OXA (400 mg) and ISO in 2 mL of solvent, left stirring at 250 rpm on a hot-plate with DrySyn attachment set to 30 ℃ for one week. After this stirring period, the resultant product was isolated from the solvent using vacuum filtration and left to dry for 24 hours before being analysed *via* PXRD and DSC.

The PXRD analysis shows OXA starting material is produced *via* slurrying methods (Figure 6.55; but note that this conclusion is affected by the similarity of the OXA and OXA-ISO predicted PXRD patterns). In contrast, the DSC analysis on the same samples, showed consistency in endotherms across each of the solvent systems with a single melting event at 123 ℃, which does not coincide with the melting event of OXA, which is expected at 160 ℃ (Figure 6.56).

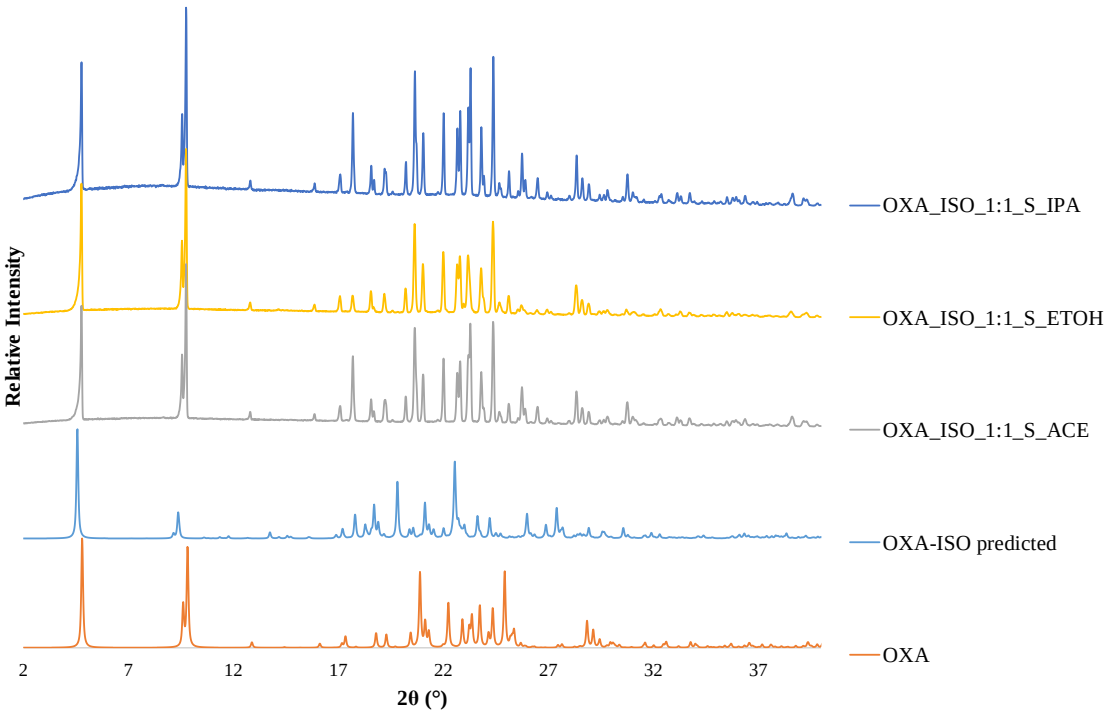

Figure 6.55 – PXRD patterns of the OXA-ISO 1:1 molecular complex prepared *via* slurrying crystallisations for 1 week in three different solvents systems compared to the PXRD pattern of the OXA-ISO predicted pattern simulated in Mercury and OXA (Ref code: OJURAO) powder pattern.

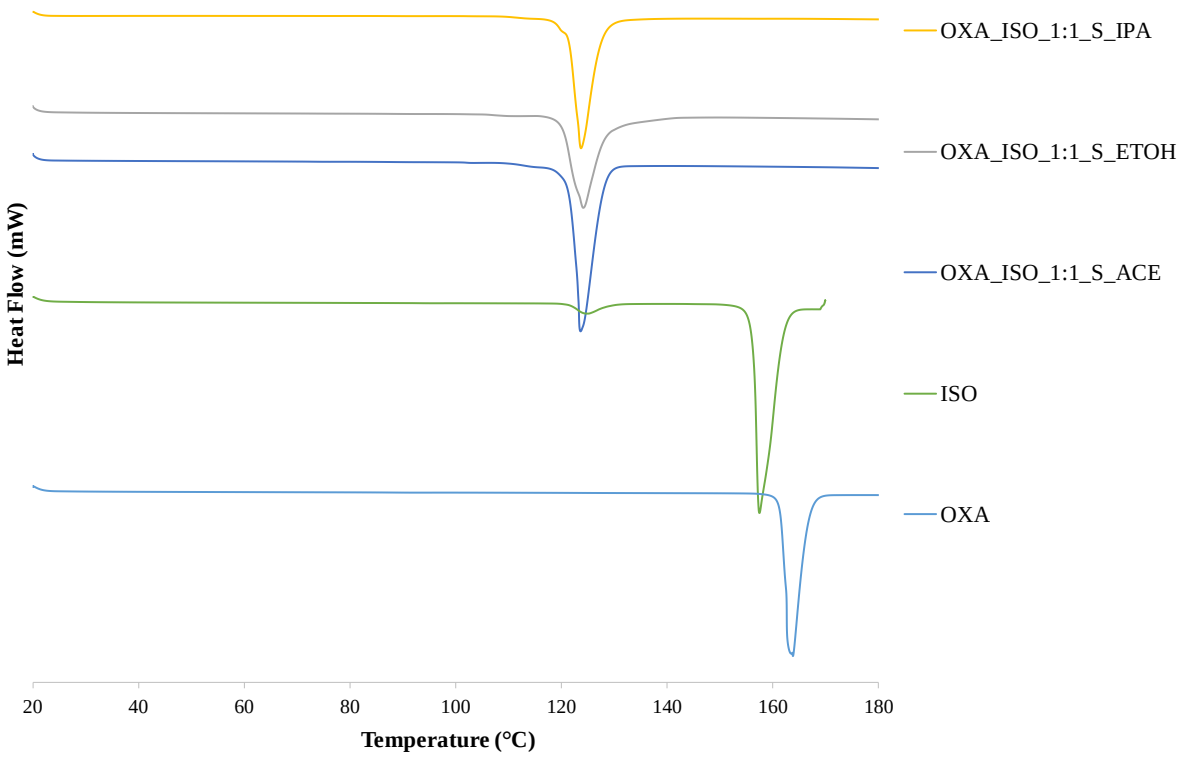

Figure 6.56 – DSC heat profile for the molecular complex OXA-ISO 1:1 prepared *via* slurrying crystallisation for 1 week in three different solvent systems.

6.5.4 OXA-ISO crystallisations in 60:40 water:isopropanol (HI)

The crystallisation of the OXA-ISO co-crystal was evaluated in 60:40 HI across the range of crystallisation methods already investigated. The PXRD data confirms OXA-ISO co-crystal formation *via* evaporative methods, although the co-crystal has not been accessed in purity, indicated by the presence of additional diffraction peaks. Mechanochemical methods produced OXA-ISO largely in purity while OXA_ISO slurry mediated in 60:40 HI produces OXA starting material (Figure 6.57). These observations were confirmed by DSC data (Figure 6.58).

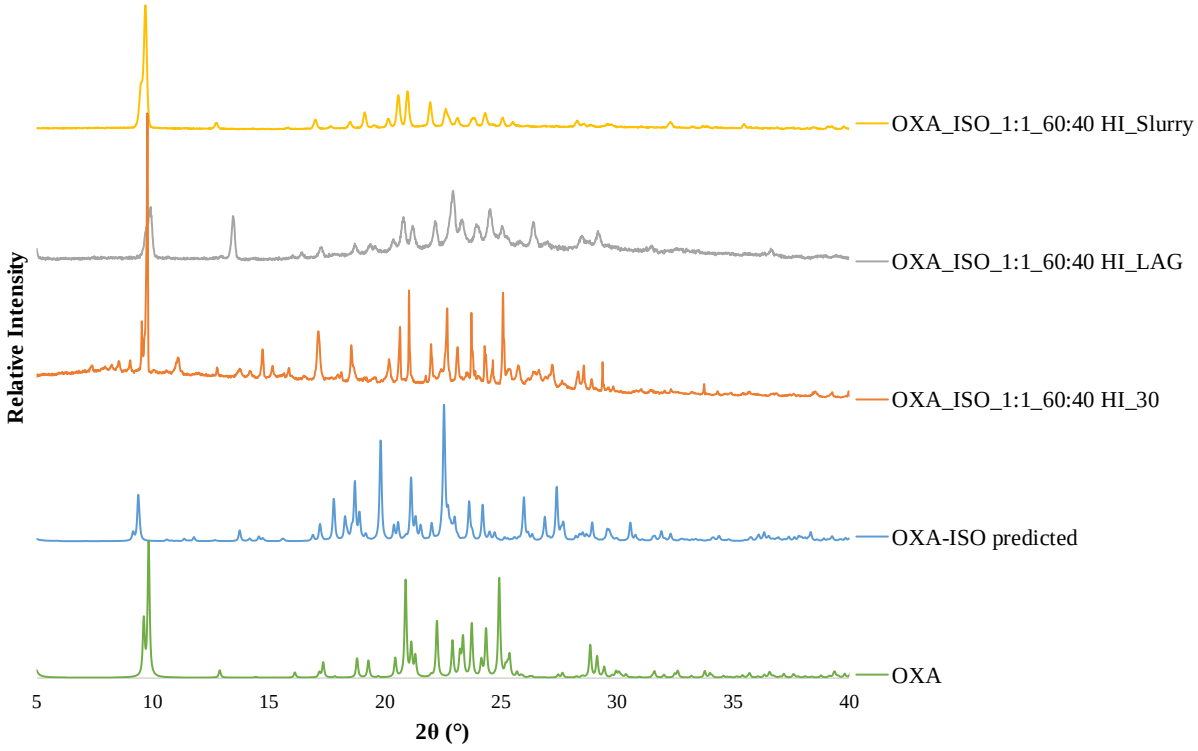

Figure 6.57 – PXRD patterns of the OXA-ISO 1:1 prepared in 60:40 HI *via* various crystallisation methods: evaporative, LAG, slurrying at 20 °C at 10 mL scale for a slurry time of 24 hours, compared to the PXRD pattern of the OXA-ISO predicted pattern simulated in Mercury and OXA (Refcode: OJURAO) starting material.

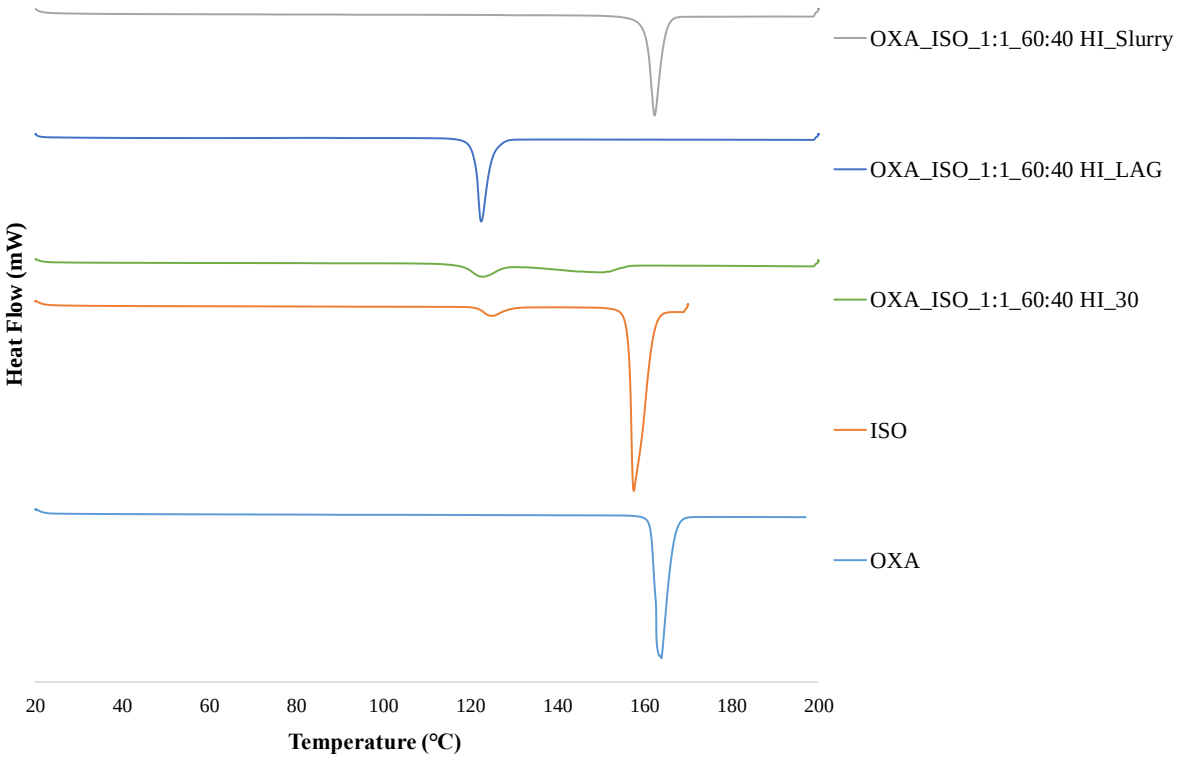

Figure 6.58 – DSC heat profiles of the OXA-ISO 1:1 molecular complex prepared in 60:40 HI *via* various crystallisation methods: evaporative at 30 °C, LAG, slurrying at 20 °C at 10 mL scale for a slurry time of 24 hours, compared to the DSC traces of pure OXA and pure ISO starting materials.

6.5.4.1 Relative Thermal Stability Studies and Humidity Studies of OXA-ISO

It is evident that the samples prepared by mechanochemical crystallisations compared to the solution-based preparations show marked differences in crystalline outcome, producing the OXA-ISO co-crystal and recrystallisation of the OXA starting material respectively. This highlights a distinct difference between solid and solution phase co-crystal preparation.

Both thermal stability and humidity stability studies of the OXA-ISO co-crystal, carried out as outlined for ISO-IBU above, showed small but not significant changes in the diffraction peaks presented in the PXRD analysis. Similarly, thermal analysis using DSC did not show any significant changes to the phase adopted when investigating thermal ageing monitored over time.

6.5.4.2 Solubility measurements of OXA ISO in 60:40 HI

Solubility analysis to obtain a combined solubility of a physical mixture of OXA and ISO in a 1:1 molar ratio was carried out by turbidity measurements at 1 mL scale using the Crystal16® platform at the University of Strathclyde (Figure 6.59). This solubility curve of OXA_ISO 1:1

in 60:40 HI will be used in the design of the cooling regime used to access the OXA-ISO co-crystal by cooling at scale.

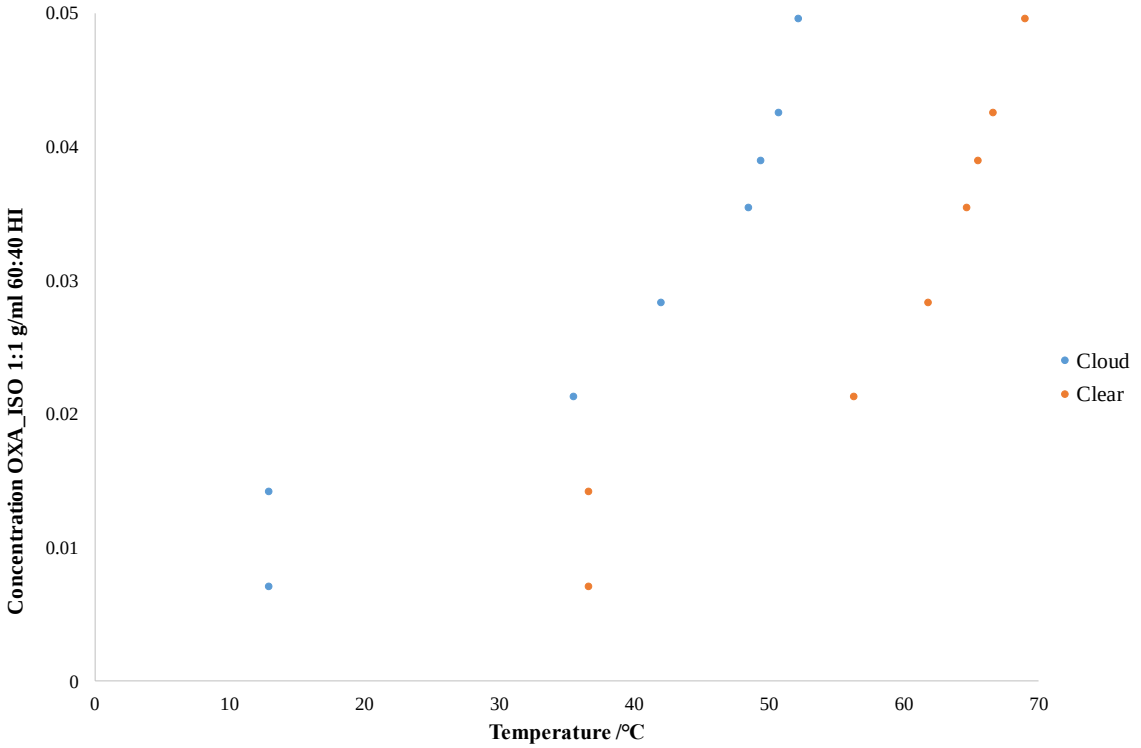

Figure 6.59 – Solubility curve of OXA and ISO 1:1 physical mixture in 60:40 HI at 1 mL scale in Crystal16®.

6.5.4.3 Cooling Crystallisations of OXA-ISO

6.5.4.3.1 Batch *via* Polar Bear Plus from Cambridge Reactor Design (CRD)

The OXA-ISO co-crystal was translated into cooling crystallisation, with the quantities of OXA and ISO initially based upon the solubility at room temperature of the physical mixture of OXA_ISO in 60:40 HI at 1 mL scale in the Crystal16®. A concentration range was selected to ascertain how concentration choice influences OXA-ISO co-crystal formation. The OXA_ISO 1:1 in 1 mL 60:40 HI samples were heated to 70 °C, followed by a 1 hour dwell time, to ensure complete dissolution before cooling to 5 °C at a cooling rate of 0.05 °C min^{-1}. Attempts to crystallise OXA-ISO co-crystal by cooling in 60:40 HI produced OXA starting material, confirmed by both PXRD and DSC.

6.5.4.3.2 Solubility by Visual Observation of OXA in ACE

Investigations into accessing the OXA-ISO co-crystal *via* a solvent swap from 60:40 HI led to studies into the solubility behaviour of OXA in ACE by visual observation (Figure 6.60).

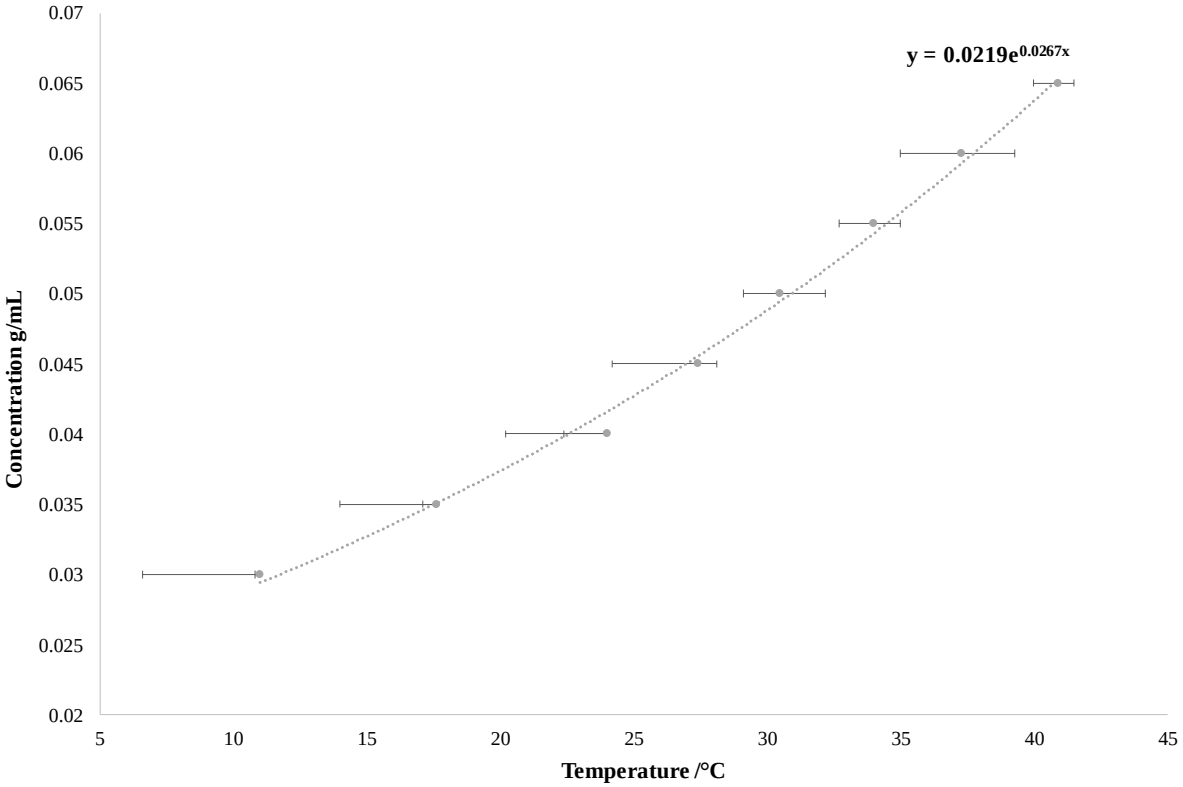

Figure 6.60 – Solubility of OXA in ACE *via* visual observation, three repeats Obs 1, 2, 3 with an exponential trend curve to fit the median data.

The concentration of OXA in OXA_ISO 1:1 physical mixture was based upon the solubility of OXA at 40 °C. However, initial attempts did not crystallise enough material for both PXRD and DSC analysis, so the concentration range was increased from approximately 0.06 g/mL to 0.08 g/mL of OXA in a 1:1 molar ratio with ISO in ACE. A cooling regime was adopted whereby the samples were heated to 45 °C, followed by a 1 hour dwell time, to ensure complete dissolution before cooling to 5 °C at a cooling rate of 0.05 °C min^{-1}, followed by a further 1 hour dwell time.

The PXRD data (Figure 6.61) again show a potential mixture of OXA and OXA-ISO co-crystal across the concentration range examined, while as before the DSC data shows the OXA-ISO co-crystal is formed in purity, with no OXA melting event present (Figure 6.62). The initial melting endotherm is consistent with the DSC traces presented for the OXA-ISO co-crystal prepared by evaporative, mechanochemical and slurrying crystallisations in Sections 6.5.1-6.5.3 respectively.

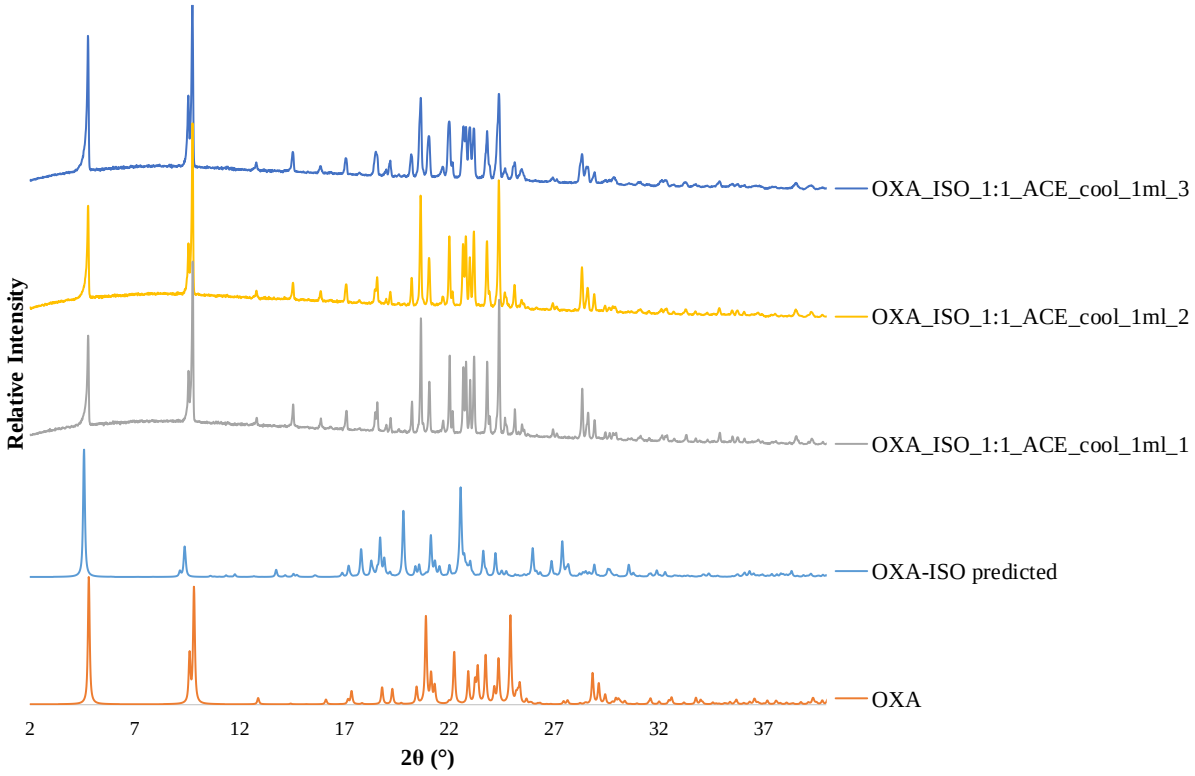

Figure 6.61 – Cooling crystallisations of OXA_ISO 1:1 in ACE at 1 mL scale over a concentration range for samples 1, 2 and 3 performed in the CRD Polar Bear Plus crystalliser.

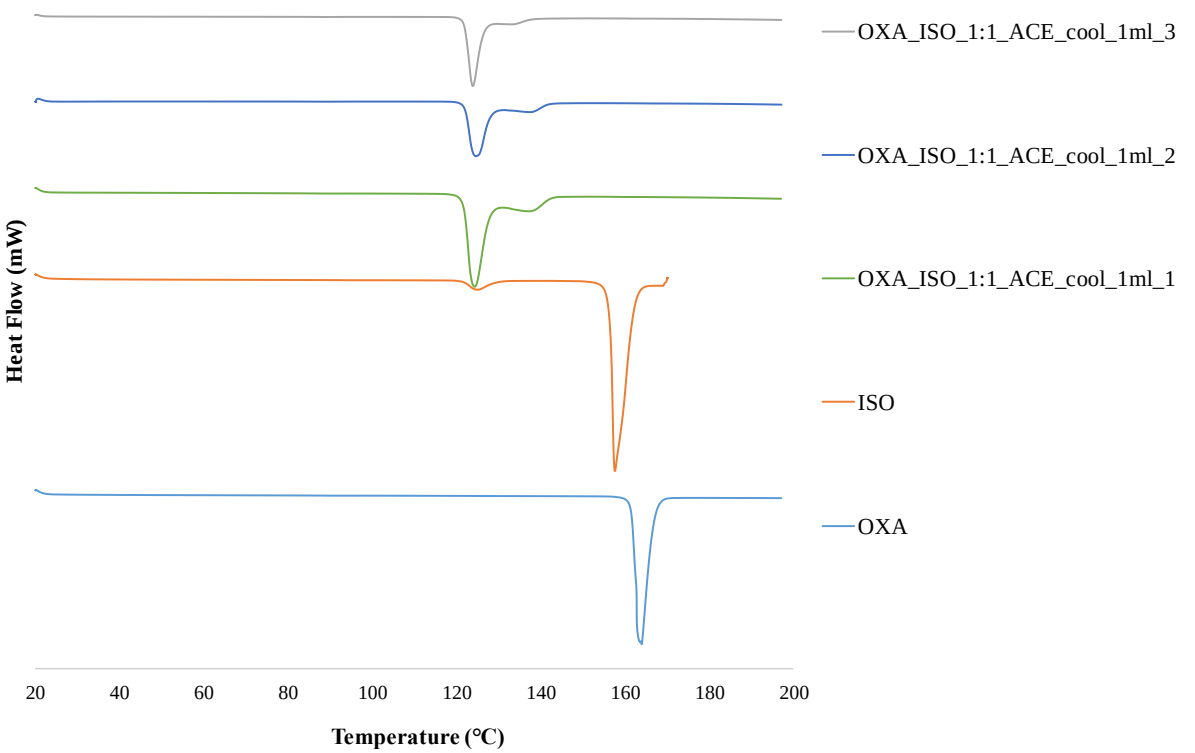

Figure 6.62 – DSC heat profiles of OXA_ISO 1:1 in ACE at 1 mL scale over a concentration range for samples 1, 2 and 3 performed in the CRD Polar Bear Plus crystalliser *versus* starting material DSC traces of OXA and ISO.

The OXA-ISO co-crystal has successfully been accessed by slow (0.05 °C min^{-1}) 1 mL batch cooling across a concentration range and thus has the potential to be scaled-up. Cooling crystallisations at increased scales were undertaken at an increased rate of 1 °C min^{-1} using a concentration of OXA of 0.08 g/mL in the physical mixture of OXA_ISO 1:1 in ACE. The PXRD and DSC data both confirm the formation of the OXA-ISO co-crystal up to 100 mL scale as shown in Figure 6.63 and 6.64 respectively. The PXRD data presented in Figure 6.63 show co-crystal formation of OXA-ISO most clearly of all the crystallisation methods presented in the study of OXA-ISO.

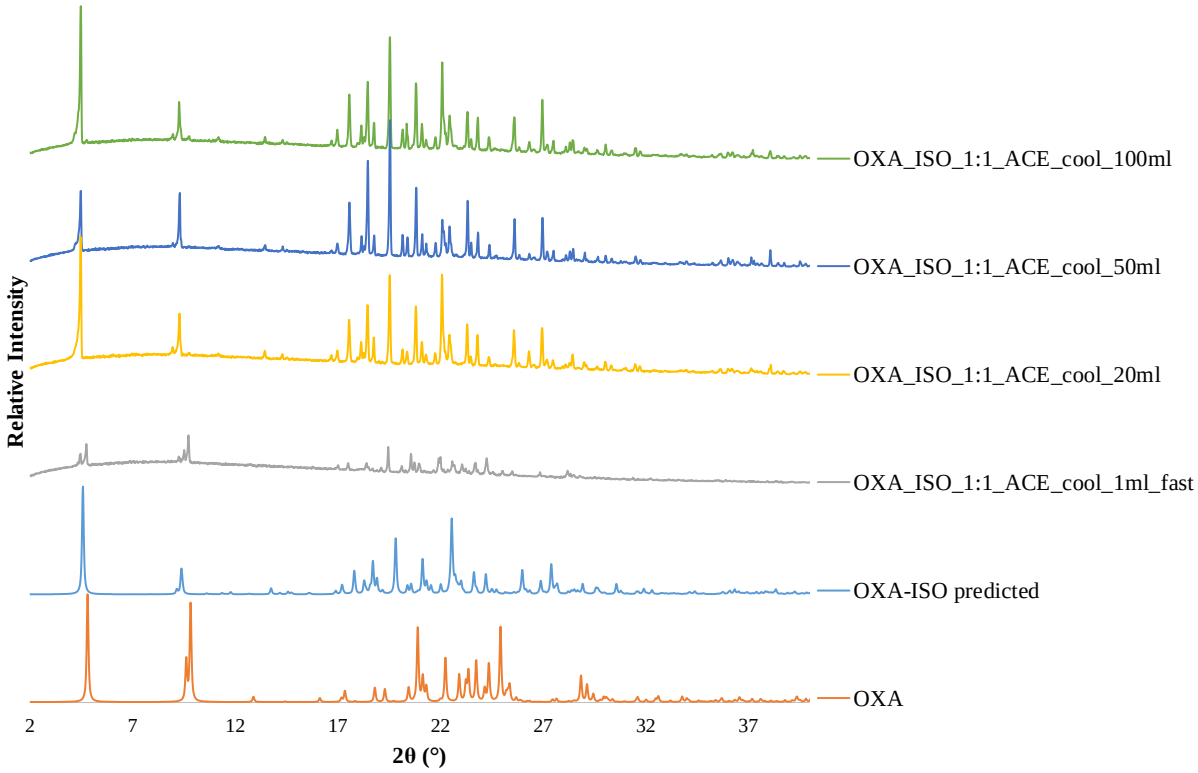

Figure 6.63 – Cooling crystallisation of OXA_ISO 1:1 in ACE scale-up with overhead stirring, with exception of 1 mL scale, which utilised magnetic bottom stirring.

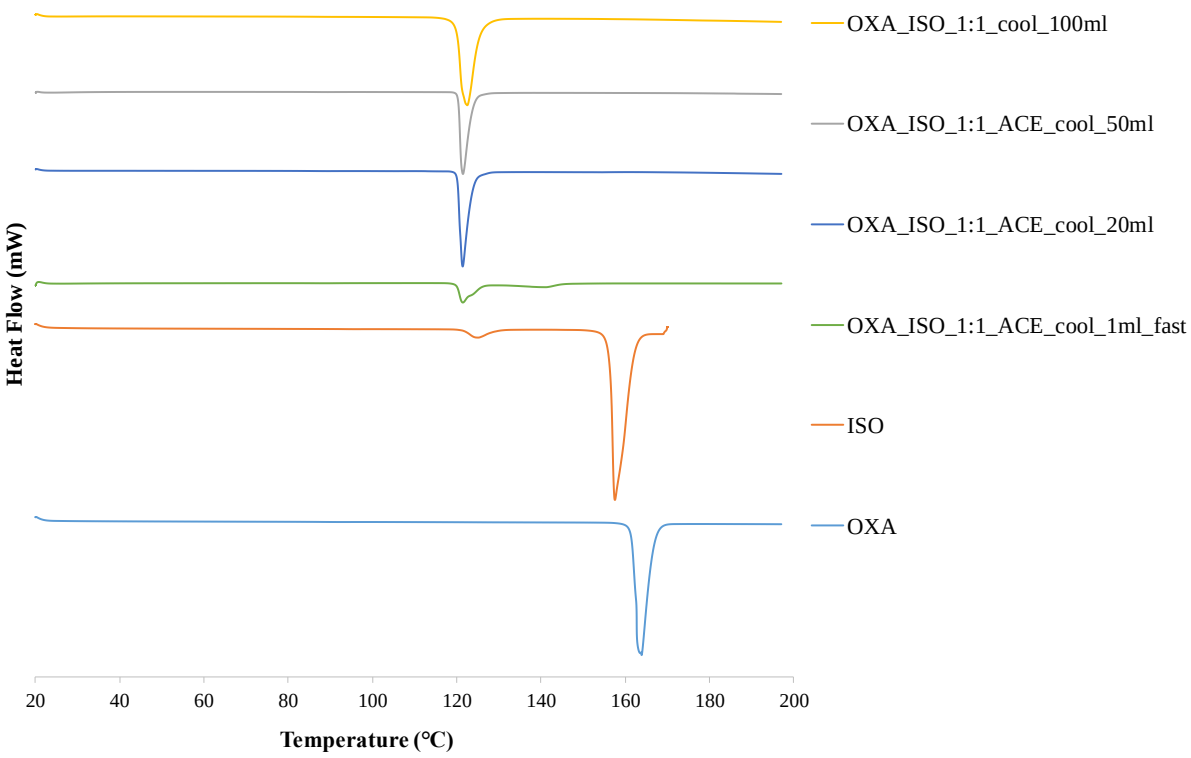

Figure 6.64 – DSC profiles of OXA_ISO 1:1 in ACE scale-up with overhead stirring, with exception of 1 mL scale, which utilised magnetic bottom stirring compared to the starting material DSC traces of OXA and ISO.

6.6 Oxaprozin Imidazole (OXA-IMID)

Preliminary work for the discovery of the OXA-IMID system was performed by A. Alam (MChem 2018) under the direction of the author, including the VT-SCXRD measurements, which were supported by Dr. Lauren Hatcher.

6.6.1 Evaporative Crystallisations of OXA-IMID

The PXRD patterns for OXA (20 mg) and IMID in a 1:1 molar ratio dissolved in approximately 1 mL of EtOH, IPA and ACE solvent systems, evaporated at 30 °C, confirm that each of these attempted co-crystallisations yielded a new potential co-crystal *via* evaporative methods, when compared to the PXRD patterns of the starting materials. The evidence of co-crystal formation is especially prominent from peaks around 15° 2θ, where these peaks are not present in any of the starting material PXRD patterns (Figure 6.65). Excess OXA is evident in the sample evaporated from IPA, from the representative OXA peak at 10° 2θ.

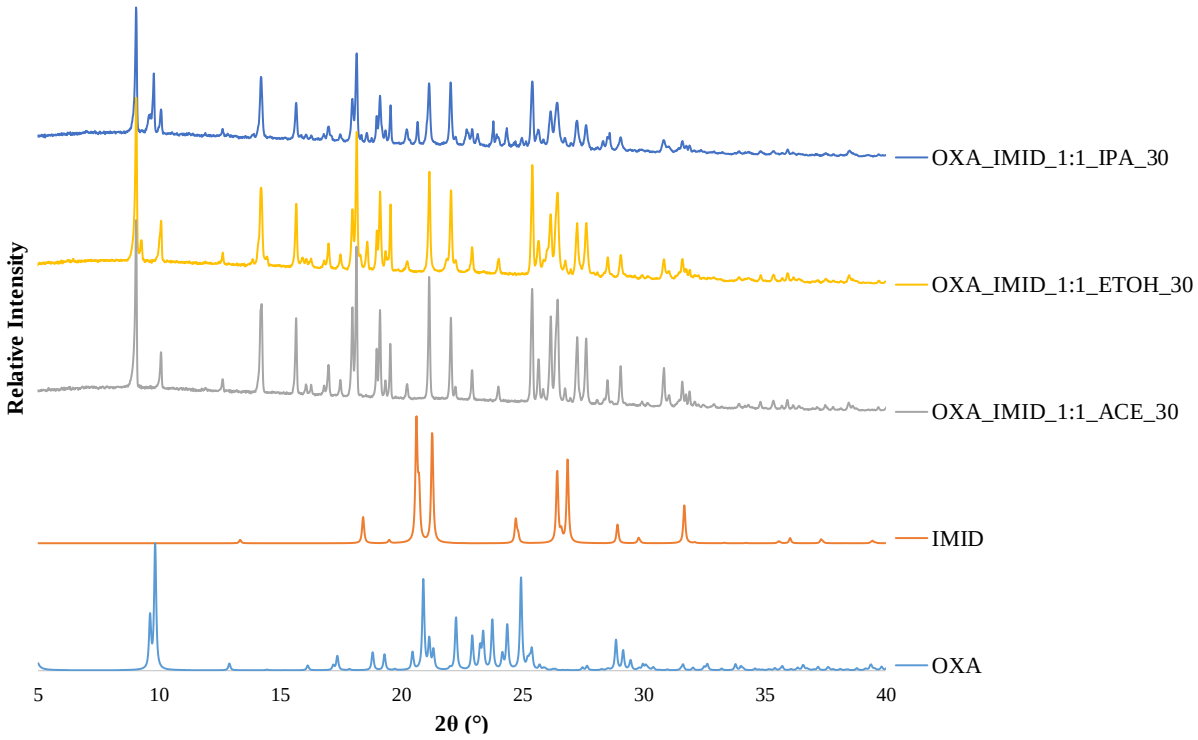

Figure 6.65 – PXRD patterns of the OXA-IMID 1:1 molecular complex prepared *via* evaporative crystallisation in three different solvents each at 30 °C, compared to the PXRD patterns of the constituent starting materials (Refcodes: OJURAO (OXA) and IMAZOL01 (IMID)).

The same samples analysed *via* PXRD, were also analysed by DSC using a ramp rate of 10 °C min^{-1}, the results of which show an endotherm similar to the melting event of IMID for each of the evaporative samples (Figure 6.66); the DSC traces do, however, show multiple endothermic events around 90 °C for each of these attempted co-crystallisations. Due to the excess OXA in the IPA evaporated sample and the melting events in the DSC traces similar to the melting event of IMID, the stoichiometric ratio of the OXA and IMID starting materials requires further investigation and optimisation.

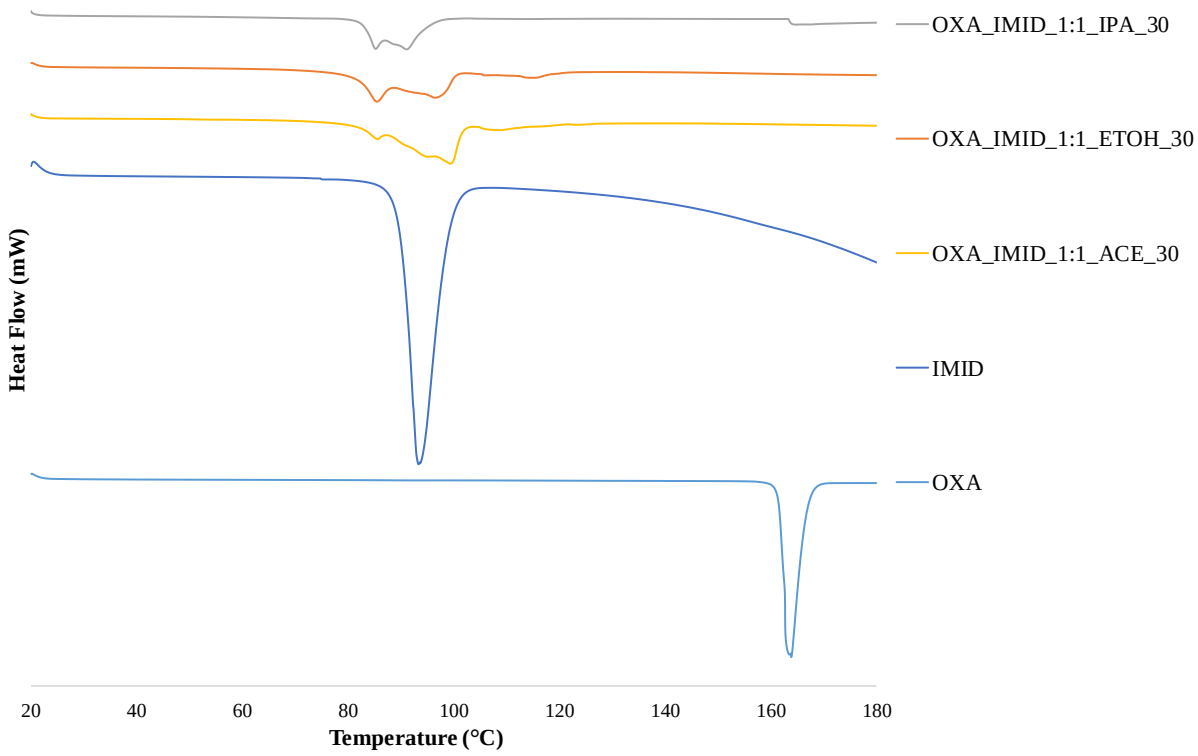

Figure 6.66 – DSC heat profiles for the molecular complex OXA-IMID 1:1 prepared *via* evaporative crystallisations at 30 °C in ACE, EtOH and IPA solvent systems.

Structural determination of OXA-IMID

Initial attempts to produce single crystals of suitable quality for single crystal structural analysis *via* evaporative methods at 30 °C were unsuccessful. Instead, the use of an anti-solvent was used to promote crystallisation. The use of EtOH with butanol acting as the anti-solvent promoted crystallisation from solution.

20 mg of OXA and 4.6 mg of IMID in a 1:1 ratio were dissolved in 2 mL of an ethanol:butanol 50:50 solvent mixture and the solvent allowed to evaporate at 4 °C, produced single crystals of suitable quality for analysis (Figure 6.67). Due to the markedly different crystal morphologies resulting from the anti-solvent evaporative crystallisations prepared under the same experimental conditions, the samples from three repeats were subjected to a Single Crystal X-ray Diffraction (SCXRD) pre-screening experiment and were confirmed to all have the same novel unit cell parameters. A suitable single crystal was subjected to SCXRD analysis to determine the full 3D crystal structure of the novel co-crystal; the crystal data for OXA-IMID are summarised in Table 6.11.

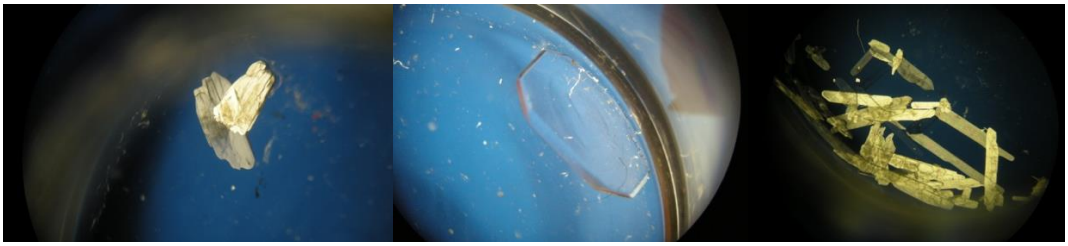

Figure 6.67 – Single crystals with varying crystal morphologies formed from repeat samples of OXA_IMID 1:1 in an ethanol:butanol 50:50 (v/v) solvent mixture: yellow blocks (left) clear plates (middle) and yellow lathes (right).

Table 6.11 – Crystal data and structure refinement parameters for OXA-IMID.

Empirical formula	**$C_{21}H_{19}N_3O_3$ ($C_{18}H_{15}NO_3 \cdot C_3H_4N_2 \cdot H_2O$)**
Formula weight	361.39
Temperature /K	150.00(10)
Crystal system	Monoclinic
Space group	$P2_1/n$
a /Å	15.7924(10)
b /Å	6.7945(4)
c /Å	18.6655(12)
α /°	90
β /°	110.461(8)
γ /°	90
Volume /Å^3	1876.5(2)
Z	4
ρ_{calc} /g cm^{-3}	1.279
μ/mm^{-1}	0.087
F(000)	760.0
Crystal dimensions /μm^3	200 × 40 × 20
Radiation	MoKα (λ = 0.71073)
2θ range for data collection /°	6.434 to 52.744
Index ranges	$-19 \leq h \leq 15$, $-6 \leq k \leq 8$, $-18 \leq l \leq 23$
Reflections collected	7604
Independent reflections	3832 [R_{int} = 0.0232, R_{sigma} = 0.0377]
Data/restraints/parameters	3832/0/260
Goodness-of-fit on F^2	1.044
Final R indexes [I>=2σ (I)]	R_1 = 0.0469, wR_2 = 0.1144
Final R indexes [all data]	R_1 = 0.0621, wR_2 = 0.1261
Largest diff. peak/hole / e Å^{-3}	0.61/-0.51

The OXA-IMID 1:1 solvate crystallises in the monoclinic space group $P2_1/n$, with one molecule of OXA, one molecule of IMID and one molecule of water (solvent) in the asymmetric unit (Figure 6.68). In the asymmetric unit, OXA and IMID are bonded through a

hydrogen bonding intermolecular interaction between the N-H from IMID with the carbonyl oxygen on the carboxylic acid moiety of OXA, with an N2-H…O1 bond length of 2.577(2) Å. The other N-H bond in IMID (N3-H) produces an intermolecular hydrogen bond with the oxygen atom on the water molecule, with an N3-H…O4 bond length of 2.692(2) Å. The water acts as a linking molecule between adjacent OXA-IMID units. These two intermolecular N-H…O bonding interactions from the IMID molecule positioned in the middle of the other two molecules in the asymmetric unit are highlighted by blue dotted lines in Figure 6.68. Beyond the asymmetric unit, the packing diagram (Figure 6.69) as observed down the crystallographic *b*-axis is dominated by hydrogen bonding interactions forming a chain-like network of molecules, with no obvious π–π stacking observed.

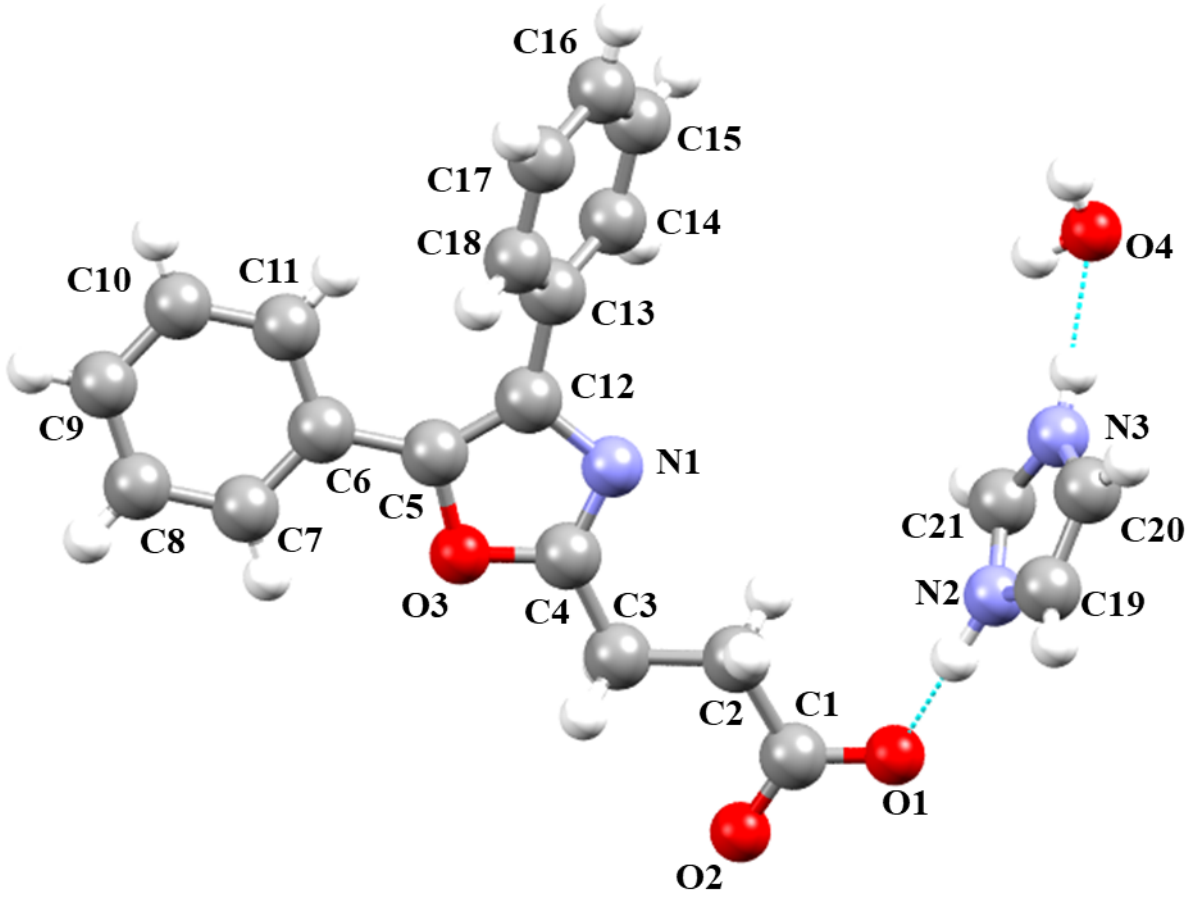

Figure 6.68 – The asymmetric unit of the OXA-IMID solvate molecular complex.

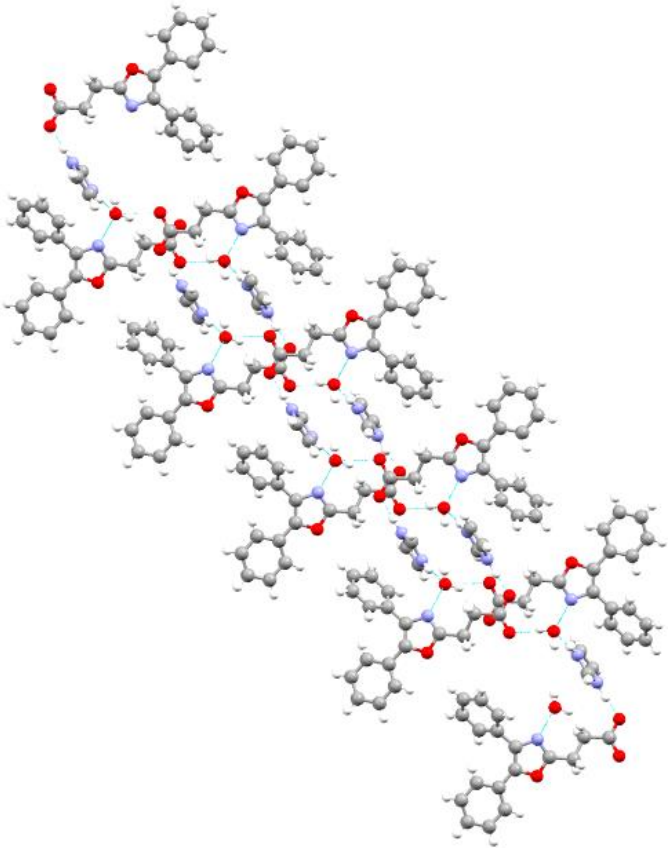

Figure 6.69 – The crystal packing of the OXA-IMID solvate molecular complex as viewed down the crystallographic *b*-axis.

The structure of IMID contains a single N-H group, allowing IMID to exist in two equivalent tautomeric forms, with the hydrogen bound to either of the imidazole nitrogen atoms. The asymmetric unit of OXA-IMID solvate contains hydrogen atoms on both of the pyrrole nitrogen atoms, indicating that hydrogen transfer has occurred from the oxygen, O1, of the OH group of the carboxylic acid of OXA to N2 on IMID upon co-crystal formation. This results in carboxylate anion formation on OXA and as a result of this ionic transfer, the OXA-IMID solvate system is strictly a salt.

However, inspection of the N2-H and O1-H distances in this hydrogen bonding interaction suggest that the hydrogen is shared between both functionalities, rather than exhibiting formal bonding to N2. This is supported by an N2-H bond length of 1.04(2) Å, which is longer than expected for an N-H bond and lies above the upper parameter for a strong, mostly covalent hydrogen bond (see Table 1.1). The hydrogen bonding interaction between OXA and IMID, represented by N2-H···O1 has a bond distance of 2.575(1) Å.

Proton migration involves the gradual shift in position of a hydrogen atom across a hydrogen bond. Proton migration is a tuneable affect, which can be induced by external influences such as through the application of temperature.[175, 176] The use of Variable Temperature (VT) Single Crystal X-ray Diffraction (SCXRD) analysis can elucidate whether the hydrogen transferred from the alcohol functionality on the carboxylic acid of OXA to IMID, can transition back towards the carboxylate. This potential to restore the neutrality of the component materials through the application of temperature would subsequently result in the system classified as a co-crystalline solvate rather than a solvated salt and may show potential as a material with electronic properties.

6.6.1.1 Variable Temperature (VT) Single Crystal X-ray Diffraction (SCXRD) analysis of OXA-IMID

Analysis of the N2-H, O1-H and N2-O1 distances were conducted as a function of temperature by VT-SCXRD collected at 20 K intervals, with the temperature of collection ranging from 160-340 K. By reviewing these distances (Table 6.12), the positioning of the hydrogen atom and subsequently the nature of its interaction with both the N-heterocyclic and carboxylate functionality on IMID and OXA respectively was investigated.

Table 6.12 – Variation in N2-H, O1-H and O1-N2 bond distances in the OXA-IMID molecular complex through the application of temperature.

Temperature /K	N2-H distance /Å	O1-H distance /Å	O1-N2 distance /Å
340	1.21(3)	1.36(3)	2.565(3)
320	1.13(2)	1.44(2)	2.570(3)
300	1.14(2)	1.43(2)	2.564(2)
280	1.12(2)	1.45(2)	2.565(2)
260	1.11(2)	1.46(2)	2.568(2)
240	1.11(2)	1.46(2)	2.570(2)
220	1.07(2)	1.51(2)	2.571(2)
200	1.09(2)	1.48(2)	2.570(2)
180	1.10(1)	1.47(1)	2.571(2)
160	1.06(2)	1.51(2)	2.573(1)
150	1.04(2)	1.53(2)	2.575(1)

With increasing temperature, there is an increase in the N2-H bond distance (Figure 6.70) and corresponding decrease in the O1-H bond distance (Figure 6.71). As these bond distances converge with an increase in temperature, this provides evidence of the hydrogen atom migrating significantly towards the carboxylate oxygen on OXA, positioning itself more centrally between the two molecules of OXA and IMID.

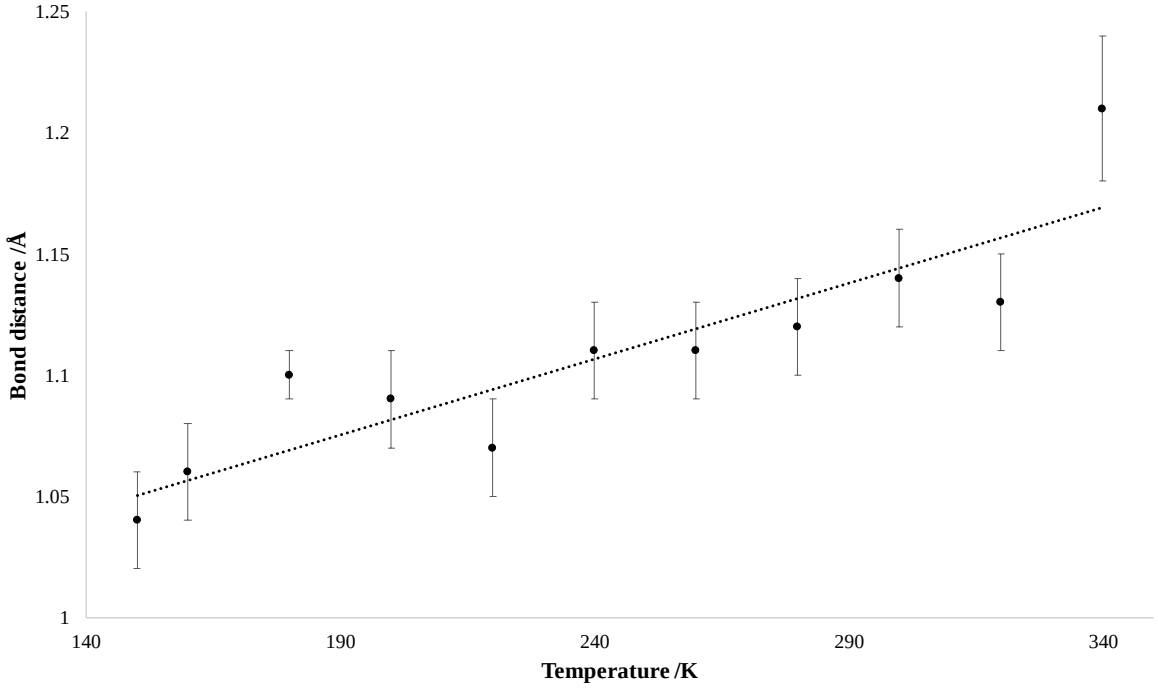

Figure 6.70 – Variation in N2-H bond distance with temperature for OXA-IMID molecular complex.

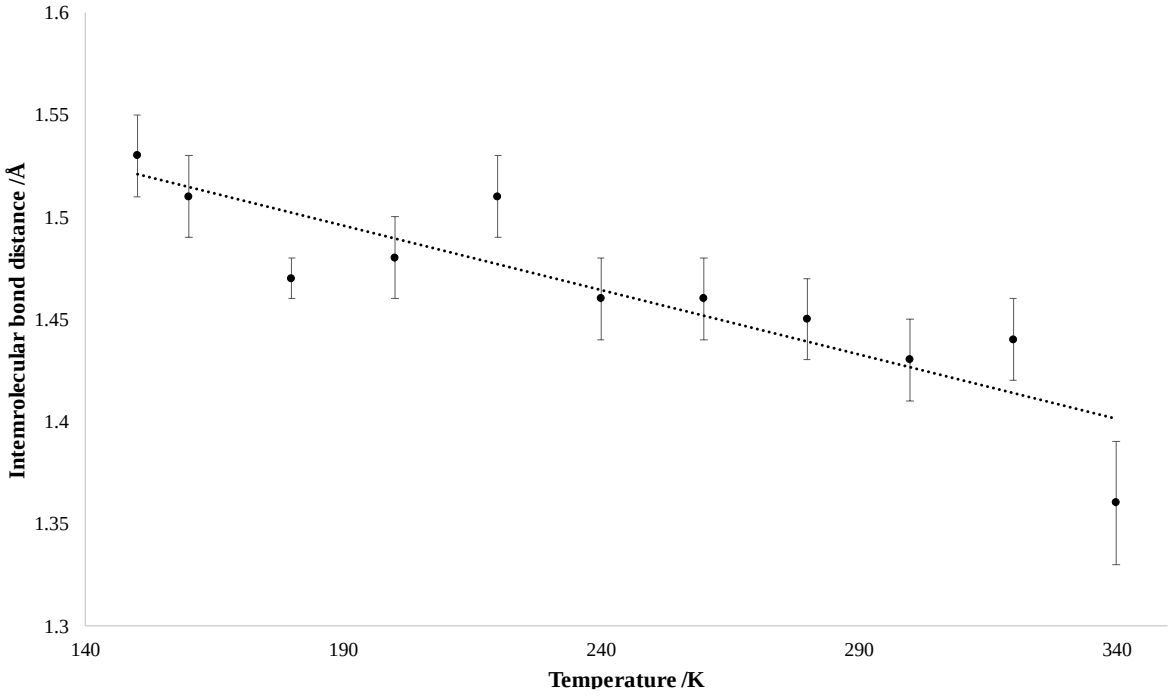

Figure 6.71 – Variation in O1-H bond distance with temperature for OXA-IMID molecular complex.

This increased sharing of the hydrogen atom between the OXA and IMID molecules with temperature is further supported by the overall distance between the heterocyclic nitrogen and the carboxylate oxygen, which is seen to decrease marginally with increasing temperature (Figure 6.72). This contrasts to the expected trend of an increase in bond distance with temperature, resulting from unit cell expansion, which would result in molecular separation of the OXA and IMID components increasing.

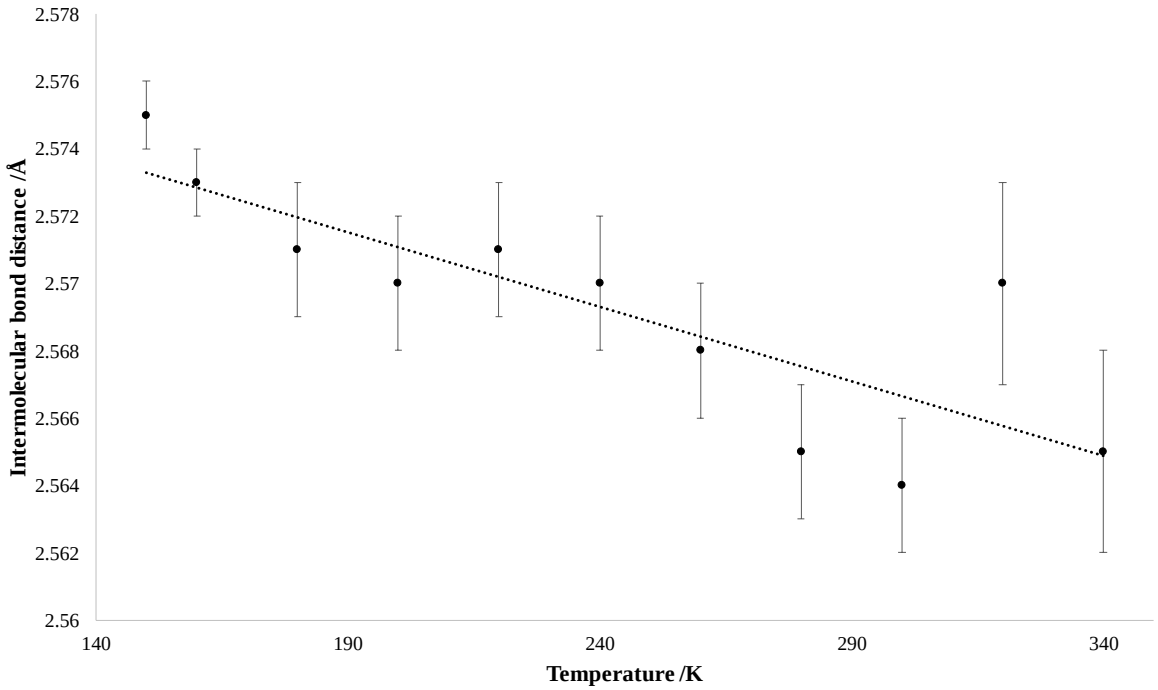

Figure 6.72 – Variation in O1-N2 intermolecular bond distance with temperature for OXA-IMID molecular complex.

The most significant shift in hydrogen position between N2 and O1 was observed from 320-340 K. The final temperature for data collection was 340 K, as data collection attempts at 360 K were unsuccessful as the single crystal became dull and a loss of extinction under the polariser on the microscope was observed. This structural change observed at 360 K can be attributed to loss of water from the solvate structure, indicating that the presence of water is integral to the crystal structure. Hot-stage Microscopy (HSM) was used to observe the solvent evolution from the single crystal at 86 °C (361 K) (Figure 6.73).

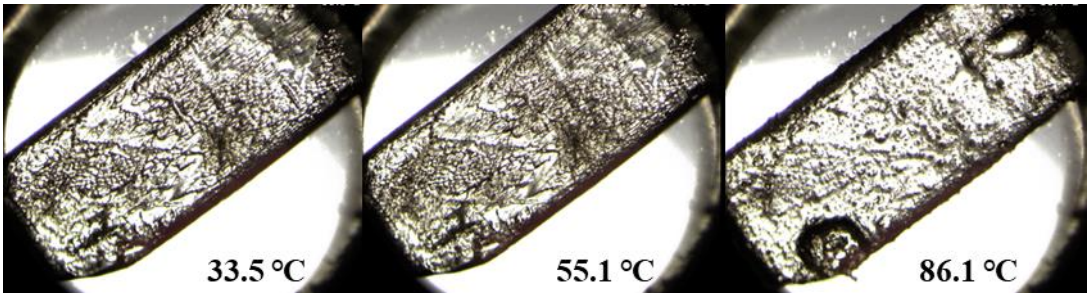

Figure 6.73 – HSM images of OXA-IMID solvate at different temperatures, with solvent emerging at 86 °C.

Further investigation into desolvation of the OXA-IMID and molecular complex including relative stoichiometries of the components was carried out using TGA.

6.6.1.2 Thermogravimetric Analysis (TGA) of OXA-IMID solvate

The TGA trace for the OXA-IMID solvate sample produced from evaporative crystallisation of OXA_IMID 1:1 from EtOH at 30 °C shows a distinct mass loss of 4 % around 100 °C, consistent with water being driven out of the crystal structure (Figure 6.74), which is in agreement with previous VT-SCXRD and HSM studies.

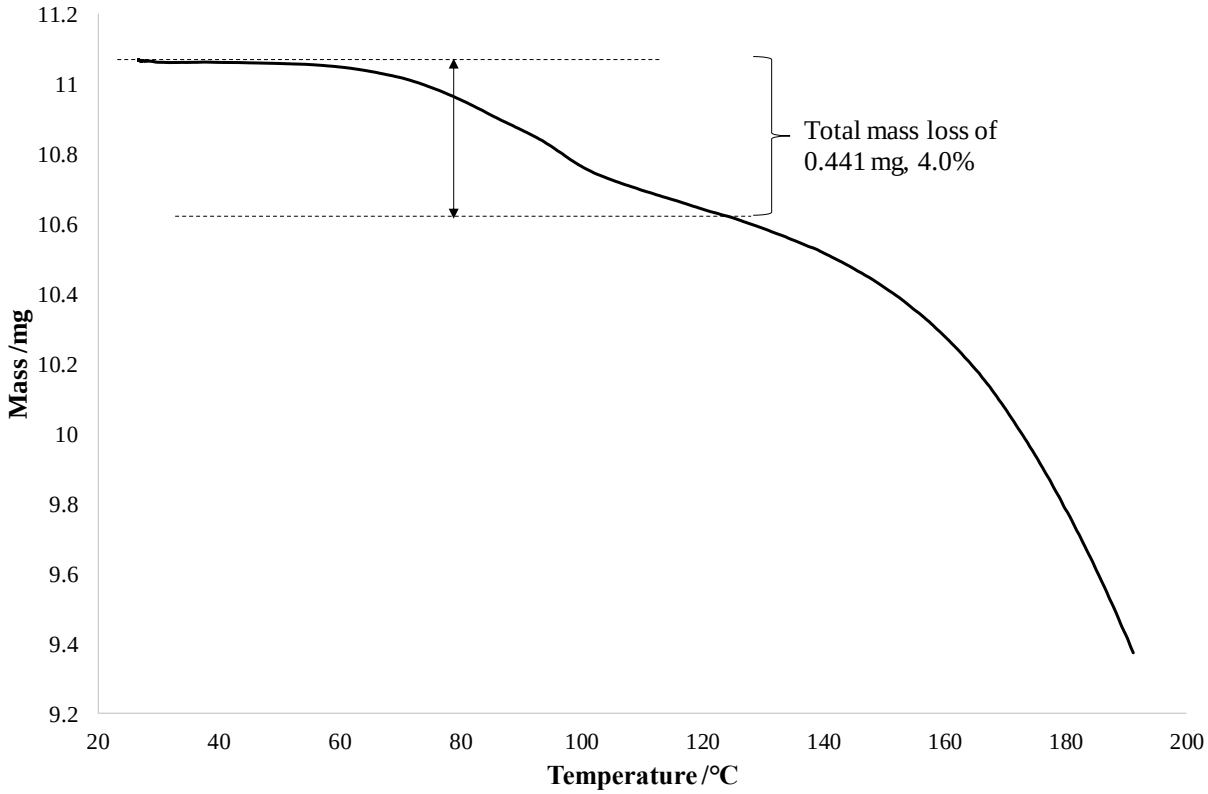

Figure 6.74 – TGA spectra of the novel OXA-IMID solvate (10 °C min^{-1}, under air).

6.6.1.3 IR Spectroscopy of OXA-IMID

Multi-component solvate formation is further confirmed by IR spectroscopy, in which the carbonyl stretching frequency was shifted to a significantly lower wavelength compared to free OXA from 1719 cm^{-1} to 1648 cm^{-1} (Appendix 6.6 and Table 6.13) due to its increased single bond behaviour, which can be rationalised using resonance structures (Figure 6.75).

Table 6.13 – Comparison of IR stretching frequencies of key functional groups in OXA-IMID compared to the OXA target.

Vibration Frequency (cm^{-1})	OXA	OXA-IMID
N-H stretch	-	3438 (N2-H···O1)
C=O stretch	1719	1648 (C1=O1)

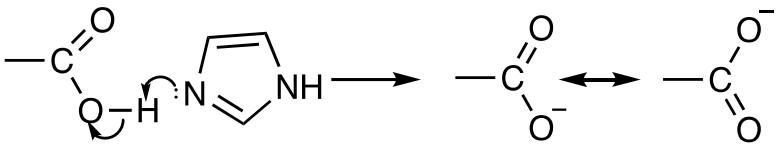

Figure 6.75 – Resonance structures arising from the hydrogen bond donation from the hydrogen on the OXA carboxylic acid group (donor) to the IMID (acceptor).

The predicted powder pattern from the solved single crystal structure of the OXA-IMID novel solvate is clearly shown by PXRD to match that observed experimentally, and to be distinct from the pure starting components (Figure 6.76).

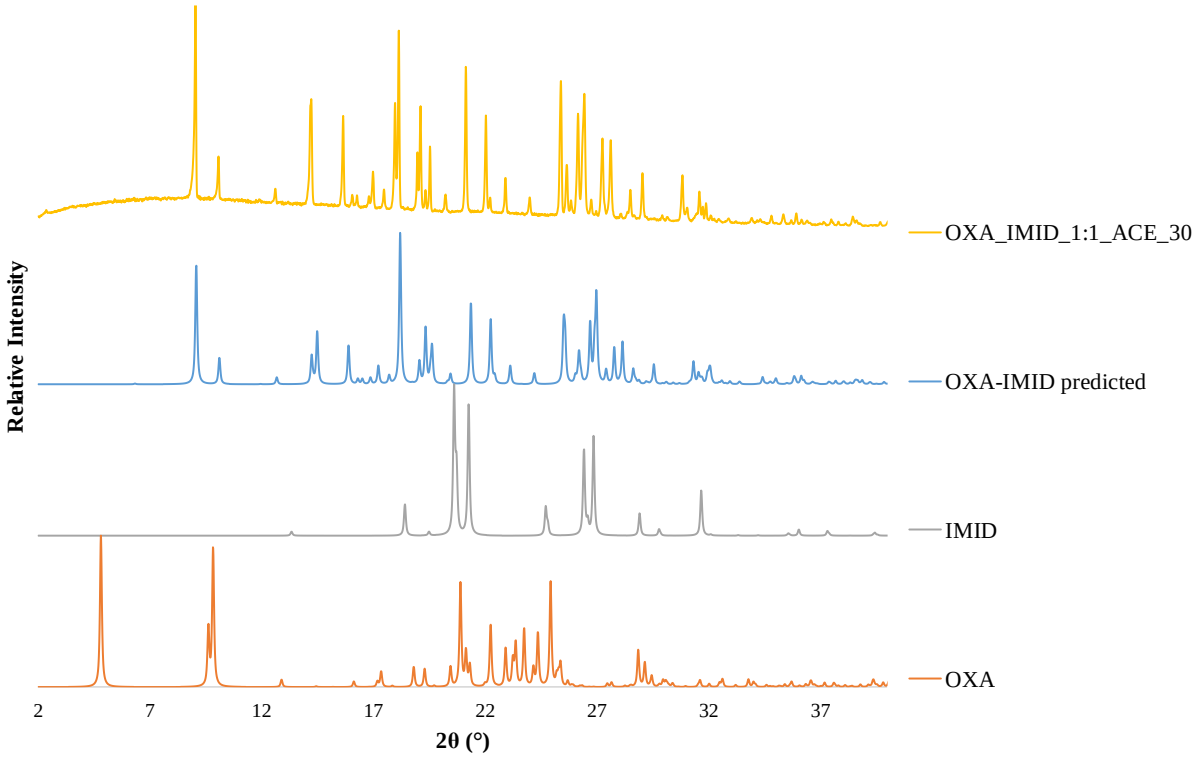

Figure 6.76 – PXRD patterns comparing OXA-IMID predicted pattern simulated in Mercury, with OXA-IMID crystallised from evaporation of ACE, as well as the PXRD patterns of the pure starting materials obtained from Mercury (Refcodes: OJURAO (OXA) and IMAZOL01 (IMID)).

6.6.2 Mechanochemical Crystallisations of OXA-IMID

Once co-crystal formation for the OXA-IMID co-crystal had been achieved through evaporation and confirmed through SCXRD, PXRD, DSC and TGA analytical techniques; this system was translated into grinding approaches. The OXA_IMID 1:1 sample prepared *via* NG and LAG across each of the solvents yields the same diffraction patterns, which can be identified as the OXA-IMID solvate (Appendix 6.7). The DSC traces also confirm co-crystal formation *via* mechanochemical crystallisations (Appendix 6.7), where samples exhibit the same thermal behaviour as OXA-IMID solvate samples prepared by evaporation. However, the NG method has not facilitated access to the OXA-IMID solvate in purity as is observed for the LAG approaches, evident from PXRD and DSC analysis.

6.6.3 Slurrying Crystallisations of OXA-IMID

Investigations into whether the OXA-IMID co-crystal could be accessed using small-scale slurry techniques were conducted using the same three solvents (ACE, EtOH, IPA) as those investigated in evaporative and mechanochemical techniques used to access the co-crystal previously. The slurries were prepared using a 1:1 molar ratio of OXA (400 mg) and IMID in

2 mL of solvent, left stirring at 250 rpm on a hot-plate with DrySyn attachment set to 30 ℃ for one week. After this stirring period, the resultant product was isolated from the solvent using vacuum filtration and left to dry for 24 hours before being analysed *via* PXRD and DSC.

The PXRD analysis carried out after slurrying a physical mixture of OXA and IMID in various solvents for 1 week showed that in addition to evaporative and mechanochemical preparations, slurrying can also be used to access the OXA-IMID solvate in purity (Figure 6.77). The DSC analysis on the same samples (Figure 6.78), showed endotherms consistent with OXA-IMID formation across solvent systems. The DSC traces of the slurrying crystallisations feature the same additional endotherm as was observed in the NG, at 58 ℃, which cannot be attributed to OXA, IMID or the solvents utilised in the slurrying. This feature was not able to be investigated further in this work.

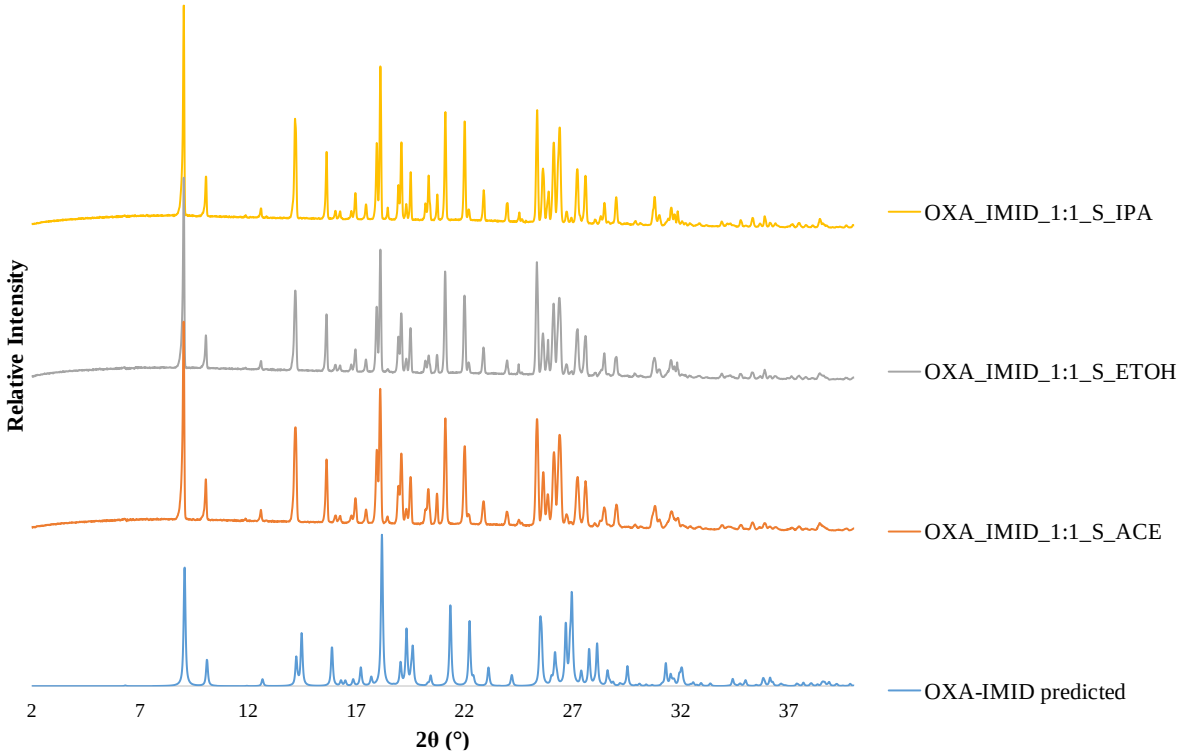

Figure 6.77 – PXRD patterns of the OXA-IMID molecular complex prepared *via* slurrying crystallisations for 1 week in three different solvents systems compared to the predicted PXRD pattern of the OXA-IMID solvate simulated in Mercury.

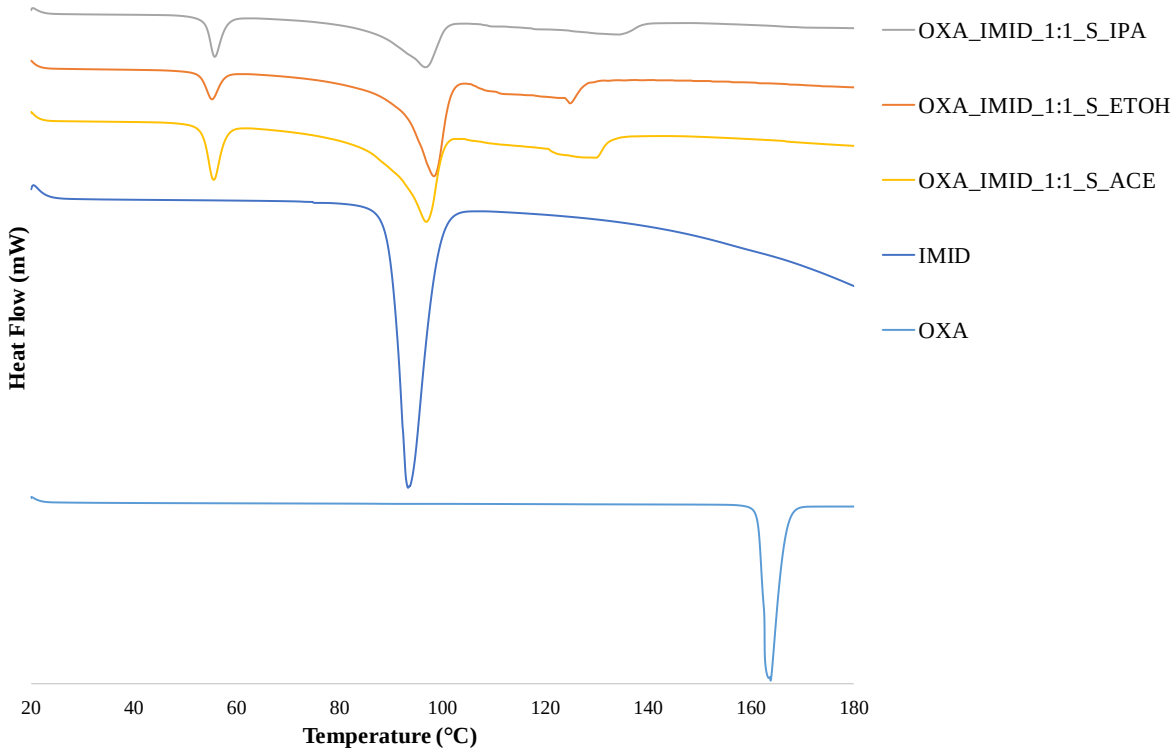

Figure 6.78 – DSC heat profiles for the molecular complex OXA-IMID prepared via slurrying crystallisation for 1 week in ACE, EtOH, IPA solvents.

6.6.4 OXA-IMID crystallisations in 60:40 H_2O:IPA (HI)

The crystallisation of the OXA-IMID co-crystal was evaluated in 60:40 HI across the range of crystallisation methods already investigated, to elucidate the potential for this system to be crystallised *via* cooling at scale. The PXRD patterns of OXA_IMID 1:1 prepared in 60:40 HI *via* slurrying and evaporative methods yield OXA-IMID in purity, whilst LAG in this solvent mixture yields OXA (Appendix 6.8). DSC traces for products from the various methods were inconsistent and not able to be interpreted in terms of the PXRD findings (Appendix 6.8).

6.6.4.1 Relative Thermal Stability Studies of OXA-IMID

The thermal stability of the OXA-IMID co-crystal prepared by LAG in 60:40 HI using a mortar and pestle for 30 minutes monitored over a month is presented in Figure 6.79, showing that the OXA-IMID co-crystal is resistant to thermal ageing at 45 °C for up to two weeks, by which time additional peaks emerge. Interestingly by day 21 the sample has reverted back to the pure co-crystal once more, however by four weeks of oven ageing the co-crystal has dissociated into OXA starting material with an unassigned peak at 3° 2θ also emerging. These findings show discrepancy with the thermal DSC analysis, where DSC traces at t=0 and day 21 both contain

the same endothermic events, notably a melting event at 55 °C, whilst day 7, 14 and 28 look largely similar. Interestingly there is no OXA melting event evident in the one month DSC trace (Figure 6.80), which contrasts with the diffraction data that yields OXA starting material.

In light of these contradictory indications, it can be postulated that the thermal ageing of OXA-IMID is affected by the tendency of OXA-IMID to 'oil out' during sample preparation *via* grinding.

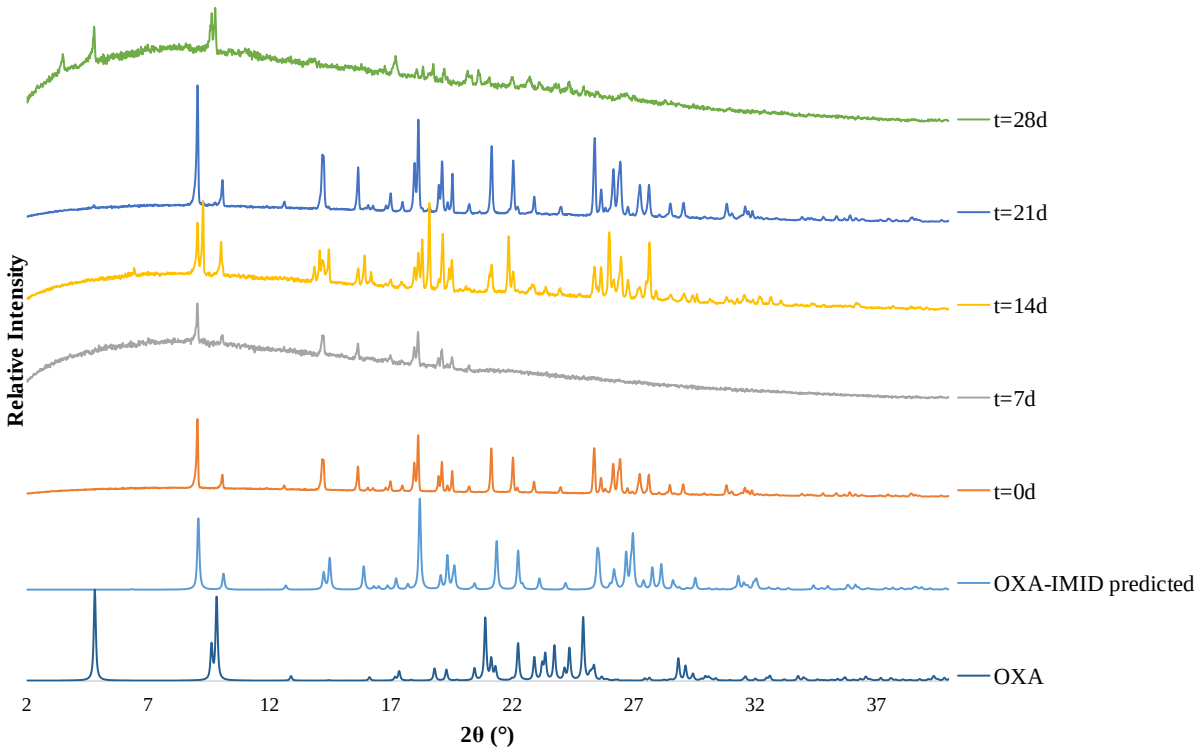

Figure 6.79 – OXA-IMID prepared in 60:40 HI *via* LAG for 30 minutes – Thermal studies at 45 °C monitored over 28 days.

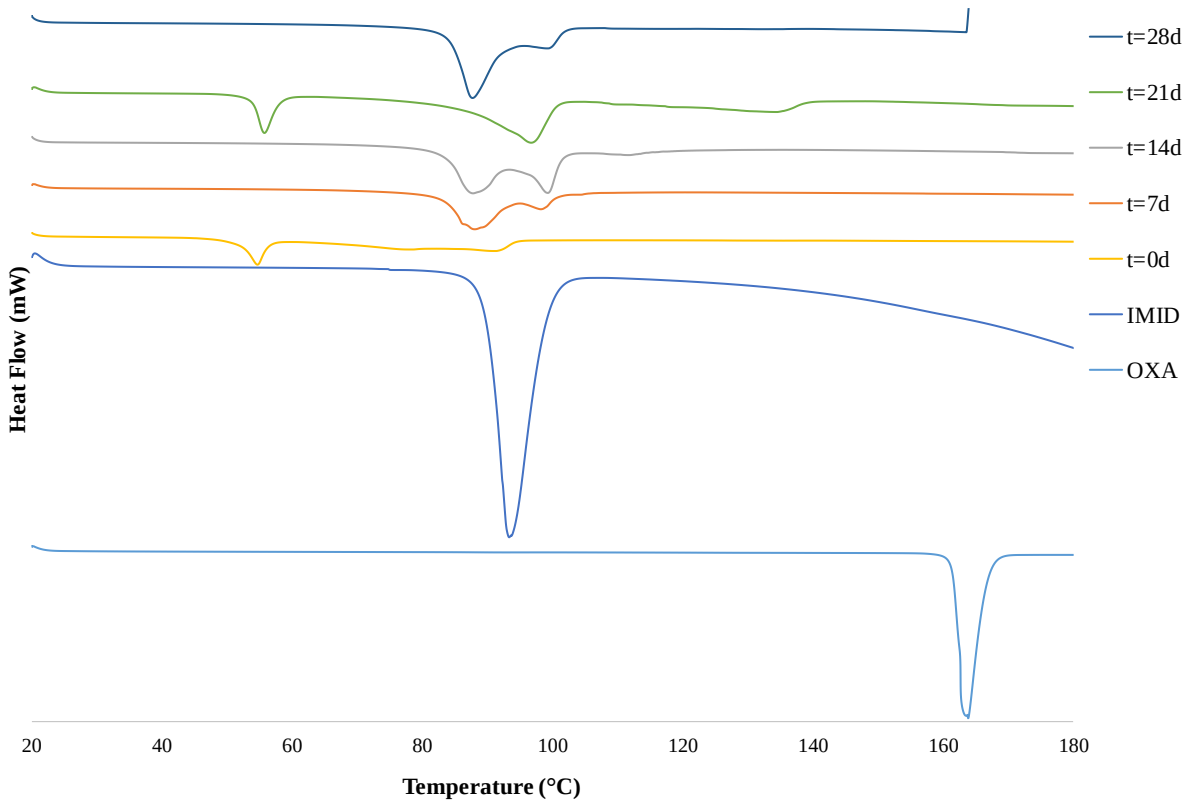

Figure 6.80 – DSC heat profiles for OXA-IMID prepared in 60:40 HI *via* LAG for 30 minutes – Thermal studies at 45 °C monitored over 28 days. All samples were heated to 200 °C, with no thermal events evident above 160 °C for any of the samples.

6.6.4.2 Relative Humidity Stability studies of OXA-IMID

OXA-IMID prepared by LAG subjected to both 46 % and 80 % RH conditions, show resistance to humidity ageing under both moderate and severe humidity conditions, as observed from no discernible differences in the PXRD patterns over the various time points (Appendix 6.9), with only some peak broadening observed over time.

6.6.4.3 Cooling Crystallisations of OXA-IMID

6.6.4.3.1 Batch *via* Polar Bear Plus from Cambridge Reactor Design (CRD)

Attempts to ascertain the solubility behaviour of OXA_IMID 1:1 physical mixture in 60:40 HI were unsuccessful due to the substantial aqueous solubility of the solvate structure; the concentration requirements were extremely high at >0.8 g/mL OXA in OXA_IMID 1:1 in 60:40 HI. Initial batch cooling crystallisations aimed at accessing the OXA-IMID multi-component material used the solubility behaviour of OXA in ACE (Figure 6.60 in section 6.5.4.3.2) as a start point in designing the cooling crystallisations.

A concentration range 0.08 g/mL (sample 1), 0.085 g/mL (sample 2) and 0.09 g/mL (sample 3) of OXA in OXA_IMID 1:1 in ACE was selected to ascertain how overall concentration might influence OXA-IMID co-crystal formation. The OXA_IMID 1:1 in 1 mL ACE samples were heated to 45 °C, followed by a 1 hour dwell time, to ensure complete dissolution before cooling to 5 °C at a cooling rate of 0.05 °C min^{-1}, followed by a further 1 hour dwell time. The OXA-IMID co-crystal was produced across each of the concentrations, confirmed by both PXRD and DSC (Appendix 6.10). Further attempts to scale-up the cooling crystallisation process of OXA-IMID were not pursued as the concentration requirements were substantial.

6.7 Discussion and Conclusions of Crystal Engineering for Materials Discovery in the Profen Family

This Chapter has investigated the use of crystal engineering for materials discovery of the profen family, exploring whether co-crystal formation could be an alternative approach to the improvement of physicochemical properties of the profen targets, most notably with respect to the BCS class II solubility classification.

This work reports the discovery of three co-crystals accessed by a range of crystallisation methods: ibuprofen-isonicotinamide (IBU-ISO), oxaprozin-isonicotinamide (OXA-ISO) and oxaprozin-imidazole (OXA-IMID) solvate. IBU-ISO was reported simultaneously by Walsh *et al.* as a model system to investigate spray drying *versus* hot-melt extrusion.[170] Each of the profen co-crystals have been fully structurally characterised and the transferability of crystallisation methods and possible physical property enhancement on these systems investigated. Solid-state stability testing was investigated through thermal stability tests to ascertain the co-crystal shelf-life compared to the pure API, as well as humidity stability tests to establish whether the co-crystals demonstrate resistance to moderate and severe humidity conditions.

IBU-ISO

The IBU-ISO co-crystal can be accessed by evaporative, mechanochemical, slurrying in a range of solvents, as well as *via* cooling crystallisation in 60:40 HI up to 200 mL scale. Investigations into the translation of this system into continuous cooling co-crystallisation were less successful as a result of the ‘oiling out’ behaviour established during the extensive solubility testing by a range of methods including turbidity and visual observation. The use of

in-line particle visualisation in the Crystalline® platform capturing dissolution, crystallisation and 'oiling out' events during repeated heat cool cycles in the turbidity measurements, proved invaluable in gaining an improved understanding of the unusual behaviour of this co-crystal system. The IBU-ISO co-crystal exhibits an improved solubility in 60:40 HI compared to the IBU target. The IBU-ISO co-crystal also features an improved thermal stability compared to IBU, from DSC analysis which quantified the melting events to be 123 ℃ and 78 ℃ respectively. The IBU-ISO co-crystal showed robustness to thermal ageing. Slurry stability testing of pre-prepared co-crystal of IBU-ISO found that IBU-ISO undergoes partial dissociation to IBU from 2 hours of slurrying at both room and body temperature, which is an acceptable result on the premise of drug delivery in the gut.

OXA-ISO

The OXA-ISO co-crystal features very large unit cell dimensions for a small-molecule organic, due to the slight positional disorder of the phenyl rings in the structure. The OXA-ISO co-crystal can be accessed by evaporative, mechanochemical and slurrying in a range of solvents and while cooling crystallisation of OXA_ISO 1:1 in 60:40 HI yielded OXA, a solvent swap from 60:40 HI to ACE led to the production of the co-crystal, which was scaled to 100 mL. Similar to IBU-ISO, an increase in grinding time could lead to complete conversion to the OXA-ISO co-crystal *via* mechanochemical methods, or a change in stoichiometric ratio of the starting components could mitigate the excess starting material observed. The OXA-ISO co-crystal exhibits a reduced thermal stability compared to OXA, as confirmed by DSC melting events of 124 ℃ and 163 ℃ respectively. The OXA-ISO co-crystal showed robustness to thermal ageing, but showed sensitivity towards humidity ageing.

The analysis of OXA-ISO co-crystallisation *via* the range of crystallisation methods was particularly challenging, partly because of the similarity in the PXRD patterns of the OXA-ISO co-crystal and OXA target. The PXRD data for the OXA-ISO co-crystal accessed *via* cooling crystallisation in ACE at scale with the use of overhead stirring yielded the most successful pattern matching to the OXA-ISO predicted pattern of all the crystallisation methods investigated.

To elucidate the diffraction behaviour of the OXA-ISO system, the use of Rietveld structural refinement would facilitate the refinement of the lattice parameters, as well as providing a correlation between the particle size and the peak parameters. This structural refinement

analysis would be particularly beneficial applied to the thermal ageing diffraction data, which showed some interesting behaviour over time. In addition, as both the structure of OXA and the OXA-ISO co-crystal are known, for samples where a mixture of OXA and OXA-ISO are present, multiple phase refinement could be carried out, whereby the relative quantities of the various components present in the bulk sample can be quantified, which is useful for co-crystal purity optimisation.

OXA-IMID

OXA-IMID solvate is a hydrate as confirmed by TGA analysis, in which water is driven out of the structure around 100 °C, which is confirmed and visualised by HSM. The use of VT-SCXRD helped to understand the hydrogen bonding within the structure and the temperature induced proton migration behaviour of the OXA-IMID salt. The proton migration with temperature found in this complex establishes a salt-co-crystal continuum that offers an opportunity for property tuning; the OXA-IMID co-crystal is a dynamic solid-state material, which may exhibit temperature induced switchable properties.[177] IR spectroscopy also helped confirm this finding by comparing the N-H stretching frequencies between the OXA-IMID and the OXA starting component. The thermal behaviour of OXA-IMID is similar to IMID, but shows reduced thermal stability compared to the OXA API target, as confirmed by DSC. The OXA-IMID DSC trace is complex and can vary with crystallisation method employed for preparation of this novel material, which is particularly interesting when the PXRD data indicate the multi-component material consistently in purity. OXA-IMID is also not resistant to thermal ageing, but exhibits resistivity to humidity ageing.

Due to the low boiling point of ACE, translation of both OXA-ISO and OXA-IMID into continuous cooling co-crystallisation in the KRAIC / KRAIC-D platforms was not pursued, nor were cooling crystallisations above 100 mL scale. As OXA-IMID has demonstrated hydrogen transfer capabilities with temperature, this salt-like behaviour explains why the concentration requirements of OXA-IMID were much greater than OXA-ISO due to the greater solubility in aqueous environments. Cooling crystallisations of OXA-IMID were thus not investigated above 1 mL scale in batch.

Interestingly, the profen family co-crystals with the ISO co-former (IBU-ISO and OXA-ISO), exhibit identical thermal stability, as confirmed by their DSC endotherm melting events between 120-124 °C. This physical property similarity between the profen family targets co-

crystallised with ISO reflects very similar intermolecular interactions, which directly impacts the melting points of these materials. The IBU-ISO and OXA-ISO co-crystals crystallise in the $P\bar{1}$ and $P2_1/c$ space groups respectively. The strong to moderate intermolecular O-H···N hydrogen bonding interaction has a similar corresponding hydrogen bond length of 2.608(5) Å and 2.628(3) Å for IBU-ISO and OXA-ISO respectively. The bond angle for this O-H···N hydrogen bond is also similar at 166.2° and 176(2)° for IBU-ISO and OXA-ISO respectively. The hydrogen-to-hydrogen donor length (H···N) varies slightly at 1.804 Å and 1.591(3) Å for IBU-ISO and OXA-ISO respectively.

Structural Comparisons

Comparing the hydrogen bonding behaviour of the IBU-ISO co-crystal, with the previously reported SODDIZ[178] structure, in which the IBU target is co-crystallised with the structural isomer of ISO, Nicotinamide (NICO), showed some structural differences, as well as similarities. IBU-NICO (SODDIZ) crystallises in the non-centrosymmetric space group $Pca2_1$, whilst IBU-ISO is crystallised in the centrosymmetric space group $P\bar{1}$. The single crystal structure of IBU-NICO features a long cell axis of 56.5 Å, which is an uncommon feature for small organic molecules; the OXA-ISO system studied in the present work also possesses a large unit cell, in that case due to slight variations of phenyl group geometries in neighbouring molecules.

The packing observed in both the IBU-ISO and IBU-NICO crystal structures are dominated by the attachment of IBU to the ISO / NICO co-former molecule through a simple O-H···N hydrogen bond, rather than through a carboxylic acid-pyridine synthon, as well as a dimerisation interaction of the co-former molecule. Similar to the ISO dimers formed through a $[R^2_2(8)]$ homosynthon in IBU-ISO, dimers of NICO molecules formed through a $[R^2_2(8)]$ homosynthon are present in the IBU-NICO crystal structure. The strong to moderate intermolecular O-H···N hydrogen bonding interaction has a similar corresponding hydrogen bond length of 2.608(5) Å and 2.658(11) Å for IBU-ISO and IBU-NICO respectively. The bond angle for this O-H···N hydrogen bond is also similar at 166.2° and 165.2° for IBU-ISO and IBU-NICO respectively. The hydrogen-to-hydrogen donor length (H···N) is also similar at 1.804 Å and 1.835 Å for IBU-ISO and IBU-NICO respectively.[178]

Similar to the improved solubility of IBU-ISO relative to the pure IBU target, the use of NICO in the IBU-NICO co-crystal also improves the solubility of IBU. In addition, both IBU-ISO

and IBU-NICO exhibit improved thermal stability compared to pure IBU, where the melting of IBU occurs at 78 °C, whilst for IBU-ISO and IBU-NICO the melting events of these co-crystals occurs at 120 °C and 89.5 °C respectively.[178] The notable difference in melting point of the IBU-ISO and IBU-NICO structures implies that hydrogen bonding is more extensive in the IBU-ISO structure, than the IBU-NICO structure.

Comparing the OXA-ISO with the previously reported OXA co-crystals OJUQOB[166] and OJUQAN[166], in which the OXA target is co-crystallised with 4,4-bipyridine (BP) and 1,2-bis(4-pyridyl)ethane (BPE) respectively, showed structural differences. OXA-BP 1:0.5 (OJUQOB) crystallises in the monoclinic *C2/c* space group with one molecule of OXA and half a molecule of BP present in the asymmetric unit. OXA-BPE 1:0.5 (OJUQAN) crystallises in the triclinic $P\bar{1}$ space group with one molecule of OXA and half a molecule of BPE present in the asymmetric unit.[166] The OXA-ISO 1:1 co-crystal reported in the present work crystallises in the monoclinic space group $P2_1/c$, with six molecules of OXA and six molecules of ISO in the asymmetric unit corresponding with a high Z' value of 6.

Similar to OXA-ISO, the OXA-BP and OXA-BPE co-crystals exhibit reduced thermal stability, with 124 °C, 148.5 °C and 134.5 °C melting temperatures respectively, in comparison to the melting event of the OXA target at 160 °C.

Comparing the OXA-IMID salt with the previously reported molecular salts of OXA with piperazine (PIP), 2-amino-3-picoline (2A3P) and salbutamol (SAL), showed some distinct differences in structural, solubility and thermal behaviour. OXA-PIP 1:1 crystallises in the triclinic $P\bar{1}$ space group with one molecule of OXA^- and half a molecule of $PIP–H^+$ in the asymmetric unit. Proton transfer from the carboxyl of the OXA to the N of the PIP was shown. OXA-SAL 1:1 crystallises in the triclinic $P\bar{1}$ space group with one molecule of OXA^- and one molecule of $SAL–H^+$ present in the asymmetric unit. The presence of multiple hydrogen bond donors and acceptors sites on $SAL–H^+$ results in a four component supramolecular unit recurring throughout the crystal structure.[166] The OXA-IMID 1:1 solvate reported in the present work crystallises in the monoclinic space group $P2_1/n$, with one molecule of OXA, one molecule of IMID and one molecule of water (solvent) in the asymmetric unit.

In both the OXA-PIP and OXA-SAL salts, all the potential hydrogen bonding sites are involved in strong ionic and neutral hydrogen bonds, with no free hydrogen donor or acceptor site with

which water may interact. This contrasts with OXA-IMID, in which water forms an intermolecular hydrogen bond with one of the nitrogen atoms in the ring of the IMID molecule.

The thermal behaviour of OXA-IMID was shown to be complex, whilst the melting events of the OXA-PIP, OXA-2A3P and OXA-SAL molecular salts exhibited much simpler thermal behaviour, comprising a single melting event at 204.8 °C, 111.7 °C and 172.7 °C respectively.

Interestingly, Aitipamula *et al.*[166] reported the salts of OXA-PIP and OXA-SAL to exhibit reduced solubility compared to the OXA target, whereas, although not quantified, the OXA-IMID salt is shown in the present work to exhibit significantly increased solubility in 60:40 HI compared to OXA in the same solvent system. Importantly, the equilibrium solubility measurements of OXA-PIP and OXA-SAL were quantified in a phosphate buffer, whilst OXA-IMID was not considered in the same buffer solution; therefore, only relative comparisons in the same solvent systems can be made. For the OXA-PIP and OXA-SAL molecular salts, no correlation was found between the melting point of the salt and the solubility of the salt. Instead, the lower solubility of the salts was attributed to the more extensive hydrogen-bond arrangement and efficient packing of the molecular fragments in the crystal lattice compared to the pure OXA target.[166]

Chapter 7 – *In situ* X-ray Diffraction (XRD) analysis for capturing Solution Mediated Phase Transformations (SMPTs) during slurrying crystallisations in capillaries at High Resolution Powder Diffraction Beamline, I11 – Ibuprofen-isonicotinamide (IBU-ISO)

The research presented in Chapter 7 was supported by Pollyanna Payne and Dr. Lauren Hatcher during beamtime experiments at Beamline I11 at the Diamond Light Source.

7.1 Introduction and Aims

The overriding goal of the development of solid-state forms of pharmaceutical materials is to establish which solid form has the optimal characteristics for the intended use,[21] which usually is the most thermodynamically stable polymorph.[13] This is because the thermodynamic polymorph is the only form that does not tend to undergo spontaneous polymorphic transformation. On the other hand, a significant disadvantage of using the thermodynamic polymorph for a pharmaceutical application is that the most stable polymorph is the least soluble due to its high crystal packing density and hence potential issues with low bioavailability are possible. Control over polymorphism is paramount in overcoming problems associated with polymorphism in industrial-scale production.

Systems that exhibit polymorphism in solution will undergo solution mediated phase transformations (SMPTs), dictated by Ostwald's Law of Stages: first, the metastable phase will undergo dissolution; second, nucleation of the stable phase; third, growth of the stable phase will occur. This implies that a low-energy route to interconversion between polymorphic forms exists.[53] This transformation from the metastable to stable polymorph is possible in solution as molecules possess a number of degrees of freedom in this phase. Therefore, molecules in solution have the opportunity to re-orientate and re-align themselves so that as the molecules crystallise the free energy of the system is minimised.

These SMPTs can be investigated *via* solution-mediated crystallisation techniques, also known as slurrying. This method of crystallisation is a suspension technique allowing for the investigation of thermodynamically related polymorphs, solvates and multi-component crystalline systems. The SMPT is thermodynamically driven by the solubility difference between polymorphs or co-crystals.

Slurrying can produce preferred polymorphic outcomes, as well as different polymorphic outcomes, dependent on varying slurrying time, mixing and temperature conditions, amount of solid loading, as well as scale of operation[8]; in addition, the polymorphic transformation time can very much depend upon the nucleation behaviour of the stable polymorph.[179]

These SMPTs can be monitored *in situ via* slurrying in capillaries on synchrotron beamlines, where many more crystallising phases, including transient phases, can be captured in the fast data collection times available during synchrotron studies.

Chapter 6 reported a novel pharmaceutical co-crystal of ibuprofen and isonicotinamide (IBU-ISO) accessed *via* a range of crystallisation methods including slurrying crystallisation. The IBU-ISO co-crystal exhibits an improved solubility in 60:40 water:isopropanol (HI) compared to the IBU target. Slurry stability testing of the pre-prepared co-crystal of IBU-ISO found that IBU-ISO undergoes partial dissociation to IBU from 2 hours of slurrying at both room and body temperature, which is an acceptable result on the premise of IBU drug delivery in the gut. Through consideration of the relative solubility curves of IBU and IBU-ISO in 60:40 HI, a SMPT from the more soluble IBU-ISO co-crystal to the IBU starting material would be expected as the SMPT is thermodynamically driven by the solubility difference between the single and multi-component systems. This indicates that IBU-ISO slurry mediated in 60:40 HI shows potential for undergoing SMPTs, which can be monitored *via in situ* characterisation at the high-resolution powder diffraction beamline I11.

The IBU-ISO co-crystal exhibits an improved thermal stability compared to IBU, demonstrated from extensive DSC analysis presented in Chapter 6, which quantified the melting events to be 123 ℃ and 78 ℃ respectively. The IBU-ISO co-crystal also showed robustness to thermal ageing *via* monitoring periodically over 1 month. The IBU-ISO co-crystal also indicates potential in undergoing SMPTs and solid state phase transformations, thus variable temperature powder X-ray diffraction (VT-PXRD) analysis is appropriate for this co-crystal material.

7.2 Slurry preparation and capillary loading

7.2.1 Preparation of Slurrying Crystallisations

The slurries were prepared using a 1:1 and 1:2 molar ratio of IBU (1 g and 0.5 g respectively) and ISO in 5 mL of a 60:40 water:isopropanol (HI) solvent stock, left stirring at 300 rpm at

room temperature for 5 minutes to allow equilibration of the slurry. After this stirring period, the resultant product was transferred into the 1 mm borosilicate capillary using a glass pipette.

7.2.2 Capillary Loading

The samples were prepared by cutting a sealed end of a 1 mm borosilicate capillary to allow the slurry solution to be fed into the open-ended capillary using a glass pipette; the capillary was then sealed at both ends using wax, fed into a brass holder, sealed with superglue and secured into a brass holder stand, ready to be mounted onto the diffractometer for data collection (Figure 7.1). The capillary was mounted onto the capillary spinner on the diffractometer as swiftly as possible before data collection in order to capture the crystallisation process as early as possible in the experiment. The use of the capillary spinner positioned on the diffractometer provided gentle mixing of the slurry suspension, whilst the intensity of mixing provided by stirring inherent in batch slurrying experiments is notably more intense. Routine batch slurrying experiments are subsequently filtered and analysed offline by PXRD, without capturing insight into the crystallisation pathway of the slurrying crystallisation process.

Weight percent (wt %) solid loading of a slurry within a capillary cannot be ascertained as the loading process is not guaranteed to maintain the same solid loading as the stock vial, due to separation of solid upon capillary preparation (slurries were stirred on a stirrer plate before capillaries were prepared). Glass pipettes were used instead of the initially trialled syringe and needle to improve slurry homogeneity transferred into the borosilicate capillary.

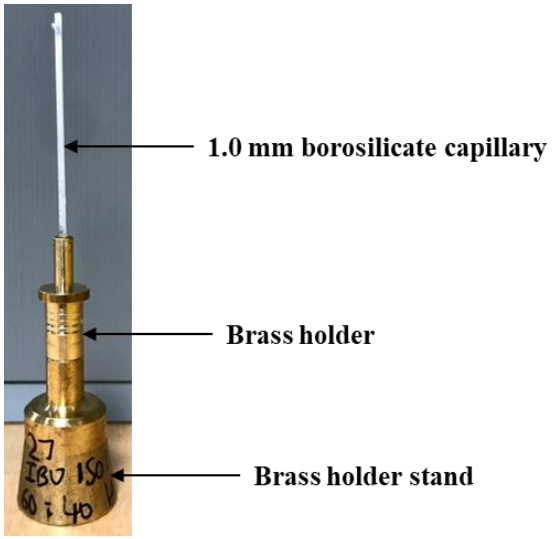

Figure 7.1 – Capillary containing slurry sample set-up.

7.3 Data Capture and Analysis Procedure

7.3.1 Data Capture

In situ XRD characterisation was performed at Diamond beamline I11, using an X-ray beam of 15 keV energy and 0.8265 Å wavelength with a position sensitive detector (PSD) based on Mythen, appropriate for this time-resolved work. The size of the X-ray beam used was 0.5 mm x 2.5 mm, to ensure compatibility with the 1 mm ID borosilicate capillaries. For Variable Temperature Powder X-ray Diffraction (VT-PXRD) measurements, a Cryostream Plus was employed to provide controlled heating to the sample in the range 293-408 K.

7.3.2 Data Analysis Procedure

Background diffraction was an important consideration as the sample, in addition to containing crystalline material, also comprised of a solvent mixture of water and isopropanol. As a result of the inherent background associated with solvents used within crystallisation experiments; the use of solvent background subtraction allows for patterns to be obtained containing only the scattering resulting from the crystalline material.

Various strategies for removing the background experimentally, as well as *via* a mathematical approach were attempted. The experimental approach involved subtracting acquired patterns of an air filled 1 mm borosilicate capillary and a borosilicate capillary containing pure 60:40 HI, from the diffraction obtained during the slurrying experiments. However, due to the slurry mediator comprising a solvent mixture containing water and isopropanol, this did not achieve suitable subtraction of the background, possibly due to inhomogeneity of the solvent mixture within the borosilicate capillary.

Instead of achieving background subtraction experimentally, a mathematical approach to background subtraction was therefore carried out using the in-house Data Analysis WorkbeNch (DAWN) created at the Diamond Light Source.[91] The raw data was loaded into the processing window and the background rolling ball baseline subtraction was set to a ball radius of 50 pixels and applied to each of the files. A local background value is determined for every pixel by averaging over a very large ball around the pixel. This value is subtracted from the original image, removing large spatial variations of the background intensities. The radius is selected on the premise that it is at least the magnitude of the largest object that is not considered to be resulting from the background. The background-subtracted files were subsequently loaded into the Data Visualisation window and the data combined into an image using the concatenate tool,

which allows alterations to be made to the number of pixels, as well as the interval and range of scans presented.

The resulting diffraction patterns were then compared with PXRD patterns of the anticipated crystalline materials simulated in Mercury from available structural information of IBU and the IBU-ISO co-crystal (Chapter 6), and also to experimental reference patterns measured from pure IBU and pure ISO, each slurry mediated in 60:40 HI loaded into a 1 mm borosilicate capillary.

7.4 Solution Mediated Phase Transformation (SMPT) monitoring of IBU-ISO

7.4.1 Offline XRD analysis of slurrying crystallisation of IBU_ISO in 60:40 HI

Ex situ PXRD measurements of IBU_ISO 1:1 slurry mediated in 60:40 HI over 24 hours at 20 ℃ and 30 ℃ yielded IBU in polymorphic purity, whilst slurrying at 40 ℃ produced a mixture of IBU and the IBU-ISO co-crystal evident from the representative IBU-ISO peaks, particularly prominent at 10° 2θ (Figure 7.2). This indicates that the IBU-ISO co-crystal is favoured at higher slurrying temperatures and highlights the potential of *in situ* VT-PXRD analysis to study the slurrying crystallisation of IBU_ISO in 60:40 HI.

To elucidate the solution-based phases of IBU_ISO physical mixture in solution, *in situ* measurements can capture early solution-based phases, which are missed in offline measurements. *In situ* measurements of a slurry suspension also allows for the relative stability of solution-based phases to be established.

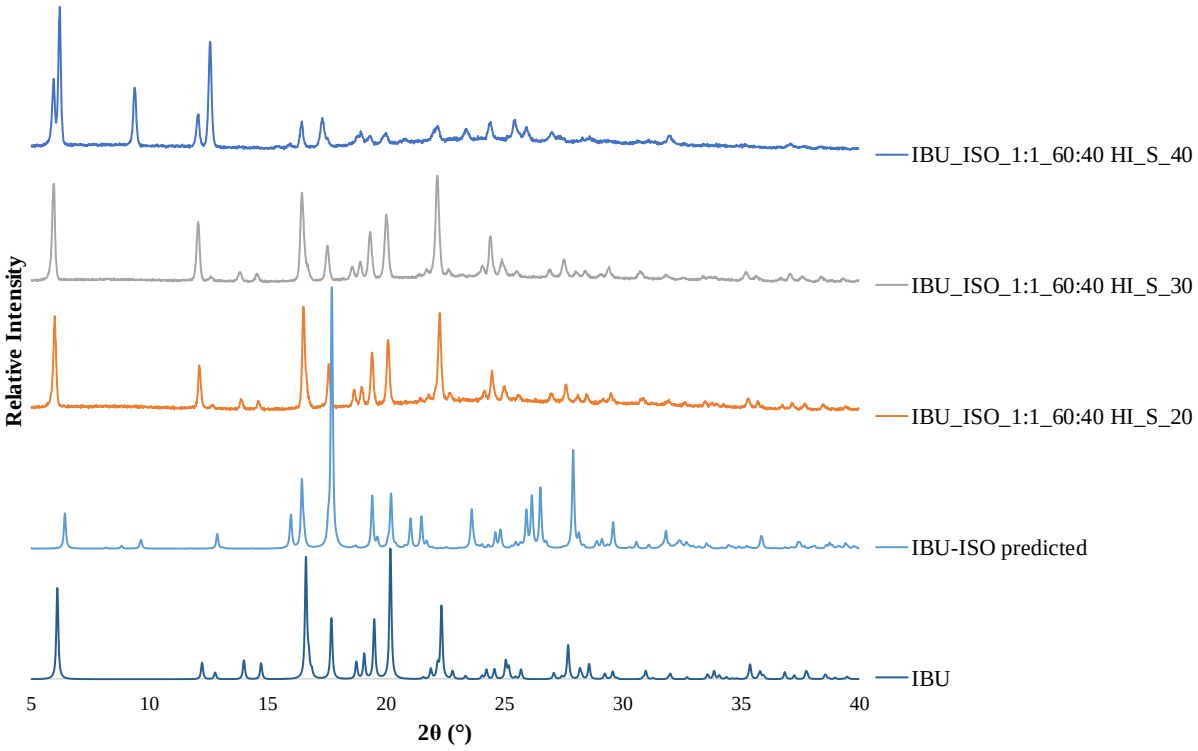

Figure 7.2 – Offline PXRD patterns of a physical mixture of IBU_ISO 1:1 slurry mediated for 24 hours in 60:40 HI at 20 ℃, 30 ℃ and 40 ℃ compared to IBU (Refcode: IBPRAC) and IBU-ISO predicted PXRD pattern simulated in Mercury.

7.4.2 *In situ* XRD monitoring of early stage crystallisation: IBU_ISO in 60:40 HI

In situ XRD monitoring of a physical mixture of IBU_ISO 1:1 in 60:40 HI was carried out continuously for 10 minutes to determine early stage phase changes in the crystallisation process. Data visualisation in DAWN was set to present PXRD patterns accumulated over each 30 second period over the 10 minute data collection time (Figure 7.3).

A diffraction peak at 6.5° 2θ corresponding to IBU disappears between 5 minutes 30 seconds and 6 minutes into the *in situ* XRD monitoring. Similarly, a diffraction peak present at 9.5° 2θ, representative of IBU-ISO emerges between 4 minutes 30 seconds and 5 minutes into the analysis of the slurrying crystallisation process. This *in situ* XRD analysis highlights that the IBU-ISO co-crystal is not formed in purity; the characteristic IBU diffraction peak at 3° 2θ is present throughout the 10 minute collection time.

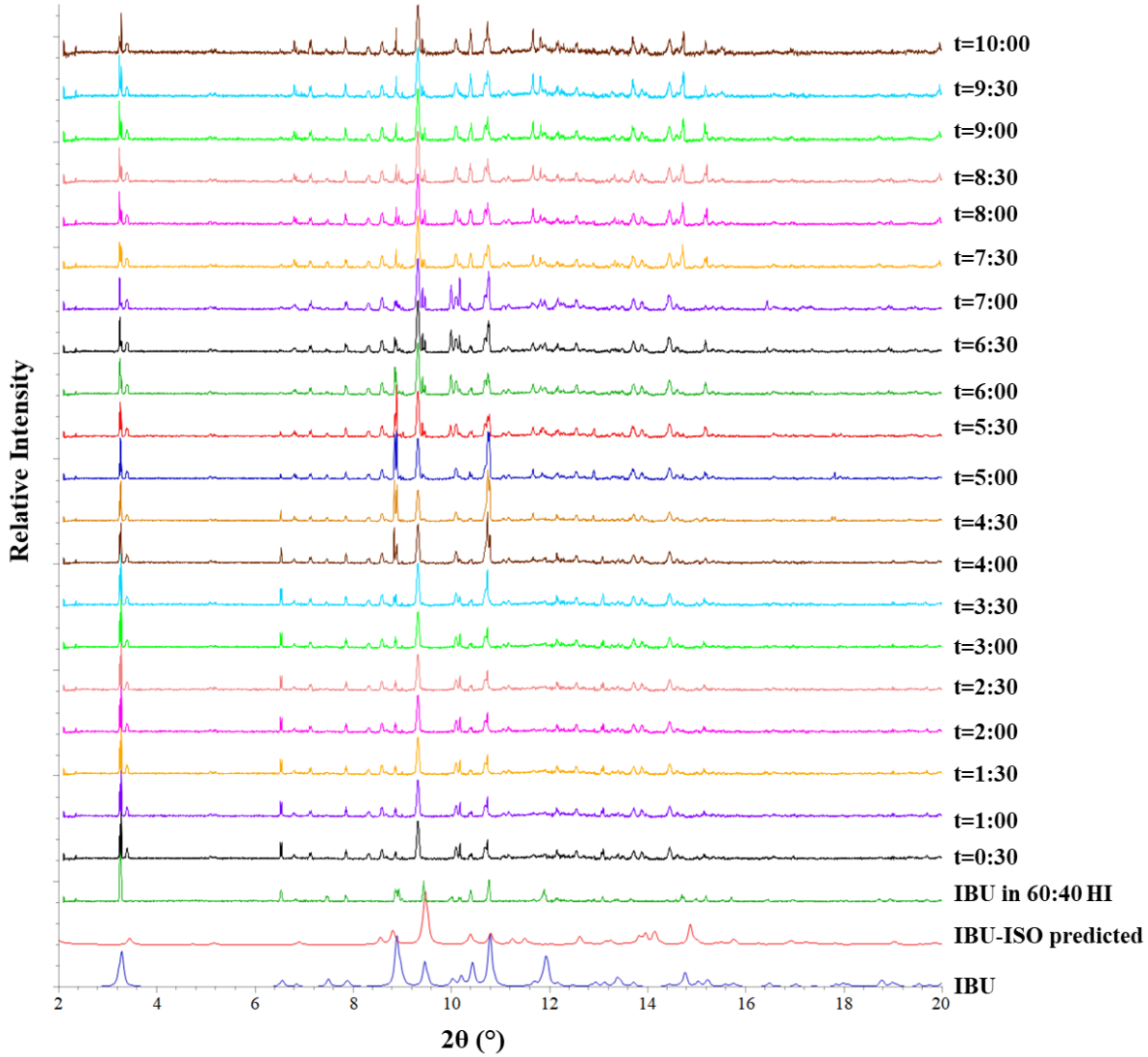

Figure 7.3 – *In situ* PXRD characterisation of a physical mixture of IBU_ISO 1:1 in 60:40 HI loaded into a borosilicate slurry and monitored at room temperature over a 10 minute data collection time (t = 10:00) at I11, compared to the IBU in 60:40 HI experimental reference collected at I11 and the IBU-ISO predicted powder pattern simulated in Mercury.

7.4.3 *In situ* VT-XRD monitoring of early stage crystallisation: IBU_ISO in 60:40 HI

In situ VT-XRD monitoring of a physical mixture of IBU_ISO 1:1 in 60:40 HI was carried out at a heating / cooling rate of 0.8 °C min^{-1} with a PXRD pattern collected at every 5 °C change in temperature (Figure 7.4). The VT-PXRD measurements show three defined areas, where a mixture of IBU and the IBU-ISO co-crystal are evident on heating. Interestingly, between 323 K and 328 K a phase transformation occurs to yield the pure IBU-ISO co-crystal. The disappearance of IBU evident form the PXRD pattern at 328 K does not correspond to the melting of pure IBU at 351 K. After the sample is heated to 328 K, the PXRD data indicate the

sample is now amorphous, as seen through the loss of the consistent baseline of the diffraction patterns and the absence of sharp diffraction peaks. This amorphous state could be attributed to dissolution of the crystalline sample and subsequent scattering from the 60:40 HI solvent mixture, as well as possible 'oiling out' seen previously in Chapter 6 for the IBU-ISO system. Upon cooling, the pure IBU-ISO co-crystal re-crystallises at 313 K and no further phase changes are evident over the temperature range 313-293 K.

Visual observations using a camera alongside the *in situ* XRD measurements would be a useful approach to provide insight to the state of the slurry within the capillary at the temperature at which the diffraction data is showing an amorphous state is present. It is difficult to make comparisons between this *in situ* XRD data and the temperature of 'oiling out' monitored *via in situ* turbidity measurements coupled with *in situ* image acquisition measurements using particle visualisation measurements (PVM) in the Crystalline®, as presented in Chapter 6. In addition, the metastable zone width (MSZW) of a 5 mL vial in the Crystalline® will be largely different to that in a 1 mm borosilicate capillary, which also experience largely different mixing conditions.[180-183]

Ni *et al.* showed that the improved mixing and heat transfer conditions accessible in the continuous oscillatory baffled crystalliser (COBC) resulted in a narrow MSZW compared to traditional stirred tank crystallisers employed for the unseeded cooling crystallisation of L-glutamic acid.[181, 182] On this basis, the more efficient mixing achievable in the 5 mL vials in the Crystalline® with agitation provided by magnetic bottom stirring in comparison to the less homogeneous mixing accessible for the slurries of high solid content loaded in the 1 mm capillaries, would suggest that the MSZW for the 5 mL vials will be smaller than in the 1 mm borosilicate capillaries. Importantly, for the VT-XRD measurements of the slurrying crystallisation process, the slurry did not dissolve before cooling, whilst for the VT studies in the Crystalline®, it was ensured that complete dissolution was achieved before the cooling cycle had begun; thus, the method of crystallisation is also a significant differentiating factor during this comparison of the amorphous behaviour of the IBU-ISO system.

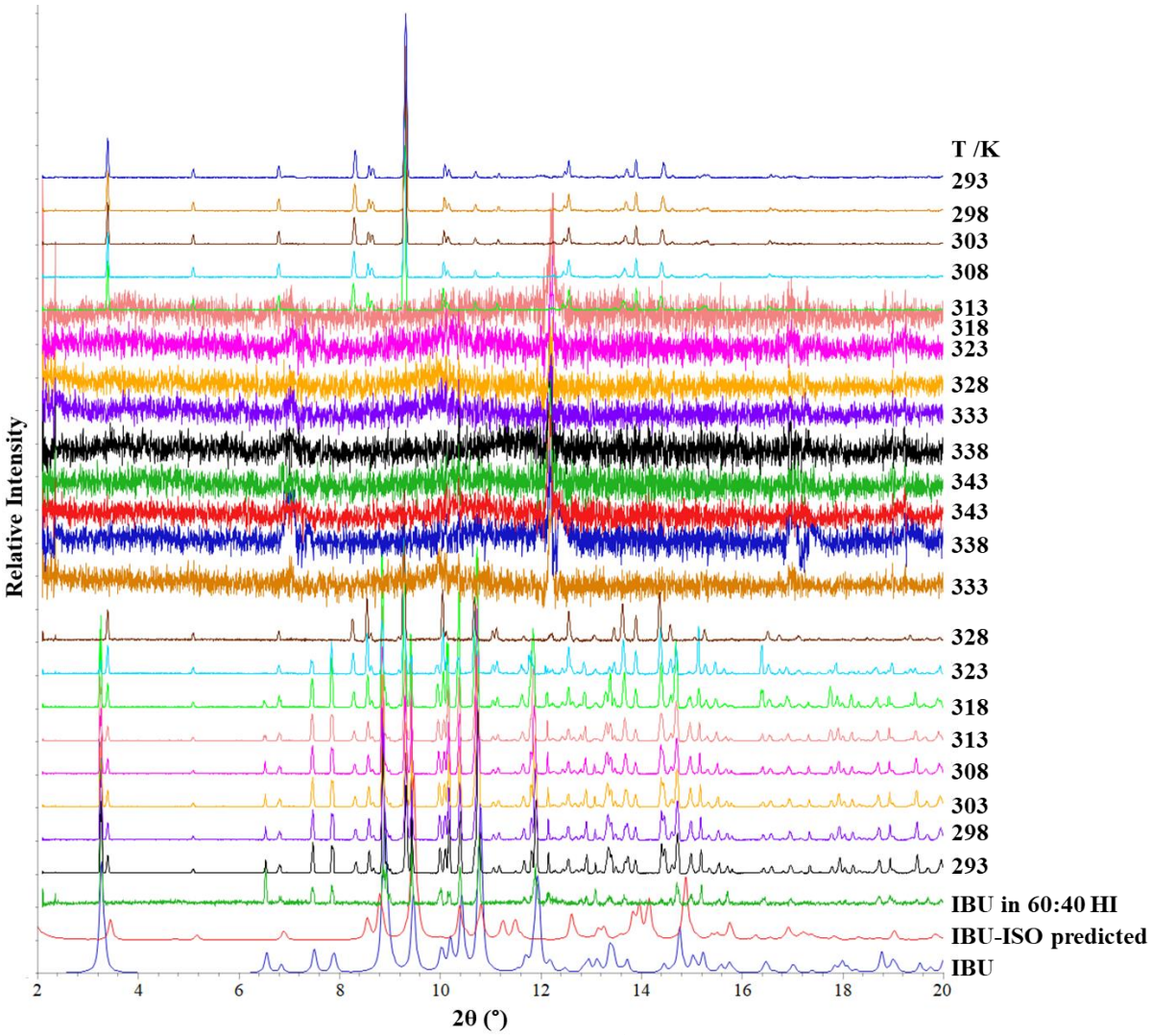

Figure 7.4 – *In situ* VT-PXRD measurements collected in capillary mode at I11 of a physical mixture of IBU_ISO 1:1 slurry mediated in 60:40 HI. The 313 K and 318 K patterns overlap in this plot as DAWN uses a set stacking for the diffraction patterns and the 318 K amorphous pattern with a higher background overlaps that at 313 K.

7.4.4 *In situ* VT-XRD monitoring of IBU-ISO

In situ VT-XRD monitoring of a pre-prepared co-crystal of IBU-ISO was analysed neat using a heating rate of 0.8 °C min^{-1} with a PXRD pattern collected at every 5 °C change in temperature (Figure 7.5). Diffraction peaks corresponding with IBU (at 3° and 9° 2θ) are seen to disappear after 338 K; this temperature could coincide with the melting event of IBU expected at 351 K, which would show a depression in melting temperature as the sample is impure with the majority of the crystalline sample containing the IBU-ISO co-crystal. Furthermore, this

disappearance of certain diffraction peaks after 338 K coincides with the dissolution observed by 333 K for the i*n situ* VT-XRD monitoring of a physical mixture of IBU_ISO 1:1 in 60:40 HI shown above in Section 7.4.3. The approximate 5 K discrepancy in the disappearance of diffraction peaks could be attributed to the 60:40 HI solvent environment experienced by the IBU_ISO 1:1 physical mixture, whilst the pre-prepared IBU-ISO co-crystal was monitored dry without the presence of solvent in the capillary. This difference could lead to changes in the moisture content in the atmosphere within the capillary, which is facilitating this SMPT.

The IBU-ISO co-crystal is present throughout the PXRD monitoring between temperatures of 293 K to 388 K, and is observed to melt at 393 K (120 ℃). The melting event from VT-PXRD analysis is consistent with the melting event of 123 ℃ observed in the DSC data presented in Chapter 6.

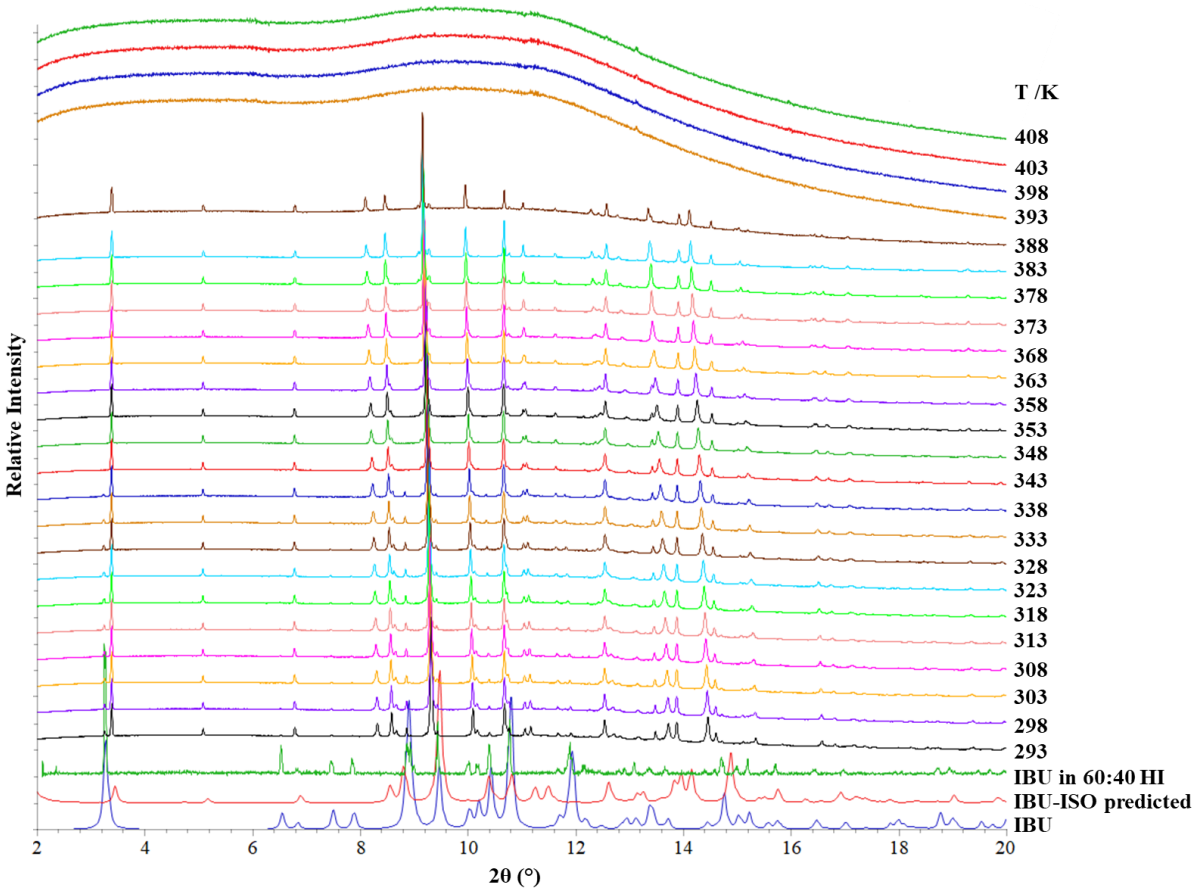

Figure 7.5 – VT-PXRD measurements collected in capillary mode at I11 of the pre-made IBU-ISO co-crystal prepared by grinding of the constituent IBU and ISO starting components for 30 minutes.

7.5 Conclusions of IBU-ISO *in situ* XRD characterisation

Chapter 7 investigated the use of *in situ* XRD as a monitoring approach to analyse SMPTs occurring during slurrying crystallisation of the pharmaceutical co-crystal IBU-ISO in 60:40 HI. The findings are in agreement with those presented in Chapter 6. The IBU-ISO co-crystal is shown to exhibit thermal stability to 388 K, before melting at 393 K (consistent with the melting temperature of IBU-ISO at 120 °C reported in Chapter 6) evident from the VT-PXRD measurements of a neat sample loaded into a borosilicate capillary. IBU-ISO is shown to re-crystallise on cooling in a solution of 60:40 HI, evident from VT-PXRD measurements at a temperature of 40 °C. The *in situ* XRD measurements captured over a 10 minute collection period showed the formation of the IBU-ISO co-crystal in 60:40 HI *via* slurry crystallisation.

7.6 Overall discussion and conclusions

Chapter 7 presented diffraction data from *in situ* XRD analysis of slurries loaded into borosilicate capillaries. The pharmaceutical co-crystal of IBU-ISO was used during method development, in which the data demonstrates that scattering from crystalline material suspended in a solvent can be achieved, as well as phase changes monitored *via in situ* XRD measurements at beamline I11 at Diamond Light Source. This work provides an improved insight into the various transient solution phases found in solution-based crystallisations, which can be overlooked during traditional solid-state analysis and highlights the potential of this technique for capturing transient phases and polymorphic transformations observed in the slurrying crystallisation pathway of other systems in the future.

Chapter 8 – Conclusions and Future Work

8.1 Conclusions

The work presented in this research project has demonstrated the potential of *in situ* synchrotron X-ray diffraction techniques to reveal information on the crystallisation pathway adopted by the crystallisation process. The development of capabilities for *in situ* diffraction of flow processes at Diamond Light Source, through use of segmented flow crystallisers known as the KRAIC-D (Kinetically Regulated Automated Input Crystalliser – for Diffraction) and KRAIC-S (Kinetically Regulated Automated Input Crystalliser – Single Crystal) have been presented. The design of these continuous platforms were developed and optimised for implementation on the Diamond beamlines I11 (High Resolution Powder Diffraction) and I19 (Small Molecule Single Crystal Diffraction).

As a result of the steady-state operation of the KRAIC-D and KRAIC-S platforms, an analytical set point will be at the same stage of the crystallisation process irrespective of the experiment time, which allows events that evolve with the crystallisation time, such as polymorphic transformations and crystal growth to be investigated.

Polymorphic transitions and stability during cooling crystallisation processes in an industrially relevant crystalliser, known as the KRAIC-D, were uncovered through *in situ* synchrotron powder X-ray diffraction (PXRD) analysis. Using the KRAIC-D installed at I11, the crystallisation pathways of the highly polymorphic pharmaceutical compounds carbamazepine (CBZ) in EtOH and urea-barbituric acid (UBA) in MeOH were monitored with respect to polymorphic form and crystal growth during unassisted crystallisation and also in response to various seeding regimes. Using both unseeded and seeded (pre- and post-nucleation) cooling crystallisation methodologies, the evolving crystal structures of CBZ in EtOH and UBA in MeOH were uncovered as a function of residence time by probing different set positions comprising Kapton® windows along the length of this milliscale tubular flow crystalliser, KRAIC-D.

The CBZ in EtOH experiments confirmed the established CBZ form II to CBZ form III nucleation and growth pathway, whilst also demonstrating the sensitivity of this pathway to seeding. The nucleation of CBZ form II could be bypassed completely or existent CBZ form II crystallites could undergo rapid transformation to CBZ form III depending on the location

of the CBZ form III seeding, corresponding with pre-nucleation and post-nucleation seeding respectively. Through analysis of a single 100 ms diffraction frame from the KRAIC-D, sufficient data is available for polymorph identification from flowing droplets. Furthermore, through this segmented flow cooling crystallisation technique, an unusual CBZ form III needle morphology can be accessed and when combined with CBZ form III blocks in a single solution slug, can lead to morphology separation *via* segmentation as a result of the interaction of the different habit with the flow path in the solution slug.

Monitoring UBA in MeOH in the KRAIC-D at I11, helped to determine solution state *versus* solid state stability of this pharmaceutical co-crystal. During solution-based cooling crystallisation and slurrying, UBA form III readily transforms to UBA form I in both unassisted and UBA form III seeded experiments. In contrast, dry crystals of UBA form I undergo solid state transformation to UBA form III under ambient laboratory storage for 12 months. These findings highlight the need for accurate knowledge of the media-dependent stability (in this case in MeOH *versus* air) of a pharmaceutical as integral to the design and process optimisation of the development of an effective pharmaceutical product.

The use of *in situ* synchrotron single crystal analysis using the KRAIC-S installed at I19 has demonstrated both the implementation and optimisation of a unique method for collecting single crystal data of small organic molecule single crystals crystallised and monitored *in situ*. The development of a slug triggering mechanism facilitated the trigger of the motorised stage, which artificially suspended a single crystal in the X-ray beam for sufficient time to achieve indexation from a single diffraction frame. An optimised slug triggering design, whereby the optical trigger was positioned adjacent to the X-ray beam, whilst residing on the motorised stage greatly improved the crystal hit rate and reduced the time delay between data acquisitions.

Paracetamol (PCM) in 60:40 water:isopropanol (HI) was a suitable model system to yield single crystals in solution slugs in the KRAIC-S, whereby this highly reproducible crystallisation environment was suitable for these serial-crystallography type experiments. Monitoring the unseeded cooling crystallisation process at two set points (6.7 m and 8.7 m), allowed the extent of lattice rotation with crystal growth to be established. The use of relative integrated intensities across *hkl* reflection sets at the two set points, compared to single crystals of known size was explored as an approach for crystal size prediction. Seeding the cooling crystallisation process of PCM in 60:40 HI with the metastable PCM form II highlighted the

need for seed delivery optimisation and compatibility of certain crystal habits for this *in situ* single crystal diffraction technique, as a result of the interaction of the single crystal with the flow path in the solution slug.

Two data processing methodologies were employed to process the *in situ* single crystal diffraction data, whereby CrysAlisPro required manual handling, whilst DIALS has been employed for full automation. The significant advantage of employing DIALS is the fully automated data processing, which includes spot finding, indexation, refinement, integration and merging can be carried out in a few minutes. The significance of this means that data checks can be automatically triggered after a 4 second data collection and thus data capture and processing can be carried out for each single crystal in under 5 minutes, allowing experimental conditions to be altered during the beamtime if the data suggests this is necessary. On the premise that the merged datasets at 8.7 m and 6.7 m achieved a completeness of 2 % and 7 % respectively, it would be expected that structural solution could be achieved from 20-50 of these datasets to sample the entire sphere, although due to symmetry of the lattice, this number of datasets could be reduced, whilst still achieving structural solution.

The use of crystal engineering for materials discovery of the profen family, exploring whether co-crystal formation could be an alternative approach to the improvement of physicochemical properties of the profen targets, most notably with respect to the BCS class II solubility classification, was investigated. The discovery of three co-crystals accessed by a range of crystallisation methods: ibuprofen-isonicotinamide (IBU-ISO), oxaprozin-isonicotinamide (OXA-ISO) and oxaprozin-imidazole (OXA-IMID) solvate was reported. Each of the profen co-crystals have been fully structurally characterised and the transferability of crystallisation methods and possible physical property enhancement on these systems investigated. Solid-state stability testing was investigated through thermal stability tests to ascertain the co-crystal shelf-life compared to the pure API, as well as humidity stability tests to establish whether the co-crystals demonstrate resistance to moderate and severe humidity conditions.

The IBU-ISO co-crystal exhibits an improved solubility in 60:40 HI compared to the IBU target. The IBU-ISO co-crystal also features an improved thermal stability compared to IBU, from DSC analysis, which quantified the melting events to be 123 ℃ and 78 ℃ respectively. The IBU-ISO showed robustness to both thermal and humidity ageing. The IBU-ISO co-crystal can be accessed by evaporative, mechanochemical, slurrying in a range of solvents, as well as

via cooling crystallisation in 60:40 HI up to 200 mL. Investigations into the translation of this system into continuous cooling co-crystallisation were less successful as a result of the 'oiling out' behaviour, highlighting that the segmented flow employed in the KRAIC-D is not appropriate for every crystal system.

The OXA-ISO co-crystal features very large unit cell dimensions for a small-molecule organic, due to the slight positional disorder of the phenyl rings in the structure. The OXA-ISO co-crystal exhibits a reduced thermal stability compared to OXA, as confirmed by DSC melting event of 124 ℃ and 163 ℃ respectively. The OXA-ISO showed robustness to thermal ageing, but showed sensitivity towards humidity ageing. The diffraction analysis for the OXA-ISO co-crystal system was particularly challenging attributed to the similarity in diffraction patterns for the OXA-ISO co-crystal and OXA target.

The OXA-IMID solvate is a hydrate as confirmed by TGA analysis, in which water is driven out of the structure around 100 ℃, which is confirmed and visualised by HSM. The use of VT-SCXRD helped to understand the hydrogen bonding within the structure and the temperature induced proton migration behaviour of the OXA-IMID salt. The proton migration with temperature found in this complex establishes a salt-co-crystal continuum that offers an opportunity for property tuning.

The use of *in situ* synchrotron powder X-ray diffraction techniques have also been applied to batch slurrying crystallisations through a novel sample preparation technique, whereby pre-prepared slurries were loaded into borosilicate capillaries and monitored at various time points at I11 have been explored. The model system employed for method development focused on the novel co-crystal system ibuprofen isonicotinamide (IBU-ISO) accessed by co-crystallisation attempts to improve physicochemical properties. This *in situ* synchrotron powder X-ray diffraction technique has facilitated the collection of diffraction data obtained from crystalline material within the slurry contained in the capillary. The data capture approach highlighted that changes in crystalline phase can be observed for the various IBU-ISO experiments, over various time frames and temperature conditions.

8.2 Future Work

The work presented on PCM in 60:40 HI in the KRAIC-S in Chapter 5 demonstrates the potential of the novel technique in terms of data collection and the associated information

obtained from the data processing, and promises applications for other systems in the future. The serial-crystallography approach to data capture will be particularly valuable for the analysis of X-ray and photosensitive samples. The slug triggering mechanism presented in Chapter 5 for single crystal analysis can also be employed in future KRAIC-D experiments to optimise the data collection at I11. This avoids the collection of background frames of the air slugs and the carrier fluid, thus removing time-consuming post-data collection analysis and allowing quick interpretation of the data quality allowing alterations to the experimental set-up to be made promptly.

To supplement the *in situ* synchrotron powder X-ray diffraction analysis of slurrying crystallisations in capillaries, a novel and bespoke milliscale tubular segmented flow crystalliser known as the KRAIC-T (Kinetically Regulated Automated Input Crystalliser – Temperature Cycling) has been designed and built to investigate slurrying in flow (Figure 8.1). The key difference in the design of the KRAIC-T compared to the KRAIC-D is the cylinders are made of aluminium, which allows the temperature of the two coils to be set at different temperatures to facilitate temperature cycling. During temperature cycling experiments, the two holding pillars will be set to disparate temperatures to reflect the different energetic minima of, for example, enantiotropic systems. The outlet from each pillar traverses directly through the X-ray transparent Kapton® windows to capture the alternating phases without risk of transformation prior to detection. Non-invasive time-resolved PXRD studies of slurrying concomitant systems and temperature cycled enantiotropic systems will facilitate the identification and understanding of the crystallisation pathways of crystallising systems that have a very close energy relationship between polymorphs.

The capabilities established for the study of crystallisation processes *in situ* at Diamond Light Source can become a valuable tool for a wider user base, following their successful establishment, and demonstration of their capabilities in this work. The KRAIC-D concept is also now being transferred to a laboratory diffractometer set-up by the collaborative team, as part of the FlowXl project.

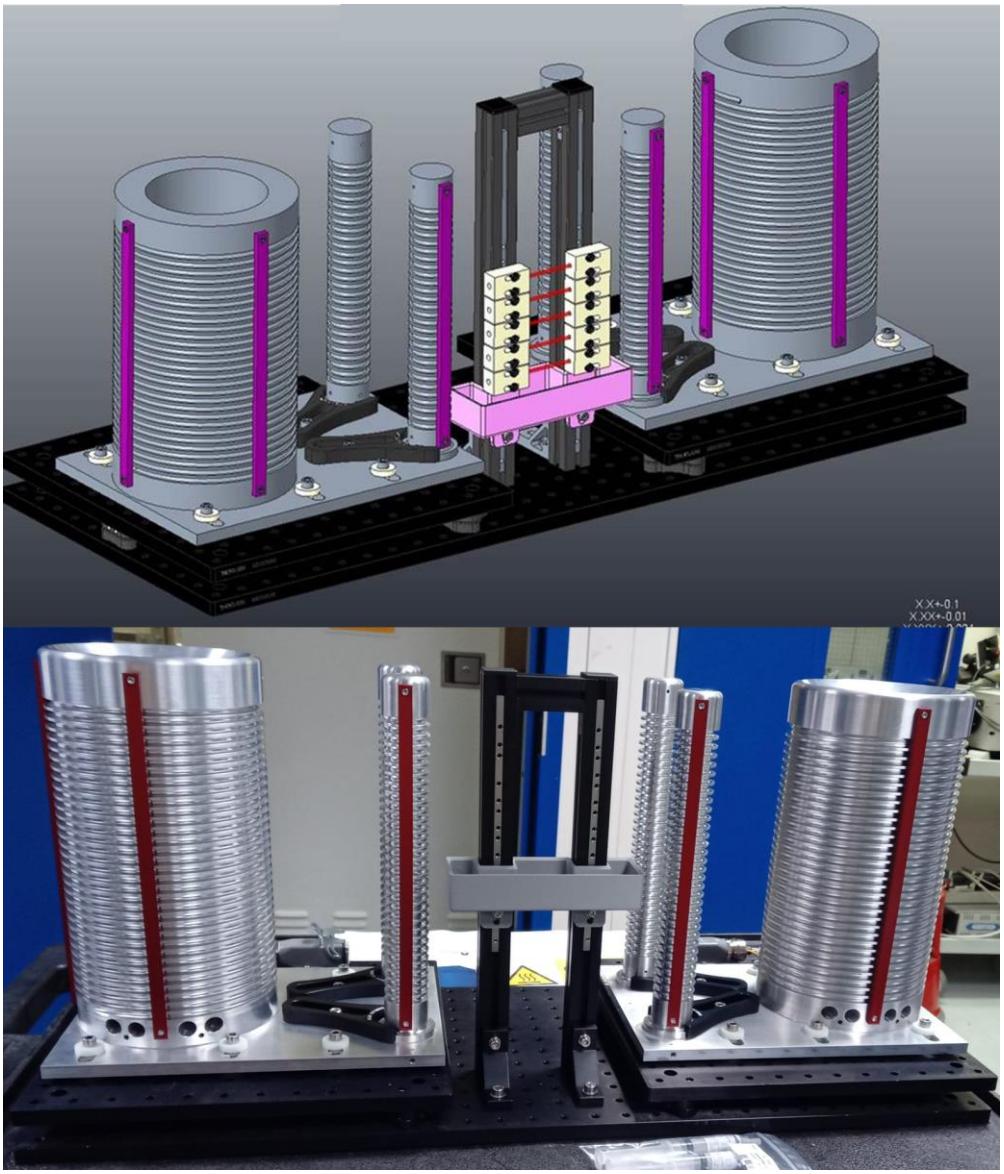

Figure 8.1 – Schematic (top) and image (bottom) of KRAIC-T.

Chapter 9 – References

1. K. Sypek, I. S. Burns, A. J. Florence and J. Sefcik, *Crystal Growth & Design*, 2012, **12**, 4821-4828.

2. P. Kavuru, S. J. Grebinoski, M. A. Patel, L. Wojtasb and K. Chadwick, *CrystEngComm*, 2016, **18**, 1118.

3. E. A. Losev, M. A. Mikhailenko, A. F. Achkasov and E. V. Boldyreva, *New J. Chem.*, 2013, **37**, 1973.

4. N. K. Thakral, R. L. Zanon, R. C. Kelly and S. Thakral, *Journal of Pharmaceutical Sciences*, 2018, **107**, 2969-2982.

5. Z. Gao, S. Rohani, J. Gong and J. Wang, *Engineering*, 2017, **3**, 343-353.

6. J. F. Bauer, *Journal of Validation Technology*, 2008, **14**, 15-23.

7. J. Bauer, S. Spanton, R. Henry, J. Quick, W. Dziki, W. Porter and J. Morris, *An Official Journal of the American Association of Pharmaceutical Scientists*, 2001, **18**, 859-866.

8. M. A. O'Mahony, A. Maher, D. M. Croker, Å. C. Rasmuson and B. K. Hodnett, 2012, **12**, 1925-1932.

9. H.-H. Tung, E. L. Paul, M. Midler and J. A. McCauley, *Crystallization of Organic Compounds: An Industrial Perspective*, Wiley, New Jersey, 2009.

10. J. W. Mullin, *Crystallization*, Butterworth-Heinemann, Great Britain, Third edn., 1992.

11. W. Beckmann, *Crystallization: Basic Concepts and Industrial Applications*, Wiley-VCH, Germany, 2013.

12. B. Y. Shekunov and P. York, *Journal of Crystal Growth*, 2000, **211**, 122-136.

13. H. G. Britain, *Polymorphism in pharmaceutical solids*, Taylor & Francis, New York, Second edn., 2009.

14. N. Qiao, M. Li, W. Schlindwein, N. Malek, A. Davies and G. Trappitt, *International Journal of Pharmaceutics*, 2011, **419**, 1-11.

15. N. Shan and M. J. Zaworotko, *Drug Discovery Today*, 2008, **13**, 440-446.

16. L. H. Thomas, A. R. Klapwijk, C. Wales and C. C. Wilson, *CrystalEngComm*, 2014, **16**, 5924-5932.

17. N. Schultheiss and A. Newman, *Crystal Growth & Design*, 2009, **9**, 2950-2967.

18. R. Hilfiker, *Polymorphism: in the Pharmaceutical Industry*, Wiley-VCH, Weinheim, Germany, 2006.

19. A. Y. Lee, D. Erdemir and A. S. Myerson, *The Annual Review of Chemical & Biomolecular Engineering*, 2011, **2**, 259-280.

20. A. Singh, I. S. Lee and A. S. Myerson, *Crystal Growth & Design*, 2009, **9**, 1182-1185.

21. L. H. Thomas, C. Wales, L. Zhao and C. C. Wilson, *Crystal Growth & Design*, 2011, **11**, 1450-1452.

22. L. R. Agnew, T. McGlone, H. P. Wheatcroft, A. Robertson, A. R. Parsons and C. C. Wilson, *Crystal Growth & Design*, 2017, **17**, 2418-2427.

23. L. R. Agnew, D. L. Cruickshank, T. McGlone and C. C. Wilson, *Chem. Commun.*, 2016, **52**, 7368-7371.

24. C. R. Groom, I. J. Bruno, M. P. Lightfoot and S. C. Ward, *Acta Crystallographica Section B*, 2016, **72**, 171-179.

25. R. Davey and J. Garside, *From Molecules to Crystallisers: An Introduction to Crystallisation*, Oxford University Press, New York, United States, 2000.

26. The Biopharmaceutics Classification System (BCS) Guidance http://www.fda.gov/AboutFDA/CentersOffices/OfficeofMedicalProductsandTobacco/CDER/ucm128219, (accessed 29th February, 2016).

27. N. K. Duqqirala, M. L. Perry, Ö. Almarsson and M. J. Zaworotko, *Chem. Commun.*, 2016, **52**, 640-655.

28. C. L. Jones, C. C. Wilson and L. H. Thomas, *CrystEngComm*, 2014, **16**, 5849-5858.

29. G. P. Stahly, *Crystal Growth & Design*, 2007, **7**, 1007-1026.

30. P. Vishweshwar, J. A. McMahon, J. A. Bis and M. J. Zaworotko, 2006, **95**, 499-516.

31. O. Almarsson and M. J. Zaworotko, *Chem. Commun*, 2004, 1889-1896.

32. D. O'Nolan, M. L. Perry and M. J. Zaworotko, *Cryst. Growth Des.*, 2016, **16**, 2211-2217.

33. C. F. Macrae, I. J. Bruno, J. A. Chisholm, P. R. Edgington, P. McCabe, E. Pidcock, L. Rodriguez-Monge, R. Taylor, J. van de Streek and P. A. Wood, *Journal of Applied Crystallography*, 2008, **41**, 466-470.

34. M. Schmidtmann, D. S. Middlemiss and C. C. Wilson, *CrystEngComm*, 2015, **17**, 5273-5279.

35. G. R. Desiraju, *Acc. Chem. Res.*, 2002, **35**, 565-573.

36. G. A. Jeffrey, *Introduction to Hydrogen Bonding*, Oxford University Press, New York, 1997.

37. G. J. Desiraju, *Crystal Engineering The Design of Organic Solids*, Elsevier, The Netherlands, 1989.

38. C. Wales, L. H. Thomas and C. C. Wilson, *CrystEngComm*, 2012, **14**, 7264-7274.

39. K. Wittering, J. King, L. H. Thomas and C. C. Wilson, *Crystals*, 2014, **4**, 123-140.

40. T. Steiner, *Acta Crystallographica Section B-Structural Science*, 2001, **57**, 103-106.

41. C. C. Wilson, L. Cronin and P. J. Kitson, *Process Understanding: For Scale-up and Manufacture of Active Ingredients*, Wiley -VCH, Houson, 2011.

42. T. McGlone, N. Briggs, C. Clark, C. Brown, J. Sefcik and A. Florence, *Organic Process Research & Development*, 2015, **19**, 1186-1202.

43. B. M. Couillaud, P. Espeau, N. Mignet and Y. Corvis, *ChemMedChem*, 2019, **14**, 8-23.

44. X.-W. Ni, A. Valentine, A. Liao, S. B. C. Sermage, G. B. Thomson and K. J. Roberts, *Crystal Growth & Design*, 2004, **4**, 1129-1135.

45. D. Erdemir, A. Y. Lee and A. S. Myerson, *Accounts of Chemical Research*, 2009, **42**, 621-629.

46. J. Chen, B. Sara, J. M. B. Evans and A. S. Myerson, *American Chemical Society*, 2011, **11**, 887 -895.

47. K. R. Seddon and M. Zaworotko, *Crystal Engineering: The Design and Application of Functional Solids*, Kluwer Academic Publishers, The Netherlands, 1999.

48. J. H. ter Horst, R. M. Geertman, A. E. van der Heijden and G. M. van Rosmalen, *Journal of Crystal Growth*, 1999, **198/199**, 773-779.

49. D. Braga and F. Grepioni, *Making Crystals by Design: Methods, Techniques and Applications*, WILEY-VCH Verlag GmbH & Co. KGaA, Weinheim, 2007.

50. A. Myerson and G. Rajiv, *Handbook of Industrial Crystallisation*, Butterworth-Heinemann, United States of America, Second edn., 2002.

51. K. Powell, G. Bartolini, K. Wittering, A. Saleemi, C. Wilson, C. Rielly and Z. Nagy, *Crystal Growth & Design*, 2015, **15**, 4821-4836.

52. K. E. Wittering, L. R. Agnew, A. R. Klapwijk, K. Robertson, A. J. P. Cousen, D. L. Cruickshank and C. C. Wilson, *CrystEngComm*, 2015, **17**, 3610-3618.

53. J. C. Burley, M. J. Duer, R. S. Stein and R. M. Vrcelj, *European Journal of Pharmaceutical Sciences*, 2007, **31**, 271-276.

54. W. Du, Q. Yin, H. Hao, Y. Bao, X. Zhang, J. Huang, X. Li, C. Xie and J. Gong, *Industrial & Engineering Chemistry Research*, 2014, **53**, 5652-5659.

55. G. G. Z. Zhang, R. F. Henry, T. B. Borchardt and X. Lou, *Journal of Pharmaceutical Sciences*, 2007, **96**, 990-995.

56. E. Garcia, C. Hoff and S. Veesler, *Journal of Crystal Growth*, 2002, **237**, 2233-2239.

57. H. G. Brittain, in *Polymorphism in Pharmaceutical Solids*, ed. H. G. Brittain, Informa Healthcare USA, Inc., United States of America, Second edn., 2009, ch. 4, pp. 76-138.

58. S. L. James, C. J. Adams, C. Bolm, D. Braga, P. Collier, T. Friščić, F. Grepioni, K. D. M. Harris, G. Hyett, W. Jones, A. Krebs, J. Mack, L. Maini, A. G. Orpen, I. P. Parkin, W. C. Shearouse, J. W. Steed and D. C. Wadde, *Chemical Society Reviews*, 2012, **41**, 413-447.

59. D. Braga, L. Maini and F. Grepioni, *Chemical Society Reviews*, 2013, **42**, 7638-7648.

60. T. Friščić and W. Jones, *Crystal Growth & Design*, 2009, **9**, 1621-1637.

61. D. Braga, S. L. Giaffreda, F. Grepioni, M. R. Chierotti, R. Gobetto, G. Palladinoa and M. Politoa, *CrystEngComm*, 2007, **9**, 879-881.

62. *The Future of High Value Manufacturing in the UK Pharmaceutical, Biopharmaceutical & Medical Device Sectors, UK, The Technology Strategy Board*, 2012.

63. F. Darvas, V. Hessel and G. Dormán, *Flow chemistry. Volume 1, Fundamentals*, De Gruyter, Berlin, First edn., 2014, ch. 2, pp. 8-58.

64. M. Movsisyan, E. I. P. Delbeke, J. K. E. T. Berton, C. Battilocchio, S. V. Ley, and C. V. Stevens, *Chem. Soc. Rev*, 2016, **45**, 4892-4928.

65. K. Robertson, *Chemistry Central Journal*, 2017, **11**, 1-18.

66. T. Noël, *Topics in Organometallic Chemistry*, Springer International Publishing, Switzerland, 2016.

67. V. Hessel and S. V. Ley, *J. Flow Chem.*, 2016, **6**, 135.

68. M. B. Plutschack, B. Pieber, K. Gilmore and P. H. Seeberger, *Chemical Reviews*, 2017, **117**, 11796-11893.

69. P. Kleinebudde, J. Khinast and J. Rantanen, *Continuous manufacturing of pharmaceuticals*, Hoboken, NJ : John Wiley & Sons Ltd, Hoboken, NJ, 2017.

70. R. E. Hayes, *Introduction to chemical reactor analysis*, Boca Raton, FL : CRC Press, an imprint of Taylor and Francis, Boca Raton, FL, Second edn., 2012.

71. H. A. Santos, D. Liu and H. Zhang, *Microfluidics for Pharmaceutical Applications: From Nano/Micro Systems Fabrication to Controlled Drug Delivery*, Elsevier Science, 2018.

72. K. Robertson, P.-B. Flandrin, A. R. Klapwijk and C. C. Wilson, *Crystal Growth & Design*, 2016, **16**, 4759-4764.

73. J.-i. Yoshida, *Basics of Flow Microreactor Synthesis*, Tokyo : Springer Japan : Imprint: Springer, Tokyo, First edn., 2015.

74. L. Rogers and K. F. Jensen, *Green Chemistry*, 2019, **21**, 3481-3498.

75. W. Clegg, *Crystal Structure Determination*, Oxford University Press Inc., New York, 1st edn., 1998.

76. L. E. Smart, *Solid State Chemistry, 3rd Edition*, London : CRC Press, London, Third edn., 2005.

77. D. E. Sands, *Introduction to Crystallography*, Dover Publications, 1975.

78. G. Stout and L. Jensen, *X-ray Structure Determination: A Practical Guide*, John Wiley & Sons, Canada, Second edn., 1989.

79. G. Burns and M. Glazer, *Space Groups for Solid State Scientists*, Academic Press, China, 2013.

80. W. Clegg and A. J. Blake, R. O Gould and P. Main, *Crystal Structure Analysis: Principles and Practice*, Oxford University Press, Oxford, 2001.

81. C. Hammond, *The Basics of Crystallography and Diffraction*, Oxford University Press, United States, Third edn., 2009.

82. K. I. White, V. Bugris, A. A. McCarthy, R. B. G. Ravelli, K. Csankó, A. Cassetta and S. Brockhauser, *Journal of Applied Crystallography*, 2018, **51**, 1421-1427.

83. S. M. Gruner, M. W. Tate and E. F. Eikenberry, *Review of Scientific Instruments*, 2002, **73**, 2815-2842.

84. C. Broennimann, E. F. Eikenberry, B. Henrich, R. Horisberger, G. Huelsen, E. Pohl, B. Schmitt, C. Schulze-Briese, M. Suzuki, T. Tomizaki, H. Toyokawa and A. Wagner, *Journal of Synchrotron Radiation*, 2006, **13**, 120-130.

85. P. Muller, R. Herbst-Irmer, A. L. Spek, T. R. Schneider and M. R. Sawaya, *Crystal Structure Refinement: A Crystallographer's Guide to SHELXL*, Oxford University Press, Oxford, 2006.

86. P. Willmott, *An Introduction to Synchrotron Radiation: Techniques and Applications*, John Wiley and Sons, Ltd, 2011.

87. C. A. Murray, J. Potter, S. J. Day, A. R. Baker, S. P. Thompson, J. Kelly, C. G. Morris, S. Yang and C. C. Tang, *Journal of Applied Crystallography*, 2017, **50**, 172-183.

88. Diamond Light Source. About Diamond, How Diamond Works: http://www.diamond.ac.uk/Home/About/How-Diamond-Works.html, (accessed 25/11/2016, 2016).

89. S. P. Thompson, J. E. Parker, J. Potter, T. P. Hill, A. Birt, T. M. Cobb, F. Yuan and C. C. Tang, *Review of Scientific Instruments*, 2009, **80**.

90. C. Tang, Welcome to I11, http://www.diamond.ac.uk/Beamlines/Engineering-and-Environment/I11.html, (accessed 02/08/2017).

91. J. Filik, A. W. Ashton, P. C. Y. Chang, P. A. Chater, S. J. Day, M. Drakopoulos, M. W. Gerring, M. L. Hart, O. V. Magdysyuk, S. Michalik, A. Smith, C. C. Tang, N. J. Terrill, M. T. Wharmby and H. Wilhelm, *Journal of Applied Crystallography*, 2017, **50**, 959-966.

92. Rigaku Oxford Diffraction, https://www.rigaku.com/en/rigakuoxford/smc, (accessed 24/10/2019, 2019).

93. Agilent Technologies, https://www.agilent.com/, (accessed 24/10/2019, 2019).

94. CrysAlisPro, http://www.rigaku.com/en/products/smc/crysalis, (accessed 24/10/2019, 2019).

95. Advanced Light Source (ALS), https://als.lbl.gov/, (accessed 22/10/2019, 2019).

96. H. Nowell, S. A. Barnett, K. E. Christensen, S. J. Teat and D. R. Allan, *Journal of Synchrotron Radiation*, 2012, **19**, 435-441.

97. Crystallography, I19, Beamline Layout, https://www.diamond.ac.uk/Instruments/Crystallography/I19/layout.html, (accessed 22/10/2019, 2019).

98. Newport, https://www.newport.com/s/synchrotron-application-solutions, (accessed 24/10/2019, 2019).

99. Dectris, https://www.dectris.com/, (accessed 24/10/2019, 2019).

100. Albula software, https://www.dectris.com/products/albula-software, (accessed 24/10/2019, 2019).

101. DIALS, Diamond Light Source, https://dials.github.io/, (accessed 24/10/2019, 2019).

102. D. G. Waterman, G. Winter, R. J. Gildea, J. M. Parkhurst, A. S. Brewster, N. K. Sauter and G. Evans, *Acta Cryst. D, Structural Biology*, 2016, **72**, 558-575.

103. Beamline 12.2.1, Advanced Light Source, https://als.lbl.gov/beamlines/12-2-1/, (accessed 25/10/2019, 2019).

104. L. J. McCormick, N. Giordano, S. J. Teat and C. M. Beavers, *Crystals*, 2017, **7**.

105. C. N. Banwell, *Fundamentals of molecular spectroscopy*, Maidenhead : McGraw-Hill, Maidenhead, Fourth edn., 1994.

106. M. A. Levenstein, Doctor of Philosophy, University of Leeds, 2019.

107. P.-B. Flandrin, Doctor of Philosophy, University of Bath, 2018.

108. N. Guo, B. Hou, N. Wang, Y. Xiao, J. Huang, Y. Guo, S. Zong and H. Hao, *Journal of Pharmaceutical Sciences*, 2018, **107**, 344-352.

109. T. D. Davis, K. R. Morris, H. Huang, G. E. Peck, J. G. Stowell, B. J. Eisenhauer, J. L. Hilden, D. Gibson and S. R. Byrn, *Pharmaceutical Research*, 2003, **20**, 1851-1857.

110. L. Ouyang, T. Zheng and L. Shen, *CrystEngComm*, 2018, **20**, 2705-2712.

111. K. Užarević, V. Štrukil, C. Mottillo, P. A. Julien, A. Puškarić, T. Friščić and I. Halasz, *Crystal Growth & Design*, 2016, **16**, 2342-2347.

112. T. Friščić, I. Halasz, P. J. Beldon, A. M. Belenguer, F. Adams, S. A. J. Kimber, V. Honkimäki and R. E. Dinnebier, *Nature Chemistry*, 2012, **5**, 66.

113. P. Nørby, M. Roelsgaard, M. Søndergaard and B. B. Iversen, *Crystal Growth & Design*, 2016, **16**, 834-841.

114. P. Nørby, S. Johnsen and B. B. Iversen, *ACS Nano*, 2014, **8**, 4295-4303.

115. B. F. B. Silva, *Physical Chemistry Chemical Physics*, 2017, **19**, 23690-23703.

116. S. L. Childs, P. A. Wood, N. Rodriguez-Hornedo, L. S. Reddy and K. I. Hardcastle, *Crystal Growth and Design*, 2009, **12**, 4211–4224.

117. H. Yang, C. L. Song, Y. X. S. Lim, W. Chen and J. Y. Y. Heng, *CrystEngComm*, 2017, **19**, 6573-6578.

118. F. C. Meldrum and H. Cölfen, *Chemical Reviews*, 2008, **108**, 4332-4432.

119. World Health Organization Model List of Essential Medicines, 21st List, 2019. Geneva: World Health Organization, (accessed 17/09/2019).

120. R. Lunt, Doctor of Philosophy, University of Bath, 2019.

121. M. Gryl, A. Krawczuk-Pantula and K. Stadnicka, *Acta Crystallographica Section B-Structural Science Crystal Engineering and Materials*, 2011, **67**, 144-154.

122. M. Gryl, A. Krawczuk and K. Stadnicka, *Acta Crystallographica Section B*, 2008, **64**, 623-632.

123. M. A. Levenstein, C. Anduix-Canto, Y. Y. Kim, M. A. Holden, C. González Niño, D. C. Green, S. E. Foster, A. N. Kulak, L. Govada, N. E. Chayen, S. J. Day, C. C. Tang, B. Weinhausen, M. Burghammer, N. Kapur and F. C. Meldrum, *Advanced Functional Materials*, 2019, **29**.

124. L. Mazutis, J. Gilbert, W. L. Ung, D. A. Weitz, A. D. Griffiths and J. A. Heyman, *Nature Protocols*, 2013, **8**, 870.

125. H. N. Chapman, P. Fromme, A. Barty, T. A. White, R. A. Kirian, A. Aquila, M. S. Hunter, J. Schulz, D. P. DePonte, U. Weierstall, R. B. Doak, F. R. Maia, A. V. Martin, I. Schlichting, L. Lomb, N. Coppola, R. L. Shoeman, S. W. Epp, R. Hartmann, D. Rolles, A. Rudenko, L. Foucar, N. Kimmel, G. Weidenspointner, P. Holl, M. Liang, M. Barthelmess, C. Caleman, S. Boutet, M. J. Bogan, J. Krzywinski, C. Bostedt, S. Bajt, L. Gumprecht, B. Rudek, B. Erk, C. Schmidt, A. Homke, C. Reich, D. Pietschner, L. Struder, G. Hauser, H. Gorke, J. Ullrich, S. Herrmann, G. Schaller, F. Schopper, H. Soltau, K. U. Kuhnel, M. Messerschmidt, J. D. Bozek, S. P. Hau-Riege, M. Frank, C. Y. Hampton, R. G. Sierra, D. Starodub, G. J. Williams, J. Hajdu, N. Timneanu, M. M. Seibert, J. Andreasson, A. Rocker, O. Jonsson, M. Svenda, S. Stern, K. Nass, R. Andritschke, C. D. Schroter, F. Krasniqi, M. Bott, K. E. Schmidt, X. Wang, I. Grotjohann, J. M. Holton, T. R. Barends, R. Neutze, S. Marchesini, R. Fromme, S. Schorb, D. Rupp, M. Adolph, T. Gorkhover, I. Andersson, H. Hirsemann, G. Potdevin, H. Graafsma, B. Nilsson and J. C. Spence, *Nature*, 2011, **470**, 73-77.

126. A. Johnston, B. F. Johnston, A. R. Kennedy and A. J. Florence, *CrystEngComm*, 2008, **10**, 1.

127. W. W. L. Young and R. Suryanarayanan, *Journal of Pharmaceutical Sciences*, 1991, **80**, 496-500.

128. A. L. Grzesiak, M. Lang, K. Kim and A. J. Matzger, *Journal of pharmaceutical sciences.*, 2003, **92**, 2260-2271.

129. Z. Li and A. J. Matzger, *Molecular pharmaceutics*, 2016, **13**, 990.

130. W. Liu, H. Wei, J. Zhao, S. Black and C. Sun, *Organic Process Research & Development*, 2013, **17**, 1406-1412.

131. A. Getsoian, R. M. Lodaya and A. C. Blackburn, *International Journal on Pharmaceutics*, 2008, **348**, 3-9.

132. R. A. Halliwell, R. M. Bhardwaj, C. J. Brown, N. E. B. Briggs, J. Dunn, J. Robertson, A. Nordon and A. J. Florence, *Journal of Pharmaceutical Sciences*, 2017, **106**, 1874-1880.

133. J.-B. Arlin, L. S. Price, S. L. Price and A. J. Florence, *Chemical Communications*, 2011, **47**, 7074-7076.

134. Y. Zhao, Y. Bao, J. Wang and S. Rohani, *Pharmaceutics*, 2012, **4**, 164-178.

135. Y. Zhao, J. Yuan, Z. Ji, J. Wang and S. Rohani, *Industrial & Engineering Chemistry Research*, 2012, **51**.

136. F. L. Muller, M. Fielding and S. Black, *Organic Process Research & Development*, 2009, **13**, 1315-1321.

137. N. E. B. Briggs, Doctor of Philosophy, University of Strathclyde, 2015.

138. W. Liu, L. Dang, S. Black and H. Wei, *Journal of Chemical & Engineering Data*, 2008, **53**, 2204-2206.

139. K. Robertson, P.-B. Flandrin, H. J. Shepherd and C. C. Wilson, *Chimica Oggi, Chemistry Today*, 2017, **35**, 19-22.

140. P. P. Nievergelt and B. Spingler, *CrystEngComm*, 2017, **19**, 142-147.

141. R. Nair, S. Gonen and S. W. Hoag, *International Journal of Pharmaceutics*, 2002, **240**, 11-22.

142. M. L. Grünbein and G. Nass Kovacs, *Acta crystallographica. Section D, Structural biology*, 2019, **75**, 178-191.

143. C. J. J. Gerard, G. Ferry, L. M. Vuillard, J. A. Boutin, L. M. G. Chavas, T. Huet, N. Ferte, R. Grossier, N. Candoni and S. Veesler, *Acta crystallographica. Section F, Structural biology communications*, 2017, **73**, 574-578.

144. A. Ghazal, J. P. Lafleur, K. Mortensen, J. P. Kutter, L. Arleth and G. V. Jensen, *Lab on a Chip*, 2016, **16**, 4263-4295.

145. D. S. Khvostichenko, E. Kondrashkina, S. L. Perry, A. S. Pawate, K. Brister and P. J. A. Kenis, *Analyst*, 2013, **138**, 5384-5395.

146. T. Beuvier, E. A. C. Panduro, P. Kwaśniewski, S. Marre, C. Lecoutre, Y. Garrabos, C. Aymonier, B. Calvignac and A. Gibaud, *Lab on a Chip*, 2015, **15**, 2002-2008.

147. R. Stehle, G. Goerigk, D. Wallacher, M. Ballauff and S. Seiffert, *Lab on a Chip*, 2013, **13**, 1529-1537.

148. O. Saldanha, R. Graceffa, C. Y. J. Hemonnot, C. Ranke, G. Brehm, M. Liebi, B. Marmiroli, B. Weinhausen, M. Burghammer and S. Koster, *ChemPhysChem*, 2017, **18**, 1220-1223.

149. N. Pham, D. Radajewski, A. Round, M. Brennich, P. Pernot, B. Biscans, F. Bonneté and S. Teychené, *Analytical Chemistry*, 2017, **89**, 2282-2287.

150. R. J. Gildea, D. G. Waterman, J. M. Parkhurst, D. Axford, G. Sutton, D. I. Stuart, N. K. Sauter, G. Evans and G. Winter, *Acta crystallographica. Section D, Biological crystallography*, 2014, **70**, 2652-2666.

151. L. R. Agnew, D. L. Cruickshank, T. McGlone and C. C. Wilson, *Chem. Commun.*, 2016, **52**, 7368-7371.

152. L. R. Agnew, Doctor of Philosophy, University of Bath, 2017.

153. E. Joiris, P. D. Martino, C. Berneron, A.-M. Guyot-Hermann and J.-C. Guyot, *Pharmaceutical Research*, 1998, **15**, 1122-1130.

154. I.-C. Wang, M.-J. Lee, D.-Y. Seo, H.-E. Lee, Y. Choi, W.-S. Kim, C.-S. Kim, M.-Y. Jeong and G. J. Choi, *AAPS PharmSciTech*, 2011, **12**, 764-770.

155. G. Nichols and C. S. Frampton, *Journal of Pharmaceutical Sciences*, 1998, **87**, 684-693.

156. M.-A. Perrin, M. A. Neumann, H. Elmaleh and L. Zaske, *Chemical Communications*, 2009, 3181-3183.

157. J. M. Fachaux, A. M. Guyot Hermann, J. C. Guyot, P. Conflant, M. Drache, J. P. Huvenne and R. Bouche, *International Journal of Pharmaceutics*, 1993, **99**, 99-107.

158. G. Winter, D. G. Waterman, J. M. Parkhurst, A. S. Brewster, R. J. Gildea, M. Gerstel, L. Fuentes-Montero, M. Vollmar, T. Michels-Clark, I. D. Young, N. K. Sauter and G. Evans, *Acta crystallographica. Section D, Structural biology*, 2018, **74**, 85-97.

159. G. Winter, *Journal of Applied Crystallography*, 2010, **43**, 186-190.

160. X. Y. Lawrence, G. L. Amidon, J. E. Polli, H. Zhao, M. U. Mehta, D. P. Conner, V. P. Shah, L. J. Lesko, M.-L. Chen, V. H. L. Lee and A. S. Hussain, *Pharmaceutical research*, 2002, **19**, 921-925.

161. A. V. Trask, W. D. S. Motherwell and W. Jones, *Crystal Growth & Design*, 2005, **5**, 1013-1021.

162. N. J. Babu, P. Sanphui and A. Ashwini Nangia, 2012, **7**, 2274-2285.

163. D. Li, M. Han, P. Balakrishnan, Y. Yan, D. Oh, J. Joe, Y. Seo, J. Kim, S. Park, C. Yong and H.-G. Choi, *Archives of Pharmacal Research*, 2010, **33**, 95-101.

164. M. Tirunagari, N. Mehveen, M. F. Qureshi, J. Sultana and V. Tirunagari, *International Journal of Pharmacy and Pharmaceutical Sciences*, 2012, **4**, 97-100.

165. J. Nerurkar, J. W. Beach, M. O. Park and H. W. Jun, *Pharmaceutical Development and Technology*, 2005, **10**, 413-421.

166. S. Aitipamula, A. B. H. Wong, P. S. Chow and R. B. H. Tan, *RSC Advances*, 2016, **6**, 34110-34119.

167. R. Rachmaniar, D. Tristiyanti, S. Hamdani and Afifah, *AIP Conference Proceedings*, 2018, **1927**.

168. P. Derollez, E. Dudognon, F. Affouard, F. Danède, N. T. Correia and M. Descamps, *Acta Crystallographica Section B*, 2010, **66**, 76-80.

169. A. Karagianni, M. Malamatari and K. Kachrimanis, *Pharmaceutics*, 2018, **10**, 1-30.

170. D. Walsh, D. R. Serrano, Z. A. Worku, A. M. Madi, P. O'Connell, B. Twamley and A. M. Healy, *International Journal of Pharmaceutics*, 2018, **551**, 241-256.

171. L. Greenspan, *Journal of Research of the National Bureau of Standards - A. Physics and Chemistry*, 1977, **81A**, 89-96.

172. E. Deneau and G. Steele, *Organic Process Research & Development*, 2005, **9**, 943-950.

173. J. Lu, Y.-P. Li, J. Wang, Z. Li, S. Rohani and C.-B. Ching, *Organic Process Research & Development*, 2012, **16**, 442-446.

174. M. Jiang and R. D. Braatz, *CrystEngComm*, 2019, **21**, 3534-3551.

175. I. Majerz and I. Olovsson, *Acta Chim. Slov.*, 2011, **58**, 379-384.

176. A. O. F. Jones, M.-H. Lemée-Cailleau, D. M. S. Martins, G. J. McIntyre, I. D. H. Oswald, C. R. Pulham, C. K. Spanswick, L. H. Thomas and C. C. Wilson, *Physical Chemistry Chemical Physics*, 2012, **14**, 13273-13283.

177. C. L. Jones, J. M. Skelton, S. C. Parker, P. R. Raithby, A. Walsh, C. C. Wilson and L. H. Thomas, *CrystEngComm*, 2019, **21**, 1626-1634.

178. D. J. Berry, C. C. Seaton, W. Clegg, R. W. Harrington, S. J. Coles, P. N. Horton, M. B. Hursthouse, R. Storey, W. Jones, T. Friščić and N. Blagden, *Crystal Growth & Design*, 2008, **8**, 1697-1712.

179. M. A. O'Mahony, C. C. Seaton, D. M. Croker, S. Veesler, Å. C. Rasmuson and B. K. Hodnett, *Crystal Growth and Design*, 2013, **13**, 1861-1871.

180. C. J. Brown and X.-W. Ni, *CrystEngComm*, 2012, **14**, 2944-2949.

181. X. Ni and A. Liao, *Crystal Growth & Design*, 2008, **8**, 2875-2881.

182. X. Ni and A. Liao, *Chemical Engineering Journal*, 2010, **156**, 226-233.

183. P. Barrett and B. Glennon, *Chemical Engineering Research and Design*, 2002, **80**, 799-805.

Chapter 10 – Appendix

Chapter 4 Appendix (A4)

4.1 Seeding Inlet Development – UV-vis Data for PP T-piece Configuration

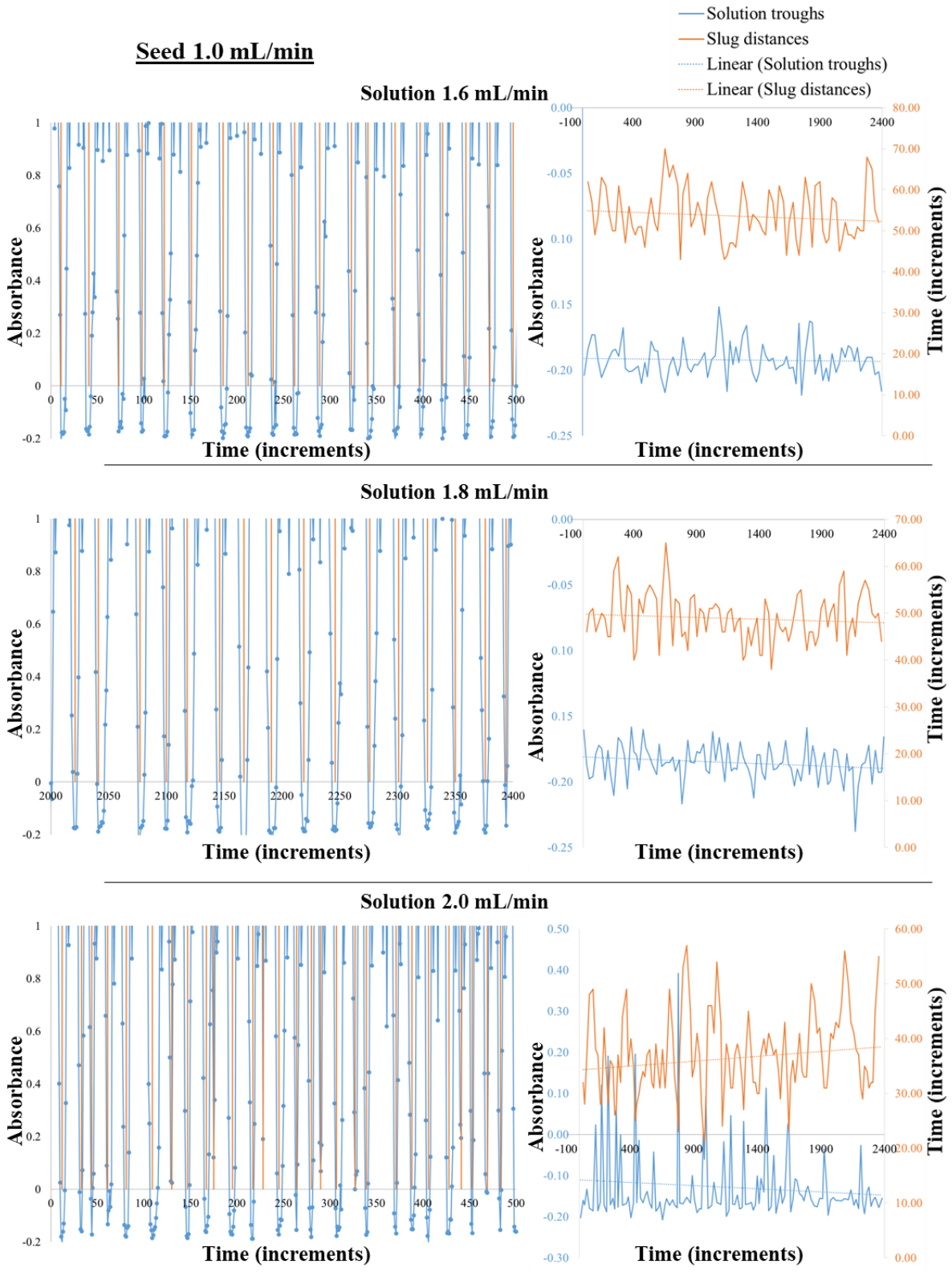

Figure A4.1 – 870 nm peak absorbance *versus* time (5 ms increments) for 1 mL/min seed flow rate, with 1.6, 1.8 or 2.0 mL/min solution flow rate, with a PP T-piece (used for optimal seeding configuration). N.B. orange vertical bars show location of detected local minima (left) and the corresponding slug analysis chart for each flow rate combination featuring solution troughs (blue) and slug distances (orange) (right).

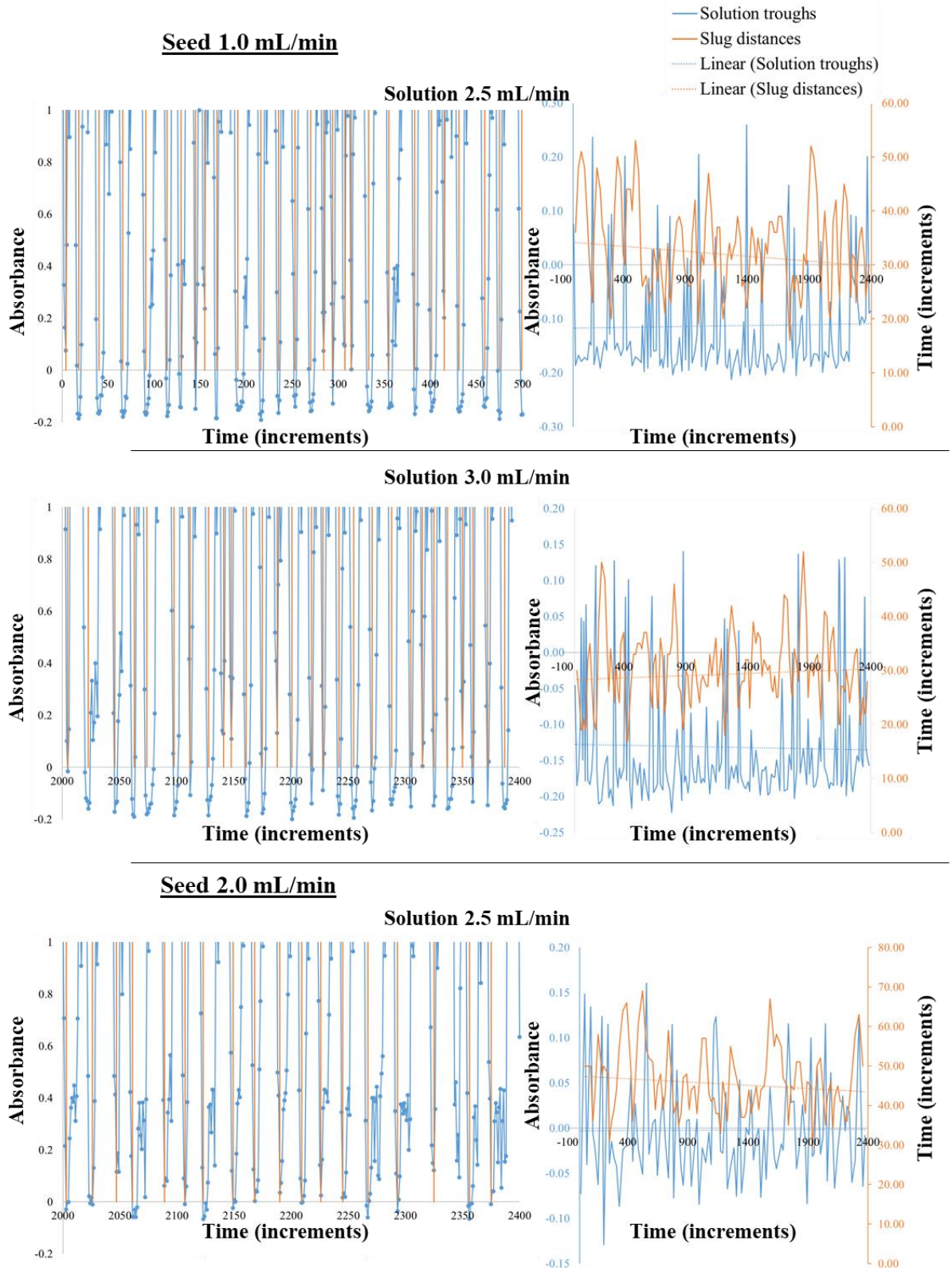

Figure A4.2 – 870 nm peak absorbance *versus* time (5 ms increments) for 1 mL/min seed flow rate, with 2.5 or 3.0 mL/min solution flow rate, or 2.0 mL/min seed flow rate and 2.5 mL/min solution flow rate, with a PP T-piece (used for optimal seeding configuration). N.B. orange vertical bars show location of detected local minima (left) and the corresponding slug analysis chart for each flow rate combination featuring solution troughs (blue) and slug distances (orange) (right).

4.2 Seeding Inlet Development – UV-vis Data for Glass T-piece Configuration

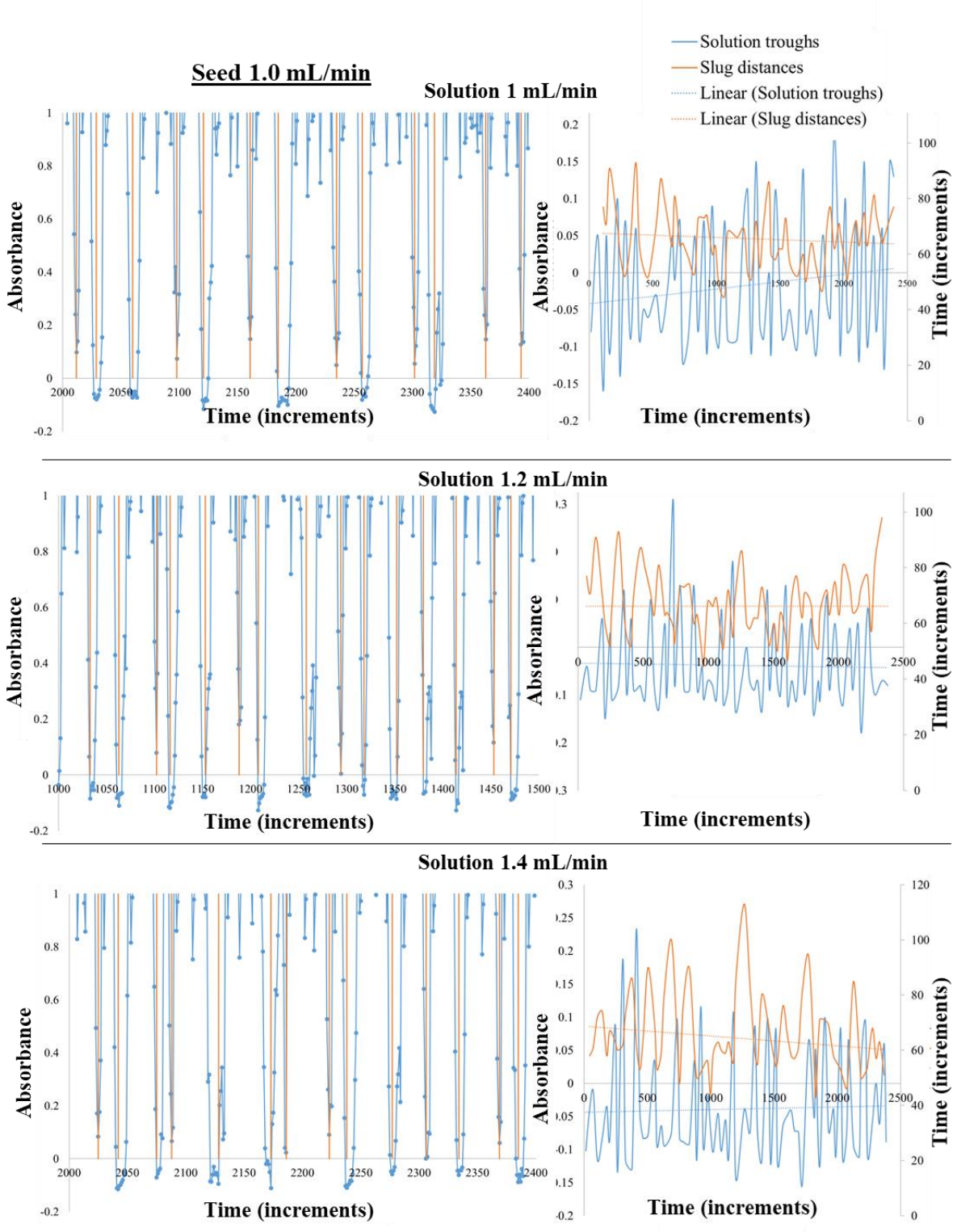

Figure A4.3 – 870 nm peak absorbance *versus* time (5 ms increments) for 1 mL/min seed flow rate, with 1.0, 1.2 or 1.4 mL/min solution flow rate, with a glass T-piece (used for optimal seeding configuration). N.B. orange vertical bars show location of detected local minima (left) and the corresponding slug analysis chart for each flow rate combination featuring solution troughs (blue) and slug distances (orange) (right).

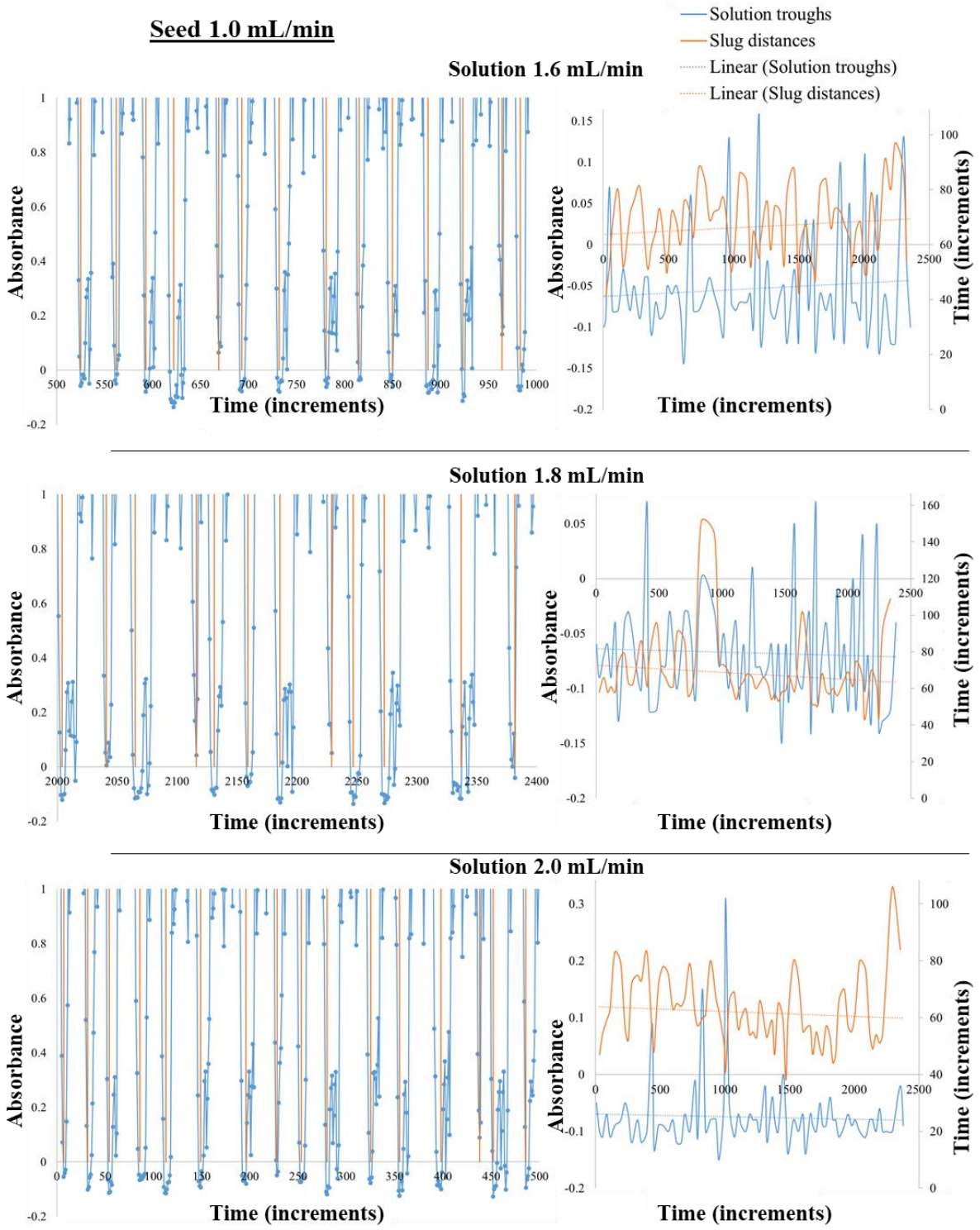

Figure A4.4 – 870 nm peak absorbance *versus* time (5 ms increments) for 1 mL/min seed flow rate, with 1.6, 1.8 or 2.0 mL/min solution flow rate, with a glass T-piece (used for optimal seeding configuration). N.B. orange vertical bars show location of detected local minima (left) and the corresponding slug analysis chart for each flow rate combination featuring solution troughs (blue) and slug distances (orange) (right).

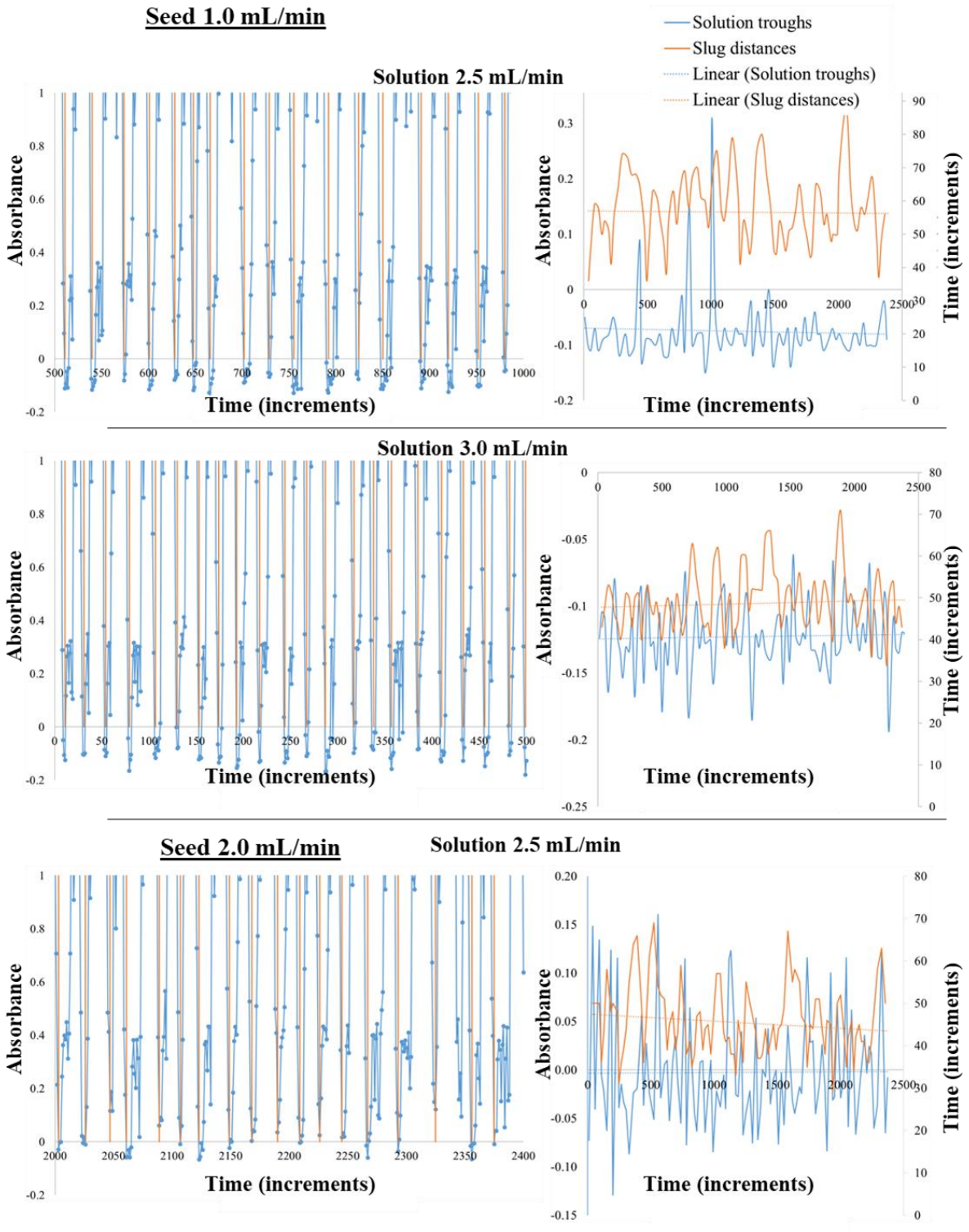

Figure A4.5 – 870 nm peak absorbance *versus* time (5 ms increments) for 1 mL/min seed flow rate, with 2.5 or 3.0 mL/min solution flow rate, or 2.0 mL/min seed flow rate and 2.5 mL/min solution flow rate, with a glass T-piece (used for optimal seeding configuration). N.B. orange vertical bars show location of detected local minima (left) and the corresponding slug analysis chart for each flow rate combination featuring solution troughs (blue) and slug distances (orange) (right).

Table A4.1 – Images of segmentation corresponding with a range of flow rate combinations for the solution feed and seed addition using a glass T-piece.

Segmentation Image Number	Flow rate of solution feed mL/min	Flow rate of seed mL/min
1	1.0	1.0
2	1.2	
3	1.4	
4	1.6	
5	1.8	
6	2.0	
7	2.5	
8	3.0	
9	2.0	2.0

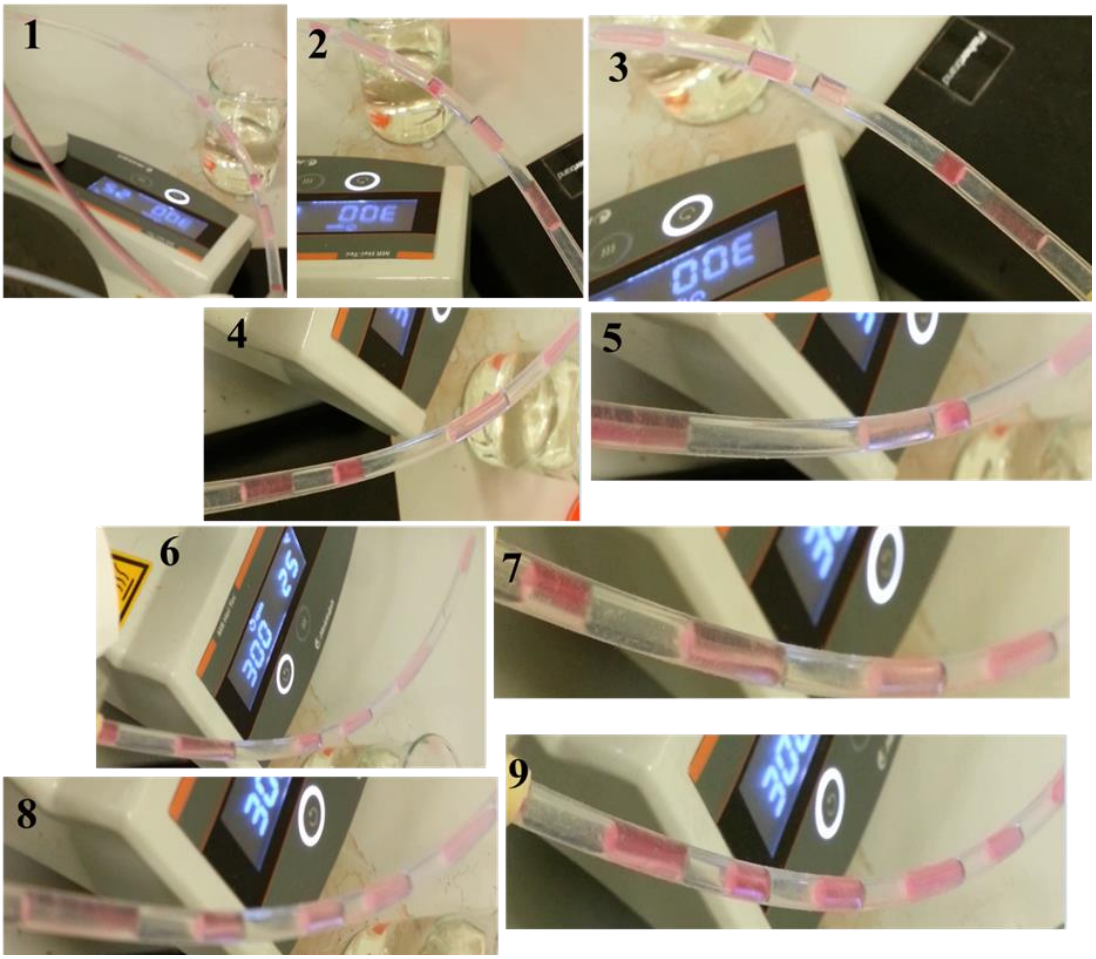

Figure A4.6 – Images of segmentation corresponding with a range of flow rate combinations for the solution feed and seed addition using a glass T-piece.

4.3 Seeding Inlet Development – UV-vis Data for PP Y-piece Configuration

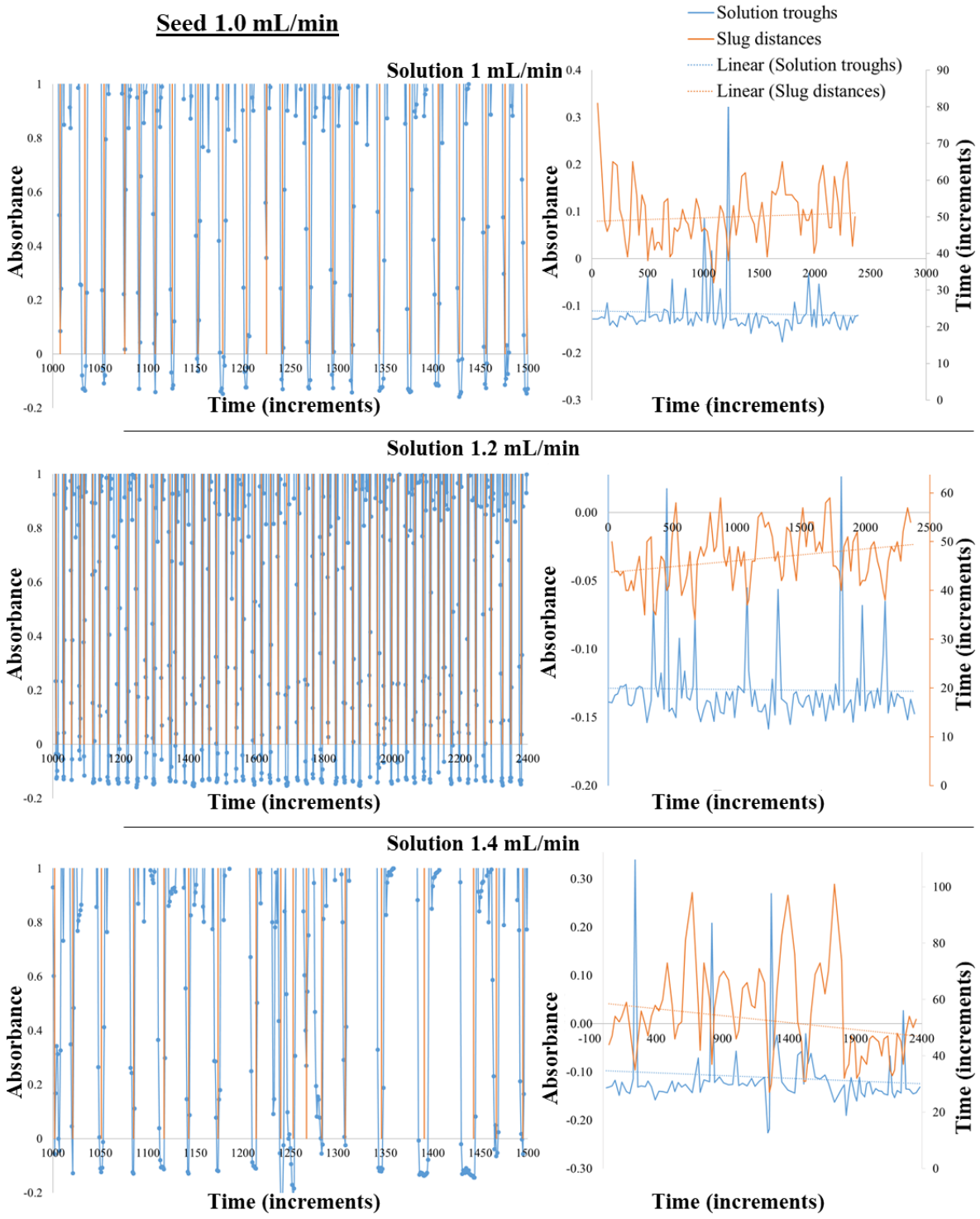

Figure A4.7 – 870 nm peak absorbance *versus* time (5 ms increments) for 1 mL/min seed flow rate, with 1.0, 1.2 or 1.4 mL/min solution flow rate, with a PP Y-piece (used for optimal seeding configuration). N.B. orange vertical bars show location of detected local minima (left) and the corresponding slug analysis chart for each flow rate combination featuring solution troughs (blue) and slug distances (orange) (right).

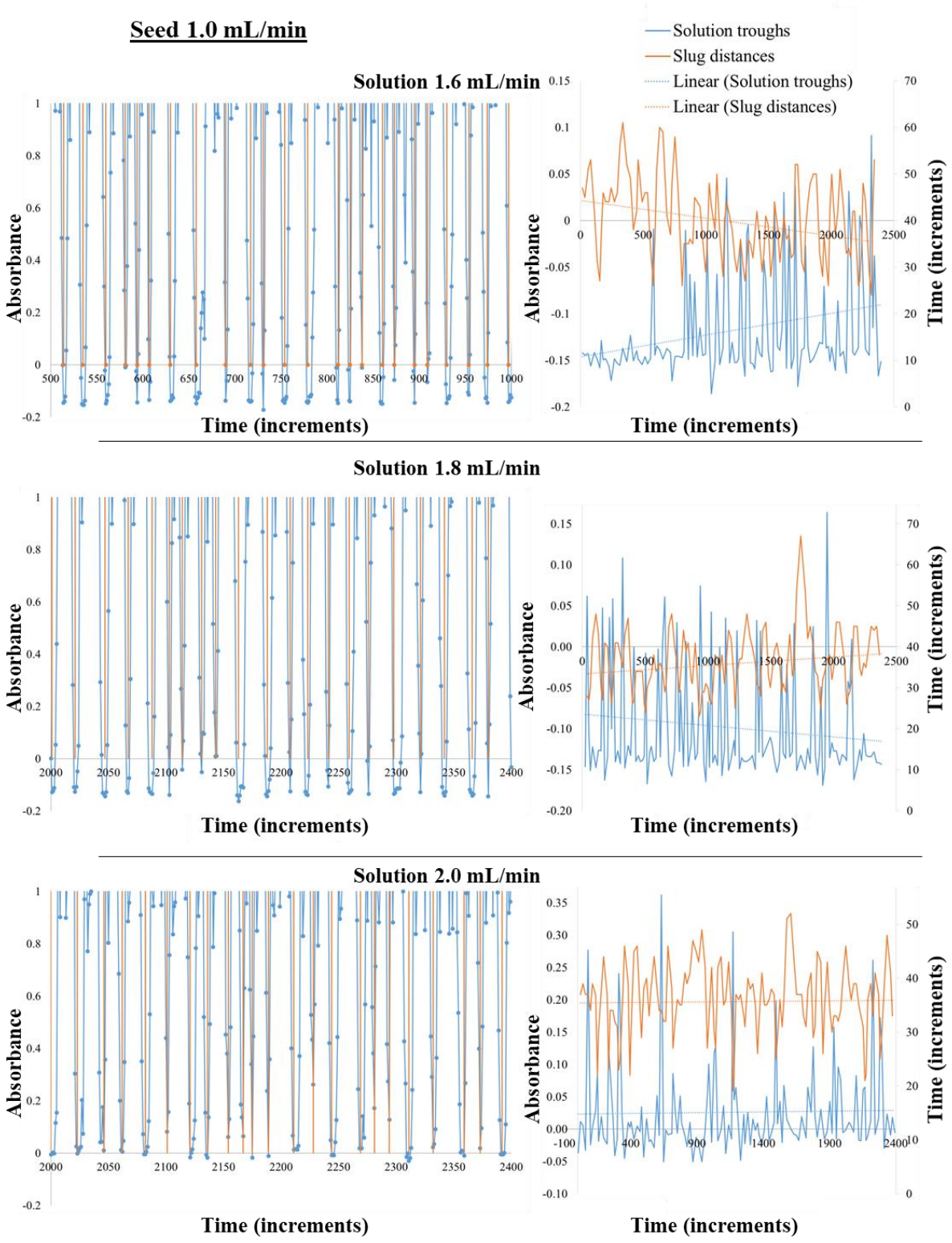

Figure A4.8 – 870 nm peak absorbance *versus* time (5 ms increments) for 1 mL/min seed flow rate, with 1.6, 1.8 or 2.0 mL/min solution flow rate, with a PP Y-piece (used for optimal seeding configuration). N.B. orange vertical bars show location of detected local minima (left) and the corresponding slug analysis chart for each flow rate combination featuring solution troughs (blue) and slug distances (orange) (right).

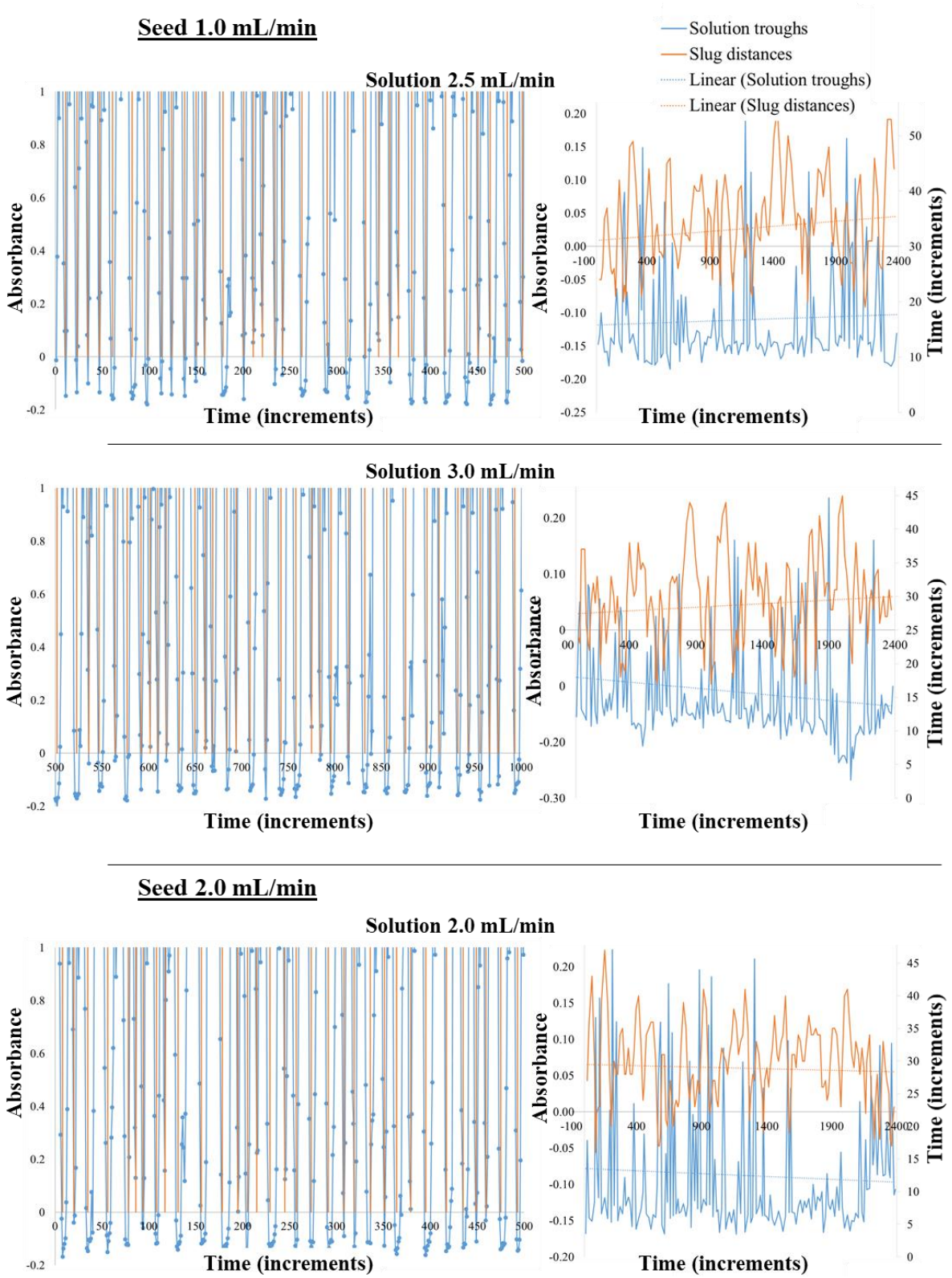

Figure A4.9 – 870 nm peak absorbance *versus* time (5 ms increments) for 1 mL/min seed flow rate, with 2.5 or 3.0 mL/min solution flow rate, or 2.0 mL/min seed flow rate and 2.5 mL/min solution flow rate, with a PP Y-piece (used for optimal seeding configuration). N.B. orange vertical bars show location of detected local minima (left) and the corresponding slug analysis chart for each flow rate combination featuring solution troughs (blue) and slug distances (orange) (right).

Table A4.2 – Images of segmentation corresponding with a range of flow rate combinations for the solution feed and seed addition using a PP Y-piece.

Segmentation Image Number	Flow rate of solution feed mL/min	Flow rate of seed mL/min
1	1.0	1.0
2	1.2	
3	1.4	
4	1.6	
5	1.8	
6	2.0	
7	2.5	
8	3.0	

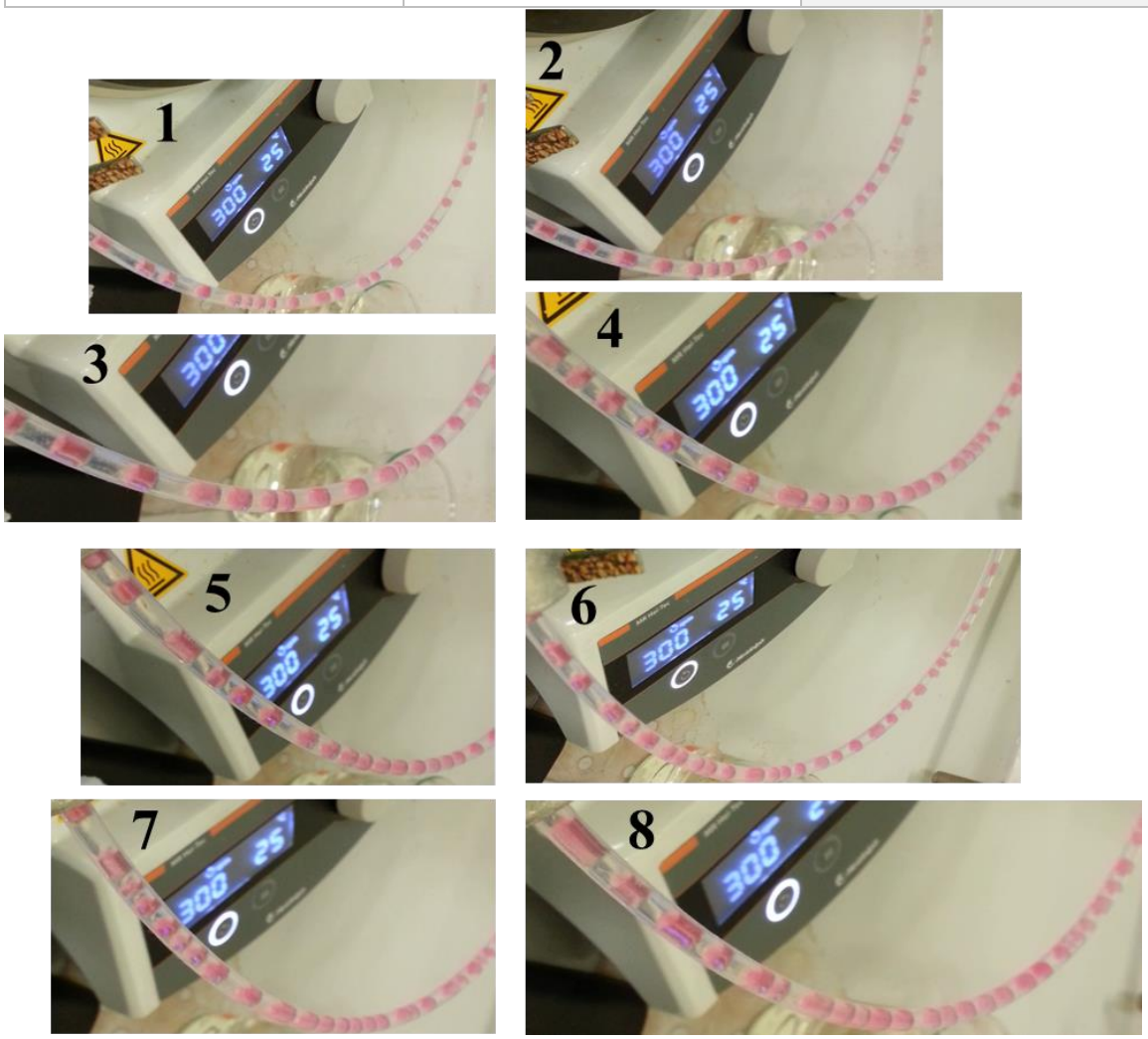

Figure A4.10 – Images of segmentation corresponding with a range of flow rate combinations for the solution feed and seed addition using a PP Y-piece.

4.4 Absorbance data for each seed inlet geometry and flow rate ratio

Table A4.3 –Absorbance data for PP Y-piece.

PP Y-piece									
seed slurry (mL/min)	1	1	1	1	1	1	1	1	2
solution (mL/min)	1	1.2	1.4	1.6	1.8	2	2.5	3	2
min abs	0.355	0.026	0.339	0.045	0.108	0.362	0.190	0.160	0.224
max abs	-0.176	-0.159	-0.226	-0.186	-0.167	-0.050	-0.185	-0.207	-0.169
av abs	-0.116	-0.130	-0.113	-0.117	-0.099	0.026	-0.111	-0.110	-0.088
std dev	0.060	0.030	0.080	0.054	0.070	0.074	0.074	0.081	0.106
max dist (s)	2.204	1.656	2.653	1.650	1.745	1.501	1.502	1.341	1.247
min dist	0.742	0.600	0.641	0.497	0.450	0.396	0.399	0.397	0.344
av dist	1.253	1.166	1.284	0.992	0.892	0.891	0.830	0.717	0.722
std dev	0.278	0.215	0.430	0.282	0.229	0.238	0.246	0.209	0.191

Table A4.4 –Absorbance data for PP T-piece.

PP T-piece									
seed slurry (mL/min)	1	1	1	1	1	1	1	1	2
solution (mL/min)	1	1.2	1.4	1.6	1.8	2	2.5	3	2
min abs	-0.107	-0.157	-0.157	-0.152	-0.158	0.392	0.259	0.140	0.372
max abs	-0.216	-0.219	-0.217	-0.219	-0.238	-0.208	-0.213	-0.222	-0.179
av abs	-0.180	-0.189	-0.190	-0.192	-0.185	-0.128	-0.113	-0.131	-0.106
std dev	0.015	0.013	0.012	0.013	0.013	0.104	0.108	0.091	0.095
max dist (s)	2.097	2.154	2.150	2.007	1.793	1.607	1.446	1.348	1.247
min dist	0.650	0.903	1.000	0.900	0.849	0.393	0.340	0.345	0.358
av dist	1.455	1.487	1.420	1.339	1.220	0.911	0.797	0.732	0.795
std dev	0.248	0.249	0.205	0.229	0.199	0.242	0.236	0.206	0.189

Table A4.5 –Absorbance data for Glass T-piece

Glass T-piece									
seed slurry (mL/min)	1	1	1	1	1	1	1	1	2
solution (mL/min)	1	1.2	1.4	1.6	1.8	2	2.5	3	2
min abs	0.189	0.312	0.233	0.156	0.075	0.309	-0.009	-0.061	0.161

max abs	-0.160	-0.176	-0.152	-0.137	-0.148	-0.145	-0.149	-0.194	-0.129
av abs	-0.018	-0.037	-0.039	-0.053	-0.067	-0.075	-0.098	-0.123	-0.002
std dev	0.089	0.094	0.084	0.067	0.050	0.061	0.033	0.026	0.060
max dist (s)	3.702	2.698	3.348	3.092	5.303	3.057	2.694	1.992	1.999
min dist	0.655	0.596	0.608	0.600	0.705	0.649	0.645	0.755	0.602
av dist	1.749	1.663	1.602	1.654	1.699	1.540	1.413	1.214	1.137
std dev	0.611	0.555	0.554	0.550	0.667	0.440	0.375	0.239	0.321

4.5 CBZ Seed Generation and Stability Testing

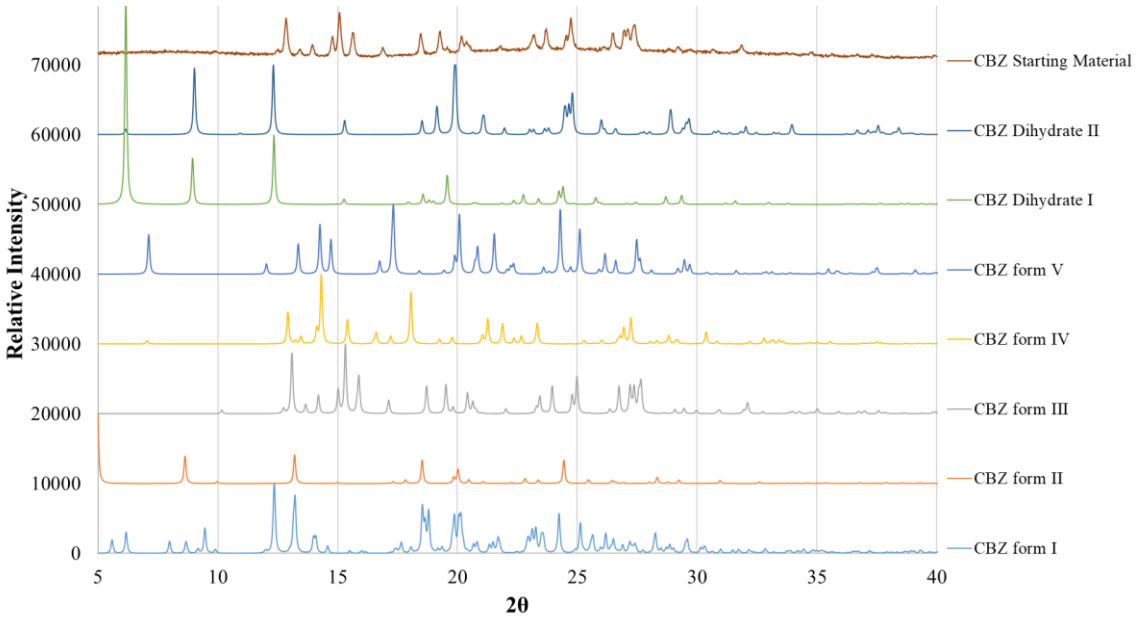

Figure A4.11 – PXRD pattern of CBZ starting material compared to the pure polymorphs both anhydrous and CBZ DH forms simulated in Mercury.

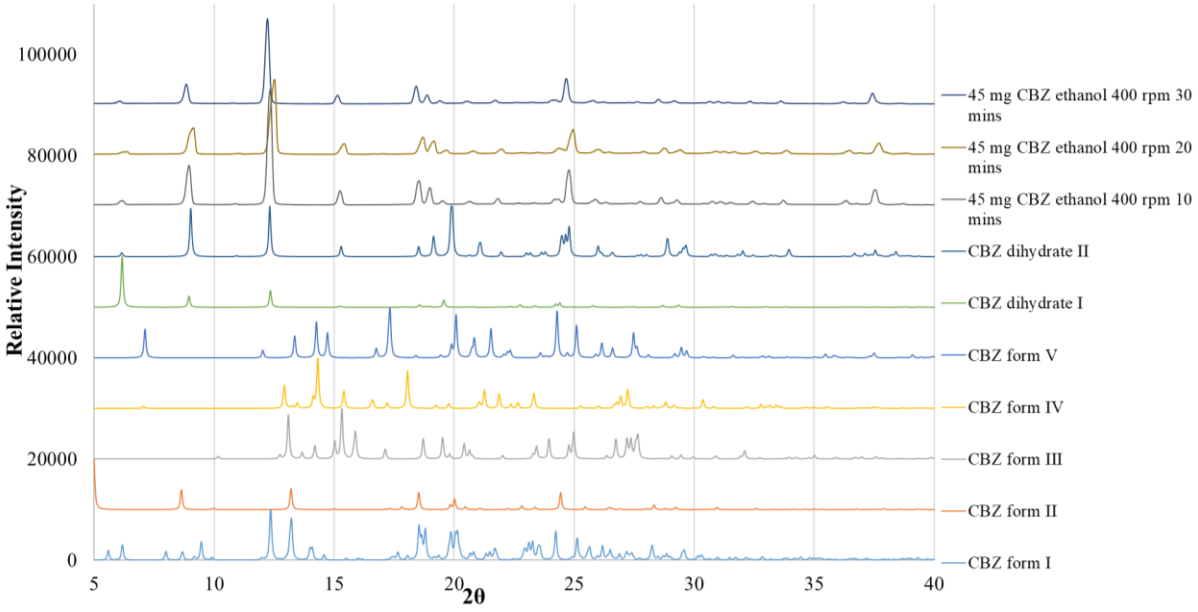

Figure A4.12 – PXRD patterns of 45 mg/mL CBZ in EtOH at 400 rpm for various slurrying times at 20 ℃.

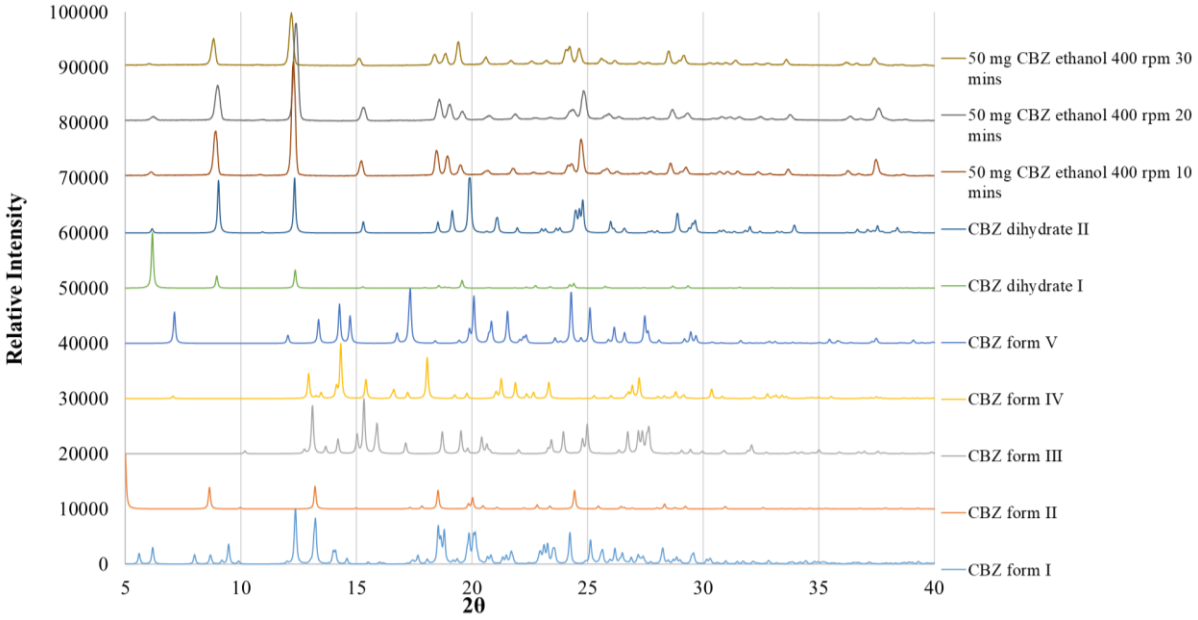

Figure A4.13 – PXRD patterns of 50 mg/mL CBZ in EtOH at 400 rpm for various slurrying times at 20 ℃.

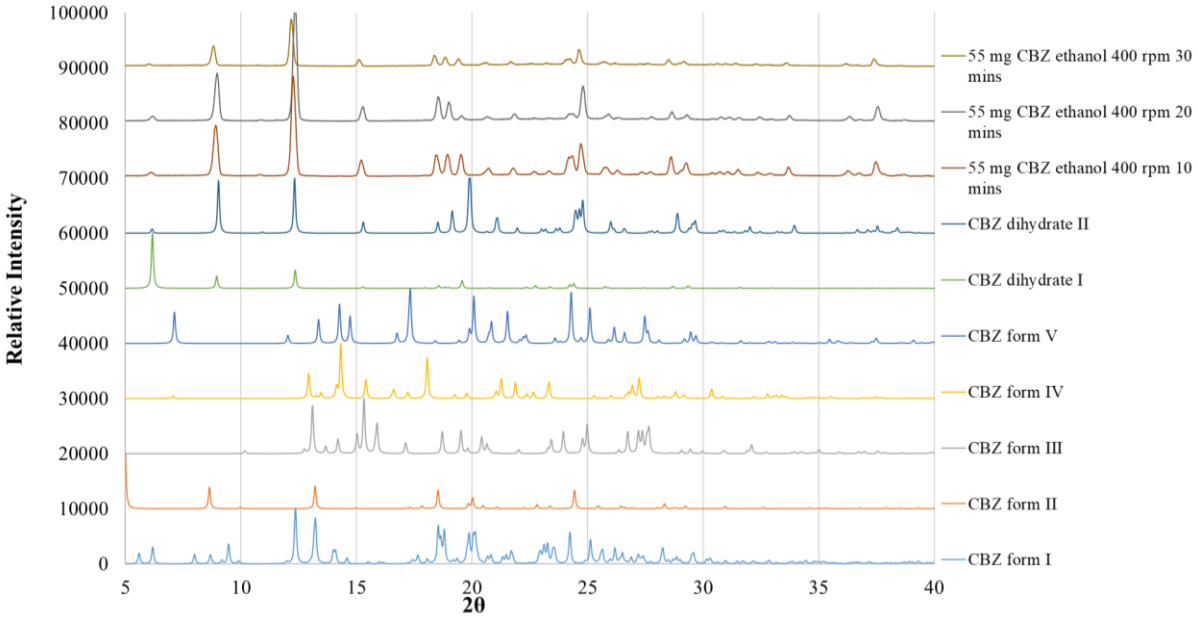

Figure A4.14 – PXRD patterns of 55 mg/mL CBZ in EtOH at 400 rpm for various slurrying times at 20 ℃.

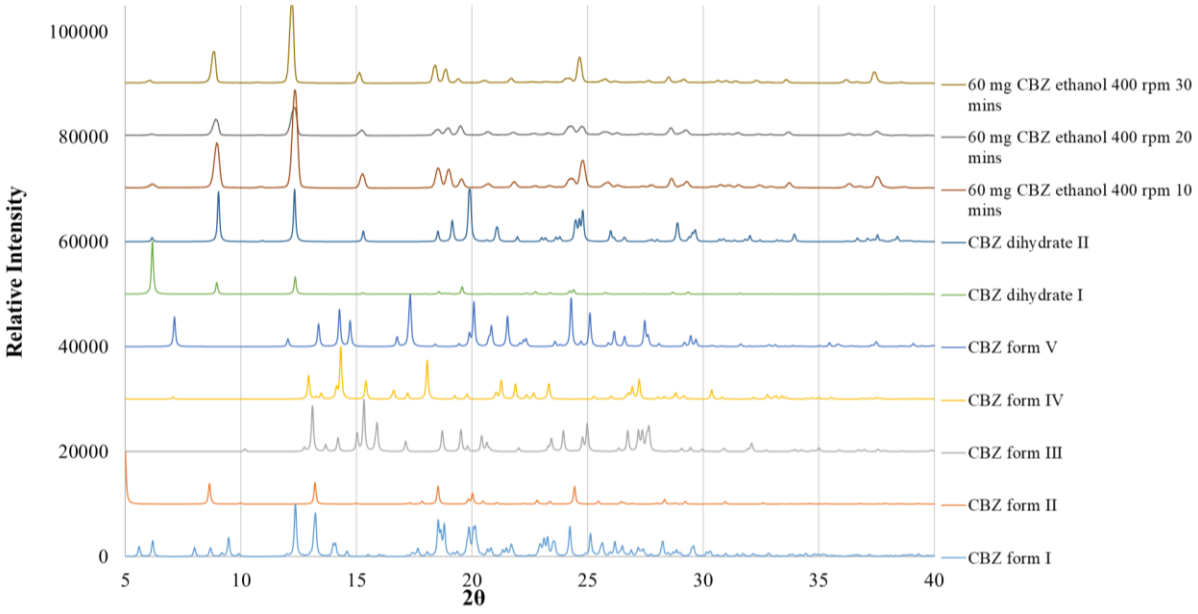

Figure A4.15 – PXRD patterns of 60 mg/mL CBZ in EtOH at 400 rpm for various slurrying times at 20 ℃.

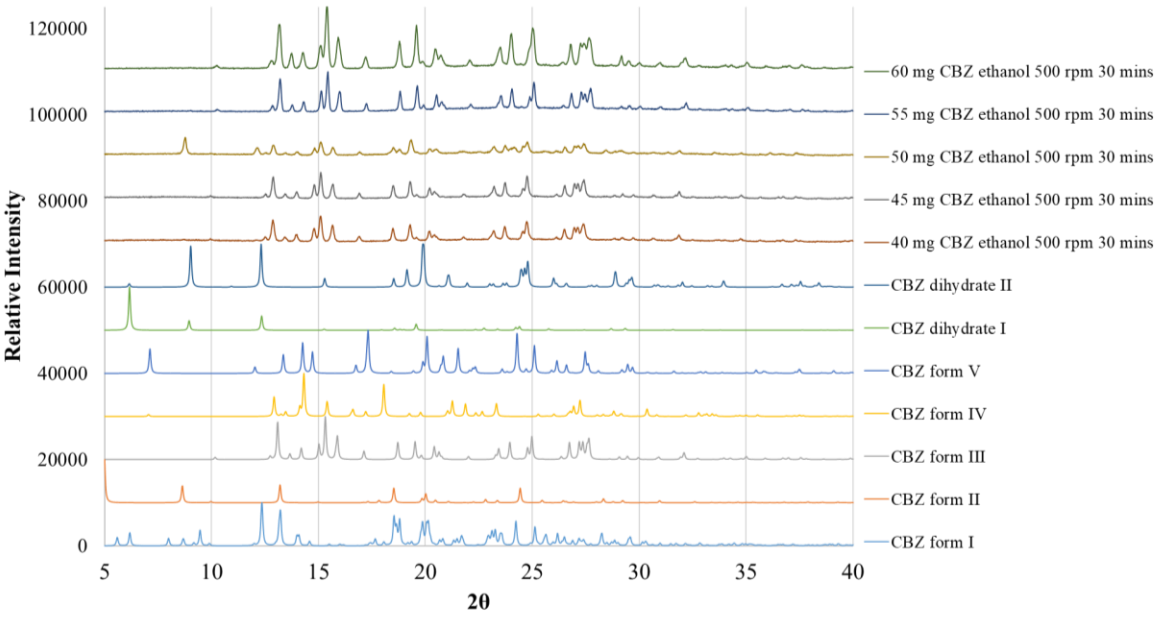

Figure A4.16 – PXRD patterns of varying concentrations of CBZ in EtOH at 500 rpm for 30 minutes slurrying time at 20 ℃.

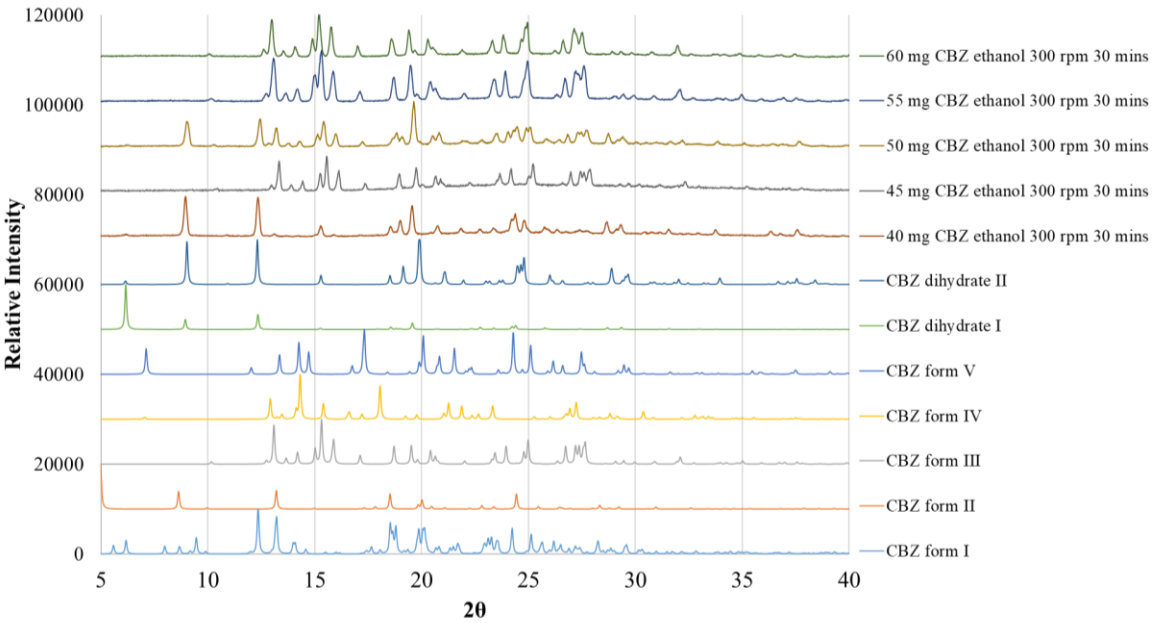

Figure A4.17 – PXRD patterns of varying concentrations of CBZ in EtOH at 300 rpm for 30 minutes slurrying time at 20 ℃.

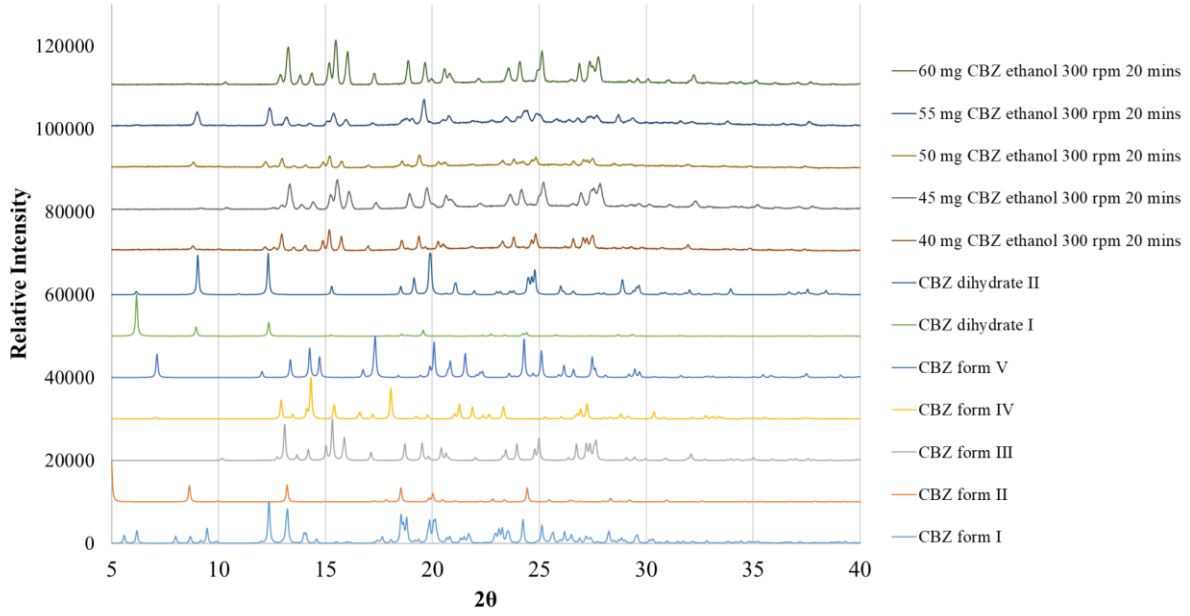

Figure A4.18 – PXRD patterns of varying concentrations of CBZ in EtOH at 300 rpm for 20 minutes slurrying time at 20 ℃.

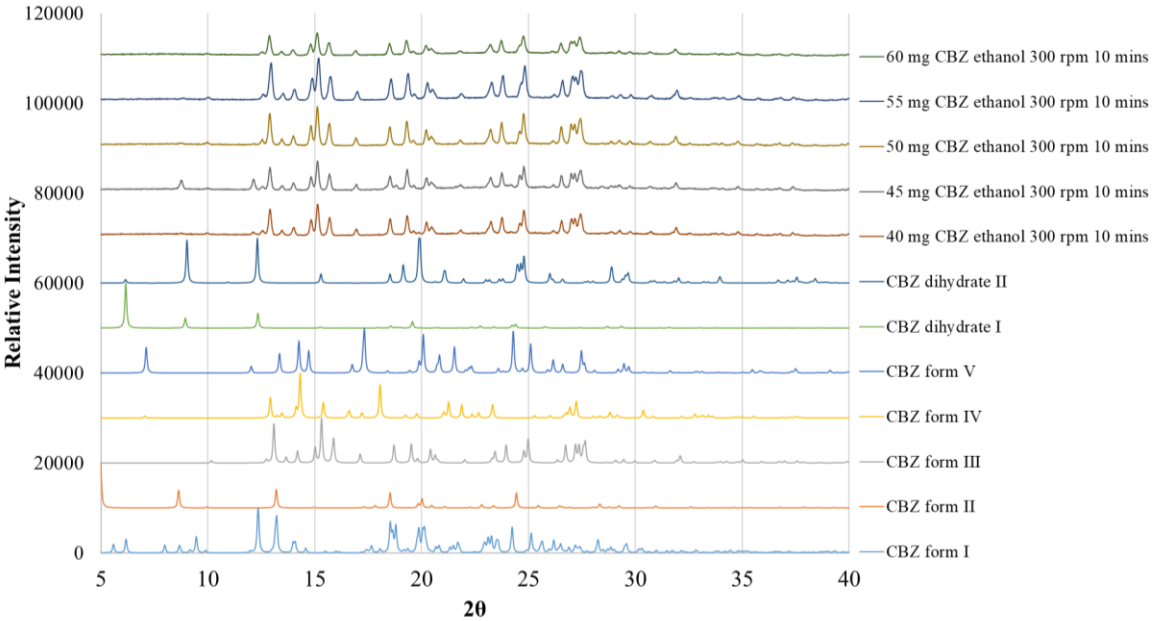

Figure A4.19 – PXRD patterns of varying concentrations of CBZ in EtOH at 300 rpm for 10 minutes slurrying time at 20 ℃.

4.6 Integrated intensity values for growth plots for all crystallisation runs

Table A4.6 – Integrated intensity values for growth plots for all crystallisation runs.

Hit rate	Scan Number	Background threshold (intensity)	Polymorphic form
NRP = Not right position			
Unseeded 66.6 g/kg CBZ in EtOH (CBZKDB1)			
	Diffraction poor		
NRP = 8	W1 (8)		
NRP = 4	W2 (8)		
3/5	W3 (5)		
Unseeded 71.9 g/kg CBZ in EtOH (CBZKDB2)			
Total scans = 10 Diffraction rate = 3/8 2 NRP Diffraction rate in 5 sampling (2/5)	W1 (30017)	25 (0.0617)	CBZ form II
	W1 (30025)	25 (0.0439)	CBZ form II or III (single peak)
	W1	0	
	W1	0	
	W1	0	
10 8/10 (4/5)	W2 (30007)	25 (0.8219)	CBZ form I or II
	W2 (30008)	20 (3.3936)	CBZ form I, II, V
	W2 (30009)	20 (5.8870)	CBZ form II
	W2 (30040)	25 (0.0283)	CBZ form I, II
	W2	0	
6 5/5 1 NRP	W3 (30052)	25 (11.1291)	CBZ form III (some additional)
	W3 (30053)	25 (13.0532)	
	W3 (30054)	25 (17.1724)	
	W3 (30055)	25 (3.5890)	
	W3 (30060)	25 (5.6932)	
CBZ Pre-nucleation seeded form III (CBZKDB3)			
7 6/7 1 NRP	W1 (29757)	25 (97.8690)	CBZ form III
	W1 (29758)	25 (3.4011)	
	W1 (29760)	25 (76.1559)	
	W1 (29765)	25 (257.3721)	
	W1 (29766)	25 (240.5746)	
5 4/5	W2 (29795)	25 (120.1241)	CBZ form III
	W2 (29799)	25 (418.6823)	
	W2 (29800)	25 (246.9676)	
	W2 (29803)	25 (77.0891)	
	W2	0	
8	W3 (29767)	25(95979)	CBZ form III

2 NRP 5/6 (4/5)	W3 (29769)	25(7.0249)	
	W3 (29780)	25(48.3571)	
	W3 (29794)	25(220.3667)	
	W3 (29796)	0	
Seeded Post-nucleation CBZ form III (CBZKDB4)			
	W1 No data		
9 1 SC (Shutter Closed)	W2 (29967)	25 (0.2439)	CBZ form III
	W2 (29968)	25 (1.6443)	
	W2 (29970)	25 (0.1650)	
	W2 (29955)	0	
	W2 (29971)	0	
6 1 NRP 5/5	W3 (29920)	25 (86.4557)	CBZ form III
	W3 (29921)	25 (238.8568)	
	W3 (29930)	25 (122.9822)	
	W3 (29931)	25 (310.2949)	
	W3 (29953)	25 (169.5978)	
Unseeded UBA in MeOH (UBAKDB1)			
7 2/7	W1 (30425)	25 (0.6106)	UBA form III
	W1 (30426)	25 (0.6100)	
	W1	0	
	W1	0	
	W1	0	
7 7/7 (5/5)	W2 (30453)	25 (3.5770)	UBA form III
	W2 (30454)	25 (4.3701)	
	W2 (30470)	25 (3.1886)	
	W2 (30477)	25 (9.6535)	
	W2 (30478)	25 (7.6253)	
7 5/7 (3/5)	W3 (30485)	25 (48.2470)	UBA form I, III
	W3 (30490)	25 (29.1441)	
	W3 (30500)	0	
	W3 (30501)	0	
	W3 (30502)	173.0879	
UBA Pre-nucleation seeded form III (UBAKDB2)			
5 5/5	W1 (30264)	25 (3.7726)	UBA form III
	W1 (30265)	25 (10.6449)	
	W1 (30280)	25 (2.4514)	
	W1 (30281)	25 (5.0458)	
	W1 (30290)	25 (25640)	
5	W2 (30292)	25 (43.5318)	UBA form III, some I

5/5	W2 (30300)	25 (33.6745)	
	W2 (30301)	25 (72.5553)	
	W2 (30318)	25 (29.4925)	
	W2 (30291)	25 (62.5991)	
5 5/5	W3 (30319)	25 (59.0006)	UBA form III, some I
	W3 (30320)	25 (49.7182)	
	W3 (30330)	25 (64.8975)	
	W3 (30345)	25 (164.4119)	
	W3 (30346)	25 (220.3533)	
UBA Post-nucleation seeded form III (UBAKDB3)			
6 0/5 1NRP	W1 No diffraction		
12 2/7 5NRP	W2 (30237)	25 (0.1667)	UBA form III
	W2 (30238)	25 (0.0468)	
	W2	0	
	W2	0	
	W2	0	
5 5/5	W3 (30196)	20 (34.5925)	UBA form I and III
	W3 (30197)	25 (33.0175)	
	W3 (30210)	25 (2.6199)	
	W3 (30211)	25 (4.5048)	
	W3 (30223)	25 (90.4002)	
UBA Pre-nucleation seeded form I (UBAKDB4)			
5/5	W1 (30347)	20 (13.5733)	UBA form I
	W1 (30348)	20 (8.8730)	
	W1 (30356)	20 (6.7179)	
	W1 (30357)	20 (15.4396)	
	W1 (30358)	20 (13.2893)	
5/5	W2 (30380)	20 (182.0228)	UBA form I
	W2 (30381)	20 (156.4067)	
	W2 (30391)	20 (207.3885)	
	W2 (30392)	20 (304.2517)	
	W2 (30390)	20 (213.6479)	

4.7 UBA form III pre-nucleation seeded experiment UBAKDB2 showing combined data from 10 scans

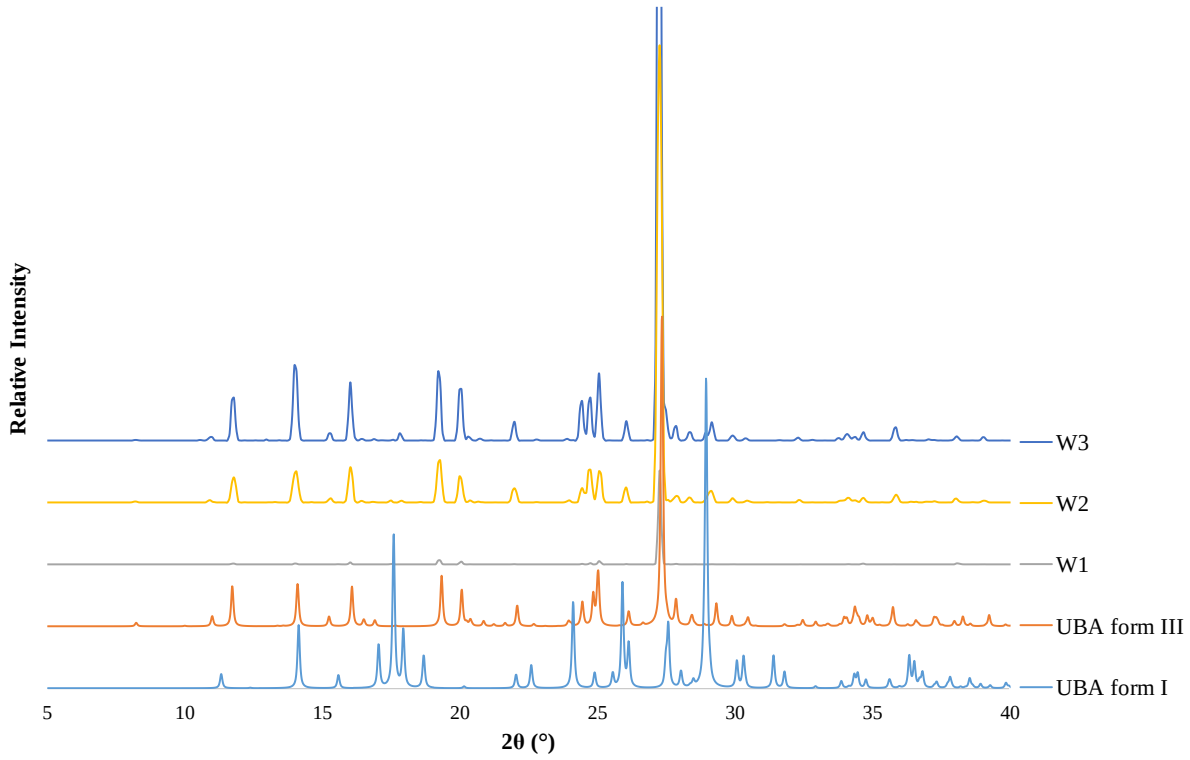

Figure A4.20 – UBA form III pre-nucleation seeded experiment UBAKDB2 showing combined data from 10 scans across W1, W2 and W3 compared to the PXRD patterns of the pure polymorphs UBA form I and UBA form III. N.B. the peak at 27° has been truncated to give clarity to lower intensity peaks.

Chapter 5 Appendix (A5)

5.1 Automated Data Processing Trials *via* Xia2

Table A5.1 – Cytidine: the full 124° dataset was collected on a PILATUS 300K diffractometer and processed across a range of wedge sizes using Xia2. Attempts to index a 5° wedge of data *via* manual input of unit cell parameters failed.

Parameter	**Wedge of data**		
	90°	**20°**	**10°**
Unit cell finding	Yes	Yes	Manual
a /Å	5.1195(7)	5.1126(12)	5.1158(14)
b /Å	13.9918(13)	14.001(19)	13.99(2)
c /Å	14.8013(12)	14.785(3)	14.769(5)
α /°	90.0	90.0	90.0
β /°	90.0	90.0	90.0
γ /°	90.0	90.0	90.0
Number of spots	544	103	51
Number of images	449	100	49

Table A5.2 – PCM: the full 180° dataset was collected on a PILATUS 2M diffractometer and processed across a range of wedge sizes using Xia2.

Parameter	**Wedge of data**			
	180°	**90°**	**20°**	
Unit cell finding	Yes	Yes	Yes	
a /Å	7.10362(9)	7.10361(10)	7.10362(9)	
b /Å	9.38220(15)	9.3779(3)	9.38220(15)	
c /Å	11.7093(2)	11.7078(3)	11.7093(2)	
α /°	90.0	90.0	90.0	
β /°	97.4296(13)	97.4317(15)	97.4296(13)	
γ /°	90.0	90.0	90.0	
Parameter	**Wedge of data**			
	10°	**5°**	**2°**	**1°**
Unit cell finding	Manual	Manual	Manual	Manual
a /Å	7.0989(5)	7.0976(8)	7.0904(15)	7.12
b /Å	9.3851(7)	9.3874(11)	9.398(3)	9.37
c /Å	11.7074(9)	11.7111(14)	11.714(4)	11.71
α /°	90.0	90,0	90.0	90.00
β /°	97.434(6)	97.463(9)	97.486(17)	97.45
γ /°	90.0	90.0	90.0	90.00

5.2 Slug Triggering Testing

5.2.1 Identifying constituent media in segmented flow on oscilloscope read-out

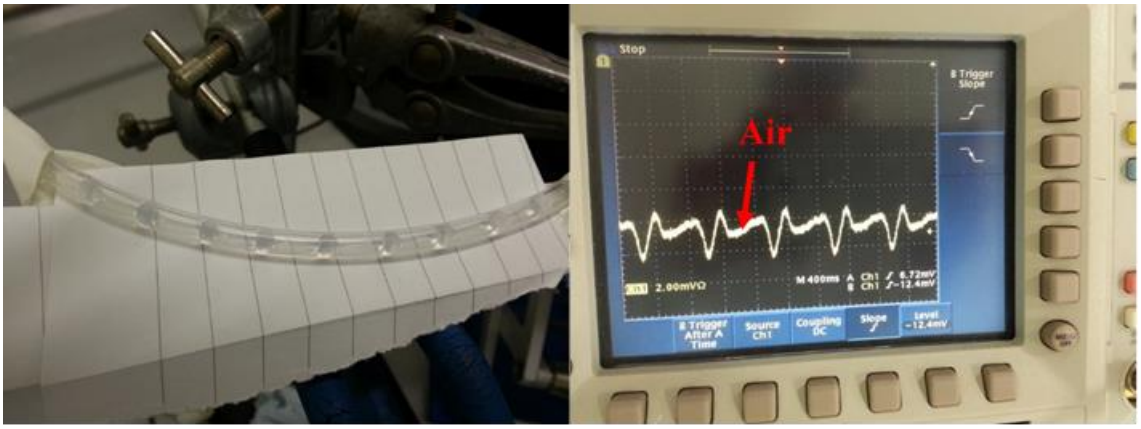

Figure A5.1 – Image of segmented flow (left) *versus* oscilloscope read-out (right), flow rates of air and solution are 4.18 mL/min and 1.6 mL/min respectively.

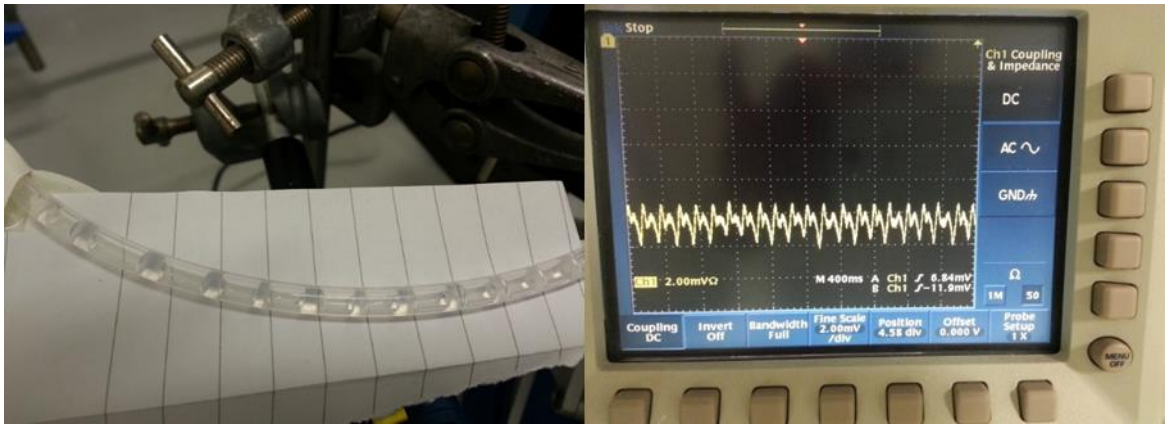

Figure A5.2 – Image of segmented flow (left) versus oscilloscope read-out (right), flow rates of air and solution are 12.5 mL/min and 6.4 mL/min respectively.

5.2.2 *In vitro* Data Processing Optimisation

For the top, middle and bottom measured segmentation patterns (Figure A5.3); the distance between adjacent slugs is 3.2 cm for each of the images, coupled with an adjacent peak separation of 1.5 seconds, equating to a slug translation speed of 21 mm/s. This translation rate is both too fast for the speed capabilities of the motorised stage and will not allow sufficient data to be collected for indexing of a single solution slug.

To decrease the speed of the solution slugs, subsequent experiments were carried out as follows:

The flow rates were decreased to air pump 4.18 mL/min, carrier fluid pump 2.1 mL/min and solution pump 1.6 mL/min. The distance between adjacent solution slugs increased to 4.2 cm,

but the time between adjacent solution slugs also increased to 2 seconds. Therefore, the speed of the solution slugs remains too fast at 21 mm/s; in addition, the size of the air slugs under these conditions was too large.

The flow rates were decreased to air pump 2.1 mL/min, carrier fluid pump 2.1 mL/min and solution pump 1.6 mL/min. The distance between adjacent solution slugs decreased to 2.6 cm; with the time between adjacent solution slugs remaining at 2 seconds, the speed of the solution slugs is reduced to 13 mm/s, within the capabilities of both the speed of the motorised stage and the data collection.

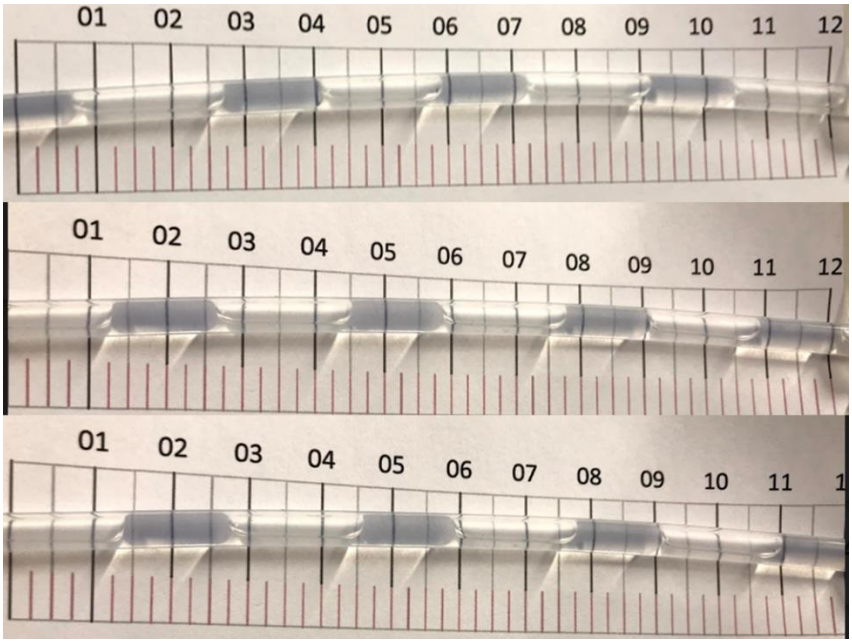

Figure A5.3 – Images of segmented flow for flow rates of air pump (4.18 mL/min), carrier fluid pump (2.1 mL/min) and solution pump, water (3.2 mL/min).

5.3 DIALS Commands

5.3.1 DIALS Data Processing Trials

dials.import /path/to/data/image_01_00001.cbf

Command A5.1 – DIALS import.

dials.find_spots imported.expt min_spot_size=1 d_max=15 sigma_strong=8

Command A5.2 – DIALS spot finding.

dials.index imported.expt strong.refl

Command A5.3 – DIALS index.

5.3.2 Xia2 Data Processing Trials

xia2 small_molecule=true image=/path/to/data/image_01_00001.cbf

Command A5.4 – General Xia2 command.

5.3.3 DIALS Data Analysis Procedure

dials.import /path/to//image_01_00001.cbf reference_geometry=/path/to/instrument_model.expt distance=124.61

Command A5.5 – DIALS single image import.

dials.find_spots imported.expt spotfinder.filter.min_spot_size=1 spotfinder.filter.d_max=15 sigma_strong=5 resolution_range=5.28,4.72 rectangle=0,612,824,858 circle=620,851,27

Command A5.6 – DIALS spot finding.

dials.index imported.expt strong.refl unit_cell=7.08,9.2,11.54,90,97.9,90 space_group=P21/n scan_varying=false refinement.parameterisation.beam.fix=all refinement.parameterisation.auto_reduction.action=fix

Command A5.7 – DIALS indexing.

dials.refine indexed.refl indexed.expt refinement.parameterisation.beam.fix=all refinement.parameterisation.auto_reduction.action=fix refinement.parameterisation.scan_varying=false refinement.parameterisation.detector.fix=all refinement.parameterisation.crystal.unit_cell.force_static=true

Command A5.8 – DIALS refine.

dials.import /path/to/raw/data/folder/ reference_geometry=/path/to/instrument_model.expt distance=124.61

Command A5.9 – DIALS import all images.

dials.find_spots imported.expt spotfinder.filter.min_spot_size=1 spotfinder.filter.d_max=15 sigma_strong=5 resolution_range=6.232,5.1 rectangle=0,612,824,858 circle=620,851,27

Command A5.10 – DIALS peak hunting after removal of resolution band from FEP and beamstop background.

dials.index imported.expt strong.refl unit_cell=7.08,9.2,11.54,90,97.9,90 space_group=P2/m outlier.algorithm=null beam.fix=all detector.fix=all index_assignment.method=local local.epsilon=0.15

Command A5.11 – DIALS local index assignment.

5.4 Lattice Rotations from Commissioning Time

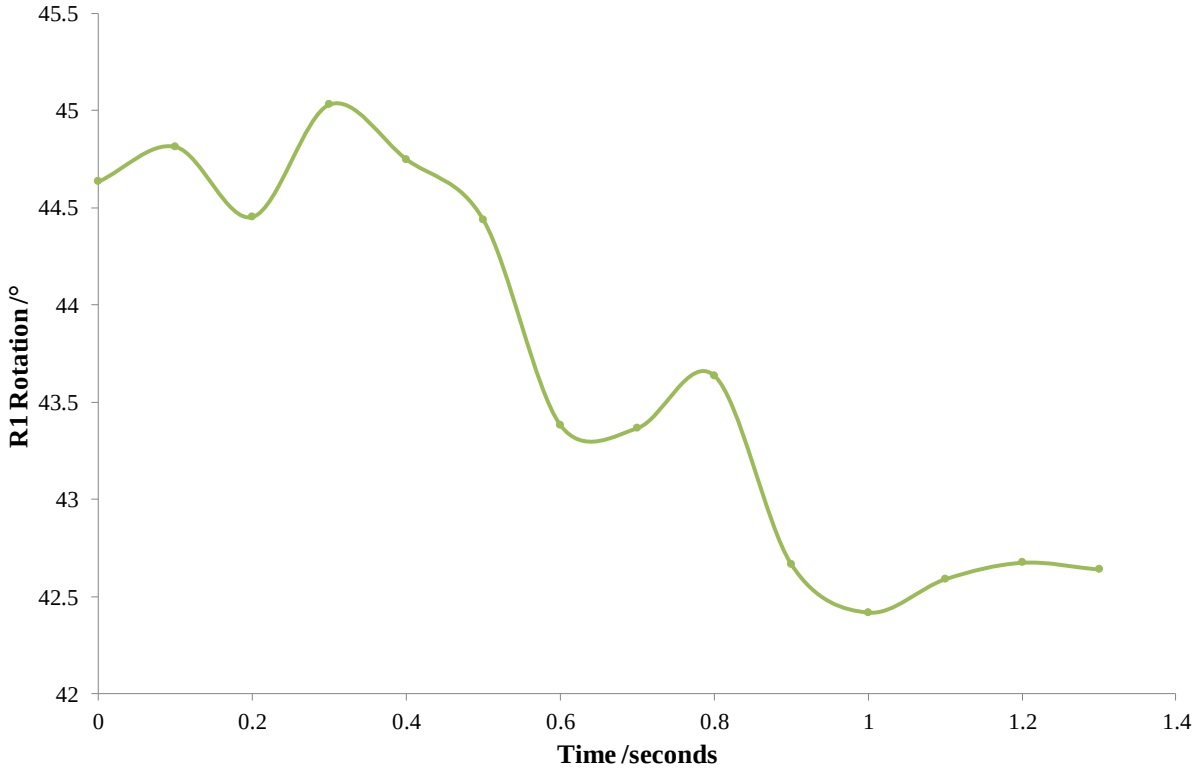

Figure A5.4 – R1 lattice rotation with respect to the instrument over time.

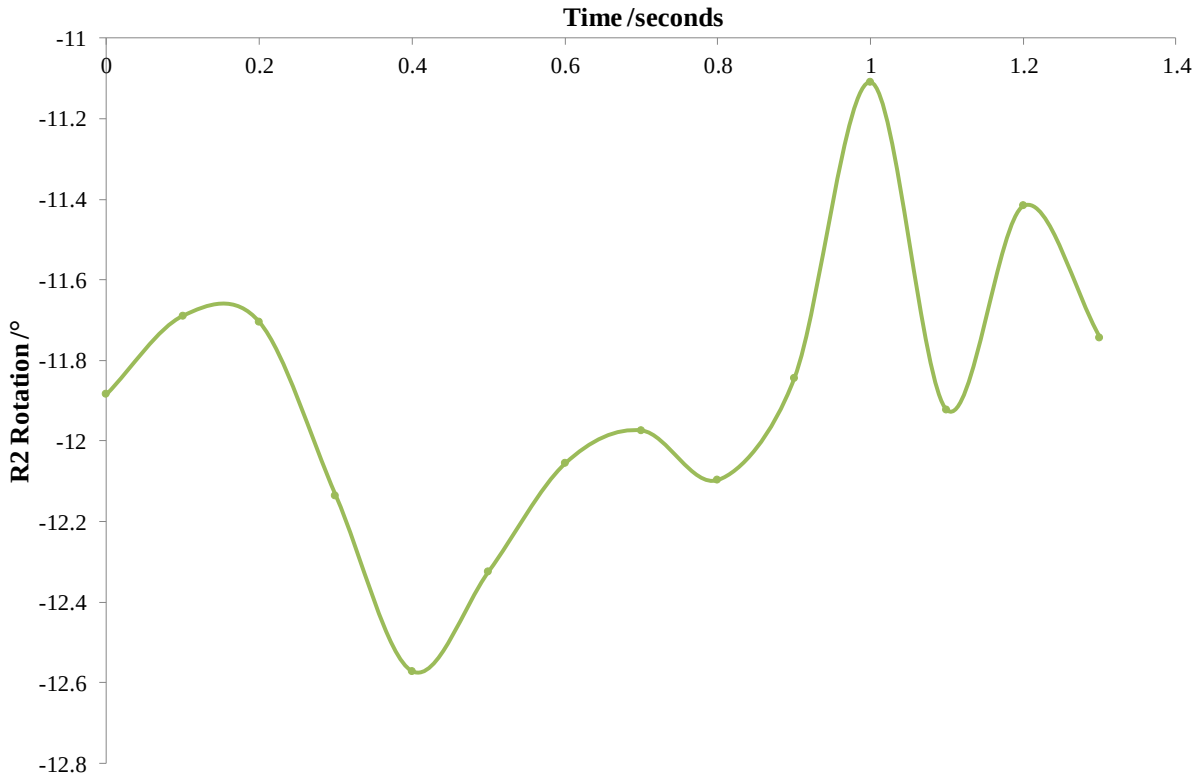

Figure A5.5 – R2 lattice rotation with respect to the instrument over time.

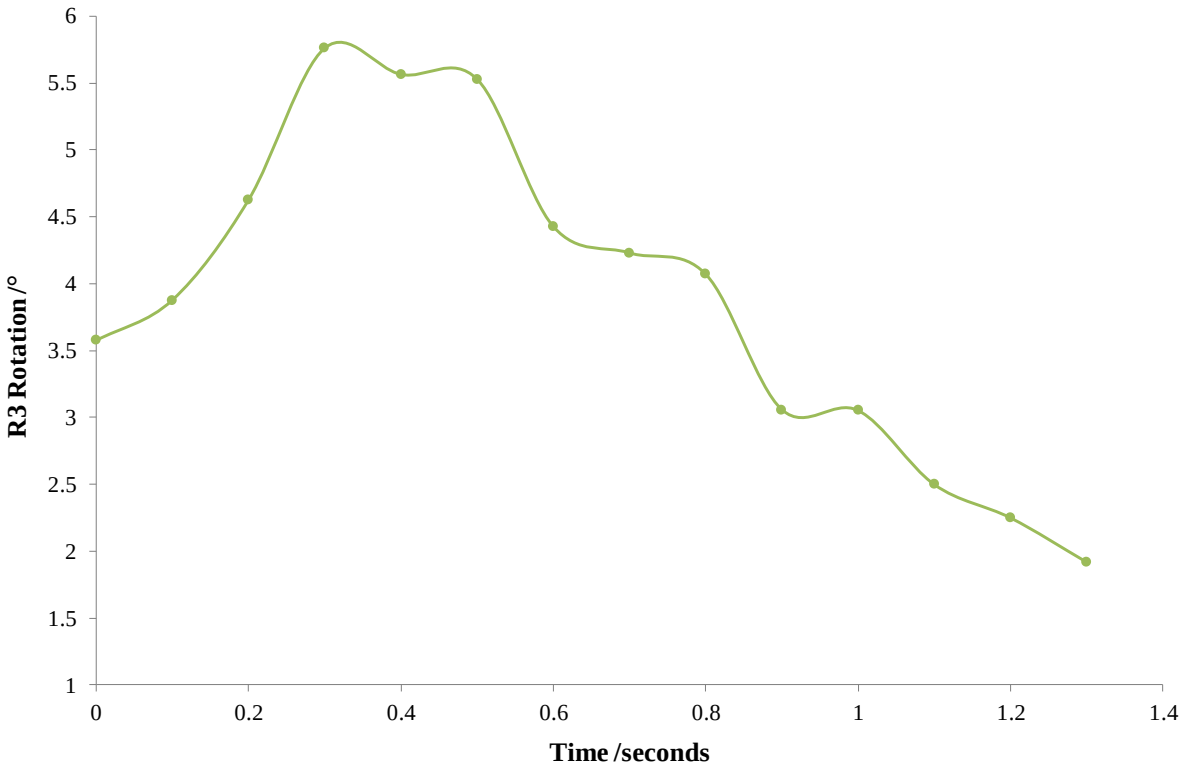

Figure A5.6 – R3 lattice rotation with respect to the instrument over time.

5.5 Diode read-out for PCMKSB1

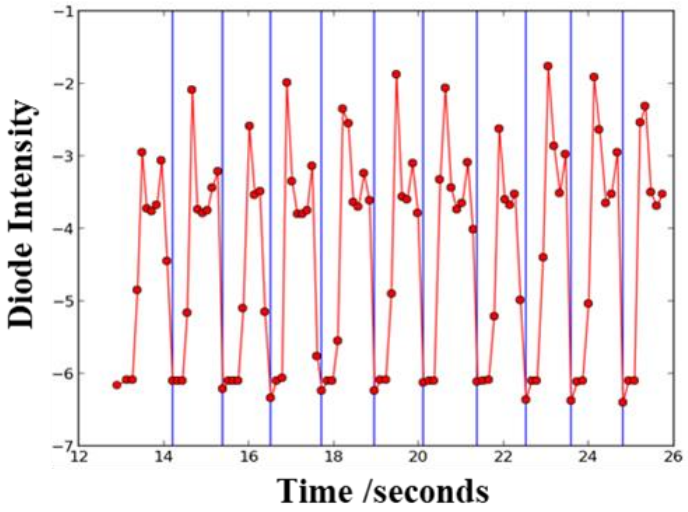

Figure A5.7 – Diode-readout of intensity *versus* time for the segmentation in crystallisation run PCMKSB1.

5.6 Unseeded PCM in 60:40 HI at 8.7 m (Beamtime)

5.6.1 Unit cell parameters over time for each of the five datasets at 8.7 m

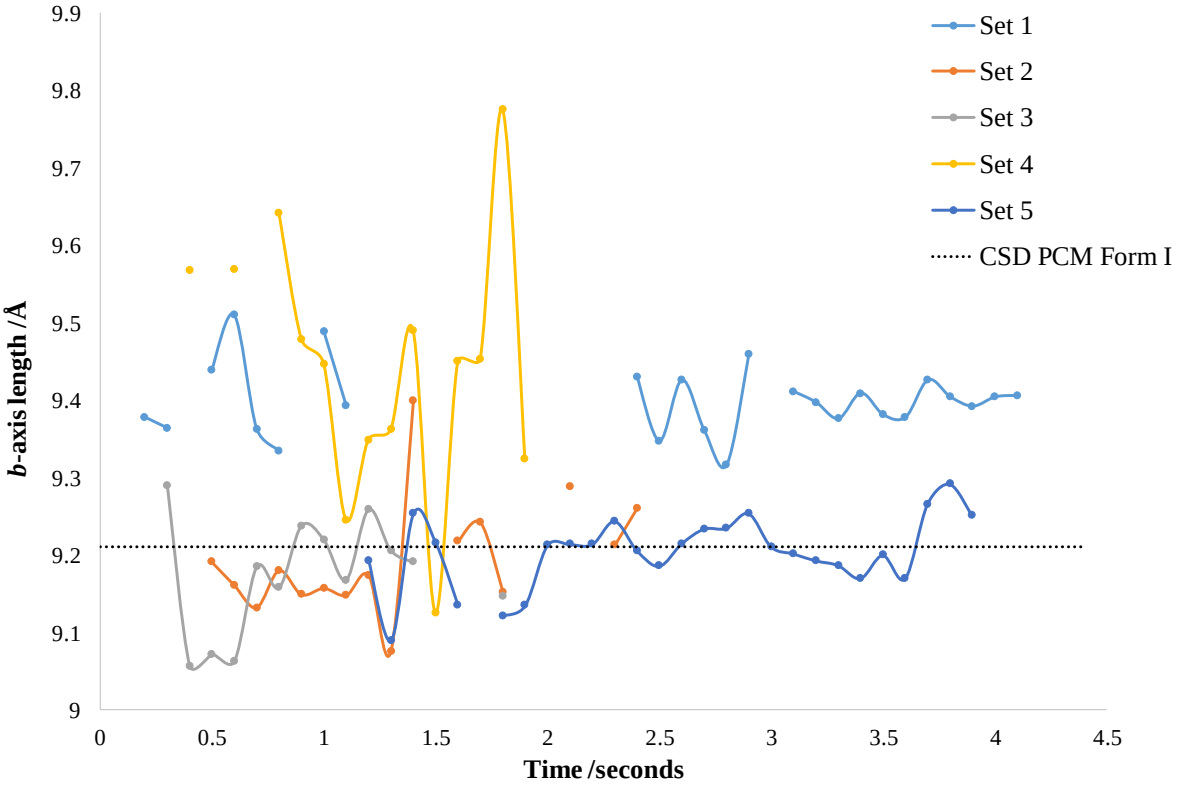

Figure A5.8 – *b*-axis lattice parameter over time for each of the five datasets compared to the magnitude of the *b*-axis for PCM form I obtained from the CSD (PCMKSB3).

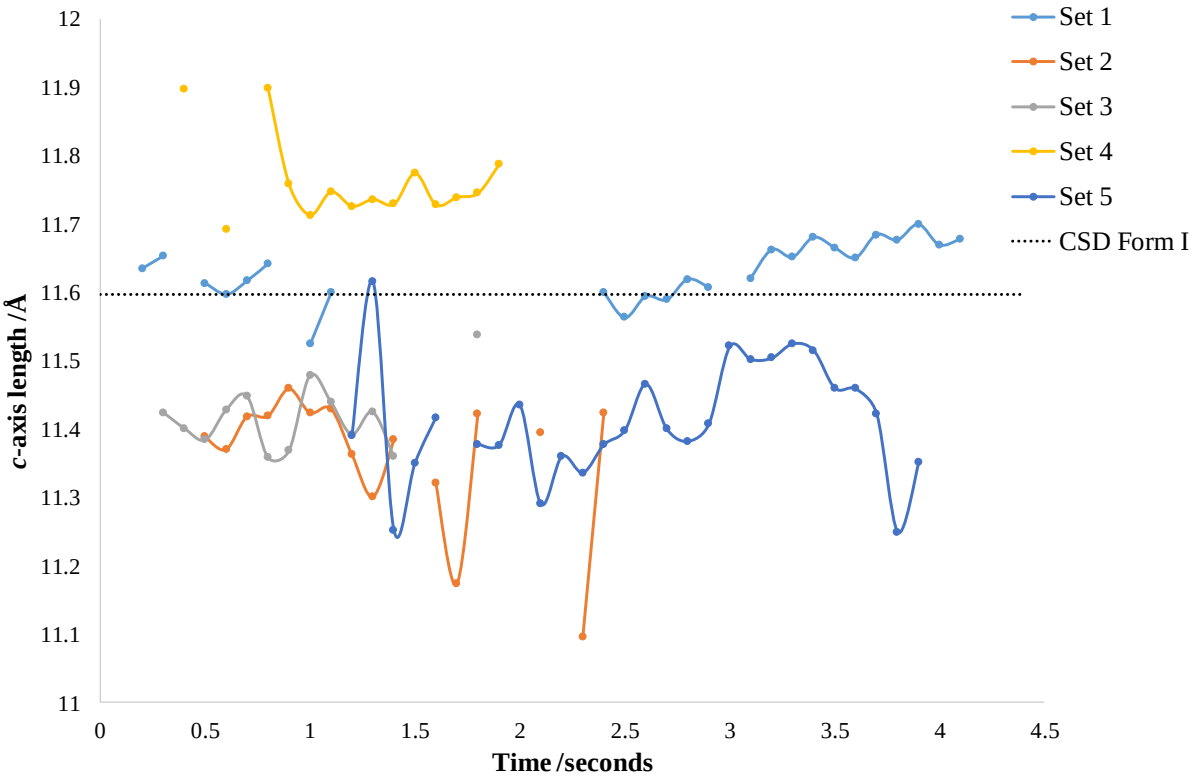

Figure A5.9 – *c*-axis lattice parameter over time for each of the five datasets compared to the magnitude of the *c*-axis for PCM form I obtained from the CSD (PCMKSB3).

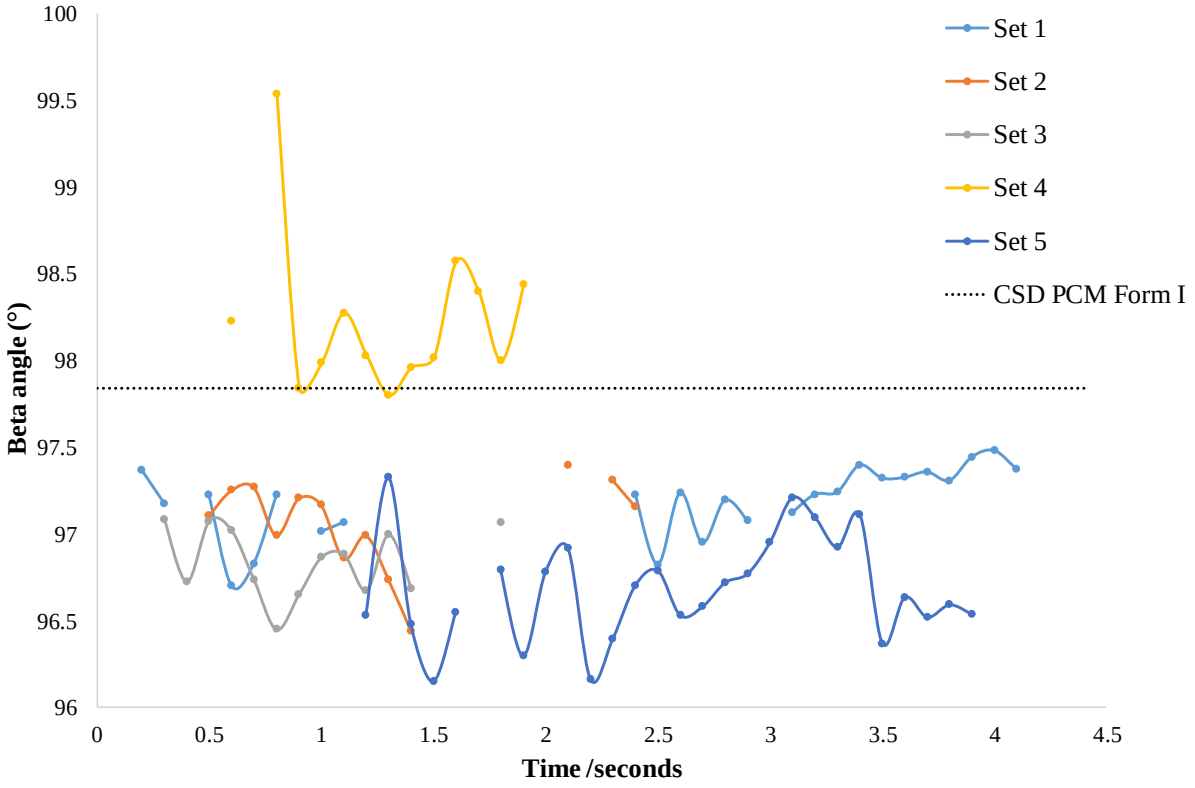

Figure A5.10 – Beta angle lattice parameter over time for each of the five datasets compared to the magnitude of the beta angle for PCM form I obtained from the CSD (PCMKSB3).

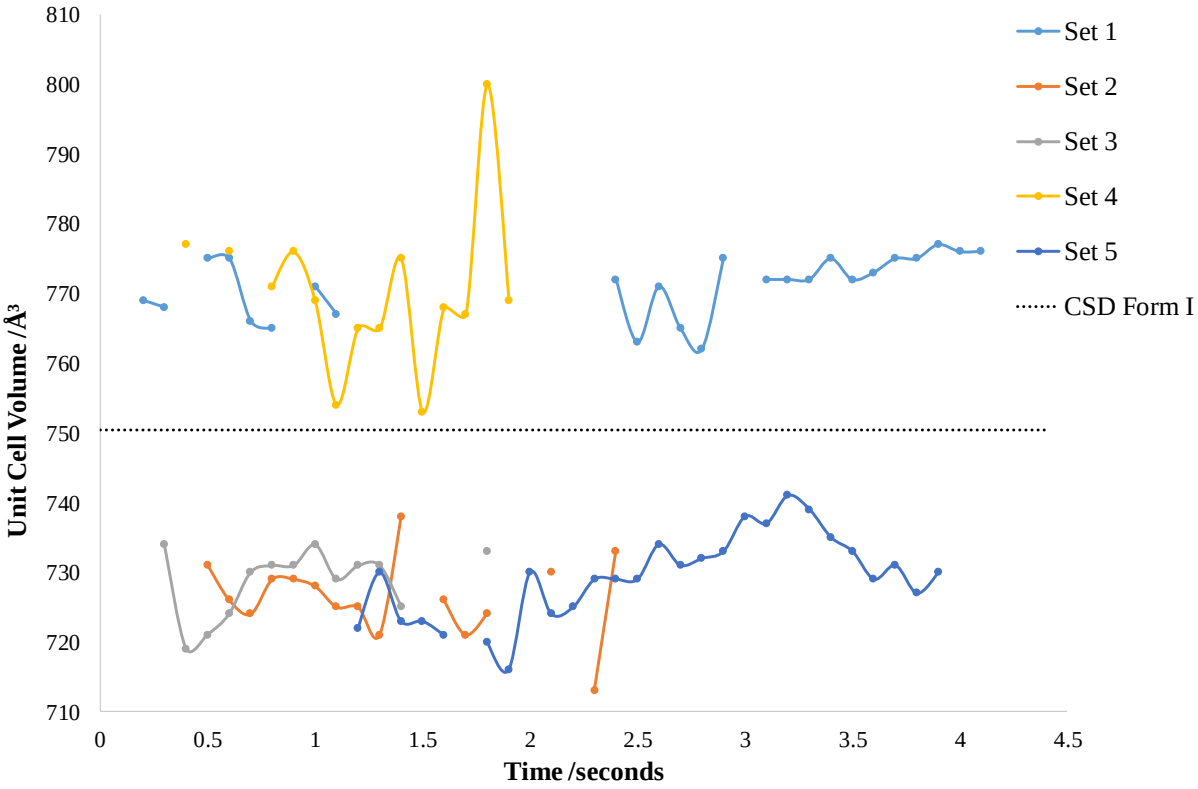

Figure A5.11 – Unit cell volume over time for each of the five datasets compared to the magnitude of the unit cell volume for PCM form I obtained from the CSD (PCMKSB3).

5.6.2 Lattice rotations over time for each of the five datasets at 8.7 m

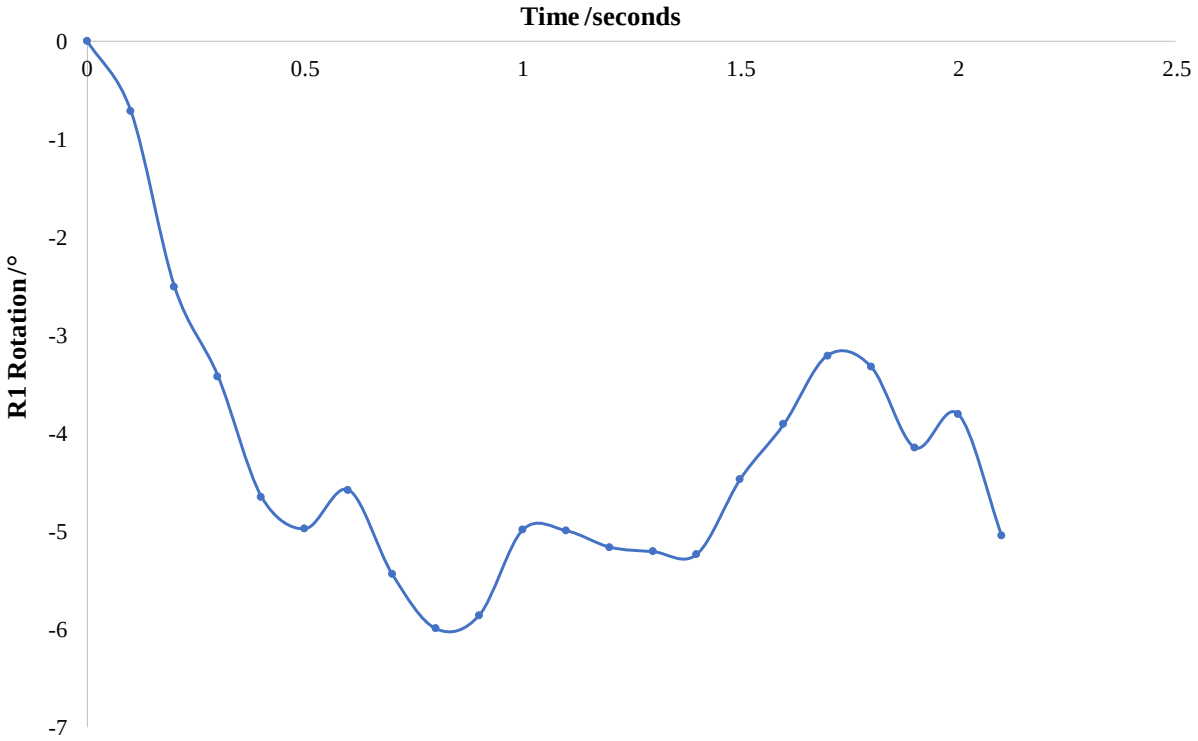

Figure A5.12 – R1 lattice rotation with respect to the instrument over time.

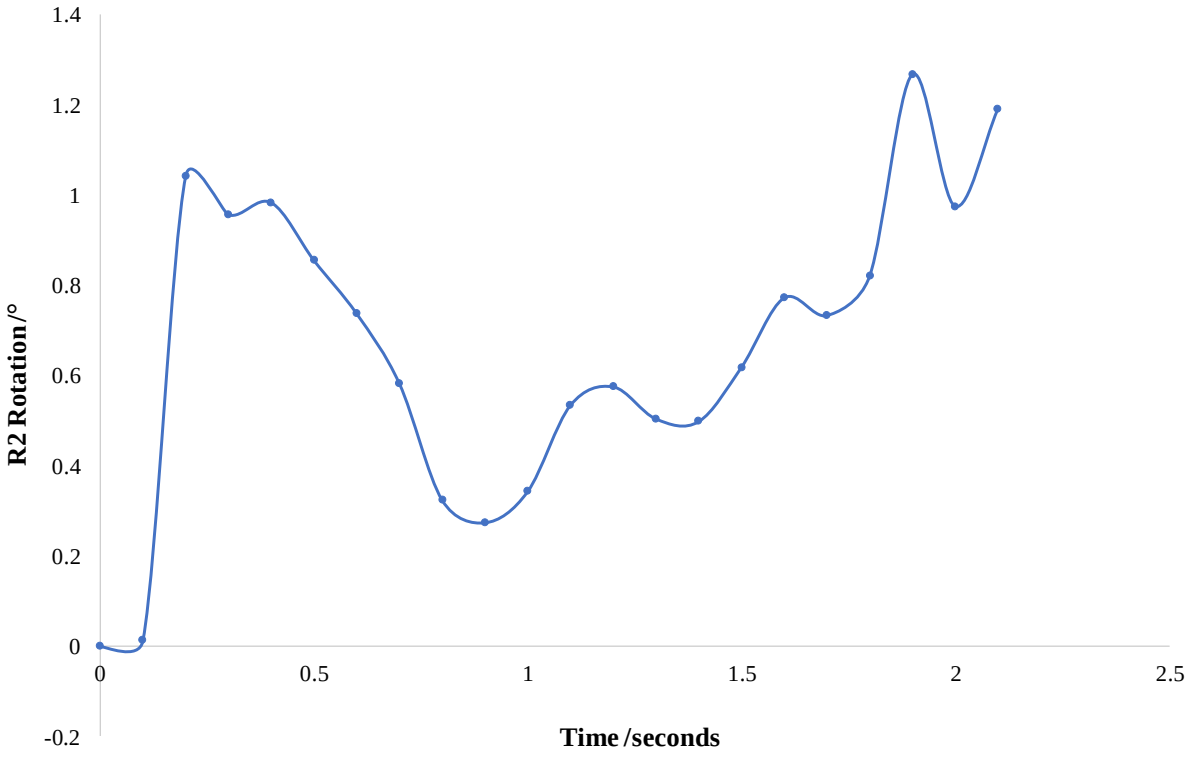

Figure A5.13 – R2 lattice rotation with respect to the instrument over time.

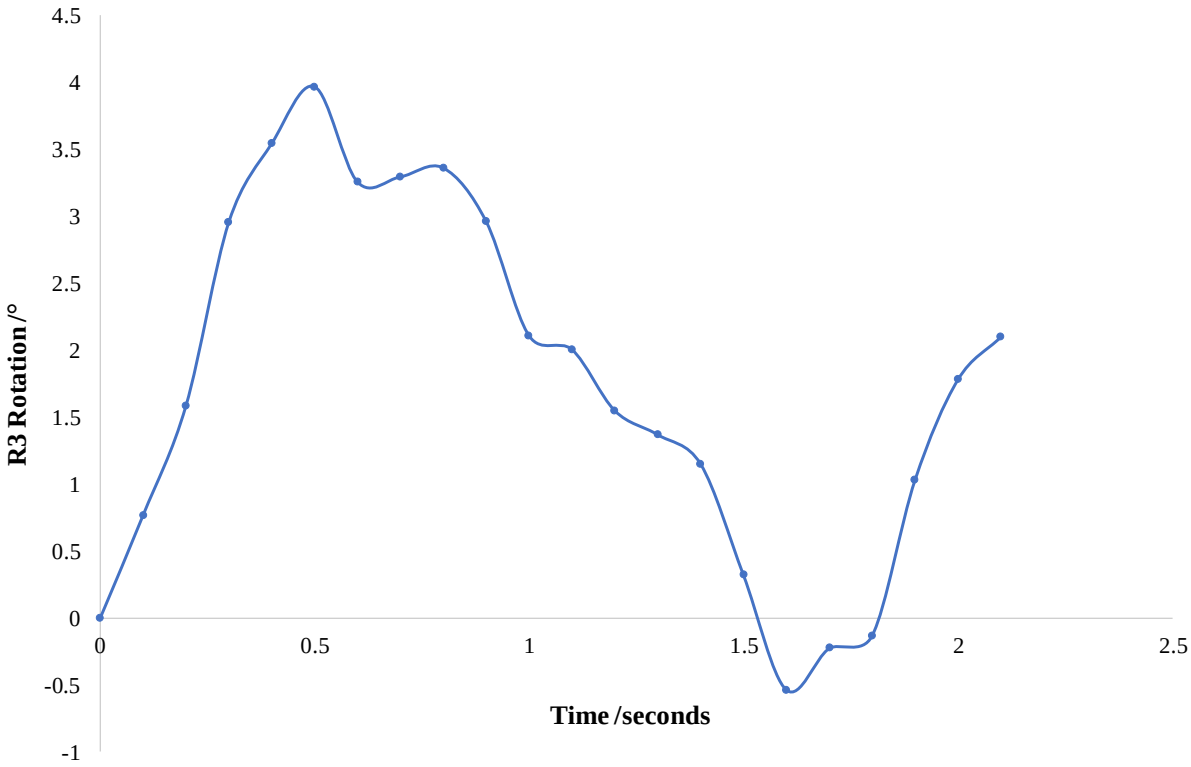

Figure A5.14 – R3 lattice rotation with respect to the instrument over time.

5.7 Unseeded PCM in 60:40 HI at 6.7 m (Beamtime)

5.7.1 Unit cell parameters over time for each of the five datasets at 6.7 m

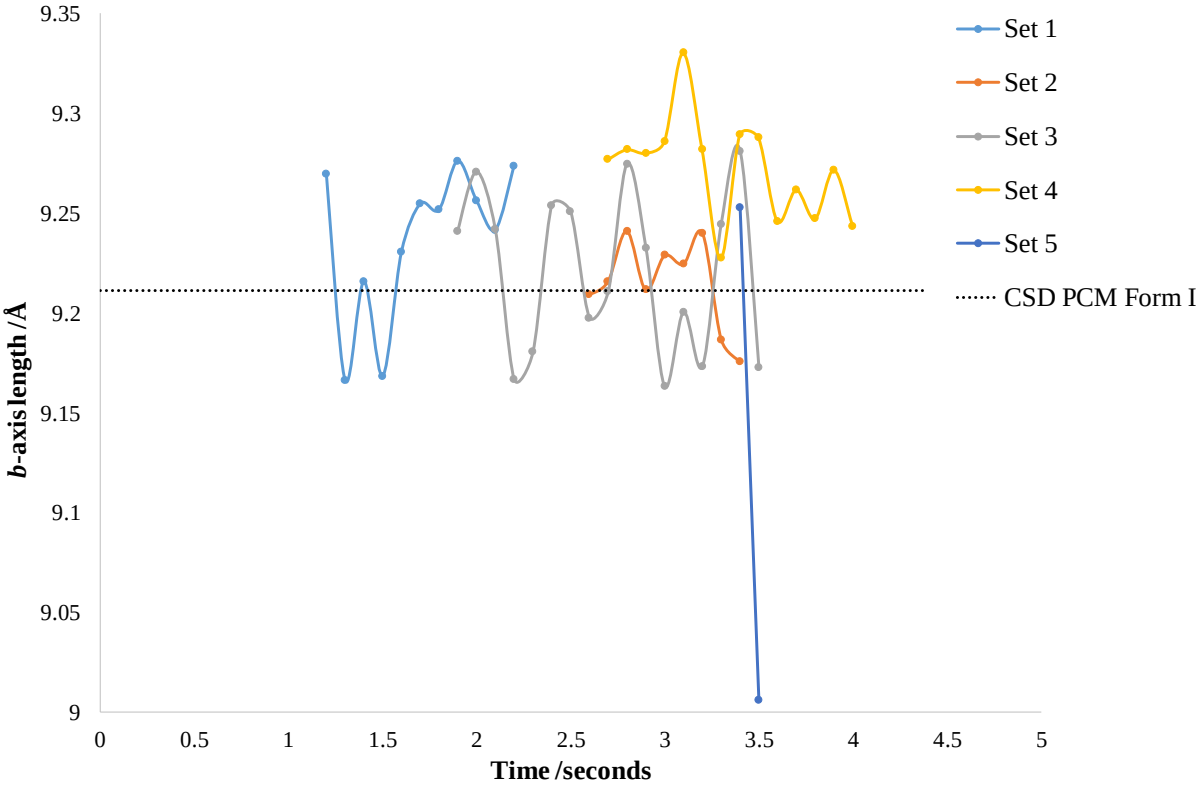

Figure A5.15 – *b*-axis lattice parameter over time for each of the five datasets compared to the magnitude of the *b*-axis for PCM form I obtained from the CSD (PCMKSB6).

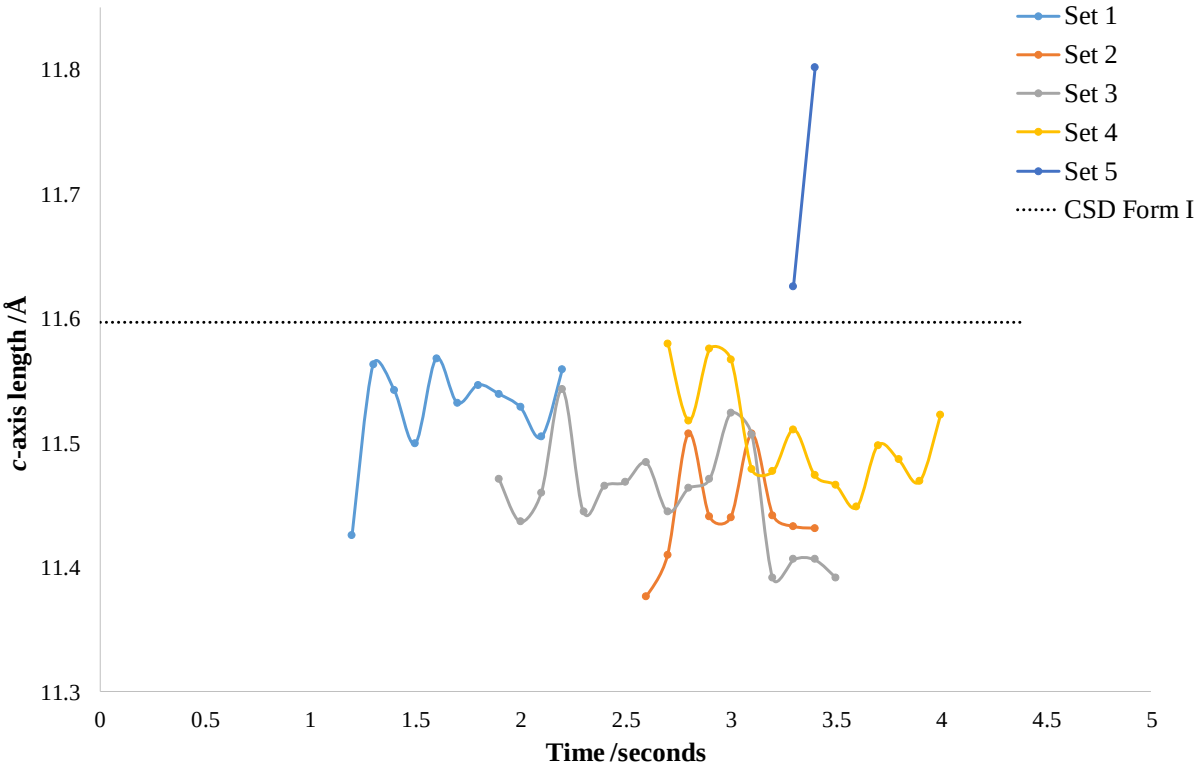

Figure A5.16 – *c*-axis lattice parameter over time for each of the five datasets compared to the magnitude of the *c*-axis for PCM form I obtained from the CSD (PCMKSB6).

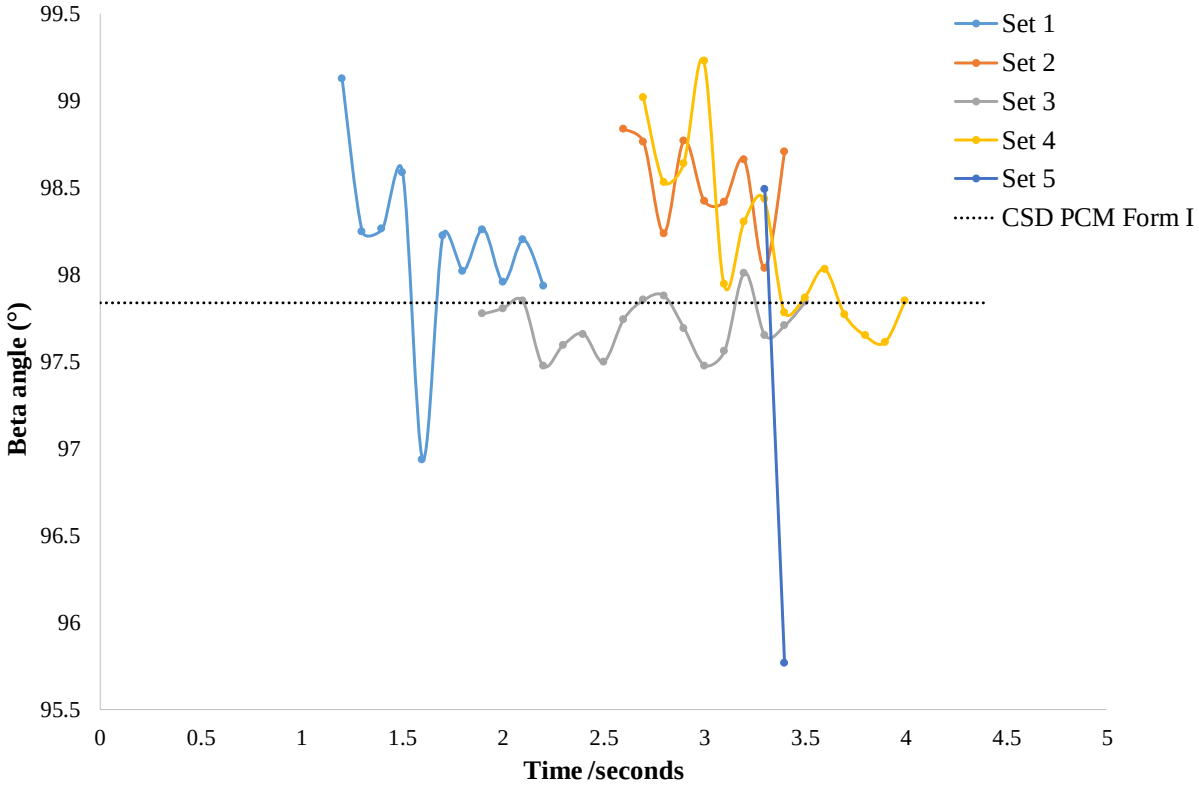

Figure A5.17 – Beta angle lattice parameter over time for each of the five datasets compared to the magnitude of the beta angle for PCM form I obtained from the CSD (PCMKSB6).

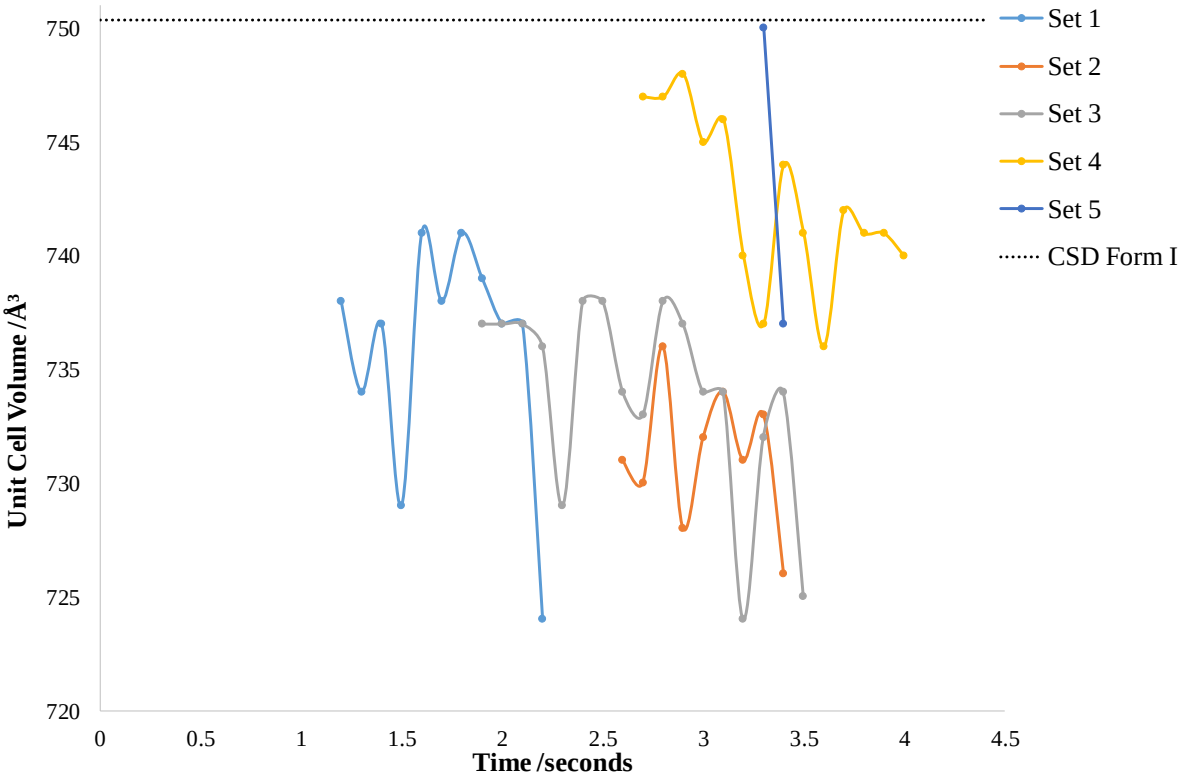

Figure A5.18 – Unit cell volume lattice parameter over time for each of the five datasets compared to the magnitude of the unit cell volume for PCM form I obtained from the CSD (PCMKSB6).

5.7.2 Lattice rotations over time for each of the five datasets at 6.7 m

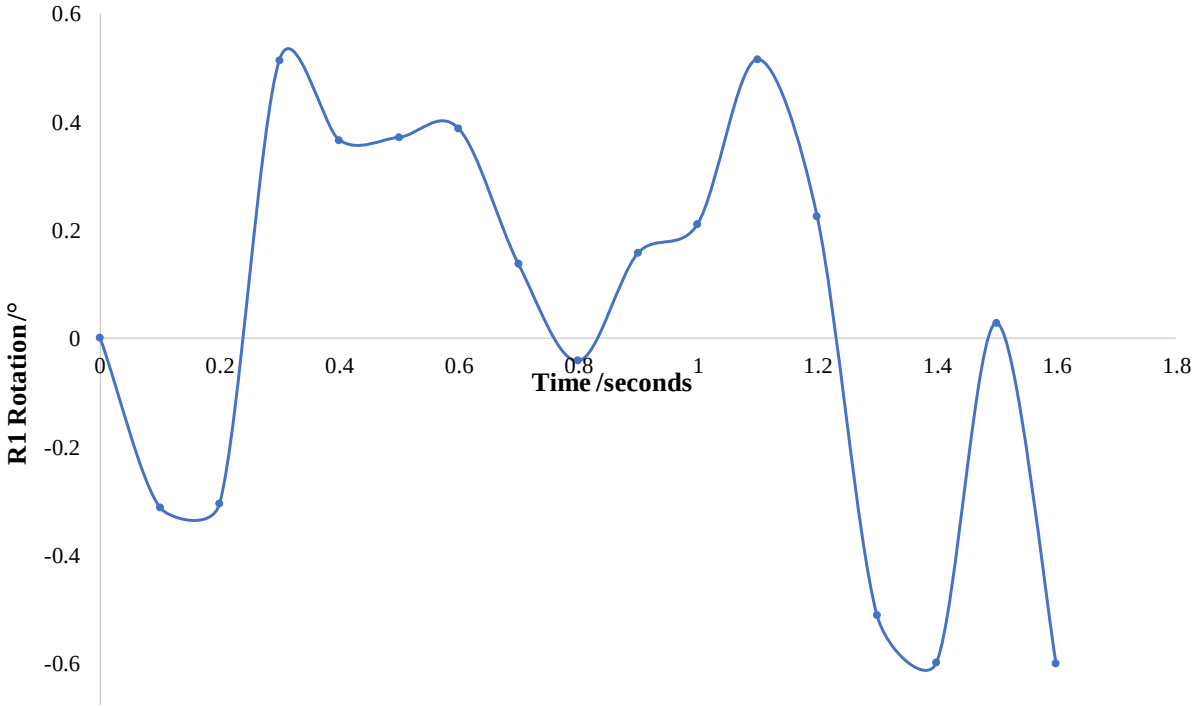

Figure A5.19 – R1 lattice rotation with respect to the instrument over time.

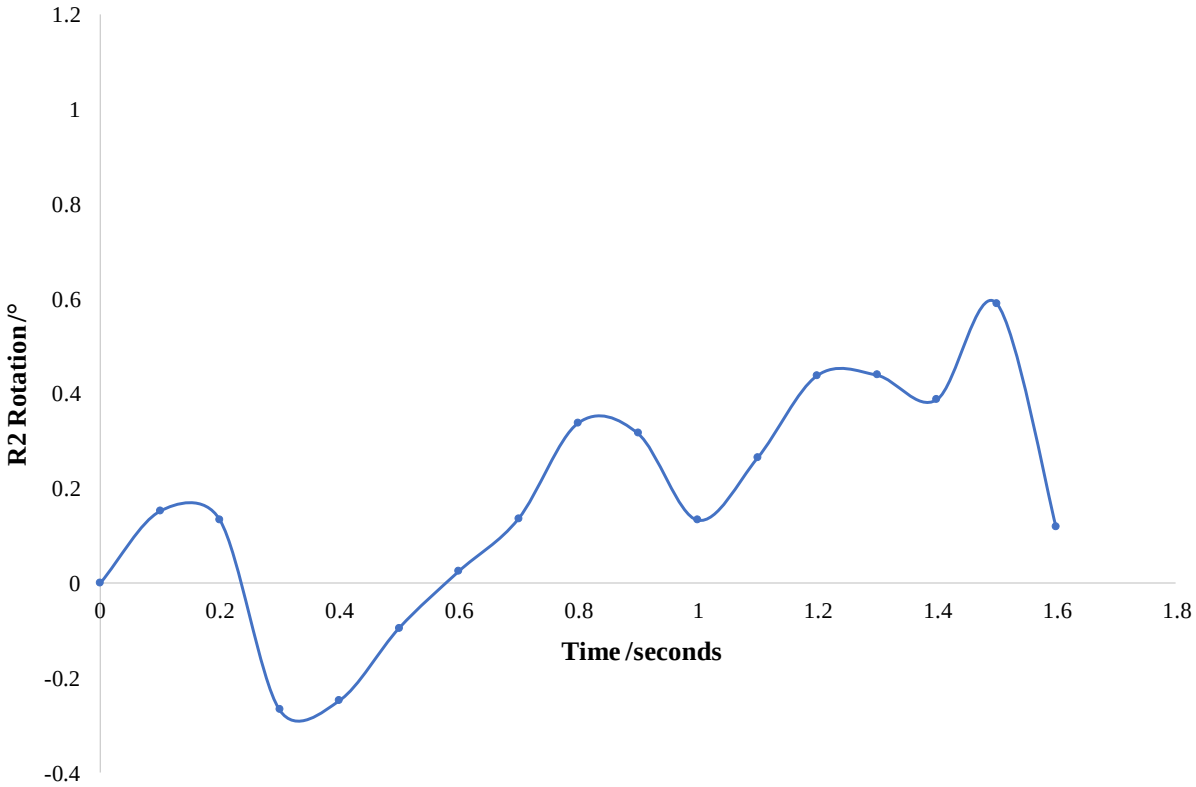

Figure A5.20 – R2 lattice rotation with respect to the instrument over time.

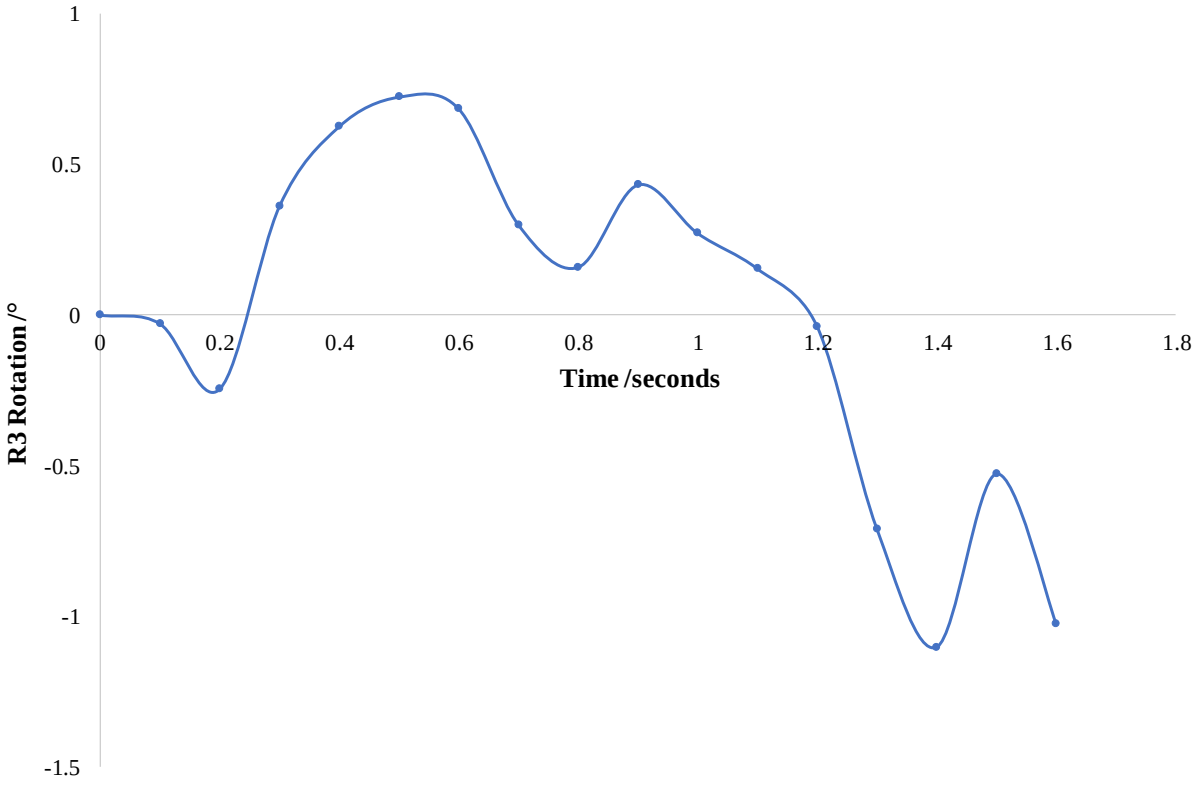

Figure A5.21 – R3 lattice rotation with respect to the instrument over time.

5.8 Details of Electronic Supplementary Information (ESI) – Videos of single crystals tracked in solution slugs

Wayment, L., in press. *Dataset for "Continuous flow for materials synthesis, assembly and crystallisation at Diamond: discovery and delivery of high value materials"*. Bath: University of Bath Research Data Archive.

The videos associated with Chapter 5 include single crystals produced from the range of experiments investigated. Each video tracks a different single crystal in a solution slug; where through use of the slug triggering mechanism, whereby an optical trigger prompts translation of the motorised stage to artificially suspend the single crystal in the X-ray beam during data collection. These videos complement the diffraction data and can provide explanation for data collections, which do not achieve cell indexation as the single crystal is shown to move in and out of the X-ray beam in these videos.

N.B videos are rotated by 180° and thus is observed as residing in the top of solution slug, when in fact the single crystals position themselves in the rear end of a solution slug at the bottom.

Unseeded PCM Form I

6.7 m

- 20190728_1517_0003_Unseeded PCM_6_7m_Set 1 Video
- 20190728_1521_0003_Unseeded PCM_6_7m_Set 2 Video
- 20190728_1521_0009_Unseeded PCM_6_7m_Set 3 Video
- 20190728_1559_0003_Unseeded PCM_6_7m_Set 4 Video
- 20190728_1614_0001_Unseeded PCM_6_7m_Set 5 Video

8.7 m

- Set 1 - No video to accompany diffraction data
- Set 2 - No video to accompany diffraction data
- 20190726_1839_0014_Unseeded PCM_8_7m_Set 3 Video
- 20190726_1928_0010_Unseeded PCM_8_7m_Set 4_Video
- 20190726_2023_0043_Unseeded PCM_8_7m_Set 5_Video
- 20190726_1405_0014_Unseeded PCM_8_7m_Video with no accompanying diffraction data

Seeded PCM Form II

- 20190727_2340_0004_Seeded PCM form II_Set 1_Get Form I_Video
- 20190727_2355_0010_Seeded PCM form II_Set 2_Get Form II_Video
- 20190728_0038_0007_Seeded PCM form II_Set 3_Get Form II_Video
- 20190728_0038_0008_Seeded PCM form II_Set 4_Get Form II_Video
- 20190727_1347_0050_Seeded PCM form II_Video with no accompanying diffraction data

Chapter 6 Appendix (A6):

6.1 Linear cooling profiles for cooling crystallisations

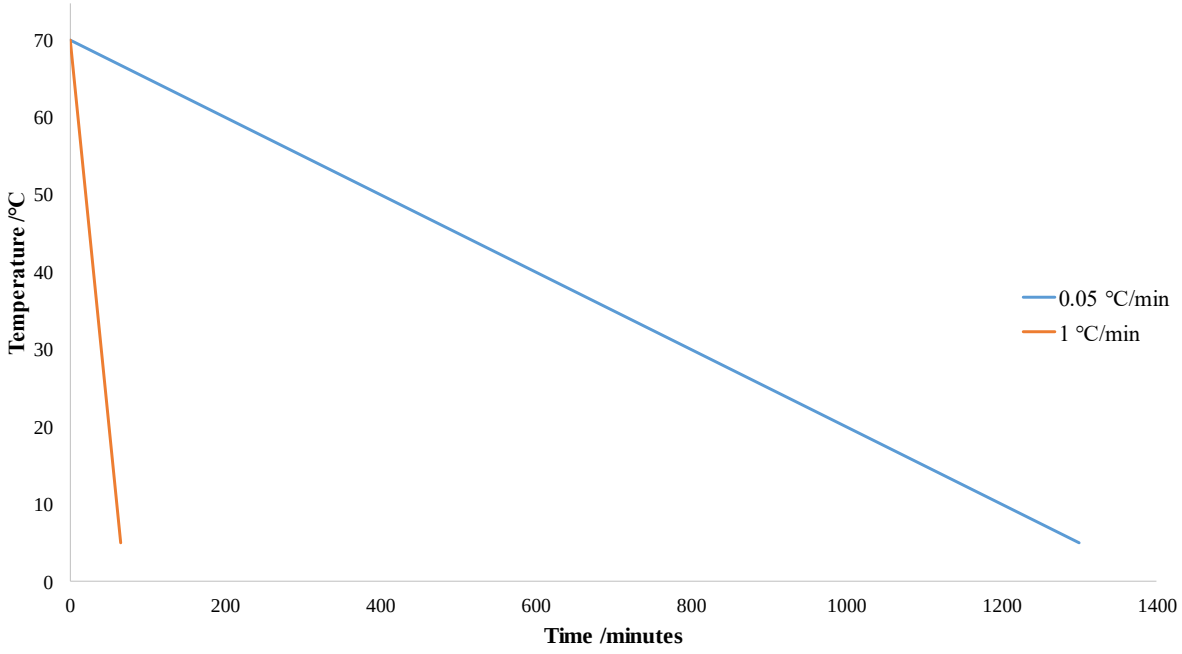

Figure A6.1 – Linear cooling rates adopted for cooling crystallisations, slow (0.05 °C min^{-1}) and fast (1 °C min^{-1}).

6.2 Thermal Behaviour of ISO Co-former

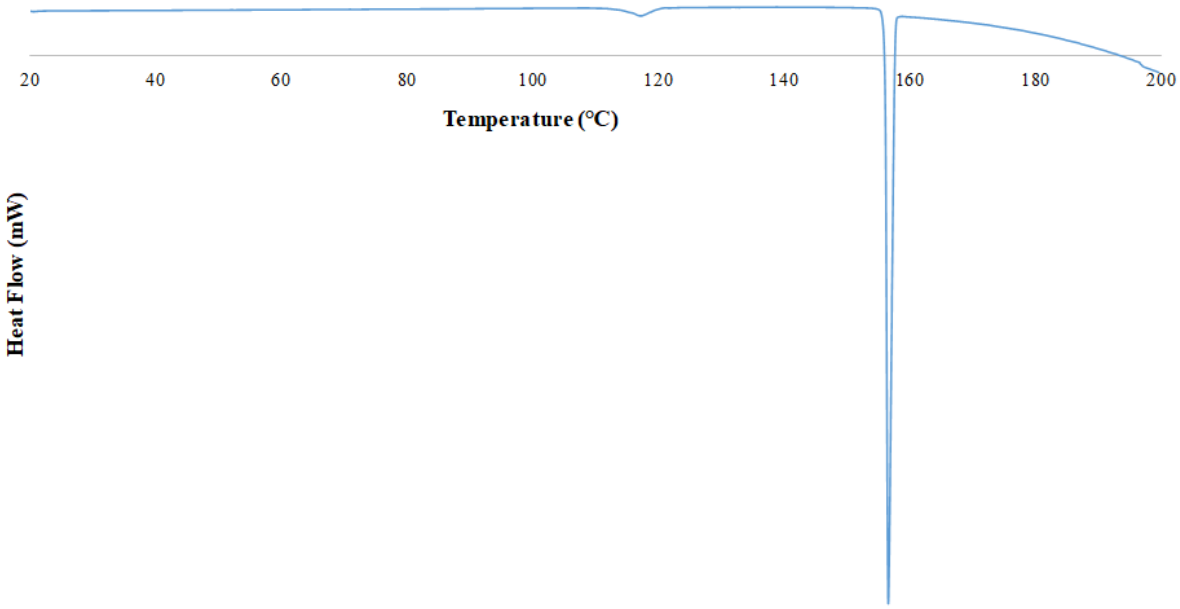

Figure A6.2 – DSC trace of ISO *via* a slower 1 °C min^{-1} heating ramp to 200°C.

6.3 Microscope Images of IBU-ISO

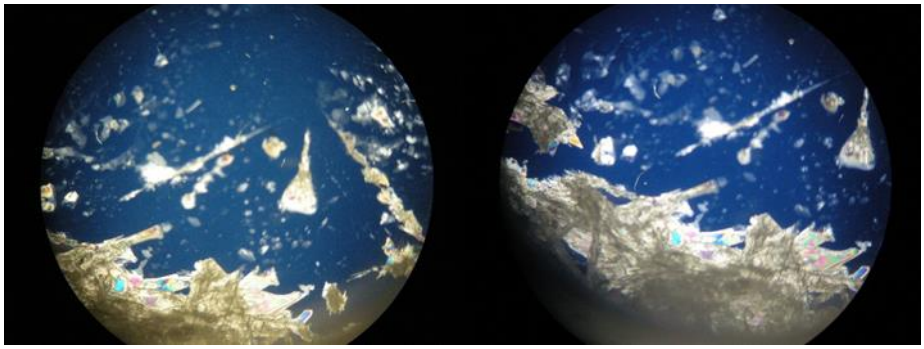

Figure A6.3 – Microscope images of IBU_ISO 1:1 in ACE evaporative crystallisations at 30 °C.

6.4 Thermal stability studies of IBU-ISO monitored over one month

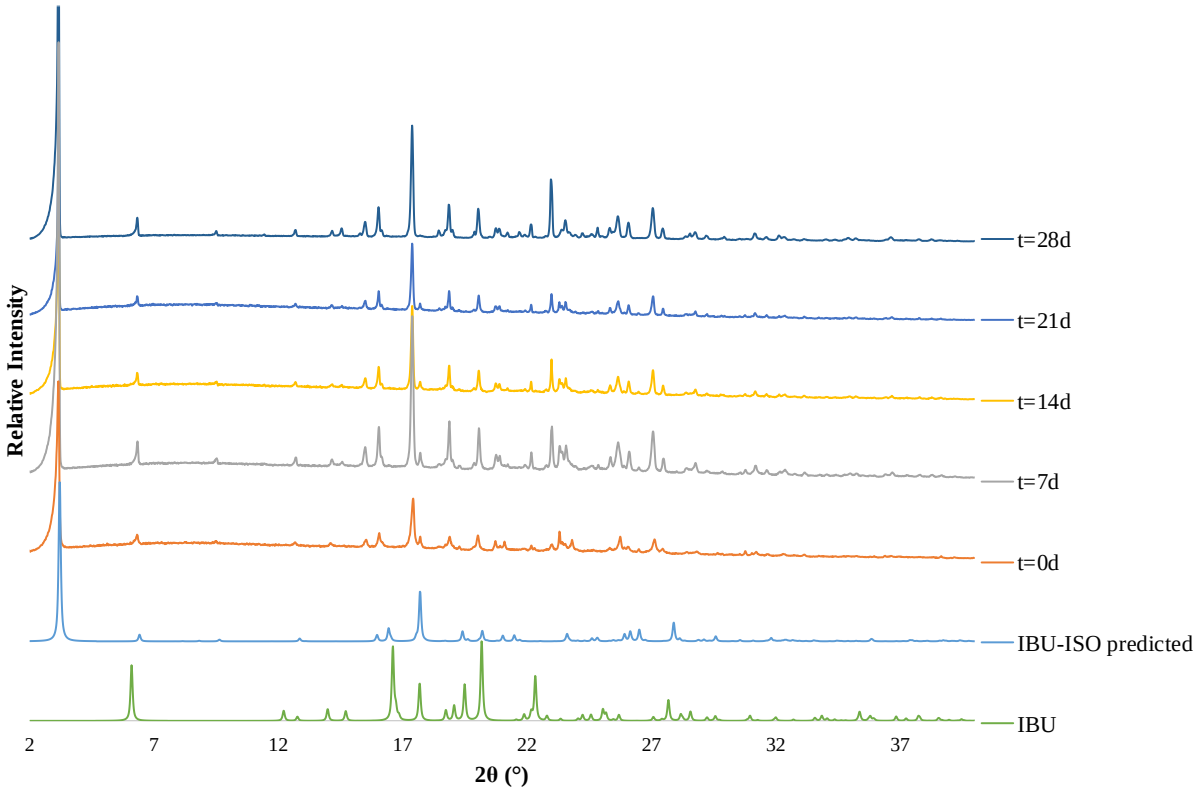

Figure A6.4 – IBU-ISO 1:1 prepared in 60:40 HI *via* LAG for 30 minutes – Thermal studies at 45 °C monitored over 28 days.

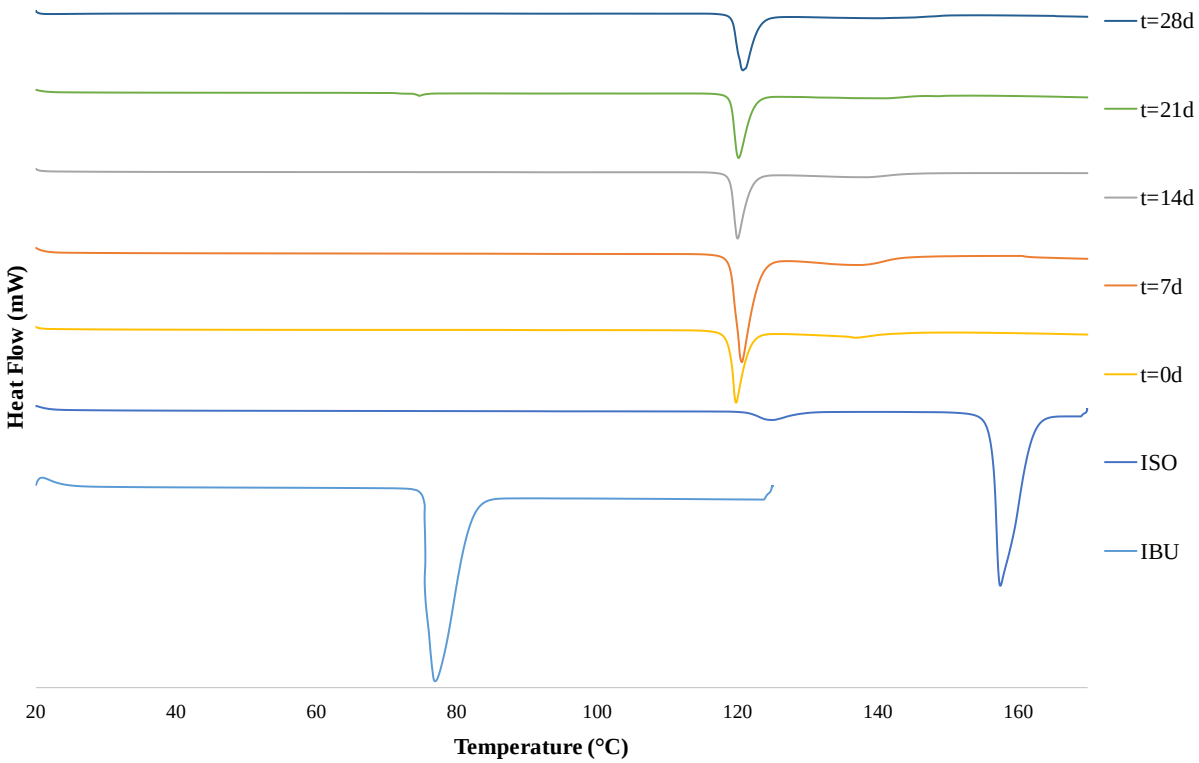

Figure A6.5 – DSC heat profiles for IBU-ISO 1:1 prepared in 60:40 HI *via* LAG for 30 minutes – Thermal studies at 45 °C monitored over 28 days.

6.5 Thermal stability studies of IBU monitored over one month

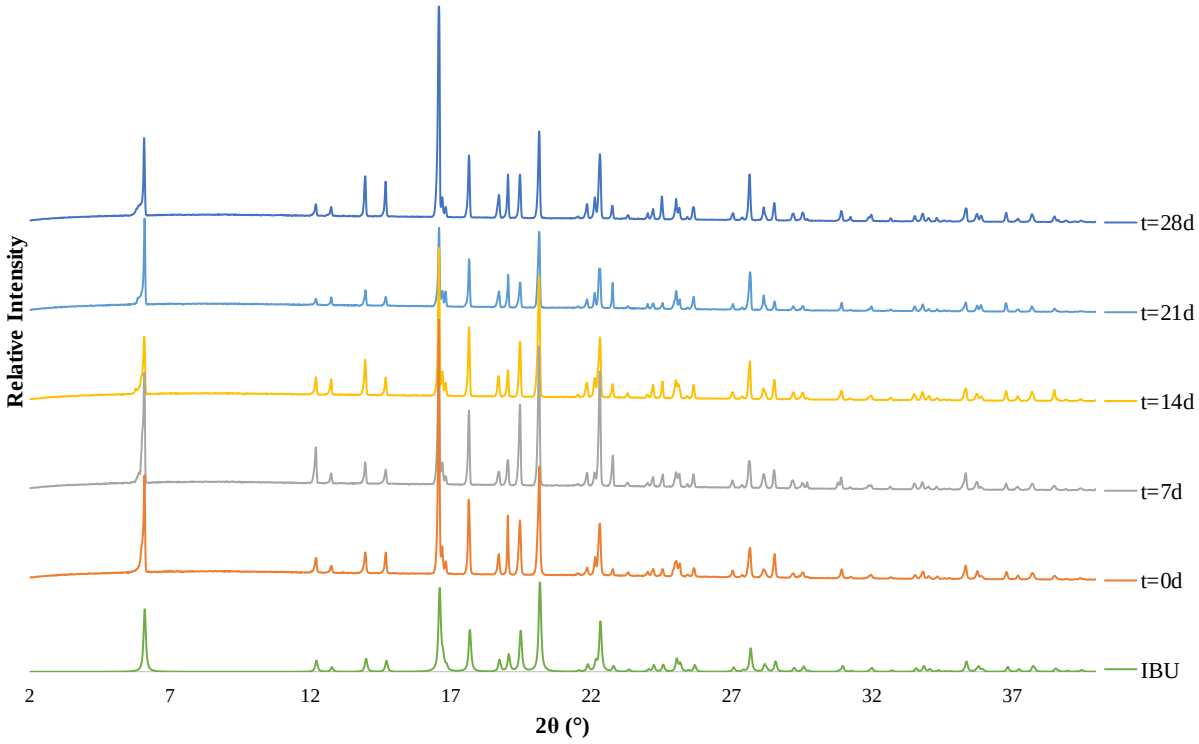

Figure A6.6 – IBU subjected to 60:40 HI LAG for 30 minutes – Thermal studies at 45 °C monitored over 28 days.

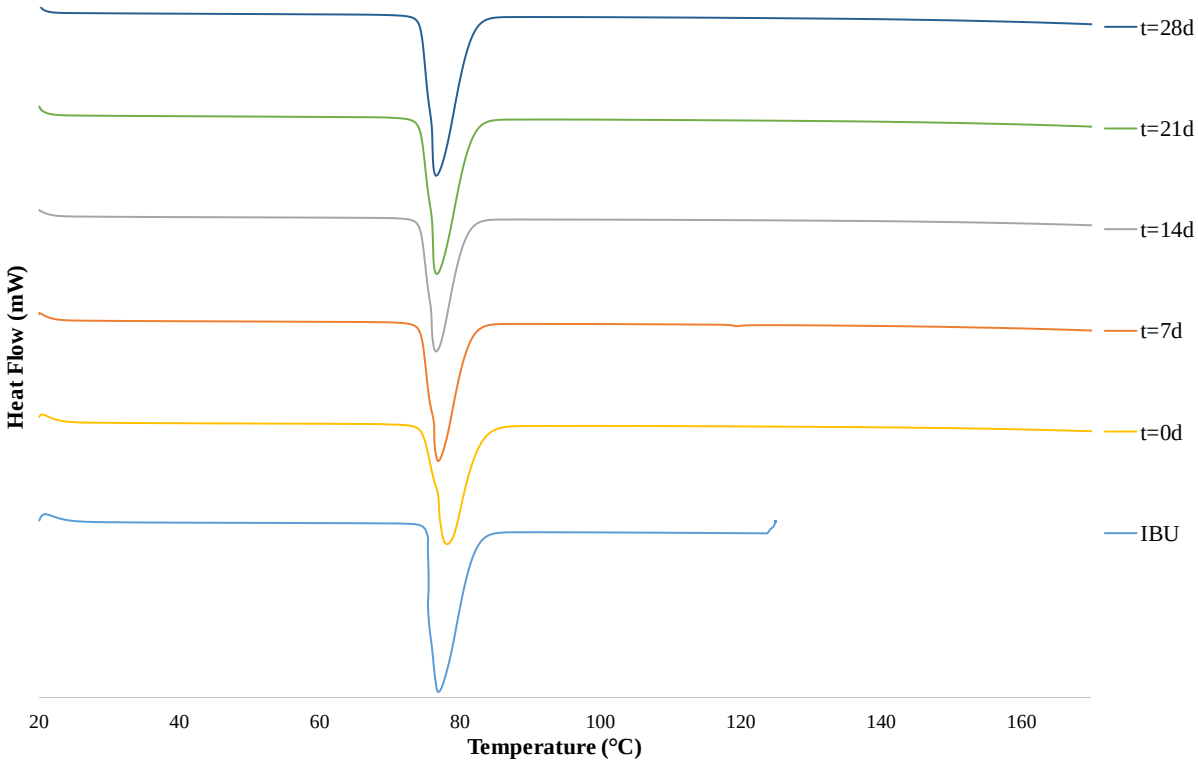

Figure A6.7 – DSC heat profiles for IBU prepared in 60:40 HI *via* LAG for 30 minutes – Thermal studies at 45 °C monitored over 28 days.

6.6 IR Spectroscopy for the OXA-IMID multi-component material

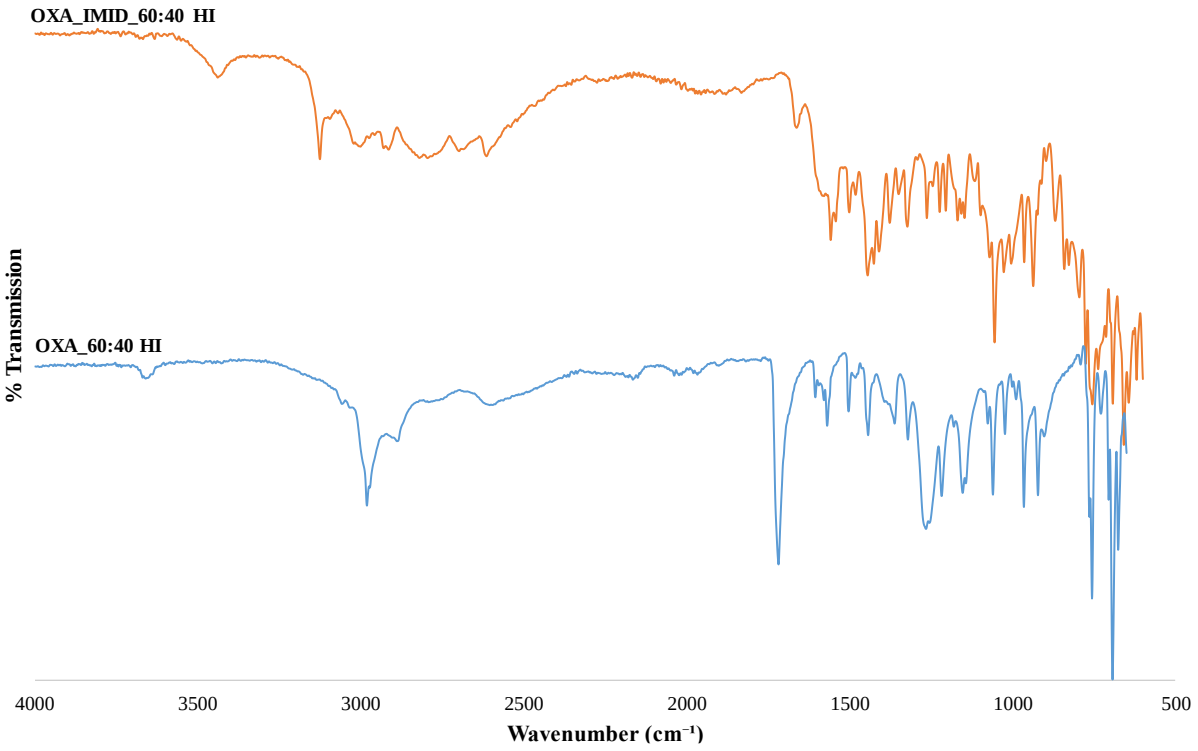

Figure A6.8 – FTIR spectra of OXA-IMID compared to the OXA target.

6.7 Mechanochemical Crystallisations of OXA-IMID

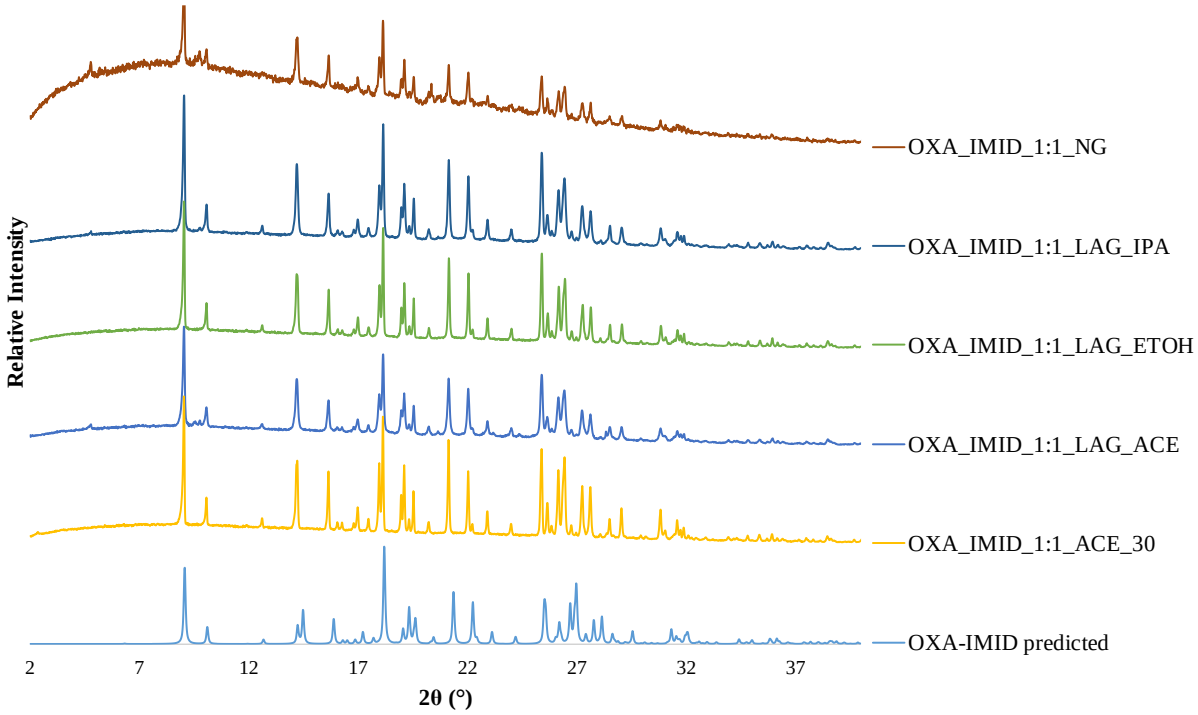

Figure A6.9 – PXRD patterns of the OXA-IMID molecular complex prepared *via* mechanochemical crystallisation both NG and LAG in 3 different solvents, compared to the PXRD pattern of OXA_IMID 1:1 crystallised from evaporation of ACE, as well as the OXA-IMID predicted pattern simulated in Mercury.

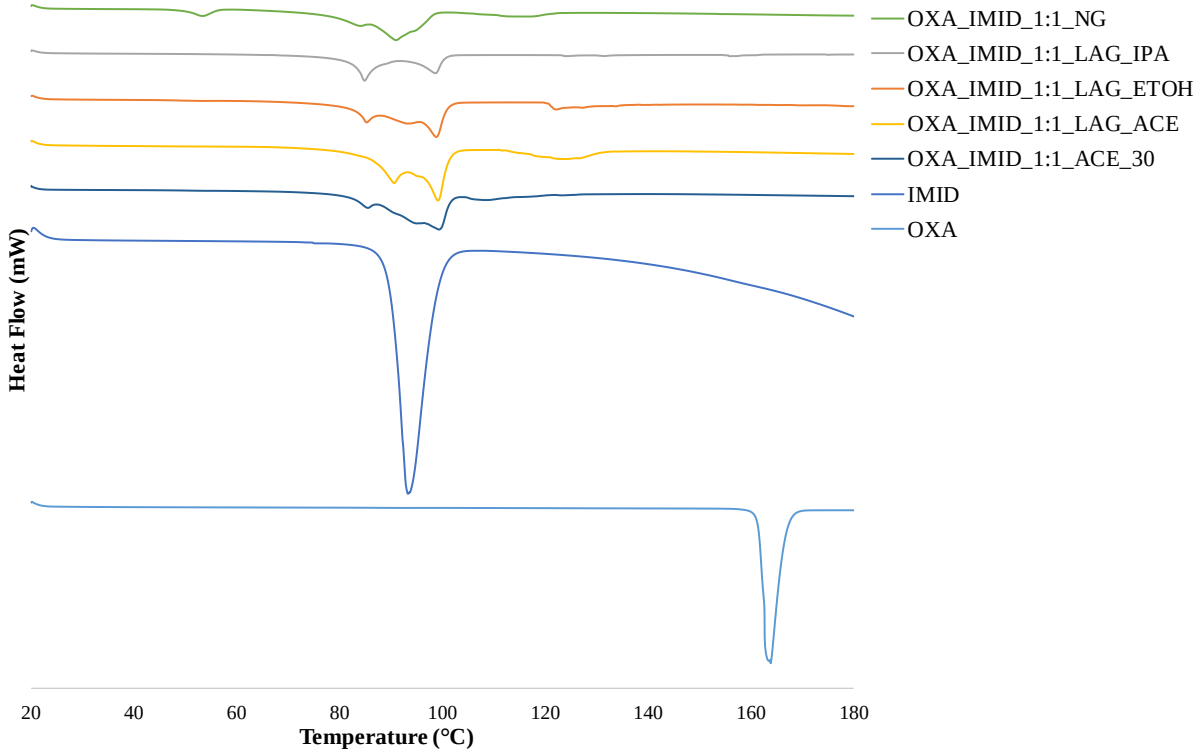

Figure A6.10 – DSC heat profile for the molecular complex of OXA-IMID prepared *via* mechanochemical crystallisation using both NG and LAG in ACE, EtOH and IPA solvent systems compared to the DSC trace of

OXA_IMID 1:1 crystallised from evaporation of ACE at 30 °C, as well as the DSC traces of OXA and IMID starting materials.

6.8 OXA-IMID crystallisations in 60:40 H2O:IPA (HI)

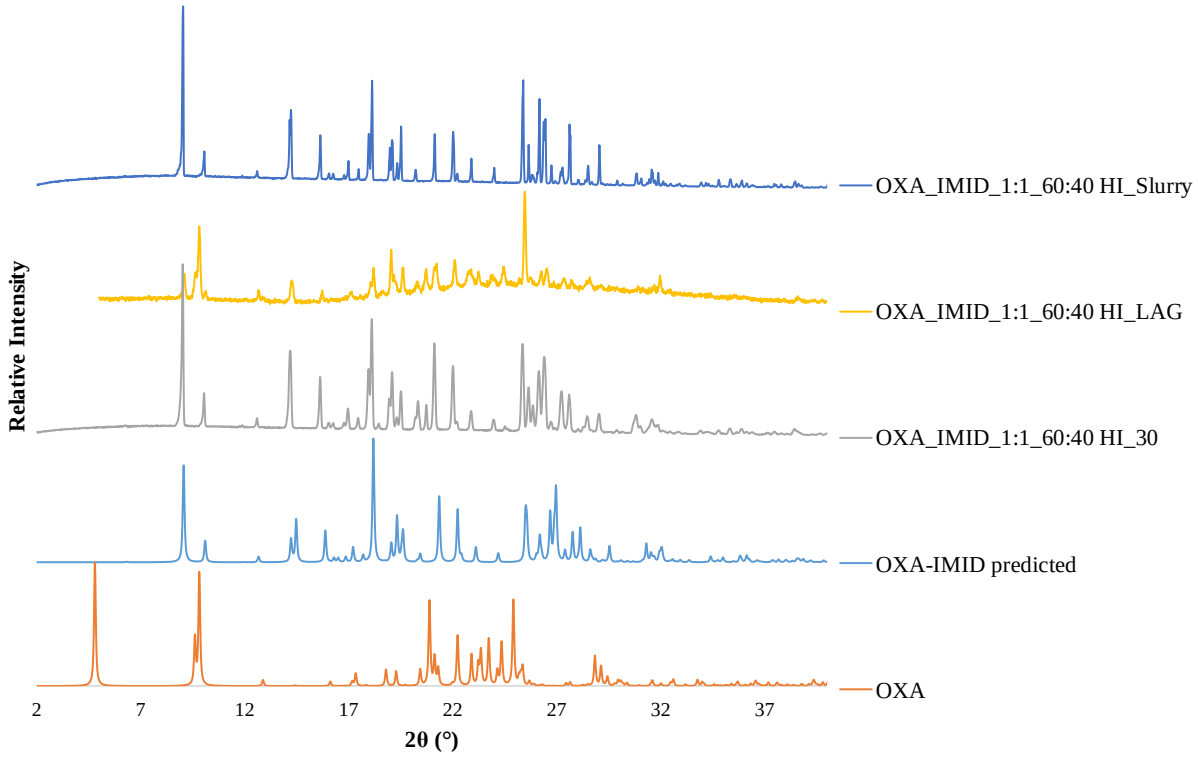

Figure A6.11 – PXRD patterns of the OXA-IMID prepared in 60:40 HI *via* various crystallisation methods: evaporative, LAG, slurrying at 20 °C at 10 mL scale for a slurry time of 24 hours, compared to the PXRD pattern of the OXA-IMID predicted pattern simulated in in Mercury and OXA (Refcode: OJURAO) starting material.

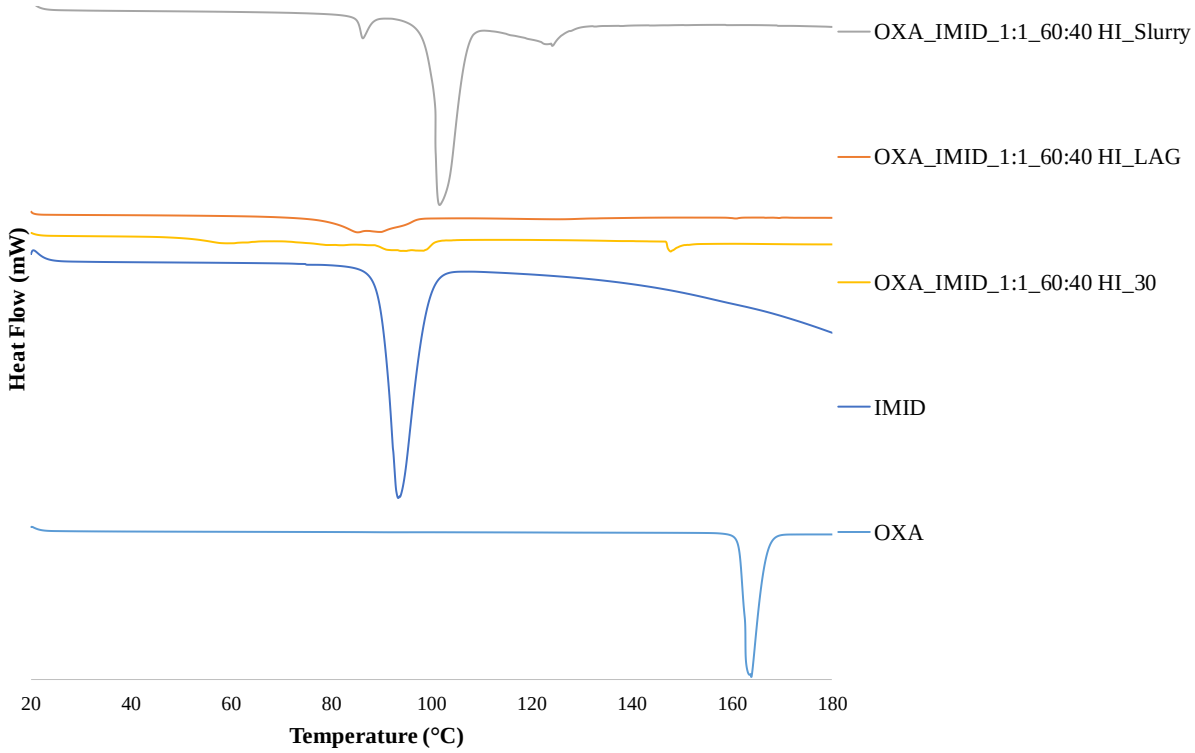

Figure A6.12 – DSC profiles of the OXA-IMID 1:1 molecular complex prepared in 60:40 HI *via* various crystallisation methods: evaporative, LAG, slurrying at 20 °C at 10 mL scale for a slurry time of 24 hours, compared to the DSC trace of pure OXA and pure ISO starting materials.

6.9 Relative Humidity Stability studies of OXA-IMID

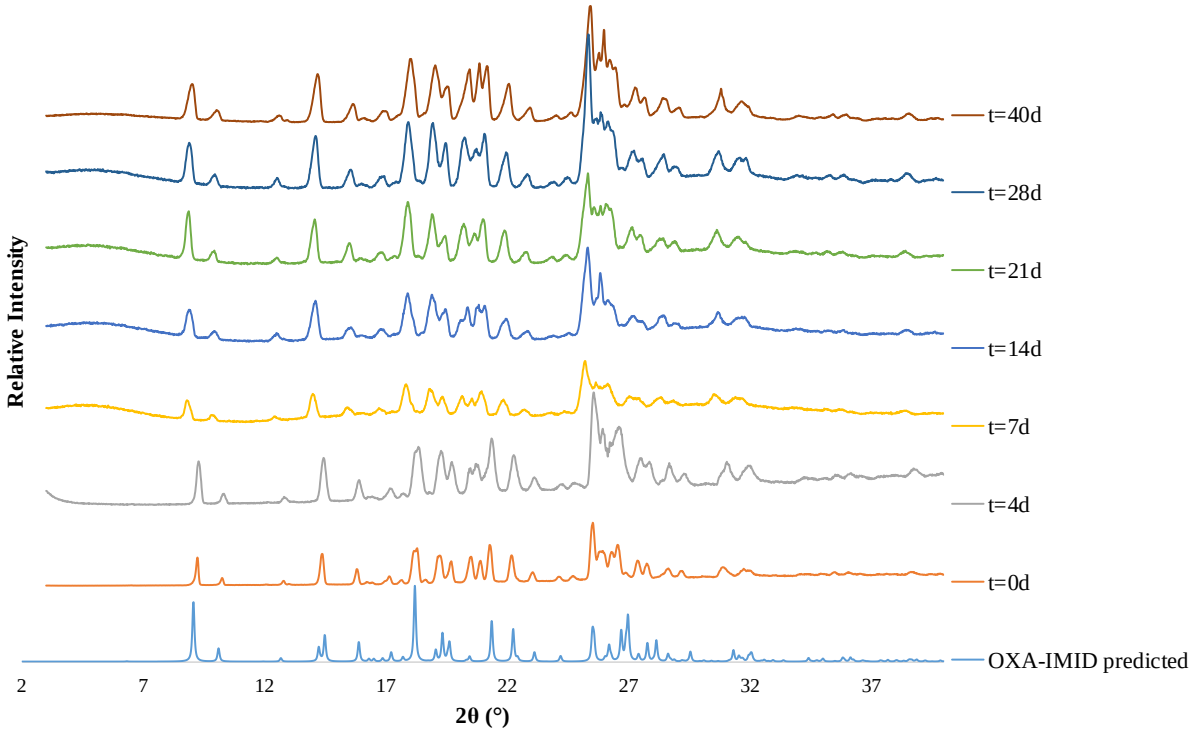

Figure A6.13 – OXA-IMID 1:1 prepared in 60:40 HI *via* LAG for 5 minutes – Humidity studies at 46 % RH monitored over 40 days.

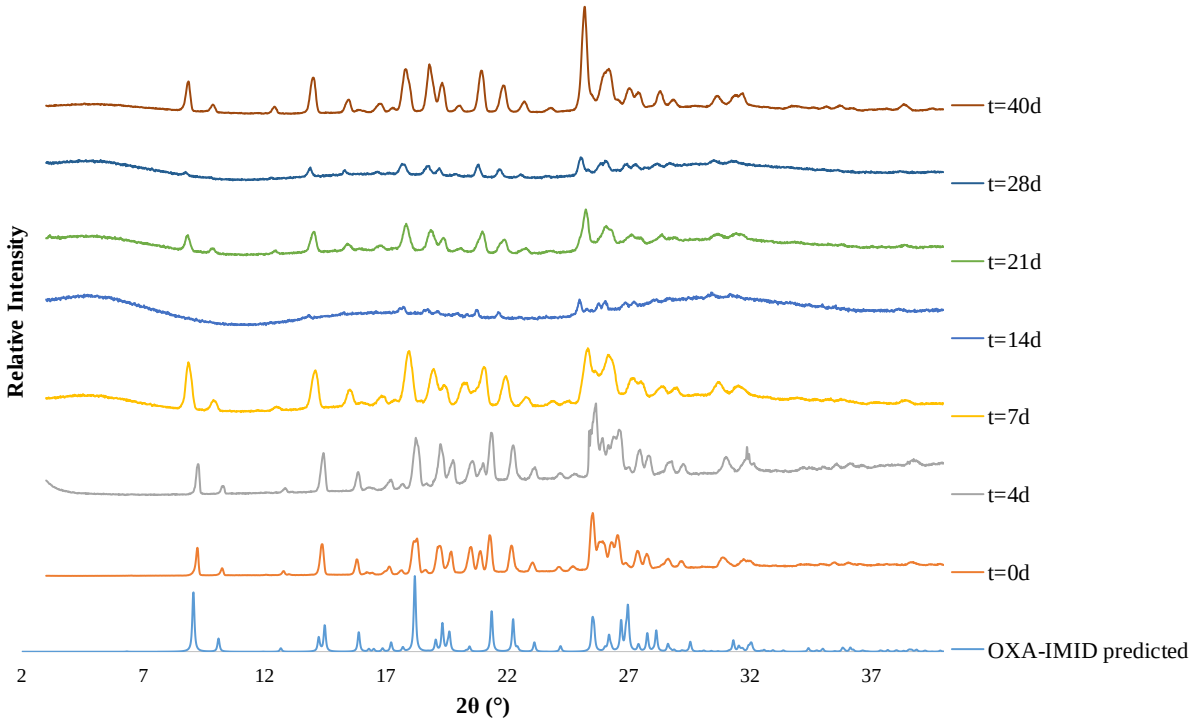

Figure A6.14 – OXA-IMID 1:1 prepared in 60:40 HI *via* LAG for 5 minutes – Humidity studies at 80 % RH monitored over 40 days.

6.10 Cooling Crystallisations of OXA-IMID

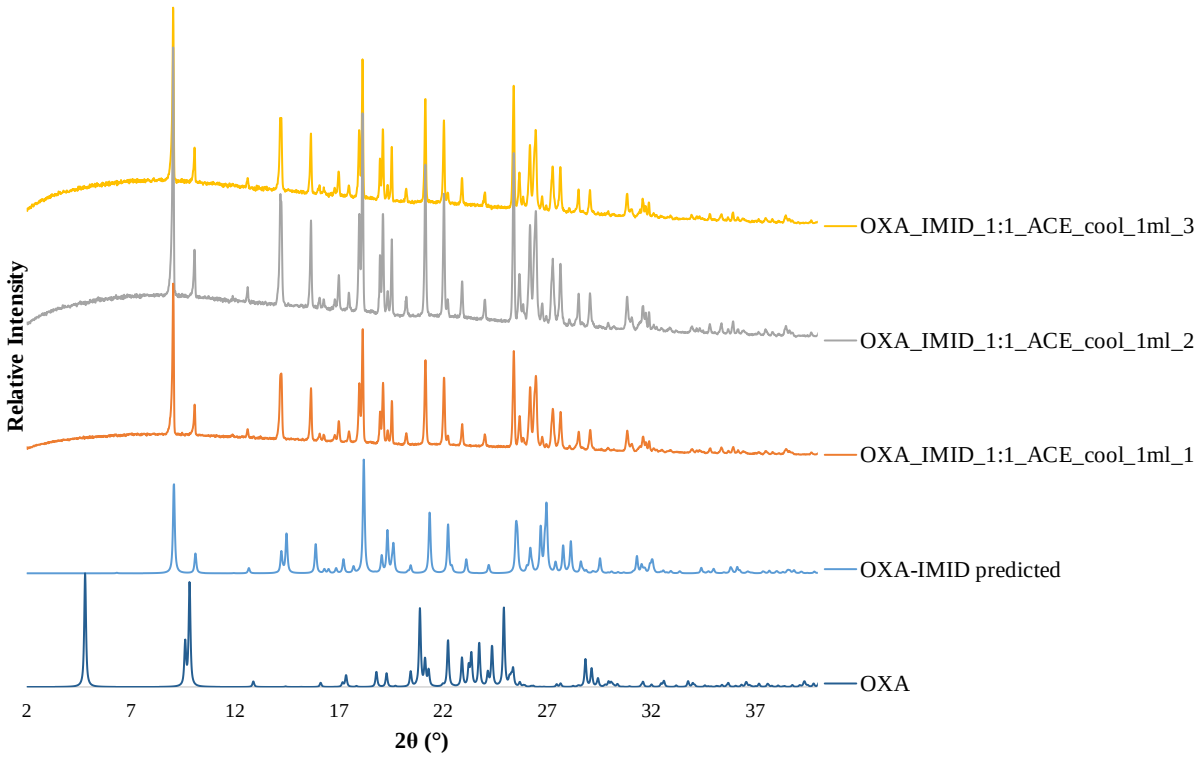

Figure A6.15 – Cooling crystallisations of OXA_IMID 1:1 in ACE at 1 mL scale over a concentration range for samples 1, 2 and 3 performed in the CRD Polar Bear Plus crystalliser.

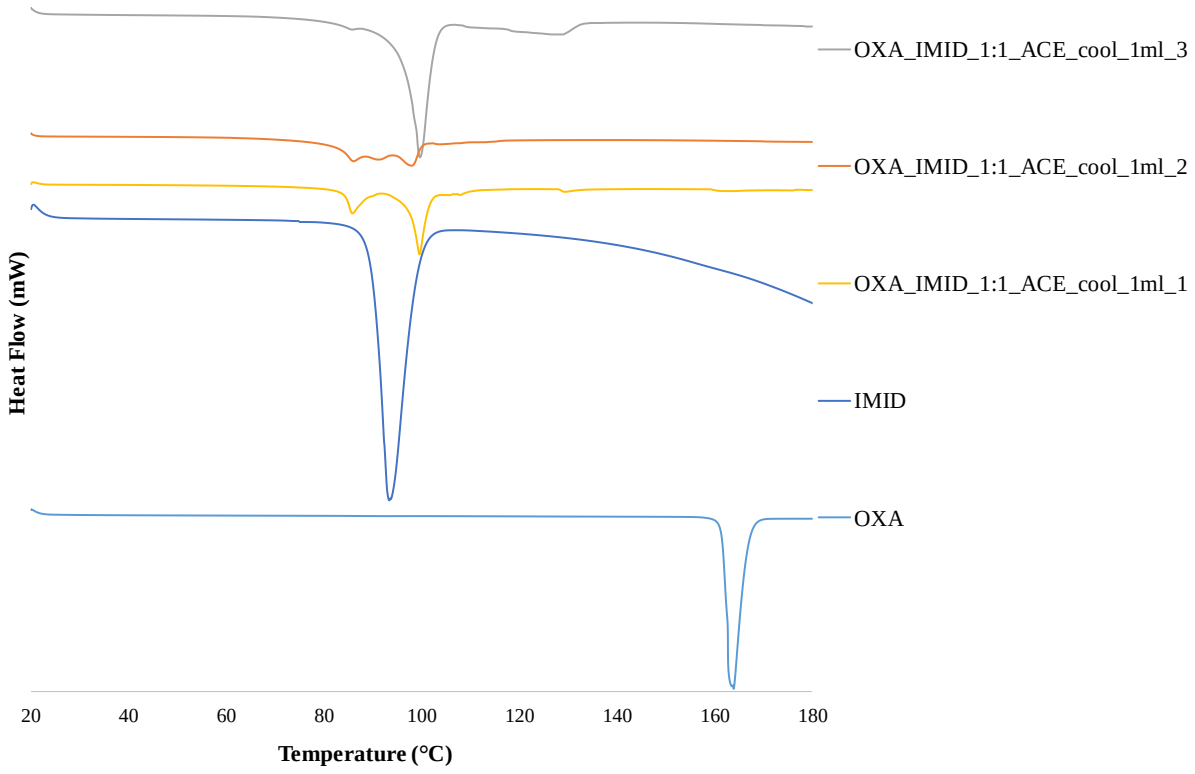

Figure A6.16 – DSC of OXA_IMID 1:1 in ACE at 1 mL scale over a concentration range for samples 1, 2 and 3 performed in the CRD Polar Bear Plus crystalliser *versus* starting material traces of OXA and IMID.